Springer Series in Materials Science 214

R.G. Sharma

Superconductivity

Basics and Applications to Magnets

Springer

Springer Series in Materials Science

Volume 214

The Springer Series in Materials Science covers the complete spectrum of materials physics, including fundamental principles, physical properties, materials theory and design. Recognizing the increasing importance of materials science in future device technologies, the book titles in this series reflect the state-of-the-art in understanding and controlling the structure and properties of all important classes of materials.

More information about this series at http://www.springer.com/series/856

R.G. Sharma

Superconductivity

Basics and Applications to Magnets

Springer

R.G. Sharma
Cryogenics and Applied Superconductivity
Laboratory
Inter-University Accelerator Centre
New Delhi
India

and

Previously at National Physical Laboratory
New Delhi
India

ISSN 0933-033X ISSN 2196-2812 (electronic)
Springer Series in Materials Science
ISBN 978-3-319-13712-4 ISBN 978-3-319-13713-1 (eBook)
DOI 10.1007/978-3-319-13713-1

Library of Congress Control Number: 2014958887

Springer Cham Heidelberg New York Dordrecht London

Printed on acid-free paper

Springer International Publishing AG Switzerland is part of Springer Science+Business Media (www.springer.com)

Dedicated to the readers of this book and the distinguished scientists/professors/engineers engaged in large superconducting magnet application programmes who readily provided inputs for the book in the form of data, important parameters of their large magnet systems and quality pictures.

Preface

Superconductivity has fascinated physicists and engineers for over a century and continues to do so. New superconductors with ever-increasing transition temperatures and in very unconventional systems continue to be discovered. Theorists keep struggling hard to find an acceptable theory of superconductivity in cuprates and many new superconductors discovered recently. Such is the nature of these mysterious materials. Yet, the exploitation of these materials for building magnets producing intense field or magnets of large size for fusion reactors and particle accelerators has been going on at a fast pace. A large workforce of young researchers working in areas of superconductivity has thus grown over the decades. Books have also been published by distinguished professors and scientists at regular intervals on different topics of superconductivity to cater to this growing community.

During the last 40 years of my involvement with superconducting materials and magnets I have, however, always felt the need for a self-sufficient and concise volume which can impart all the background knowledge to young researchers who want to take a plunge into projects on magnet applications. Often, one has to search for different books for different topics. In the present book I have tried to cover most topics on superconductivity beginning from the basic phenomenon to conductor production to magnet development for a variety of applications such as high field production, accelerators, fusion reactors, NMR, MRI, SHGMS and SMES. The contents of the book are largely based on the numerous lectures that I had been delivering to young scholars preparing for their master/doctorate degrees in India and abroad. It was during the period 2002–2009 that I gave a very large number of lectures on superconductivity to the Laurea students at INFN Labratori Nazionali di Legnaro, Padova University, which I visited almost every year on the invitation of Prof. Enzo Palmieri. The material for these lectures had been collected over the years from many books, journals, my own work and lectures from international schools on various topics of superconductivity and magnets.

Since superconductivity is a low temperature phenomenon, for the sake of completeness, I have started with an introduction in Chap. 1, why do we need low temperature, how to produce such low temperatures, how to liquefy gases, and how

ultimately Kamerlingh Onnes succeeded in liquefying helium and discovered the phenomenon of superconductivity. This, I believe, will be entertaining to any beginner.

Chapter 2 is about the phenomenon and the physical properties of this class of materials. Important topics like the Meissner effect, two-fluid model, critical magnetic field, penetration depth, concept of coherence length, energy gap, positive surface energy and flux quantization have been discussed. The chapter ends with the description of dc and ac Josephson effect and the SQUID used for mapping the feeble magnetic field in the human brain. Chapter 3 introduces Abrikosov's concept of negative surface energy leading to strange superconductivity in alloys and compounds called type II superconductors. Only type II superconductors can carry very large current in presence of high magnetic field when suitably doped with defects or impurities.

When the superconductivity community was reeling under the despondency of getting nowhere beyond T_c = 23 K (for Nb_3Ge), Bednorz and Muller discovered superconductivity at T_c = 35 K in 1986–1987 in La_2CuO_4, an insulator, when doped with Sr or Ba. What we witnessed next was unprecedented. Superconductivity was found in curates one after another starting with YBaCuO (T_c = 93 K) to BiSrCaCuO (T_c = 110 K) to TlCaBaCuO (T_c = 125 K) and to HgCaBaCu (T_c = 135 K). The entire saga offered vast opportunities for experimentalists and technocrats but left the theorists completely bewildered. This and much more about the discoveries of superconductivity in MgB_2 (T_c = 39 K) and several iron-based compounds (T_c = 50–60 K) have been discussed in Chap. 4.

Chapter 5 is a brief review of theories of conventional and high T_c cuprates such as Londons' theory, the Ginzberg-Landau theory, the BCS theory, Resonance Valence Bond (RVB) theory and the Spin Fluctuation (SF) theory. No attempt has been made to give rigorous mathematical treatment. Chapter 6 discusses the unprecedented improvement in current-field behaviour of conventional superconductors, Nb–Ti, Nb_3Sn, V_3Ga and Nb_3Al through ingenious techniques. At the end, I report very high J_c in REBCO coated wires which have turned out to be far superior to Nb_3Sn when used below 64 K.

Chapter 7 explains how to build laboratory magnets using Nb–Ti and Nb_3Sn conductors starting from the design concept to winding, impregnation, quench protection to the operation of the magnet. Specific examples for the fabrication of 7 T Nb–Ti magnet, 11 T Nb–Ti/Nb_3Sn magnet and a warm bore 6 T Cryofree magnet have been taken up for discussion. All important high field LTS/HTS magnets generating intense magnetic field peaking at 32 T at NHMFL (FSU) have been discussed. Chapter 8 is on the magnets for accelerators. A short description of all superconducting accelerators built so far, namely Tevatron, HERA, SSC, RHIC and LHC has been given in the chapter. The magnet system of the most powerful collider, LHC, finds prominence. All futuristic dipole designs too have been described. Futuristic International Linear Collider (ILC) has been included in this chapter. Important superconducting cyclotron beginning with K-500, K-1200 and K-2500 cyclotrons have been discussed with special reference to magnet design and specifications.

Chapter 9 is on the magnets for fusion reactors. All superconducting fusion machines, based on tokamak concept, starting with the Soviet (Russian) tokamak T-7, Tore Supra (now WEST), JT-60SA, EAST, KSTAR, SST-1 and finally the largest machine, called ITER have been discussed. Exception has however been made for two machines, viz TFTR at PPPL, Princeton and JET at Culham (UK) which are not superconducting, nevertheless, both had contributed enormously to fusion science leading to the final design of the ITER. Two futuristic fusion machines, W7-X (Wendelstein 7-X) Stellerator and IGNITOR, have also been included. The last Chap. 10 is on magnet applications to systems widely used for analytical and diagnostic purposes like NMR and MRI. Other very promising applications, HGMS and SMES have been described.

One unique feature of the book is that each chapter starts with a background introduction to the application discussed in the chapter so that the reader does not have to search for supporting literature. I hope the researchers will enjoy reading the book A to Z.

New Delhi R.G. Sharma

Acknowledgments

Writing the book on superconductivity my thoughts go to two great personalities, first, late Prof. N.E. Alekseevskii of the Kapitza Institute, Moscow who introduced me to the field of A-15 (Nb_3Sn) superconductors and fabricating high homogeneity laboratory magnets during 1973–1974. Secondly, Prof. Kyoji Tachikawa of the erstwhile NRIM (now NIMS) with whom I enjoyed working on V_3Ga wires using composite process during 1979–1980. Professor Tachikawa has helped me a great deal in writing this book by providing a lot of inputs on Chap. 6 and some rare photographs. My grateful thanks to him.

The inspiration for writing this book came from my two senior colleagues here at IUAC, Girijesh Mehta and Suresh Pancholi, who had published books in their respective fields a few years ago. I greatly benefited from their experience and advice. A large number of professors, scientists and engineers involved in magnet applications in accelerators, fusion research and high field laboratory magnets helped me by providing data, the latest status of their systems and several photographs from their archives as well as from the recent collection. I am completely overwhelmed by their quick response even when they were on holiday tours. They had readily granted copyright permissions. In fact some of them even went through the portion of the manuscript relevant to their project. I would like to mention some names below and express my gratitude to all of them.

Philippe Labrun and Lucio Rossi (LHC, CERN), Kurt Riesselmann and Andre Salles (ILC, Fermi Lab.), Amaud Devred, Sborchia Carlo, Neil Mitchell and Michel Claessens (ITER), Jean-Luc Duchateau, Valerie Lamaison and Christophe Roux (Tore Supra, CEA, Cadarache France), Yeong-Kook and Kwon Myeun (K-Star, NFRI, Korea), Jiangang Lee (EAST, IPP, CAS, China), Y.C. Saxena, Dheeraj Bora, Biswanath Sarker and Subrata Pradhan, (SST-1, IPR, India), Kita MacPherson (TFTR and NSTX, PPPL, Princeton), Kiyoshi Yoshida (JT-60SA, JAEA), Nick Holloway (JET, CCFE, Culham), Thomas Klinger (Wendelstein 7-X, MPI for Plasma Physics, Greifswald), Bruno Coppi and M. Advardsen (IGNITOR, PSFC, MIT, IAEA), Marti Felix and Gelbke Konrad (K-500, K-1200, NSCL, MSU), Hiroki

Okuno (K-2500, RIKEN, SRC, Japan), Dinesh Srivastava, Rakesh Bhandari and Subimal Saha (VECC, Kolkata), R.P. Aloysius (NPL, Delhi), Peter Kes (Kamerlingh Onnes Laboratory Leiden University), Yifei Zhang and Prateek Dokania (SuperPower Inc.), Rainer Kuemmerle (1 GHz NMR, Bruker Biospin), Ernst Wolfgang Strautner (MRI, GE Global Research), Hemut Krauth (Bruker and Vacuumschmelze), Kenichi Sato (Cryo. Supercond. Society of Japan), Chandra Mohan Varma (University of California), Shinji Matsumoto and Takao Takeuchi (NIMS Tsukuba), Alex Braginski (editor-in-chief, ESNF), Hubertus W. Weijers, David Larbalestier and Denis Markkiewicz (NHMFL, FSU), Ramesh Gupta (BNL), Ian Worpole (Sci. American), D. Bruce Montgomery (MIT), Renuka Rajput Ghosal (Jaffersen Lab.), Pierre Manil, A. Milanese and J.F. Millot (CEA/IRFU, France).

I am impressed by the promptness with which all the publishers granted copyright permissions to use material for this book. Help came fast from Elsevier, Springer Publishing, Oxford University Press, Cambridge University Press, Nature Publishing Group, American Physical Society, Institute of Physics (IOP), American Chemical Society (ACS) and American Institute of Physics (AIP). In particular, I thank Guffi Chohdari (OUP), Lucy Evans (IOP), Ashley Bressingham (Springer), Adam Hischberg (Cambridge University Press), Jennifer Jones (Elsevier), Jamie Casey (Associate Publisher) and Susann Brailey (AIP) for their cooperation. Many media/communication centres from several national laboratories in USA also provided high quality pictures for the book. RightsLink too provided wonderful service.

The book has been written at Inter-University Accelerator Centre (IUAC), my workplace since 2001. The Director and the administration of IUAC provided all possible logistic support. I thank them all. The Department of Science and Technology (DST) sponsored this book writing project under its USERS Programme. I thank the DST for the same.

I started my low temperature physics career at National Physical Laboratory 50 years ago in 1964 and retired officially in 2001. I thank Dr. M.S.R. Chari, my Ph.D. Teacher and several friends at NPL (India) who cooperated with me at different times. These include Y. Showry Reddy, Manmohan Krishna, Rajan Babu Saxena, Harikishan and Mubeen A. Ansari and Dipten Bhattacharya. I have also referred to the work of some of my Ph.D. students (Sudip R. Jha, Shriram Shukla, Biswanath Sarkar, Renuka Rajput, Saswati Lahiry, Shyam S. Dubey, Arvind Pandey and Devraj Mishra) on HTS at relevant places in the book. Yogesh C. Saxena, Dipten Bhattacharya, G. Rodrigues and Renuka Rajput also went through a chapter each and made valuable suggestions. I thank them all.

My own colleagues at the centre, Triptishekar Datta, Anup Choudhury, Rajesh Kumar and Pameendra Konduru helped me a lot during the writing of the book in different ways. It has been a pleasure to have interacted with them. In particular, help came rather fast from my friend, Soumen Kar as and when needed. I also thank Murthi Goirik, graphic designer with long experience in publishing, who prepared the illustrations for the book and helped in the preparation of the manuscript.

Above all, I want to thank my wife, Bimlesh and the rest of my family, who supported and encouraged me in spite of all the time it took me away from them. It must have been a long journey for them. I hope one day my grandchildren, Oorja, Tanvi, Tavisha and Olli will enjoy reading this book and realise why I spent so much time in front of my computer.

New Delhi R.G. Sharma

Contents

Chapter 1
Introduction

Abstract The study of matter at very low temperature is fascinating because the phonon activity dies down at very low temperatures and one can look into the electronic behaviour minutely. Cryogenic baths of liquefied gases provide excellent medium to cool down samples. Liquefaction of a gas is a combination of an isothermal compression followed by an adiabatic expansion. Cascade process were adopted in liquefying oxygen by Cailletet and Pictet independently in 1877. The final cooling stage has always been a Joule-Thomsen (J-T) valve. Another important breakthrough came in 1898 when James Dewar succeeded in liquefying hydrogen making a temperature range of 20–14 K accessible. The moment of triumph came in July, 1908 when years of hard work by Kamerlingh Onnes at Leiden ultimately resulted in the liquefaction of helium. A temperature range of 4.2–0.8 K thus became accessible in the laboratory. A cascade process using Lair, LO2, LN2 and LH2 and the J-T expansion valve was employed. Within 3 years of this discovery came the defining moment of the discovery of superconductivity in April, 1911 in pure Hg at just below 4.2 K.

1.1 Why Low Temperature Is So Exciting?

Temperature is one of the most important variable parameter like pressure and magnetic field which can be manipulated to change the phase of the material and thus its mechanical, thermodynamical, chemical, electronic and phonon properties. To carry out studies at low temperatures is particularly interesting. At ambient temperatures lattice vibrations (which are quantized and are called phonons) in any material are dominant and usually mask its fine properties. As the temperature is lowered the amplitude of these vibrations is reduced and at very low temperature (close to absolute zero) die down completely. In other words the dominant phonon contribution almost disappears and one can observe the quantum behaviour of matter. Normal laws valid at ordinary temperatures may not hold any more. Some of the properties in fact violates all our norms about the matter as to how it ought to behave. Superconductivity and Superfluidity are perhaps the most striking

R.G. Sharma, *Superconductivity*, Springer Series in Materials Science 214,
DOI 10.1007/978-3-319-13713-1_1

phenomena observed at low temperature which display the quantum behaviour at a macroscopic scale. An electric current can flow persistently in a superconductor (without dissipation) without a voltage and similarly a superfluid can flow effortlessly (no viscosity) through fine pores, impervious to normal liquid, without a pressure head.

1.2 How to Conduct Experiment at Low Temperatures?

The best way to carry out studies at low temperature is to have a suitable cryogenic bath which can cover the temperature range of interest. A cryogenic bath is best provided by a liquefied gas. One can pump over the liquid surface to reduce vapour pressure and obtain still lower temperature until it freezes. Thus for example, nitrogen (N_2) gas boils at 77 K (Kelvin) and can be pumped down to 65 K, hydrogen (H_2) boils at 20 K and be pumped down to 14 K. Helium (He) is the only stable gas which boils at the lowest temperature, that is, 4.2 K. One can pump liquid helium and can achieve a temperature of 0.8 K. There is a rare isotope of helium with a mass number of 3 called ^{3}He. It boils at a temperature of 3.2 K and can be pumped down to 0.3 K. Most interesting thing about these two liquids is that they refuse to freeze even at zero absolute. Both can be solidified only at very high pressure. For their unique and very peculiar properties they are referred to as Quantum Liquids.

To go to temperature lower than 0.3 K, one can use what we call as ^{3}He/^{4}He dilution refrigerator (DR) and is based upon the finite solubility of ^{3}He (6.4 %) into ^{4}He down to absolute zero. ^{4}He at 1 K is used as a pre-cooling agent. We can use a DR to produce a temperature of a few milli Kelvin (mK). To go to still lower temperatures this DR is used as a pre-cooling stage to an adiabatic nuclear demagnetization system and temperature of a few micro Kelvin (μK) is achieved. By using a cascade of demagnetization stages one can go down to nano Kelvin (nK) and pico Kelvin (pK). A world record of ultra low temperature $\sim$100 pK is held by the Low Temperature Laboratory of the Helsinki University of Technology, Finland. Whenever the scientific community entered a new regime of low temperature, some discovery or the other of very fundamental importance took place.

1.3 Gas Liquefaction

Broadly speaking, a gas liquefaction is a combination of two thermodynamic processes, an isothermal compression followed by an adiabatic expansion. In the first step a gas is compressed at high pressure at constant temperature. This is achieved by removing the heat of compression by a suitable cooling mechanism. In the second stage the compressed gas is allowed to expand under adiabatic conditions wherein heat is neither allowed to enter nor escape from the system.

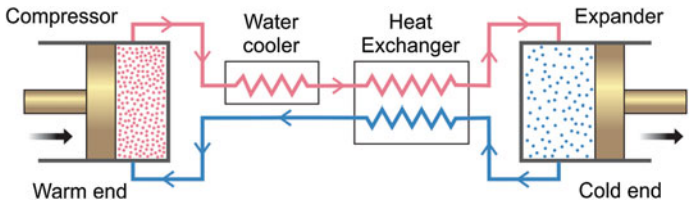

Fig. 1.1 Principle of gas liquefaction

The temperature therefore drops. The process goes on till the gas liquefies. This is schematically shown in Fig. 1.1. The expansion could be of either isenthalpic or isentropic type.

1.3.1 Isenthalpic Process

In isenthalpic expansion one uses an expansion valve or a Joule-Thomson valve through which the high pressure gas throttles and gets cooled. There is no change in the enthalpy (zero heat transfer and zero work transfer) in this expansion process. This process is sometimes also referred to as the internal-work method as it does not remove the energy from the gas. It only moves the molecules apart against the interatomic forces. This process is irreversible and therefore not an efficient thermodynamical cycle. Further, the isenthalpic expansion does not always lower the temperature. If the temperature of the gas is above the maximum inversion temperature, it will heat up the gas. The temperature of the compressed gas before expansion should therefore be below its inversion temperature. It is for this reason that gases like helium (45 K), hydrogen (205 K) and neon (250 K) cannot be liquefied using a J-T valve expansion, their inversion temperatures being below the ambient temperature ($\sim$300 K). These gases have to be pre-cooled to below their inversion temperature before they suffer J-T expansion. A J-T valve is however integral to any liquefier and always forms the last stage of cooling since the liquid formation in the expander cannot be sustained. Table 1.1 lists the maximum inversion temperatures (at $P = 0$) of a few permanent gases. The gases therefore have to be pre-cooled to below their respective inversion temperature before entering the J-T valve.

1.3.2 Isentropic Process

In the isentropic process the energy is extracted as external work and always produces cold in contrast to the isenthalpic process. This is also referred to as the external work method. Gas expands in an expander which can be of reciprocating engine type or can be a turbine. The process is reversible and thus

Table 1.1 Maximum inversion temperature of some gases

S. no.	Gas	Max. inversion temperature (K)
1	^{4}Helium	45
2	Hydrogen	205
3	Neon	250
4	Air	603
5	Nitrogen	621
6	Oxygen	761
7	Argon	794
8	Carbon dioxide	1,500

thermodynamically more efficient. With the same initial temperature of the gas this process always leads to lower temperature than obtainable with the isenthalpic process. As stated above, the operational problem associated with the expansion of the two phase mixture (liquid and gas) in an expander makes it mandatory to use a J-T expander as the last stage of the cooling cycle.

1.3.3 The Linde-Hampson Process

Oxygen was first time liquefied by Louis Cailletet of France and Raoul Pictet of Switzerland independently within days of each other in the year 1877. Pictet used a cascade process wherein a precooling stage is cooled by another precooling stage. He used liquid SO_2 and then dry ice (−80 °C, solid CO_2) for precooling. Cailletet used liquid SO_2 for precooling oxygen before it throttles through a J-T valve. A good historical account of the liquefaction processes can be found in "Cryogenic Engineering" [1]. Carl von Linde [2] and Hampson [3] perfected the oxygen liquefaction technology by using more reliable ammonia cycle for precooling compressed oxygen and the counter current heat exchangers before the gas expands through a J-T valve. Linde founded Linde Eismaschinen AG in 1879 and later obtained a German Patent in 1895. Basic principle in this process is that air/oxygen is alternatively compressed, pre-cooled and expanded in a J-T valve This results each time in reducing the temperature till the gas gets liquefied. The pressure used in Linde process is rather high. For example, for air at 300 K the optimized pressure is about 40 MPa (∼5,880 psi) but the actual machines use a pressure of about 20 MPa. A typical Linde-Hampson cycle is shown in Fig. 1.2.

1.3.4 The Claude Process

Claude Process [4] is an isentropic process which is adiabatic and thermodynamically reversible and therefore more efficient than the isenthalpic process to produce cold.

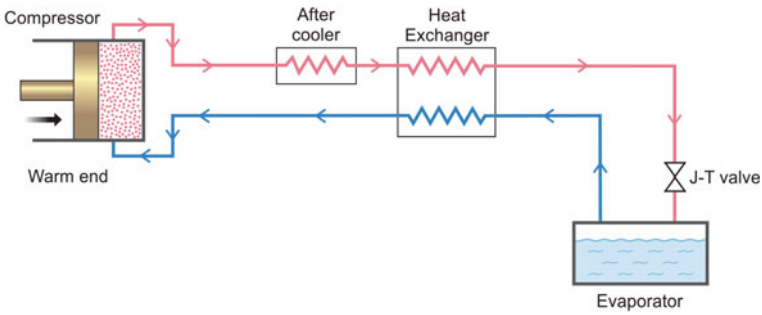

Fig. 1.2 Linde-Hampson liquefaction cycle consisting of a compressor, a counter current heat exchanger and a J-T valve at the final stage

Another added advantage is the lower operating pressure needed for this cycle ~1.7 MPa (~250 psi). In this process the gas does an external work in an expansion engine. The engine can either be of reciprocating piston type or of a rotating type. As shown in Fig. 1.3 the gas is compressed to the required pressure and passes through the first heat exchanger. A portion of the gas (60–80 %) is then sent to an expander and the rest continues to move along the main stream path. The expanded low pressure cold gas is fed back to the returning gas just after the second heat exchange. The return gas cools down the high pressure incoming gas via the two heat exchangers. Thus the cold high pressure gas proceeds via the third heat exchanger and expands in a J-T expander and gets liquefied. The cold vapours from the liquid reservoir return to the compressor via the heat exchangers giving out cold to the incoming high pressure gas. A J-T expansion valve is still necessary because liquid formation in the cylinder of the expansion engine is not desirable. The stresses caused by the low compressibility of the liquid can damage the cylinder. Rotary turbine expander can, however, tolerate almost 15 wt% liquid without causing damage to the turbine.

Two great inventions which took place in the history of gas liquefaction need to be mentioned here. First in 1892 when James Dewar developed a double walled vacuum-insulated cryogenic-fluid storage vessel (popularly known as Dewar Flask). This made it possible to store, transport or pour cryogenic-fluid from one vessel to another. Experiments with cryogenic-fluids for long duration became possible. Second invention [5, 6] by Dewar was the first time liquefaction of hydrogen in 1898, lowering the temperature range for studies to 20 K and to 14 K under reduced pressure. Dewar used the Linde cycle (that is, high pressure and J-T expansion) with liquid nitrogen as the pre-cooling stage.

A masterpiece treatise on the liquefaction cycles has been written by Randall F. Barron [7]. Readers are advised to consult this book for greater details on gas liquefaction and most of the cryogenics topics.

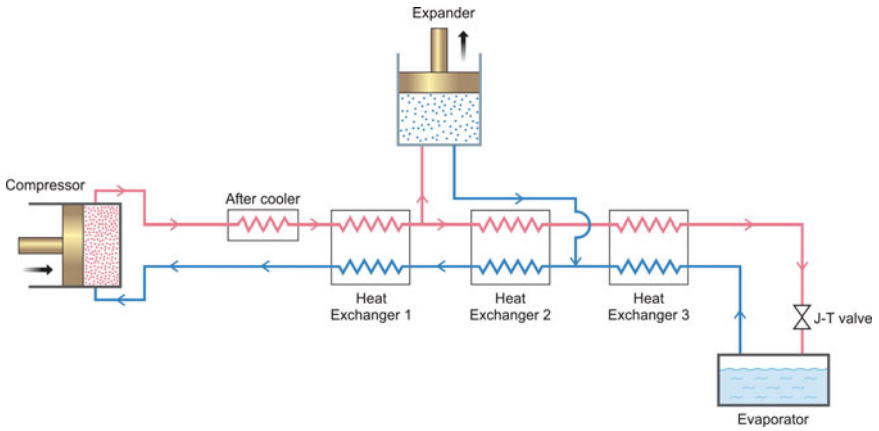

Fig. 1.3 The Claude cycle consisting of a compressor, a series of heat exchangers, an expansion engine and a J-T valve in the final stage

1.3.5 Liquefaction of Helium (1908)

Heike Kamerlingh Onnes at Leiden Institute, The Netherlands had great fascination for the study of Van der Waals equation of corresponding states down to lowest ever temperatures. Nernest heat theorem and Planck's zero point energy theory further added to his curiosity to achieve lowest possible temperature. His passion to liquefy helium became all the more stronger. He made use of the Linde technique, that is, pre-cooling compressed helium to the freezing point of hydrogen (14 K) and subjecting it to J-T expansion. He succeeded in liquefying helium on July 10, 1908. This turned out to be a turning point for the entire condensed matter physics community. This opened the flood gate for getting to lower and lower temperatures. Discoveries one after another followed in quick succession. The first one was, of course the discovery of superconductivity in 1911 by Kamerlingh Onnes himself. Kamerlingh Onnes got Noble Prize in 1913 for this work. The Noble Prize citation dated Dec. 10, 1913 states "*For his investigations on the properties of matter at low temperature which led inter alia, to the production of liquid helium*". Figure 1.4 shows the schematic diagram of the apparatus used by him for helium liquefaction [8].

As seen in Fig. 1.4, compressed helium gas flows through the liquid air cooled charcoal dewar to get rid of moisture, gets cooled through a spiral immersed in pumped hydrogen (15 K) and expands in the inner most dewar through a J-T expansion valve and gets liquefied. Kamerlingh Onnes with his original liquefier is seen in Fig. 1.5. The boiling temperature of helium is 4.2 K at atmospheric pressure. For the next 20 years the Leiden Laboratory remained a most sought after place for research by the condensed matter physics community from Europe and USA and Kamerlingh Onnes enjoyed complete monopoly.

John Cunningham Mclinnan built the second helium liquefier at the Toronto University in 1923. The design of this machine was borrowed from Kamerlingh

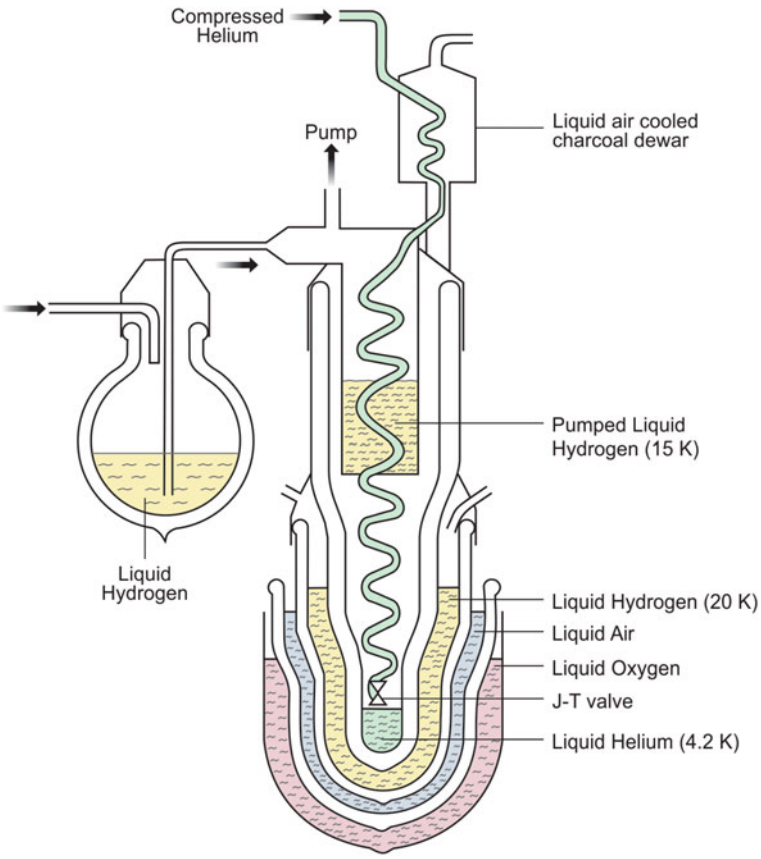

Fig. 1.4 A schematic diagram of the apparatus used by Kamerlingh Onnes for the liquefaction of helium first time (*Courtesy* Peter Kes, Kamerlingh Onnes Laboratorium, Leiden University)

Onnes but looked little more elegant. In reality low temperature research started flourishing around 1934–35. Four German scientists, namely, Franz Simon, Heinrich Kuhn, Nicolas Kurti and Kurt Mendelssohn joined Clarendon Laboratory at Oxford University at the invitation of Lindemann. Low temperature research started at Oxford when Simon built a mini He-liquefier. Around the same time Pjotr Kapitza too built a He-liquefier [9] at the Cambridge University. This machine was based upon a rotating expansion engine or the so called 'turbine'. He made a similar liquefier at the Institute for Physical Problems, Moscow during 1935. The commercial machine [10] built by Samuel Collins (MIT) and marketed by M/S Arthur D Little of the USA was the beginning of the spread of low temperature studies using liquid helium the world over. Many countries around the globe bought this machine and the low temperature research now flourished all around. My earlier place National Physical Laboratory, Delhi too acquired Collin's helium liquefier in 1952 and started low temperature under the leadership of David Shoenberg.

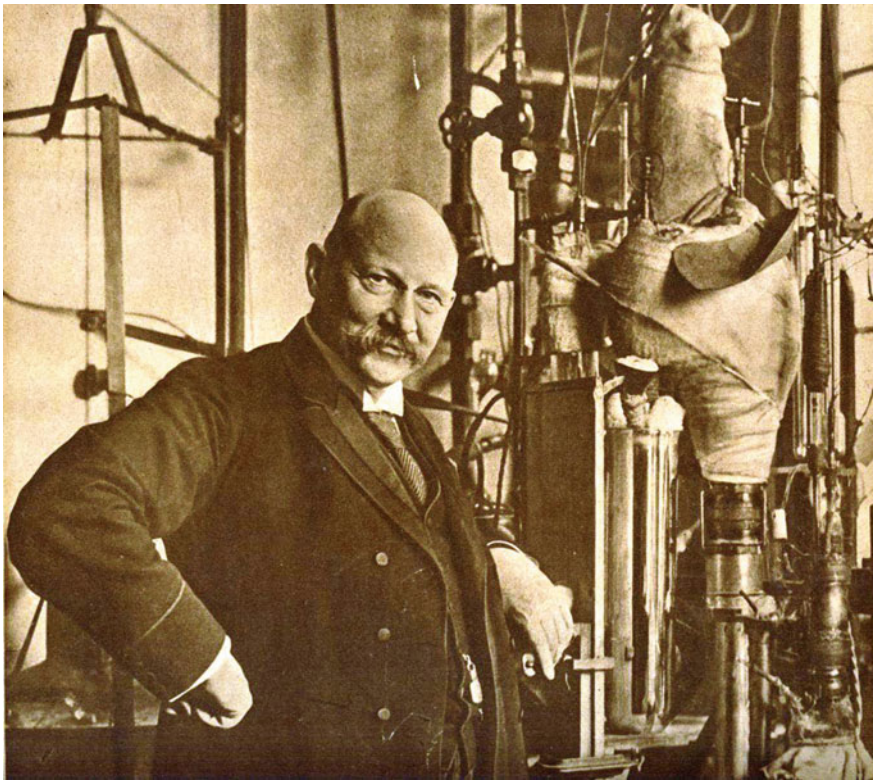

Fig. 1.5 Kamerlingh Onnes in his Low Temperature Laboratory (*Courtesy* Peter Kes, Kamerlingh Onnes Laboratorium, Leiden University)

1.3.6 Collins Liquefaction Cycle

The liquefaction cycle used by Collins and shown in Fig. 1.6 is an extension of the Claude cycle (Fig. 1.3). The machine uses three stages of cooling for helium liquefaction, two expansion engines of the reciprocating piston type followed by the J-T expansion valve. Pure helium gas is compressed to about 225 psi pressure, precooled to 77 K and passes through the first heat exchanger. Thereafter, part of this cold gas expands in the first expander cooling the gas further to about 60 K. This low pressure gas goes back to the compressor via the second and first heat exchangers cooling in-turn the incoming high pressure gas. Rest of the gas continue to proceed through yet another (third) heat exchanger and again a fraction of the gas expands in the second expander bringing down the temperature of the gas to about 20 K. This temperature is well below the inversion temperature of helium gas. Low pressure gas again returns to the compressor via the series of the heat exchangers transferring its cold to the incoming high pressure gas. The cold gas now at 6 K

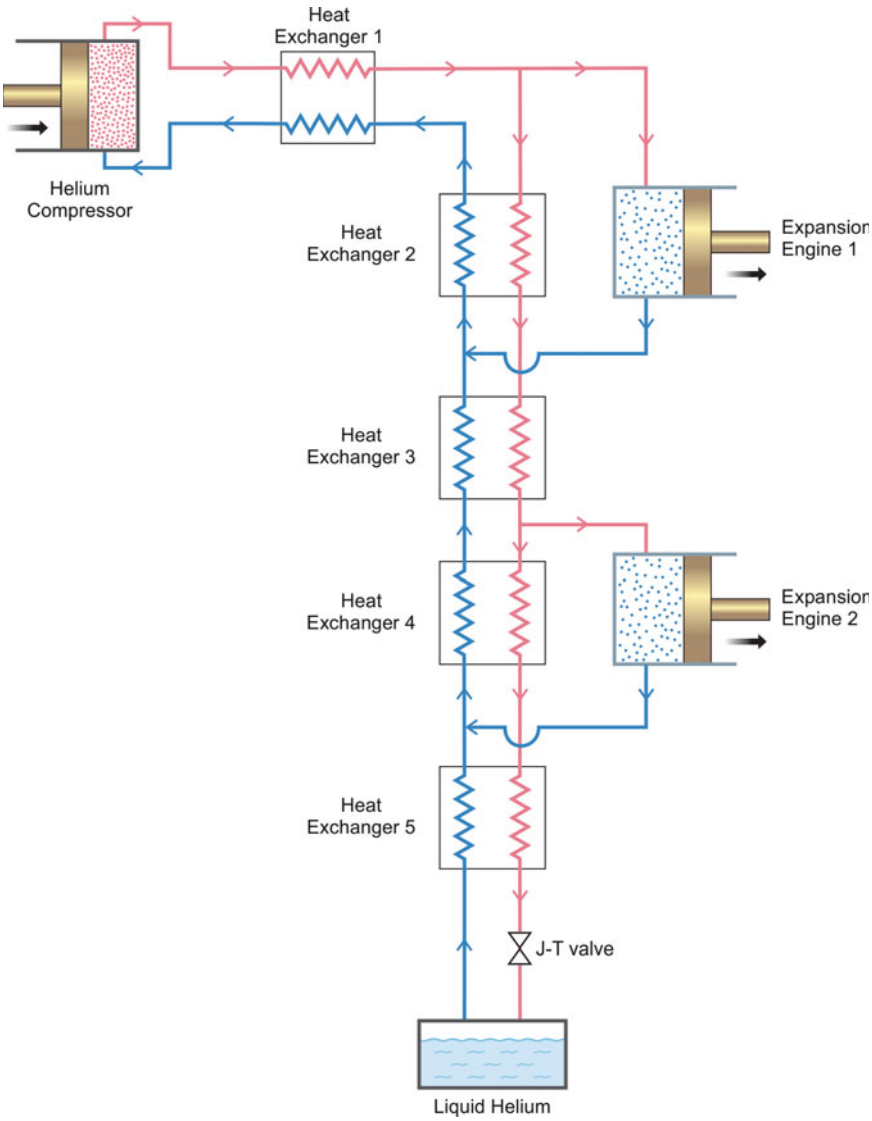

Fig. 1.6 The flow diagram of the Collins helium liquefaction cycle

finally throttles through the J-T valve, liquefies and gets collected in the vessel. The liquid helium can be siphoned out of the container for use. The evaporated gas from this container continues to travel to the compressor via the heat exchangers for a continuous operation.

Precooling helium gas with liquid nitrogen though not essential, nevertheless increases the yield of liquid helium, by almost a factor of two. Figure 1.7 is the photograph of this first generation Collins liquefier of the ADL make. This machine

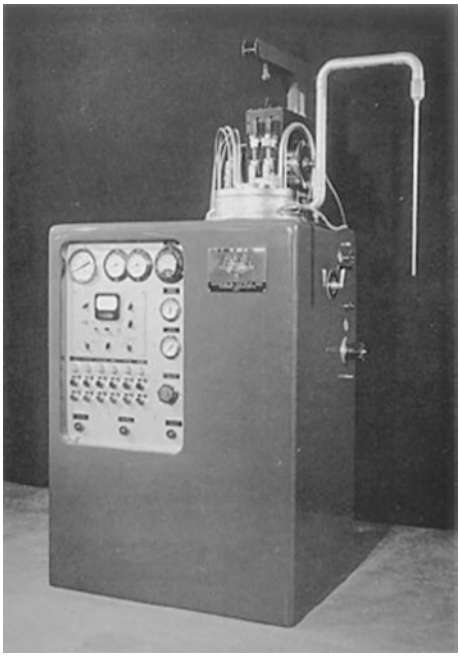

Fig. 1.7 First generation commercial Collin's helium liquefier ADL make with 4 l/h LHe capacity

used to produce 4 l/h liquid with a single compressor. In recent years reciprocating engines have been replaced by the turbo-expanders which rotate at speeds varying between 250,000 and 300,000 rpm. These machines can produce several hundred litres of liquid helium per hour. Figure 1.8 is a photograph of a modern turbo-cooled helium liquefier custom manufactured and installed by Linde Kryotechnik AG with a refrigeration capacity of 900 W (∼300 l/h) at our Centre, IUAC in 2012.

1.4 Discovery of Superconductivity—A Fall Out of Helium Liquefaction

The liquefaction of helium gas in 1908, and just discussed above, was the culmination of a well designed programme of Kamerlingh Onnes of studying properties of materials at lower and lower temperatures achieved by the successive liquefaction of permanent gases, viz; oxygen, air, hydrogen and finally helium. Till this time, there were only conjectures that the electrical resistance of metals will drop to zero as the temperature approached absolute zero or will show a minimum and rise again and so on. Kamerlingh carried out electrical resistivity measurements on pure platinum and gold and found that the resistivity attains a temperature independent constant value below about 10 K. Purer the material smaller is the value of this residual resistivity. He then took up pure mercury for his studies as it was possible to obtain mercury in ultra-pure form through multiple distillations. What he found

Fig. 1.8 A modern day turbine based helium liquefier with a refrigeration capacity of 900 W (∼300 l/h) manufactured by Linde Kryotechnik AG installed at IUAC in 2012 (*Photo courtesy* IUAC Delhi)

was quite startling and unexpected. The resistance in mercury just close to 4.2 K 'abruptly' dropped to zero (one thousand-millionth part of the normal temperature value) with no potential difference. He thus proclaimed that mercury just below 4.2 K has entered a new state which he named 'suprageleider' and when translated from Dutch to English became 'superaconductivity' and finally changed to superconductivity [11]. His original resistance versus temperature plot for mercury is shown in Fig. 1.9. Lead and Tin were next metals from the periodic table to have shown superconductive transition at 7.2 and 3.7 K respectively.

Kamerlingh Onnes also realized soon that this zero potential difference lasts only up to a threshold current in the sample beyond which it rises sharply. Lead, for example, stood superconducting up to a threshold current density of 4.2 A/ mm^2 only.

He also observed that superconductivity stays in lead up to a threshold magnetic field of 600 Gauss without a sign of magneto-resistance. Beyond this field, the resistance appears and rises fast with magnetic field. Notwithstanding these limitations, Kamerlingh Onnes did realize that superconducting coils can be used to produce fields in excess of 10,000 Gauss without Joule heating. His dream did come true and it is all for us to see the great revolution these materials have brought about. How this phenomenon unfolded, understood, different classes of superconductors

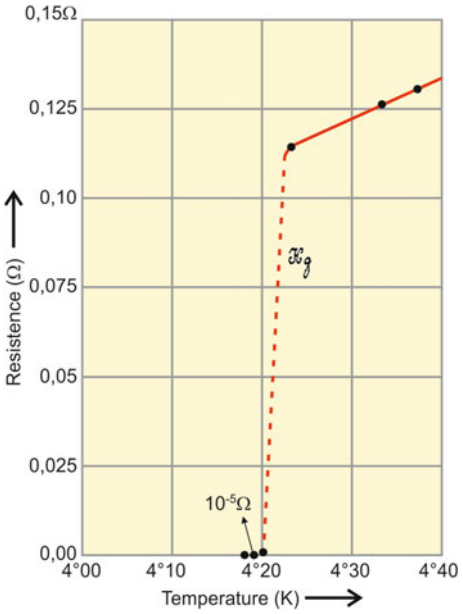

Fig. 1.9 First observation of superconductivity in pure Mercury by Kamerlingh Onnes (*Courtesy* Peter Kes, Kamerlingh Onnes Laboratorium, Leiden University)

discovered and put to use in producing high magnetic fields, in accelerators, in fusion reactors and such other applications (NMR, MRI, SMES, levitation etc.) is discussed in the following chapters.

References

1. K. Timmerhause, R.P. Reed (eds.), *Cryogenic Engineering, Fifty Years of Progress*. International Cryogenics Monograph Series, Chapter 1 (Springer, New York, 2007)
2. C. Linde, G. Claude, *Liquid Air, Oxygen, and Nitrogen*, trans. by H.E.P. Cotrell (J & A Churchill, London, 1913), p. 75
3. W. Hampson, and G. Claude, *Liquid Air, Oxygen, and Nitrogen*, trans. by H.E.P. Cotrell (J & A Churchill, London, 1913), p. 88
4. G. Claude, C.R. Acad. Sci. Paris. **134**, 1568 (1902)
5. J. Dewar, Preliminary Notes on Liquefaction of Hydrogen and Helium. In: *Proceedings of Chemical Society* No. 158, 12 May 1898
6. J. Dewar, *Collected Papers of Sir James Dewar*, ed. by L. Dewar (Cambridge University Press, Cambridge, 1927), p. 678
7. R.F. Barron, *Cryogenic Systems*, Chapter 3, (Oxford University Press, 1985), pp. 60–150
8. H. Kamerlingh Onnes, Comm. Leiden No. 1206 (1911), Noble Prize Lecture, 11 Dec 1913, http-nobleprize.org/noble_prizes/physics/laureate/1913/ones-lecture-pdf
9. P. Kapitza, *Russian J. Phys.* (English transl.) **1**, 7, (1939)
10. S.C. Collins, Rev. Sci. Instrum. **18**, 157 (1947)
11. H.K. Kamerlingh Onnes, Commun. Phys. Lab. Univ. Leiden, **29**, (1911)

Chapter 2
The Phenomenon of Superconductivity

Abstract A superconductor is not only a perfect conductor ($\rho = 0$) but also a perfect diamagnet ($B = 0$) below T_c. Meissner and Ochsenfeld discovered in 1933 that the magnetic field is expelled out of the body of the superconductor. Field penetrates the material only a small distance, called London's penetration depth, λ which is of the order of 30–60 nm in metal superconductors. The transition to superconducting phase has been found to be of the second order as confirmed by the absence of a latent heat and by the appearance of a peak in the specific heat at T_c. These materials also exhibit flux quantization in so far as the field entering a superconducting ring or a cylinder has to be an integral multiple of a flux quantum $\Phi_0 = h/2\pi$ ($= 2 \times 10^{-15}$ T m^2). The strong evidence of the role of phonons in the occurrence of superconductivity came from the isotope effect which shows that T_c is inversely proportional to the square root of the atomic mass. Pippard introduced the concept of long range coherence among the super electrons and defined a characteristic length, the coherence length ξ over which the order parameter changes in a superconductor. This parameter is of the order of 1,000 nm much larger than the parameter λ for these metal superconductors. Optical experiments strongly hinted at the existence of an energy gap in the energy spectrum of these materials. All these experimental facts led the three physicists, Bardeen, Cooper and Schrieffer, to formulate the first successful microscopic theory, the BCS theory of superconductivity. The chapter ends with a short discussion on dc and ac Josephson effect. The design of SQUID, an ultra low magnetic field/voltage measuring device, based upon the Josephson junction behavior, has also been discussed. A large number of SQUIDs are mounted on a helmet shaped cryostat and used for mapping feeble magnetic field inside the brain. This technique is called "magneto-encephalography".

R.G. Sharma, *Superconductivity*, Springer Series in Materials Science 214,
DOI 10.1007/978-3-319-13713-1_2

2.1 Electrical Resistance Behaviour at Low Temperature: Electrical Conduction in Metals

Conduction in materials is a wonderful gift of nature. All materials conduct but the conductivity can vary from one extreme to another. Pure metals like silver, copper and gold, for example, are the best conductors of electricity. The electrical conductivity in semiconductors, on the other hand, is several orders of magnitude smaller and other materials do not conduct at all and are perfect insulators. An indication to what extent the conductivity (or the resistivity) varies as one moves away from metals to semiconductors to ionic solids, glasses and finally insulators, can be seen from Fig. 2.1. It can vary by about 25 orders of magnitude. According to Drude hypothesis conduction electrons in a metal wander randomly in the background of positively charged ions rigidly fixed to their (ordered) lattice positions. These ions vibrate at quantized frequencies limited to a maximum frequency called the Debye frequency. In the absence of an electrical potential electrons do get scattered by these ions but randomly, such that they do not drift in a particular direction. So, there is no current flow. In the presence of an electric potential electrons still get scattered by the ions but now they drift in a particular direction which is opposite to that of the applied potential. A net current thus flows through the conductor. When electrons are scattered by ions they lose energy which is absorbed by the lattice in the form of heat, called dissipation. Thus in a sense, electrons face resistance in their free movement when scattered by the lattice ions vibrating at quantized frequencies, called phonons. In what follows, we will refer to this mechanism as electron-phonon interaction. Figure 2.2 shows schematically the electron motion in a lattice under these two different situations. If impurities are present in the lattice, they too will scatter electrons and will add an additional term to the resistivity. What is surprising is that the electrical resistance of most materials is governed by a simple law, the Ohms Law ($V = I \times R$) and strangely enough this relationship is found valid over a large resistance range of the order of 10^{24}.

Temperature variation of resistance in metals has been the next most exciting problem researchers aimed at after the liquefaction of helium. Since the dominant component of resistivity comes from the scattering of electrons by phonons (lattice vibrations) and the amplitude of lattice oscillations being strongly temperature dependent, such studies yield information on the nature of electron-phonon interaction. Around ambient temperature resistivity usually show a linear variation with temperature. The behaviour may become quite different at low temperature. In metals well below Debye temperature ($T \ll \theta_D$) the resistance varies as $\sim T^5$. What will happen to resistance just a few K above the absolute zero had been a curiosity of the physicists all along. In fact, this curiosity has been a motivation for getting to lower and lower temperatures. Before Kamerlingh Onnes succeeded in liquefying helium there were different conjectures as to what will happen to resistivity at absolute zero. As shown in Fig. 2.3 James Dewar had predicted the resistivity to

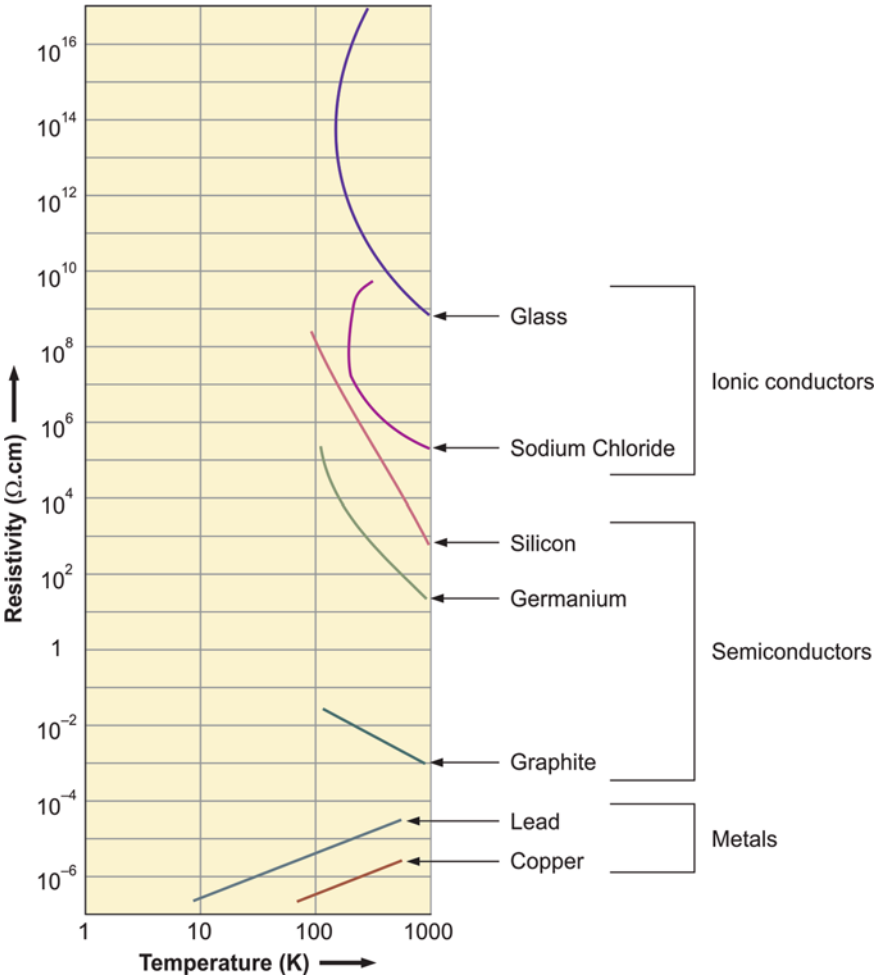

Fig. 2.1 Electrical resistivity in different class of materials varying as it does from very low value for metal to extremely high values for insulators, semiconductors lie some where in the middle

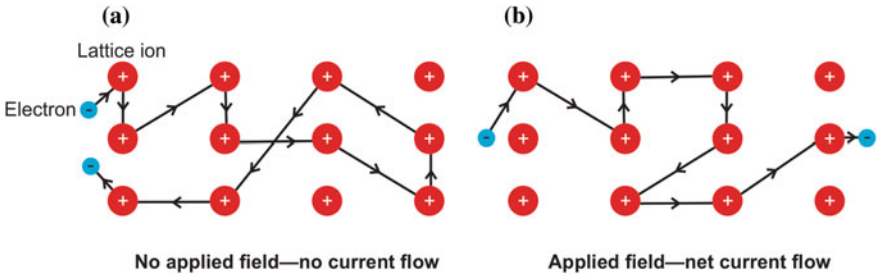

Fig. 2.2 Free electron motion in a lattice of a metal. **a** In the absence of an electric field. **b** In the presence of an electric field

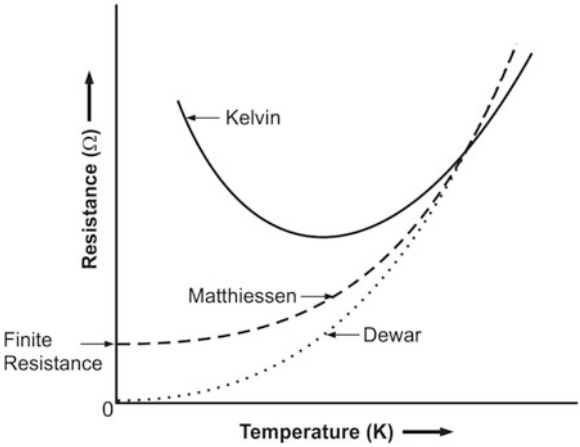

Fig. 2.3 Three different predictions about the possible resistivity-temperature behaviour in metals as one approaches zero absolute

become zero as the temperature approaches zero K because the phonon scattering too should die down. Kelvin believed that the resistivity should decrease to a minimum and rise again at still lower temperature as the electron motion will freeze. Matthiessen's prediction that resistance will saturate at a finite value close to absolute zero turned out to be the most accurate one.

According to Matthiessen's Rule the resistivity at low temperature consists of two dominant components, viz; ρ_0, the residual resistivity which is temperature independent and is caused by the scattering of electrons by impurities and imperfections and another $\rho_{i,}$ the intrinsic resistivity caused by the scattering of electrons by phonons and is strictly temperature dependent.

$$\rho = \rho_0 + \rho_i \tag{2.1}$$

The intrinsic resistivity ρ_i always decreases with the fall of temperature. Dewar, after liquefying hydrogen, measured the resistivity of pure silver and gold down to 16 K but always found it to be saturating to a finite value (Fig. 2.4). He believed that there is always an impurity. This was precisely the reason that Kamerlingh Onnes chose to study resistivity of mercury which can be obtained in ultra high purity form by multiple-distillation process. What he observed in mercury at 4.2 K became a history and is the subject matter of the book.

2.2 The Phenomenon of Superconductivity

As discussed in Chap. 1 superconductivity was discovered by Kamerlingh Onnes [1] in mercury in 1911 at 4.2 K. The temperature at which superconductivity occurs is called the 'transition temperature' or the 'critical temperature', T_c. Kamerlingh

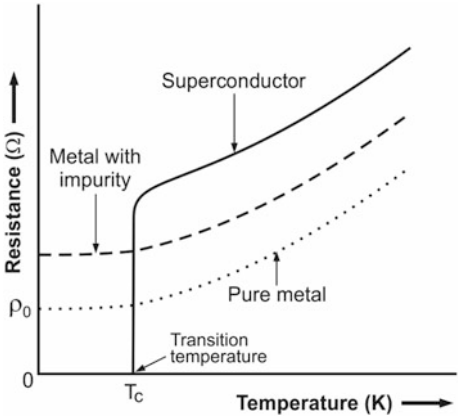

Fig. 2.4 Electrical resistance behavior at low temperature (close to 0 K) of pure metals and a superconductor. Impurity in a metal raises the residual component of the resistance, ρ_0

Onnes also concluded that the purity of mercury was not of consequence and superconductivity was an intrinsic property of mercury. Soon, he found superconductivity in Sn at 3.7 K and in Pb at 7.2 K. Intense research continued for discovering more and more superconductors across the periodic table. There was no rule to govern which particular element should become superconductor and which should not. Characteristic parameters like melting point and crystal structure did not show a particular trend for the occurrence of superconductivity. The position of the superconducting elements in the periodical table has been marked with their transition temperature (T_c), the critical field (B_c), the penetration depth (λ) and the coherence length (ζ) values in Table 2.1. The critical field parameter (B_c) will be introduced and discussed in next section. As seen from the table, the T_c of these elements varies from as low a value as 0.0003 K for Rh to a maximum of 9.3 K for Nb. In addition, there are elements which are superconducting only under high pressure [2]. These are shown as shaded in the Table 2.1. Pressure at which they become superconducting has been indicated in kbar unit. One striking feature of the periodical table, however, is the absence of superconductivity in the best known electrical conductors, namely copper, silver and gold.

2.3 The Critical Magnetic Field

Soon after the discovery of superconductivity Kamerlingh Onnes realized the importance of these materials for winding magnets to produce high fields without dissipation but to his dismay he found in early 1913 that superconductivity gets destroyed when exposed to small magnetic field. Each superconductor was found to have a characteristic value of this field, called B_c, the critical magnetic field. B_c is maximum at $T = 0$ K and continuously decreases with the increase of temperature and becomes zero at T_c. It is shown in Fig. 2.5 that the material at point P in the superconducting state can be driven to normal state by either increasing the

Table 2.1 Elements in the periodic Table showing superconductivity, with their T_c, B_c, λ and ξ values. (Parameter values compiled from my lecture notes, large number of publications and [2]). (Copyright Wiley-VCH Verlag GmbH & Co. KGaA. Reproduced with permission)

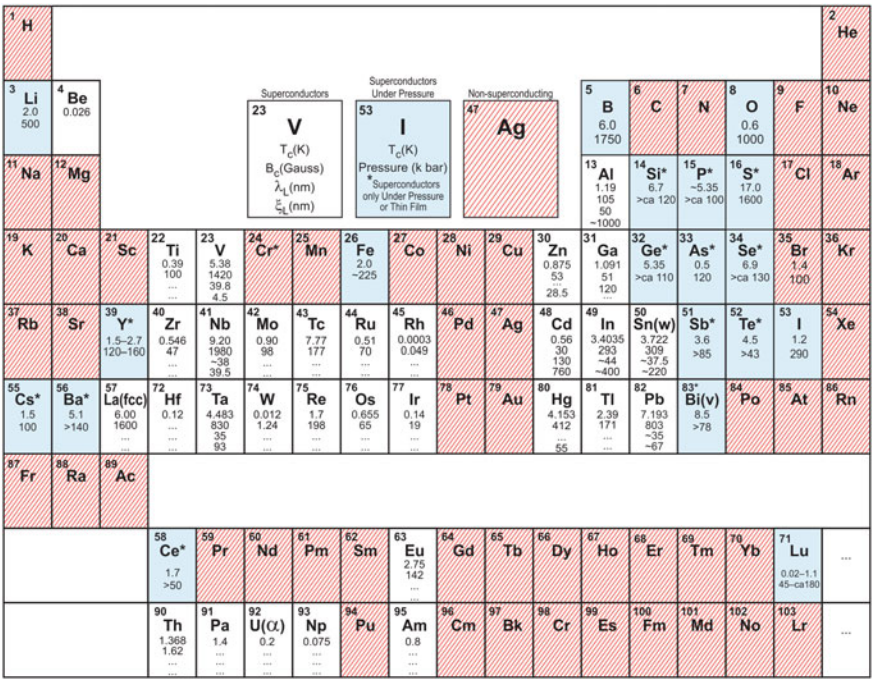

Shaded elements show superconductivity at high pressure only, T_c(K) and pressure values (kbar) are mentioned. Elements with* turn superconducting under high pressure or in thin film form only.

temperature or the magnetic field and taking it outside the parabolic curve. Unfortunately, the value of B_c for most of the elemental superconductors is very low, of the order of few hundred Gauss. B_c of Nb metal happens to be maximum $\sim$1980 Gauss. Values of the B_c for most superconductors are shown in the periodic Table 2.1. The variation of B_c with temperature is parabolic and can be expressed by the expression (2.2).

$$B_c = B_0\left\{1 - (T/T_c)^2\right\} \tag{2.2}$$

B_c is maximum (= B_0) at $T = 0$ and drops to zero at the T_c. The transition to normal state in magnetic field can be very sharp depending upon the purity and perfection of the material. Transition also depends strongly upon the direction of the applied magnetic field. Transition is sharp if the field is parallel to the axis of the cylindrical sample. Transition starts at $B_c/2$ if the field is perpendicular to the axis. Figure 2.6 shows the plots of B_c versus temperature for a number of metal superconductors.

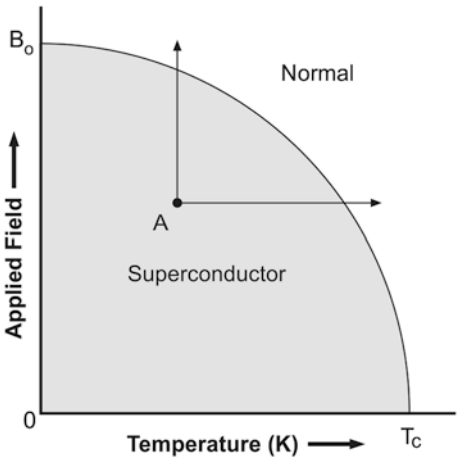

Fig. 2.5 The parabolic *B–T* curve represents the boundary between the superconducting state and the normal state

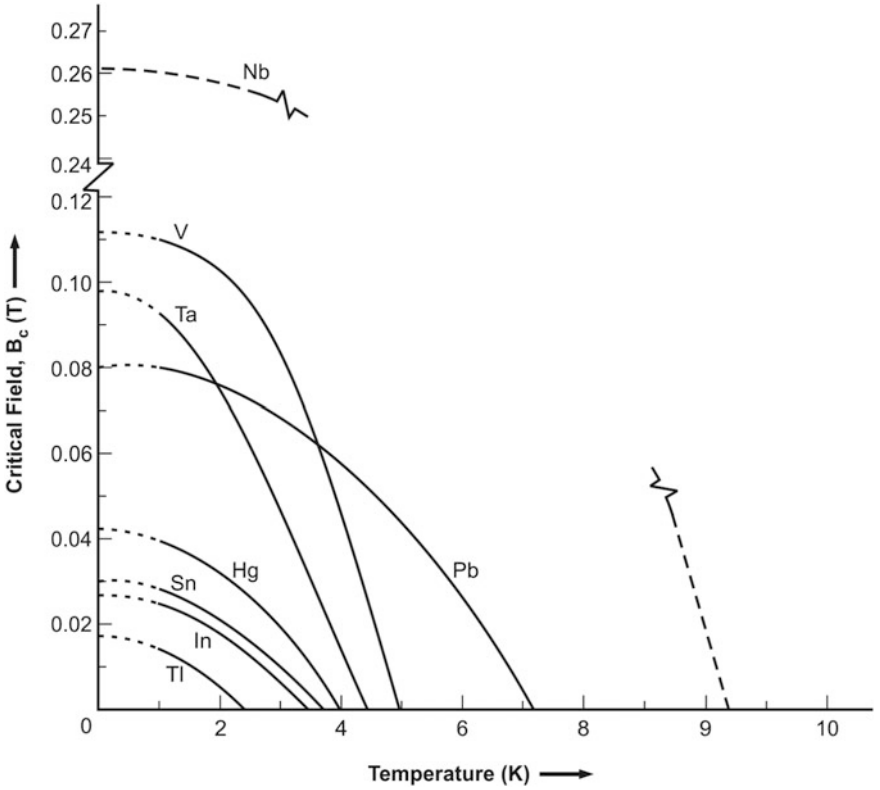

Fig. 2.6 The B_c versus temperature plots of some of the metallic superconductors. (Data from 'Superconductivity' by Shoenberg, 1952, p. 224. (Reproduced with the permission of Cambridge Uni. Press))

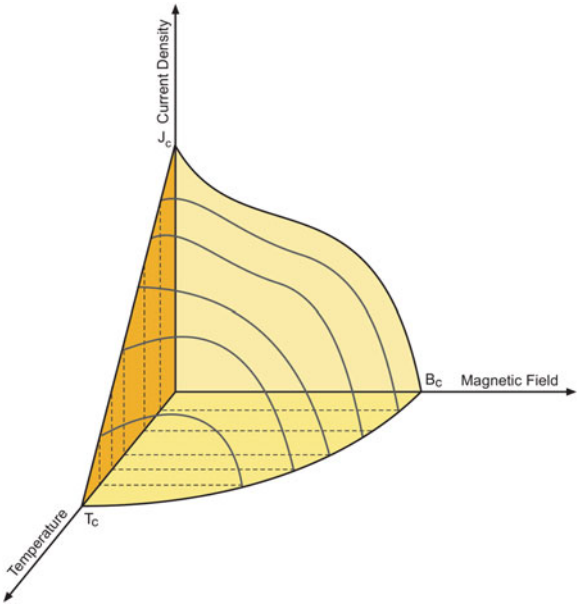

Fig. 2.7 Critical surface of a superconductor. Notice that the three critical parameters are inter-dependent

Francis Silsbee [3] proposed in 1916 that a superconductor has a critical value of current too which will produce a self field equivalent to B_c and destroy superconductivity. We thus have three critical parameters characterizing a superconductor, namely, critical temperature (T_c), the critical field (B_c) and the critical current (I_c). All the three parameters are inter dependent. Thus a superconductor remains superconducting within the confine of these three critical parameters and turns normal, the moment any of critical parameter is exceeded as shown in Fig. 2.7.

2.4 The Meissner Effect (Field Expulsion)

Low temperature research spread beyond the confines of the Low Temperature Laboratory of Leiden around the world after 1930. Race to discover superconductivity in variety of materials and especially in alloys continued unabated. Some thing very extraordinary happed in 1933 when Walter Meissner and Robert Ochsenfeld [4] at Berlin found out that a magnetic field is not frozen within the body of a superconductor when cooled down to below its critical temperature T_c. Instead, the field is expelled from the interior of the superconductor. This observation was quite startling and unexpected. It was expected that a magnetic field will freeze inside a superconductor (being a perfect conductor) until the superconductor is warmed up above T_c. We know a perfect conductor cannot sustain an electric voltage, that is $E = 0$, it therefore follows from Maxwell Equations

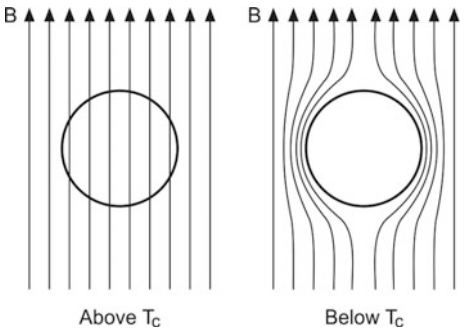

Fig. 2.8 Magnetic flux is expelled from the body of a superconductor the moment it enters the superconducting state when cooled to below T_c

$$\nabla \times E = -\frac{\partial B}{\partial t} \tag{2.3}$$

$$E = 0 \Rightarrow \frac{\partial B}{\partial t} = 0 \tag{2.4}$$

This implies that $\partial B = 0$ or the magnetic flux B inside a superconductor should be constant. This means that if a perfect conductor is placed in a magnetic field and then cooled down to T_c the magnetic flux remains trapped inside even when the field is removed. Meissner and Ochsenfeld however observed that it does not happen in a superconductor. They found that the flux is expelled from the body of the superconductor the moment it is cooled down to below T_c. Irrespective of the fact whether the superconductor is kept in a magnetic field and cooled below T_c or it is cooled below T_c first and then a field is applied, the magnetic flux does not enter a superconductor. The lines of force now pass around the sample as shown in Fig. 2.8. A superconductor thus behaves like a perfect diamagnet.

We can therefore state that a superconductor is a perfect conductor as well as a perfect diamagnet below its transition temperature T_c. Field expulsion can be explained in terms of screening current running across the surface so as to produce a magnetic field equal and opposite to the applied field. The consequence of this induced field is that a magnet will levitate over a superconductor provided, of course, the weight of the magnet is less than the force of levitation. Figure 2.9 is a typical picture of a superconductor floating over a permanent magnet. One can also levitate a magnet over a superconductor.

2.4.1 Perfect Diamagnetism

One immediate consequence of Meissner effect is that superconductivity is a thermodynamical phase in so far as the final state of magnetization does not depend upon the sequence of cooling below T_c and applying magnetic field. This behaviour is totally different to that observed in a normal metal. The fact, that the magnetic

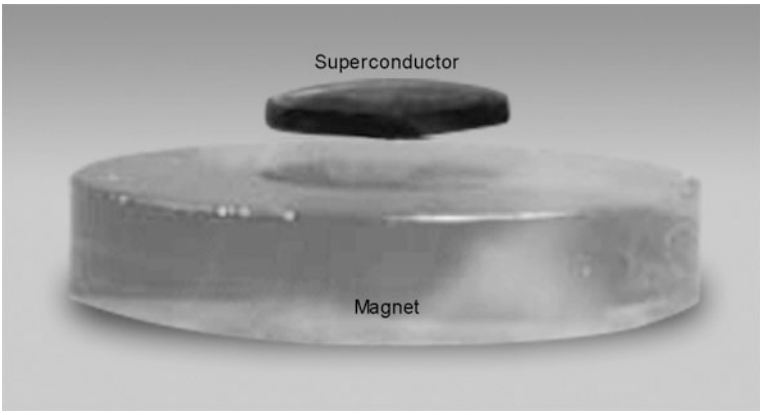

Fig. 2.9 Levitation of a superconductor over a magnet

flux inside a superconductor remains zero ($B = 0$) when an external field B_a is applied, implies that a magnetization is induced in the superconductor which exactly cancels out this magnetic flux. Thus,

$$\text{The magnetic flux} = \mu_0(B_a + M) = 0 \tag{2.5}$$

$$\text{Or} \quad \chi = M/B_a = -1 \tag{2.6}$$

A superconductor thus has a magnetic susceptibility of −1 and is a perfect diamagnet and quite distinct from the known diamagnetic materials.

As stated earlier, the screening currents flow along the surface of a superconductor to prevent the entry of the flux. Since the resistance of a superconductor is zero, these currents never decay (supercurrents) and flow persistently without Joule heating.

2.4.2 The Penetration Depth

The just discussed Meissner effect or the so called perfect diamagnetic property of a superconductor implies that screening currents flow along the external surface of the superconductor. If these currents were to flow only at the surface the current density will be infinite which will be an impossible proposition. Current sheet should therefore extend into the material to a depth on an atomic dimension. In fact, the magnetic field penetrates a superconductor a very small distance, falling exponentially to zero with a characteristic depth, called the 'penetration depth' λ. This is shown in Fig. 2.10. This penetration depth in most pure metals turns out to be of the order of 10–100 nm. The flux at a distance of x inside the material is given by the expression:

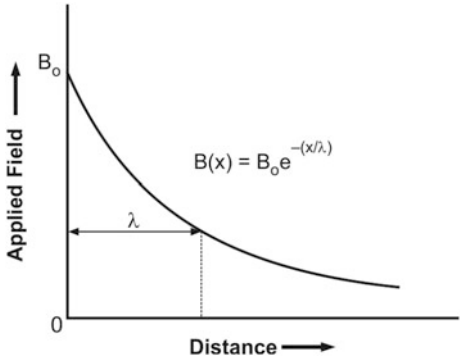

Fig. 2.10 Field penetration in a superconductor. The magnetic flux drops exponentially inside the material. Penetration depth λ is defined as the depth at which the flux density drops to its eth value

$$B(x) = B_0 \mathrm{e}^{-(x/\lambda)} \tag{2.7}$$

It is rather difficult to measure the penetration depth in bulk material, flux penetration being so small. In specimens of the dimension of λ, the field penetration could be across the material and can therefore be estimated to some accuracy.

The penetration depth is not constant but varies widely with temperature. Well below T_c and until 0 K there is hardly any variation but close to T_c (>$0.8T_c$) λ rises exponentially to infinity at T_c. Figure 2.11 is a typical λ–T curve for a superconductor. Equation (2.8) and (2.9) represent the observed λ–T behaviour.

$$\lambda(T) = \frac{\lambda_0}{\left[1 - \left(\frac{T}{T_c}\right)^4\right]^{\frac{1}{2}}} \tag{2.8}$$

Very close to T_c

$$\lambda(T) = \frac{\lambda_0}{\left[1 - \left(\frac{T}{T_c}\right)\right]^{\frac{1}{2}}} \tag{2.9}$$

Table 2.2 gives typical values of λ at 0 K for Pb, In and Al. The exponential variation of λ near T_c makes measurements close to T_c most difficult. The technique employed to measure field penetration is to have cylindrical superconductor of possibly high purity snugly fitted into a solenoid magnet. The inductance of this system will depend upon the extent of field penetration. If this inductance is connected to a LCR circuit, change in inductance can be evaluated in terms of frequency which can be measured with high accuracy.

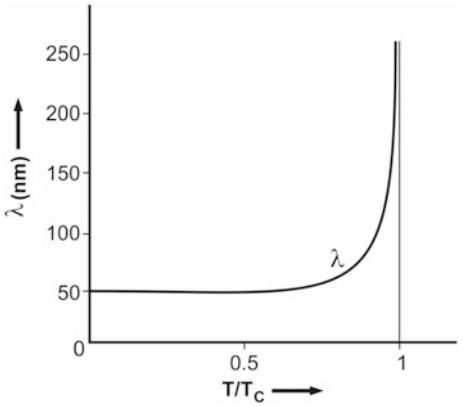

Fig. 2.11 Penetration depth is nearly constant until about $0.8T_c$ and rises sharply thereafter, reaching infinite at T_c

Table 2.2 Penetration depth of some metals at 0 K

S. no.	Metal	Penetration depth at 0 K (nm)
1.	Pb	39
2.	In	64
3.	Al	50

2.4.3 Magnetization in Superconductors

We have already discussed in Sect. 2.4.1 that superconductivity is an equilibrium thermodynamic state and a magnetization is induced in the superconductor when an external field B_a is applied. This behavior too is different from that of the normal metal. From Fig. 2.5 we find that at temperature higher than T_c and in field higher than B_c, a normal state is more stable. The magnetic flux inside a superconductor remains zero but the flux enters the material rather sharply as soon as the field exceeds B_c. The material turns normal. This is shown in Fig. 2.12a. The magnetization versus field behavior is shown in Fig. 2.12b. In the superconducting state magnetization rises with the increase of magnetic field to oppose the field penetration and drops to zero as soon as B_c is approached. Interestingly both these processes turn out to be reversible confirming the thermodynamical nature of superconductivity.

2.4.4 The Intermediate State

The value of critical field B_c usually gets modified because of the concentration of field lines at the surface. This, so called, the demagnetization effect, depends upon the shape of the material and the field orientation. For example a long thin cylindrical superconductor has no demagnetization effect if the magnetic field is parallel to its axis. In perpendicular field, however, the field penetration starts at $\frac{1}{2}B_c$, that

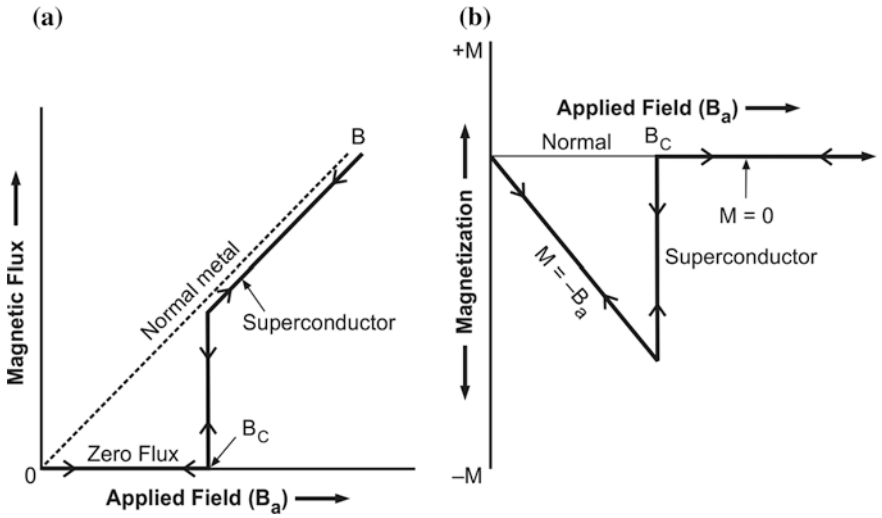

Fig. 2.12 Magnetic flux (**a**) and magnetization (**b**) behaviour of a superconductor in an applied magnetic field

is, the demagnetization factor is 1/2. For a sphere the demagnetization factor is 1/3. The uniform field B_i inside the superconductor in an applied field B_a is given by the expression

$$B_i = B_a/(1 - n) \tag{2.10}$$

where n is the demagnetization factor. Since $n = 1/3$ for a superconducting sphere, at $B_a = B_c$, $B_i = 2/3B_c$ and the sphere has to turn normal. If, however, it turns normal $M \approx 0$ and $B_i = 2/3B_c$ which is less than the critical field B_c and the sphere has to stay superconducting. This simply means that between B_c and $2/3B_c$ the sphere can neither be fully normal nor fully superconducting. Instead, the sphere undergoes an intermediate state. Figure 2.13 schematically shows the splitting of the material into laminae of alternate normal and superconducting material parallel to the field in a long thin cylinder when the field exceeds $½B_c$. As field increases superconducting fraction diminishes and the normal regions grow at the expense of the superconducting regions. At B_c, the entire material turns normal. Consequently, there is a continuous increase of resistance. These laminae are parallel to field. Since magnetic induction in the normal regions is parallel to field and goes to zero in superconducting regions the boundary has to be parallel to the field direction only. That the laminae extend right through the sample is confirmed by the observation of a finite resistance in the intermediate state. Finite resistance obviously comes from the current flow through the normal regions, without being short circuited by the superconducting regions.

Free energy calculations show that the intermediate state is more favourable than the wholly superconducting state as the effective field on the superconducting regions is greatly reduced. Stability of such a structure requires a positive surface

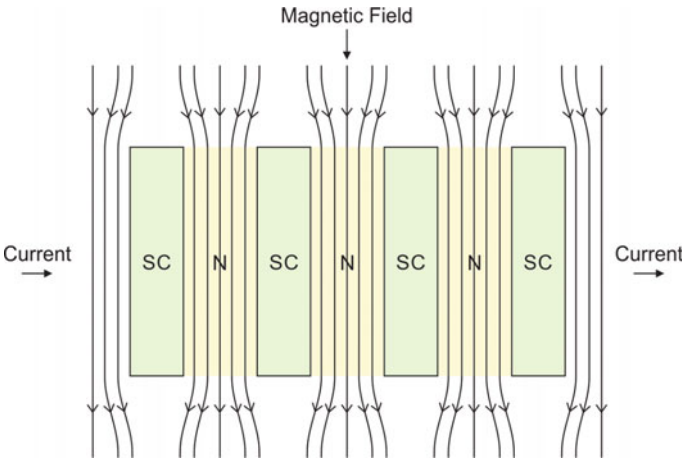

Fig. 2.13 A superconductor between the initial penetration and B_c splits into the laminae of alternate normal and superconducting material parallel to the field

energy which in turn implies finite width δ of the boundary layer between the laminae given by the expression

$$\alpha_{ns} = \delta(B_c)^2/8\pi \tag{2.11}$$

where α_{ns} is the boundary energy per unit area and $(B_c)^2/8\pi$ is the free energy difference between the normal and superconducting state. δ turns out to be of the order of 1,000 nm and can be identified with Pippard's coherence length to be discussed in a later section.

2.5 Two Fluid Model

To explain the zero resistivity and the perfect diamagnetism in superconductors, Gorter and Casimir [5] in 1934 at Leiden proposed a hypothesis what is popularly called as Two Fluid Model. According to the model. below the transition temperature the normal electrons start condensing into superelectrons which only, carry supercurrent. At $T = 0$ K all the electrons are superelectrons and at T_c all the electrons are normal electrons. These superelectrons can be identified with Cooper pairs of the BCS microscopic theory, to be discussed in chapter five. The variation of the normal electron density and the superelectron density with temperature is shown in Fig. 2.14. At any given temperature the electron density is given by;

$$n = n_n + n_s \tag{2.12}$$

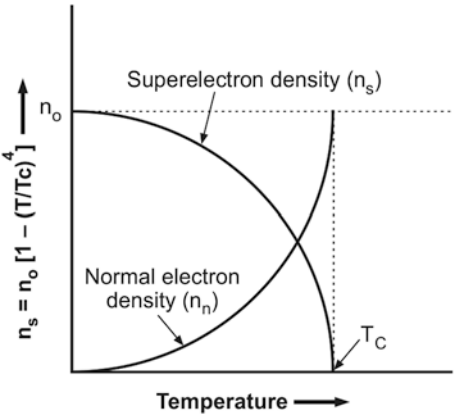

Fig. 2.14 The variation of the densities of the normal electrons and the superelectrons with temperature

The superconducting electron density, n_s at any temperature is given by the Expression;

$$n_s = n_0\left\{1 - (T/T_c)^4\right\} = n_0\left(1 - t^4\right) \tag{2.13}$$

where ($t = T/T_c$).

Here n_0 is the superconducting electron density at $T = 0$ K. n_s is also taken as an order parameter. Using this model Gorter and Casimir were able to account well for the specific heat anomaly at T_c discovered in Tin [6] and later in Thallium [7]. The peak in specific heat at T_c is caused by the extra energy required to excite the superelectrons to normal state at T_c. The above model was also adapted to explain the phenomenon of superfluidity occurring in liquid ^{4}He below Lambda point (its transition temperature, 2.18 K). Here the assumption is that the fluid below λ-point consists of two interpenetrating fluids, one, the normal fluid and another a superfluid each possessing its own inertia and the velocity field. There is at most very little or no exchange of momentum between the two fluids. The superfluid component has no viscosity. Superfluidity disappears at T_c similar to superconductivity in metals. The other component, the normal fluid behaves like a normal electron gas in a metal and thus has normal viscosity and gets scattered by irregularities and heat waves. Normal component disappears fast at the temperature approaches 0 K.

2.6 Thermodynamics of Superconductors

2.6.1 The Gibbs Free Energy

In Sect. 2.4.2 we have seen that the magnetization induced in a superconductor depends upon the magnetic field and is reversible thermodynamically under the two variables, temperature and magnetic field. The destruction of superconductivity at

the critical field B_c indicates that the normal state is energetically more favourable at B_c. Let us see how much is the increase in the potential energy of the superconductor in presence of B_c. The work done in bringing a superconductor in an applied field B_a is given by

$$W = -\mu_0 \int_0^{B_a} M dB \tag{2.14}$$

Since $M = -B$ in a superconductor W turns out to be

$$W = \mu_0 B_a^2/2 \tag{2.15}$$

The Gibbs free energy of a superconductor in an applied field B_a is thus given by

$$g_s(T, B_a) = g_s(T, 0) + \mu_0 B_a^2/2 \tag{2.16}$$

The Gibbs free energy in the normal state remains magnetic field independent and is practically constant as the magnetization is negligible. Thus we have

$$g_n(T, B_a) = g_n(T, 0) \tag{2.17}$$

From (2.16) we find that the free energy difference between the normal and superconducting phase is

$$g_n(T, 0) - g_s(T, 0) = \mu_0 B_c^2/2 \tag{2.18}$$

B_c thus turns out to be an important parameter linking up the free energies of the normal and the superconducting states in a superconductor and can be measured experimentally with precision. Figure 2.15 shows Gibbs free energy in the superconducting state and the normal state plotted against magnetic field. At B_c normal state becomes more stable

2.6.2 Specific Heat

From the free energy difference equation it is easy to calculate the difference in entropies and the specific heats in the normal and superconducting states. From the first law of thermodynamics entropy

$$S = -\left(\frac{\partial g}{\partial T}\right)_{p,B_a} \tag{2.19}$$

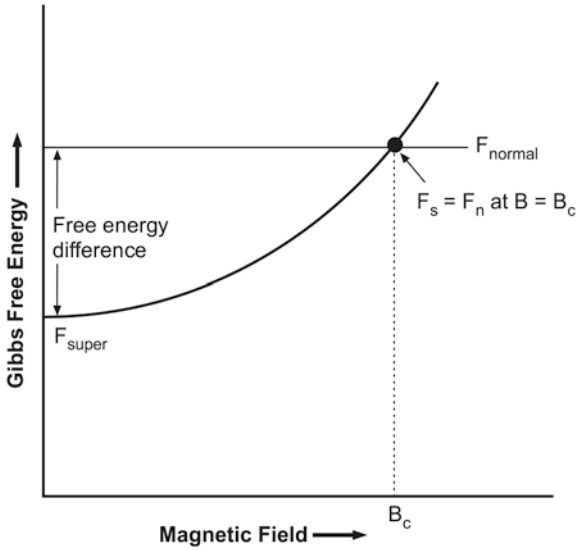

Fig. 2.15 Gibbs free energy in the superconducting state and the normal state plotted against magnetic field. Beyond B_c normal state becomes more stable

Thus differentiating g_n and g_s with respect to T we get

$$S_n - S_s = -\mu_0 B_c \left(\frac{dB_c}{dT}\right) \tag{2.20}$$

Since B_c always decreases with the rise of temperature in all the known superconductors the quantity $\left(\frac{dB_c}{dT}\right)$ is negative. This means $S_n - S_s$ is always positive, that is the entropy of a material is lower in superconducting state than in its normal state. Superconducting state is therefore an ordered state as also predicted by the Two Fluid Model discussed in Sect. 2.5. It also follows from (2.20) that at T_c the critical magnetic field B_c is zero therefore the two entropies are same at T_c. Similarly from the Third Law of thermodynamics the two entropies should again converge to the same value, that is, zero at 0 K. The entropies in the two states of S_n are shown in Fig. 2.16 between T_c and 0 K. The entropy of the superconducting state is lower than in the normal state between T_c and 0 K. Between these two temperatures one can go from the superconducting state to normal state by applying an appropriate magnetic field. The above curves have an interesting consequence. For example, if we move from low entropy point 1 in superconducting state to high entropy point 2 in normal state by applying a field, cold will be produced if the process is carried out under an adiabatic condition. This may be called as "adiabatic magnetization" as opposed to the usual "adiabatic demagnetization", a popular method to produce ultra cold using paramagnetic salt or the nuclear spins.

We can now derive an expression for the specific heat difference using expression (2.20). We know that the specific heat of a material is given by

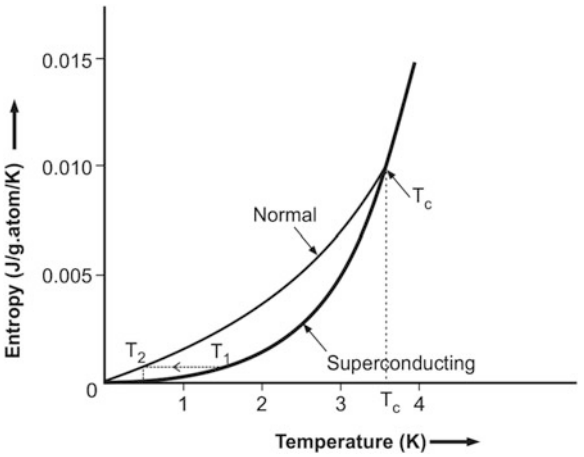

Fig. 2.16 Typical entropy curve of S_n. The entropies of the normal state and the superconducting state are the same at T_c and at 0 K

$$C = VT\frac{\partial s}{\partial T} \tag{2.21}$$

where V is the volume per unit mass. Differentiating (2.20) we obtain

$$C_s - C_n = VT\mu_0 B_c \frac{d^2 B_c}{dT^2} + VT\mu_0 \left(\frac{dB_c}{dT}\right)^2 \tag{2.22}$$

At the transition temperature T_c, the magnetic field $B_c = 0$. At T_c, the (2.22) will therefore reduce to

$$(C_s - C_n)_{T_c} = VT_c\mu_0 \left(\frac{dB_c}{dT}\right)^2_{T_c} \tag{2.23}$$

Which is a positive quantity. Superconducting state thus has higher specific heat value than the normal state. This jump in the specific heat at T_c (Fig. 2.17) is a characteristic feature of all the superconductors and has been well explained on the basis of Two Fluid Model [6, 7]. The specific heat of a metal is composed of two components. One is the lattice contribution proportional to T^3 and the other, electronic contribution proportional to T. The specific heat can therefore be represented by the following equation:

$$C_n(T) = \gamma T + \beta T^3 \tag{2.24}$$

Here γ is the density of electron states at Fermi level. The first term is the electronic term and the second lattice term. A plot of $\left[\frac{C_n(T)}{T}\right]$ versus T^2 gives a straight line with a slope β and the intercept γ. Since superconductivity affects only

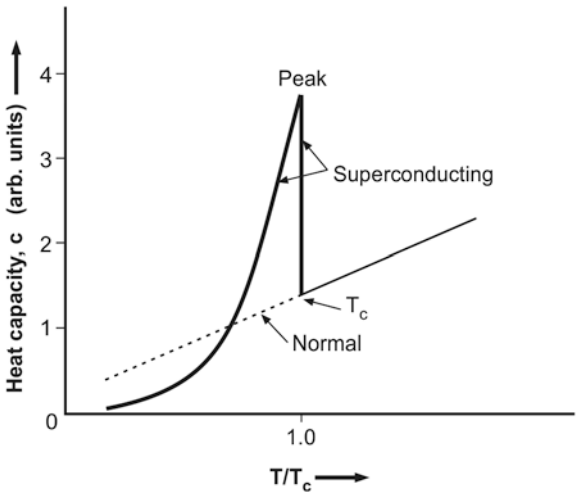

Fig. 2.17 The specific heat of a superconductor shows a jump at T_c and decreases exponentially below its value for the normal state as it approaches 0 K

the electrons and not the lattice at the transition, it is reasonable to assume that the lattice contribution to specific heat, βT^3 is the same in the normal state as well as in the superconducting state. Using this substitution electronic specific heat has been evaluated experimentally well below T_c and it turns out to be of the form

$$C_{es}(T) = A \exp\left(\frac{-\Delta}{k_B T}\right) \tag{2.25}$$

Experimental data fit well to (2.25) as shown in Fig. 2.18. This form of exponential dependence implies the existence of an energy gap between the energy levels of the so called superelectrons and the normal electrons. Super electrons exist in special lower energy state separated by a gap from the normal electrons. Extra heat is to be supplied to convert superelectrons into normal electrons to maintain the superelectrons density compatible with the temperature (as per $x = 1 - (T/T_c)^4$). At low temperature the change in 'x' is small and exponential at high temperature. Number of normal electron thermally excited rises exponentially with temperature and hence the exponential behaviour of the specific heat. Thermal conductivity below T_c is expected to be lower as the number of normal electrons carrying entropy is reduced.

2.6.3 Phase Transition

Let us recall (2.18) which gives the difference between the free energy in superconducting state and the normal state to be $\mu_0 B_c^2/2$. Since at T_c the value of B_c is zero the two free energies, g_s and g_n are equal. This means the free energy at T_c is

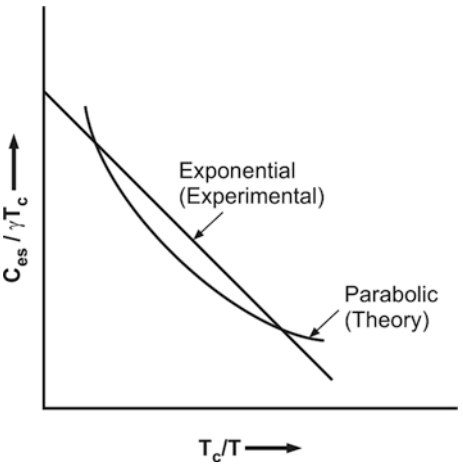

Fig. 2.18 Exponential behaviour of the electronic specific heat in superconducting state below T_c

continuous. From the (2.20) the difference between the entropies of the two states at T_c again turns out to be zero, B_c being zero. The fact that not only the free energy but also the entropy is continuous at the transition temperature shows that in the absence of the magnetic field the normal to superconducting transition is of the second order. There is no latent heat involved either at the transition ($dQ = T\,dS = 0$). Second order phase transition is also confirmed by the jump in the specific heat at T_c as discussed in Sect. 2.6.2 and shown in Fig. 2.17.

Phase transition from superconducting to normal state at T_c in presence of a magnetic field, however, turns out to be of the first order. The latent heat $dQ = T(S_n - S_s)$ now is finite (2.18), B_c being no longer zero.

2.7 Thermal Conductivity

Thermal conductivity in superconducting state is found to be smaller than in the normal state. The reason is that the superelectrons do not interact with the lattice and therefore do not transport heat from one part of the material to another. As the temperature goes down, the thermal conductivity keeps decreasing. Far below T_c, it becomes orders of magnitude smaller. For example, in Pb the thermal conductivity at 1 K is reduced by a factor of 100. So much so that superconductors like Pb and Sn are routinely used as thermal switches in the milli Kelvin and lower temperature region to break the thermal contact between different cooling stages. Thermal conductivity can, however, be restored by applying a small magnetic field just above B_c or by winding a small heating coil to raise the temperature just above T_c.

2.8 Thermoelectric Power

There is no thermo-emf in a thermocouple made up of two superconductors, when the two junctions are held at different temperatures. This is for the simple reason that any thermo-emf howsoever small will lead to current flowing at a critical value irrespective of the magnitude of the temperature difference at the junctions. In other words the Seeback coefficient S (= dV/dT) is zero. Likewise the two other thermoelectric effects, namely, Peltier effect and the Thomson effect are also absent in the superconductors, all the three effects being inter-related. The Peltier coefficient ($\Pi = S\ T$) and the Thomson coefficient ($\mu = dS/dT$), both are zero in superconductors. This property makes a superconductor an ideal standard to measure the absolute thermoelectric power of a material if coupled with it and had been widely used for calibration of temperature sensors below T_c.

2.9 The Energy Gap

The exponential behaviour of specific heat with temperature in superconducting state gave the first hint of the existence of an energy gap in the energy spectrum of the electrons. One needs as though an energy equal to the gap to excite a super electron to the normal state. The energy gap turns out to be of the order of 3.5 $k_B T_c$. This energy gap is reminiscent of a similar gap between the valence band and the conduction band in semiconductors, but the gap here is of the order of 10^{-4} eV, some three orders of magnitude smaller than in semiconductors. Table 2.3 gives the values of the energy gap ratio of some of the metal superconductors [8]. The presence of an energy gap implies that a photon of energy less than 2Δ is not absorbed by the superconductor. A superconductor is thus more reflective than in its normal state for frequencies $<2\Delta/h$. Figure 2.19 shows [9] the absorption of EM radiation in superconductors normalized to that in the normal state $(P_s - P_n)/P_n$ plotted against frequency (in wave numbers) of the EM radiation for Pb, V, Sn, Nb, Hg, In and Ta. All the curves show a peak followed by a steep drop to zero at a characteristic frequency which is different for different metal. This frequency is a

Table 2.3 Energy gap ratio ($2\Delta/k_B T_c$) for metal superconductors at zero temperature ($T = 0$ K)

Metal	Energy gap ($2\Delta/k_B T_c$) ratio	Metal	Energy gap ($2\Delta/k_B T_c$) ratio
Aluminum	3.3	Thallium	3.57
Zinc	3.2	Lead	4.38
Gallium	3.5	Vanadium	3.4
Cadmium	3.2	Niobium	3.80
Indium	3.6	Molybdenum	3.4
Tin	3.5	Lanthanum	3.7
Mercury	4.6	Tantalum	3.60

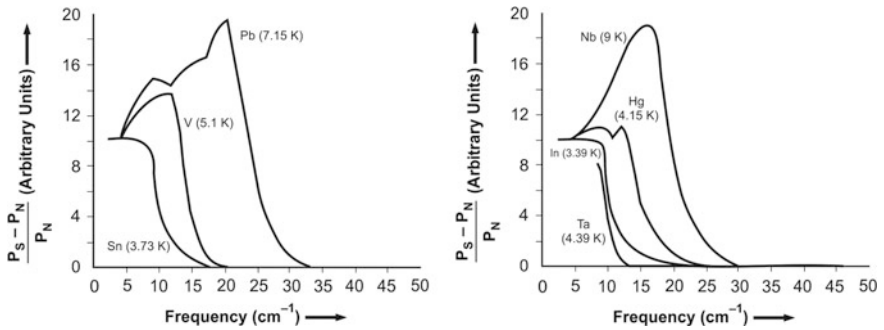

Fig. 2.19 Absorption curves for seven metal superconductors normalized to the normal state plotted against the frequency (in wave number). T_c of each metal is written *within the bracket* [9] (With permission from APS) http://journals.aps.org/pr/abstract/10.1103/PhysRev.119.575

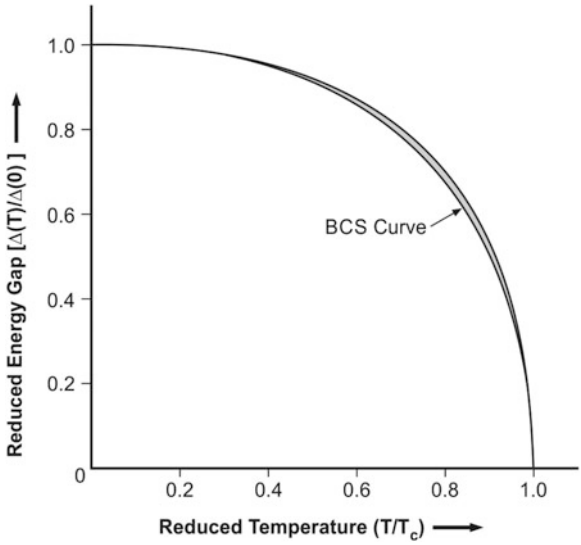

Fig. 2.20 Reduced energy gap $\Delta(T)/\Delta(0)$ plotted against the reduced temperature T/T_c for most metal superconductors lie on a universal curve and fit well with BCS theory within the width in the curve

function of temperature increasing as the temperature approaches zero. At T_c this frequency drops to zero.

The energy gap and its variation with frequency at different temperatures can be measured directly by electron tunneling measurements. The energy gap is maximum at 0 K and decreases with the rise of temperature and becomes zero at T_c. Reduced energy gap $\Delta(T)/\Delta(0)$ plotted against reduced temperature T/T_c for a number of pure metal superconductors has a universal behavior. Interestingly, the data for all the superconductors lie on a universal curve (within the width of the curve in the middle) and are also in good agreement with the BCS theory, shown in Fig. 2.20.

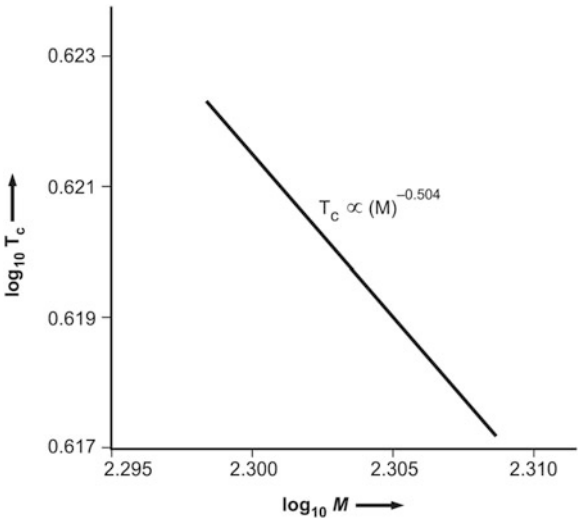

Fig. 2.21 Logarithmic plot of T_c of the different isotopes of mercury and the average mass number. The data fit well with the formula $T_c \propto \frac{1}{\sqrt{M}}$. [11] (With permission from APS) http://journals.aps.org/pr/abstract/10.1103/PhysRev.84.691

2.10 The Isotope Effect

Different isotopes of several metal superconductors showed a variation in T_c with the atomic mass number [10, 11]. Most of the data can be fitted to the expression of the type $M^{\alpha}T_c$ = constant. Experimentally the average value of α turns out to be 0.5, that is, T_c is inversely proportional to the square root of the atomic mass.

$$T_c \propto \frac{1}{\sqrt{M}} \tag{2.26}$$

This leads to an interesting conclusion that the lattice does not seem to play a direct role in the phenomenon of superconductivity as the lattice does not show change in going from normal to superconducting state but does influence the behaviour of the electron in a very subtle way. The isotope effect in fact, provided an important clue to the role of lattice in superconductivity. Figure 2.21 is the logarithmic plot of T_c of the different isotopes of mercury [11] and the average mass number. The data fits well with the formula $T_c \propto \frac{1}{\sqrt{M}}$. The experimental values of exponent α in the formula $M^{\alpha}T_c$ = constant for a few metal superconductors are listed in Table 2.4.

2.11 Flux Quantization

London going through the peculiar behaviour of superconductors postulated [12] that a magnetic flux inside a superconducting cylinder or in a ring (Fig. 2.22) will always be an integral multiple of (h/e) where h is the plank constant and e the

Table 2.4 Measured values of α in the formulae $M^{\alpha}T_c$ = constant of some metal superconductors

Metal (Superconductor)	Value of α in $M^{\alpha}T_c$ = constant
Zinc	0.45 ± 0.05
Cadmium	0.32 ± 0.07
Mercury	0.50 ± 0.03
Thallium	0.61 ± 0.10
Tin	0.47 ± 0.02
Lead	0.49 ± 0.02

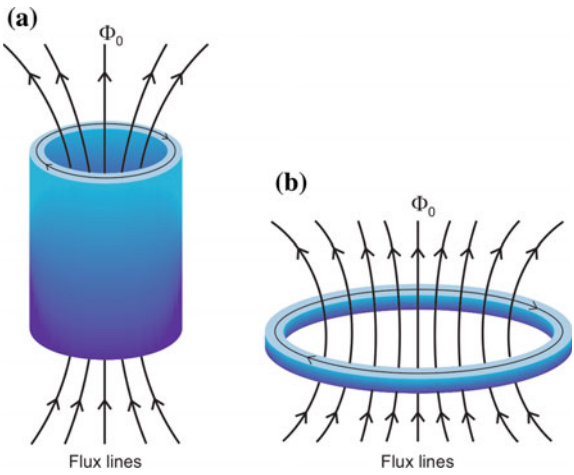

Fig. 2.22 The flux inside a superconducting cylinder (**a**) or a superconducting ring (**b**) is always found to be an integral multiple of the quantum of flux, $\Phi_0 = h/2e$

electronic charge. It was indeed a remarkable prediction that the magnetic flux in the free space is a multiple of h/e simply because it is surrounded by a superconducting cylinder. This quantum of flux is small only about 4×10^{-15} Weber or 4×10^{-15} T m^2. The experimental confirmation of this so called flux quantization came through precision experiments by Deaver and Fairbank [13] at Stanford and Doll and Näbauer [14] at Munich in 1961. The trapped flux was however found to be quantized in units of ($h/2e$) and not in units of (h/e). The flux quantum thus turns out to be exactly 2.067833×10^{-15} T m^2 and is represented by Φ_0.

Deaver and Fairbank [13] carried out measurement on a *S*n (hollow) cylinder by depositing a 5 μm thick tin layer over a copper wire (cylinder) of 13 μm diameter. The composite wire was cooled below T_c in a small magnetic field of about 0.1 Gauss. The magnetic flux in copper was determined by measuring the emf in an electrical pick up coil while moving the sample up and down in the coil at a rate of 100 cycles/s The measured flux remained confined to values to $nh/2e$ for integral values of n = 1, 2, 3. Döll and Näbauer [14], on the other hand used a torque method to determine the magnitude of flux contained in a lead cylinder. They coated lead on a quartz fiber and suspended with a quartz fiber and made to oscillate

in a liquid helium bath. The frozen flux was measured by the torque produced by the application of a magnetic field perpendicular to the axis of the cylinder. Flux was again found to be quantized in the unit of $h/2e$.

The factor $2e$ above is of great significance in so far as it represents the charge of the superelectron responsible for superconductivity. These superelectrons are identified with Cooper pairs in the theory of superconductivity, the BCS theory [15] which will be discussed in Chap. 5.

2.12 The Concept of Coherence Length and Positive Surface Energy

The coherence length represented by ξ is yet another fundamental characteristic length which defines a superconductor. The other similar characteristic length already introduced is the penetration depth λ. One of the many observed unique features of superconductivity that the transition temperature could be as sharp as 10^{-5} K in a pure metal, led Brian Pippard [16] to believe that superconductivity is a cooperative phenomenon. A large number of entity (superelectrons) over a long range take part in the process. There is a long range coherence among the superelectrons. All superelectrons move in phase. According to the two fluid model, superelectron density n_s increases as the temperature decreases below T_c and so does the degree of order of the superconducting phase. The superelectron density, n_s in fact can be identified with this order. Pippard arrived at the conclusion [16] that this order parameter cannot change abruptly at the S–N boundary but will do so smoothly over a finite distance of the order of 1,000 nm in pure metals. This distance is referred to as the coherence length, ξ. It has the maximum value at $T = 0$ K, for the purest form of the metal and is represented by ξ_0. The value of ξ_0 is an intrinsic property of a superconductor. As the temperature increases the coherence length decreases and drops to zero at T_c.

Another property of coherence length is that it is strongly dependent upon the purity of the metal. ξ is found to be proportional to the electronic mean free path ℓ_e and is shorter for impure material. At high level of impurity the coherence length becomes equal to ℓ_e. Coherence length ξ is related to ξ_0 through the equation of the type

$$\xi = (\xi_0 \ell_e)^{1/2} \tag{2.27}$$

The value of the intrinsic coherence length ξ_0 can be calculated from (2.28) by substituting the values of the Fermi velocity and T_c

$$\xi_0 = 0.18 \frac{\hbar v_f}{k_f T_c} \tag{2.28}$$

Table 2.5 Typical values of the intrinsic coherence length ξ_0 and penetration depth, λ at 0 K for some metal superconductors

Metal (Superconductor)	Intrinsic coherence length, ξ_0 (nm)	London penetration depth, λ (nm)	Ratio ξ_0/λ
Aluminium	1,600	16	100
Niobium	38	39	0.98
Cadmium	760	110	6.9
Tin	170	30	5.67
Lead	510	37	13.8
Indium	360	24	15

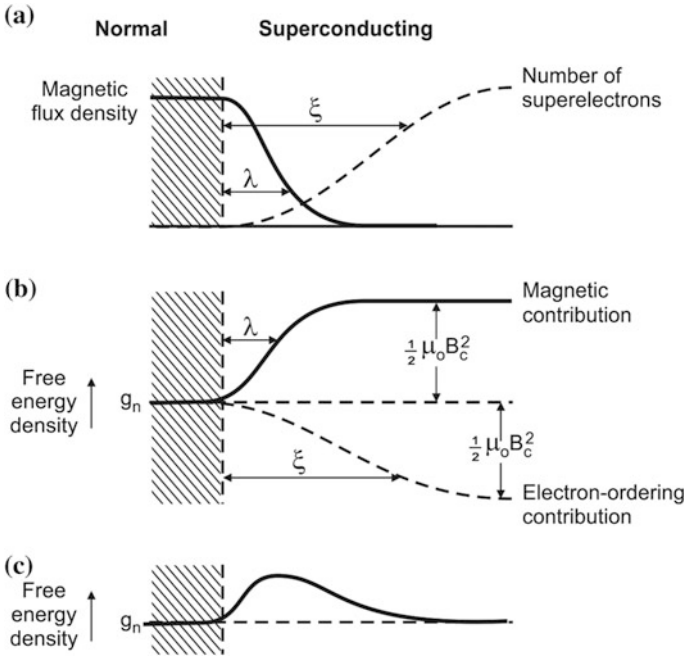

Fig. 2.23 The interface at the superconducting and normal boundary has a positive surface energy for metallic superconductors (Type I superconductors) ([17], p. 80) (with permission from Elsevier). **a** Penetration depth and coherence range at boundary. **b** Contributions to free energy. **c** Total free energy

Table 2.5 gives typical values of ξ_0 and λ for a few metal superconductors. We will see in subsequent Chap. 3 that the ratio of ξ/λ determines the nature of superconductor whether it belongs to type I or type II class of superconductors.

Let us now attend to the surface energy issue. Figure 2.23 shows [17] the boundary between the normal and the superconducting regions. In order to have a stable boundary it is necessary that the two regions are in equilibrium. This means

that at the boundary the free energy per unit volume in both the regions are same. Inside the superconducting regions, however, there are two contributions to the free energy. Since electron ordering takes place in the superconducting region over a distance of ξ there is a decrease in free energy equal to $g_n - g_s = \mu_0 B_c^2/2$. The other contribution to free energy is due to the magnetization, which it acquires to expel the flux. It contributes a positive magnetic energy equal to $\mu_0 B_c^2/2$ over a distance of the penetration depth λ. So well inside the superconductor both these contributions cancel each other but since $\xi \gg \lambda$ in most of the metal superconductors, close to the boundary there is a net small positive energy. The value of this energy is approximately equal to $\mu_0 B_c^2/2(\xi - \lambda)$ per unit area of the boundary. Positive surface energy turned out to be an important characteristic parameter of the metallic superconductors as opposed to alloy superconductors which are characterized with a negative surface energy which are termed as type II superconductors. Metallic conductors are likewise termed as type I superconductors. Type II superconductors will be the subject matter of the next chapter.

2.13 Determination of Energy Gap (Single Particle Tunneling)

One easy and simple technique to measure the energy gap in superconductors is through the single particle tunneling experiment. As shown in Fig. 2.24 a thin film of metal is deposited on a suitable substrate. The metal surface is then oxidized to form an insulating layer of the order of 10 Å thick. A superconducting layer is now deposited on this oxide layer. *I–V* characteristics of the junction are studied after making usual current and voltage contacts with the layers. Giaever [18] found the *I–V* behaviour of such a junction (MIS) as shown by solid line in Fig. 2.25. The *I–V* characteristics of a tunnel junction consisting of a metal-insulator-metal (MIM) has also been shown in this figure. The *I–V* plot for MIM junction is a straight line, that is, current and voltage are proportional. For the MIS junction, the current jumps sharply at a voltage of Δ/e where 2Δ is the energy gap of the superconductor.

The energy versus density of electronic states have been plotted in Fig. 2.26. The energy gap in the superconductor is distinctly seen in the figure. At 0 K no current flows unless the voltage is raised to $E_g/2e = \Delta/e$. The current rises sharply [19] at $eV = \Delta$ (Fig. 2.25). The gap separates the normal electrons from the superelectrons. At non zero temperature there is a small current flowing even at lower voltage because the normal electrons are thermally excited across the energy gap.

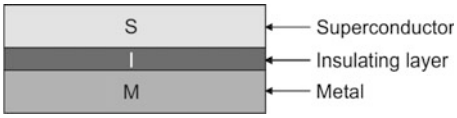

Fig. 2.24 Cross-section of a tunnel junction consisting of a metal, an insulator and a superconductor. The insulator is usually the oxidized metal surface itself

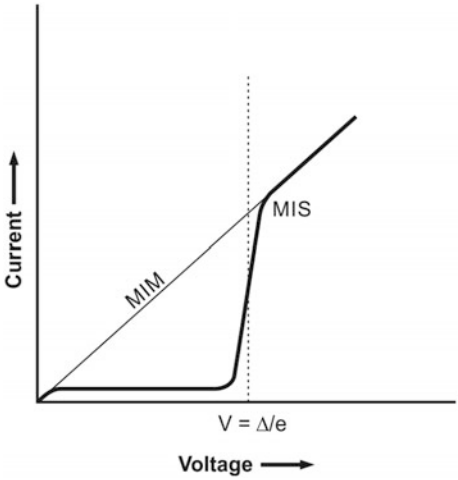

Fig. 2.25 Typical current–voltage behaviour of a Metal-Insulator-superconductor (MIS) tunnel junction. The straight line is the *I–V* characteristic of a Metal- Insulator-Metal (MIM) junction

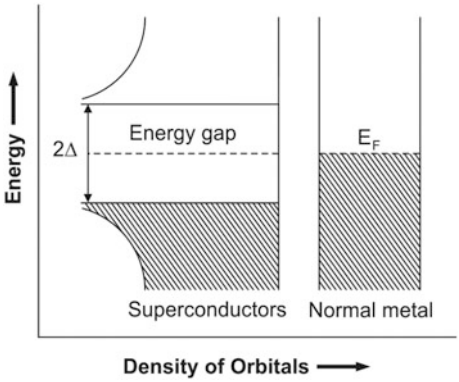

Fig. 2.26 The energy versus density of electronic states plots for a superconductor (S) and in a normal metal (N)

2.14 The Josephson Effect (Pair Tunneling)

2.14.1 DC Josephson Effect

In 1962, Brian D. Josephson [20], a graduate student at the University of Cambridge made a startling prediction that a supercurrent (zero voltage) will flow across a tunnel junction consisting of two superconductors, A and B separated by an insulating layer, about 10 Å thick (Fig. 2.27). These two superconductors can either be identical or different. The prediction came true and the effect was observed experimentally. In the picture of BCS theory [15] of superconductivity (to be discussed in Chap. 5) the electrons start pairing up via a virtual phonon interaction process as the temperature is reduced to below T_c. These pairs condense to a ground state. These electron pairs, referred to as Cooper pairs, are responsible for the supercurrent flow in superconductors and can be identified with the superelectrons

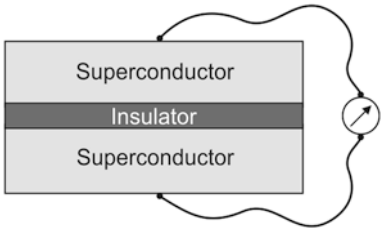

Fig. 2.27 A Josephson junction has two superconductors separated by a thin oxide insulating layer

in the Gorter's two fluid model. Interestingly, all the pairs in a superconductor are in the same quantum-mechanical phase ϕ (phase coherence) and can be represented by a single macroscopic wave function or the order parameter.

$$\psi(\vec{r},t) = |\psi(\vec{r},t)\exp[i\phi(\vec{r},t)] \tag{2.29}$$

This theory explained well most of the observed behaviour of the metallic superconductors, like zero resistance, Meissner effect and flux quantization.

Josephson effect [20] was yet another important manifestation of the same macroscopic quantum nature of superconductors. Here the pairs tunnel through the insulating barrier without encountering resistance. This flow of pairs constitutes a supercurrent. The supercurrent I generates a phase difference $\Delta\phi$ between the order parameters of the two superconductors according to the equation

$$I = I_c \sin(\Delta\phi) \tag{2.30}$$

where I_c is the critical current of the junction which depends upon the temperature and the junction parameter. For current less than I_c the phase difference $\Delta\phi$ adjusts to facilitate the passage of the Cooper pairs across the junction with a constant value of $\Delta\phi$ or for a zero voltage. For currents larger than the critical current a finite voltage appears. This is dc Josephson effect. A typical ideal current-voltage (I–V) characteristic of a tunnel junction is shown in Fig. 2.28. The dc Josephson effect was first observed experimentally in a crossed film junction by Philip Anderson and John Rowell [21].

2.14.2 AC Josephson Effect

At finite voltage supercurrent still exists but oscillates with time with a frequency given by

$$v = \frac{2eV}{h} = \frac{V}{\phi_0} \tag{2.31}$$

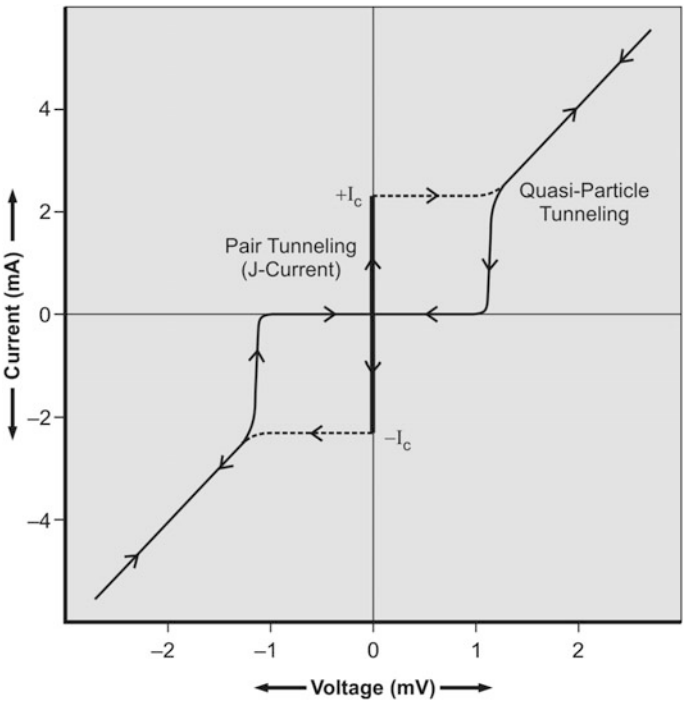

Fig. 2.28 A typical *I–V* behaviour in a Josephson tunnel junction. Note the hysteresis when the current is swept from −5 to +5 mA and back

This frequency turns out to be 484 MHz/μV. These oscillations persist up to frequencies of the order of 10^{12} Hz or more. This is ac Josephson effect and can be experimentally observed by irradiating the Josephson junction (J-J) by microwave of frequency, f. The *I–V* characteristic now shows a series of current steps at constant voltage

$$|V_n| = \frac{nhf}{2e}, \text{where } n \text{ is an integer} \tag{2.32}$$

The *I–V* characteristics with and without microwave irradiation are shown in Fig. 2.29. The height of the current steps and the range of current for which voltage remains constant oscillates with microwave frequency, f. This microwave frequency mixes up with the Josephson currents whose frequency v depends upon the voltage across the J-J. Whenever $v \pm nf = 0$, there is a zero frequency beat and a current step appears. When the J-J is biased at voltage V, energy difference between Cooper pairs on the two sides is = $2eV$ and whenever $2eV = nhf$, pairs can tunnel through the barrier coherently with the emission or absorption of n microwave photons. Please notice here, that the voltage is related to frequency through the universal constants h and e which are invariant of time and place. As a consequence,

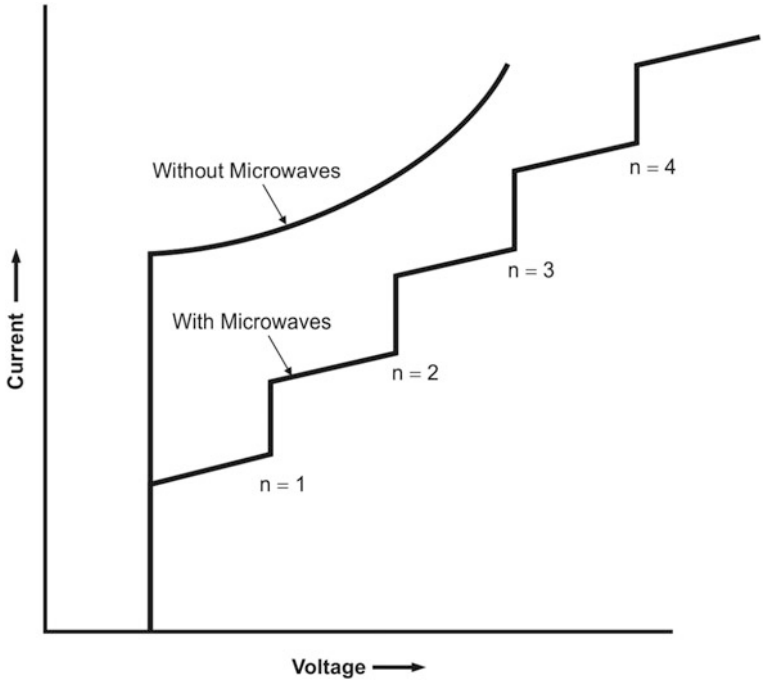

Fig. 2.29 The *I–V* characteristics of a Josephson Junction with and without microwave radiation. Current steps appear at constant voltage $|V_n| = \frac{nhf}{2e}$. These steps are shown for n = 1, 2, 3 and 4

international standard volt has now been defined as the voltage step that will be produced in a J-J irradiated by microwave of frequency 483,597.9 GHz. It is, however, necessary to prepare an array of a large number of Josephson junctions. An array of a large number of Nb J-J are used to generate 10 V for voltage standard routinely by the international laboratories. The voltage can be measured to better than 0.03 ppm accuracy. Josephson effect studies can be carried out on a variety of junctions prepared by different routes and three of such most popular fabrication techniques [22] are depicted in Fig. 2.30a is a crossed film Josephson-junction consisting of an insulating layer sandwiched between two superconductors. The first superconductor film is oxidized to form an insulating barrier and a film of second superconductor is then deposited. Figure 2.30b is yet another form of J-J which has a broad superconducting film with a constriction in the middle and is called a "weak link" or a "microbridge". Figure 2.30c is a point contact J-J consisting of a superconducting screw pressing a bulk superconducting slab, mostly niobium, at a point. A niobium oxide film formed on the slab at room temperature serves as the barrier between the slab and the screw.

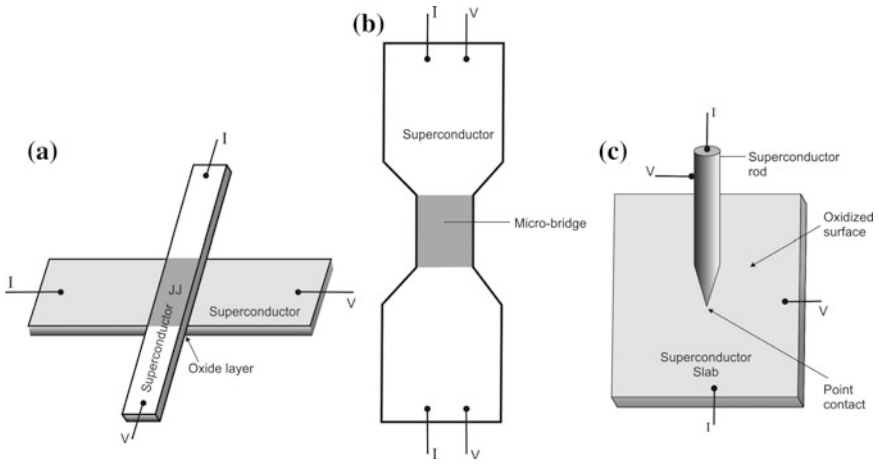

Fig. 2.30 Three different configurations of the J-J, **a** a "crossed film Junction", **b** a "weak link" or a "microbridge", **c** a "point contact" [22] (With permission of AIP)

2.14.3 The SQUID

SQUID stands for "Superconducting Quantum Interference Device" and is perhaps the most widely exploited application of Josephson effect and the flux quantization. SQUID is a device which can measure feeble magnetic field of the order of 10^{-15} T, such as produced by the neural activity in human brain, to unprecedented accuracy. SQUID is used in biomagnetism and geomagnetism for prospecting as also in solid state physics. By coupling a small coil a SQUID can as well be used as an ultra low noise parametric amplifier for voltage and current signals from a variety of transducers. A SQUID could be either a dc SQUID or an rf SQUID. The prefix indicates the method of coupling of the electronics to the device. Figure 2.31 is the schematics of dc SQUID [23] which consists of two Josephson-junctions (weak links), J-J1 and J-J2 mounted on a superconducting ring with two side arms. External current applied to the SQUID (bias current) enters from the left and branches out into two arms of the device and combine again together and exit at the right end. When the current in the weak links (J-J1) and (J-J2) is greater than the critical current a voltage appears across the SQUID. The Junction critical current (supercurrent) is extremely sensitive to the flux applied to the ring and is maximum for zero flux. If now the magnetic flux threading the ring is increased the critical current starts decreasing and reaches to a minimum at half the integer of flux quantum Φ_0. Critical current increases again to a maximum at full integer of Φ_0. The voltage across the SQUID thus oscillates with a periodicity of one flux quantum Φ_0 as shown in the lower part of Fig. 2.31. The above effect is similar to the one observed in optics when a coherent light beam from a laser source passes through two parallel slits and interfere with each other to produce dark and bright fringes. In a superconductor all the Cooper pairs are in phase and are described by a single wave

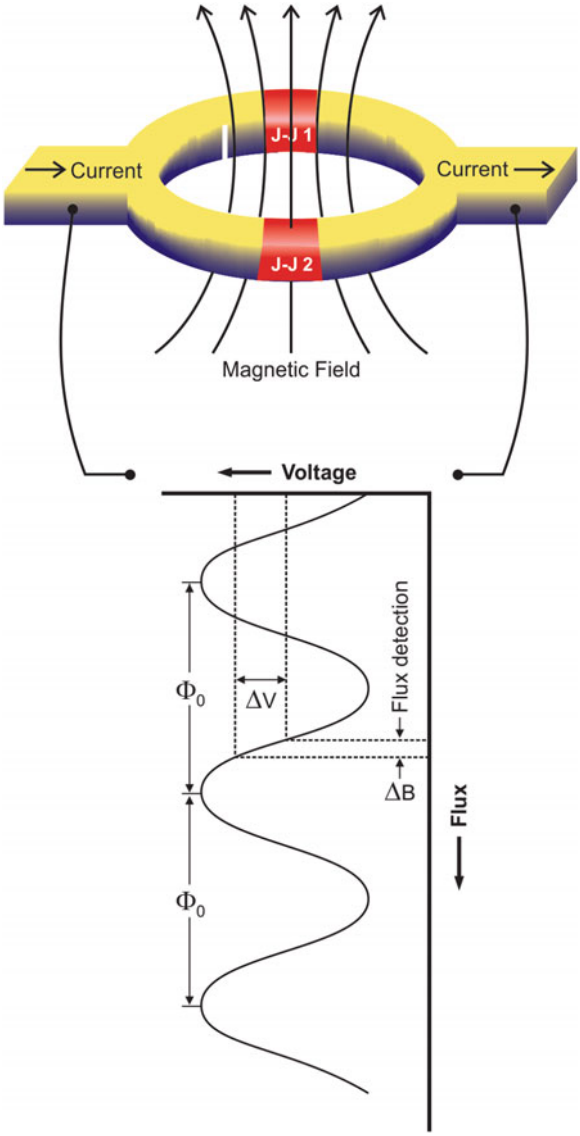

Fig. 2.31 A dc SQUID with two Josephson-junctions (J-J1 and J-J2) mounted on a superconducting ring (*top*) and the SQUID voltage oscillations with flux (*bottom*). One can measure a fraction of the flux quanta accurately in terms of voltage [23] (*Courtesy* Ian Worpole/ Scientific American)

function. In a SQUID the wave functions at the two weak links (JJ) interfere with each other and produce current and voltage fluctuations. As shown in Fig. 2.32 a SQUID in a magnetic field has a critical current versus magnetic field pattern very much similar to the diffraction pattern formed by the interference between the monochromatic light coming from the two slits. In a SQUID the quantum mechanical interference takes place between the currents flowing through the two separate Josephson junctions. This interference gives rise to the periodicity of current associated with flux enclosed in the area between the two junctions. The

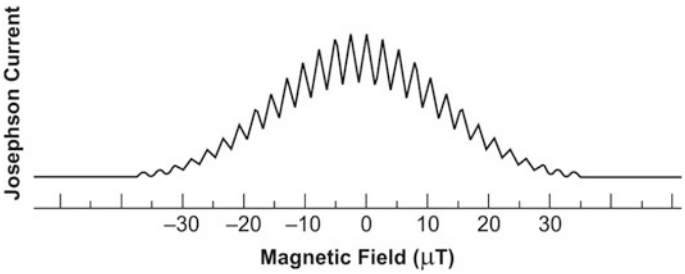

Fig. 2.32 A typical Josephson current versus magnetic field pattern in a dc SQUID

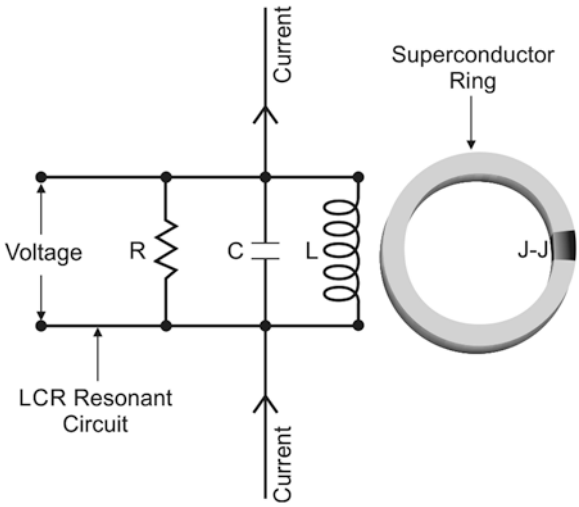

Fig. 2.33 An rf SQUID has a single J-J on a superconducting ring and is coupled to an LCR circuit

other periodicity, of course, is associated with the flux contained in a single junction. It is clear from the above discussion that a SQUID can detect and measure a fraction of a flux quantum digitally and accurately. SQUIDs are widely used as sensitive magnetometers. Very good reviews on SQUIDs have been written by John Clarke [22, 23], who contributed a great deal to this field.

With the commercial availability of SQUIDs a new field of research "Magnetoencephalography (MEG)" has emerged wherein one can map feeble magnetic field generated by neuroelectric activities in the brain. Neuro-surgeons can pin point the source of epileptic seizure and can study real time brain activity. A combination of MEG and MRI can enable a surgeon to have detailed brain map and remove only the damaged tissues. MEG machines with as much as 400 SQUIDs on a helmet-shaped head gear are commercially available to map the entire area of the brain.

It is easier to fabricate rf SQUIDs as it uses a single Josephson junction as shown in Fig. 2.33. Here the interferometer is coupled to a capacitance-inductance-resistance resonant circuit. An ac current flows in the circuit at its resonant frequency. The

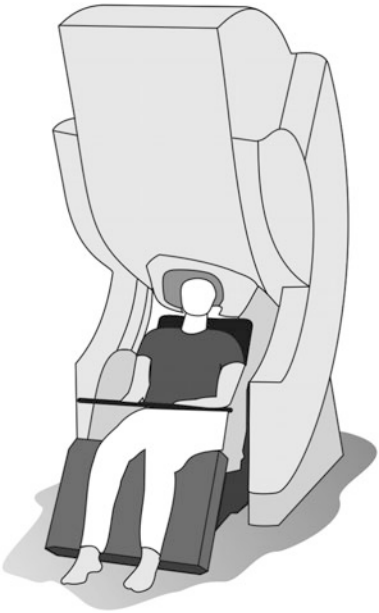

Fig. 2.34 A sketch of a typical commercial MEG machine. The patient head fits in a helmet shaped gear which has a few hundred SQUIDS mounted on it for mapping the whole brain area

voltage across this circuit oscillates with a period of one flux quantum Φ_0 with the flux threading the superconducting ring. The applied flux modulates the critical current of the J-J as also the voltage. In rf SQUID the resonant circuit too is kept at liquid helium temperature. Both the dc and the rf SQUIDS have comparable sensitivity.

The sketch of a typical commercial MEG machine is shown in Fig. 2.34. The patient sits comfortably with the head fitted into a helmet-shaped gear housing few hundred SQUIDS cooled to 4.2 K.

References

1. H.K. Kamerlingh Onnes, Commun. Phys. Lab. Univ. Leiden, **29**, (1911)
2. W. Buckel, R. Kleiner, *Superconductivity Fundamental and Applications* (Wiley_VCH Verlag GmbH & Co KGaA, Weinheim, 2004)
3. F.B. Silsbee, J. Wash. Acad. Sci. **6**, 597 (1916)
4. W. Meissner, R. Ochsenfeld, Naturewissenschaften **21**, 787 (1933)
5. C.J. Gorter, H.B.G. Casimir, Phys. Z. **35**, 963 (1934)
6. W.H. Keesom, J.v.d. Ende, Comm. Leiden, 219b
7. W.H. Keesom, J.A. Kok, Comm. Leiden, 221e Physica **1**, 175 (1934)
8. D.H. Douglass Jr, L.M. Felicov, Prog. Low Temp. Phys. **4**, 97 (1964)
9. P.L. Richards, M. Tinkham, Phys. Rev. **119**, 575 (1960)
10. E. Maxwell, Phys. Rev. **78**, 477 (1950)
11. C.A. Reynold, B. Serin, W.H. Wright, L.B. Nesbitt, Phys. Rev. **84**, 691 (1951)
12. F. London, *Superfluids*, vol. 1 (Willey, New York, 1950)

13. B.S. Deaver Jr, W.M. Fairbank, Phys. Rev. Lett. **7**, 43 (1961)
14. R. Doll, M. Nabauer, Phys. Rev. Lett. **7**, 51 (1961)
15. J. Bardeen, L.N. Cooper, J.R. Schrieffer, Phys. Rev. **108**, 1175 (1957)
16. A.B. Pippard, Physica **19**, 765 (1953)
17. A.C. Rose-Innes, E.H. Rhoderidz, *Introduction to Superconductivity.* Copyright © 1969, Pergamon Press, Library of Congress Catalog Card No. 79-78591
18. I. Giaever, Phys. Rev. Lett. **5**, 464 (1960)
19. I. Gaiever, K. Megerle, Phys. Rev. **122**, 1101 (1961)
20. B.D. Josephson, Phys. Lett. **1**, 251 (1962)
21. P.W. Anderson, J.M. Rowell, Phys. Rev. Lett. **10**, 230 (1963)
22. J. Clarke, Phys. Today **24**, 30 (1971)
23. J. Clarke, Sci. Am. **271**, 46 (1994)

Chapter 3
Type II Superconductors

Abstract Superconductivity with high T_c was found in a number of alloys and compounds which displayed a strange type of behavior. They were found to be perfect diamagnetic only up to a small field, called lower critical field, B_{c1} but remained superconducting up to a high magnetic field called the upper critical magnetic field, B_{c2}. Abrikosov explained this behavior in terms of the formation of negative surface energy at the normal-superconducting interface in these materials. Beyond B_{c1} field starts entering the material in the form of flux lines each carrying a quantum of flux, $\Phi_0 = h/2e = 2 \times 10^{-15}$ T m^2. Since formation of normal zone (flux lines) reduces the energy, this, so called the "mixed state", is more stable. The flux lines form a triangular lattice and are produced by the circulating persistent currents around the normal cores. Mixed state has a fine structure with a periodicity of $<10^{-6}$ and is an intrinsic property of these so called type II superconductors. At B_{c2} the material is overtaken completely by the flux and turns normal. If a current flows in a superconductor in the mixed state the flux lines experience Lorentz force, forcing them to move. A voltage appears and the material turns normal. Flux lines are, however, pinned by impurities or imperfections introduced in the material and the critical current density is increased to desired level. Only type II superconductors are capable of carrying large currents without dissipation in presence of high magnetic field and are of technological importance.

3.1 Strange Behavior of Superconductors: Abrikosov's Concept of Negative Surface Energy

After having studied superconductivity in metals across the periodic table, and the consequent disappointment with low T_c values, the researchers in the field of superconductivity changed track and started looking for superconductivity in alloys and compounds. Superconductivity was indeed discovered in a large number of alloys and compounds. These new superconductors, however, displayed a strange behaviour in so far as they did not show perfect diamagnetism like pure metals.

R.G. Sharma, *Superconductivity*, Springer Series in Materials Science 214,
DOI 10.1007/978-3-319-13713-1_3

Instead, they exhibited partial flux penetration. At first instance it was thought to be either an experimental artifact or an impurity effect. Abrikosov [1], however, predicted in 1957 a new class of superconductors, now called type II with anomalous properties. He emphasized that it is a new class of superconductors and not a trivial impurity effect. He argued that in metal superconductors, referred to as type I superconductors, occurrence of perfect diamagnetism implies that there is positive surface energy at the normal-superconducting boundary. Let us consider a normal region in a type I superconductor in a magnetic field $B_a < B_c$ the free energy of normal regions/unit volume is greater than for the superconducting region (diamagnetic state) by $\frac{\mu_0}{2}\left(B_c^2 - B_a^2\right)$. Thus in a type I superconductor the free energy will increase if the normal regions were to grow. This is energetically unfavourable and therefore it remains superconducting until a field B_c is reached. Let us now assume a negative surface energy [2] at the superconducting—normal boundary. This will imply that the energy will reduce if normal regions are formed in the superconductor. When a field is applied, a large number of normal regions are formed resulting in a large negative energy. It thus becomes energetically favourable to allow partial flux penetration than carrying the burden of expelling the field completely.

To understand the concept of negative surface energy, we should recall that type II superconductivity is observed mostly in alloys and compounds (with a few exceptions like Nb, V and T_c) where the mean free path is very small and so is the coherence length. Thus type II superconductors are characterized by a coherence length ξ much smaller than the penetration depth λ. Let us now refer to positive surface energy in type I superconductors discussed in Chap. 2 (Fig. 2.23). Compare it with Fig. 3.1 for type II superconductors where $\xi \ll \lambda$ resulting in a negative surface energy close to the N–S boundary. Here we see that well inside the material the two contributions to free energy namely, electron ordering contribution and the magnetic contribution cancel each other but close to the boundary there is now a net negative energy.

3.2 Lower and Upper Critical Magnetic Field

Figure 3.2 shows the magnetic phase diagrams of the type I and type II superconductors. Figure 3.2a is the same as Fig. 2.5 for the type I superconductor whereas Fig. 3.2b is the phase diagram for type II superconductors. As seen in the figure, type II superconductors are now characterized by two critical magnetic fields instead of one for type I. The type II superconductor shows perfect diamagnetism only up to a magnetic field, B_{c1}, called the lower critical magnetic field. This field is a fraction of the thermodynamical magnetic field B_c. Material however stays superconducting (zero resistance) up to a magnetic field which is significantly higher than B_c and is called upper critical magnetic field, B_{c2}. A type II superconductor can thus sustain a very high magnetic field and can still carry large current. It is for this reason that only type II superconductors are of technological

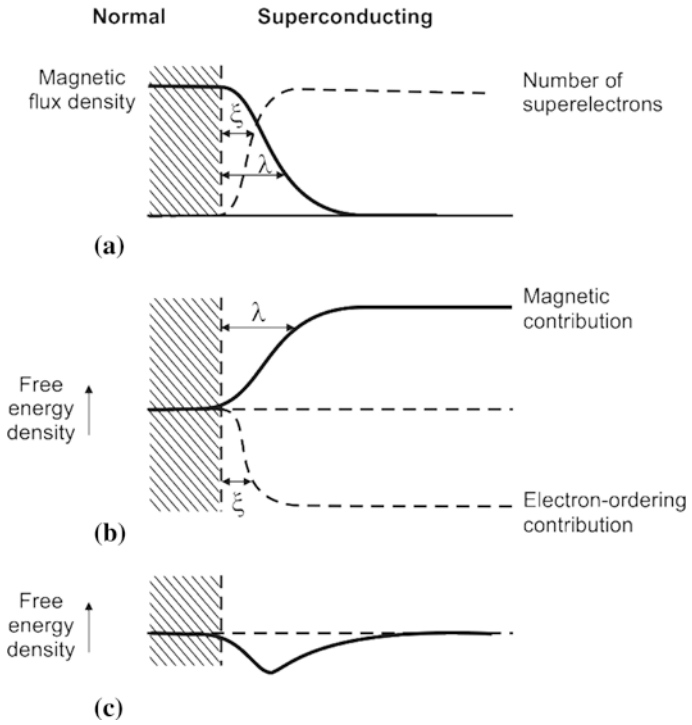

Fig. 3.1 Lowering of energy, due to pair formation, is more than the increase in energy due to magnetic contribution close to the N–S boundry resulting in a negative surface energy [2, p. 175]. **a** Penetration depth and coherence range at boundary. **b** Contributions to free energy. **c** Total free energy (With permission from Elsevier)

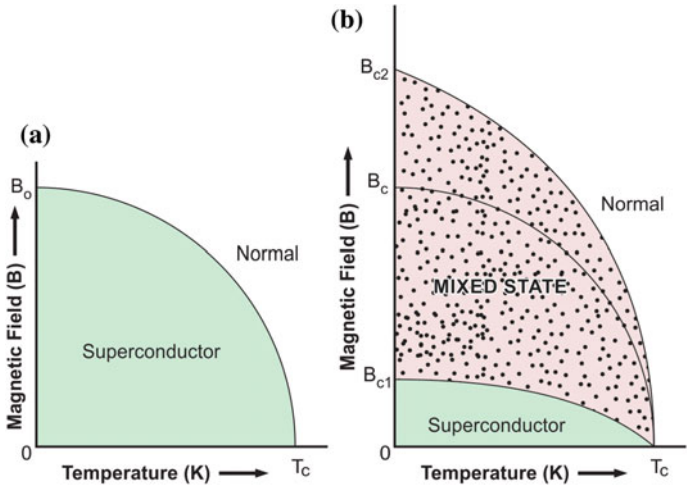

Fig. 3.2 Magnetic phase diagrams of type I (**a**) and type II (**b**) superconductors

importance and are widely used for magnet construction. All the three critical magnetic fields are inter-related in the following way;

$$B_c = [8\pi(g_n - g_s)]^{\frac{1}{2}} \tag{3.1}$$

$$B_{c1} = \frac{B_c}{\left(\kappa\sqrt{2}\right)^{0.65}} \tag{3.2}$$

$$B_{c2} = \left(\sqrt{2}\right)\kappa B_c \tag{3.3}$$

$(g_n - g_s)$ is the energy difference between the normal state and the superconducting state and κ is the G–L parameter ($=\lambda/\xi$). As κ increases B_{c1} decreases with respect to B_c and B_{c2} increases. The value of κ is given by the G–L theory:

$$\kappa = \frac{\left(\sqrt{2}\right)2\pi\lambda^2\mu_0 B_c}{\Phi_0} \tag{3.4}$$

where $\Phi_0 = h/2e = 2 \times 10^{-15}$ T m^2, the flux quanta. It is pertinent to note here that in alloys electron mean free path is short which means the coherence length ξ decreases and λ increases thus making κ large. For type I superconductor $\kappa < 0.71$ and for type II $\kappa > 0.71$. However, κ can be more than 0.71 even for pure metals in exceptional cases as shown in Table 3.1.

For pure metals κ increases with impurity and thus with normal state resistivity as per the relation below:

$$\kappa = \kappa_0 + 7.5x\sqrt{10}x10^5\gamma^{\frac{1}{2}}\rho \tag{3.5}$$

where κ_0 is the value of κ for pure metal, ρ and γ are normal state resistivity and coefficient of electronic specific heat respectively. Further, some metals and alloys behave like type I superconductor at T_c but turn type II at lower temperature. For example $Pb_{0.99}$ $Tl_{0.01}$ $\kappa = 0.58$ at T_c (=7.2 K) but increases to 0.71 at $T = 4.3$ K. For pure vanadium $\kappa = 0.85$ at T_c (=5.4 K) and increases to 1.5 at $T = 0$ K.

Table 3.1 κ values for type II pure metal superconductors

Metal superconductor	κ value
Nb	0.78
V	0.85
Tc	0.92

3.3 The Mixed State

It will be interesting to know what happens to a type II superconductor between the lower critical field B_{c1} and the upper critical field B_{c2}. The existence of a negative surface energy at the N–S boundary favours partial field penetration of the material. As shown in Fig. 3.3, between B_{c1} and B_{c2} the material undergoes 'mixed state'. It is energetically favourable that the flux lines, each carrying a unit quantum of flux Φ_0 (=$h/2e$) parallel to the applied field penetrate the material. These flux lines form a triangular lattice and are normal cores of small dimension of the order of diameter 2ξ. Mixed state is a fine structure with a periodicity of $<10^{-6}$ and a is an intrinsic property of type II superconductors.

The favourable configuration for the normal cores to thread the superconductor is a cylinder with a maximum surface to volume ratio, parallel to the applied field. Each flux line is produced by a vortex of persistent current with a sense of rotation opposite to the surface screening current. The material still remains diamagnetic being protected by the surface screening current, and the supercurrent still flows. In type II superconductors current flows through the entire cross section as compared to type I where the current flows along the surface. As field strength increases the density of normal cores increases at the expense of superconducting volume fraction and at the upper critical field B_{c2} the entire structure collapses. The material turns normal.

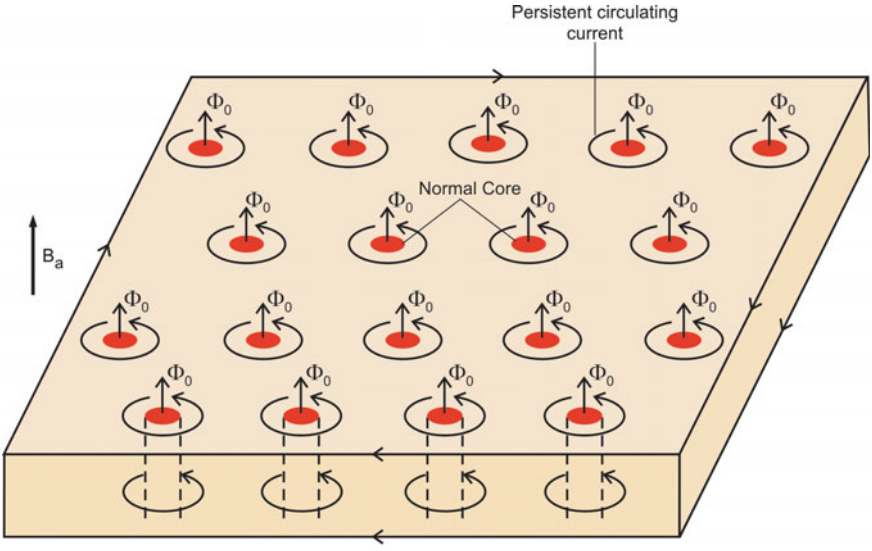

Fig. 3.3 Between B_{c1} and B_{c2} a type II superconductor undergoes mixed state. The material is threaded by *flux lines* (Φ_0) produced by vortices of persistent current with a sense of rotation opposite to surface screening

3.4 Current Flow and Mixed State

Type II superconductors are known to carry very large current in presence of high magnetic fields. Let us see how current is carried by the superconductor in mixed state. In the mixed state the current is not impeded by the presence of flux lines, the size of the normal cores being very small ($\sim 2\xi$). The vortices repel each other so that the normal cores are confined to small area and the current flows without hindrance as long as it does not disrupts vortices. The flux lines, however, experience a Lorentz force, F_L under the influence of the transport current and the perpendicular transverse field which tries to move it in the third perpendicular direction (Fig. 3.4). The movement of the flux lines generates a finite voltage and a resistance appears. The flux lines are however held back by the crystal lattice through a pinning force F_P. Imperfections, defects and impurities are introduced into the superconducting materials to create pinning sites. The pinning force is thus increased significantly and the superconductor can carry a much larger current.

The flux lines do not move until the time Lorentz force becomes equal to the pinning force. This happens at a current density value, called the critical current density J_c. Once the J_c is exceeded flux lines start moving, a voltage appears and the material reverts back to normal state.

Figure 3.5 shows two typical plots of J_c versus the magnetic field. The lower plot is for a clean, defect free type II superconductor and the upper plot is drawn for the dirty' superconductor with defects or the so called pinning centres. As seen from the figure J_c drops sharply to low value for a pure superconductor at low field and is hardly of use for practical applications. The dirty superconductors, normally referred to as "hard superconductors" with pinning sites (defects) on the other hand carries large useful current at high magnetic field. Defects are, in fact, substituted intelligently in a

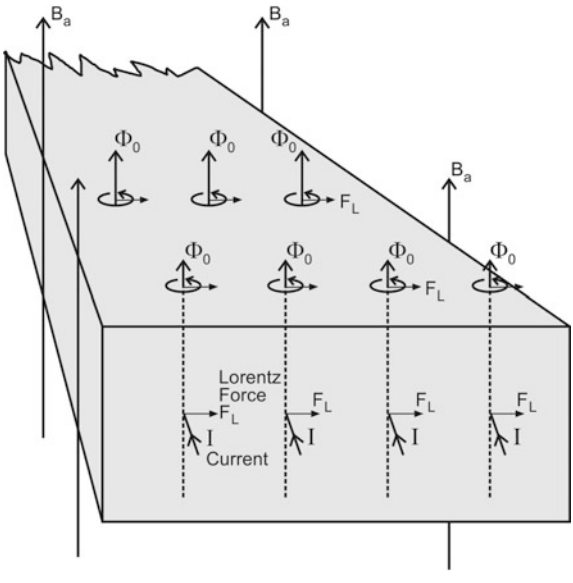

Fig. 3.4 In the mixed state *flux lines* (*normal cores*) experience Lorentz force (F_L) when a longitudinal current flows through the superconductor. Movement of *flux line* is prevented by flux pinning mechanism

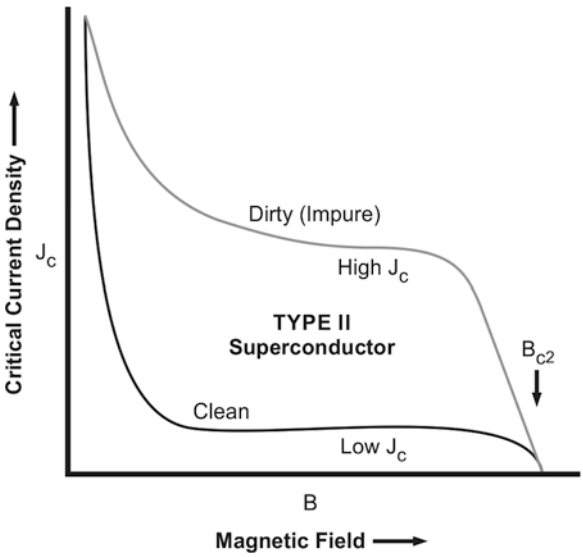

Fig. 3.5 J_c versus magnetic field for type II superconductors in clean limit and the dirty limit with pinning centres. J_c in both the cases drops to zero at B_{c2}. Notice high J_c in dirty (hard) superconductors

superconductor to create pinning sites which increase the pinning force many fold. The critical current increases dramatically whereby the superconductor can be used for magnet applications like in accelerators and the fusion reactors where the superconducting cables carry several kA current and in high magnetic field.

3.5 Measuring Transport Critical Current

Critical Current density is the single most important parameter for characterizing a superconducting (multifilamentary) wire against the magnetic field. Experimentally, the superconducting wire sample is mounted on a sample probe shown schematically in Fig. 3.6 in a hair-pin geometry. While measuring critical current in a MF wire with several concentric layers of filaments around the central core it is important that the voltage contacts are made far away from the current contacts. There is a current transfer length which can be many times the wire diameter depending upon the matrix resistance. All the layers of filaments must share the current uniformly. Voltage contacts are in fact made on the horizontal part of the sample which is kept in the perpendicular magnetic field. The sample is kept dipped in liquid helium at 4.2 K. A variable dc current is passed through the sample from a power supply and the voltage across the sample is monitored using a nano-voltmeter. There is practically no voltage across the sample with increasing current until a current equal to critical current I_c is reached. There is a sharp jump in voltage at I_c as shown in Fig. 3.7. This voltage rise is caused by flux flow resistivity which is different from the Ohmic resistivity and is proportional to the normal state resistivity. I_c is determined at different values of the magnetic field. It is advisable to start from the highest

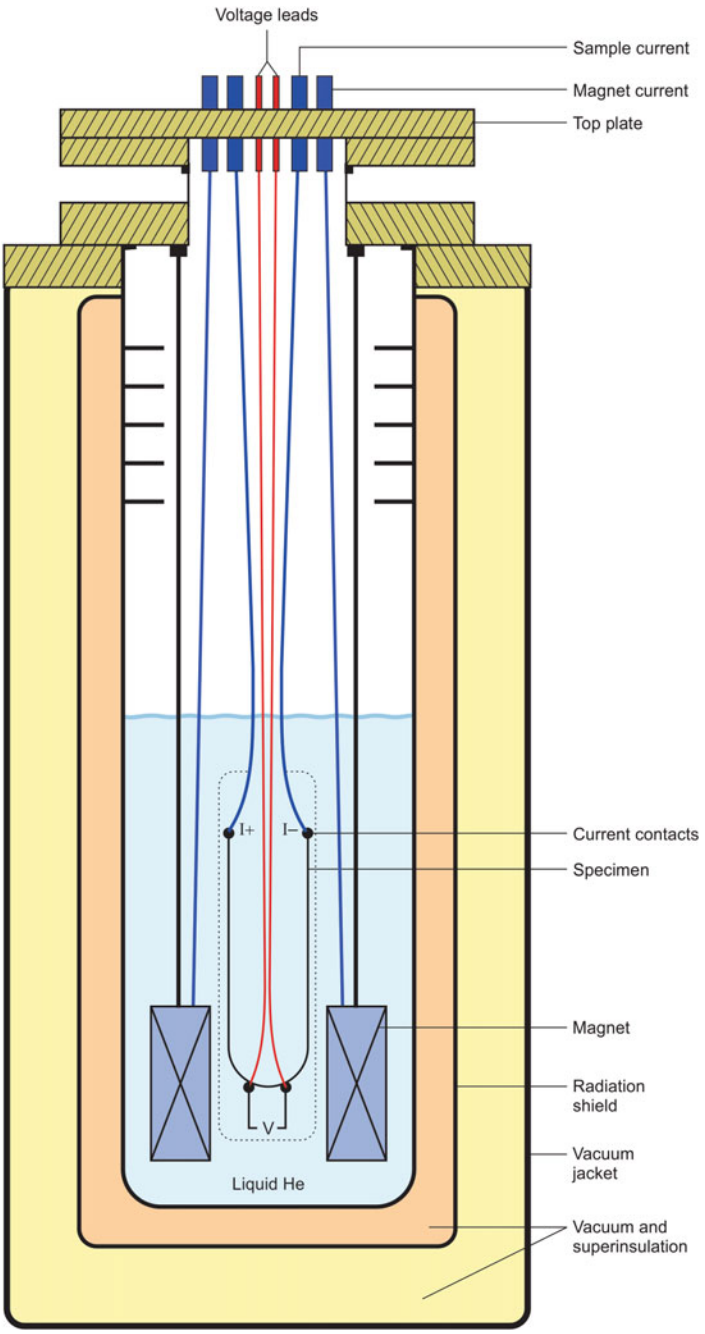

Fig. 3.6 A schematic of the superconducting magnet system used for critical current measurement. Voltage contacts on the sample are made far away from the current contacts

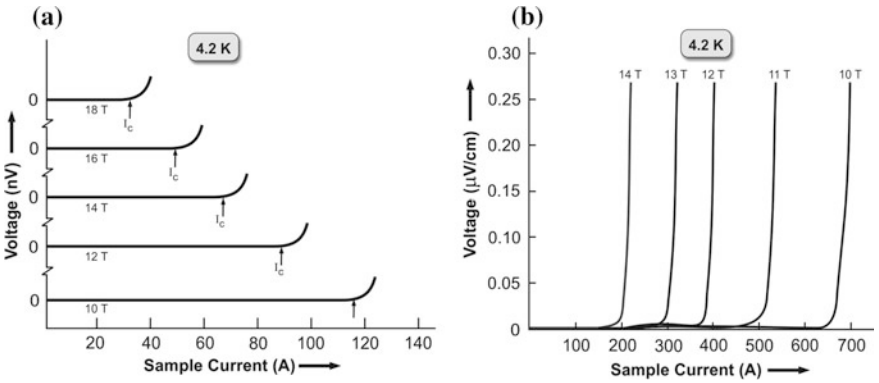

Fig. 3.7 Typical critical current, (I_c) plots at different fields. I_c decreases as the magnetic field increases

magnetic field so that the current to be passed is minimum. As the field is reduced sample carries larger currents and so also the possibility of sample burnt-out. A shunt across the sample is therefore always advisable to save the sample from burnt-out. The criterion to determine I_c is usually 0.1–0.01 μV/cm voltage drop across the sample. The critical current density, J_c is calculated by dividing I_c by the area cross section of the wire.

3.6 Magnetization in Type II Superconductors

A type II superconductor behaves exactly like type I below the critical field B_{c1} and is a perfect diamagnet with magnetization equal to $-B_a$. Beyond B_{c1} flux lines start penetrating the material (mixed state) and the magnetic flux inside the material is no longer zero as shown in Fig. 3.8a. As the magnetic field is increased magnetic flux density rises and continues till B_{c2} is reached. The material is completely taken over by the flux, turning it into the normal state. The curve retraces its reverse path in pure ideal superconductors. The corresponding magnetization versus field behaviour is shown in Fig. 3.8b. As shown, magnetization increases with magnetic field until B_{c1} and starts decreasing in field higher than B_{c1} and continues to decrease until it becomes zero at B_{c2}. Between B_{c1} and B_{c2} flux lines (normal cores) enter the material. The density of flux line is governed by the equilibrium between the reduction in free energy and the mutual repulsion between the vortices. In increasing field, normal cores pack closer together, so the average flux density increases in the material and the magnetization decreases. At B_{c2} there is a discontinuous change in the slope of the flux density and the magnetization. The material now is in normal state with flux density equal to $\mu_0 B_a$ and magnetization zero.

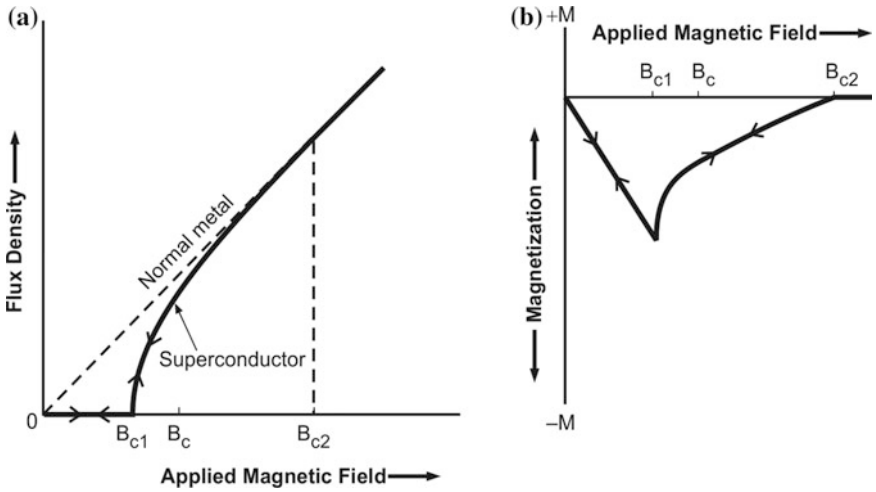

Fig. 3.8 **a** The magnetic flux density inside a type II superconductor is zero up to B_{c1} and increases in higher field. At B_{c2} flux penetrates the whole of the material. The process is reversible in ideal pure material. **b** Negative magnetization increases with magnetic field, peaks at B_{c1} and then decreases to zero at B_{c2}. This process too is reversible for pure ideal material

Magnetization measurement can be used for the determination of κ by finding the slope of the M–H curve near the field B_{c2} as per the formula

$$\left[\frac{dM}{dH}\right]_{B_{c2}} = \frac{-1}{1.16(2\kappa^2 - 1)} \tag{3.6}$$

The procedure is, however, valid only if the magnetization is reversible. The same curve should be traced while increasing and decreasing the magnetic field.

3.6.1 Irreversible Magnetization

Only ideal type II superconductors without pinning show reversibility but real type II superconductors (hard superconductors) show irreversibility in their magnetization behaviour as shown in Fig. 3.9. The reason for this magnetic irreversibility is that the flux lines or the normal cores are pinned in the bulk by imperfections and are not free to move. Consequently on increasing the field from zero there is no sudden entry of flux inside the material at B_{c1}. Thus there is rounding in the flux density and the magnetization curves at B_{c1}. Likewise on reducing the field from above B_{c2}, the two curves do not retrace their paths, but show hysteresis instead. Flux may be left trapped permanently as some flux line remain pinned down and are not able to detach and move out. Imperfections like dislocations, grain boundaries

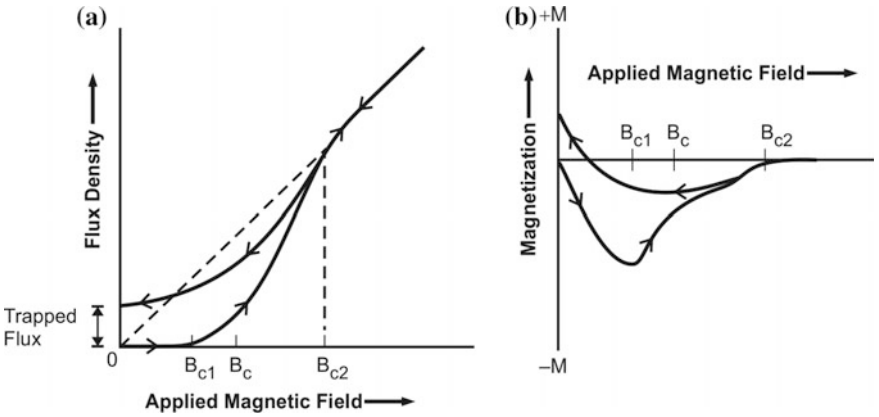

Fig. 3.9 A real type II superconductor has imperfection and show magnetic irreversibility in flux density (**a**) and in magnetization (**b**). Material can retain finite flux and magnetization even after the field is reduced to zero

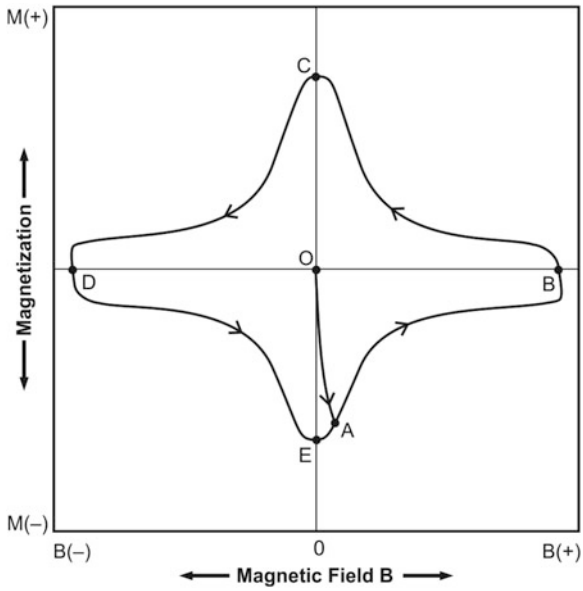

Fig. 3.10 Typical plot of magnetization versus magnetic field of a multifilamentary hard superconductor between $+B$ and $-B$. Starting from $M = 0$ to $B = 0$ point the curve traverses an irreversible path showing hysteresis. M does not drop to zero even at $B = 0$ after tracing the full cycle

and impurities can cause this type of magnetic irreversibility. The magnetic field has to be reversed to bring down magnetization M to zero but the situation at $B = 0$ and no trapped flux is retrieved only by warming the material to normal state.

Figure 3.10 shows a typical magnetization versus magnetic field loop observed in a multifilamentary conductor. To draw the full M–B loop we start from point O ($M = 0$, $B = 0$). The negative magnetization M increases with field up to the field B_{c1} (point A) and starts decreasing with the further increase of the field. Magnetization

drops to zero at B_{c2} (point B). The anomalous behaviour of these hard superconductor is that when the field starts decreasing the M–B curve does not retrace the earlier path. Instead magnetization changes sign and starts increasing to oppose the changing magnetic field attaining a peak value at C. Now if we reverse the direction of the magnetic field and start increasing it, M again drops to zero at point D. With the decreasing field M again increases in the negative direction to a peak value at point E. Thus we find that even after a full cycle from $+B$ to $-B$, the magnetization does not drop to zero at zero field. Warming of the superconductor to normal state seems to be the only way-out.

Notice that the curve is almost a straight line till a small field ($=B_{c1}$) and then it traverses an irreversible path showing hysteresis. It is seen from Fig. 3.10 that the irreversibility behavior is associated with the hysteresis and the consequent dissipation. It is interesting to note that the curve is not symmetric around the horizontal axis. This asymmetry is caused by the magnetic moments produced by the surface screening currents opposing the flux entry. Area of the hysteresis loop is the measure of the dissipation. The dissipation can be estimated from the area of the loop using the formula:

$$Q_{\text{hys}} = \oint M(B)\mathrm{d}B \tag{3.7}$$

This energy dissipation appears as frictional heat and is caused by the movement of the flux bundles in and out of the conductor. This is important for superconducting magnets in accelerators where the conductor is exposed to time-varying field. Precise calculation of heat generation is thus extremely important to work out the cryogenic refrigeration requirement. Hysteresis is an indication of an effective pinning of flux lines by imperfections which causes sharp increase of critical current density in type II superconductors, making them most suitable for magnet applications.

3.6.2 Bean's Critical-State Model and Magnetization

Superconducting magnets built during initial years during 1960s using hard superconductors performed poorly and quenched at operating currents far below the expected values. Flux jumping was found to be the main reason behind this disappointing performance, which arises because of the magnetization currents penetrating the surface deeper as the external field keeps increasing. The problem was solved in the subsequent years and ingenious techniques were perfected to produce conductors in a particular configuration which show no flux jumping and the magnets perform just as predicted. AC losses in hard superconductors is another problem faced and is a manifestation of the magnetization effects too.

The first phenomenological theory of magnetization was given by Beans [3, 4]. Even though the mixed state is well explained by the vortex structure postulated by

Abrikosov and verified experimentally, Bean assumed a 'filamentary mesh structure' (also referred to as 'Sponge model') postulated by Mendelssohn [5] for the sake of simplified calculations. According to this model the mesh consists of filaments which have diameter less than the London penetration depth. These filaments sustain supercurrent up to a critical current density J_c which is a function of magnetic field and becomes zero at the critical field of the filament. The sponge model is equivalent to a picture of multiply connected internal structure of high critical field material surrounded by a matrix of soft superconductor with low critical magnetic field.

Bean had, however, assumed that the critical current density is independent of the magnetic field which would simply mean that the field is far less than the critical field of the filaments. He also envisaged that the mesh interstices are filled with soft superconductor of critical field B_c which shields the material against the magnetic field up to B_c but the shielding beyond B_c is provided by the magnetizing currents induced in the filaments at a critical value J_c in a depth necessary to reduce the field to B_c. Bean drew the magnetization curve of a virgin hard superconductor cylinder of radius R in a magnetic field parallel to the axis by calculating internal field B_i as a function of external field B_e and the position of the superconductor.

$$4\pi M = \frac{\int_0^v (B_i - B)\mathrm{d}v}{\int_0^v \mathrm{d}v} \tag{3.8}$$

where v is the sample volume. For field less than B_c the shielding will be full if the radius R is much greater than the London penetration depth, that is

$$B_i = 0,\ 0 \le r \le R \text{ and } 0 \le B \le B_c \tag{3.9}$$

For field greater than B_c the soft superconductor surrounding the filaments becomes normal and for higher fields shielding currents are induced in the filaments flowing within a depth D_p, given by the circuital form of Ampere's law

$$D_p = 10\,(B - B_c)/4\pi J_c \tag{3.10}$$

This field dependent and macroscopic penetration depth is an interesting result of this model. Here we can define a new field $B^* = 4\pi J_c R/10$. This step simplifies the analytic expressions and B^* signifies the field that should be applied in excess of the bulk critical field which induces magnetization current to flow throughout the entire sample. Under such condition the penetration depth D_p will simply be equal to R. When all the bulk superconducting characteristics are destroyed, only shielding currents flow through the filaments under different conditions of external field.

$$B_i = B - B^*(1 - r/R); \quad 0 \le r \le R \quad B^* + B_c \le B \tag{3.11}$$

After a few mathematical steps the expressions for magnetization turn out to be

$$\text{(i)} \quad \text{For } 0 \le B \le B_c \quad 4\pi M = -B \tag{3.12}$$

$$\text{(ii)} \quad \text{For } B_c \le B \le B^* + B_c \quad 4\pi M = -B + \frac{\left(B^2 - B_c^2\right)}{B^*} + \frac{\left[B_c^2(3B - 2B_c) - B^*\right]}{3B^{*2}} \tag{3.13}$$

$$\text{(iii)} \quad \text{For } B \ge B^* + B_c \quad 4\pi M = -B^*/3 \tag{3.14}$$

The most striking result of this model is that the magnetization in hard superconductors is dependent on the macroscopic dimension of the sample. Rightly so, because critical current is carried by all the filaments which are proportional to the sample size. There is an excellent fit between the experimental magnetization data on Nb_3Sn specimens and the theoretical calculations.

The essence of Bean's critical state model thus turns out to be (i) that each hard superconductor is characterized by a limiting critical current density $J_c(B)$ and (ii) that any smallest electromotive force induces this full current that flows locally. The consequences of this model are that the regions inside a superconductor not experiencing magnetic field will carry zero current, full current at J_c will flow in regions perpendicular to the field axis. The polarities of the current depend on the polarity of the electromotive force caused by the earlier field change. The field profile in a slab of large dimensions along the Y and Z axes and finite thickness, 2a along the x-axis is shown in Fig. 3.11a for $B = 0$, $B = B^*/2$, $B = B^*$ and $B = 2B^*$. The magnetic field is parallel to the surface. The corresponding critical currents

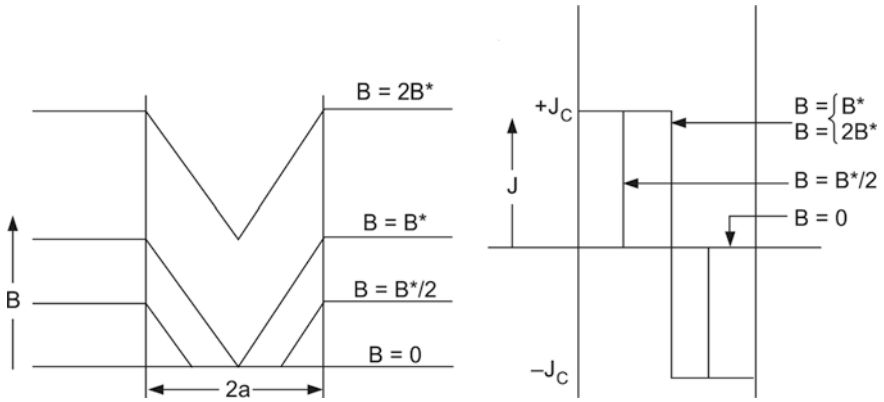

Fig. 3.11 The local field and critical current density configuration in a hard superconductor for increasing external field, $B = 0$. $B = B^*/2$, $B = B^*$ and $B = 2B^*$ in Bean's model. The J_c is assumed independent of field [4]. (With permission from APS) http://journals.aps.org/rmp/abstract/10.1103/RevModPhys.36.31

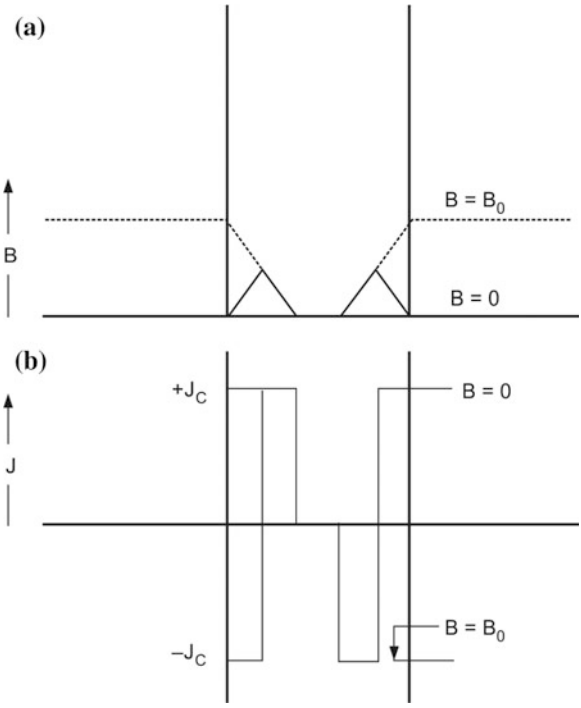

Fig. 3.12 Local fields (**a**) and current density (**b**) configuration in the slab after a field B_0 has been applied and removed [4]. (With permission from APS) http://journals.aps.org/rmp/abstract/10.1103/RevModPhys.36.31

with opposing polarities ($+J_c$ and $-J_c$) for different fields are shown in Fig. 3.11b. It can be noticed that the polarities of the critical currents along the outer and inner surface sheaths on the right and left of the mid-axis are in opposite directions.

Figure 3.12 shows the plots of the local field and critical current density in a slab of hard superconductor after a field B_0 is applied in a virgin state and removed. When the field B_0 is applied it penetrates the slab to a depth determined by the critical current to oppose this field shown in Fig. 3.12a. As we remove the field an electromotive force is generated directed in opposite direction to the one at the time of increasing field. As a result, the surface currents reverse as shown in Fig. 3.12b wherein the two surface sheaths have oppositely directed currents. The remnant flux density or the trapped flux as seen in Fig. 3.12a is exactly half the flux penetration at $B = B_0$.

3.6.3 Kim Model

Kim et al. [6] generalized Bean's critical state model and assumed that the entire region of the superconductor carries critical current which is determined only by the local field in the region. They compared experimental data on a thin walled hollow cylinder with theory. When an increasing external field (along the axis) is applied, currents are induced in the surface to counter the field. As the field keeps increasing

current penetrates the specimen deeper inside, eventually reaching a critical state. Any further increase in the field brings down the critical current density. Based upon their experimental data on hollow Nb-Zr and Nb_3Sn tubes, they postulated that the critical state is a body current in saturation and the concept of critical current applies to each macroscopic part of the sample. This critical current density is unique and a function of local magnetic field only. The state of magnetization can then be determined from this unique $J_c(B)$. A rapid sweep in the magnetic field in critical state generates an electric field which may result in a normal current flow and heating. The heating is found severe in regions where the magnetization curve is steep. This is supported by experiments which indicate that a critical state is difficult to be realized when the magnetization curve is steep. This implies that going from one critical state to another is very difficult unless the heat generated by the normal current is dissipated away fast. If the heat removal is not fast enough, the raise in temperature might quench a part of the superconductor which in turn will generate more heat. Since this additional heat is proportional to M^2, flux jumps have been found frequent in materials with large magnetization. This is the primary reason why the critical state is difficult to be realized in bulk material of large dimensions. Another interesting result of Kim model is that Lorentz force is an important parameter for the determination of the critical current density. They found a simple relationship

$$\alpha(T) = J_{cr}(B + B_0) \tag{3.15}$$

where $\alpha(T)$ and B_0 are constants. Parameter $\alpha(T)$ is strongly dependent on temperature and structure sensitive. The strong temperature dependence of $\alpha(T)$ and the fact that the critical current decays slowly in hard superconductors prompted Anderson [7, 8] to propose the theory of 'flux creep' in these materials.

We will return to the problem of flux jumping in detail in Chap. 6 (Practical Superconductors) and describe how the problem has been solved successfully by providing stability to the conductors carrying several kA current.

3.6.4 Flux Creep

Anderson built up over the critical state model proposed by Bean and modified by Kim and argued that if the critical current J or the field B exceed the critical values in (3.15), flux bundles leak through the material and the material returns to critical state. Flux lines closer than the London penetration depth may be considered bound together via their mutual field interaction and move as flux bundle of dimension $\sim 10^{-5}$–10^{-6} cm. This flux motion has been termed [7] as "flux creep". Anderson gave a theory [7, 8] of flux creep in terms of the thermally activated movement of flux bundle caused by an interplay between the Lorentz force ($J \times B$) and pinning

force. The flux movement is viscous and highly dissipative. Even when the pinning force exceeds the driving force ($FP > FL$), at a finite temperature ($T > 0$ K) the thermal energy associated with the driving force of flux density gradient may force the flux bundles to hop from one pinning centre to another or from one potential well to another potential well. Flux creep is revealed in two ways. One, the trapped magnetic flux shows a slow variation leading to a logarithmic decay [8] of flux with time (t) as

$$\partial B \, \alpha \, k_B T \, \ln(t) \tag{3.16}$$

This creep is unobservably slow unless the flux density gradient is close to the critical value. Second, the flux creep leads to a longitudinal resistive voltages caused by the drifting of the flux bundles under the influence of current flow through the conductor. This voltage is proportional to the average creep velocity of the flux bundle.

The theory of Anderson clearly establishes a marked variation of J_c with temperature in the range of 0.5–0.1 T_c. The movement of flux bundles is blocked at the pinning centres by an energy barrier (potential well). When a field is applied, the flux density in the material is not uniform because of this pinning. In the presence of a transport current the Lorentz force exerts a force on the flux bundles and modify the local free energy which turns the barrier structure spatially 'down hill' direction in a 'stair case' style. The flux bundle jumps over the barrier under thermal excitation at finite temperature below T_c. The bundle jumps at the rate

$$v = v_0 \exp\left[-U(B, T, J)/k_B T\right] \tag{3.17}$$

where v_0 is a characteristic frequency of flux bundle vibration assumed to be 10^5–10^{11} s^{-1} and $U(B, T, J)$ is the activation free energy.

In high T_c oxide superconductors (HTS), to be introduced in the next chapter, the problem of thermally activated flux creep has been found [9–12] to be severe. Several models based upon the classical theory have been developed. Two models, namely, the 'giant flux creep model' [9] and the 'thermally assisted flux flow model' [13] assume the all HTS materials have intrinsically low pinning barriers ($U_0/k_B T_c$) < 10. Here U_0 is the effective pinning potential height and $k_B T_c$ is the thermal energy. The studies have shown that the relaxation is considerably faster in HTS in comparison to the conventional superconductors, though the logarithmic law is followed in both the types of materials. In HTS single crystals, the value of U_0 has been found [9] to be 0.02 eV which is about two orders of magnitude smaller than in conventional metallic superconductors. On the other hand the expected temperature of 77 K for the operation of HTS is high. This makes the height of the pinning barrier ($U_0/k_B T_c$) extremely small which results in 'giant flux creep'. The value of U_0 in practical HTS conductors has been increased significantly by introducing suitable effective pinning centres.

3.6.5 Critical Current by Magnetization

It is possible to calculate critical current density, J_c through the magnetization method using Bean Model [3, 4]. Following expression can be used to calculate J_c from the measured magnetization in increasing and decreasing magnetic field (Fig. 3.13);

$$J_c = 2(M_+ - M_-)/d = 1.59 \times 10^6 \mu_0 \Delta M/d \tag{3.16}$$

where J_c is in A/m^2, $\mu_0 \Delta M = \mu_0(M_+ - M_-)$ is in tesla and d is the diameter of the sample grain in meters. The equation in cgs units reduces to;

$$J_c = 30\Delta M/d \left(\mathrm{A/cm^2}\right) \tag{3.17}$$

where d is in cm.

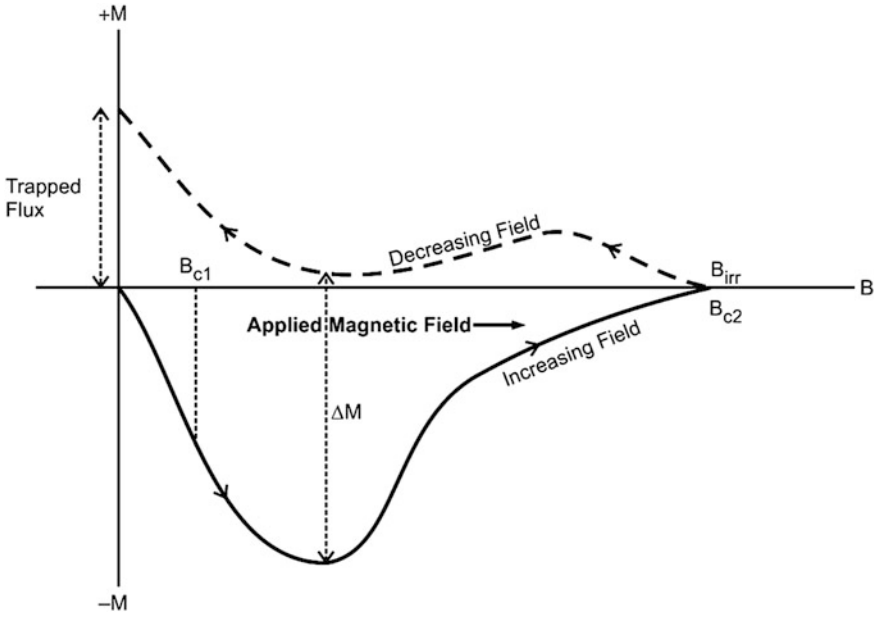

Fig. 3.13 A typical *M–B* plot of a inhomogeneous type II superconductor. J_c can be calculated from the measured ΔM value using the expression (3.17)

3.7 Surface Superconductivity—Critical Magnetic Field B_{c3}

St James and de Gennes [14] in 1963 deduced theoretically that in a finite size superconducting specimen superconductivity exists close to the surface of the superconductor in contact with a dielectric, including vacuum in field higher than B_{c2}. This new critical field is termed as B_{c3} which is 1.695 times B_{c2}. The bulk material though is normal. This superconducting surface layer is found to occur in superconductors with $\kappa > 0.42$ and usually in type II superconductors. B_{c3} depends upon the angle the applied field makes with the surface. It has a maximum value if the field happens to be parallel to the surface and is given by

$$B_{c3} = 2.4\kappa B_c = 1.7\ B_{c2} \tag{3.18}$$

B_{c3} decreases with the angle and is minimum when the applied field is perpendicular to the surface. B_{c3}(min) reduces to B_{c2} for type II superconductors. An indicative magnetic phase diagram (B-κ plots) incorporating B_c, B_{c1}, B_{c2} and B_{c3} has been shown in Fig. 3.14. A type II superconductor now has superconducting state, mixed state, surface superconductivity and the normal state at different field values. Since surface superconductivity occurs for materials with $\kappa > 0.41$ the

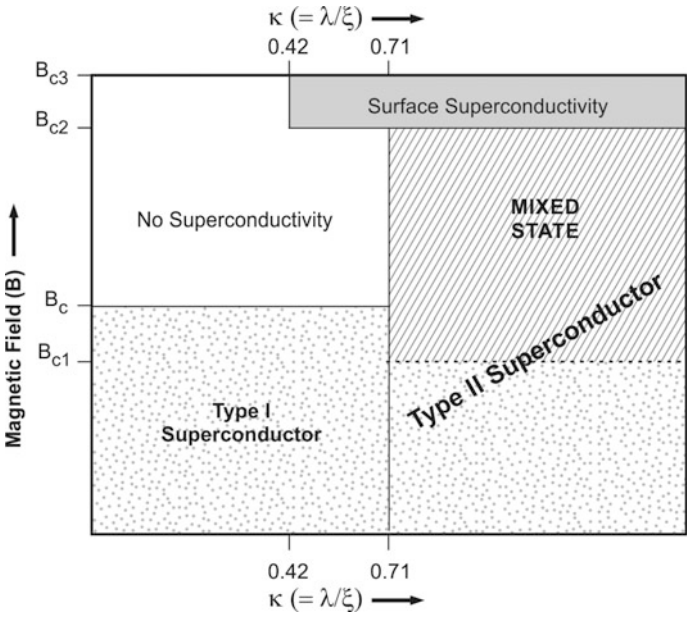

Fig. 3.14 An indicative magnetic phase diagram of a superconductor in contact with a dielectric, showing B-κ plots for B_c, B_{c1}, B_{c2}, and B_{c3} and the existence of surface superconductivity for $\kappa > 0.42$

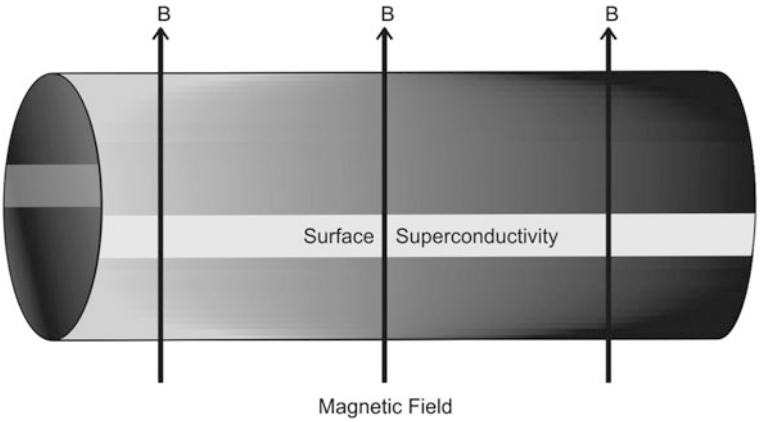

Fig. 3.15 For perpendicular field greater than B_{c2} surface superconductivity reduces to *two strips* parallel to the two sides of the specimen

phenomenon is observed even in Type I superconductors. For example, in Pb, κ increases from 0.37 (at T_c = 7.3 K) to a value of 0.58 at $T < 1.4$ K and surface superconductivity is indeed observed. Surface superconductivity is observed at the interface of the material and a dielectric (or vacuum). Surface superconductivity does not occur at the interface of the superconductor and a metal. So, no surface superconductivity is observed if a type II superconductor is coated with metal. For field higher than B_{c2} the surface layer shrinks to two strips along the length of the specimen. Close to B_{c3} these strips reduce to just two lines where the field happens to be parallel to the surface (Fig. 3.15).

3.8 Paramagnetic Limit

B_{c2} in type II though is high and still increases at reduced temperatures but cannot be increased indefinitely, even if κ too is made high. In fact, the B_{c2} of the best known superconductor is limited to a value much smaller than the predicted one. In high magnetic field the electron spins tend to align themselves along the direction of the field. This lowers the magnetic energy considerably which is not conducive to superconductivity which envisages anti parallel spins to form Cooper pairs. At high enough field it may be energetically favourable for the material to go to normal paramagnetic state rather than remaining in a superconducting state. Experimentally the highest value of B_{c2} has been found limited to what is known as the paramagnetically limited field, $B_p = 1.6 \times 10^6\ T_c$ (A m^{-1}) beyond which superconductivity does not exist, irrespective of how large is the value of κ.

References

1. A.A. Abrikosov, Zh. Eksperim. i. Fiz. **32**, 1442 (1957); Sov. Phys.—JETP. **5**, 1174 (1957)
2. A.C. Rose-Innes, E.H. Rhoderidz, *Introduction to Superconductivity*. Copyright © 1969, Pergamon Press, Library of Congress Catalog Card No. 79-78591
3. C.P. Bean, Phys. Rev. Lett. **8**, 250 (1962)
4. C.P. Bean, Rev. Mod. Phys. **36**, 31 (1964)
5. K. Mendelssohn, Proc. Roy. Soc. (London) **A152**, 34 (1935)
6. Y.B. Kim, C.F. Hemstead, A.R. Strnad, phys. Rev. **129**, 528 (1963)
7. P.W. Anderson, Phys. Rev. Lett. **9**, 309 (1962)
8. P.W. Anderson, Y.B. Kim, Rev. Modern Phys. **36**, 39 (1964)
9. Y. Yashurun, A.P. Malozemoff, Phys. Rev. Lett. **60**, 2202 (1988)
10. T.T.M. Palstra, B. Batlogg, L.F. Schneermeyer, J.V. Waszczak, Phys. Rev. Lett. **61**, 1662 (1988)
11. D. Shi, M, XuA. Umezawa and R.F. Fox. Phys. Rev. **B42**, 2026 (1990)
12. Y. Yashrun, A.P. Malozemoff, T.K. Warthington et al., Cryogenics **29**, 258 (1989)
13. P.S. Kes, J. Aarts, J. van der Berg et al., Supercond. Sci. Technol. **1**, 242 (1989)
14. D. Saint, James and P.G. de Gennes. Phys. Lett. **7**, 306 (1963)

Chapter 4
High Temperature Cuprate Superconductors and Later Discoveries

Abstract The discovery of superconductivity at 30 K in an oxygen deficient $La_4Ba_1Cu_5O_{5(3-y)}$ compound by Bednorz and Muller in 1986 lifted the despondency under which the superconductivity community was reeling since 1973 when highest $T_c = 23$ K was recorded in sputtered Nb_3Ge films and T_c went no further. Chu raised T_c of this compound to 40 K by applying pressure and Cava to 36 K after substituting Sr at the La-site. A breakthrough came in early 1987 when Wu and Chu announced a record $T_c = 93$ K in $Y_1Ba_2\ Cu_3\ O_7$. T_c thus crossed the 77 K mark first time. Soon Maeda discovered superconductivity at 110 K in another cuprate of the type $Bi_2Sr_2Ca_2Cu_3O_{10}$ (Bi-2223 with 3 CuO_2 layers). T_c thus increases with the number of CuO_2 layers but not beyond three layers. These layered curates have large anisotropy. The superconductivity is strong in the *a-b* planes (CuO_2 layers) and weak along the *c*-axis. Critical parameters B_{c2} and J_c too are high in the *a-b* plane and low along *c*-direction. Both the materials, Bi-2223 and YBCO are produced commercially and used for selected applications. The new improved 2G-YBCO wires are coated multilayered thin film conductors produced by employing sophisticated techniques and getting popularity among the community. Two more cuprates with still higher T_c and analogous to Bi-system were discovered. A $T_c = 125$ in $Tl_2Ca_2Ba_2Cu_3O_x$ (Ti-2223) and 135 K in $Hg_1Ba_2Ca_2Cu_3O_{6+\delta}$ (Hg-1223) were reported. These materials were, however, not pursued for commercial production because of the toxicity involved. Superconductivity was also found in 2001 in MgB_2 at 39 K, easily attainable with the use of a cryo-cooler. Besides, the material is quite cheap. MgB_2 has two energy gaps and appears to be a BCS superconductor. It is being produced commercially now. The chapter also reviews all the discoveries that took place in 2008 onwards. Hosano reported superconductivity in iron based oxy-pnictides of the type LaFeAsO(1111) around 25 K. T_c in excess of 50 K were reported in Sm and Nd based pnictides. The strategy adopted to enhance T_c has been to dope the insulating La_2O_2 layer suitably whereby a charge, electron/hole is transferred to the Fe_2As_2 conduction layer. Thus a $T_c = 38$ K was reported in a K-doped $(Ba_{0.6}K_{0.4})\ Fe_2As_2$ compound. Very strange behavior of the appearance, disappearance and re-appearance of superconductivity with increasing pressure was announced in an

R.G. Sharma, *Superconductivity*, Springer Series in Materials Science 214,
DOI 10.1007/978-3-319-13713-1_4

iron-chalcogenide, $Tl_{0.6}Rb_{0.4}Fe_{1.67}Se_2$ hinting at the possibility of two different types of superconducting phases appearing at different pressures. A maximum T_c = 48 K was obtained in this material at a pressure of 12.4 GPa.

4.1 Discoveries of High T_c Cuprate Superconductors: Discovery of Superconductivity in La–Ba–Cu–O System (T_c = 35 K)

The search for superconductivity among the elements in the periodical table, in alloys and compounds continued unabated after the discovery of this fascinating phenomenon. Superconductivity was indeed discovered in a variety of families (listed in Table 4.1) but the T_c still remained confined to low value, necessitating the use of liquid helium for operation. The highest T_c was obtained in 1973–1974 in thin films of Nb_3Ge by Gavaler [1] and Tastardi et al. [2] by optimizing the deposition parameters. There was a lull for next 12 years until in 1986 all of a sudden, something very unusual happened. Two research scientists at IBM, Zűrich, namely, Bednorz and Muller discovered [3] superconductivity at 30 K in an oxide compound of the type $La_{5-x}Ba_xCu_5O_{5(3-y)}$. The compound was prepared by co-precipitation of the nitrates of La, Ba and Cu taken in appropriate ratios. This was followed by the solid state reaction at 900 °C in a reduced atmosphere. Samples were finally prepared in the form of pellets sintered at 900 °C. The resistivity behaviour of these samples is shown in Fig. 4.1. Clearly, the resistivity drops with the fall of temperature nearly linearly, then rises logarithmically and then drops sharply by three orders of magnitude. The onset transition temperature is 30 K. Three phases were detected in the material. (i) a cubic phase dependent upon Ba composition, (ii) a superconducting phase $La_{1.8}Ba_{0.2}$ CuO_4 and a third (iii) Perovskite layered phase of the type K_2NiF_4 with a = 3.79 Å and c = 13.2 Å. The resistivity was found to be changing with measuring sample current indicating that the superconductivity is granular in nature. The material turns out to be an O^{2-} deficient phase with mixed valence Cu constituents, namely Jahn-Teller ions Cu^{2+} and non Jahn-Teller ions Cu^{3+} resulting in a large λ (the electron-phonon coupling parameter) and large metallic conductivity. The ideal perovskite La_2CuO_4 structure shown in Fig. 4.2 is orthorhombic at room temperature and becomes tetragonal at 500 K. Pure La_2CuO_4 is insulating and antiferromagnetic with a Neel temperature of 290 K. Ba and Sr substitute at La sites and the compound $La_{2-x}M_xCuO_4$ shows a T_c of 35 K at M = 0.15 and 0.2 for Ba and Sr respectively. The doped material has a tetragonal structure at room temperature and turns orthorhombic at 180 K. It was not the first time that superconductivity was observed in oxides. As early as 1973, Johnston et al. [4] reported superconductivity in a Li–Ti–O system with a T_c = 13.7 K. The X-ray analysis showed the presence of three crystallographic phases. One phase with a spinel structure had the highest T_c with a comparatively

Table 4.1 Different families of superconductors with corresponding T_c values (most values from [8], with permission from R.P. Aloysius)

Sr no.	Type of superconductor	Example	Max. T_c (K)
1	Pure elements	Nb	9.2
2	Transition metal alloys	MoRe	12
3	Carbides	NbC	11
4	Nitrides	NbN	15
5	Amorphous superconductors	VGa	8.4
6	Nitrocarbides	$NbN_{0.7}C_{0.3}$	18
7	Laves phase (C-15 structure)	$CeRu_2$	6.1
8	Cheveral phase	$PbMo_6S_8$	12–14
9	A-15 (β-Tungsten)	Nb_3Sn–Nb_3Ge	18–23
10	Organic superconductors	$(TMTSF)_2PF_6$	1 (at 12 kbar)
11	Intercalated superconductors	$TaS_2(C_5H_5N)_{1/2}$	3.5
12	Heavy fermionic superconductors	UPt_3–$CeCoIn_5$	0.48–2.3
13	Magnetic superconductors	$ErRh_4B_4$	8.6
14	Semi-metal superconductors	La_3Se_4	10
15	First oxide superconductors	$BiPb_{1-x}Bi_xO_3$	13 (x = 0.25)
16	K-doped Ba–Bi oxide, supercond.	$(Ba_{0.6}K_{0.4})BiO_3$	31.5
17	Boro-carbides	YNi_2B_2C	15
18	Rare earth cuperates	$YBa_2Cu_3O_{7-\delta}$	92
19	Lanthenate (discovery of high T_c superconductor)	$La_{5-x}Ba_xCu_5O_{5(3-y)}$	35
20	Bismuth oxide superconductors (Bi-2223)	$Bi_{1.7}Pb_{0.4}Sr_{1.8}Ca_2Cu_{3.5}O_y$	110
21	Mercury oxide superconductors (Hg-1223)	$HgBa_2Ca_2Cu_3O_{8+\delta}$	155 (15 GPa)
22	Thallium oxide superconductors (Tl-2223)	$Tl_2Ca_2Ba_2Cu_3O_x$	125
23	Fullerides	Rb_2C_{60}	45
24	Magnesium diboride	MgB_2	39
25	Iron pnictides	$NdFeAsO_{0.82}F_{0.18}$	51
26	F-doped La–Fe–As compounds	$NdFeAsO_{0.82}F_{0.18}$	55 K
27	Iron chalcogenides	$Tl_{0.6}Rb_{0.4}Fe_{1.67}Se_2$	33

low carrier concentration of n = 2–4 × 10^{21}/cm^3. Soon after Sleight et al. [5] reported a T_c = 13 K in a mixed valence Ba $Pb_{1-x}Bi_xO_3$ system which also has a perovskite structure. Strong electron phonon coupling was believed to be responsible for superconductivity. Prior to the discovery by Bednorz and Muller, scientists had almost given-up hopes of achieving high T_c in superconductors under the belief of the theoretical predictions made around the time. On the basis of the BCS theory even with highest values of the electron density of state and the electron-phonon coupling parameter, the T_c would not go beyond 30 K. What happened after the publication of the celebrated paper by Bednorz and Muller was something

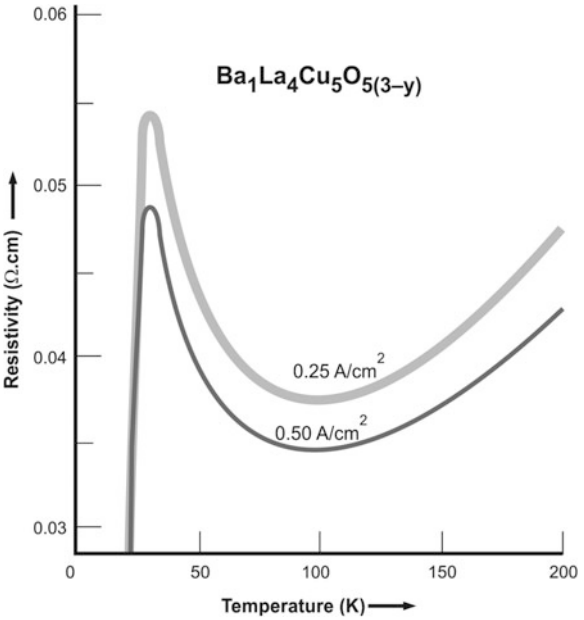

Fig. 4.1 Electrical resistivity plotted against temperature for the compound $Ba_1La_4Cu_5O_{5(3-y)}$. Superconducting transition occurs at $\sim$30 K and the resistivity shows variation with measuring current [3] (With kind permission of Springer Science+Business Media)

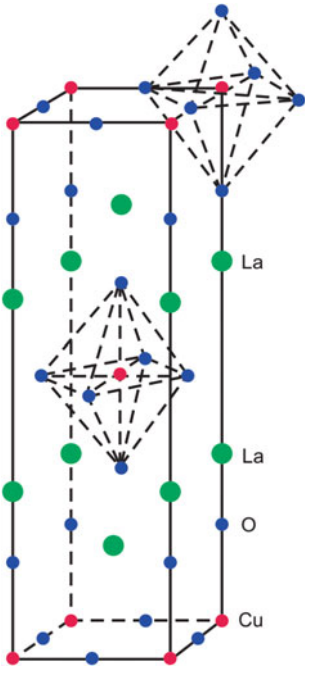

Fig. 4.2 The ideal La_2CuO_4 (K_2NiF_4) crystal structure. Superconductivity sets in with Ba/Sr substitution at the La site

unprecedented and quite unexpected. Superconductivity was reported in oxide systems one after another with higher and higher transition temperature, climbing well above the liquid nitrogen temperature (77 K). Within a couple of years T_c rose to as high as 150 K making the T_c/Year graph rising almost exponentially (Fig. 4.3).

Chu et al. [6] at the university of Houston raised the T_c of the compound $(La_{0.85}Ba_{0.15})_2CuO_{4-y}$ from 36 K at ambient pressure to 40 K after applying a pressure of 13 kbar. Cava et al. [7] on the other hand partially replaced La by Strontium (smaller ion) replicating chemical pressure. The compound studied had the chemical composition $La_{1.8}Sr_{0.2}CuO_4$. Undoped La_2CuO_4 structure is slightly orthorhombic distortion of K_2NiF_4, all the copper ions are in Cu^{2+} state and no superconductivity is observed down to 4.2 K. Substitution of La by Sr stabilizes tetragonal undistorted K_2NiF_4 and oxidizes some Cu to Cu^{3+} state resulting in a mixed valence compound. The compound had been annealed in air as well as in oxygen [7]. Sample annealed in air reveals the presence of a mixture of a metallic phase, a semiconducting phase and a superconducting phase. Oxygen anneal on the other hand leads to a metallic and a superconducting phase. Oxygen anneal also improves the onset T_c from 36.5 to 38.5 K. Thus Sr and oxygen both are important for the oxidizing condition. Oxygen pressure influences Cu^{3+}/Cu^{2+} valence ratio as well as charge compensation by O-vacancies.

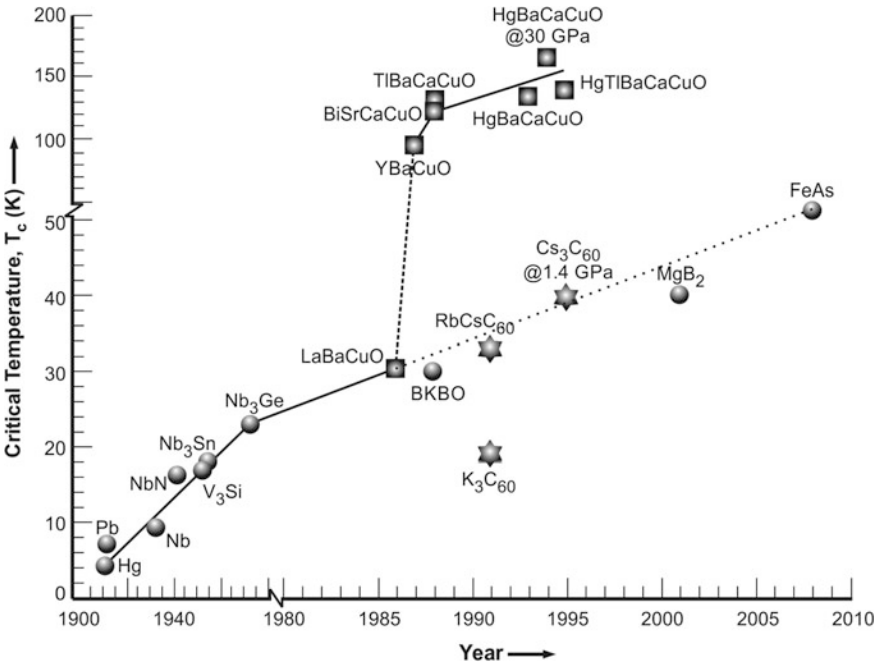

Fig. 4.3 Transition temperatures of important elements, alloys and compounds plotted against the year of their discovery. The *curve* rose sharply in 1986 when high T_c cuprates were discovered

The discovery of superconductivity by Bednorz and Műller in an oxide system opened the flood gate to the discovery of a larger family of oxide systems containing copper. Many superconductors containing Cu–O layers, now called cuprates with higher and higher T_c values rising far above the boiling temperature of nitrogen, 77 K were discovered. This evoked great excitement among the scientific community of all shades who hoped that an engineering revolution will soon take place where the conventional superconductors used in large scale applications will be replaced by these oxide superconductors. Although the hope of using these superconductors at 77 K for producing high magnetic fields is yet to be realized, yet selected cuprates have been produced commercially and are being increasingly used in a variety of power applications where high current densities in presence of high magnetic field are not required. They have nevertheless been found suitable for high field production, when operated below 65 K. A vast family of cuprate superconductors is tabulated along with their T_c values in Table 4.2.

Below we briefly discuss the discovery of important superconductors which surpassed the T_c of the previous superconductors.

4.2 The Y–Ba–Cu–O (YBCO) System—First Superconductor with T_c Above 77 K

A real breakthrough occurred in the history of superconductivity in March 1987 when Wu et al. [9] discovered superconductivity in a $Y_1Ba_2Cu_3O_{7-x}$ (or simply YBCO or also called just Y123) system at 93 K making it possible first time to cool down a superconductor below its T_c using liquid nitrogen instead of liquid helium. Figure 4.4 shows the resistivity—temperature plots at different magnetic field reported by Wu et al. [9]. The superconducting phase was identified to be $Y_1Ba_2Cu_3O_7$ which is an oxygen deficient triplet perovskite unit cell of the type ABO_3. The triplet cell would have been $(Y_1Ba_2)Cu_3O_9$ but the superconducting phase is oxygen deficient that is, $Y_1Ba_2Cu_3O_7$ and has a T_c = 93 K. $Y_1Ba_2Cu_3O_7$ has an orthorhombic distorted structure and is shown in Fig. 4.5. Clearly Cu ion has two distinct crystallographic and dissimilar sites Cu(1) and Cu(2). Cu(1) is surrounded by a squashed square planar O configuration in the *b*-*c* plane and linked to similar sites in a one dimension along the *b*-axis. Cu(2) site is 5 coordinated by a square pyramidal arrangement of O. The vertex of the pyramid is at O(4) site along the *c*-axis. The Y ion is at the centre of the two Cu–O sheets eight O-coordinated and Ba ten O-coordinated. We thus find that Cu–O network is important for cuprates. Cu(1)–O(1) chains are crucial to superconductivity in this material. Cu(2)–O(2)/O(3) do not seem to be so crucial for 90 K transition. Cu(1)–O(4) bond is much stronger than Cu(1)–O(1), bond lengths being 1.85 and 1.943 Å respectively. Oxygen vacancies occur in O(1) sites easily which

Table 4.2 A large variety of cuprate superconductors with their T_c values

Sr. no.	Compound	T_c (K)
1	$La_{1.85}(Ba/Sr)_{0.15}CuO_4$	35
2	$La_2CuO_{4+\delta}$	45
3	$La_{1.6}Sr_{0.4}CaCu_2O_{6+\delta}$	60
4	$Y_1Ba_2Cu_3O_7$	92
5	$Y_1Ba_2Cu_3O_8$	82
6	$TlBa_2Ca_{n-1}Cu_nO_{2n+3}$	120 (n = 3)
7	$TlBa_2Ca_{n-1}Cu_nO_{2n+4}$	127 (n = 3)
8	$Bi_2Sr_2Ca_{n-1}Cu_nO_{2n+4}$	110 (n = 3)
9	$HgBa_2Ca_{n-1}Cu_nO_{2n+2+\delta}$	134 (n = 3)
10	$CuBa_2Ca_{n-1}Cu_nO_7$	120
11	$Sr_2Ca_{n-1}Cu_nO_4$	90
12	$Pb_2Sr_2(Ca, Y, Nd)Cu_3O_8$	70
13	$Pb_2(Sr, La)_2Cu_2O_6$	32
14	$PbBaSrYCu_3O_8$	50
15	$(Pb, Cu)(Ba, Sr)_2(Y, Ca)Cu_2O_7$	53
16	$Pb_{0.5}Sr_{2.5}(Y, Ca)Cu_2O_7$	104
17	$(Pb, Cu)(Sr, La)_2CuO_5$	32
18	$(Nd, Ce)_2CuO_{4-\delta}$	24
19	$(Nd, Ce, Sr)CuO_{4-\delta}$	28
20	$(Pb, Cu, Eu, Ce)_2(Sr, Eu)_2Cu_2O_9$	25
21	$(EuCe)_2(Ba, Eu)_2Cu_3O_{10}$	43
22	$Bi_2Sr_2(Gd, Ce)_2Cu_2(CO_3)O_7$	34
23	$Tl_{0.5}Pb_{0.5}Sr_4Cu_2(CO_3)O_7$	70
24	$(BaSr)_2CuO_2(CO_3)$	40
25	$Sr_{4-x}Ba_xTlCu_2(CO_3)O_7$	62
26	$Tl_{0.5}Pb_{0.5}Sr_2Gd_{2-x}Ce_xCu_2O_{9-\delta}$	45
27	$NbSr_2(Gd, Ce)_2Cu_2O_y$	27
28	$Bi_2Sr_{6-x}Cu_3O_{10}(CO_3)_2$	40
29	$(Cu_{0.5}C_{0.5})Ba_2Ca_{n-1}Cu_nO_{2n+3}$	117 (n = 4)
30	$YCaBa_4Cu_5(NO_3)_{0.3}(CO_3)_{0.7}O_{11}$	82
31	$CuSr_{2-x}La_xYCu_2O_7$	60
32	$GaSr_2Ln_{1-x}Ca_xCu_2O_7$	73
33	$(C_{0.35}Cu_{0.65})$ $Sr_2(Y_{0.73}Ce_{0.27})_2Cu_2O_x$	18
34	$Bi_4Sr_4CaCu_3O_{14+x}$	84

n represents the number of CuO_2 layers in the compound (data from [8], with permission from R.P. Aloysius)

brings down the transition temperature. At stoichiometric O_7, copper exists in divalent and trivalent state as per the expression below:

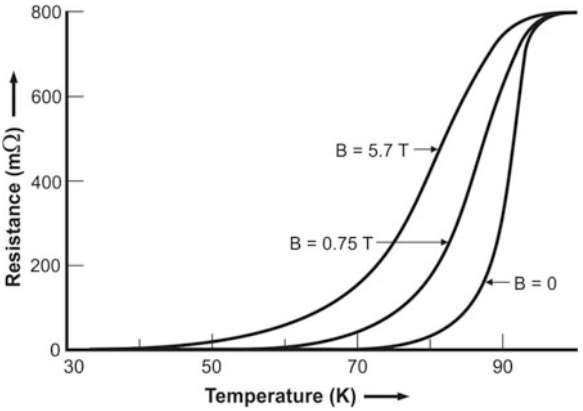

Fig. 4.4 Resistivity/temperature plot of Y–Ba–Cu–O at different magnetic fields by Wu et al. [9]. (With permission from APS) http://journals.aps.org/prl/abstract/10.1103/PhysRevLett.58.908

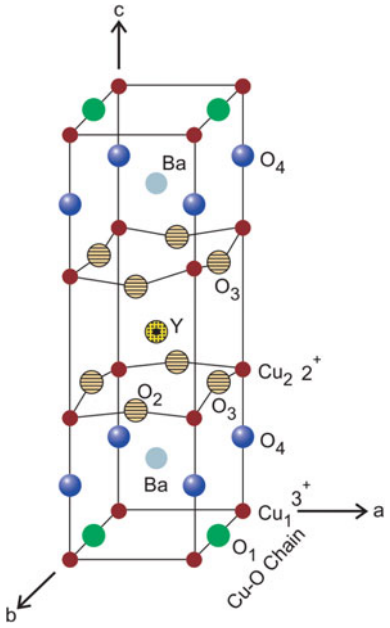

Fig. 4.5 Crystal structure of $Y_1Ba_2Cu_3O_7$. Notice two Cu–O sheets in the *a*–*b* plane sandwiching Y-atom and the Cu–O chains along the *b*-axis

$$\text{At } O_7 \qquad Y_1Ba_2Cu_3O_7 = Y^{3+}Ba_2^{2+}Cu^{3+}(1)Cu_2^{2+}(2)O_7^{2-} \qquad (4.1)$$

Oxygen depletion leads to change in structure from orthorhombic to tetragonal. T_c starts decreasing with oxygen loss and so does the oxidation state of Cu. As O content decreases from 7 to 6.5, T_c decreases from 93 to 55 K and Cu(1) and Cu(2) are in divalent state. At $O = 6.5$ the material becomes semiconducting. In fact there is a plateau in the T_c versus O-content curve at $O_{6.5}$. As O-content decreases further, T_c decreases too and at $O = 6$, the material turns into an insulator. The oxidation

state of Cu reduces to univalent. The oxidation states of Cu at O_6 and $O_{6.5}$ can be expressed like this:

$$\text{At } O_{6.5} \qquad Y_1Ba_2Cu_3O_{6.5} = Y^{3+}Ba_2{}^{2+}Cu^{2+}(1)Cu_2{}^{2+}(2)O_{6.5}{}^{2-} \tag{4.2}$$

$$\text{At } O_6 \qquad Y_1Ba_2Cu_3O_6 = Y^{3+}Ba_2{}^{2+}Cu^{1+}(1)Cu_2{}^{2+}(2)O_6{}^{2-} \tag{4.3}$$

There is a striking correlation between the T_c and the oxidation state of Cu. T_c is found to be maximum when the oxidation state of Cu is $^{+}2.2$ which is found to correspond to O_7 stoichiometry. Both T_c and the copper oxidation state scales with the oxygen stoichiometry almost identically as seen from Fig. 4.6. T_c thus seems to be strongly dependent on the valence state of Cu which is controlled by the oxygen stoichiometry. One can explain this correlation between the valence state and T_c on the basis of the so-called charge transfer model. A detailed crystal structure of YBCO system, a repeat unit cell, is shown in Fig. 4.7. The CuO_2 planes sandwiching the Y-atom constitute the conduction layers. These double CuO_2 planes are separated by the so called charge reservoir or the intercalating layers which consists of metal-oxygen layers of Cu, Ba and oxygen. Many cuprate superconductors have been discovered by manipulating the number of CuO_2 planes, metal atoms in the charge reservoir layer and crystal structure. Quite a few of these cuprates are tabulated along with their T_c values in Table 4.2. YBCO has two Cu-atoms per unit cell in the conduction layer and one Cu-atom in charge transfer layer forming Cu–O chains. A reduction of O from 7 to 6 leads to equal distribution of O along the a and b-axes and the structure changes from orthorhombic to tetragonal. The tetragonal phase is not superconducting. Holes are created in the conduction layers as the electrons are transferred to charge reservoir layers. This changes the oxidation state of Cu to optimum value ($Cu^{+2.2}$) in the conduction layer causing the material to turn superconducting.

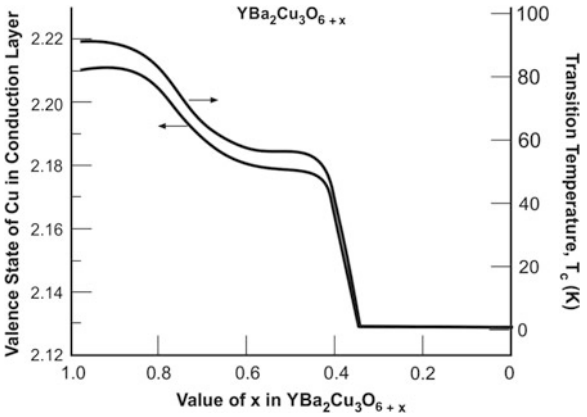

Fig. 4.6 T_c and the valence state of Cu in YBCO plotted against O-contents. T_c decreases as the oxygen content decreases from 7 to 6. Note the similarity in the two *curves*. Highest T_c occurs at $Cu^{+2.2}$ (from my lecture-notes, original data source could not be traced)

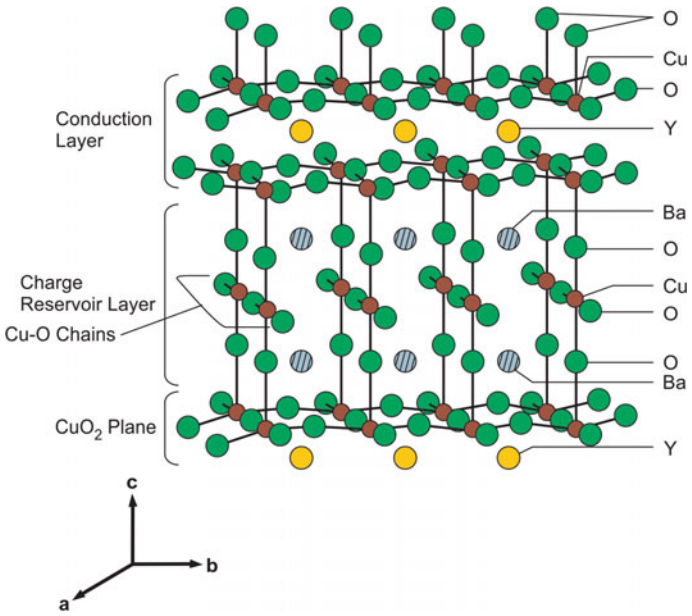

Fig. 4.7 A repeat unit cell structure of $Y_1Ba_2Cu_3O_{7-x}$. The CuO_2 planes on either side of Y-atom are the conduction layers and the Cu–O chains and the Ba–O planes constitute the charge reservoir layers

Even though YBCO remains to be the most studied and developed system, yet Y can be replaced by almost all the rare earth elements except Pr and Cs yielding this 123 compound with a T_c = 90 K. Even the magnetic material Gd yields Gd123 superconductor with T_c = 90 K.

4.2.1 Method of Synthesis of YBCO

The most popular technique for synthesizing Y123 is the standard technique of solid state diffusion [10]. Appropriate quantities of Y_2O_3, $BaCO_3$ and CuO, as per the formula unit $Y_1Ba_2Cu_3O_{7-x}$ are mixed thoroughly and ground in a pestle mortar. The fine powder so prepared is calcined at around 900 °C for about 20 h. This powder is finely crushed and calcined again. This process is repeated about three times when a homogenous mixture is obtained. The powder is now pressed into the form of a pellet or a bar and sintered at 920 °C for 20–25 h under flowing oxygen. Pieces of desired dimensions can now be cut from this pellet for different types of measurements. It is important to cool the sample slowly from the sintering temperature to have the stoichiometric oxygen (O_7) in the compound. Our experience shows around 60 °C/h. cooling rate is optimum [11]. Fast cooling changes the orthogonal phase into the tetragonal phase and makes the material non

superconducting. Target pellets are also prepared for thin film deposition following this method. Adequate oxygen supply during the sintering process is essential to get oxygen stoichiometry to 7.0. This becomes rather difficult while supplying oxygen to Ag-clad wires. The author has used successfully an addition of HgO to the bulk YBCO before calcinations which provides an internal source of oxygen [12–14]. A perfect O_7 stoichiometry has been obtained using this technique.

4.2.2 Some Peculiar Properties of YBCO

These cuprate superconductors are highly anisotropic materials and have widely different characteristic parameters and properties in the *a-b* plane and along the *c*-axis. Amongst the family of cuprates YBCO is, however the least anisotropic. A well oxygenated stoichiometric YBCO superconductor, for example, has the following typical parameters (Table 4.3).

Another peculiar property observed in these cuprates was the linear variation of the normal state resistivity with temperature down to T_c. Even though normal metals have linear ρ–T at higher temperature ($\sim\theta_D$) and $\rho\ \alpha\ T^5$ at low temperatures. The linear ρ–T behaviour in these compounds cannot be explained on the basis of electron-phonon interaction since the mean free path ($\sim$100–200 Å) is much greater than the lattice parameter ($\sim$3.8 Å).

4.2.3 YBCO Wires and Tapes

High hopes were generated, first time, to use this material for high field superconducting magnets and operate them at 77 K but the results were disappointing. The critical current in bulk YBCO superconductor drops down sharply with the application of magnetic field for a variety of reasons. One important reason is that

Table 4.3 Typical parameters of a stoichiometric $Y_1Ba_2Cu_3O_7$ in the *a-b* plane and along the *c*-axis

Parameter	$Y_1Ba_2Cu_3O_7$
Critical temperature, T_c (K)	93 K
Lattice parameters	a = 3.8591 Å
	b = 3.9195 Å
	c = 11.8431 Å
Coherence length (0 K)	$\xi_{ab}(0)$ = 15 Å
	$\xi_c(0)$ = 3 Å
London penetration depth	$\lambda_{ab}(0)$ = 1,400 Å
	$\lambda_c(0)$ = 7,000 Å
Normal state resistivity	ρ_{ab} = 0.5 m Ω cm and metallic
	ρ_c = 20 m Ω cm and semiconducting

these materials happen to be grainulus [10, 15] with grain boundaries which are weakly superconducting or even insulating. High critical current densities have however been reported in epitaxially grown YBCO films [16] and in YBCO single crystals [17]. This resulted in high expectation of developing this material with high critical current densities needed for high field applications. The critical current within the grain has been found to be quite high $\sim 10^6$ A cm^{-2} at 77 K. After a few years of intensive research, the focus of R&D activity shifted from research laboratories to industry for their commercial production. American Superconductors, Furukawa, SuperPower and Sumitomo are some leading companies marketing HTS wires, tapes and current leads. 2G YBCO or rather 2G REBCO coated conductors are increasingly used for power devices like FCL (fault current limiter), transformer and rotating machine. The fabrication techniques employed to produce these materials will be discussed in Chap. 6 titled 'Practical Superconductors'.

4.3 The Bi–Sr–Ca–Cu–O (BSCCO) System

Soon after the discovery of superconductivity in YBCO system at 93 K, Maeda et al. [18] reported superconductivity above 100 K in a Bi–Sr–Ca–Cu–O system, first high T_c material without a rare earth element. Figure 4.8 shows the version of the original curve of the resistance versus temperature behaviour of this compound which happens to be a multi phase superconductor. This was the first observation made by Maeda's group on 24th Dec 1987. An onset of superconducting transition was observed at 114 K with a tendency to go to zero resistivity at 105 K. A second transition is observed showing zero resistivity at 80 K. Their initial attempts to isolate

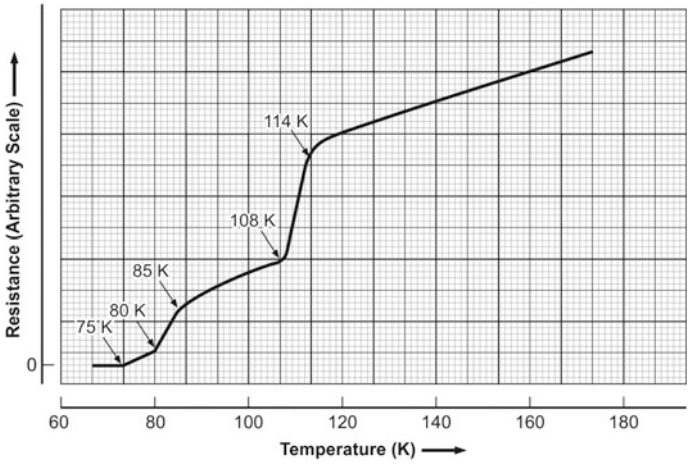

Fig. 4.8 Replicated original resistance versus temperature plot of Bi–Sr–Ca–Cu–O by Maeda et al. The *curve* shows multiple superconducting transitions at 114, 108 and 85 K [18]

the high T_c phase failed and they announced the discovery on Jan 21, 1988. Takano et al. [19] however succeeded in stabilizing the high T_c phase (=110 K) through the partial substitution of Bi by Pb. Further studies established the coexistence of three distinct crystallographic phases, namely the $Bi(Pb)_2Sr_2Ca_2Cu_3O_x$ phase, $Bi_2Sr_2Ca_1Cu_2O_y$ phase and $Bi_2Sr_2CuO_z$ or simply referred to as Bi-2223, Bi-2212, and Bi-2201 phases with T_c values of 110, 80 and 10 K respectively. In our laboratory we have been obtaining phase pure Bi-2223 material by solid state and also by solution technique with a T_c of 110 K. Best results have been obtained on nominal composition like $Bi_{1.6}Pb_{0.4}Sr_2Ca_{2.2}Cu_{3.5}O_y$ [20] and $Bi_{1.7}Pb_{0.4}Sr_{1.8}Ca_2Cu_{3.5}O_y$ [21] which are rich in Ca and Cu and deficient in Sr. These Bi-cuprates have orthorhombic structure, have Cu–O layers separated by Sr–O and Ca–O layers and two double Bi–O layers at the two ends of the unit cell. As seen from Fig. 4.9 the *c*-axis increases with the number of Cu–O layers. The *c*-axis is 24.6 Å for the 2201 phase, 30.89 Å for 2212 phase and 37.1 Å for the 2223 phase. There is one Cu–O layer in the 2201 phase, two Cu–O layers in 2212 phase and three Cu–O layers in the 2223 phase. It appears T_c goes up as the number of Cu–O layers increase. T_c has however been found decreasing if the number of layers increases beyond three. Crystals of Bi-cuprates have mica like morphology.

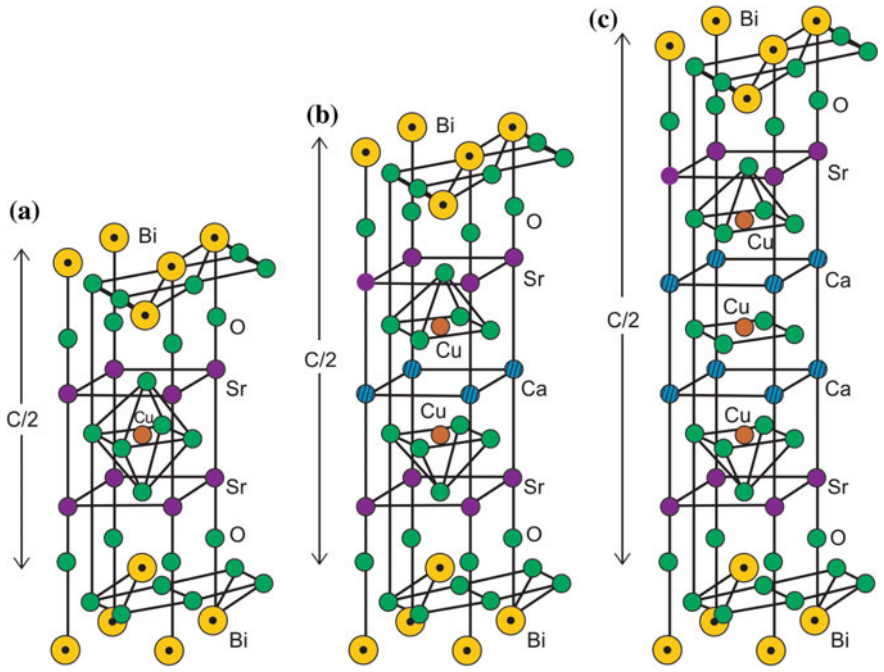

Fig. 4.9 The unit cells of the three Bi-compounds with compositions 2201, 2212 and 2223 having one, two and three Cu–O layers and increasing *c*-axis value respectively. **a** 2201 $Bi_2Sr_2Cu_1O_6$ (semiconductor phase) C = 24.6 Å, **b** 2212 $Bi_2Sr_2Ca_1Cu_2O_8$ (low T_c phase) C = 30.89 Å, **c** 2223 $Bi_2Sr_2Ca_2Cu_3O_{10}$ (high T_c phase) C = 37.1 Å

The 80 K Bi-2212 compound show modulation in the *ab* plane structure with 4b periodicity. The modulation is related to oxygen content and the Bi–O layers but does not play role in superconductivity. Inter-growth of the phases is a problem in the synthesis of Bi compounds. Some times this intergrowth has been found [21, 22] to provide effective flux pinning enhancing critical current density, J_c in Bi-2223 system.

4.3.1 Bi-2223 Wires and Tapes

Until the recent arrival of 2G, YBCO wires, Bi-2223 was the only material which has been commercially produced and used in applications like magnets, current leads high gradient magnetic separators, fault current limiters and the likes. Bi-2223 had been the favorite high T_c material for manufacturing because one needs to use a simple PIT technique followed by mechanical drawing, rolling and re-bundling with intermediate heat treatments. Typical cross section of a circular wire and a rectangular tape with multifilaments are shown in Fig. 4.10. Another more subtle reason is that the *c*-axis grain alignment can easily be achieved when shaped into the form of tapes. Grain alignment is achieved during the rolling process when compressive stress forces the plate like Bi-2223 grains to align parallel to the tape surface. Weak link problem is thus minimized in this material. Bi-2212 on the other hand needs heat treatment of the partially melted material followed by solidification after the tape forming to get the grain alignment. NRIM (now NIMS) together with Asahi Glass and Hitachi Cable Group in Japan produced a field of 21.8 T at 1.8 K by using a Bi-2212 coil [23] as the inner most insert. A back ground field of 18 T was provided by a combination of Nb–Ti and Nb_3Sn coils. The tapes were fabricated following the doctor-blade technique.

The problem with high T_c material is that the critical current density, J_c in these materials drops rather sharply in increased magnetic field when operated at high temperature, 77 K. This is primarily due to the weak pinning at these temperatures and the large anisotropy of J_c. Both are caused by the 2D nature of the structure of BSCCO system. The CuO_2 layers where the superconductivity resides, are separated by weakly superconducting or non superconducting oxide layers. When a

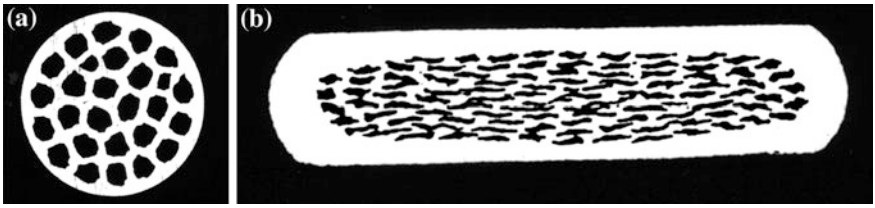

Fig. 4.10 Cross-section of the multifilamentary Ag/B(P)SCCO wires (**a**) and tapes (**b**) [8] (*Courtesy* R.P. Aloysius)

magnetic field is applied parallel to the layers (along the *ab*-plane), vortices pass through the weakly superconducting layers (charge transfer layers) but CuO_2 layers prevent the vortex movement in the perpendicular direction. This is the new type of pinning force called 'intrinsic pinning' [24]. BSCCO tapes in parallel field configuration can thus be used even at 77 K and still carry significant current. In field parallel to *c*-axis the vortex is divided into segments by non superconducting layers because of extremely small coherence length along this axis. This segment is referred to as 'pancake vortex' [25] and is confined within the CuO_2 layer and free to move because it is not strongly connected with the vortex in the next layer. In our initial studies on MF Ag/BSCCO tapes [21] we found a variety of impurity induced defects which probably served good pinning centres in a low purity commercial (CuO 99 %) grade material tapes. Figure 4.11a shows dislocation network in a (001) basal plane in a Ag/BSCCO-2223 tape with a core thickness of 140 μm. The same tape is further rolled to small thickness where the core thickness is reduced to 7 μm. As shown in Fig. 4.11b the dislocation density increases and improves the flux pinning. The dislocation network corresponds to the low-angle grain boundaries. The J_c value of the 7 μm (b) sample is 6.14×10^3 A cm^{-2} (77 K, self field) and 1.49×10^5 A cm^{-2} (4.2 K, self field). Yet another type of defect structure observed in the (b) sample is the intergrowth of the two phases viz; the low T_c (2212) and the high T_c (2223) phase with a *c*-axis parameters of 30.89 and 37.1 Å respectively. The J_c value after the rolling and re-sintering process is found to increase substantially. The commercial grade CuO (99 %) was found to have 60 ppm Fe which preferentially occupies the Cu(II) square pyramidal site as revealed by Mössbauer studies. This results in stacking faults and the intergrowth of the 2212 and 2223 phases (Fig. 4.12). These defects can be expected to provide effective flux pinning sites and raise J_c, as observed experimentally.

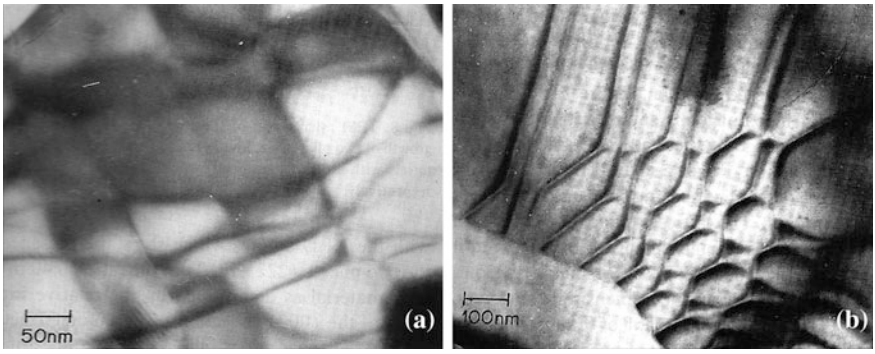

Fig. 4.11 Transmission Electron Micrographs of the core material of a Ag/BSCCO-2223 tape prepared using commercial grade oxides and carbonates. **a** is a tape with 140 μm thick core and shows dislocation network in (001) basal plane. **b** is the same tape rolled down to a core thickness of 7 μm and re-sintered. The density of dislocation increases in (**b**) sample. The dislocation network corresponds to the low angle twist grain boundaries. J_c too increases [21] (With permission from Elsevier)

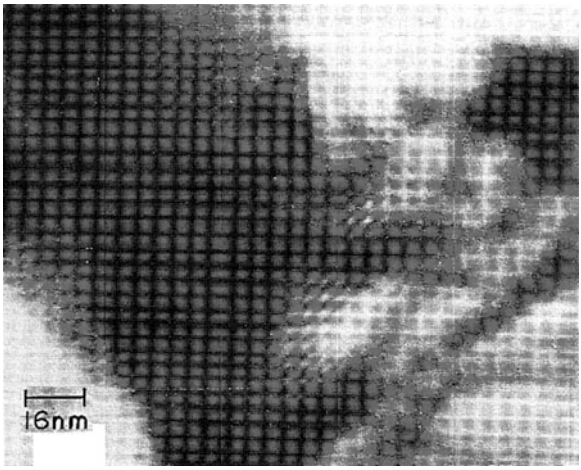

Fig. 4.12 TEM micrograph of (**b**) sample of Ag/BSCCO-2223 tape, rolled to fine size (7 μm core) and re-sintered which shows the intergrowth of low T_c (2212) and high T_c (2223) phases [21] (With permission from Elsevier)

Among several manufacturers of the Ag/BSCCO wire, American Superconductors (AMSC) of USA and Sumitomo Electric Company (SEC) of Japan were the main players supplying this material for different applications. AMSC mainly supplied two types of wires. One code named 1G-HSP HTS (high strength plus HTS wire) meant for applications where high mechanical strength was required. This wire had BSCCO-based multifilaments (MF) and was encased in a Ag-alloy matrix with a SS lamination. Typically, the wire thickness was 0.26 mm, width 4.2 mm and a room temperature maximum tensile stress of 200 MPa which goes up to 250 MPa at 77 K. The wire had a maximum tensile strain of 0.4 % and an engineering current density, J_c of 13.3×10^3 A cm^{-2} (77 K and self field). The second type of MF BSCCO wire with high current density too was encased in a Ag-alloy matrix. This wire was 0.22 mm thick, 4.0 mm wide, had a maximum RT tensile strength of 65 MPa and a maximum tensile strain of 0.1 %. Maximum I_c was 155 A which corresponds to a $J_c = 17.2 \times 10^3$ A cm^{-2} (77 K and self field). The wire length available was 800 m. AMSC has now stopped producing this material and has switched over to 2G YBCO wires already discussed in Sect. 4.2.3. The BSCCO conductor now receded to background is now referred to as G-1 (first generation) high T_c superconductor. We will present the present status of 2G REBCO conductors in Chap. 6 on "Practical Superconductors".

SEC of Japan had been marketing Ag-matrix clad BSCCO wires in 2 km lengths under the code name DI-BSCCO wires [26]. DI here means Dramatically Innovative CT-OP (controlled over pressure sintering) process. Sintering is carried out under a gas pressure (partially oxygen) of 30 MPa. The wire has an excellent J_c behaviour up to a field of 10 T. The wire carries an I_c of 218 A (1 mm^2). The wires are laminated with either SS or brass as per the strength requirement. Wires with 50 μm SS lamination can withstand a stress of 400 MPa.

4.3.2 First Generation (1G)-BSCCO Current Leads

One most popular use of HTS had been in current leads employed in superconducting magnets both bath-cooled and conduction-cooled. The (1G) BSCCO current leads capable of transporting current in excess of 3,000 A have been commercially marketed for decades now. 'Can Superconductors' of Czech Republic, American Superconductors of USA and Bruker Energy and Supercon Technologies are some of the suppliers of these current leads. Current leads are generally used to transport current from 77 K thermal shield to magnet maintained at ~4 K with no Joule heating. Moreover, the thermal conduction through the leads too is poor which makes the magnet system energy efficient. Current carrying capacity almost doubles if the higher temperature end is kept at around 64 K instead of 77 K. Typically, a current lead with I_c = 1,500 A between 77 and 4 K has a conductive heat leak of 0.6 W, whereas if used between 64 and 4 K the heat leak reduces to only 0.4 W. Current leads can be bulk tube type or encased for protection (Fig. 4.13). Copper studs or copper braids are provided for jointing/soldering purpose. Figure 4.14 is a 100 A pair of BSCCO-2223 current leads developed [8] by the NIIT, Trivandrum. The development of BSCCO current leads made it possible to build cryo-free superconducting magnets which found popularity in low temperature laboratories in last two decades. The reduction in heat generation in the current leads had been so significant that a closed cycle refrigerator (CCR) with a cooling capacity of 1.5 W can cool a large size magnets to ~3 K in a reasonable time of few hours. Chap. 7 will discuss the construction of such a cryo-free magnet with a special reference to a 6 T room temperature bore magnet built in author's laboratory using a 1.5 W CCR of Sumitomo make some years ago.

Fig. 4.13 Bulk and encased current leads marketed by M/S 'Can Superconductors' and used in author's lab (IUAC Delhi)

Fig. 4.14 A pair of 100 A, BSCCO-2223 current leads developed by NIIST, Trivandrum. Leads with higher current rating available [8] (*Courtesy* R.P. Aloysius)

4.4 The Tl–Ba–Ca–Cu–O System

The race to discover still higher T_c superconductors continued and yet one more cuprate superconductor of the type Tl–Ba–Ca–Cu–O with T_c of greater than 90 K was discovered by Sheng and Hermann [27] in 1988 itself. The zero resistivity in this compound was obtained at 81 K. Soon a T_c of 120 K was reported by the same authors [28] in a compound $Tl_{1.86}CaBaCu_3O_{7.5+y}$. This was the highest T_c cuprate without a rare earth constituent. Since Tl_2O_3, the ingredient of the compound has a low melting point of 717 °C and starts decomposing at 100 °C, the preparation method for this compound is different. Sheng and Hermann have followed a 'short high temperature and quenching technique'. Appropriate amounts of $BaCO_3$ and CuO were mixed, ground and heated to 925 °C for >24 h in air with several intermediate grindings. Black compound like $BaCu_3O_4$ or $Ba_2Cu_3O_5$ are formed during this process. Right amount of Tl_2O_3 was then added, pressed into a pellet and kept in a tubular furnace already heated to about 900 °C under flowing oxygen. The pellet was kept for 2–5 min and quenched in air to room temperature and used for studies.

Still higher T_c of 125 K was reported [29] in quick succession in the same compound with stoichiometry $Tl_2Ca_2Ba_2Cu_3O_x$ (Tl-2223) quite analogous to Bi-2223 compound. The unit cell of this compound is bcc tetragonal containing three Cu perovskite like units separated by bilayers of TlO. T_c ranges between 118 and 125 K depending on the preparation parameters. Another compound with composition $Tl_2Ba_2Ca_1Cu_2O_x$(2212) is a bulk superconductor with T_c = 95–108 K. This compound has two Cu perovskite units similar to Bi-2212 compound.

Figure 4.15 shows how T_c increases with the number of CuO layers from one to three. Tl compounds can be expressed with the general formula $Tl_2Ba_2Ca_{n-1}Cu_nO_{2n+4}$ and are tetragonal with two Tl–O layers and n Cu–O layers. T_c values are 80, 110 and 125 K for three compounds with n = 1, 2 and 3 respectively. T_c is found increasing with the increase of Cu–O layers only up to n = 3. T_c decreases for n > 3. Tl being a toxic material, no attempts have been made to produce this material either on a laboratory scale or on a commercial scale for applications.

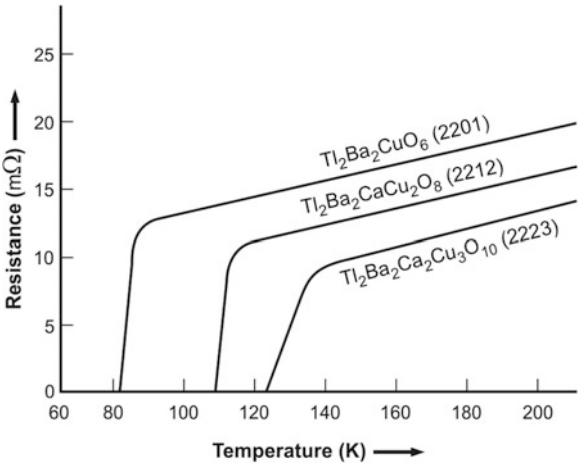

Fig. 4.15 Superconducting transition in three compositions of Tl compounds viz; 2201, 2212 and 2223. T_c increases with the number of Cu perovskite units 1, 2 and 3 respectively

4.5 The Hg–Ba–Ca–Cu–O System

After a lull of about 5 years, once again a new superconductor was discovered with T_c of 94 K by Putillin et al. [30] in a compound, $HgBa_2CuO_{4+y}$ or simply called Hg-1201 (as Ca is absent). This is very high T_c in contrast to the similar Tl-1201 compound which has a T_c of <10 K. This compound has one Cu–O_2 sheet. Mercury compounds can in general be described by a formula of the type $HgBa_2Ca_{n-1}Cu_nO_{2n+2+y}$ where n can take different values starting from 1 onwards. Soon superconductivity was discovered at 130 K by Schilling et al. [31] in a multiphase Hg-compound with $n = 1, 2$ and 3. Soon the pure phase $HgBa_2Ca_2Cu_3O_{8+\delta}$ was synthesized with $n = 3$ and a $T_c = 135$ K was obtained. The unit cell structure of the three Hg-compounds with $n = 1$, 2 and 3 are shown in Fig. 4.16. Evidently c-axis increases with the number of CuO_2 layers. Analogous to Tl-system Hg-system too has a tetragonal structure with 'a' and 'c' parameters as given in the figure. An enhancement in T_c with pressure in copper containing superconductors with hole conductivity is well known. Chu et al. [32] reported a T_c of 153 K for the compound $HgBa_2Ca_2Cu_3O_{8+\delta}$(1223) at a pressure of 150 kbar. In a systematic study Gao et al. [33] found continuous increase in T_c of all the Hg-compound(1201, 1212 and 1223) up to a pressure of 45 GPa, viz; 164 K for 1223, 154 K for 1212 and 118 K for the compound 1201. T_c values with increasing pressure for Hg-compounds with $N = 1, 2, 3$ and 4 are plotted in Fig. 4.17 [34]. In all the compounds T_c increases with pressure and tend to saturate at high pressure. It has been conjectured that it may be possible to get T_c values as high as 164 K under ambient pressure in optimally doped compounds through substitution if the Cu–O distances can stabilize.

Synthesis of Hg-compound is little complicated because of the toxicity of Hg and decomposition of HgO into Hg and oxygen at comparative low temperature

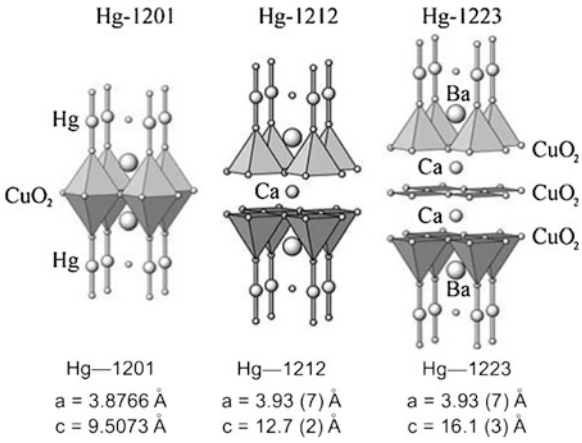

Fig. 4.16 Unit cell structure of $HgBa_2CuO_{4+\delta}$(1201), $HgBa_2Ca_1Cu_2O_{6+\delta}$(1212) and $HgBa_2Ca_2Cu_3O_{8+\delta}$(1223) with one, two and three CuO_2 layers respectively [34] (With permission from IOP)

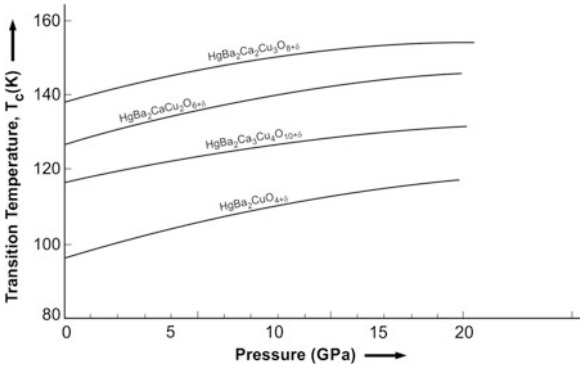

Fig. 4.17 T_c increases with pressure for Hg-compounds and with the number of CuO_2 layers up to $n = 3$. T_c decreases with pressure for compound Hg-1234 ($n = 4$). T_c is thus highest for Hg-1223 ($n = 3$) [34] (With permission from IOP)

(430 °C). Samples are prepared in sealed quartz ampoules, and of either platinum or gold containers to prevent reaction. The synthesis is a two-step process. In the first step stoichiometric mixture of barium carbonate (oxalate, nitrate or oxide), copper and calcium oxides is prepared and annealed at 600–1,000 °C in air, Oxygen flow or vacuum. The precursor so prepared is extremely hydroscopic and absorb CO_2 fast. All the operations are therefore carried out in a dry box. HgO is then added to the mixture and sealed in an ampoule for further annealing. T_c of these compounds has been found extremely sensitive to the presence of carbon and steps should therefore be taken to avoid carbon contents in the starting materials. An excellent topical review on the structure and synthesis of Hg-compounds has been written by Antipov et al. [34] on Hg-compounds. As far as the commercial production of

cuprates is concerned, Bi-2223 had been the most favoured materials for magnet based applications and the current leads until recently. Hg-compound wires and tapes have not been exploited for commercial production or applications.

4.6 Discovery of Superconductivity in Magnesium Diboride (MgB_2)

Nature surprised us yet again when Nagamatsu et al. [35] reported the discovery of superconductivity at 39 K in magnesium diboride, MgB_2 outside the cuprate family. This material had been known to us since early 1950s but not as a superconductor. Figure 4.18a shows the original magnetic susceptibility versus temperature curves for MgB_2 by Nagamatsu et al. [35] under zero-field cooled (ZFC) and field cooled (FC) conditions. Figure 4.18b on the other hand shows the electrical resistivity behaviour with temperature. Both the measurements give a sharp superconducting transition at 39 K. In fact, interest had been growing to look for superconductivity in intermetallic compounds with light elements like boron since 1994 when superconductivity was discovered in borocarbides [36, 37] These materials are of the type RE-Tm_2B_2C where RE is a rare earth such as Y, Lu, Er, Dy, Tm is Ni or Pd. The study of these materials had been of interest because of high T_c observed among the intermetallics (e.g. T_c = 23 K in YPd_2C), the unique anisotropic layered structure and an interplay between superconductivity and magnetism.

Excitement to exploit MgB_2 for applications grew for a variety of reasons. It is a cheap material compared to HTS cuprates where Ag constitutes almost 70 %, it has low anisotropy in its superconducting properties and T_c is in the range when one can operate MgB_2-based systems using close cycle refrigerators thus doing away with the use of liquid helium. We will therefore discuss this material a little more in

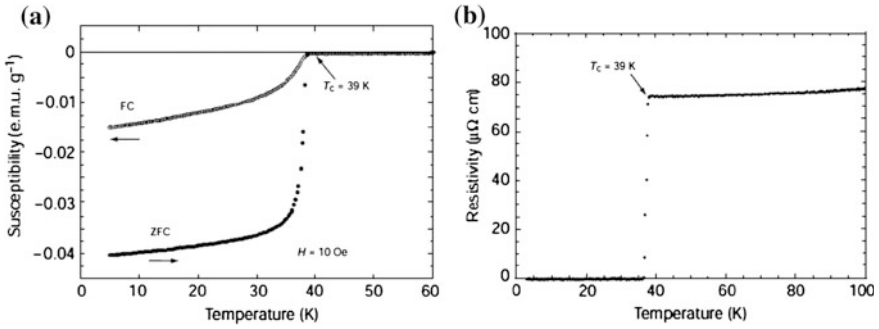

Fig. 4.18 **a** Magnetic susceptibility of MgB_2 under zero field (ZFC) and field cooled (FC) conditions plotted against temperature, **b** The electrical resistivity variation with temperature of MgB_2 both the measurements show a sharp superconducting transition at 39 K [35] (With permission from Nature Publishing Group)

detail. Search for similar diborides with comparable T_c turned out to be futile. Superconductivity was indeed found in niobium diborides (NbB_2) but with T_c (0.62 K), disappointingly low.

4.6.1 The Crystal Structure and the Origin of Superconductivity in MgB_2

MgB_2 is metallic and has a layered hexagonal structure [38]. The B atoms form a graphite like honeycombed layers and the magnesium atoms occupy the centre of the hexagons in between the boron planes as shown in Fig. 4.19. MgB_2 is quite similar to conventional metallic superconductors except that it has high T_c, remains metallic all through unlike the cuprates which are insulator without doping. It has nevertheless one dissimilarity with them in so far as MgB_2 is characterized by two energy gaps. This indicates that it has two different species of electrons with different kinds of bonding forming pairs and leading to superconductivity. Choi et al. [38] for the first time carried out calculations from the first principle and obtained numerical values of the two energy gaps and their effects on the measurable parameters. These authors have been able to account for the high T_c, the anomalous specific heat versus temperature behaviour and for the isotopic substitution. The observed isotope effect also led them to believe that the pairing is mediated via the

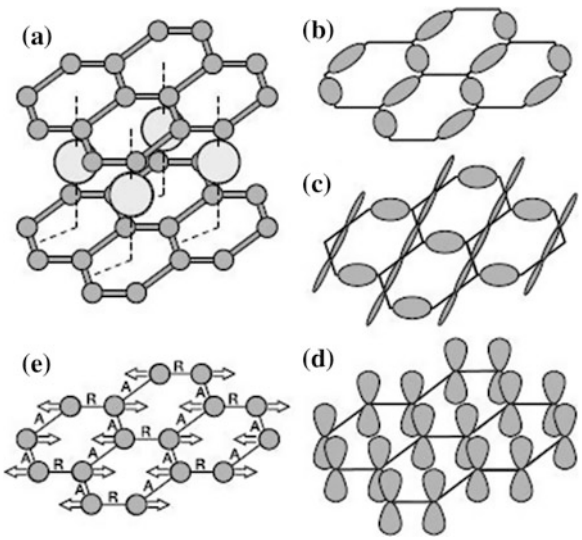

Fig. 4.19 Crystal structure of MgB_2 [38]. **a** The crystal structure of MgB_2, **b**, **c** σ-bonding states of the Fermi level derived from boron p_{xy} orbitals, **d** a π-bonding state of the Fermi level derived from boron p_z orbitals, **e** a vibrational mode of boron atoms that couples to σ-bonding electronic states at the Fermi level (With permission from Nature Publishing Group)

lattice vibrations and the superconductor is of BCS type. An important feature of their analysis is that the electronic states formed by the orbitals in the boron plane interact strongly with the specific phonon modes leading to pair formation and the superconductivity.

The authors have used Eliasberg approach of strong coupling superconductivity based upon the BCS theory. Their argument is that the electronic states at the Fermi level are mainly either σ or π-bonding boron orbitals. σ-bonding states resides within the boron planes. The σ-bonding states couple rather strongly with the in-plane vibrations of the boron atoms. This coupling leads to strong electron-pair formation of the σ-bonding states resulting in the appearance of an average energy gap of 6.8 MeV. This strong pairing in the boron planes, occupying the Fermi surface only partially is believed to be the main source of superconductivity. π-bonding states residing on the remaining part of the Fermi surface, on the other hand, form much weaker pairs with an average energy gap of 1.8 MeV. This pairing too can become stronger by coupling with the σ-bonding states. These average values of two energy gaps are found to be consistent with the experimental values. The calculated energy gaps-temperature variation is plotted in Fig. 4.20. As seen in the figure the large energy gap corresponding to σ-bonding states drops with the increase of temperature and quite fast close to T_c as compared to the smaller energy gap for the π-bonding states. Both the energy gaps merge and vanish at T_c, despite having very different values at low temperature.

The experimental energy gap parameters fit well with the calculated values and follow a temperature variation given by the equation of the type:

$$\delta(T) = \delta(0)[1 - (T/T_c)^p]^{\frac{1}{2}} \tag{4.4}$$

where $p = 2.9$ for the larger gap for the σ-bonding states and $p = 1.8$ for the smaller gap for the π-bonding states. This temperature dependence of the energy gaps has been verified by experimental data on tunneling, optical and specific heat

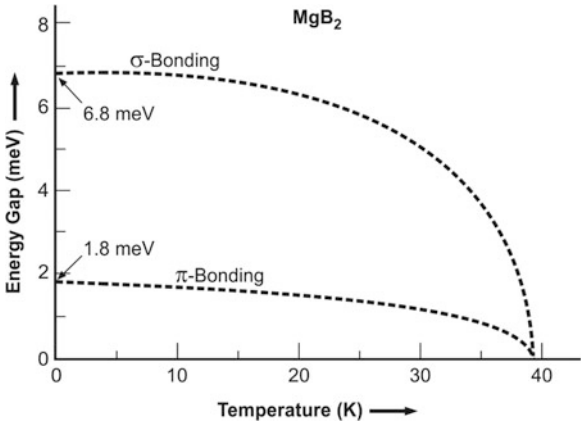

Fig. 4.20 The calculated average superconducting energy gap parameters plotted against temperature. Both the gaps merge and become zero at T_c [38] (With permission from Nature Publishing Group)

measurements. There is overwhelming evidence that MgB_2 is a BCS type superconductor with an intermediate to strong s-wave coupling. The existence of pairs with charge 2 e too has been established through ac and dc Josephson effect [39] studied on break junctions of MgB_2. Extensive studies have been carried out on almost all aspects of this material and a very large number of papers have been published. A few comprehensive reviews [40–42] have already been published on MgB_2 system. Nevertheless, we review in next section some important properties and related studies carried out on MgB_2.

4.6.2 A Summery of Studies on MgB_2

4.6.2.1 Preparation of Bulk MgB_2 and Fabrication of Wires/Tapes

Magnesium diboride is commercially available from chemical suppliers but the purity has to be ascertained. In the laboratory MgB_2 has been synthesized in various forms such as polycrystalline bulk, single crystal, thin film, wires and tapes following different techniques. Nagamatsu et al. [35] had prepared the first MgB_2 sample by the solid state reaction method. Appropriate quantities of Mg and B in the ratio 2:1 were mixed, ground and pressed in pallet form. The pellet was heated to 973 K under 196 MPa argon pressure using a hot isostatic pressing furnace for 10 h. The material can also be synthesized under ambient in an inert atmosphere. One can prepare bulk MgB_2 in a sealed ampoule to prevent the loss of Mg because of its volatile nature. Single crystals of the size $1.5 \times 0.9 \times 0.2$ mm^3 and weighing up to 230 μg have been grown [43] at high pressure through the peritectic decomposition of MgB_2. The single crystals have a T_c in the range of 37–39 K.

Methods followed to deposit MgB_2 film, are co-evaporation, pulse laser deposition (PLD), magnetron sputtering, deposition from suspension and Mg diffusion. Films have been deposited on a variety of substrates such as, SiC, Si, $LaAlO_3$, $SrTiO_3$, MgO, Al_2O_3 and SS. The choice of substrate is thus very wide because perhaps the hexagonal structure of MgB_2 can grow on a variety of substrates with different lattice parameters. The volatility of Mg has to be kept in mind. Target for sputtering therefore has to be kept Mg rich. Bulk MgB_2 is also prepared in a sealed ampoules for the same reason. Mg-diffusion technique (diffusion of Mg in B) has proved to be the best technique, be it bulk, films or wires.

For magnet coils we need superconducting material in the form of stabilized multifilamentary wire or a tape. Two methods are available to prepare the material in this form. One is the coating technique and the other PIT (powder-in-tube) technique. In the first technique, a moving ribbon mostly hastelloy is coated with MgB_2. Komori et al. [44] prepared MgB_2 tapes on hastelloy with a $J_c = 1.1 \times 10^5$ A/cm^2 at 4.2 K and 10 T field. H_{c2} as high as 55 T and an irreversible field of 40 T has been reported by Ferrando et al. [45] in a carbon alloyed MgB_2 coated conductor by a hybrid physical-chemical vapour deposition technique.

The coating technique discussed above though provides tapes with superior quality, nevertheless is not an ideal technique to produce long lengths (several km). PIT is a viable and preferred technique for commercial production. In this technique well prepared fine powder is packed at a high density in a metal tube and rolled/drawn to fine size of wires or tapes in a series of steps of rolling and intermediate annealing to maintain ductility. The sheath material should be such that it does not react with the core material and provides sufficient mechanical strength to the composite wire/tape. Copper has to be incorporated some how in the cross section of the wire/tape to provide thermal stability to the superconductor. Several metals such as Fe, Mo, Nb, Ta, Hf, W, Cu, Ag, Cu–Ni and SS have been used for cladding with varying degree of performance. The starting core material can be either preformed MgB_2 or a mixture of Mg and B in right proportion. In the later case a heat reaction at 900–1,000 °C is required so as to form stoichiometric MgB_2 core. High temperature treatment is not needed [46] in the case of preformed MgB_2. Stoichiometry, however, improves with heat treatment after the drawing process. Kumakura et al. [47] reported $J_c = 10^4$ A cm^{-2} at 4.2 K and 5 T values in a single core and a 7-core MgB_2 tapes fabricated using PIT technique with SS and Cu–Ni sheath material (Fig. 4.21). No heat treatment was carried out. The higher value of J_c for SS sheathed tape is achieved because of the higher packing density attainable. SS also provides higher mechanical strength. Feng et al. [48] prepared 1 mm dia. wires by PIT technique using 1020 Fe-sheath and following a wind and react method. Annealing was done under Ar atmosphere at a temperature of 850 °C for 30 min. They report a J_c value of 1×10^4 A cm^{-2} (4.2 K, 6 T) and 1.8×10^5 A cm^{-2} (20 K, 0 T). Fe, Ni and SS turn out

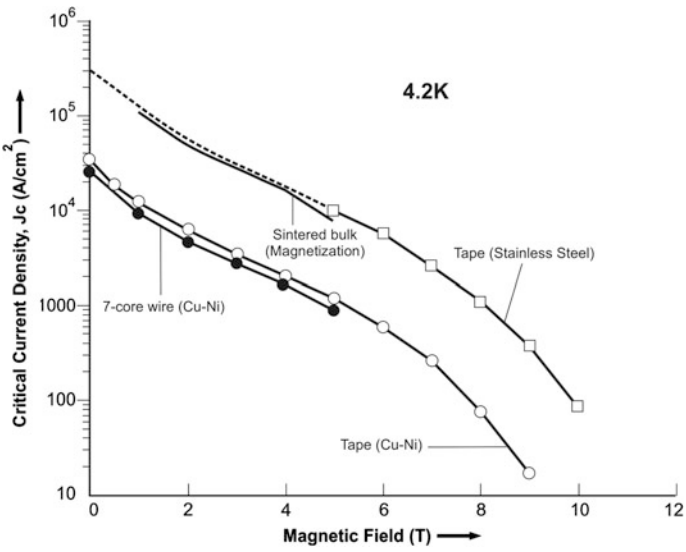

Fig. 4.21 Transport J_c versus magnetic field plots for Cu–Ni sheathed mono-core tape and Cu–Ni sheathed 7-core wire and SS sheathed mono-core tape at 4.2 K [47]. Reproduced with permission AIP Publishing LLC

to be the most suitable cladding materials. Copper has to be used with Nb or Ta barrier for thermal stability.

Sumption et al. [49] developed 7, 19 and 37 filament MgB_2 wires following the ex situ route. In some sample 30 μm size particles and in some samples excess Mg was incorporated. Single step heat treatment at 700–800 °C for 10–30 min was given. All the wires used either Nb or Fe as filament barrier. Filament size ranges between 80 and 150 μm. A $J_c = 1.75 \times 10^5$ A cm^{-2} (4.2 K, 5 T) has been achieved. At 20 K the intrinsic J_c appears to be reaching 10^6 A cm^{-2}. All these studies auger well for the potential application of MgB_2 superconducting wires for magnets operating with close cycle refrigerators.

4.6.2.2 Some Physical Properties of MgB_2

We briefly describe some physical properties and interesting studies that have been carried out on this material.

The Hall effect measurements [50] on MgB_2 single crystal reveal that it has two types of charge carriers, holes in the plane and electrons along the *c*-axis. There is anisotropy in electrical resistivity along the plane and in the perpendicular direction which turns out $\rho_c/\rho_{ab} = 3.5$. Normal state Hall coefficient is positive in plane (*B*//*c*, *I*//*ab*) and negative in the out-of-plane (*B*//*ab*, *I*//*c*) confirming that the electronic structure of MgB_2 is multi-band.

MgB_2 shows isotope effect quite convincingly confirming the phonon mediated Cooper pair formation in this material. Bud'ko et al. [51] through magnetization and specific heat measurements find a shift of T_c by 1 K in $Mg^{11}B$ and $Mg^{10}B$ prepared with two isotopes of B. The T_c values obtained are 39.2 and 40.2 K for the two intermetallics respectively. Conventional BCS superconductors follow the relation $T_c\ \alpha\ M^{-\alpha}$ where the isotopic exponent, α turns out to be 0.5. The value of boron isotope exponent α_B for MgB_2, however, comes out to be = 0.26 ± 0.03. This value of the exponent is very close to the values reported for YNi_2B_2C and $LuNi_2B_2C$ borocarbides. Mg does not display significant isotope shift in T_c and the isotope exponent for Mg is though non-zero but very small. This indicates that the phonons mediating for the occurrence of superconductivity are boron like. Some theories do hint at the possibility that the phonons responsible for superconductivity are high frequency boron A1 g optical modes.

Pressure is another important parameter which has been exploited to study this material. Lorenz et al. [52] have made detailed studies on ac susceptibility and Seeback coefficient with increasing pressure up to 1.84 GPa. T_c always decreases with increasing pressure and is linear with pressure. As shown in Fig. 4.22 T_c drops down with the increase of pressure till the highest pressure of 1.84 GPa. This drop in T_c is rather fast at a rate of −1.6 K/GPa and is close to the theoretically calculated value of −1.4 K/GPa. The Seeback coefficient has been found to be positive and relatively small. It decreases with the decrease of temperature similar to a metal with hole-type carriers.

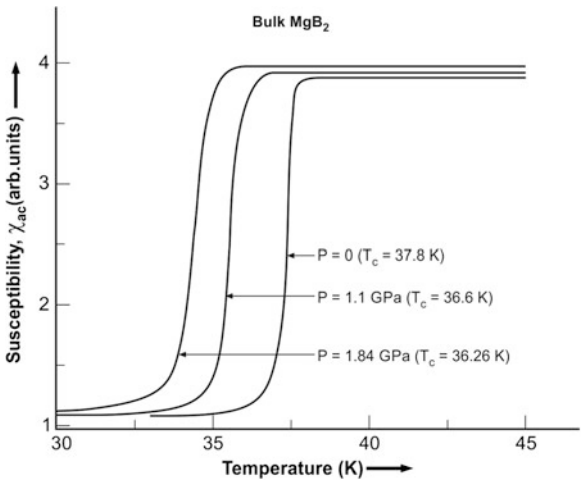

Fig. 4.22 Plots of ac susceptibility of bulk MgB_2 against temperature with increasing pressure up to 1.84 GPa. T_c shifts to lower temperature with increasing pressure [52]. (With permission from APS) http://journals.aps.org/prb/abstract/10.1103/PhysRevB.64.012507

Substitution at Mg as well as B sites with a host of elements always resulted in the decrease of T_c. Some of the materials tried are C, Al, Li, Si, Be, Cu, Mn, Nb, Ti, Fe, Co, Ni, and Zn. Decrease in T_c is severe in case of substitution with Mn, Co and C and slow with Si and Li. Least decrease in T_c occurs with Zn substitution

The coherence length values, as calculated from B_{c2}, range between 6.1 and 6.5 nm in *ab*-plane and between 2.5 and 3.7 nm along the *c*-axis. The most accurate data for a single crystal gives $\xi_{ab}(0)$ = 6.1–6.5 nm and $\xi_c(0)$ = 2.5–3.7 nm.

The penetration depth as evaluated from B_{c1} values range between 85 and 203 nm.

The lower critical magnetic field as reported by several investigators range from 25 to 48 mT.

Upper critical magnetic field B_{c2} has been reported for material in different forms like bulk, single crystal and thin films and in different orientations over a wide range of values ranging from 2.5 to 32 T. The highest value of B_{c2}, 32 T has been reported for films with T_c = 39 K. Higher B_{c2} = 40 T has been reported by Patnaik et al. [53] for films with lower T_c. B_{c2} drops almost linearly with increasing temperature saturating at low temperature. The B_{c2} anisotropy ratio = $\frac{B_{c2}^{ab}}{B_{c2}^{c}}$ = 1.1–1.7 is reported for textured bulk and partially oriented crystallites. Higher ratio = 1.8–2.0 has been reported [53] for *c*-axis oriented MgB_2 film. The irreversible field extrapolated to 0 K, range from 6 to 12 T for MgB_2 in bulk, thin film, powder, tape and wire. B_{irr} thus is =0.5 B_{c2} in MgB_2 instead of =0.8 B_{c2} for conventional low temperature superconductors. Impurity additions are known to increases the B_{c2} in type II superconductors as the mean free path is reduced and so does the coherence length $\xi(0)$. Braccini et al. [54] do report significant enhancement of B_{c2} in C-alloyed MgB_2 films irradiated with He-ions. The disorder thus introduced, raises in-plane B_{c2} to 51 T (4.2 K) and along the *c*-axis to 35 T (4.2 K). These are very promising values and show the potentiality of use of this material with high J_c in

Table 4.4 Some important superconducting parameters of MgB_2 (data compiled from references cited in the text)

Parameter	Unit	Value
Transition temperature, T_c	K	39
Penetration depth	nm	85–203
Coherence length, ξ_{ab}	nm	6.1–6.5
Coherence length, ξ_c	nm	2.5–3.7
Coherence length, ξ_{ab} single crystal	nm	6.1–6.5
Coherence length, $\xi_c(0)$ single crystal	nm	2.5–3.7
Lower critical field, B_{c1}	mT	25–48
Highest upper critical field (film)	T	32–40
$\frac{B_{c2}^{ab}}{B_{c2}^{c}}$ anisotropy (textured bulk/partially oriented crystellites)		1.1–1.7
$\frac{B_{c2}^{ab}}{B_{c2}^{c}}$ anisotropy (c-axis oriented films)		1.8
Irreversible field, B_{irr} (0 K)	T	6–12
Estimated paramagnetic limited field, H_{c2}^{ab}	T	70

high magnetic field. Extrapolation of data to $T = 0$ K shows that H_{c2}^{ab} might lead to paramagnetic limit of 70 T. Table 4.4 summarizes most of the important superconducting parameters of MgB_2.

4.7 The Discovery of Iron Based Superconductors

4.7.1 The LaFeAsO(1111) Compounds

One more surprise came from the Japanese group headed by Hideo Hosano [55] when they reported superconductivity in a new class of materials, the iron-based oxy-pnictides, of the type LaOFeP. The material has a tetragonal structure consisting of alternate layers of lanthanum oxide ($La^{3+}O^{2-}$) and iron pnictide ($Fe^{2+}P^{3-}$). The material had an on-set of T_c at 5 K and complete disappearance of resistivity at 3.2 K. The two dimensional ($Fe^{2+}P^{3-}$) layer is believed to be the conduction layer in which the charge carriers travel. Doping of the ($La^{3+}O^{2-}$) layer causes the transfer of carriers to the conduction layer. Replacing O^{2-} with F^- will provide a positive charge to the insulating La_2O_2 layer and a negative charge to the Fe_2As_2 conduction layer. This will lead to the strong electron interaction and modulation of the interaction through the density of state. T_c was found to increase with fluorine-doping. Soon the group reported [56] a high T_c of 26 K in iron-based $La(O_{1-x}F_x)FeAs$ layered superconductor. Here x varies from 5 to 12 %. The crystal structure of this superconductor is shown in (Fig. 4.23). The conduction layers Fe_2As_2 are sandwiched between the insulating La_2O_2 layers. It has a tetragonal structure of the type (ZrCuSiAs) with p4/nmm space group. The room temperature lattice parameters of

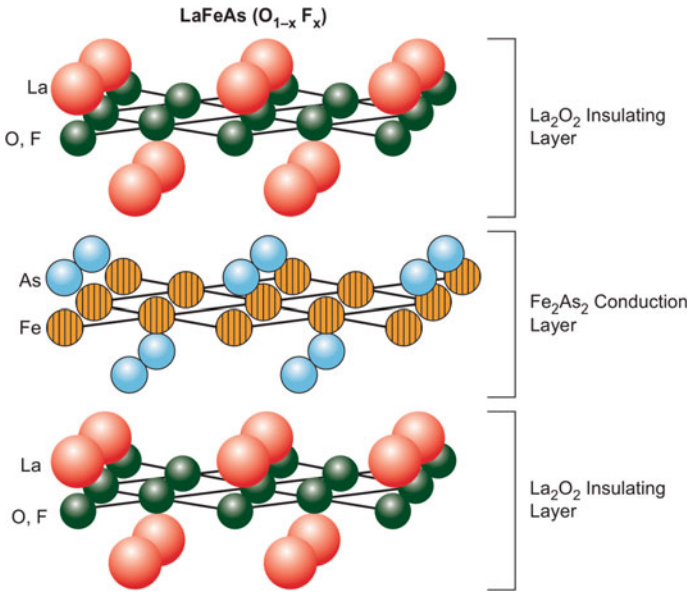

Fig. 4.23 The crystal structure of LaFeAsO system. The Fe_2As_2 conduction layers are sandwiched between the insulating La_2O_2 layers. The structure is of the type (ZrCuSiAs) [56] (With permission from American Chemical Society)

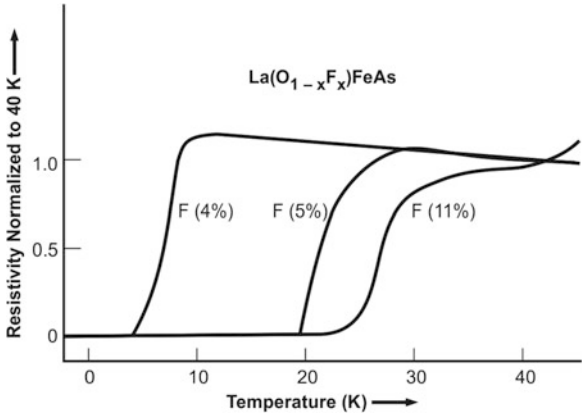

Fig. 4.24 Electrical resistivity plotted against temperature for La($O_{1-x}F_x$) FeAs for 0, 4, 5 and 11 %) of F-doping [56] (With permission from American Chemical Society)

the un-doped samples are $a = 0.403552(8)$ nm and $c = 0.87263(3)$ nm. The lattice constants decrease with F-doping. Thus for example, the lattice parameters for 5 % F-doping are: $a = 0.40320(1)$ nm and $c = 0.87263(3)$ nm.

The electrical resistivity of La($O_{1-x}F_x$)FeAs are plotted against temperature up to 40 K in Fig. 4.24. The un-doped sample does not show superconductivity down to the lowest temperature. Samples with F 4 % and above doping show superconductivity

between 5 and 22 K. Highest value of T_c (=26 K) is obtained for 11 at.% F-doped sample. Higher doping leads to a drop in T_c. Similar results on superconducting transition have been obtained from susceptibility measurements. The value of χ_{mol} for the 5 % F-doped sample starts decreasing at 25 K and is negative, confirming the onset of superconductivity.

Another interesting finding of these studies is that superconductivity was not observed when doping was done with Ca^{2+} instead of with F. This gives a strong signal that superconductivity is induced by electron (F^-)-doping and not by hole (Ca^{2+})-doping. The material LaOFeAs was prepared following the solid state method. Powders of dehydrated La_2O_3, lanthanum arsenide and iron arsenide were thoroughly mixed and sealed in a silica tube filled with Ar-gas. The tube was heated to 1,250 °C for 40 h. Right quantities of CaO and 1:1 mixture of LaF_3 and La were added to the starting material for doping with Ca^{2+} and F^- respectively. This was followed again by the same heating schedule.

4.7.2 High T_c (>50 K) in Sm and Nd Based Oxypnictides

Significantly, high values of T_c have been reported for these oxypnictides by replacing La by different rare earths. For Ce-compound the T_c rises to above 40 and 50 K for Nd, Pr, Sm and Gd. Jaroszynski et al. [57] reported T_c higher than 50 K for their Sm and Nd based materials. They carried out high field studies on three REFeAsO(1111) materials with RE as La, Sm and Nd. Superconductivity was induced either by doping F at O-sites or creating O-vacancies by synthesizing O-deficient materials. Three compounds studied, viz; $LaFeAsO_{0.89}F_{0.11}$, $SmFeAsO_{0.85}F_{0.15}$ and $NdFeAsO_{0.94}F_{0.06}$ yield T_c = 28, 53.5 and 50.5 K respectively. These values have been tabulated in Table 4.5. It is to be mentioned that these materials were synthesized at high pressure and high temperature following the solid state reaction route. Pre-sintered powders of LaAs. SmAs and NdAs were mixed together with powders of Fe, Fe_2O_3 and FeF_2 in right stoichiometric proportions ground and pressed into pellet form. The pellets were sealed in BN (boron nitride) tubes and heated at 1,250 °C under 6 GPa pressure for 2 h. Interestingly, the highest values of T_c obtained for optimal doping show that the optimal level is different for different doping materials, viz; 11, 15 and 6 % for La, Sm and Nd respectively. A detailed review article on oxypnictides has recently appeared in the literature [58].

Table 4.5 Superconducting parameters of REFeAsO(1111) oxypnictides with RE as La, Sm and Nd [57]

Parameter	Unit	$LaFeAsO_{0.89}F_{0.11}$	$SmFeAsO_{0.85}F_{0.15}$	$NdFeAsO_{0.94}F_{0.06}$
Transition temperature, T_c	K	28	53.5	50.5
Optimum doping of F	%	11	15	6
Upper critical field, B_{c2}	T	36	150	204

Table 4.6 Superconducting parameters of REFeAsO (1111) oxypnictides with RE as La, Sm, Nd, Pr and Ce [61]

Oxypnictide	T_c (K)	B_{c2} (0 K)
$LaFeAsO_{0.89}F_{0.11}$		36
$SmFeAsO_{0.85}F_{0.15}$		150
$NdFeAsO_{0.94}F_{0.06}$		204
$PrFeAsO_{0.94}F_{0.06}$		72
$CeFeAsO_{0.8}F_{0.2}$	42.5	43
$CeFeAsO_{0.9}F_{0.1}$	38.4	94
$NdFeAsO_{0.82}F_{0.18}$ [58]	51	230

The upper critical field B_{c2} of La $FeAsO_{1-x}F_x$ (1111) compounds turns out to be high. The B_{c2} values as evaluated from resistive (ρ-B plots) using Werthamer-Helfend-Hohenberg (WHH) formula,

$$B_{c2} = -0.693 T_c [dB_{c2}/T]_{T_c} \tag{4.5}$$

and extrapolated to 0 K for La, Sm, Nd, Pr, and Ce(1111) compounds are [61] 36, 150, 204, 72 and 107 T respectively (Table 4.6). B_{c2} has been found to decrease with increasing F^- doping even though T_c shows an opposite trend. For $CeFeAsO_{0.8}F_{0.2}$ the B_{c2} is 43 T and T_c is 42.5 K and for $CeFeAsO_{0.9}F_{0.1}$ the B_{c2} value is 94 T and T_c is 38.4 K. Similar variation of B_{c2} is reported for $LaFeAsO_{1-x}F_x$. For $LaFeAsO_{0.95}F_{0.05}$ the B_{c2} is 63–65 T and for $LaFeAsO_{0.89}F_{0.11}$ it is 73 T. Sm(1111) compound also show similar behaviour. Like the T_c of this compound B_{c2} of the (1111) compounds also increases if the compound is prepared by high pressure route. B_{c2} up to 230 T and T_c of 51 K have been reported [58] in $NdFeAsO_{0.82}F_{0.18}$. The field anisotropy B_{c2ab}/B_{c2c} is about five, much smaller than in YBCO compound. The values of irreversible field, B_{irr} are also correspondingly high as compared to MgB_2. Above tables indicate beyond doubt that these materials can have high T_c and B_{c2} once the parameters are optimized.

In spite of high B_{c2} and high T_c these compounds suffer from the problem of granularity similar to cuprates. Thus the inter-grain critical current J_{cgb} is far smaller than the intra-grain critical current J_{cg}. Through magneto-optical measurements (low temperature laser scanning electron microscopy) on Sm(1111) compounds Kametani et al. [59] have shown that the transport current though is high within the grains but is low at the grain boundary in very low field. The grain boundaries are identified as Fe–As normal wetting phase surrounding Sm(1111) grains. These grain boundaries produce a dense array of Josephson-coupled superconducting-normal-superconducting (SNS) junctions. Transport J_c of $SmFeAsO_{0.85}$, prepared by high pressure technique drops sharply with small magnetic field. The authors had earlier established that the irreversible field B_{irr} at 39 K in this material is 25 T. J_c, nearly independent of field between 1 and 5 T does support this observation. The self field transport J_c obtained is 463 A cm^{-2} at 39 K and whole-sample global J_c of 600 A cm^{-2} are consistent with each other. Authors also observe fine micro-cracks along the grain boundaries which too must lower the transport J_c. It is fair to

conclude that to exploit these materials for practical applications more efforts are required to get rid of the unwanted Fe–As normal metal wetting phase and the micro-cracks.

4.7.3 Superconductivity in K-Doped $BaFe_2As_2$(122) Compounds

A new member of the Fe–As superconductor family was discovered in 2008 shortly after the discovery of superconductivity in LaFeAsO system at 26 K through F-doping and raising the T_c to all time high 55 K in $SmFeAsO_{1-x}$ system. This was achieved by F^-doping or creating oxygen deficiency (electron-doping) in the Fe_2As_2 conducting layer which suppresses the structure phase transition (at 135–140 K) and induces superconductivity. Hole doping too has been reported to induce superconductivity in the $(La_{1-x}Sr_x)FeAsO$ system but the T_c was limited to 25 K.

Rotter et al. [60] discovered superconductivity first time in an oxygen free pnictide. A T_c of 38 K has been reported in a compound, $(Ba_{0.6}K_{0.4})Fe_2As_2$ prepared by partially replacing Ba with K. The parent compound $BaFe_2As_2$ has a tetragonal $ThCr_2Si_2$ type crystal structure with I4/mmm space group and consisting of $(FeAs)^-$ layers separated by Ba^{2+} ions as shown in Fig. 4.25. $BaFe_2As_2$ is a poor metal with Pauli paramagnetism. It shows a spin density wave (SDW) anomaly at 140 K similar to the anomaly in LaFeAsO compound at 150 K. The anomaly is accompanied with a structural and magnetic phase transition and anomalous specific heat, resistivity and susceptibility. Hole doping in $(FeAs)^-$ layers by partial substitution of K^+ on the Ba^{2+} sites suppresses this SDW anomaly and induces superconductivity. This SDW anomaly seems to be a pre-requisite for superconductivity. The structural phase transition can be suppressed by electron-doping or hole-doping in the Fe–As layer which leads to the appearance of superconductivity. Through this Substitution, the authors [60] have found superconductivity in $(Ba_{0.6}K_{0.4})Fe_2As_2$ at 38 K. The resistive superconducting transition is shown in Fig. 4.26. Thus a new category of oxygen-free Fe–As compounds was added to the list of Fe–As based superconductors.

4.7.4 Superconductivity in Iron-Chalcogenides and Mysterious Behaviour at High Pressures

After the discovery of superconductivity in Fe-oxypnictides of the type LaFeAsO these compounds became the most studied materials with an object of getting higher T_c. Report of T_c as high as 55 K in oxygen-deficient $SmFeAsO_{0.85}$ [57] inspired researchers to continue to look for Fe-based superconductors with still

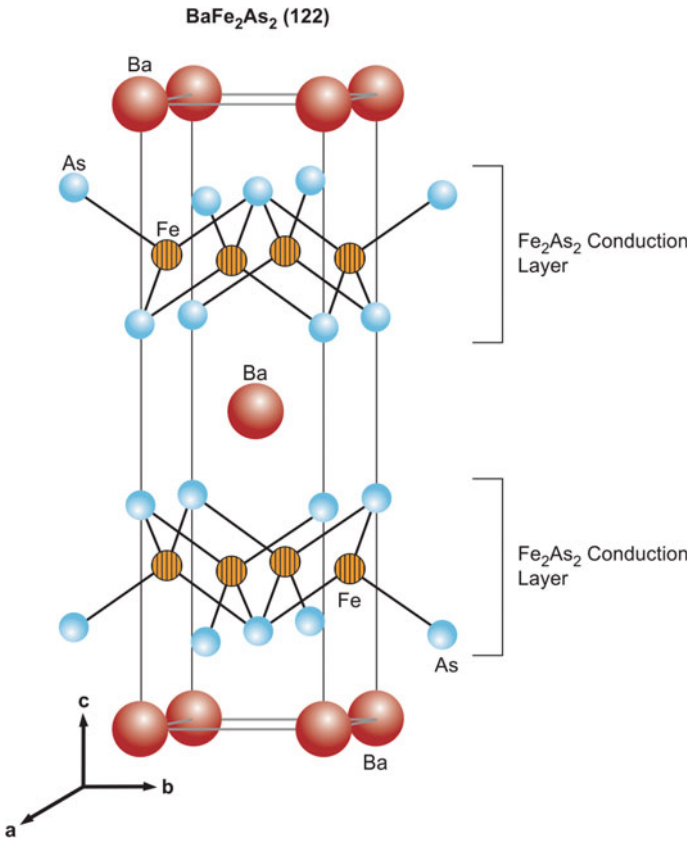

Fig. 4.25 Crystal structure of $BaFe_2As_2$(122) compound (of the type $ThCr_2Si_2$) with space group I4/mmm [60]. (With permission from APS) http://journals.aps.org/prb/abstract/10.1103/PhysRevB.82.180520

higher T_c. Superconductivity was indeed reported in a new material, Fe–Se or referred to as [11] iron-chalcogenide at 8 K by Hsu et al. [61]. This compound has a simple structure of Fe–Se layers without intercalating cations, something quite different from the oxypnictides. Static magnetic ordering too does not occur up to a pressure of 38 GPa. Tellurium doping ($FeSe_{0.42}Tl_{0.58}$) raises the T_c to 15 K and the high pressure up to 37 K. Guo et al. [62] reported superconductivity in a compound of the composition $K_{0.8}Fe_2Se_2$ at 30 K at ambient pressure. The compound was synthesized through intercalation of Fe–Se by K. Figure 4.27 shows the crystal structure of this compound. Single crystal grown by flux method shows a tetragonal structure with a = 3.9136(1) Å and c = 14.0367(7) Å and space group I4/mmm. Obviously, the intercalation increases the c-axis parameter significantly. The carrier density as evaluated from Hall effect measurement turns out to be $1.76 \times 10^{21}/cm^3$. The Hall coefficient R_H is negative and constant above 105 K. The electrical conduction is thus electron dominated. The compound has a semiconductor

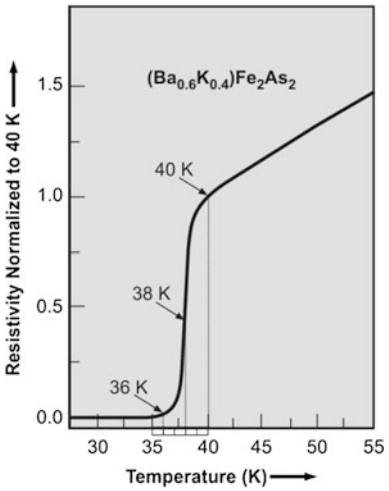

Fig. 4.26 Resistive superconducting transition in $(Ba_{0.6}K_{0.4})Fe_2As_2$ [60]. (With permission from APS) http://journals.aps.org/prb/abstract/10.1103/PhysRevB.82.180520

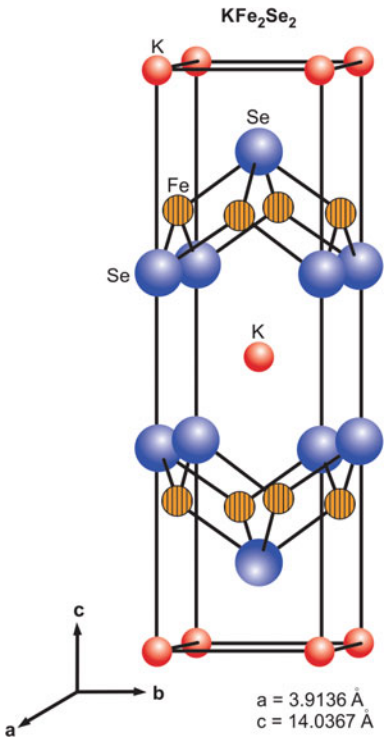

Fig. 4.27 The crystal structure of KFe_2Se_2 of the type ($ThCr_2Si_2$) a = 3.9136 (1) Å and c = 14.0367 Å [62]. (With permission from APS) http://journals.aps.org/prb/abstract/10.1103/PhysRevB.82.180520

behaviour in electrical resistivity between room temperature and 105 K below which it turns metallic and finally superconducting (at 30 K). The resistive transition of the $K_{0.8}Fe_2Se_2$ compound is shown in Fig. 4.28. The lower critical

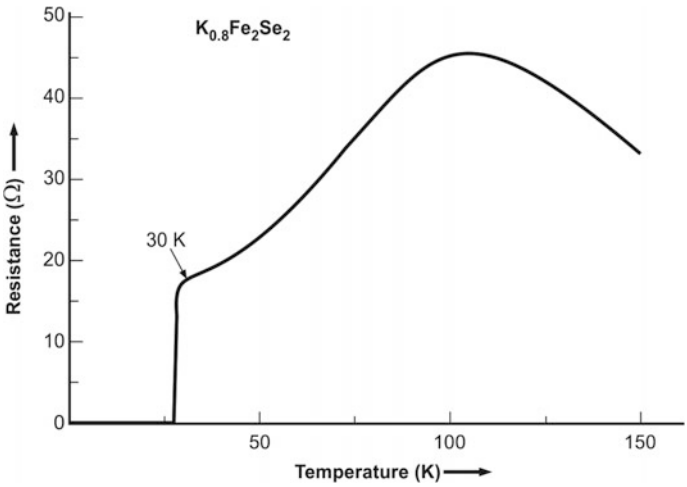

Fig. 4.28 Resistance/temperature behaviour of $K_{0.8}Fe_2Se_2$, below 150 K. Superconducting transition occurs at 30 K [62]. (With permission from APS) http://journals.aps.org/prb/abstract/10.1103/PhysRevB.82.180520

magnetic field B_{c1} and upper critical magnetic field B_{c2} have been calculated to be 0.2 and 9 T respectively.

A mysterious behaviour of repeat appearing and disappearing of superconductivity in iron-chalcogenide has been reported very recently by Sun et al. [63]. They probed the basic electronics and structural properties of iron-chalcogenides by the application of pressure. Pressure application is perhaps the cleanest way to probe such properties. They carried out their studies on the single crystals of $(Tl_{0.6}Rb_{0.4})Fe_{1.67}Se_2$, $K_{0.8}Fe_{1.7}Se_2$ and $K_{0.8}Fe_{1.78}Se_2$ grown by the Bridgman technique and conducted resistivity and magnetic susceptibility measurements at low temperature and under varying applied pressure. The results shown in Fig. 4.29 were stunning. Superconductivity for example in the compound $Tl_{0.6}Rb_{0.4}Fe_{1.67}Se_2$, $K_{0.8}Fe_{1.7}Se_2$ sets-in at an optimum pressure of 1.6 GPa with a T_c of 33 K, T_c decreases with increasing pressure and superconductivity vanishes at a pressure of 9 GPa. What was astounding, was that while the pressure was raised further beyond 9 GPa superconductivity again surfaced at 48 K, an high T_c indeed, at a pressure of 12.4 GPa. There seem to be two distinct superconducting phases in this material. One can call them the superconducting phase I and phase II respectively. These superconductors possess rather high magnetic moment something like 3.3 μ_B per Fe atom and have Fe-vacancy ordering in the Fe square lattice. Existence of superconductivity in materials with such high magnetic moment is a riddle to be sorted out. Quite similar behaviour has been observed in other two systems, namely, $K_{0.8}Fe_{1.7}Se_2$ and $K_{0.8}Fe_{1.78}Se_2$. This type of re-emergence of superconductivity has been found earlier in strongly correlated electron systems like heavy-Fermions [64] and some organic systems [65]. It appears that by manipulating the thermodynamical parameters like pressure, T_c can be raised to high values hitherto not attainable.

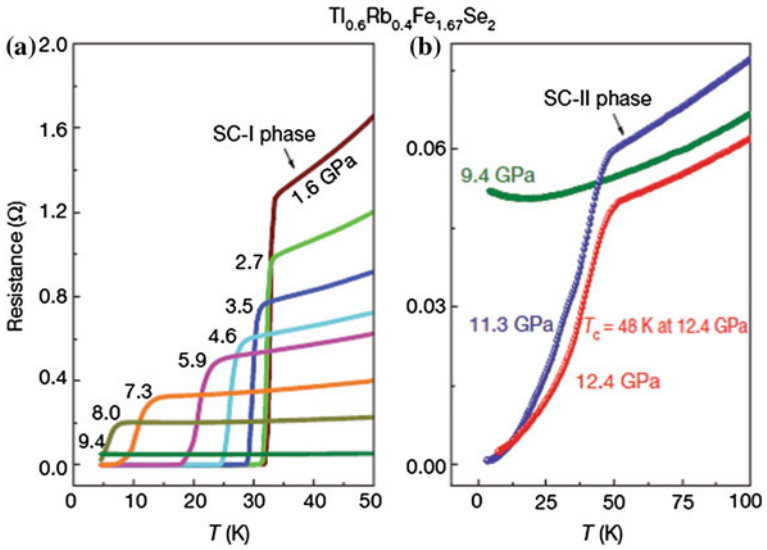

Fig. 4.29 The resistivity-temperature plots of $Tl_{0.6}Rb_{0.4}Fe_{1.67}Se_2$ at varying pressures. **a** Superconductivity occurs at 33 K at a pressure of 1.6 GPa and disappears at a pressure of 9 GPa. **b** A second phase of superconductivity sets-in at a pressure of 12.4 GPa. The compound looses superconductivity at a still higher pressure of 13.2 GPa [63]. (With permission from Nature Publishing Group)

References

1. J.R. Gavaler, Appl. Phys. Lett. **23**, 480 (1974)
2. L.R. Tastardi, J.H. Wernick, W.A. Royer, Solid State Commun. **15**, 1 (1974)
3. J.G. Bednorz, K.A. Muller, Z. Phys. B: Condens. Matter **64**, 189 (1986)
4. D.C. Johnston, H. Prakash, W.H. Zachariasen, R. Viswanathan, Mater. Res. Bull. **8**, 777 (1973)
5. A.W. Sleight, J.L. Gillson, F.E. Bierstedt, Solid State Commun. **17**, 27 (1975)
6. C.W. Chu, P.H. Hor, R.L. Meng et al., Phys. Rev. Lett. **58**, 405 (1987)
7. R.J. Cava, R.B. van Dover, B. Batlogg, E.A. Rietman, Phys. Rev. Lett. **58**, 408 (1987)
8. R.P. Aloysius, Ph.D. thesis, Cochin University of Science and Technology, Cochin (2002)
9. M.K. Wu, J.R. Ashburn, C.J. Torng et al., Phys. Rev. Lett. **58**, 908 (1987)
10. R.G. Sharma, Y.S. Reddy, S.R. Jha, S.S. Dubey, Pramana-J. Phys. **30**, L-81 (1988)
11. S.R. Jha, Y.S. Reddy, D.K. Suri, K.D. Kundra, R.G. Sharma, D. Kumar, Pramana-J. Phys. **32**, 277 (1989)
12. A. Pandey, R. Rajput, B. Sarkar, Y.S. Reddy, R.G. Sharma, Physica **C256**, 335 (1996)
13. A. Pandey, Y.S. Reddy, R.G. Sharma, J. Mater. Sci. **32**, 3701 (1997)
14. R.G. Sharma, S. Lahiry, A. Pandey, D. Bhattacharya, Bull. Mater. Sci. **22**, 265 (1999)
15. R.G. Sharma, Y.S. Reddy, S.R. Jha, Rev. Solid State Sci. **2**, 409 (1988)
16. P. Chaudhuri, R.H. Koch, R.B. Laibowitz et al., Phys. Rev. Lett. **58**, 2684 (1987)
17. T.R. Dinger, T.K. Worthington, W.J. Gallagher, R.L. Sandstorm, Phys. Rev. Lett. **58**, 2687 (1987)
18. H. Maeda, Y. Tanaka, M. Fukutomi, T. Asano, Jpn. J. Appl. Phys. **27**, L665 (1987)
19. M. Takano, J. Takada, K. Oda et al., Jpn. J. Appl. Phys. **27**, L1652 (1988)

20. B. Sarkar, Y.S. Reddy, R.G. Sharma, Mater. Res. Bull. **28**, 629 (1993)
21. S.R. Shukla, D.K. Pandya, N. Kumar, S.K. Sharma, R.G. Sharma, Physica **C219**, 483 (1994)
22. S.R. Shukla, Y.S. Reddy, N. Kumar, S.K. Sharma, R.G. Sharma, Pramana-J. Phys. **41**, 285 (1993)
23. H. Maeda, K. Innoue, T. Kiyoshi, T. Asano et al., Phys. B **216**, 141 (1996)
24. M. Tachiki, S. Takahashi, Solid State Commun. **70**, 291 (1989)
25. K. Kadowaki, in *Electronic Properties and Mechanism of High T_c Superconductors,* ed. by T. Oguchi, K. Kadowaki, T. Sasaki (North-Holland, Amsterdam, 1992), p. 209
26. M. Kikuchi, N. Ayai, T. Ishida et al., SEI Tech. Rev. **66**, 73 (2008)
27. Z.Z. Sheng, A.M. Hermann, Nature **332**, 55 (1988)
28. Z.Z. Sheng, A.M. Hermann, Nature **332**, 138 (1988)
29. S.S.P. Parkin, V.Y. Lee, E.M. Engler et al., Phys. Rev. Lett. **60**, 2539 (1988)
30. S.N. Putillin, E.V. Antipov, O. Chmaissem, M. Marezio, Nature **362**, 226 (1993)
31. A. Schilling, M. Cantoni, J.D. Guo, H.R. Ott, Nature **363**, 56 (1993)
32. C.W. Chu, L. Gao, F. Chen et al., Nature **365**, 323 (1993)
33. L. Gao, Y.Y. Xue, F. Chen et al., Phys. Rev. **B50**, 4260 (1994)
34. E.V. Antipov, A.M. Abakumav, S.N. Putillin, Supercond. Sci. Technol. **15**, R-31 (2002)
35. J. Nagamatsu, N. Nakagawa, T. Muranaka et al., Nature **410**, 63 (2001)
36. R. Nagarajan, C. Mazumdar, J. Hossain et al., Phys. Rev. Lett. **72**, 274 (1994)
37. R. Cava, H. Takagi, H.W. Zandbergen et al., Nature **367**, 252 (1994)
38. H.J. Choi, D. Roundy, H. Sun, M.L. Cohen, Nature **418**, 758 (2002)
39. R.S. Gonelli, A. Calzolari, D. Deghero et al., Phys. Rev. Lett. **87**, 097001 (2001)
40. C. Buzea, T. Yamashita, Supercond. Sci. Technol. **14**, R 115 (2001)
41. K. Vinod, N. Verghese, U. Syamaprasad, Supercond. Sci. Technol. **20**, R31 (2007)
42. K. Vinod, R.G. Abhilash Kumar, U. Syamaprasad, Supercond. Sci. Technol. **20**, R1 (2007)
43. J. Kapinski, S.M. Kazakov, J. Jun et al., Phys. C (Supercond.) **385**, 42 (2003)
44. K. Komori, K. Kawagishi, Y. Takano et al., Appl. Phys. Lett. **82**, 1047 (2002)
45. V. Ferrando, P. Orgiani, A.V. Pogrebnyakov et al., Appl. Phys. Lett. **87**, 252509 (2005)
46. G. Glasso, A. Malagoli, C. Ferdeghini et al., Cond-Mat/0103563
47. H. Kumakura, A. Matsumoto, H. Fuji, K. Togano, Appl. Phys. Lett. **79**, 2435 (2001)
48. H. Fang, P.T. Putman, S. Padmanabhan et al., Supercond. Sci. Technol. **17**, 717 (2004)
49. M.D. Sumption, M. Bhatia, X. Wu et al., Supercond. Sci. Technol. **18**, 730 (2005)
50. Y. Elstev, K. Nakao, S. Lee et al., Phys. Rev. B **66**, 180504 (2002)
51. S.L. Bud'ko, G. Labertot, C. Petrovic, et al., Phys. Rev. Lett. **86**, 1877 (2001)
52. B. Lorenz, R.L. Meng, C.W. Chu, Phys. Rev. B **64**, 012507 (2001)
53. S. Patnaik, L.D. Cooley, A Gurevich, et al., Supercond. Sci. Technol. **14**, 315 (2001)
54. V. Braccini, A. Gurevich, J.E. Giencke et al., Phys. Rev. B **71**, 012504 (2005)
55. Y. Kamihara, H. Hiramatsu, M. Hirano et al., J. Am. Chem. Soc. **128**, 10012 (2008)
56. Y. Kamihara, T. Watanabe, M. Hirano, H. Hosono, J. Am. Chem. Soc. **130**, 3296 (2008)
57. J. Jaroszynski, C. Scott, F. Riggs et al., Phys. Rev. B **78**, 064511 (2008)
58. P.M. Aswathy, J.B. Anuja, P.M. Sarun, U. Syamaprasad, Supercond. Sci. Technol. **23**, 073001 (2010)
59. F. Kametani, P. Li, D. Abrrimov et al., Appl. Phys. Lett. **95**, 142502 (2009)
60. M. Rotter, M. Tegel, D. Johrendt, Phys. Rev. Lett. **101**, 107006 (2008)
61. F.C. Hsu, J.U. Luo, K.W. Yeh et al., Proc. Natl. Acad. Sci. U.S.A. **105**, 14262 (2008)
62. J. Guo, S. Jin, G. Wang et al., Phys. Rev. B **82**, 180520(R) (2010)
63. L. Sun, X.J. Chen, J. Guo et al., Nature **483**, 67 (2012)
64. H.Q. Yuan, F.M. Groche, M. Deppe et al., Science **302**, 2104 (2003)
65. T. Okuhata, T. Nagai, H. Taniguchi et al., J. Phys. Soc. Jpn. **76**(Suppl. A), 188 (2007)

Chapter 5
A Review of Theories of Superconductivity

Abstract The first ever phenomenological theory of superconductivity was propounded by London brothers (Fritz and Heinz) by correlating the current in a superconductor with a vector potential and using Maxwell equations. Theory explained well the vanishing of resistivity and the occurrence of Meissner effect in metallic superconductors. An expression for London penetration depth λ was given which was confirmed experimentally. Another phenomenological theory was proposed by Ginzberg and Landau (G-L theory) introducing the concept of an order parameter and a temperature dependent coherence length which close to 0 K is similar to the temperature independent Pippard coherence length. The most successful theory, the microscopic BCS theory ultimately came from three physicists Bardeen, Cooper and Schrieffer in 1957. They argued that two electrons with equal and opposite momenta form a bound pair (Cooper pair), a boson, via the exchange of a virtual phonon overcoming the Coulomb repulsion. These pairs (bosons) condense into a ground state, a gap appears in the energy spectrum and the system turns superconducting. The energy gap goes down to zero at T_c. Theory however could not explain the so called high temperature cuprate superconductors (HTS) which are similar to BCS superconductors in several respects but differ drastically in many others. There is no evidence of phonon mediation in pair formation in these materials as evidenced from the absence of isotope effect. After many attempts and a long turmoil two theories have found some acceptance. First, is the RVB resonance valence bond (RVB) theory proposed by P.W. Anderson and the other is spin fluctuation theory proposed by P. Monthoux. The two concepts are qualitatively described briefly in this chapter. Last word on theory is, however, yet to come.

5.1 A Chronology of Theories of Superconductivity

In this chapter, we will review the development of important theories culminating into a successful microscopic theory formulated by Bardeen et al. [1] which explained all the important features of metal superconductors quite successfully. The first theory to explain the occurrence of superconductivity in metallic

R.G. Sharma, *Superconductivity*, Springer Series in Materials Science 214,
DOI 10.1007/978-3-319-13713-1_5

superconductors was given by London brothers [2] (Fritz London and Heinz London) in 1935. They had set out to formulate a law similar to the versatile Ohm's law valid for normal conductors. Ohm's law, however, cannot account for superconductors because current in a superconductor flows without a voltage. The formulation has also to explain Meissner effect which characterizes a superconductor and distinguishes it from a perfect conductor. Since Meissner state is a fundamental equilibrium state, the current flow must correlate with the applied magnetic field and not with the voltage. They drew a connection between the current density J and an electromagnetic vector potential A and employed Maxwell's expressions. The theory accounted well for the infinite conductivity as also for the Meissner effect. Another important landmark in this journey was the so called GL theory proposed by Ginzburg and Landau [3]. The theory in its original form was a phenomenological theory in which they argued that free energy of a superconductor can be expressed in terms of a complex wave function $\Psi(r)$ which is an order parameter $\left(n_s = |\Psi(r)|^2\right)$ within the general theory of Landau of second-order phase transition. Gorkov [4] in 1959 did, however, show that the GL theory was a limiting case of the microscopic theory of BCS valid near T_c, where $\Psi(r)$ is proportional to the energy gap parameter. But the answer to the question that how a single wave function describes a superconductor not only at $T = 0$ but also at all temperatures below T_c came in 1957 from the BCS theory. These three gentle men proposed that in a superconductor electron pairing takes place via the exchange of a virtual phonon and the pairs condense to a ground state. This was the first successful microscopic theory which accounted well for all the peculiar properties of the superconductor observed experimentally. These theories will be briefly discussed below. A concise description of the theories has been given by Ramakrishnan and Rao [5]. A summary of theories proposed by various schools of thought to explain the occurrence of superconductivity in the cuprate superconductors or the so called high temperature superconductors (HTS) will be discussed towards the end of this chapter. Rigorous treatment of any theory is outside the scope of the book.

5.2 Londons' Theory

London brothers started with the logic that if the electrons do not encounter resistance (superelectrons) they will continue to accelerate in an applied electric field such that

$$\frac{dv}{dt} = \frac{eE}{m} \tag{5.1}$$

where e, m and v are the charge, mass and velocity of the electron respectively and E the electric field. If we multiply both sides with the density of these superelectrons and the charge e, we get

$$\frac{\mathrm{d}}{\mathrm{d}t}(n_s ev) = \left[\frac{n_s e^2}{m}\right] E \tag{5.2}$$

But since $(n_s ev)$ in (5.2) is just the electric current density J_s, we now have

$$\frac{\mathrm{d}}{\mathrm{d}t}(J_s) = \left[\frac{n_s e^2}{m}\right] E \tag{5.3}$$

London(s) expressed the electromagnetic field in terms of a vector potential A. We thus have the relation between magnetic flux and the electric field;

$$B = \nabla x A \tag{5.4}$$

and

$$E = -\left|\frac{\partial A}{\partial t}\right| \tag{5.5}$$

Combining (5.3) and (5.5) we get

$$\frac{\mathrm{d}}{\mathrm{d}t}(J_s) = -\frac{n_s e^2}{m}\left[\frac{\partial A}{\partial t}\right] \tag{5.6}$$

The expression for J_s can now be obtained by integrating (5.6). J_s is thus given by

$$J_s = -\left(\frac{n_s e^2}{m}\right) A \tag{5.7}$$

London(s) assumed the constant of integration to be zero so that the relation (5.7) is unique and which accounts well for the zero electrical resistivity.

The expression for the magnetic field B can be obtained by employing Amperes law

$$(\nabla x B) = \mu_0 J_S \tag{5.8}$$

Using (5.4) and (5.7) we can eliminate J_s and have an expression for B

$$\nabla x(\nabla x B) = -\left[\frac{n_s e^2}{m}\right] \mu_0 B \tag{5.9}$$

Assuming the field along the z direction we get London equation for field inside the superconductor along the x direction as given by

$$\frac{d^2B(x)}{dx^2} = \frac{\mu_0 n_s e^2}{m} B(x) \tag{5.10}$$

which has a solution of the type

$$B(x) = B_0 \exp(-x/\lambda) \tag{5.11}$$

The solution matches with the experimental observation that the magnetic flux is maximum at B_0 on the superconductor surface and drops exponentially inside it to $1/e$th value at a distance of λ, called London's penetration depth or just the penetration depth. The equation for the penetration depth λ thus turns out to be

$$\lambda^2 = \frac{1}{\mu_0}\left[\frac{m}{n_s e^2}\right] \tag{5.12}$$

The penetration depth thus turns out to be inversely proportional to the square root of n_s, the superelectron density which changes with temperature. As the temperature increases n_s decreases and the flux penetration increases. At T_c, n_s decreases to zero and the whole material is penetrated with magnetic field thus turning the superconductor into the normal state. Although Londons' theory did explain the infinite electrical conductivity and the Meissner effect, yet the expressions (5.11) and (5.12) are only approximate in so far as the calculated values of λ differ from the experimentally determined values. This may be due to the uncertainty of the values of n_s, e and m taken for free electrons, which obviously cannot be justified. The parameters like the superelectron density, n_s, their effective charge and effective mass have to be taken into account. After all, a superconductor cannot be treated as a free electron metal. Instead, superelectrons in a superconductor, interact coherently.

5.3 Ginzburg-Landau Theory

The Ginzburg-Landau theory of superconductivity or called just G-L theory [3] is a phenomenological theory and valid close to the transition temperature. Nevertheless, it accounts well for the main characteristic properties of the superconductors. Recognition of this theory came after Gorkov [4] showed that the theory can as well be derived from the microscopic BCS theory. Since superconductivity is caused by a second order phase transition, this theory draws an analogy with the similar second order ferromagnetic phase transition in metals like iron and nickel. The order parameter M, the magnetization in ferromagnets has now been replaced by a macroscopic quantum wave function $\psi(r)$. The theory expresses the free energy of a superconductor in terms of the expansion of $\psi(r)$. Ginzburg and Landau treated the order parameter $\psi(r)$ as the wave function of the superconducting state which

can vary with the location r. They expressed the order parameter $\psi(r)$ as $|\psi(r)|e^{i\phi(r)}$ where $\phi(r)$ is the phase. The gradient of the phase at r is related to the momentum, that is, the current flowing at the point r. Ginzburg and Landau expanded the free energy as a functional power series for small values of $\psi(r)$ and for it's slow spatial variation as below

$$F\{\psi(r)\} = \int a|\psi(r)|^2 + (b/2)|\psi(r)|^4 + \mathrm{d}\xi^2|\nabla\psi(r) - (ie^*/\hbar)A\psi(r)|^2 + (1/2)\mu_0 \int |B(r)|^2 \mathrm{d}r \tag{5.13}$$

Terms a, b and d are the energy density terms. It is assumed that the term 'a' is temperature dependent and given by $a = a_0\,[(T - T_c)/T_c\,]$ and the terms b and d are assumed to be temperature independent. The third term which is proportional to the squire of the gradient of ψ indicates the uniform value of $\psi(r)$ at minimum energy. The quantity ξ has the dimensions of length and represents a characteristic length scale over which $\psi(r)$ varies and can thus be identified with the coherence length. It is to be noticed that this square term also has the electromagnetic potential A because $\nabla\psi(r)$ is proportional to current which too depends upon A. Magnetic field energy is represented by the last term in (5.13). The free energy expression above assumes a configuration $\psi(r)$, yielding minimum free energy condition controlled by external parameters like temperature and magnetic field. Quite a few solutions of (5.13) are possible which yield various superconducting parameters.

The term ξ in (5.13), called Ginzburg Landau coherence length is given by

$$\xi_{GL} = \frac{\hbar}{|2m^* a(T)|^{1/2}} \tag{5.14}$$

This characteristic length is the distance over which $\psi(r)$ can change without appreciable energy increase. In a pure superconductor close to 0 K, $\xi_{GL} \approx \xi_0$ similar to temperature independent Pippard coherence length. ξ_{GL}, however, diverges as $(T_c - T)^{-1/2}$ since 'a' vanishes as $(T - T_c)$. These two coherence lengths though based on the same concept yet are two different quantities. Coherence length decreases with the addition of impurity to the superconductor as the electronic mean free path decreases. In pure metal superconductors the coherence length is of the order of few hundred nm and can be reduced to few tens of nm on alloying.

5.3.1 Flux Exclusion and Zero Electrical Resistance

The GL theory too leads to a London type relation between the electromagnetic vector potential 'A' and the electric current. Taking current density of a system of charges in a vector potential as the rate of change of its energy with vector potential 'A', we can write

$$j_s(r) = -[\partial F/\partial A(r)] \tag{5.15}$$

$$= -d\xi^2 \frac{ie^*}{\hbar}\left[\psi^*(r)\left(\nabla - \frac{ie^*}{\hbar}A\right)\psi(r) + c\right] \tag{5.16}$$

In a region where order parameter is uniform, that is, $\nabla\psi(r) = 0$, J_s is given by

$$j_s = -d\xi^2|\psi|^2\left(\frac{e^{*2}}{\hbar^2}A\right) \tag{5.17}$$

Which is the London equation. The constant of proportionality depends upon the order parameter $|\psi|^2$. As the order parameter decreases penetration length increases. Since near T_c, $|\psi|^2 \propto (T_c - T)$ the penetration depth λ should be proportional to $(T_c - T)^{-1/2}$. This variation of λ with temperature is indeed experimentally observed as shown in Fig. 2.11. The assumption that ψ does not vary spatially implies that London results are valid if ξ, the length scale of the variation of ψ, is much smaller than $\lambda(\xi \ll \lambda)$. This condition is satisfied only in type II superconductors.

5.3.2 *Flux Quantization*

Londons' postulate that the flux inside a superconducting ring is quantized also follows as a consequence of GL theory. We know from our discussion on Meissner effect that the flux penetrates a superconductor a small depth λ only and so does flow the screening current. Deep inside the ring (contour C) the supercurrent as well as the field will be zero. Thus

$$j_s = \psi^*(r)\left[\nabla - \frac{ie^*A}{\hbar}\right]\psi(r) = 0 \tag{5.18}$$

Since $\psi(r) = |\psi|e^{i\phi}(r)$, (5.18) can be written as,

$$\nabla\phi(r) - \frac{e^*A(r)}{\hbar} = 0 \tag{5.19}$$

The order parameter should have a unique value with minimum energy at every point along the circular path. In going round the circular path phase $\phi(r)$ should change only by an integral multiple of 2π. Thus from (5.19)

$$\oint \nabla\phi \cdot dl = \Delta\phi = 2n\pi \tag{5.20}$$

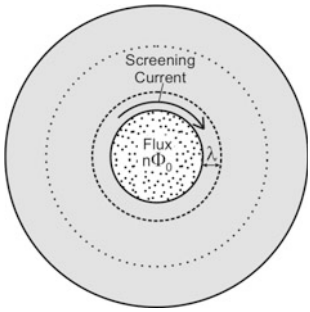

Fig. 5.1 The flux contained inside a superconducting hollow cylinder or a circular ring is always an integral multiple of the unit quantum of flux, $\phi_0 = \frac{h}{2e}$

or

$$\frac{e^*}{\hbar}\oint A \cdot dl = \frac{e^*}{\hbar}\phi \tag{5.21}$$

or

$$\phi = \frac{nh}{e^*} = \phi_0 \tag{5.22}$$

We thus find that the single valuedness of the order parameter leads to the flux quantization. The quantity e^* turns out to be equal to $2e$ in the microscopic theory (Fig. 5.1).

5.3.3 GL—Parameter and Type II Superconductors

The ratio of London's penetration length, λ and the GL coherence length ξ is called the GL parameter represented by κ, that is,

$$\kappa = \lambda/\xi \tag{5.23}$$

Since both the parameters λ and ξ diverge as $(T_c - T)^{-1/2}$, the GL parameter, κ remains temperature independent. For typical classical metallic superconductors λ is much smaller than ξ, the ratio κ is smaller than 1. In fact, the value of the GL parameter distinguishes between two class of superconductors type I and type II. For most metallic superconductor $\kappa < 1/\sqrt{2}$ and for type II superconductors (like alloy superconductors and high T_c superconductors) this ratio $\kappa > 1/\sqrt{2}$. Thus $\kappa = 1/\sqrt{2}$ (<0.71) is the dividing line between the two classes of superconductors.

5.3.4 Josephson Effect

From the aforesaid discussion we understand now quite clearly that a superconductor is defined by an order parameter $\Psi(r)$ with a phase which is constant within a superconductor. This phase can however be changed by an external electromagnetic field. Variation of phase causes a current to flow. If two superconductors with two different phases ϕ_1 and ϕ_2 are coupled weakly (like in a microbridge or a point contact) a current tends to flow across the weak link or the junction. This current is dependent on the phase difference $(\phi_1 - \phi_2)$. The expression for the current that flows through the weak link can be written as

$$i = i_c \sin(\phi_1 - \phi_2) \tag{5.24}$$

No current will flow if the phase difference $\phi_1 - \phi_2$ is zero. I_c in the above equation is the critical current of the junction and depends upon the junction strength. This is dc Josephson effect [6] and we have discussed it in some details in Chap. 2, Sect. 2.14. This current flows without a potential difference. In a geometry, like a superconducting ring, the phase difference will change with the flux in the ring which is quantized. Equation (5.24) will now take the form

$$i = i_c \sin\left[(\phi_1 - \phi_2) + 2\pi\phi_{\text{junction}}/\phi_0\right] \tag{5.25}$$

In a SQUID (Fig. 2.31) the two arms acquire different phases equal to 2π times the unit quantum of flux, ϕ_0 depending on the enclosed flux. The current will be maximum when the phase difference is 2π times ϕ_0 and minimum when the phase difference is an odd multiple of π. The current pattern is thus oscillatory when plotted against the magnetic field passing through the SQUID (Fig. 2.32).

An expression for the ac Josephson effect can be driven from the (5.22) by differentiating with respect to time, that is,

$$\nabla \frac{\partial \phi}{\partial t} = \frac{e^*}{\hbar}\left(\frac{\partial A}{\partial t}\right) \tag{5.26}$$

Since the rate of change of vector potential A is V

$$\frac{\partial \phi}{\partial t} = \frac{e^* V}{\hbar} \tag{5.27}$$

Thus the phase difference between the two superconductors in a Josephson junction turns out to be,

$$\Delta\phi = \left[\frac{2eV}{\hbar}\right] t \tag{5.28}$$

Thus if a voltage V is applied across the junction, an ac current with a frequency $2eV/\hbar$ will flow. We thus find that G-L theory accounts well for most of the characteristic parameters of a superconductor and establishes the fact that the free energy of a superconductor can be expressed as a function of an order parameter which is influenced by external electromagnetic field.

5.4 BCS Theory of Superconductivity

The sharp transition temperature ($\sim 10^{-5}$ K) in superconductors had long established the fact that superconductivity is a cooperative phenomenon in which a large number of entities (conduction electrons) take part. There are, however, two major difficulties. One, that the electrons are fermions and obey Fermi-Dirac statistics according to which no two electrons can occupy the same quantum energy state. A cooperative phenomenon or the coherence among electrons is thus not feasible. Secondly, electron experience Coulomb repulsion which will prevent them from coming together howsoever weak the Coulomb repulsion may be. Suggestion, that two electrons can have an attractive interaction via a lattice distortion overcoming the Coulomb repulsion, first time came from Fröhlich [7] in 1950. Fröhlich argued that electron-phonon interaction which is associated with either the emission or the absorption of a phonon can lead to a new state of superconductivity. As the two electrons attract and form a bound pair they behave like a Boson obeying Bose-Einstein statistics. All the Bosons can then condense coherently into a single quantum state. Confirmation of the electron-phonon (lattice) interaction responsible for superconductivity came from the discovery of isotope effect [8, 9] (discussed in Chap. 2, Sect. 2.10) in metal superconductors. In the same year (1950), Bardeen independently developed a theory [10] of electron-electron interaction via the exchange of a virtual phonon on similar lines.

5.4.1 Cooper Pairs

Electron-electron attractive interaction via the lattice vibrations originally proposed by Fröhlich [11] can be understood using the following argument [12]. Let us assume that an electron passes through the lattice distorting it by attracting positive ions (Fig. 5.2). This lattice distortion, because of the large inertia will leg behind the moving electron by a distance

$$d \approx v_F \frac{2\pi}{\omega_D} \approx 100-1{,}000 \text{ nm} \tag{5.29}$$

where ω_D is the Debye frequency. This lattice deformation, because of the accumulation of positive charge, will attract another electron passing through this

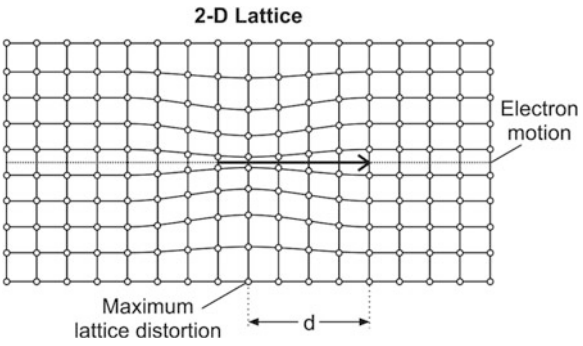

Fig. 5.2 Lattice deformation caused by the passage of an electron

region. This attraction will be maximum when the second electron moves along the track left by the first electron and is a distance '*d*' away. This attractive force is a polarization force and lasts much longer as compared to the repulsive coulomb force between these two electrons which is instantaneous. It is for this reason that even if the lattice distortion is weak, the attractive force mediated by it overcomes a stronger instantaneous Coulomb repulsion.

Cooper [13] studied to find what happens when two electrons with equal and opposite momenta $\vec{p}_1 = -\vec{p}_2$ with magnitude slightly more than the Fermi momentum p_F, are added to a filled Fermi sphere. Because of the Pauli exclusion principle these electrons cannot occupy energy state below the Fermi level being fully occupied. Instead, they tend to come together via the exchange of a virtual phonon and form a bound state. These pairs, called Cooper pairs have a binding energy of 10^{-3}–10^{-4} eV. To preserve this binding energy against thermal excitations it is necessary to maintain the temperature low. The binding is strongest when the electrons have equal and opposite momentum so that the total momentum of the pair is zero and the pairs are in spin singlet state. The size of the Cooper pair, '*r*' can be calculated using the relationship

$$r = \left[\frac{\hbar v_F}{E_B}\right] \tag{5.30}$$

where E_B is the binding energy and v_F the Fermi velocity. Taking the E_B as 10^{-3}–10^{-4} eV and $v_F = 10^8$ cm/s in a metal, '*r*' turns out to be 100–1,000 nm, the same as '*d*' in (5.29).

Thus we find that the size of the Cooper pair is quite large compared to the distance between two electrons ($\sim$0.01 nm) and thus is an extended entity. This implies that there will be a considerable overlapping of the Cooper pairs. As shown in Fig. 5.3 there will be hundreds of thousands of other pairs within the space occupied by one Cooper pair. Once electrons form a bound pair all other electrons tend to realign into bound pairs as well. Bardeen Cooper and Schrieffer showed that the energy of the system is lowest when all the pairs have the same momentum, that is, zero and have phase coherence.

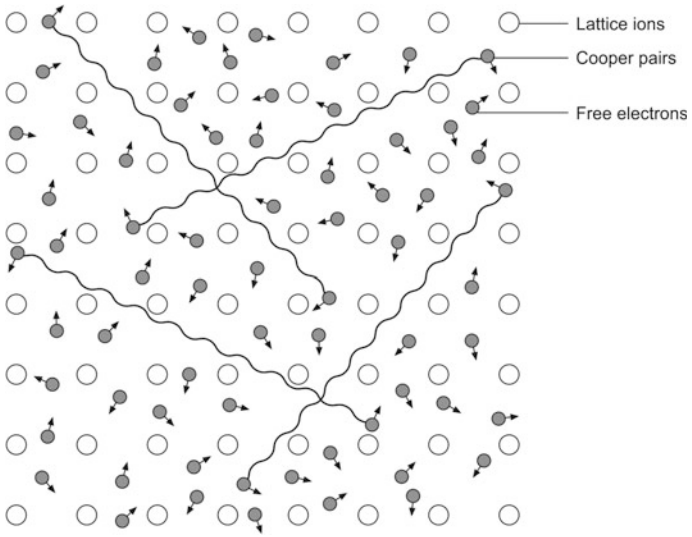

Fig. 5.3 Single electron and Cooper pairs in a metal lattice. Pairs extend over long distance

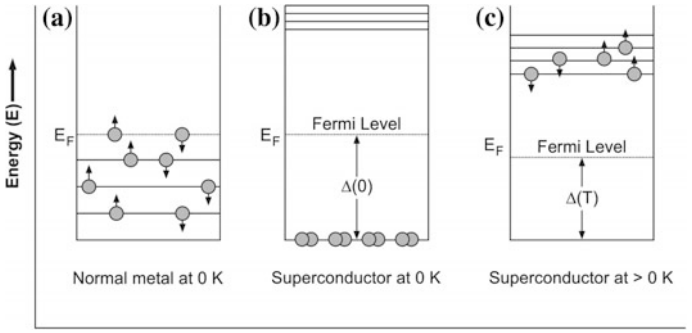

Fig. 5.4 Pictorial depiction of the energy spectrum of a metal and a superconductor

The energy level diagram of a normal metal ($T = 0$), a superconductor at $T = 0$ and at $T > 0$ has been shown in Fig. 5.4. All the levels below Fermi level are filled in a metal and those above Fermi level are empty. In a superconductor at $T = 0$ all the electrons form bound pairs and condense to the ground state and an energy gap = 2Δ appears in the energy spectrum. A pair can be broken into quasi-electrons only when an energy equal to 2Δ is supplied to the superconductor. These electrons will occupy the empty levels above the energy gap. At finite temperature (below T_c) bound pairs as well as single electrons are interspersed. All the pairs occupy the ground state and the single electrons occupy the levels above the energy gap.

5.4.2 Formulation of the Microscopic Theory

With the plethora of crucial experimental data on superconductors available and the phenomenological and semi-phenomenological theories already developed, the time was just ripe for Bardeen, Cooper and Schrieffer to formulate their microscopic theory for superconductors. BCS set for themselves the task to formulate a theory that accounts for all the experimental observations namely, (i) the zero electrical resistance below T_c, (ii) second order phase transition at T_c, (iii) Meissner effect, (iv) an energy gap of right magnitude, (v) a jump in specific heat at T_c and an exponential term in the electronic specific heat in superconducting state, (vi) dependence of T_c on isotopic mass and (vii) the penetration depth and its temperature variation.

The theory was built around the Cooper pair formation involving electron-electron interaction via the exchange of virtual phonon discussed above. This interaction is attractive when the energy difference between the electron states is smaller than the phonon energy $\hbar\omega$. Superconducting phase is formed when this attractive force is greater than the repulsive screened Coulomb interaction. With the electrons now forming bound state, the energy is lowered and pairs condense to the BCS ground state. An energy gap appears in the energy spectrum. An energy equal to this gap energy is required to break a pair. All the pairs in the ground state are indistinguishable and are in the same phase. They keep on changing their partners within a narrow energy band around the Fermi level. Momentum is conserved when a pair is formed $(k_1 + k_2) = \left(k_1' + k_2'\right)$. Here k_1 and k_2 are the wave vectors of electron one and electron two before pairing and k_1' and k_2' are the respective wave vectors after pairing. According to BCS theory all the pairs can be represented by a single wave function. The state so produced is highly ordered. This order extends over the entire lattice and is responsible for most of the exotic properties of the superconductors.

A detailed analysis of the BCS theory is outside the scope of the book and I refer to their original paper [1]. We, however, summarize below the important results and relationship between different superconducting parameters calculated by BCS.

5.4.3 Transition Temperature

In the weak coupling limit ($kT_c \ll \hbar\omega$) the expression for the transition temperature has been obtained by solving ground state energy equations and is given by the expression

$$kT_c = 1.14\hbar\omega \exp\left[-\frac{1}{N(0)V}\right] \tag{5.31}$$

where $N(0)$ is the density of electron states of one spin per unit energy at the Fermi level and V the electron-phonon interaction parameter. Here we find that T_c is proportional to the phonon frequency $\hbar\omega$ which is consistent with the observation of the isotope effect in superconductors. We also notice in (5.31) that T_c is a strong function of the electron concentration as the density of state enters in the exponential term. It is thus possible for one to make calculations for the change in T_c as a result of alloying or applying pressure.

5.4.4 The Energy Gap

Another remarkable finding of the BCS theory is that it predicts a relationship of T_c with the energy gap which is given by

$$2\Delta = 3.5kT_c \tag{5.32}$$

It is interesting to note that the energy gap normalized to the zero temperature value when plotted for various superconductors against the reduced temperature, T/T_c lie on a single universal curve as already shown in Fig. 2.20. The law of corresponding state does predict this ratio to be the same for all superconductors. As seen in the Fig. 2.20 the energy gap at $T = 0$ is almost independent of temperature. Close to T_c, gap versus temperature relationship is given by

$$2\Delta = 3.2kT_c[1 - (T/T_c)]^{\frac{1}{2}} \tag{5.33}$$

5.4.5 Critical Field and Specific Heat

BCS theory predicts the critical field B_c to vary as $1 - (T/T_c)^2$ which is in conformity with the Gorter-Casimir two-fluid model [14]. Most of the B_c experimental data fall between the BCS curve and the $1 - (T/T_c)^2$ plot. The maximum deviation is 4 %. The critical field at $T = 0$ is given by

$$B_{co} = [4\pi N(0)]^{\frac{1}{2}}\Delta(0) = 1.75[4\pi N(0)]^{\frac{1}{2}}kT_c \tag{5.34}$$

where $2\Delta(0)$ is the energy gap at $T = 0$ and the density of states $N(0)$ has been taken for a unit volume. On the basis of law of corresponding states (5.34) yields

$$\gamma T_c^2/B_{co}^2 = \frac{1}{6}\pi[kT_c/\Delta(0)]^2 = 0.170 \tag{5.35}$$

Here γ is the coefficient of the electronic specific heat of the normal state ($C_{en} = \gamma T$) and is given by

$$\gamma = \frac{2}{3}\pi^2 N(0)kT \tag{5.36}$$

The two fluid model gives the value of the ratio in (5.35) as 0.159 quite close to the BCS value.

At T_c, the energy gap disappears and the specific heat drops to normal state value. This peak in specific heat is caused by the onset of second order phase transition. The ratio of the excess specific heat to normal state value at T_c turns out to be

$$\frac{C_{es} - \gamma T_c}{\gamma T_c}|_{T_c} = 1.52 \tag{5.37}$$

The value of this ratio as given by Gorter-Casimir model is 2.00. Experimental values fall between 1.52 and 2.00. The experimental data on Sn fits extremely well with the BCS curve. BCS value near the T_c was later corrected and the intercept at $T = T_c$ became 2.52. The two curves thus almost overlap all through. The electronic specific heat can be expressed as

$$\frac{C_{es}}{\gamma T_c} = ae^{-bT_c/T} \tag{5.38}$$

Corak et al. [15] have reported their specific data on V and Sn which fit with the above expression quite well for $T_c/T > 1.4$ with parameters, $a = 9.10$ and $b = 1.50$. The BCS theory thus gives a very good account of the thermodynamical properties of the superconductors.

The BCS theory also yields expressions for all other superconducting parameters like critical current, coherence length and the penetration depth. It deals very successfully with Meissner effect and electro-dynamical properties of the superconductors. At the same time the theory does not invalidate any of the then existing phenomenological theories. BCS theory remains to-date the successful microscopic theory of superconductivity. It stood the test of time and was awarded Nobel Prize only in 1972 a good 15 years after it was formulated. It explains well the behaviour of at least type I superconductors. Theory, however does not predict which material should become superconductor and which should not. It has also not been successful in its existing form to explain the occurrence of superconductivity in so called HTS cuprate superconductors.

5.5 Peculiar High T_c Superconductors

As discussed in detail in Chap. 4 the discovery of superconductivity in La-system [16] beyond 30 K and then in Y-system [17] and Bi-system [18] to 92 and 110 K respectively caused unprecedented excitement among the superconductivity

community. A race started to look for newer materials with higher and higher T_c. The discovery also threw a challenge to theoreticians to find a suitable theory which can account for high T_c values far beyond that could have been accounted for by the BCS theory. While companies have been engaged in exploiting these materials for magnet and power applications, theoreticians remain entangled in solving the mystery. Leading theory groups have been putting forth various theories and hypothesis at times contradicting each others' view point. High T_c superconductors have several features quite common to the conventional superconductors but have many properties that are anomalous. This dual behaviour has been a riddle to be resolved. We discuss below the anomalous properties, that these superconductors display.

5.5.1 Anomalous Properties of the Cuprates

5.5.1.1 Temperature-Hole Concentration Phase Diagram

Cuprates are unique materials in so far as they transform from insulating state to a superconducting state at an optimum level of doping. Oxides in general are supposed to be insulating in their solid state but some of them, mostly binary and ternary oxides of transition metals show transition to metallic state under suitable condition of temperature, pressure and doping. What surprised us all in 1986 was that La_2CuO_4, which is an antiferromagnetic insulator with a Neel temperature of 290 K, turns metallic and subsequently goes superconducting at 30 K at a suitable doping with Ba or Sr. La is in La^{3+} valence state, Cu in Cu^{2+} valence state and O in O^{2-} valence state in the un-doped La_2CuO_4 compound. If, however, La^{3+} is replaced by Sr^{2+}, either Cu has to be in Cu^{3+} state or O has to be in O^{1-} state. Spectroscopic evidence does suggest the presence of O^{1-} state, thus adding a hole in the otherwise filled p-shell. This hole concentration is proportional to the doping concentration x in $La_{2-x}Sr_xCuO_4$. The movement of holes leads to metallicity and ultimately to superconductivity.

The Temperature-Sr doping (x) phase diagram [19] of this system is shown in Fig. 5.5. In the under-doped region the material is an antiferromagnetic insulator. Below a temperature T^* and above T_c the material has a pseudo-gap phase. The transition between the Fermi liquid and strange metal occurs gradually and there is no sharp boundary between the two phases. Superconductivity occurs between $x = 0.06$ and $x = 0.3$ and the highest value of T_c is found around $x = 0.2$. QCP indicates quantum critical point at which T^* becomes zero. At increased doping level (over-doped) different phases are obtained at different temperatures. Superconducting phase occurs below T_c for a doping level $x = 0.06$ to $x = 0.3$. Thus we find that the doping level is very crucial for the occurance of superconductivity in cuprates. For very low doping called 'under-doping', the material is in a long range antiferromagnetic state, it is superconducting for 'optimum doping' and finally, superconductivity disappears in 'over-doped' systems. T_c turns out maximum close to 0.2 holes/CuO_2 layer doping.

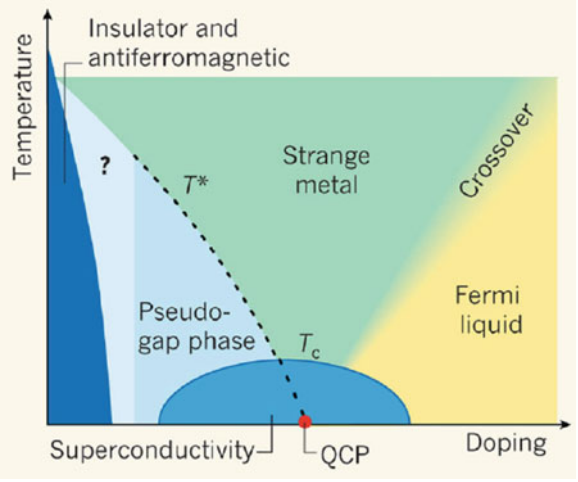

Fig. 5.5 Temperature-Sr doping (x) phase diagram of the $La_{2-x}Sr_xCuO_4$ compound [19]. (*Courtesy* Chandra Varma and with permission from Nature Publishing House)

5.5.1.2 Normal State Resistivity

The electrical resistivity of the cuprates is anomalous. As discussed earlier cuprates are highly anisotropic materials. The resistivity in the Cu–O planes (*ab*-planes) is quite different from along the *c*-axis. Resistivity in *ab* plane is metallic over a wide range of temperature down to T_c where the material goes superconducting. Resistivity along the *c*-axis, on the other hand, is semiconductor like even though the material displays superconductivity at the same temperature, T_c. Thus below T_c one observes superconductivity in both the orientations. Cuprates also exhibit strong anisotropy in their J_c and B_{c2} behaviour.

Another anomalous behaviour of normal state resistivity is that in the *ab*-plane the resistivity varies linearly over a wide temperature range of several hundred *K* down to T_c as shown in Fig. 5.6. In normal free electron metals, well above Debye temperature (Θ_D) the resistivity is linear in temperature but below Θ_D it decreases rather fast $\sim T^5$. Resistivity in metals is caused by the scattering of electrons by phonons, lattice imperfections and other electrons. None of the above scattering mechanisms accounts for the observed variation of resistivity in cuprates.

This perfect linearity of resistivity with temperature all through from the high temperature to near T_c is a function of doping as well. This is seen from Fig. 5.7 for the compound $La_{2-x}Sr_xCuO_4$ [20] for different values of doping ($x = 0.07$, 0.15 and 0.34). The R-T plot is perfectly linear throughout the large temperature range for $x = 0.15$, that is for optimum doping. For under-doped and over-doped compound the curves deviate from perfect linearity. This linear resistivity behaviour is certainly non-Landau Fermi liquid like and thus quite different from the normal metals. The under-doped regime ($x = 0.07$) marks the pseudogap causing a dip in resistivity below a certain temperature. Over-doped regime ($x = 0.34$) hints at the recovery of Landau Fermi liquid behaviour. Very strangely this linearity in R-T plot is found in all the cuprates with differing T_c values right from 20 to 120 K with almost similar slope.

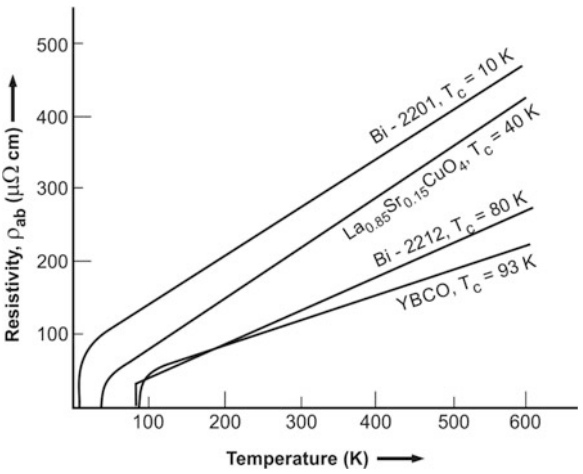

Fig. 5.6 Typical normal state resistivity of LSCO, YBCO, BSCCO-2201 and BSCCO-2212 in *ab*-plane plotted against temperature. ρ–T is linear over a wide range of temperature (adapted from [5])

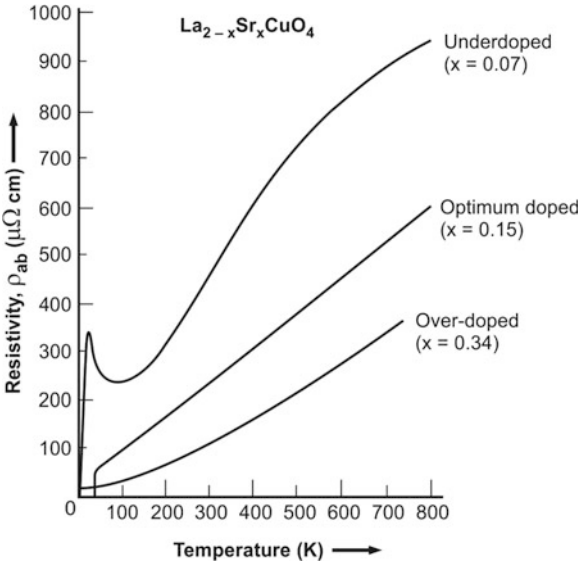

Fig. 5.7 The electrical resistivity of $La_{2-x}Sr_xCuO_4$ in *ab*-plane for different doping levels (x = 0.07, 0.15 and 0.34). The perfect linearity for optimum doping (x = 0.15) and deviations for under-doped and over-doped compound are distinctly visible [20] (With permission from Elsevier)

Besides, the anomalous linear resistivity/temperature behaviour, the cuprates also display normal state properties like Hall effect and frequency dependence of the electrical conductivity quite different from the normal metals. The electrical conductivity, $\sigma(\omega)$, for example, decreases as ω^{-1} instead of ω^{-2} expected for the normal metal. Hall effect measurements yields parameters, Hall angle $(\theta_H \propto T^{-2})$, Hall resistivity $\left(\rho_{xy} \propto T^{-1}\right)$ and the transverse magneto-resistance $(\Delta\rho/\rho \propto T^{-4})$. In addition, the photo-electron spectroscopy shows that over a large energy range the spectral function is dominated by a incoherent function. All these observations

strongly hint at the failure of the Landau-Fermi liquid theory in the optimally doped cuprates. The measurements on momentum transport scattering rate in resistivity in normal state shows the processes to be dominated by electronic scatterings and not by electron-phonon scattering. There is enough evidence that the inverse life time increases with energy linearly and not quadratically as expected in normal metals. As seen from the phase diagram (Fig. 5.5) superconductivity occurs in a narrow region of optimal doping by holes. If more holes (0.3–0.4) are doped the resistivity curve (Fig. 5.7) shows an upward turn and can be expressed by $\rho = \rho_0 + \rho' T^2$. The T^2 law is reminiscent of quasiparticle-quasiparticle scattering in Landau-Fermi liquids. The over-doped region thus tends to be closer to the Landau-Fermi liquid theory.

5.5.1.3 Presence of Pseudo-Gap in Highly Under-Doped Superconductors

Several precision experiments like the specific heat, angle-resolved photoemission spectroscopy (ARPES) and the scanning tunneling microscopy (STM) have revealed the existence of a pseudo-gap in the energy spectrum of highly under-doped cuprates (Fig. 5.5), a strange behavior indeed. This energy gap is quite different from the usual energy gap in superconductors which appears at T_c. The pseudo-gap exists over a wide range of temperature and doping. The understanding of the origin of this pseudo-gap may play a crucial role in understanding the mechanism responsible for the occurrence of superconductivity in these high T_c superconductors. This energy gap is termed 'pseudo-gap' because it has no direct relationship with T_c. Through a systematic study on a heavily under-doped Bi (2212) system with $T_c = 30$, 40 and 50 K using ARPES technique, a Stanford group had observed distinctly two energy gaps along the Fermi surface in different parts of the momentum space. Their observation hints at the presence of a small gap with a sharp coherent peak near the nodal region identified with pseudo-gap and a larger gap at the antinodal region identified as the normal superconducting gap. The two gaps, however, display opposite behavior on doping. The magnitude of the larger gap scales with T_c in conformity with the BCS theory.

The observation of two energy gaps and the presence of a pseudo-gap are two unique features of cuprates and their origin may as well throw light on the occurrence of superconductivity in these materials. Above experiments also confirm that the pseudo-gap is not a precursor to superconducting. Instead, this state competes with the superconducting state. These studies reveal that superconductivity in the under-doped state is weakened by the loss of coherence due to a reduction in the superfluid density and weakening of the pair amplitude. The reduction in the superconducting gap may be related to the shrinkage of the Fermi surface due to under-doping, leading to a reducing phase space for pairing.

5.5.1.4 Comparison with Conventional Metallic Superconductors

Cuprates have many similarities with the conventional superconductors but show significant deviations too. For example, the following three experimentally determined dimensionless ratios for cuprates are all within the range of conventional superconductors. These ratios are

$$\text{(i)} \quad \frac{2\Delta}{kT_c} \approx 3.5\text{–}4.8 \tag{5.39}$$

$$\text{(ii)} \quad \frac{2\Delta}{\gamma T_c} \approx 1.5 \tag{5.40}$$

$$\text{(iii)} \quad \frac{B_c}{4\pi N(0)^{\frac{1}{-\Delta}}} \approx 1 \tag{5.41}$$

2Δ being the energy gap.

Formation of Cooper pairs $(e^* = 2e)$ has been confirmed in cuprates experimentally through the observation of dc/ac Josephson effect.

Existence of an energy gap in the single particle energy spectrum is confirmed, though high in comparison with the transition temperature thermal energy.

Isotope ^{18}O has been substituted in place of normal ^{16}O but the decrease in T_c observed is small, putting a question mark on the exact role of lattice in pair formation in cuprates.

Flux quantization $\left(\phi = \frac{h}{2e}\right)$ too has been confirmed in these materials.

Cuprates are extreme type II superconductors, that is, $(\lambda/\xi \gg 1)$, meaning thereby that the field penetration is large because of low carrier concentration $\approx 2 - 5 \times 10^{21}/\text{cm}^3$. Consequently these superconductors also show poor Meissner shielding. In clean limit, $\xi_{T=0} \ll$ mean free path which is of the order of 10–20 nm near T_c. Following the BCS expression for coherence length $\xi = \hbar v_F/\pi\Delta(0)$ and taking the Fermi velocity $v_F = 1.1 \times 10^7$ cm/s and the gap parameter $2\Delta(0) = 6kT_c$ coherence length, ξ_{ab} turns out to be 1.5 nm which is a typical value for YBCO in *ab*-plane. However the coherence length along the *c*-axis, $\xi_c = 0.15 - 0.3$ nm is much smaller than in the *ab*-plane. This low value of ξ_c indicates that the CuO_2 layers are weakly coupled because of large charge reservoir layers.

The concept of short coherence length is interesting in so far as it indicates at low carrier concentration <1 per CuO_2 layer. Since coherence volume ξ^3 contains 5–10 CuO_2 units, it has less than 5 pairs far less than the 10^4 pairs in aluminum superconductor. This leads to pronounced fluctuation effects. The $B_{c2} = \phi_0/2\pi\xi^2$ of these superconductors turns out of the order of 100 T which is almost four to five times the B_{c2} value for conventional best superconductor, the Nb_3Sn. Peculiar features like different mobilities, the layered structure and the granular nature of

these materials make it very difficult to work out transport parameters. These materials characterized by short coherence length and high penetration depth also display most unusual vortex state.

Another complication in high T_c cuprates comes in their $J_c - B$ behaviour. These materials show sharp drop in J_c with increasing magnetic field because of the grain boundary problem. Grains are weakly coupled. J_c is thus quite different within the grain and in the inter-grain region. Intra-grain J_c is usually very high. Material being highly anisotropic J_c in *ab*-plane is much higher than along the *c*-axis. These materials show enhanced flux creep and flux flow effects because of high operating temperature (high T_c) and low pinning potential. The flux creep or the so called thermal activation leads to a time decay of J_c from J_{co}, the value without thermal activation. Several techniques have been tried to introduce defects to pin the flux motion. Highest value of J_c has been obtained by growing highly oriented epitaxial films and highly pure single crystals.

HT cuprates are thus very unconventional but fascinating materials. What causes the carriers to pair up below T_c is still a unresolved issue.

5.6 Possible Theories of HTS

A detailed account of the theories proposed during this period of about two decades by very many theorists is outside the purview of the book and we just mention about a couple of serious attempts made to explain the occurrence of superconductivity in these cuprates. The biggest challenge posed by these materials and as discussed in sections above, is that they behave quite similar to conventional superconductors in many respects but differ profoundly in many others. Formation of charge carrier pairs in these materials is well established experimentally. But to find the mechanism of formation of the pair has proved to be a daunting task.

In BCS superconductors T_c increases with the lattice frequency and the electron-phonon coupling parameter. Even after taking the largest values of these two parameters for the known materials T_c cannot exceed 35–40 K if the pair formation is assumed to be phonon mediated. Obviously a new possible mechanism for the Cooper pair formation is to be worked out and the ensued theory should be able to explain all the normal and anomalous properties of the cuprates. We just give a summary of a few credible attempts made by the theorists.

Various theories were proposed by many theory groups during last 25 years ranging from the extension of the BCS theory (attraction mediated by phonons), the excitonic mechanism based on electronic polarization, the marginal Fermi liquid theory, spin bipoloran (or spin bag), the resonating valence bond (RVB) theory and the spin fluctuation theory. After a long time of fights and turmoil, people have by now come to accept two theories on which the work still continues.

5.6.1 The Resonating Valence Bond (RVB) Theory

The concept of resonating valence bond (RVB) was originally introduced by Pauling [21] in the context of pπ bond states of some organic molecules. The valence bond develops between a pair of atoms bonded by sharing of unpaired valence electrons of the atoms at the outermost levels. The bonded electrons form a singlet which resides in between the atoms. This singlet can also be considered a dimer. In a lattice when valence bonds or dimers between a pair of atoms (nearest neighbors) stabilize into a configuration of many body singlet pairs a stable state is formed which is actually a resonating valence bond state. This state is a superposition of all the possible singlets. It also shows that these singlets move freely between the pair of atoms and thus can give rise to even a metallic state. However, this superposition gives rise to an energy gap at $T = 0$ with respect to any state with long-range charge fluctuations and, therefore, the resonating valence bond state in its pure form cannot be a metal.

Anderson [22] revived this concept for describing the ground state of the Mott insulators where electron-electron correlation in systems with one electron per unit cell yields an insulating ground state while forming singlet pairs. The spin-1/2 excitations in these systems could either form an antiferromagnetic Neel state at $T = 0$ or a fluctuating resonating valence bond state with superposition of singlet pairs. The fluctuations are quantum in nature which is further enhanced in lower dimension and geometric frustration. The Neel state is a solid while the RVB state is a liquid. In one dimension, both the states are identical and there is no energy difference between them. However, in two dimensions, the RVB state is found to be more stable with lower free energy. This can be easily understood in a triangular lattice of spin-1/2 particles. The antiferromagnetic coupling between a pair of spins cannot yield a stable configuration while satisfying the condition of spin pairing between any two nearest neighbors. Therefore, the stable state is the one which is a superposition of the fluctuating states—a resonating valence bond state. Soon after the discovery of cuprate superconductors, Anderson [23] realized that the essential physics of the origin of superconductivity is contained in the electronic states of the Cu–O planes which are ubiquitous in all the cuprates. The Cu–O planes with spin-1/2 excitations yield a fluctuating spin liquid—essentially a RVB liquid state. Once again, this state appears with a gap with respect to the long-range charge fluctuations and, therefore, is an insulator. The statistics of these spin-1/2 particles appear to be different from normal Fermi-Dirac statistics of indistinguishable particles such as electrons. These localized spin singlets (notwithstanding the fluctuations) do not conduct electricity. Only when this Mott insulator is doped by creating holes in the electron states, the electrons flow and carry current and thus induce metallicity.

Interestingly, it has been found that the collective behavior of the strongly interacting localized spins and delocalized holes leads to fractionization and these quantum particles acquire two different dispersion patterns and are clearly distinguishable from each other—spin-1/2 particles (spinons) are more like fermions

(ordinary electrons) while the charged particles are spinless bosons (holons). Separation of spin-charge spectra in two-dimensional Cu–O layers is an important outcome of the RVB concept. Depending on the doping level x, a certain number of spin singlet states thus get charged and form Cooper pairs. They condense following either Bose or Kosterlitz-Thouless condensation and give rise to the superconducting state. One important point worthy of mention here is that the RVB state of spin singlet pairs gives rise to a pseudogap at T^* ($>T_c$) at which the pairs break. Experimental observation of the pseudo gap [24] in cuprate superconductors points out that the RVB state does form and offers the background for superconductivity to emerge. However, recent experiments offer a contradictory picture as far as the superconductivity within RVB background is concerned. In Anderson's theory, the pseudo-gap is a precursor of the superconducting gap and, therefore, it should vanish at T_c. Yoshida et al. [25] on the other hand have confirmed, through ARPES experiments on LSCO system, the coexistence of pseudo-gap together with superconducting gap below T_c. It thus appears that the Cooper pairs do not originate from the charging of the spin singlet pairs. Instead, they originate elsewhere even though the collective modes of the background RVB state do provide the glue to bind them. The doped hole actually resides in oxygen ions instead of Cu 3d levels [26]. This, in turn, breaks the spin singlets and creates free-d electrons instead of d holes. These free-d electrons form the Cooper pairs while retaining the RVB background and the pseudo-gap. The theory has been built further by Anderson and co-workers [27–29].

5.6.2 The Spin-Fluctuation Theory

The second theory is the spin fluctuation theory developed by Monthoux and co-workers [30–32] which finds wider acceptability within the superconductivity fraternity. The theory is based upon the premise that the full treatment of charge and spin degree of freedom of the electrons is essential which predicts an attractive component of the interaction between electrons without invoking the phonon mediation. Cooper pair formation is possible through the involvement of spin fluctuations. The theory envisages that in an undoped cuprate the magnetic field, produced by the antiferromagnetically aligned spins of the outer most electrons of copper atoms lock the electrons in place. So it remains an insulator. Doping makes these electrons mobile rendering them free to move. A passing electron may set-up a pulsating pattern of spins quite similar to the lattice distortion in conventional superconductors. This distortion can pull another electron allowing the two electron pair-up to form a Cooper pair. This leads to unconventional type of superconductivity in materials like the cuprates which show sensitivity to the fine details of the crystal structure, the electronic and the magnetic property of the material. This theory too rules out the role of lattice in the occurrence of superconductivity for the same reason of not finding isotope effect in these materials like we found in conventional superconductors.

The focus of the theory has been to understand the origin of the physical properties of the cuprates in their normal state which can give a clue to the occurrence of superconductivity at high temperatures. It is argued that strong antiferromagnetic correlations of the nearly localized Cu^{2+} d orbitals are responsible for the unusual normal state properties. The same correlations are responsible for the occurrence of superconductivity with high T_c. The theory deals with the interaction of quasi particles having same charge and spin but not the same mass. In a real metal an electron with its moving cloud can be considered as a quasi-particle. Its effective mass can be two or more orders of magnitude higher than the mass of an electron.

It was established earlier, that quasi-particle scattering [33, 34] by paramagnons results in electrical resistivity which varies linearly with temperature. This quasi-particle interaction produced by magnetic excitations leads to superconductivity at higher T_c with a d-wave gap. The presence of conventional s-wave pairing has been ruled out by the detailed NMR studies on these materials. Enough experimental evidence exists which confirms the presence of a d-wave pairing. Schrieffer et al. [35–37] too believe that antiferromagnetic correlations play important role in the determination of the T_c of the superconductors but argue that the coupling between the quasi-particles and spin fluctuations is so strong that the normal state excitations are solitons (spin bag). They go to the second-order spin fluctuation exchange to obtain s-wave superconductivity rather than going to first-order term to obtain d-wave superconductivity.

The important results obtained by Monthoux et al. [30] can be summarized as;

(a)
$$T_c = \alpha\hbar\omega_{SF}(T_c)\frac{\xi^2(T_c)}{\alpha^2}\exp\left[-\frac{1}{\lambda(T_c)}\right] \tag{5.42}$$

$$\cong \alpha\frac{\Gamma(T_c)}{\pi^2}\exp\left[-\frac{1}{\lambda(T_c)}\right] \tag{5.43}$$

where ω_{SF} is the paramagnon energy, the dimensionless effective coupling constant $\lambda(T_c) = \eta g_{eff}^2(T_c)\chi_0(T_c)N(0)$ varies from 0.48 to 0.33 in the compounds and α and η are the constants of the material and are of the order of unity.

(b) In spite of the poor coupling below T_c the energy gap does open up rapidly reaching a maximum. This energy gap is larger than the gap in weak coupling BCS superconductors. The results are in conformity with the experiments.

(c) Smaller values of T_c and larger values of $\Delta_{max}(0)/k_{BT_c}$ are, however, obtained if the antiferromagnetic correlations happen to be strong.

(d) The temperature variation of the calculated planer spin susceptibility is found to be of right magnitude and matches well with experiments [38].

(e) The coupling constant $g_{eff}^2(T_c)$ evaluated from λ accounts well the anomalous resistivity as well as the optical properties of the normal state.

NMR experiments [39, 40] on $Y_1Ba_2Cu_3O_7$ in superconducting state have confirmed, first time, the presence of unconventional superconductivity in this material. The experimentally measured temperature dependent anisotropy of the relaxation rates of the ^{63}Cu and ^{17}O nuclei for field in plane and perpendicular to plane rule out the possibility of s-wave pairing being responsible for superconductivity in this system. Bulut and Scalapino [41] also confirm that the superconductivity is of the d-wave pairing type.

We thus find that the spin fluctuation mediated coupling model is quite an attractive one. The strong electron correlation between the local moment and the conduction electron leads to an anisotropic pair wave function in k-space with nodes on the Fermi surface. This d-wave symmetry of the pair wave function or the superconducting gap has been observed experimentally as well. A good successful theory has, however, yet to come which can explain everything and make good sense of huge data reported in literature till now.

References

1. J. Bardeen, L.N. Cooper, J.R. Schrieffer, Phys. Rev. **108**, 1175 (1957)
2. F. London, H. London, Proc. Roy. Soc. (London) **A149**, 71 (1935)
3. V.L. Ginzburg, L.D. Landau, Zh. Eksperim i Teor. Fiz. **20**, 1064 (1950)
4. L.P. Gorkov, Zh. Eksperim. i Teor. Fiz. **36,** 1918 (1959) [Sov. Phys.-JETP **9** (1364) (1959)]
5. T.V. Ramakrishnan, C.N.R. Rao, *Superconductivity Today*, Chap. 4 (Wiley Eastern Ltd., Hoboken, 1992)
6. B.D. Josephson, Phys. Lett. **1**, 251 (1962)
7. H. Fröhlich, Phys. Rev. **79**, 845 (1950)
8. E. Maxwell, Phys. Rev. **78**, 477 (1950)
9. C.A. Reynold, B. Serin, W.H. Wright, L.B. Nesbitt, Phys. Rev. **78**, 487 (1950)
10. J. Bardeen, Phys. Rev. **80**, 567 (1950)
11. H. Fröhlich, Phys. Rev. **79**, 845 (1950)
12. H. Ibach, H. Luth, *Solid State Physics*, 2nd edn. (Springer, Berlin, 1996)
13. L.N. Cooper, Phys. Rev. **104**, 1189 (1956)
14. C.J. Gorter, H.B.G. Casimir, Phys. Z. **35**, 963 (1934)
15. W.S. Corak, B.B. Goodman, C.B. Satterthwaite, A. Wexler, Phys. Rev. **102**, 656 (1956)
16. J.G. Bednorz, K.A. Muller, Z. Phys, B-Condensed Matter **64**, 189 (1986)
17. M.K. Wu, J.R. Ashburn, C.J. Torng et al., Phys. Rev. Lett. **58**, 908 (1987)
18. H. Maeda, Y. Tanaka, M. Fukutomi, T. Asano, Jpn. J. App. Phys. **27**, L665 (1987)
19. C.M. Varma, Nature **468**, 184 (2010)
20. B. Betlogg, Solid State Commun. **107**, 639 (1998)
21. L. Pauling, *Nature of Chemical Bond* (Cornell University Press, New York, 1960)
22. P.W. Anderson, Mater. Res. Bull. **8**, 153 (1973)
23. P.W. Anderson, Science **235**, 1196 (1987)
24. S. Hufner, M.A. Hossain, A. Damascelli, G.A. Sawatzky, Rep. Prog. Phys. **71,** 062501 (2008) (See, for example)
25. T. Yoshida, M. Hashimoto, S. Ideta et al., Phys. Rev. Lett. **103**, 037004 (2009)
26. M-L. Chen, arXiv: 1206.0862v3 (2012)
27. G. Baskaran, Z. Zou, P.W. Anderson, Solid State Commun. **63**, 973 (1987)
28. G. Baskaran, P.W. Anderson, Phys. Rev. **B37**, 580 (1988)
29. G. Baskaran, Phys. Rev. **B64**, 092508 (2001)

30. P. Monthoux, A.V. Balatsky, D. Pines, Phys. Rev. Lett. **67**, 3448 (1991)
31. P. Monthous, A.V. Balatsy, D. Pines, Phys. Rev. **B46**, 14803 (1992)
32. P. Monthoux, D. Pines, G.G. Lonzarich, Narture **450**, 1177 (2007)
33. H. Monien, M. Takigawa, D. Pines, Phys. Rev. **B43**, 258 (1991)
34. H. Monien, P. Monthous, D. Pines, Phys. Rev. **B43**, 275 (1991)
35. J.R. Schrieffer, X.G. Wen, S.C. Zhang, Phys. Rev. **B39**, 11663 (1989)
36. A. Kampf, J.R. Schrieffer, Phys. Rev. **B41**, 6399 (1990)
37. A. Kampf, J.R. Schrieffer, Phys. Rev. **B42**, 7967 (1990)
38. S.E. Barrett, D.J. Durand, C.H. Pennington et al., Phys. Rev. **B41**, 6283 (1990)
39. S.E. Barrett, J.A. Martindale, C.H. Pennington et al., Phys. Rev. Lett. **66**, 108 (1991)
40. M. Takigawa, J.L. Smith, W.L. Hults, Phys. Rev. B **44**, 7764 (1991)
41. N. Bulut, D.J. Scalapino, Phys. Rev. Lett. **68**, 706 (1992)

Chapter 6
Practical Superconductors

Abstract All superconductors exhibit thermal and EM instabilities because of their poor thermal conductivity and worst electrical conductivity in their normal state. These instabilities lead to premature quench in superconducting magnets. To circumvent the problem, practical superconductors are produced in the form of fine filaments in high conductivity copper matrix. Most popular superconductor Nb–Ti had been produced this way by co-processing it with Cu and used universally up to a field of 9 T. To meet the stringent requirement of high J_c and low ac losses for accelerator and fusion reactor magnets, impressive improvements have been made in the production techniques. Conductors with fine filaments smaller than 1 μm cladded with diffusion barriers, with low filament spacing to dia. ratio ($\sim$0.15), resistive matrix to reduce filament coupling and low fraction of Cu have been produced. Conductors carrying large J_c of the order of 50 kA in Rutherford and CICC (cable-in-conduit conductor) configuration have been produced. For future accelerators and fusion reactors high field A-15 Nb_3Sn superconductor cables have been produced by bronze technique, internal tin (IT) method, improved distributed tin (DT) method and the jelly roll (JR) methods. The DT technique has yielded Nb_3Sn wire with 2–3 μm filament dia. with $J_c = 10^5$ A/cm^2 (12 T, 4.2 K) and ac loss = 300 kJ/m^3 (±3 T, 4.2 K) suitable for ITER application. JAERI has produced CICC Nb_3Al cable by JR technique which produces a field of 13 T at a current of 46 kA. NRIM, KEK and FNAL are jointly developing Nb_3Al Rutherford cable (14 × 1.84 mm) using 27 strands prepared by the so called JR-RHQT (rapid heating quench technique) for the luminosity upgradation of the LHC. V_3Ga conductors too are being developed by PIT technique for the future Demo fusion power reactor to take care of the induced radioactivity by the 14 MeV neutrons released by the D + T reaction. HTS like REBCO are being developed to generate ultra high field. A record field of 35.4 T has been reported by NHMFL recently.

R.G. Sharma, *Superconductivity*, Springer Series in Materials Science 214,
DOI 10.1007/978-3-319-13713-1_6

6.1 Superconductors Useful for Magnet Application

Even before the discovery of the high temperature superconductors or the so called cuprate superconductors, over two thousand conventional metallic superconductors were known to us, yet precisely only three superconductors, namely Nb–Ti, Nb_3Sn and V_3Ga were produced commercially during 1970s and 1980s. The later two superconductors belong to A-15 class of crystal structure and are extremely brittle. In the later years even the commercial production of V_3Ga stopped in favour of Nb_3Sn. There are several other superconductors mostly belonging to A-15 class which hold promise to become available for applications in future as they have high values of B_{c2} and J_c. Their inability to be fabricated in desired multifilamentary form remains a hurdle. These superconductors are listed in Table 6.1. The upper critical field (B_{c2}) of some of these potential superconducting alloys and compounds are quite high and are plotted [1] in Fig. 6.1. Materials are available with B_{c2} as high as 60 T ($Gd_{0.2}PbMo_6S_8$) only if techniques are developed to produce them in long length and in multifilamentary configuration. Predictably, one of these materials, Nb_3Al has been recently produced by the National Institute for Materials Science (NIMS) in Japan and seems to be at the verge of being commercialized. Figure 6.2 shows the J_c versus B plots for these three commercial materials. Clearly, Nb–Ti superconductor is the obvious choice for field production up to 9 T. Since Nb–Ti is a ductile alloy and easy to be manufactured, it has been the workhorse so far in entire electro technical applications, laboratory magnets, particle accelerators and fusion reactors. However, wherever the field requirement is in excess of 9 T one had to switch over to either Nb_3Sn or V_3Ga both belonging to what is known as A-15 superconductors. We will discuss this class of materials separately in subsequent sections. Among these two materials V_3Ga was traditionally considered to be a superior material for high field application. The reason being that the value of γ (ratio of specific heats) for V_3Ga is 3.04 much higher than the corresponding value of 1.42 for Nb_3Sn and since J_c is proportional to $\gamma^{\frac{3}{2}}(T_c - T)^{\frac{5}{2}}$, the J_c of V_3Ga tends to be roughly twice the J_c for Nb_3Sn. However, since the T_c for V_3Ga is little lower

Table 6.1 High field superconducting materials having potential for technological applications

Material	Crystal structure	T_c (K)	B_{c2} (T) at 4.2 K	J_c (A cm^{-2}) at 4.2 K at B (T)
Nb–Zr	A-2	9.5	11	1×10^4 (6 T)
Nb–Ti	A-2	9.3	11	1×10^6 (7 T)
Nb_3Sn	A-15	18.3	23	2×10^4 (20 T)
Nb_3Al	A-15	18.9	32	1.5×10^4 (16 T)
Nb_3(Al, Ge)	A-15	20.5	41	1×10^4 (12 T)
Nb_3Ga	A-15	20.3	34	
Nb_3Ge	A-15	23.2	37	1×10^5 (21 T)
V_3Si	A-15	17.0	23.5	1×10^3 (10 T)
V_3Ga	A-15	15.2	23	1×10^5 (20 T)
V_2(Hf, Zr)	C-15	10.1	23	3×10^5 (6 T)

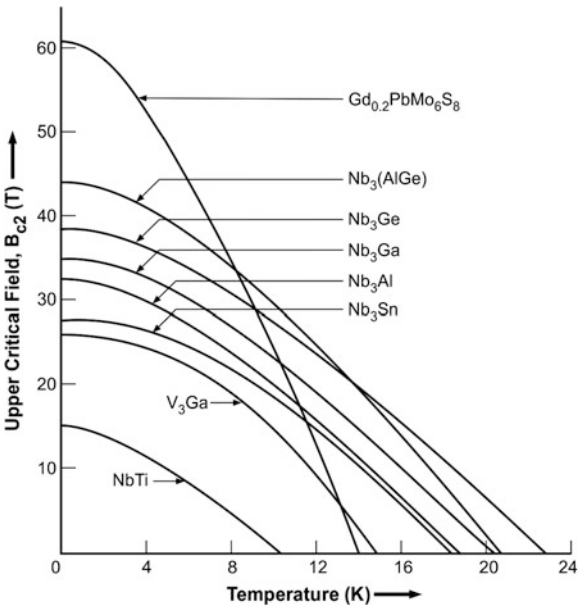

Fig. 6.1 The upper critical field B_{c2} versus temperature plots of potential superconductors for applications. Highest B_{c2} (60 T) is for Cheveral phase compound $Gd_{0.2}PbMo_6S_8$ [1] (By permission of Oxford University Press)

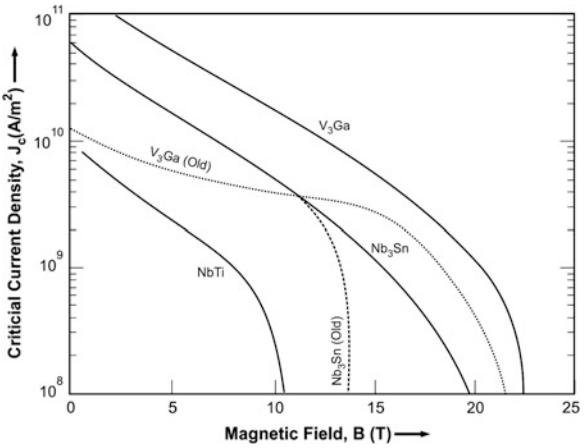

Fig. 6.2 The J_c versus B plots for the three commercial superconductors, namely: ductile Nb–Ti alloy, Nb_3Sn and V_3Ga. The last two superconductors are highly brittle intermetallic compounds

(15.2 K) than for Nb_3Sn (18.2 K) there is a crossover in the J_c–B plots for the two industrial superconductors in a field region of $\sim$12 T. This cross over is seen by the dotted lines for the two superconductors in Fig. 6.2. Great improvement in J_c has however been achieved for Nb_3Sn over the years through elemental additions and Nb_3Sn is routinely used for field production up to 20 T. The solid curves for the two materials are the improved J_c values achieved through elemental additions and the micro-structural control. Nb_3Sn being significantly cheaper than V_3Ga it becomes the material of choice for applications in high field magnets, be it for laboratory use

or other uses like in accelerators and fusion reactors. Nb_3Al is the next A-15 superconductor likely to be manufactured commercially soon.

Why out of thousands of known superconductors only three superconductors have been produced on an industrial scale, is a pertinent question. There are stringent conditions to be met while fabricating these superconductors in wire and cable form. These, so called industrial superconductors are to be fabricated in the form of wires consisting of a large number of very fine superconducting filaments embedded in a high conductivity material like copper. These wires are then twisted and transposed to make cables. Co-processing of high field brittle A-15 superconductors with copper becomes a challenge. Fine size filaments and conducting matrix are essential to counter the problem of the "thermal instability of superconductors" caused by their peculiar properties. We will discuss this topic a bit in detail in the following section.

6.2 Thermal and Electromagnetic Instability Problem—The Multifilamentary Superconductors

All superconductors are poor conductors of heat, because Cooper pairs do not transport entropy, and worst conductor of electricity in their normal state (above T_c) as most type II superconductors are either alloys or compounds. As shown in Table 6.2 the electrical resistivity of a pure metal like copper is about four orders of magnitude smaller than a superconductor in its normal state. On the other hand the thermal conductivity of a normal conductor is about three order of magnitude larger than for a superconductor. In other words, the thermal diffusivity in normal metal is 3–4 orders of magnitude higher than that in a superconductor and the magnetic diffusivity in a superconductor is higher by almost the same magnitude than in a normal metal. This, in simple words, means that heat travels faster in a normal conductor than in a superconductor and magnetic flux travels faster in a superconductor than in a normal metal. This implies that magnetic flux takes over a superconductor before the heat is dissipated away to the surrounding. As a result, the temperature of the superconductor may exceed T_c and it may turn normal. This is termed 'quenching'.

Table 6.2 Typical thermal, electrical and magnetic parameters of copper and a superconductor in its normal state

Parameter	Superconductor in normal state	Pure metal like copper
Resistivity, ρ (Ω cm)	$\sim 10^{-5}$–10^{-4}	$\sim 10^{-8}$
Thermal conductivity, λ (W cm^{-1} K^{-1})	$\sim 10^{-3}$–10^{-2}	$\sim$1–10
Heat capacity S (J cm^{-3})	$\sim 10^{-3}$–10^{-2}	$\sim 10^{-3}$
Thermal diffusivity D_H	$\sim$1	$\sim 10^{3}$–10^{4}
Magnetic diffusivity D_M	$\sim 10^{3}$–10^{4}	$\sim$1

6.2.1 Degradation and Flux Jump

Early magnets wound using superconducting wires quenched at current densities significantly smaller than the values quoted on the basis of short sample tests. This was believed to be partly due to 'flux jumps' or the 'premature quenching'. The flux jump can be understood something like this. Suppose, we apply a small magnetic field to a superconductor, surface screening currents will start flowing in a surface layer to protect the superconductor against the flux penetration. Flux will however penetrate the superconductor a small distance equal to the penetration depth λ. The resulting heat of magnetization will cause a small temperature increase in the superconductor by small amount, say ΔT_1. This increase in temperature will bring down the screening current density allowing an additional small field penetration and a further raise in temperature, say by an amount ΔT_2. If this temperature rise ΔT_2 is greater than ΔT_1, further increase in magnetic field will raise the conductor temperature further by a small amount say, ΔT_3 and the process will continue till the superconductor quenches to normal state. We refer it as 'thermal run-away' or 'flux jump'. Let us assume that ΔT_2 happens to be smaller than ΔT_1 and ΔT_3 smaller than ΔT_2, the material can be stabilized against flux jump. This can be achieved by either resorting to

1. Adiabatic stability criterion
   or
2. Dynamic stability criterion

Let us discuss these two criteria to stabilize a superconductor against flux jumps in detail. Figure 6.3 shows the magnetic field penetration of a superconductor of diameter $2a$. Field penetration increases with increasing field strength and at a

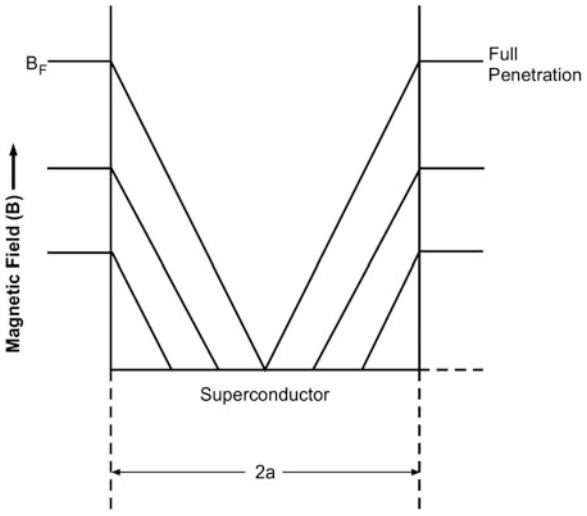

Fig. 6.3 Field penetration of a superconductor of the diameter $2a$. Field B_F corresponds to the full penetration

certain value B_F the superconductor is fully penetrated. The energy stored by the magnetization currents corresponding to this full penetration field B_F is given by

$$Q = \left(\frac{2\pi}{3} \times 10^{-9}\right) J_c^2 a^2 \tag{6.1}$$

or

$$Q = \left(B_F^2\right)/\left(24\pi \cdot 10^7\right) \tag{6.2}$$

Since

$$B = \frac{4\pi}{10} J_c x$$

It is thus seen from (6.1) that for a given value of J_c the heat produced during field penetration is proportional to the square of the thickness of the superconductor. This simply means that if the dimension of the superconductor or the radius of the circular wire is reduced to very fine filament size, the heat generated during the field sweep can be reduced to a very small value which can be absorbed by the superconductor itself without a serious raise in temperature. This will fulfill the stability criterion of $\Delta T_3 \ll \Delta T_2 \ll \Delta T_1$. This is called the 'adiabatic' or the 'intrinsic' stability criterion because it assumes that no heat escapes to the surrounding. Thus if the wire diameter is reduced by a factor of 10 the heat produced Q will be reduced by a factor of 100.

The other alternative technique to stabilize the superconductor against flux jumps is to laminate a superconductor with a high conductivity material like copper. In such a composite superconductor the heat generated during field sweep is dissipated away through copper. This is called the 'dynamic' stability criteria. Copper, in fact, not only provides dynamic stability but also provides the cryostatic stability to the superconductor by working as a shunt resistance. In the event of a part of superconductor turning normal (becoming highly resistive) the current will flow through the copper shunt instead of the superconductor. How to realize these two stability criteria will be discussed in the following sections.

6.2.2 The Adiabatic or Intrinsic Stability

Figure 6.4 shows a superconductor under an external magnetic field B. The superconductor is protected against flux penetration by the screening currents flowing at a density of J_c allowing a field penetration of x (cm). Let us see what happens if a disturbance causes a small temperature rise ΔT_1 in the conductor. Following sequence of events is likely to follow:

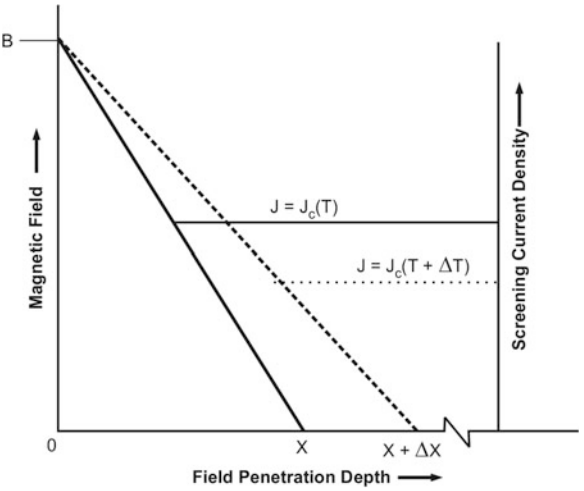

Fig. 6.4 Adiabatic stability criterion: the conductor dimensions are reduced such that the heat generated due to field penetration is so small that it is absorbed by the conductor without a serious raise in temperature

1. The screening current density, J_c will decrease by a small amount, say ΔJ_c given by

$$\Delta J_c = \left(\frac{dJ_c}{dT}\right)\Delta T_1 \tag{6.3}$$

2. This decrease in J_c allows an extra flux penetration, say Δx, given by

$$\Delta x = -\frac{10}{4\pi}\left(\frac{B}{J_c}\right)\left(\frac{\Delta J_c}{J_c}\right) \tag{6.4}$$

3. This flux movement will generate heat ΔQ per unit volume given by

$$\Delta Q = 10^{-8}\left(\frac{J_c B \Delta x}{3}\right) \text{ J/cm}^3 \tag{6.5}$$

4. Since thermal diffusivity D_H in a superconductor is very small, this heat is not likely to be dissipated away. Instead, it will be absorbed by the material itself under adiabatic situation. Thus, there will be a further rise in temperature, say ΔT_2, depending upon the heat capacity of the conductor, and will be given by:

$$\Delta T_2 = \frac{\Delta Q}{S} \tag{6.6}$$

where S is the heat capacity of the superconductor in J/cm^3/K. Thermal run away will occur if ΔT_2 happens to be greater than ΔT_1. The superconductor will, however, remain stable in case ΔT_2 turns out smaller than ΔT_1. The system will then be stable against small disturbances.

Taking the values of ΔT_1 and ΔT_2 from expressions (6.3) and (6.6), the condition $\Delta T_2 \ll \Delta T_1$ for conductor stability against small disturbance/perturbation leads to:

5. $$B < \left(12\pi\ 10^7\ SJ_R\right)^{\frac{1}{2}} \tag{6.7}$$

here

$$J_R = \frac{J_c}{-\mathrm{d}J_c/\mathrm{d}T} \tag{6.8}$$

since B and J_c are related through the relation

$$B = \left(\frac{4\pi}{10}\right) J_c x \tag{6.9}$$

Equation (6.7) can as well be written:

6. $$x < \left(\frac{3 \cdot 10^9 SJ_R}{4\pi}\right)^{\frac{1}{2}} \left(\frac{1}{J_c}\right) \tag{6.10}$$

In the above calculations we have assumed a uniform distribution of energy released by the flux motion which is not likely to happen in an adiabatic process. For a perfect adiabatic condition the above two equations, (6.7) and (6.10) will get modified to

7. $$B < \left(\pi^2 10^7 SJ_R\right)^{1/2} \tag{6.11}$$

and

8. $$x < \frac{\left(10^9 SJ_R\right)^{1/2}}{4J_c} \tag{6.12}$$

If we assume typical values of $S = 2 \times 10^{-3}$, $J_R \sim 4$ and a J_c value of 3×10^5 A cm^{-2} for Nb–Ti, a wire of 24 μm dia. will be stable against flux jump. For larger diameter 'flux jumps' will occur before the full flux penetration of the superconductor.

6.2.3 The Dynamic and Cryostatic Stability

Dynamical stability criterion is an alternate route to stabilize a superconductor by laminating it with high conductivity material such as copper. Conditions get modified when we consider composite of a superconductor and a conducting normal matrix. This arrangement slows down the flux movement in the superconductor by

reducing the value of the magnetic diffusivity, D_M. This slow-down of flux movement permits time for most of the heat to escape from the superconductor to the surrounding via thermal conduction through copper. The D_H will now be greater than the D_M and therefore energy dissipated by flux motion will distribute uniformly throughout the composite. The current density will be the mean current density $=\lambda J_c$ (λ being the superconducting fraction). Similarly, the specific heat too will have to be averaged out over the whole composite. When the flux penetration x is less than the half width of the composite the heat release will be distributed over the whole composite cross-section. This will reduce ΔT_2 by a fraction x/a ($2a$ being the composite diameter) and improve the stability of the composite. Copper lamination not only provides dynamic stability but also provides cryostatic stability to the superconductor by way of sharing the current in the event of the formation of a hot spot.

As shown in Fig. 6.5 the composite consists of alternate sheets of the superconductor and a normal matrix, usually copper for its excellent bonding properties and high thermal conductivity. The superconductor sheet has a thickness of w (cm) and constitutes a fraction λ_s of the whole composite. Let the electrical resistivity of copper be ρ (Ω cm). The composite conductor (Fig. 6.5) is shielded against an external magnetic field, B by the screening currents flowing at a mean current density of $\lambda_s J_c$ extending to a depth of x cm.

We can again start from a disturbance say, an increase of temperature by ΔT_1 and construct the following sequence of events

1. This increase in temperature, ΔT_1 will reduce the screening current J_c by an amount

$$\Delta J_c = \left(\frac{dJ_c}{dT}\right)\Delta T_1 \tag{6.13}$$

2. This decrease in shielding current will allow further field penetration by a small amount, say Δx given by

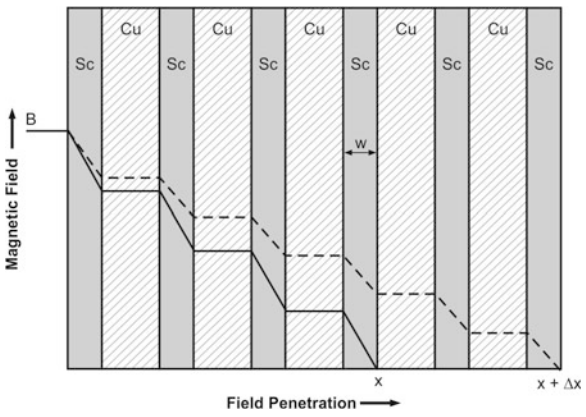

Fig. 6.5 Dynamic stability criterion: the composite now consists of alternate sheets of copper and superconductor. Heat dissipates away via copper before the conductor turns normal

$$\Delta x = -\left(\frac{10}{4\pi}\right)\left(\frac{B}{\lambda_s J_c}\right)\left(\frac{\Delta J_c}{J_c}\right) \tag{6.14}$$

3. The rate of heat release/cm^3 in the filament will be:

$$\frac{dQ}{dt} = \frac{\Delta Q}{1/2T_m} \tag{6.15}$$

here

$$\Delta Q = 10^{-8} J_c B \Delta x/3 \tag{6.16}$$

and

$$T_m = \left(\frac{16}{10^9\pi}\right)\left(\frac{x^3}{\rho}\right)(1-\lambda_s) \tag{6.17}$$

4. The effective resistivity being $(\rho/1-\lambda_s)$. Assuming that there is no temperature rise of the normal metal, the average temperature rise in the superconductor will be:

$$\Delta T_2 \cong \left(\frac{dQ}{dt}\right)\frac{w^2}{12k_s} \tag{6.18}$$

where k_s is the thermal conductivity of the superconductor in W cm^{-1} K^{-1}. According to our stability criterion, $\Delta T_2 < \Delta T_1$, we combine (6.13) and (6.18) and obtain:

5. $$B^2 \leq 12\left(\frac{J_R k_s}{\rho}\right)\left(\frac{x}{w}\right)^2 \lambda_s(1-\lambda_s) \tag{6.19}$$

here $J_R = \frac{J_c}{-dJ_c/dT}$ same as in (6.8)
since $B = \left(\frac{4\pi}{10}\right)\lambda_s J_c x$ (6.19) can as well be written as

6. $$x^2 \leq 8\left(\frac{J_R k_s}{\rho}\right)\left(\frac{1-\lambda_s}{\lambda_s}\right)\left(\frac{1}{J_c^2}\right) \tag{6.20}$$

Taking typical values of parameters for Nb–Ti superconductor, J_R = 4, $J_c \sim 3 \times 10^5$ (A cm^{-2}), $k_s \sim 10^{-3}$ (W cm^{-1} K^{-1}), $\rho \sim 2 \times 10^{-8}$ (Ω cm) and $\lambda_s \sim 0.5$, we find that a wire 40 μm in diameter will be stable. Lower λ_s values, that is, larger copper fraction will lead to larger filament diameter. For example for λ_s = 0.3 a filament diameter of 55 μm can be tolerated if one goes by the dynamical stability criterion. It is however advisable that the filament diameter be chosen as per the adiabatic stability criterion so that individual filaments are intrinsically stabilized. If we exceed the diameter given by (6.12) there is a danger that local instabilities may

occur within the individual filaments or the superconducting layer which may not be sufficiently damped by the copper lamination, if the bonding is not perfect. Further, our assumption of temperature rise only in the superconducting part, may not be valid. The conduction paths in a composite system in fact is quite complicated as the composite not only involves superconductor and the cladding metal but other components like electrical insulation, inter-layer and potting material. Notwithstanding these limitations, above equations have served admirably well for the design and the production of industrial multifilamentary superconductors capable of transporting large currents and used in dc applications. Filament diameter of the commercial wires range from 5 to 50 μm depending upon the application. For ac applications, the filament diameter is kept much smaller in the range of 1–10 μm. A good review on Nb–Ti conductors with low ac and eddy current losses has been published by Wilson [2].

6.2.4 Multifilamentary Superconducting Wires

From the above discussion we can conclude that a practical superconductor has to be manufactured in the form of fine filaments of a few micron size. However, all practical superconductors are required to carry large current and since a single filament can carry only a very small current, a superconducting wire should have a bundle of such fine filaments. The best way to produce such a material on an industrial scale is to combine both the stability criteria. Thus the practical way to produce the material is in the form of a large number of filaments embedded in pure copper.

Figure 6.6 shows the schematic of the manufacturing process for stabilized Cu/Nb–Ti superconducting wires. The Nb–Ti alloy happens to be ductile enough to be co-processed with copper. The process for manufacturing the composite copper/Nb–Ti wires can briefly be described this way. The Nb–Ti composition is roughly 50:50 with Ti concentration varying from 47 to 56 wt%. The Nb–Ti alloy is usually prepared by arc melting or the electron beam melting technique under controlled metallurgical conditions yielding mass with desired microstructure and ductility. The alloy ingot is extruded and hot rolled in to thick rods of a few cm diameter depending upon the dimensions of the composite billet needed to produce required length of the wire. These rods are annealed at about 1,000 °C and quenched at room temperature. A large number of these rods are inserted in to the holes drilled in a large size copper billet in a predetermined geometry. The billet ends are plugged with thick copper lids which are electron beam welded after proper evacuation. No trace of oxygen is left.

The sealed billet is preheated and extruded at high temperature under inert atmosphere. High temperature at this stage is needed to have good metallurgical bonding between the superconducting rods and copper matrix. These billets can be massive with large diameters and long lengths depending upon the required diameter and the length of the conductor. Typical dimensions of a large billet could

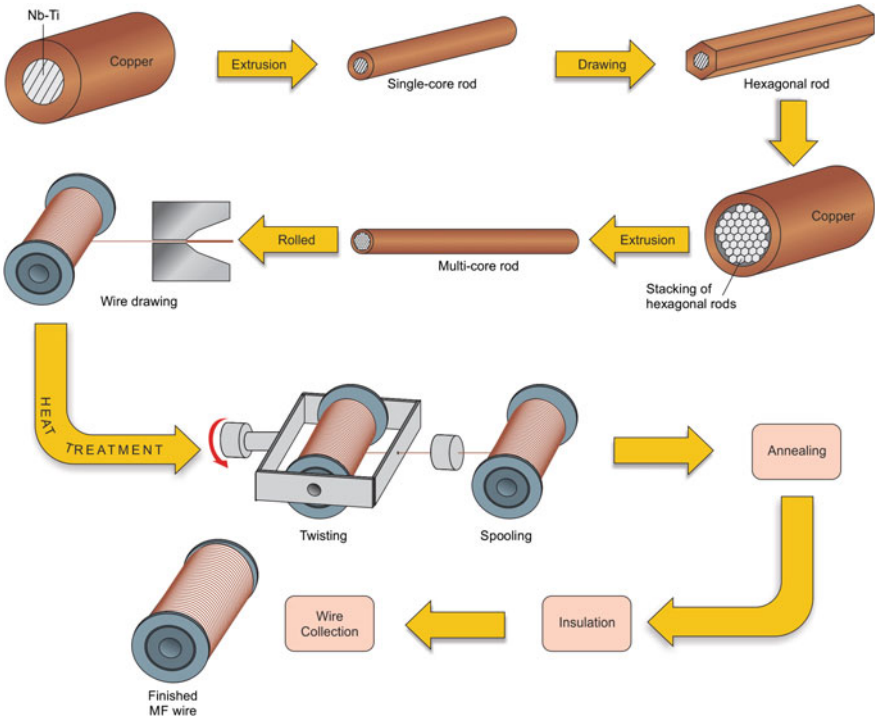

Fig. 6.6 A schematic diagram of the manufacturing process of a mutifiamentary composite superconductor

be as much as 250 mm diameter and 800 mm length. For industrial production a billet may weigh as much as 250–300 kg. After hot extrusion, the billet takes the shape of a long rod which is then rolled to a hexagonal shape and cut in to many pieces to prepare another billet. Several of these hexagonal rods are packed together and inserted inside a copper stabilizer tube. The new billet so prepared is evacuated and sealed as before and cold extruded. This multi-core rod is then rolled, swaged and drawn to wires of desired size. This process can be repeated till one gets the required number of filaments. A typical cross-section of a multifilamentary wire is shown in Fig. 6.7. The multifilamentary wire thus produced is suitably heat treated and twisted along its axis to decouple the filaments in the metal matrix. We will deal with this issue in the next section. The twisted wire is usually subjected to a series of heat treatment and cold work schedule to introduce pins (the flux pinning sites) to enhance J_c. The twisted and annealed wire is finally insulated. For high current application several of such wires are woven in the form of braids to counter the self field affects, yet to be discussed in next section.

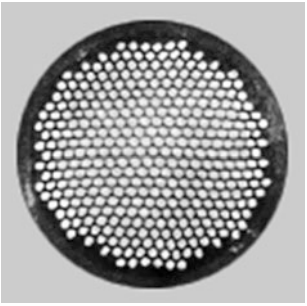

Fig. 6.7 A typical cross-section of a multifilamentary wire with copper stabilizer

6.2.5 *Twisting and Transposition of the Multifilamentary Wires*

The technique discussed above to produce multifilamentary superconducting wires with filaments embedded in copper matrix looked as though the problem of flux jumps has been solved once for all but turned out to be not enough. Magnets, wound using multifilamentary wires practically behaved quite the same way as with using the equivalent single solid core wire. These magnets too quenched prematurely. It turned out that copper did provide dynamic stability to the superconductor but also coupled the filaments electrically. In a static field the composite superconductor is protected against flux inclusion by the surface shielding (magnetization) current flowing along the surface of an individual filament. However, under the influence of a rapidly changing magnetic field enough voltage is induced which drives the shielding currents from one filament to another across the copper (resistive) matrix. Shielding current loops are formed (Fig. 6.8) occupying the whole of the composite instead of confining to individual filaments. All the filaments are thus electrically coupled and the very purpose of having isolated fine filaments is defeated. On the other hand, if the magnetic field increases sufficiently slowly there will be very small associated voltage and very little shielding current will cross the copper matrix. Shielding current loops will thus form within the individual isolated filaments. Based on these arguments Smith et al. [3] suggested that these composites should be twisted along the axis so that the induced voltage changes the polarity with the period of the twist. It has been pointed out that for a given field sweep $\dot{B}$ (=dB/dt) there is a critical length of the composite conductor which allows all the current in the filament to cross the matrix. Below this critical length the shielding currents will form a close loop within the filament. We can estimate this critical length, ℓ_c in the following way. Let us consider two superconducting slabs of thickness t (cm) each separated by the normal matrix of width d and of resistivity ρ (Ω cm) as shown in Fig. 6.8. The total length of the composite slab is 2ℓ (cm). A varying external magnetic field, $\dot{B}$ (G/s) is applied along the z direction. Under steady state let us find out the critical length ℓ_c at which the induced voltage is large enough to allow all the current to cross the matrix.

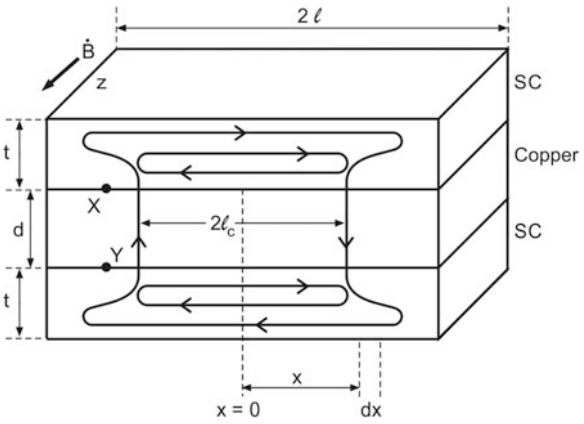

Fig. 6.8 Critical length ℓ_c, of the wire in a composite of two superconducting slabs separated by a normal matrix. Twisting the wire with a twist pitch smaller than ℓ_c prevents the coupling of filaments across the matrix

Consider a small element dx at a distance x (cm) from the midpoint. We can find out the length ℓ_c by following a few mathematical steps:

1. $$\text{The voltage across } XY = \left(\frac{\dot{B}}{10^8}\right)(xd) \tag{6.21}$$

2. $$\text{Resistance across } XY = \frac{\rho d}{z\mathrm{d}x} \tag{6.22}$$

3. $$\text{Current across } XY = \frac{\dot{B}}{10^8}\left(\frac{z}{\rho}\right)x\mathrm{d}x \tag{6.23}$$

Integrating current from 0 to ℓ and equating it to $J_c zt$ we get

4. $$J_c zt = \int_0^{\ell} \frac{\dot{B}}{10^8}\left(\frac{z}{\rho}\right)x\mathrm{d}x = \left(\frac{\dot{B}}{10^8}\right)\left(\frac{\ell^2 z}{2\rho}\right) \tag{6.24}$$

5. $$\ell^2 = \ell_c^2 = \left(\frac{2\times 10^8 \rho J_c t}{\dot{B}}\right) \tag{6.25}$$

For a multifilamentary system J_c in (6.25) is to be multiplied by a space factor, λ, the superconducting volume fraction. To account for fine size filaments the right hand side of (6.25) is to be multiplied by a factor $d/(d + t)$. Thus the final equation for ℓ_c gets modified to,

$$\ell_c^2 = \left(\frac{2\times 10^8 \rho J_c \lambda t}{\dot{B}}\right)\left(\frac{d}{d+t}\right) \tag{6.26}$$

Thus by substituting typical values for Cu/Nb–Ti composite, for the typical sweep rate of $\dot{B} = 1\ T/s$ (=10^4G/s), $J_c = 3\times 10^5$ A/cm^2, $\lambda = 0.5$ ($d = t = 50$ μm), ℓ_c turns out to be 30 mm for copper composites. A magnet built by untwisted superconductor multifilamentary wire will show solid conductor behaviour and quench at low current value. However, if the composite conductor is twisted along

its axis cutting effectively the length equal to one quarter of the twist pitch, it behaves as a collection of isolated filaments. For conductor length $\ell > \ell_c$, transverse current equal to magnetization currents cross the matrix in a distance of ℓ_c at each end. If, however, the conductor length $\ell < \ell_c$, only a small fraction, of the current can cross the matrix, the remaining current being confined to individual filament. A sweep rate range is thus specified for a given multifilamentary composite superconductor by the manufacturer. Loss or the magnetization of the composite conductor becomes smaller as the twist rate is increased. Direct experimental confirmation of (6.25) and (6.26) came from the magnetization and loss measurements carried out by Critchlow et al. [4, 5]. These authors made use of the expression for magnetization versus the field sweep rate for a fixed twist pitch for a composite conductor given by Smith et al. [3], viz;

$$M = M_0\left(1 + \frac{3\pi}{4\lambda^{1/2}}\right)\frac{\dot{B}}{\dot{B}_c} - \cdots \tag{6.27}$$

(Ignoring the higher order terms).

Here M_0 is the magnetization of the bare filament, and $\dot{B}_c$ is the magnetic sweep rate at which the effective length is equal to the critical length. Since $\dot{B}_c$ depends on the critical current density, above equation should be used for a constant external magnetic field. Figure 6.9 gives their plots between the magnetization (M) and field sweep $\dot{B}$ for Cu/Nb–Ti composite superconductor containing 121 strands each 0.009 mm dia. in a 0.2 mm copper matrix [4]. The plots qualitatively fit with the (6.27) and yield a value of right magnitude of the matrix resistivity. As seen from this figure magnetization is high for composite without twist and decreases as the twist rate increases. For high pitch rate the magnetization reduces to the bare filament value, M_0. Magnets using twisted filamentary conductors and suitably impregnated performed as per the expectation. When large cross-section composite superconductors with much larger number of filaments, in multiple layers around the central core, were developed, it was found that twisting was not enough and the conductors exhibited losses. This has been attributed to the 'self field effect'. The self field produced by the transport current causes unequal distribution of current across the cross-section of the MF wire. The outer layers of the filaments carry larger current than the inner layers. Twisting does not eliminate the self field effect as the radial positions of the filaments remain unaffected. Twisting proved to be effective only for a single layer of filaments around the central core. In such large cross-sectional wires self field can be eliminated by transposing the wires. High current multifilamentary conductors are thus produced in braided form. A typical braded cable flat-rolled in a Rutherford style is shown in Fig. 6.10. Such cables are the standard conductors used for winding magnets for accelerators. A cable contains a large number of strands, each strand contain thousands of Nb–Ti fine filaments. Several of these strands are then braided in to flat cables. The filament diameter for such application is as small as 3 μm and the cable has very low losses.

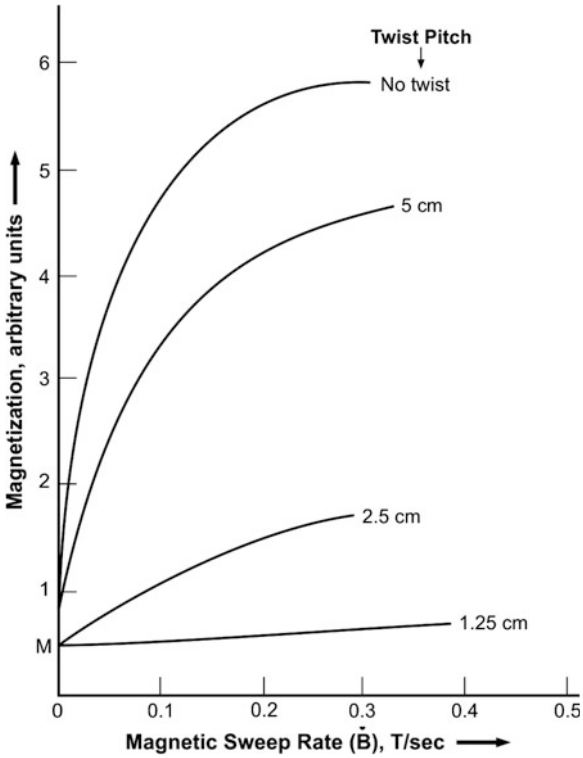

Fig. 6.9 Magnetization versus field ramp rate plots at 1 T of a Cu/Nb–Ti wire with 121 strands each 0.009 mm dia. in a 0.2 mm Cu-matrix composite [4] (With permission of Elsevier)

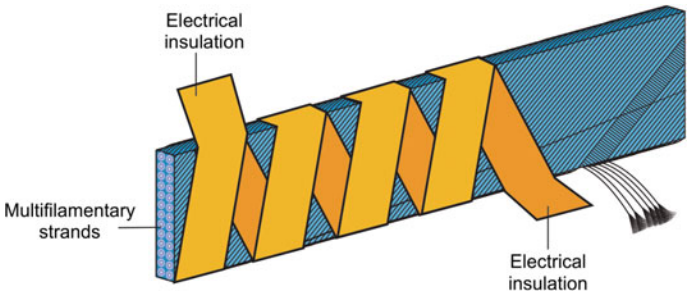

Fig. 6.10 Sketch of a braded superconducting cable in Rutherford style. Each strand in the braid contains thousands of superconducting filaments

Figure 6.11 shows the cross-sections of typical commercial superconductors. Circular wires in the diameter range of 0.4–1 mm are routinely used for small dc laboratory magnets. The square and rectangular conductors with large cross-section

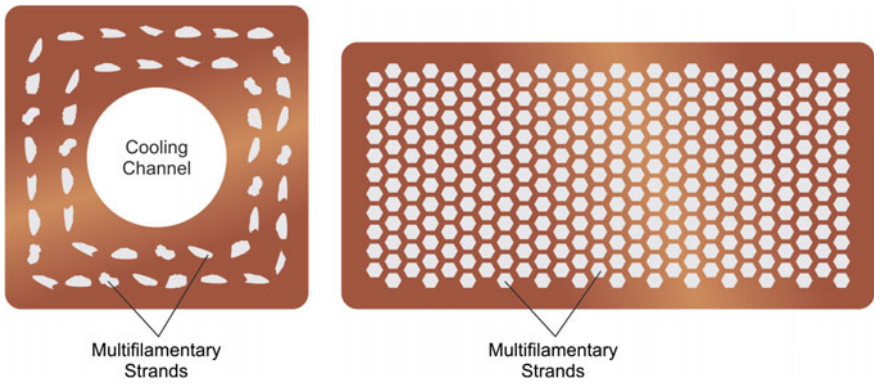

Fig. 6.11 A typical squire cross-section commercial Nb–Ti superconductors with a central cooling channel (*left*) and a rectangular superconductor with multifilamantary strands (*right*)

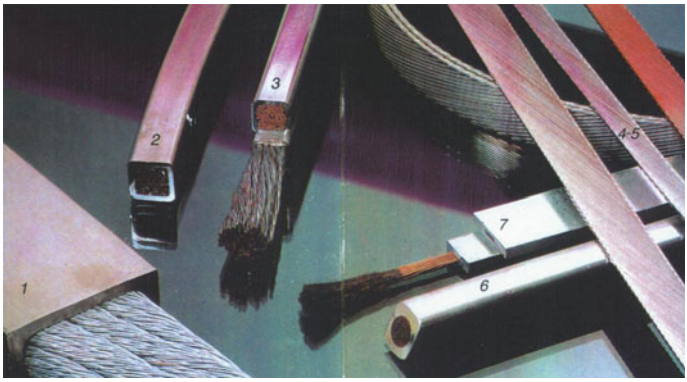

Fig. 6.12 A variety of high current multifilamentary cables manufactured by Europa Metalli, Italy for specific applications related to accelerator magnets and fusion reactors (From an old brochure of Europa Metalli)

are used for large size magnets. Typical dimensions of the conductor are 2 mm^2 and rectangular as 3.0 mm × 1.25 mm. Hollow conductors are used for the circulation of super critical helium for efficient cooling of the coil. A variety of high current multifilamentary cables manufactured by Europa Metalli (now KME), Italy for specific applications such an accelerator and fusion reactors magnets is shown in Fig. 6.12. The cable is reinforced with a stainless steel casing too which provides mechanical strength for withstanding large stresses during the operation of the magnets. Cooling channels are at times provided within the conductor cross-section. Cable-in-conduit-conductor (CICC) is a popular choice for toroidal magnets in fusion reactor.

6.3 The Ubiquitous Nb–Ti Superconductor

6.3.1 A Brief History

The superconductivity in Nb–Ti alloy system was reported first time by Hulm and Blaugher [6] while studying solid solutions of most of the incomplete d-shell metals in groups 4–7. The T_c maxima has been found at valence numbers approaching 4.7 and 6.4 except in the first long period. The authors report a T_c = 9 K for the Nb–Ti alloy in the composition range of 50 at.%. The US patent on superconducting magnet using Nb–Ti is held by Matthias [7]. Nb–Ti as a potential material with high critical magnetic field and high transport current for applications was however established by Berlincourt and Hake [8, 9]. These authors studied several alloys including U-based alloys materials under a newly built 20 T pulse magnet at that time. First time, they reported a record upper critical field of 14.5 T for this system. They argued that through appropriate metallurgical and mechanical processing Nb–Ti can be made to transport large currents. The results of their critical current studies were reported first as a post deadline paper at the Washington Meeting [9] of the APS in late April, 1962 and later in a regular paper [8] at the Evanston Meeting of the APS on 21 June, 1962. They established the suitability of Nb–Ti for building magnets up to 10 T. Heavily worked Nb–Ti wires were found carrying critical current densities more than 10^4 A cm^{-2} at 4.2 K and 10 T. This value was far superior to the competing material Nb–Zr which could support such currents only up to 6–7 T field.

The first 9.2 T superconducting magnet using Nb–Ti wire was built at Westinghouse, USA by Coffey et al. [10]. The magnet was built in five sections. A background field of >5 T was produced using two outer coils of copper-coated Nb–Zr (25 at.%) wire and the inner three coils were wound using copper-coated Nb–Ti (56 at.%) wire.

Nb–Zr was another material which caught wide attention for being exploited for magnet application around the same year, 1961. Kunzler and Matthias, in fact, obtained a patent [11] on Nb–Zr magnet. Kunzler at Bell Laboratories announced his results on high critical current density in Nb_3Sn and also on Nb–Zr at the APS meeting on 27 April, 1961. At the same time Berlincourt at Atomics International (AI) also discussed AI results obtained on Nb–Zr with Kunzler which were published [12] soon after. In due course Wah Chang started producing long lengths of Nb–Zr on a commercial scale in collaboration with AI and Westinghouse too produced the material for their research activity. Soon 6 T Nb–Zr magnets became a popular research tool in the laboratories. AI and Bell Labs. fought a patent war for 4 years. Finally, patent for Nb–Zr was granted to Bell labs. and non-exclusive royalty-free rights to AI. At this time it appeared that the future belonged to Nb_3Sn and Nb–Zr and Nb–Ti will be no-where to compete. The construction of a 10 T magnet by Coffey et al. [10] using Nb–Ti and Nb–Zr, however, changed the game for ever.

By 1967, Nb–Ti was accepted as the superior high field material and Nb–Zr slided in to history. Complete switch over from Nb–Zr magnets to Nb–Ti magnets took place rather fast in early 1970s. The invention of copper stabilized multifilamentary Cu/NbTi composite wires and cables firmly established the monopoly of this cheap, ductile, lighter and high performing material as the only material for fields up to 10 T. Today Nb–Ti M/F composites are all pervading from research laboratories to accelerators to fusion reactors. A detailed and interesting history of Nb–Ti emerging as an industrial product has been written by Berlincourt [13].

6.3.2 The Phase Diagram of Nb–Ti

The relevant useful part of the Nb–Ti phase diagram [4] is reproduced in Fig. 6.13. The useful composition of Nb–Ti is from 45 at.% to 56 wt% Ti. Different manufacturers have been using different compositions within this range. Composition with 47 wt% Ti has, however emerged as the most preferred material for commercial production. At high temperature only a single bcc—(β) phase forms whereas at lower temperatures pure Ti—(α) phase is formed. In between these two limits a mixture of both the phases α and β exists. The phase boundaries shown are not stable, rather depend upon the interstitial oxygen. Oxygen interstitials do enhance precipitation of α-phase but if oxygen exceeds 2,000 ppm, it can lead to poor ductility. Heat treatment in the $\alpha + \beta$ phase region can cause precipitation of the metastable ω phase in a very fine structure. These precipitates can serve as excellent pinning sites but causes severe work hardening which makes the extrusion process rather difficult. Formation of this phase should therefore be avoided.

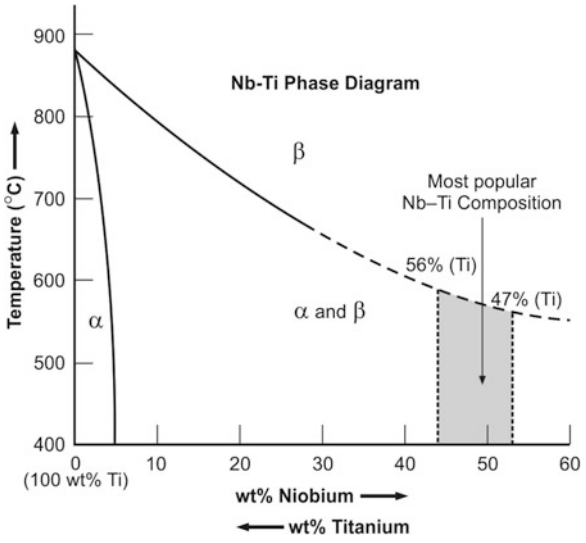

Fig. 6.13 Relevant part of the Nb–Ti phase diagram [4] (With permission of Elsevier)

The starting material and the rate of cooling determine the actual yields of the α and β phase materials. β phase is, however, retained irrespective of the cooling rate if the Nb-contents are greater than 50 at.%. This perhaps may be that the α-phase precipitation is too sluggish to occur in the low temperature region obtained by the extrapolation of the (β, $\alpha + \beta$) phase boundary. Further, the α phase precipitation can still be prevented in the 20–50 % Nb region by quenching the melt to room temperature to preserve β phase. However, as the Nb-contents are reduced α precipitation increases as the temperature is lowered. The two vertical arrows indicate the two popular compositions (47 and 56 wt% Ti) in Fig. 6.13. At 47 % Ti, B_{c2} peaks [14] at 11.7 T but the T_c drops to 9 K from its peak value of 9.68 K at a lower Ti concentration.

6.3.3 Optimization of J_c in Nb–Ti Wires

The detailed processing technique to produce multifilamentary conductors has already been discussed in Sect. 6.2.5. For processing the material for wire/cable production, Nb–Ti alloy is hot extruded and quenched to room temperature to retain the β phase. It is, however, crucial that the microstructure of the material is suitably controlled through the optimization of thermo-mechanical treatment of the final product so as to have high value of the critical current density, J_c. Cold working of the material is known to produce dislocations which have been found effective pinning sites. Dislocation cell structure provides even more effective pinning in Nb–Ti as revealed by critical current studies [15]. A dislocation net work with a cellular structure has been observed in Nb–Ti cold worked to the extent of 99 %. The average separation between cell walls is of the order of a few hundred Å. This dislocation network provides more effective flux pinning. The X-ray and electron diffraction data show the presence of only β phase. This confirms that under cold work condition the pinning is mainly caused by the dislocation cell structure and not by α or ω phase precipitations. Figure 6.14 shows the J_c versus B data of a Nb–Ti alloy containing 56 wt% Ti in cold worked state as well as after annealing it at 375 °C for 20 h. Evidently J_c increases with cold working and still more significantly after annealing them. Similar effect has been observed in Nb–Ti wires containing 45 wt% Ti (Fig. 6.15). Increase in J_c value depends strongly on the degree of cold work to which the wire was subjected. J_c is higher for heavily cold worked wires. Large billets of the composite are processed therefore not only to produce long lengths but high J_c as well. The increase in J_c after heat treatment is believed to have been caused by α (pure Ti) precipitation. This is confirmed by the X-ray and electron diffraction studies but not by the electron micrographs. This would then mean that these precipitates are very fine and nucleate at the dislocation cell walls. Intermediate annealing has been found even more beneficial for Nb–Ti conductors. The conductor after annealing treatment is cold worked to final size. Heat treatment causes some recovery and cell rearrangement in the highly deformed material. Heat treatment also produces α precipitation. If the material is deformed

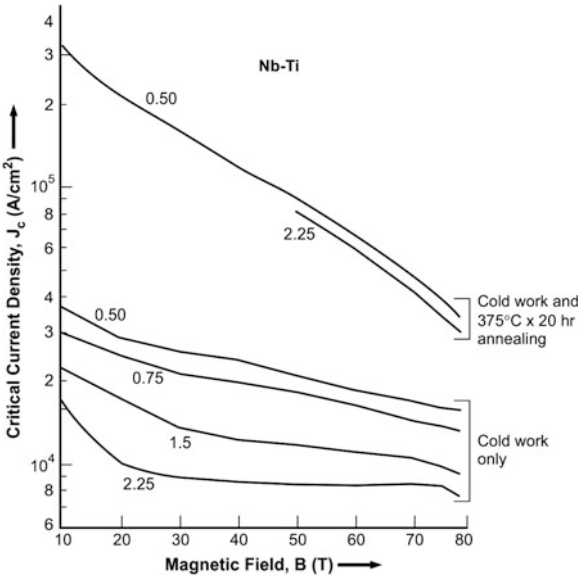

Fig. 6.14 J_c–B plots of Nb–Ti alloy containing 56 wt% Ti. Cold working leads to increased J_c. Successive annealing (375 °C × 20 h) raises the J_c to still higher values [4] (With permission from Elsevier)

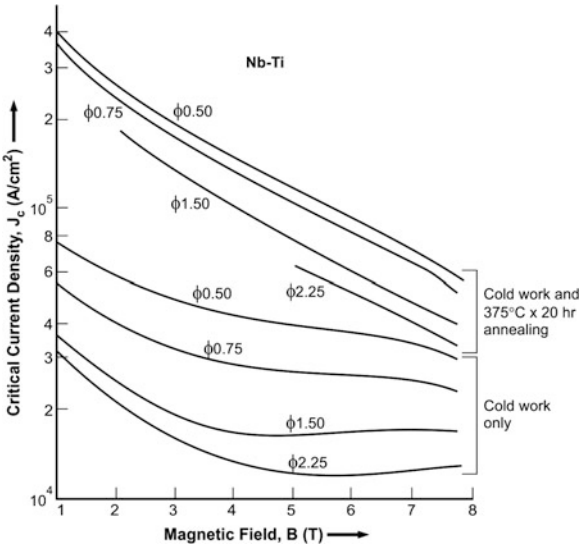

Fig. 6.15 J_c–B plots of Nb–Ti alloy containing 45 wt% Ti. Cold working followed by annealing (375 °C × 20 h) leads to enhanced J_c values [4] (With permission from Elsevier)

again, dislocations are produced which form tangles around the precipitates and along the cell walls. The new structure leads to even more effective pinning and higher J_c. During the entire thermo-mechanical process care is, however, taken that the ductility of the composite is maintained all through the processing. This intermediate heat treatment has been proven to be most effective pinning process especially in high field region. A $J_c = 10^5$ A cm^{-2} (4.2 K, 6 T) is invariably achieved in practical MF Cu/Nb–Ti conductors.

6.3.4 Some Recent Developments in the Fabrication Process of MF Cu/Nb–Ti Composite Conductors

By the end of 1970s Nb–Ti was accepted as the best choice for magnet systems designed to generate field below 10 T. The reason for this success was its extreme ductility and the consequent ability to be produced in fine filamentary structure. The challenge to this material came in early 1980s when strong interest grew in using this material for pulse magnets for particle accelerators. The hysteretic ac losses encountered in such applications turned out to be the big hurdle. The problem was, however surmounted by reducing the filament to 5–10 μm size. A filament of 5 μm dia. is stable up to a ramp rate of 1 T/s. Losses can be greatly reduced by increasing the ramp time and retaining the filament diameter to 5–10 μm range to reduce the field errors caused by superconductor magnetization. This leads to high quality field shape in the accelerator dipole magnets. Since these wires were required to transport several thousand of Ampere current, conductors were produced with thousands of these fine filaments. For small number of filament conductor (up to few hundred) Nb–Ti rods in copper tubes with outer hexagonal geometry are staked in an outer Cu-billet tube and processed as described in Sect. 6.2.4. For several thousand filamentary conductor the hexagonal composite rod becomes very small and difficult to bundle in desired geometry. In an alternate technique, to fabricate conductor with several thousand filaments, a two-stage stacking process has been followed involving hexagonal staking at two stages of the billet assembly. Figure 6.16 left shows the cross-section of a standard composite Cu/Nb–Ti conductor with 54 filaments and Fig. 6.16 right shows a conductor with 8,670 filaments fabricated with double stacking process. The conductor has 102 strands and each strand 85 filaments [16]. Supercon [17] however reports lower J_c values for this process compared to single-stage bundling process.

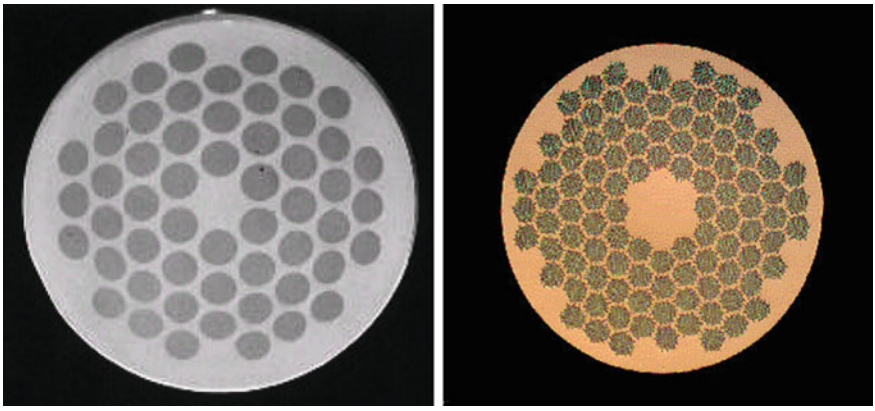

Fig. 6.16 *Left* A standard composite Cu/Nb–Ti conductor with 54 filaments. *Right* A conductor with 8,670 (102 × 85) filaments fabricated with double stacking process [16] (*Courtesy* Helmut Krauth)

The hysteretic ac loss problem becomes truly formidable in power engineering where the devices operate at 50–60 Hz. Wires with 1 million filaments of 0.1 μm dia. were developed but attempts to commercialize the technology failed on the consideration of economics.

6.3.5 *Use of Diffusion Barrier and Filament Spacing*

While developing these high current, tailor-made, conductors one drawback came to the fore. As discussed in Sect. 6.2.4 one hot extrusion of the virgin billet is invariably followed to have large area reduction ratio and also good metallurgical bonding. This hot extrusion and the successive heat treatments were found to lead to the formation of Cu–Ti intermetallic on the filament surface [16]. These hard particles cause sausages of the filaments (varying dia. of the filaments along the length) and bring down the J_c significantly. The problem is solved by using a Nb-diffusion barrier around each filament. This is achieved by preparing mono-core Nb–Ti/Nb/Cu composite rods for the initial stacking of the billet tube. The thickness of the Nb-barrier is such that down to the last diameter of the wire no Cu–Ti intermetallic is formed during the heat treatment. Figure 6.17 shows the uniformity of the filaments achieved by the use of Nb-barrier.

Another important factor affecting the J_c in Nb–Ti conductors has been reported by Gregory [17] at Supercon Inc., namely, the filament-spacing to diameter ratio (S/D). A detailed analysis of the data on conductors from different manufacturers yielded the result that the sausaging problem is far less in conductors having closely spaced

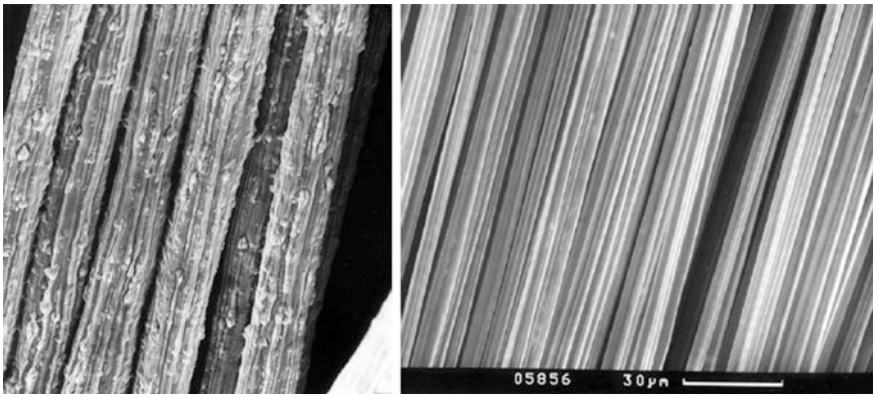

Fig. 6.17 Problem of sausages of the Nb–Ti filaments solved by using Nb-diffusion barrier around each filament. *Left* Nb–Ti filaments with sausages caused by Cu–Ti intermetallic particles. *Right* Very uniform Nb–Ti filaments when the filaments are covered by the Nb-diffusion barrier [16]. (*Courtesy* Helmut Krauth) http://cbmm.com.br/portug/sources/techlib/science_techno/table_content/sub_3/images/pdfs/014.pdf

filaments. Supercon report a $J_c = 2.3 \times 10^5$ A cm^{-2} (4.2 K, 5 T) for S/D ratio of 0.24 without the use of Nb-diffusion barrier. Supercon designed conductors for Superconducting Super Collider (SSC, abandoned in 1990s) and Relativistic Heavy Ion Collider (RHIC) with S/D ratio of 0.15 which carried a $J_c = 3.45 \times 10^5$ A cm^{-2} with good uniformity of the filaments.

The disadvantage of having closely spaced filamentary conductor is that at low filament diameter and low magnetic field, filaments get coupled as the Cooper pairs tunnel through copper via the proximity effect. Supercon solved this coupling problem by employing (1) resistive scattering of the Cooper pairs and (2) spin flip scattering by magnetic impurity like Mn, Fe and Cr which are known to posses a magnetic moment. In the first technique 40 % of the spacing between the filaments is filled up with 70/30 Cu–Ni. The filaments remain decoupled even when the filaments are spaced 0.3 μm apart without causing stability or quench problem. Problem can as well be solved for all the filament diameters. In the second technique Supercon experimented with a matrix Cu–Mn (0.5 wt%) and found filaments as small as 0.35 μm are completely decoupled. The presence of Mn can, however, affect adversely the stability and quench protection. In large billets the effect will be minor because Cu–Mn is used only between the filament. The central part of the billet and also outside the filaments is pure copper. It appears certain that by carefully choosing proper design and combining the three constituents viz; Nb–Ti, Cu–Mn and Cu in such a geometry and in right proportion, the ac losses can be cut down to the minimum. This can be accomplished without either sacrificing J_c or without risking the conductor stability and the consequent quench protection. An increase in J_c is often accompanied with a loss of ductility. The manufacturing process has therefore to be optimized such that the ductility of the conductor is not lost while achieving high J_c and realizing the desired piece length.

The state-of-art processes developed for manufacturing cables for high current ac applications in accelerators and fusion reactors has been reviewed recently by Wilson [2]. The author has discussed in detail the merits and demerits of different types of cables for different applications. Rutherford cable (Fig. 6.10) with resistive core, for example seems to be the best option for use in accelerators with fast ramp rates. It offers the best prospect for keeping losses within limits while retaining good contacts between the wires for current sharing. For future fusion reactors like ITER where the current requirement is 50 kA, Litz type cable is considered most appropriate. Magnets in fusion reactors are subjected to fast changes not only by the ramping of the magnets but also by frequent plasma disruptions. Several wires containing large number of fine filaments are twisted together to form strands and several strands are transposed around a core for uniform current sharing in the cable. In Litz wire three multifilamentary wires are twisted together and three groups of these twisted wires are twisted again. The process is repeated till a cable of required dimensions and J_c is obtained. The final cable is completely transposed but has an open structure because the groups of three cannot pack too tightly. A filler wire is kept at the centre to maintain symmetry. Further, the cable is encased in an outer stainless steel jacket which not only provides efficient cooling channels for super

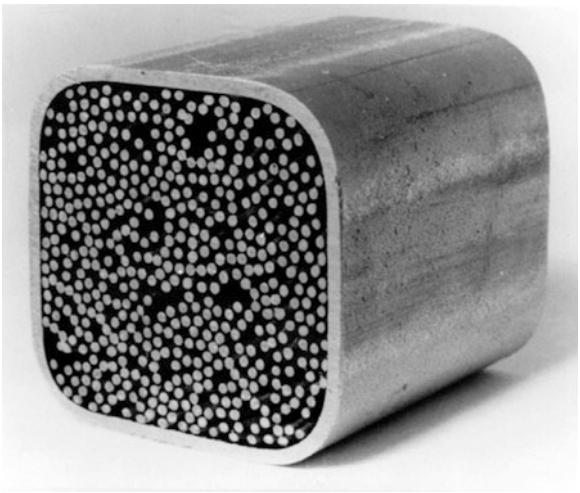

Fig. 6.18 The cross-section of a cable-in-conduit conductor (CICC), the preferred conductor for fusion magnets. Supercritical helium can be pumped through the voids [2] (With permission from Elsevier)

critical helium (SHe) but also provides mechanical strength to support large electromagnetic forces. Figure 6.18 shows [2] such a cable-in-conduit conductor (CICC). The void volume kept in these conductors varies from 30 to 40 % of the cross-section of the cable and provide channels for pumping SHe through the winding.

We thus find that Nb–Ti superconductor continues to remain unrivalled as it has demonstrated the ability to be drawn to submicron size and in the desired filament configuration. State-of-art technologies have been developed to manufacture cables of desired specifications for future accelerators and fusion reactor like ITER and beyond. Exemplary attempts will also continue to be made to achieve ultimate performance of this superconductor.

6.4 The A-15 Nb_3Sn MF Superconductor

6.4.1 The Discovery, Phase Diagram and Structure of Nb_3Sn

Superconductivity in A-15 class of intermetallic compound was discovered in 1953 by Hardy and Hulm [18]. They reported, first time, superconductivity at 17 K in vanadium silicide, V_3Si, a compound with A-15 structure. Soon, Matthias et al. [19] at Bell Laboratories reported superconductivity at still higher temperature of 18 K in Nb_3Sn in 1954. The inductive transition to superconductivity at 18 K in Nb_3Sn as reported first time by Matthias et al. is reproduced in Fig. 6.19. This was the highest ever reported T_c value till then. Because of the large mismatch of the melting points of Nb and Sn, the compound was prepared following a liquid diffusion process by dipping the Nb sample in to a molten Sn-bath kept at 1,200 °C in a quartz tube.

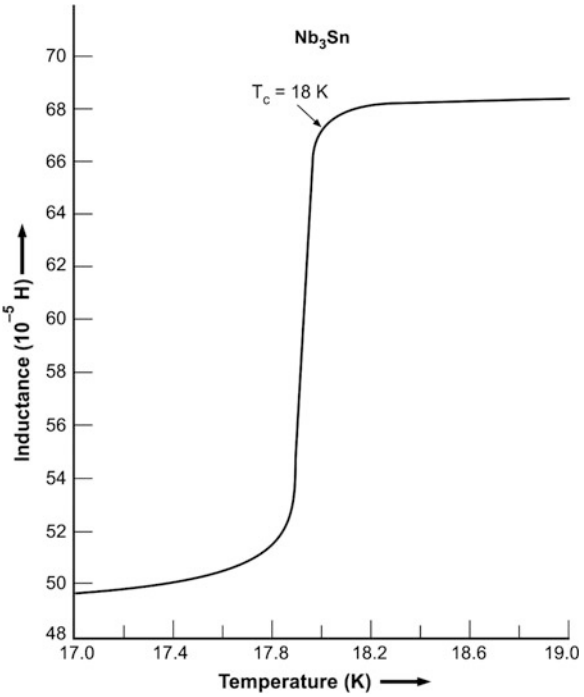

Fig. 6.19 The Superconducting transition in Nb_3Sn as reported first time by Matthias et al. at 18 K [19]. (With permission from APS) http://journals.aps.org/pr/abstract/10.1103/PhysRev.95.1435

Figure 6.20 is the Nb–Sn phase diagram taken from Charlesworth et al. [20]. Nb_3Sn phase is stable rather over a wide range, 18–23 at.% of Sn. This gives enough flexibility to prepare this material. Below 930 °C however low T_c phases like Nb_6Sn_5 (T_c = 2.6 K) and $NbSn_2$ (T_c = 2.1 K) are formed which should be prevented by cooling the ingot below 930 °C rather fast. Nb_3Sn undergoes a phase transformation from A-15 cubic phase to tetragonal phase below 43 K. Nb_3Sn happens to be the highest T_c and B_{c2} material Table 6.1 even amongst the A-15 superconductors which is commercially produced and used widely for most applications to-date. Some important superconducting parameters of Nb_3Sn are listed in Table 6.3.

At the present time, Nb_3Sn is the most successful and in fact, the only superconductor in used for field generation higher than 10 T. It belongs to the family of A_3B type of intermetallic compounds having a crystal structure of β-wolfram/Cr_3Si or the so called A-15 class. In these compounds A is a transition metal and B can be either a transition metal or a non transition metal. It has a cubic unit cell. The B-atoms occupy the corners and the centre of the cube and atoms A form chains along the faces of the cube. The peculiar feature of A-15 structure is that the A-atoms form three mutually orthogonal chains which run throughout the lattice as shown in Fig. 6.21. The lattice parameter 'a' of Nb_3Sn is 5.2908 Å. The extraordinary properties of this class of superconductors are believed to be caused by the integrity of these chains of the A-atoms. The potential A-15 superconductors, which

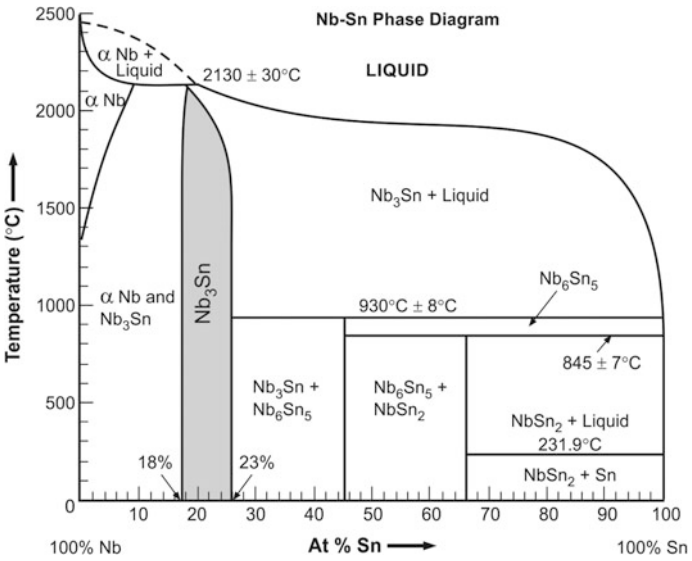

Fig. 6.20 The phase diagram of Nb–Sn [20] (With kind permission from Springer Publishing Company)

Table 6.3 Some important superconducting parameters of Nb_3Sn (B_{sh} is the superheating critical magnetic field relevant while using SC cavities, ℓ is the mean free path, other parameters carry their usual meanings

Parameter	T_c (K)	B_c (mT)	B_{sh} (mT)	B_{c1} (mT)	B_{c2} (T)	$\Delta(0)/kT_c$	ξ_o (nm)	λ nm	ℓ nm
Nb_3Sn	18.2	535	400	20	22	2–2.2	6	60	1

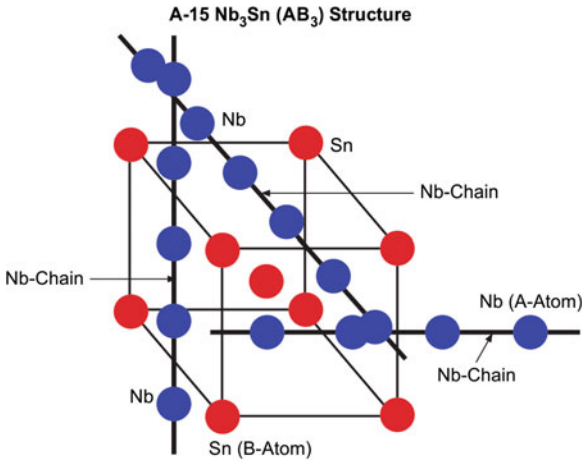

Fig. 6.21 The crystal structure of the A-15 or A_3B type of compounds. Transition metal atoms A form mutually orthogonal chains along the cubic faces and B atoms (transition or non-transition) occupy the corners and the centre of the cube

are mostly Nb or V based are listed in Table 6.1. In the rest of the chapter we will concentrate on three A-15 compounds viz; Nb_3Sn, V_3Ga and Nb_3Al only which have either been produced commercially or stand good chance of being produced in near future.

6.4.2 Emergence of Nb_3Sn as High Field Superconductor

The real breakthrough for Nb_3Sn to emerge as an industrial material for high field application came from Bell Labs. in 1961 when Kunzler et al. [21] demonstrated first time that Nb_3Sn carries a current density of $\sim 10^5$ A cm^{-2} in a field of 8.8 T and magnets producing field in excess of 10 T became a possibility. He produced Nb_3Sn by two techniques, namely (1) by the standard solid state ceramic technique and (2) by the powder-in-tube (PIT) technique. In PIT technique Nb-tubes were packed with the mixture of Nb and Sn powder having 10 % extra Sn-powder. These tubes were mechanically reduced to wires of 0.38 mm dia. and heat treated between 970 and 1,400 °C for several hours. The J_c versus field data on these samples are shown in Fig. 6.22. Evidently J_c is highest for samples heat treated at 970 °C. A J_c value of $\sim 10^5$ A cm^{-2} (at 4.2 K and 8.8 T) is reached for a sample heat treated at 970 °C for 16 h. High temperature heat treatment lowers the J_c. Great efforts were made in research laboratories, R&D institutions and companies to produce this material for high field magnets.

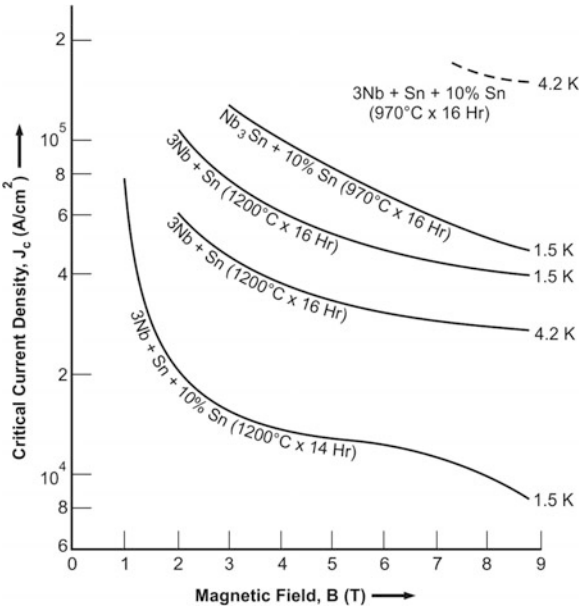

Fig. 6.22 Critical current density versus magnetic field plots of Nb_3Sn at 4.2 and 1.5 K as reported by Kunzler et al. [21]. Highest J_c ($\sim 10^5$ A cm^{-2} at 4.2 K, 8.8 T) is observed for sample heat treated at 970 °C for 16 h [21]. (With permission from APS) http://journals.aps.org/prb/abstract/10.1103/PhysRevB.82.180520

The brittle nature of Nb_3Sn hampered the development of stabilized multifilamentary Cu/Nb_3Sn composites and the material was produced in the form of flexible tapes of Nb suitably coated with Nb_3Sn either by a liquid diffusion method (perfected by General Electric Company, GEC) or by the chemical vapour deposition (CVD) process (perfected by RCA). Initial 10 T magnets were wound using these tapes in pancake structure. They were, however, not stable against flux jumps. We will not discuss these techniques because they became obsolete after the arrival of multifilamentary Nb_3Sn conductors. A brief discussion on these techniques can, however, be found in an old review [22].

In the beginning of 1970, alternate technologies were developed to realize multifilamentary composites of Cu/A-15 superconductors. The common strategy adopted in these techniques is that the brittle A-15 phase is formed at the final stage of fabrication of the application or the device. Many techniques have been tried in the past to realize multifilamentary A-15 composite conductors with varying degree of success. A review of techniques of fabrication of stabilized A-15 MF superconductors may be found [23] elsewhere. We will however discuss here only the techniques already used for commercial production or very close to being exploited in immediate future. These techniques are (1) the Bronze Process, (2) the Internal Tin (IT) process (3) the Jelly Roll (JR) Process and (4) the In Situ Process. Good reviews have been published by Tachikawa [24, 25] in recent times summarizing the state-of-the-art techniques of manufacturing metallic superconductors.

6.4.3 The Bronze Process

The bronze process was first time proposed by Kaufman and Pickett [26] for Nb_3Sn and by Tachikawa [27] for V_3Ga at the same conference, ICEC-3, in 1970. In this process for Nb_3Sn one prepares an ingot of bronze of Cu–Sn containing 13–16 wt% Sn. This bronze is used as a matrix for the billet. Desired number of holes are drilled in this billet and Nb-rods are inserted in these holes in a predetermined geometry as per the conductor design for specific application. The composite billet is extruded, rolled, swaged and drawn to final size with a few intermediate heat treatments to maintain ductility. These wires are usually bundled together repeatedly to obtained a conductor with several thousands of filaments. This bronze process is schematically shown in Fig. 6.23.

6.4.4 Parameters to be Optimized

6.4.4.1 Filament to Bronze Volume Ratio

This ratio determines the amount of Nb_3Sn formed during the heat treatment and also the compressive strain experienced by the Nb_3Sn layer when the composite

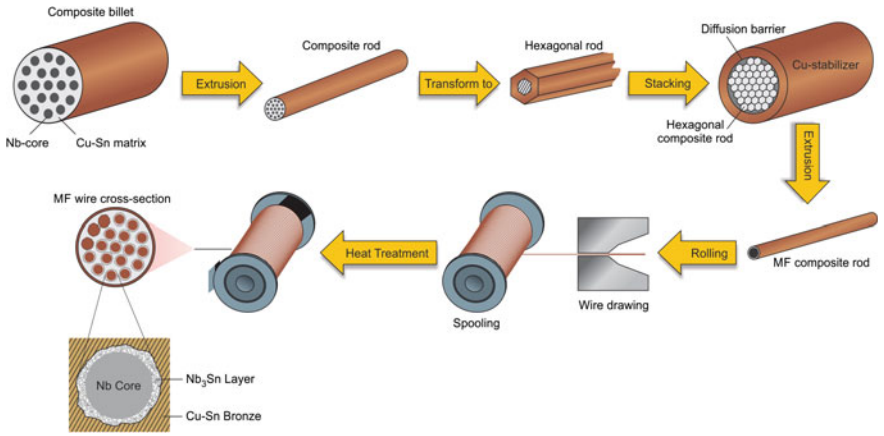

Fig. 6.23 The bronze process shown schematically. For large number of filaments composite rods are repeated bundled. Heat treatment to convert Nb in to Nb_3Sn is carried out at the last stage, that is, after winding the wire in to the device

wire is cooled to 4.2 K. The compressive strain is caused by the mismatch of the thermal contraction of Nb_3Sn and the matrix, which increases with bronze volume.

6.4.4.2 Heat Treatment Optimization

The heat treatment of bronze composites is the most critical parameter which needs to be optimized to achieve high J_c. During heat treatment, Sn from the bronze matrix diffuses in to Nb-rods and form a Nb_3Sn layer along the outer surface. The typical grain morphology of the Nb_3Sn layer formed is shown in Fig. 6.24. The Nb_3Sn layer is found to have three distinct regions, the central region consisting of equiaxed fine grains, the region with coarse grains towards the matrix interface (Sn deficient) and the third region of columnar grains towards the Nb interface. It is the central fine grain region which is responsible for high J_c as the grain boundaries are known [28] to be the best pinning sites in A-15 superconductors.

Heat treatment controls J_c through a number of metallurgical factors. First, the volume of the central fine grains of the Nb_3Sn layer which increases with the duration of heat treatment. Second, for high J_c, the grain size has to be kept minimum and therefore a lower reaction temperature is to be preferred. For Nb_3Sn a temperature of 650–700 °C has been found to be ideal. The third important parameter to be controlled is the perfect stoichiometry of the A-15 layer which too depends strongly on heat treatment. The Nb/Sn stoichiometry shows a large variation of Sn when the composite is reacted at lower temperature. Sn-concentration is

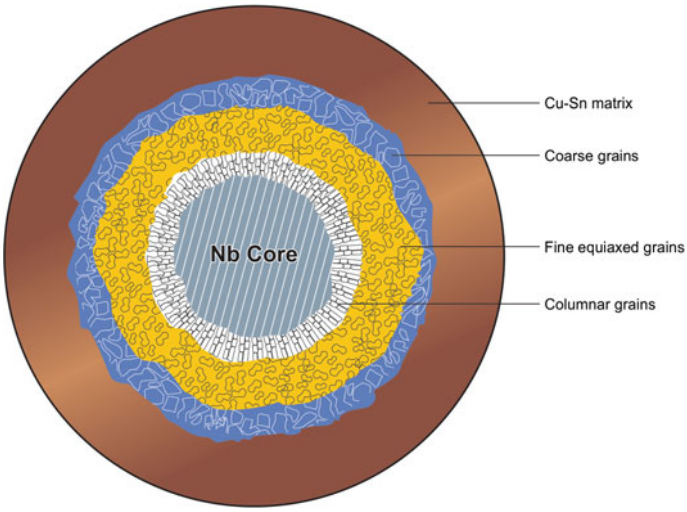

Fig. 6.24 Geometrical drawing of the cross-section of a bronze-route wire showing typical Nb_3Sn grain morphology

higher at the matrix end and lower at the Nb end. Heat treatment at higher temperature, on the other hand leads to better Nb_3Sn stoichiometry and to higher B_{c2}. J_c therefore increases. Thus, a combination of two heat treatments is preferred. A long lower temperature reaction leading to fine grain structure followed by a higher temperature reaction which improves the Nb_3Sn compositional stoichiometry and therefore B_{c2}. Table 6.4 gives the thicknesses of the Nb_3Sn layer in the three regions and the corresponding J_c values following two different heat treatment schedules of the Nb_3Sn produced by Airco [29]. The Airco bronze Nb_3Sn wire dia. was 0.7 mm with 2,869 filaments and used a matrix of Cu–Sn (13 wt%). A two-step heat treatment has been found to increase the J_c up to 14 T. The wire was heat treated in two steps, namely; 700 °C × 4 days followed by 730 °C × 2 days. The first heat treatment results in fine grains of ∼72 nm and a $J_c = 2 \times 10^4$ A/cm^2 (4.2 K, 14 T). The second heat treatment coarsens the grains a bit to ∼76 nm but still increases the J_c through an increase in B_{c2} due to improved stoichiometry. After the second treatment J_c goes up to 2.8×10^4 A/cm^2 (4.2 K, 14 T). Figure 6.25 shows how the Nb–Sn stoichiometry improves with two-step heat treatment.

6.4.4.3 Filament Size

A small filament diameter needs a shorter heat treatment and is thus ideal for attaining high J_c.

Table 6.4 Important specifications of the bronze-processed Nb_3Sn conductor developed for ITER [34]

Parameter	Unit	Value
Dia. of Cr-plated wire	mm	0.826
Bronze composition	wt%	Cu + 15−5 Sn + 0.3 Ti
Filament composition	wt%	Nb + 1.0 Ta
Barrier material		Nb
Filament diameter	μm	3
No. of filaments		19 × 583 = 11,077
Non Cu J_c	A/mm^2	820 (12 T, 4.2 K)
Hysteresis loss	kJ/m^3	620 (±3 T, 4.2 K)

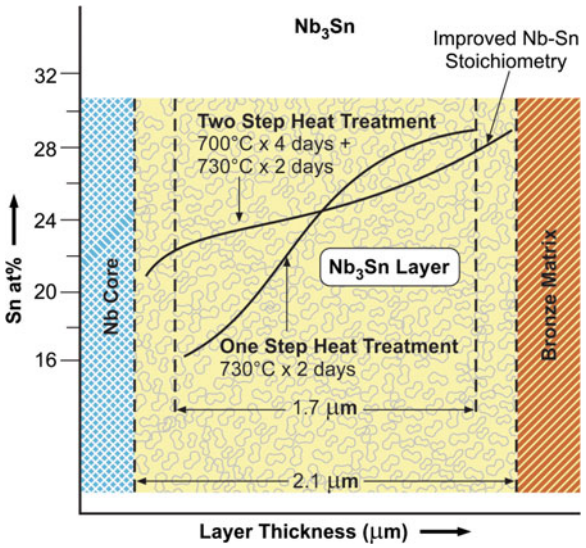

Fig. 6.25 A two-step heat treatment, 700 °C × 4 days followed by by 730 °C × 2 days leads to high J_c (*A*) and better Nb/Sn stoichiometry (*B*) [23, 29] (With permission from Elsevier and Springer)

6.4.4.4 High Tin Content in Bronze

Yet another milestone [30] was reached in enhancing the J_c of bronze processed Nb_3Sn two fold when the Sn concentration in the bronze matrix was increased from 13 to 16 wt%. Figure 6.26 shows significant increase in J_c when Sn contents are increased from 13 to 16 %. The matrix also had 0.3 wt% Ti added to it.

6.4.4.5 Elemental Additions to Nb_3Sn

Impressive improvements in J_c of bronze Nb_3Sn superconductors have been made using elemental additions to the Nb-core, to the Cu–Sn matrix or to both. These additives either refine the grains and increase J_c up to a field of 10 T or increases B_{c2} which leads to higher J_c in high fields. We will discuss below some of the

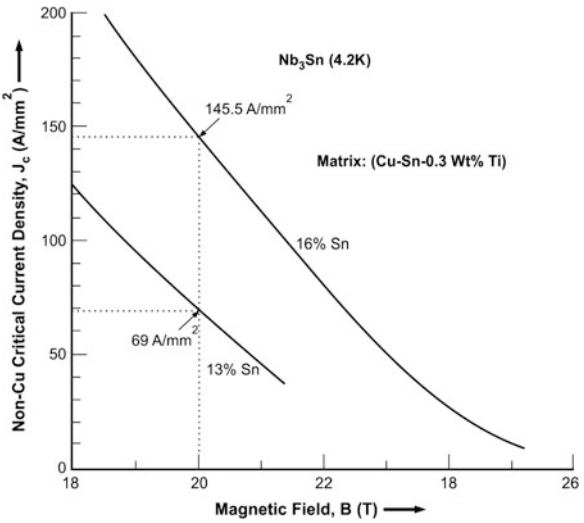

Fig. 6.26 Non-Cu J_c versus magnetic field plots of bronze processed Nb_3Sn as a function of Sn concentration. J_c rises by almost a factor of two for bronze with 16 wt% Sn. The bronze had 0.3 wt% Ti as well (Adapted from [30])

interesting developments that have taken place to produce Nb_3Sn conductors with high J_c for the International Thermonuclear Experimental Fusion Reactor (ITER). Among many elements Ti addition to the Nb-core and/or the Cu–Sn matrix has been found to raise J_c significantly [31]. Ti has been found to be incorporated in the Nb_3Sn layer better if Ti is added to the matrix. Kamata et al. [32] at Hitachi Cable Co., Japan successfully produced high J_c Nb_3Sn conductor using a Cu–Sn (7.5 at. %)–Ti (0.4 at.%) matrix heat treated at 690 °C for 200 h. The conductor had 4.7 μm diameter 10,261 filaments. An overall J_c of 3.5×10^4 A cm^{-2} (4.2 K, 15 T) was achieved in these conductors as shown in Fig. 6.27. Composites in rectangular tape form (9.5 × 1.8 mm) consisting of 5 μm diameter 349 × 361 filaments have been successfully fabricated in a full scale production using a three step hydrostatic extrusion process. These conductors have been widely used in fabricating 16 T magnets on a routine basis. V_3Ga and HTSC YBCO or BSCCO inserts have been used in a hybrid formation to reach fields in 20–21 T range with a 16 T background field provided by Nb–Ti/Nb_3Sn combination. Bronze processed Nb_3Sn conductor with 16 wt% Sn and 0.3 wt% Ti matrix has become the norm for many companies to produce high performing Nb_3Sn conductor.

Such conductors have been successfully used by Kiyoshi et al. [33] in building high frequency 930 MHz NMR magnet producing a field of 21.9 T (@ 1.5 K) using this material at NIMS, Tsukuba, Japan. Further, this material is used widely for building cryo-free, refrigerator-cooled magnets in the field range of 15 T for a variety of applications.

The international programme ITER has given new impetus to the development of high performance Nb_3Sn cables. Japan Atomic Energy Agency (JAEA) has developed bronze processed Nb_3Sn wire for the ITER programme [34]. The wire contains more than 11,000 filaments each of 3 μm dia. A large number of such

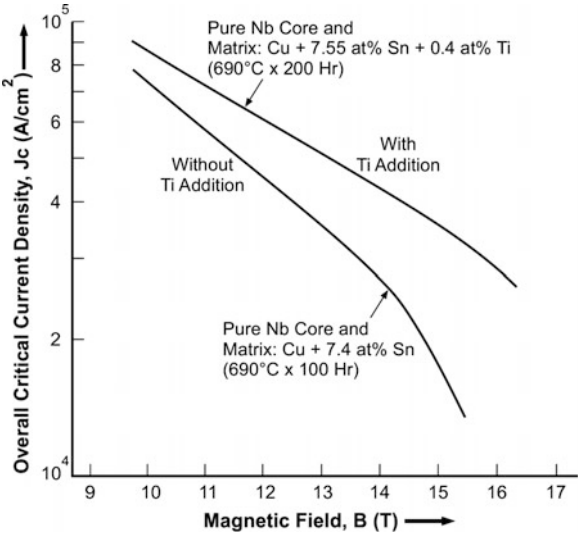

Fig. 6.27 Overall J_c (4.2 K) of 4.7 μm diameter 10,261 filament Nb_3Sn composite wire produced by Hitachi Cable Co. in Japan increases significantly by adding 0.4 at. % Ti to the Cu-7.5 at.% Sn matrix. Wire heat treated at 690 °C for 200 h (Adapted from [23, 32])

wires are encased in a long SUS 316 LN jacket together with Cu wires to fabricate a cable-in-conduit conductor (CICC). Most other parameters are listed in Table 6.4.

Bronze technique has also been used to manufacture Nb_3Sn conductors for ac applications. To minimize hysteresis losses the filament size has been reduced to as small as 0.2 μm. The Sn concentration in bronze is reduced and a small amount of Ge is added to make the matrix resistive for effective decoupling of the filaments. Because of the very small size of the filaments the heat treatment temperature is now reduced to 500–550 °C. J_c in these wires do not show degradation up to a bending strain of 4 %. This enables the wire to be used in a 'react and wind' mode. A 2 T, 50 mm bore magnet using Nb_3Sn wire has been operated by Tachikawa et al. [35] at 53 Hz with an ac loss of only 0.013 % of the coil energy.

6.4.5 Internal Tin (IT) Process

The internal tin (IT) method of fabricating Cu–Nb_3Sn composite wires is based on the old work of Hashimoto et al. [36]. In this process Sn or Sn-alloy contained as core is made to diffuse out in to the composite. The problem of intermediate annealing associated with bronze process due to work hardening is thus circumvented. In this process [36], as shown in Fig. 6.28, the copper billet consisting of Nb rods has a central hole which is filled with Sn. The composite billet is reduced to hexagonal shaped rods suitable for restacking. The desired number of these 'sub-elements' are stacked together in a stabilizing Cu tube lined with a thin tantalum diffusion barrier and cold drawn to final size of the wire. Since all the components, that is, Cu, Sn, Ta and Nb are ductile, their co-processing is easy and economical.

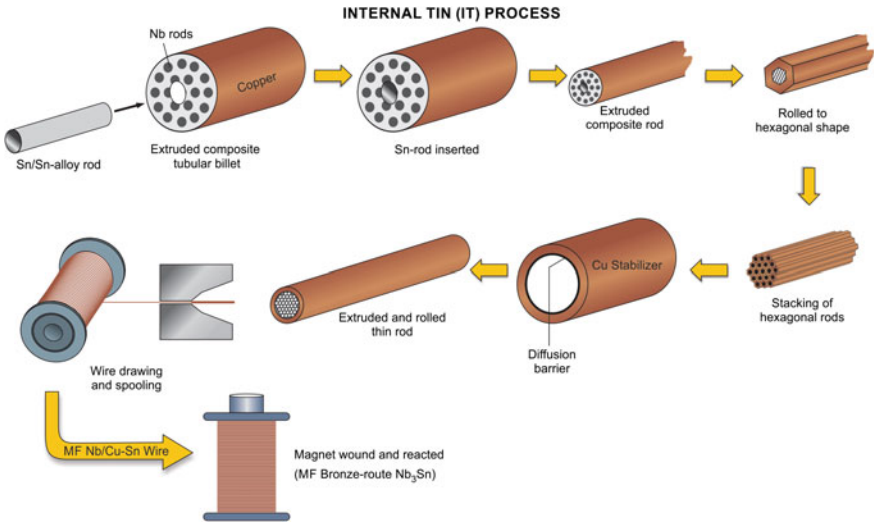

Fig. 6.28 The sequence of steps to be followed in the internal tin process to produce Cu/Nb_3Sn composite wire

No intermediate annealing is needed. For high current applications the wires can be cabled in to a desired configuration. Diffusion of Sn from the centre is carried out in a multistep homogenization process between 200 and 500 °C for several days. The final reaction to form Nb_3Sn is carried out at 650–750 °C for a few days, depending upon the subelement size, filament size, volume fraction of Sn and the desired magnetic field. IGC [37] as early as 1985 prepared 27 km long wire with this process with an overall J_c (excluding the barrier and the stabilizing Cu) = 10^5 A cm^{-2} (4.2 k, 10 T).

The bronze process has the limitation that the solubility limit of Sn in Cu is 15.8 wt% whereas larger Sn concentration is possible in the IT process which results in high non-Cu J_c in the wire. IT process is also being used for wire production for fusion programme including ITER. Similar to in bronze process addition of Ti to the Sn core leads to higher J_c values in IT processed Nb_3Sn wires.

The IT process has some drawbacks if pure Sn is used as a core too. For example, Sn melting takes place during extrusion. Therefore, the composite billet of Cu and Nb is either extruded without Sn as a tube or extruded with Cu as the central core. This Cu core is replaced after the extrusion by the Sn core for further processing. The diffusion of Sn causes a void at the centre after the heat treatment. The quality factor (n value) and the longitudinal homogeneity is superior in bronze processed conductors compared to those produced by the IT process. Nb_3Sn filaments in IT process tend to bridge after the heat treatment causing an increase in ac losses. Thus they do possess higher J_c but ac losses go-up in comparison to the bronze-processed conductors.

The benefit of Ti addition to Nb_3Sn to raise J_c is realized in IT process by adding Ti to the Sn component. Ti addition also increases the hardness of Sn to make it more compatible with Cu and Nb for co-processing.

High quality IT processed Nb_3Sn conductors have been produced by choosing intelligently the design configuration of the cross section of the conductor. Uniform distribution of Sn across the cross section is accomplished using the so called distributed tin (DT) technique [38]. Two elements, namely; Nb–Cu (Nb rods in Cu tubes) and Sn–Cu (Sn rods in Cu tubes), are packed uniformly across the cross section of a Cu stabilizer tube in a predetermined geometry as shown in Fig. 6.29. The volume ratio of Nb:Sn is kept at 3:1 across the wire. The (Table 6.5) gives the specifications of a wire prepared with a typical DT configuration. A non Cu J_c of 2.07×10^4 A/cm^2 (20 T, 4.2) have been achieved. Uniform grain size distribution has been achieved in this technique which has resulted in high J_c values. The ac losses are, however, are high reaching a level of 3,850 kJ/m^3 at ±3 T at 4.2 K.

The Mitsubishi Electric Co. later modified the DT process and developed [39] low loss Nb_3Sn wire by having a modified radially arranged Nb filaments across the cross section of the sub-elements as shown in Fig. 6.30. The Mitsubishi wire of 0.82 mm dia. had 91 sub-elements. Each sub-element has a central Sn-core with three layers of 84 Nb filaments of 2.7, 3.3 and 3.9 μm dia. from inner to outer layer respectively. The twist pitch was 25 mm. A Ta barrier has been used at the Cu stabilizer interface. The stabilizing Cu was 51.5 vol.%. The volume fraction of Cu, Nb and Sn in a sub-element was 25.4, 12.8 and 10.3 % respectively. This filament arrangement opened many Sn diffusion paths and prevented circumferential filament coupling. This resulted in higher J_c and low ac losses. A non Cu J_c of 1.15×10^5 A/cm^2 (12 T and 4.2 K) was achieved. The ac losses were reduced to 301 kJ/m^3

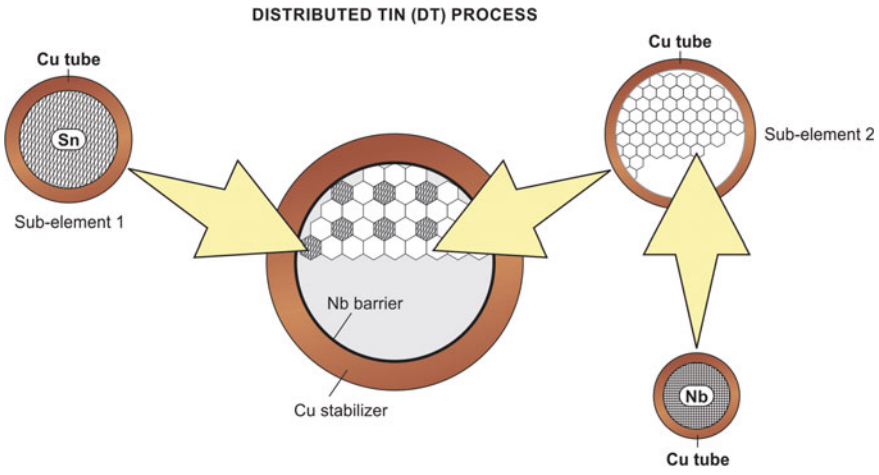

Fig. 6.29 Schematic drawing of the distribution of Nb–Cu and Sn–Cu sub-elements in a conductor cross-section prepared by the so called DT (distributed tin) technique (Adapted from [25, 38])

Table 6.5 The specifications of a typical DT type conductor (data compiled from [38])

Parameter	Unit	DT wire
Wire dia.	mm	1.0 × 0.7
No. of Nb-in-Cu tube elements		138
No. of Sn-in-Cu tube elements		61
Cu to non-Cu ratio		0.8
Filament dia.	μm	3.0/2.1
No. of filaments		27,462
Barrier material		Nb
J_c @ 4.2 K	A/cm^{-2}	2.07×10^4 (20 T)

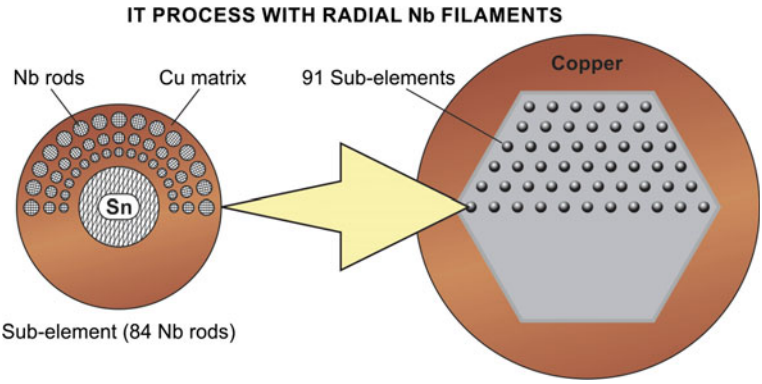

Fig. 6.30 A geometrical arrangement of Nb rods in a sub-element and the sub-elements in a wire cross-section of an IT wire used by Mitsubishi Electric Co. for the production of a low loss Nb_3Sn wire. Note the radially arranged Nb-filaments in a sub-element (Adapted from [39])

at ±3 T and 4.2 K. It thus appears that the performance of the IT conductor is strongly linked to the design of the cross section. The present day performance of the IT wires matches well with the specifications set for the ITER conductor.

Both the techniques, namely, bronze and the IT have been used successfully to produce Cu–$(Nb, Ti)_3Sn$ wire of lengths up to 20 km which are cabled to fabricate cable-in-conduit conductors (CICC) carrying currents up to 80 kA at 10 T field. Japan Atomic Energy Research Institute (JAERI) has already tested the central solenoid model coil (CSMC) for ITER. Coils have been wound using combination of conductors produced by bronze and IT processes.

Apart from the bronze and IT processes which are presently used for commercial production we discuss very briefly two more processes to produce multifilamentary Nb_3Sn conductors which have shown encouraging results in the past. These are Jelly-Roll process and the in situ process.

6.4.6 Jelly-Roll Process

The jelly-roll (JR) process was introduced by McDonald et al. [40] at Teledyne Wah Chang Albany, for producing composite Nb_3Sn MF conductors. In this process thin foils of Nb and Cu–Sn bronze are laminated and wrapped around a Cu cylinder with a Ta diffusion barrier on the cylinder and the assembly is inserted in a hexagonal shaped Cu container. Several of these hexagonal containers are bundled together in another Cu tube. The composite billet is extruded and reduced to fine wires as in conventional bronze or IT process. The advantage of this JR process is that the conventional bronze core is replaced by a Cu-core surrounded with a barrier. The barrier prevents the Sn infiltration in to copper and enhances the conductor stability. This technique also makes the availability of bronze around each filament quite uniform. By contrast, the conventional bronze core leads to a strong radial Sn-gradient which produces marked differences in the local Sn composition and the grain morphology of the Nb_3Sn layer. Detailed work on this JR technique by changing matrix to filament ratio, using pure Nb and Nb–0.8 wt% Ti sheets and using a heat treatment at 725 °C for 50–200 h has led to high J_c values = 1.3×10^4 A/cm^2 (16 T, 4.2 K).

Recently, Tachikawa et al. [41] at Tokai University, Japan used the JR technique to produce composite Nb_3Sn conductor with high J_c and B_{c2} values. Thin sheet of Nb laminated with the sheet of one of the Sn-based alloys like Sn–Ta, Sn–B or Sn–Nb are wrapped spirally over a Nb–Ta (3.3 at.%) core and covered again with the Nb–Ta sheet. The composite assembly is rolled and drawn to wires which are heat treated at 725–750 °C for long periods. A sharp T_c = 18.1 K and a B_{c2} = 26.5 T have been obtained. A non Cu $J_c = 1.5 \times 10^4$ A/cm^2 (22 T and 4.2 K) has been achieved. Still better performance can be attained by optimizing parameters leading to uniform and stoichiometric Nb_3Sn layers. The JR process used by Tachikawa et al. is schematically shown in Fig. 6.31.

6.4.7 In Situ Process

The technique is a fall out of a paper by Tsuei [42] and soon followed by Sharma and Alekseevskii [43] in which superconductivity was found at 18 K corresponding to Nb_3Sn in an alloy $Cu_{93}Nb_5Sn_2$ when drawn in to fine wires and suitably heated. The in situ technique makes use of the phase diagram of Cu–Nb. It is based upon the near negligible solubility of Nb in Cu at ambient temperature. Large amount of Nb can mix with Sn in the molten state but as soon as the liquidus line at 1,700 °C is crossed, most Nb gets precipitated out in the Cu matrix. Below the peritectic temperature (1,090 °C) the solubility of Nb in Cu is $\sim$1.5 wt% and that of Cu in Nb $\sim$2 wt%. These compositions are retained if the cooling is fast.

The cast alloy (Fig. 6.32a) shows typical dendrite structure of the Nb precipitates in Cu-matrix. Ingots when rolled and/or drawn to fine size of wire these precipitates

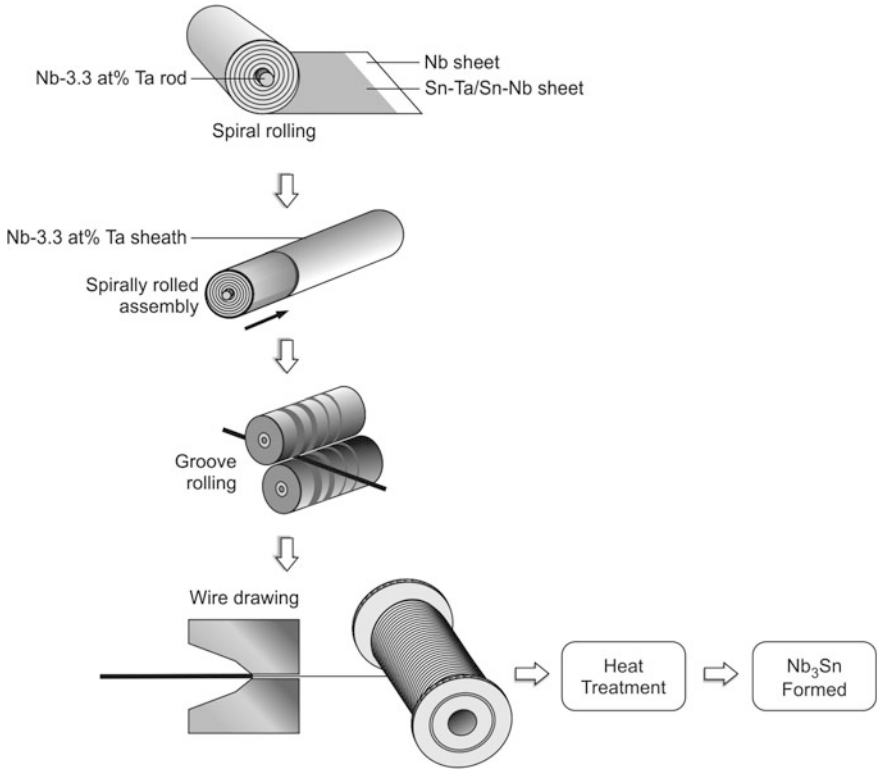

Fig. 6.31 The schematics of the JR process for producing Nb_3Sn conductor

get elongated and take the shape of fine filaments which tend to curl and fold being constrained by the matrix (Fig. 6.32b). Figure 6.32c is the micrograph of the cross section of a 0.21 mm wire and shows that the filaments have high density and are of ribbon shape. This high density of Nb filaments causes high density of Cu–Nb interfaces increasing the yield strength of the composite manifold, much more than what the rule of mixture would predict. This structure also leads to increased J_c on account of increased surface flux pinning caused by the high density of interfaces.

The drawn wires are then coated with optimized amount of Sn and heat treated at a much lower temperature ~550 °C for 50–200 h. Figure 6.33 shows the J_c–B behaviour of the in situ Cu/Nb_3Sn wires of 0.21 mm dia. coated with 36–37 vol. % Sn and reacted at 550 °C for 160 h prepared by Sharma et al. [44] Cu–Nb ingots were prepared using an arc furnace. An overall $J_c = 3 \times 10^4$ A/cm^2 at 12 T, 4.2 K has been obtained. Impressive results were reported on in situ Nb_3Sn and V_3Ga conductors by Bevk's group at Harvard University, Finnemore's group at Iowa State University, Freyhardt at Gottingen University, Roberge's group at Quebec, Canada and Tachikawa'group at National Research Institute for Metals (NRIM). For details of results from these groups, please, see the review paper by the author [23].

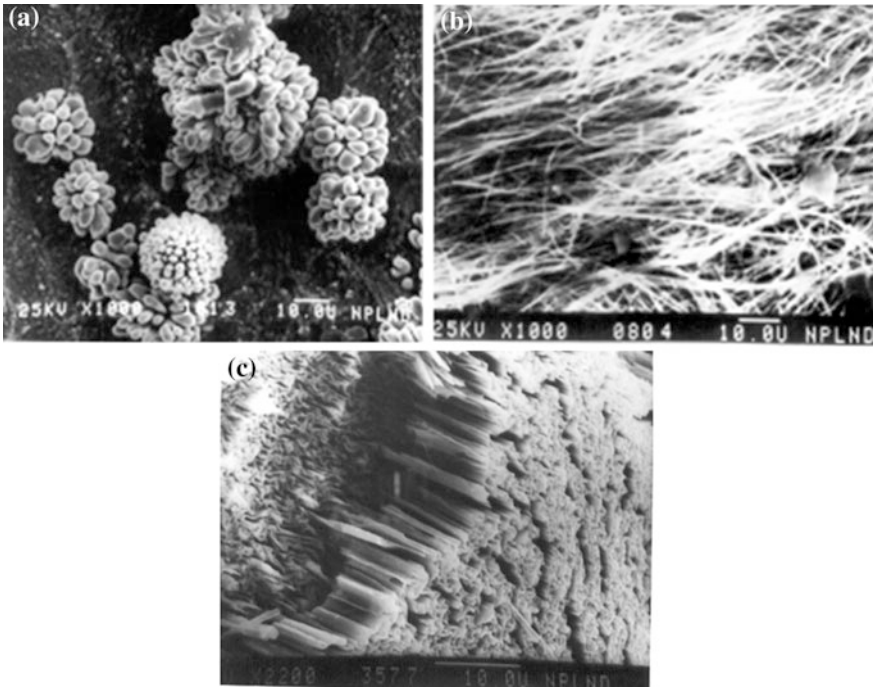

Fig. 6.32 **a** Typical Nb dendritic structure in a Cu–Nb (5 at.%). **b** Filamentary morphology of a Cu–Nb (20 at.%) wire drawn to 0.21 mm dia. **c** Cross-section of a 0.21 mm dia. Cu–Nb (20 at.%) wire. High density of ribbon shaped filaments is visible [44]

J_c of in situ conductors are comparable or better than obtainable from conventional bronze and IT techniques, nevertheless suffer from the high ac losses because of the intimate coupling between the closely spaced filaments.

This technique has several advantages not available with other techniques. The technique is much simpler as there are no repeated bundling to make MF and there are no intermediate annealing treatments. The ductility of the Cu–Nb ingot allows to process the wire down to fine size without annealing. Very fine filaments obtainable in situ conductors ($\sim$0.2–0.5 μm) need low temperature heat treatment temperature (500–600 °C) which leads to fine grain structure of the Nb_3Sn layer resulting in high J_c. Very fine size of the filaments and small inter filamentary distances lead to exceptionally high filamentary bonding. As a result local strain is transferred to the entire cross section. This results in exceptionally high mechanical strength. The ultimate tensile strength σ_{UTS} of the bronze processed Cu/Nb_3Sn composite is 292 MPa whereas the in situ composite has a σ_{UTS} of 513 MPa at room temperature and increases further by 25 % to 690 MPa at 77 K. In situ conductors are less sensitive to stress strain behaviour than their counter part in bronze process. For example, the bronze conductor shows J_c degradation at a strain level of 0.3 % whereas the in situ conductor shows the J_c degradation at only 0.6 % strain.

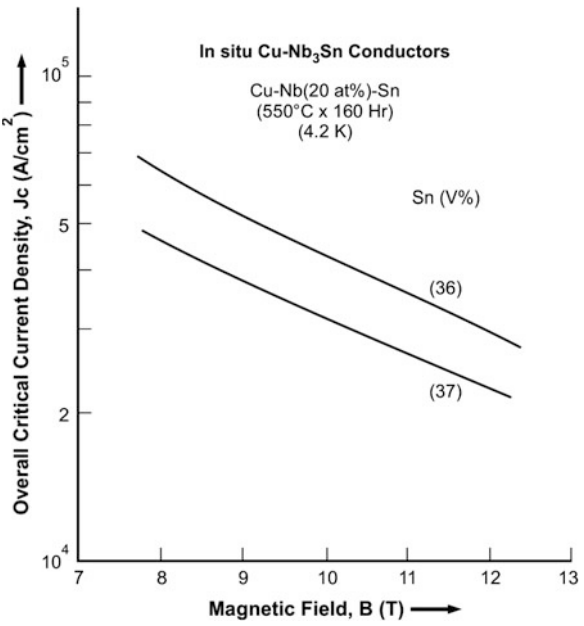

Fig. 6.33 The overall J_c of the Cu/Nb_3Sn 0.21 mm dia. in situ wires reacted at 550 °C for 160 h. *Upper curve* has Sn 36 vol.% and the *lower curve* Sn 37 vol.% [44]

Filament strength too in these composites is high because of small grain size (Hall Patch effect) and dislocation movement is also inhibited due to the high density of the filaments causing obstacles due to Orowan mechanism. All the unique properties of these in situ conductors depend upon two factors, one, the superconducting volume fraction (SVF) and the other area reduction ratio (ARR). The SVF has to be well above the percolation threshold ($\sim$17 vol.%) and as high as permitted by the need to maintain ductility. The ARR will depend upon the starting billet size but an area reduction by 3,000–4,000 has been found optimum for laboratory scale production.

There may be a revival of interest in the in situ technique in future as the reports suggest that in situ conductors are less prone to radiation damage.

6.5 The Nb_3Al MF Superconductor

6.5.1 Early Work Using Jelly-Roll (JR) Method

Nb_3Al is yet another superconductor belonging to the family of A-15 class/β-W structure compounds and is tipped to be the material of future for magnets needed for high energy particle accelerators, nuclear fusion reactors and high frequency NMR spectrometers. This material is superior to Nb_3Sn in two respects, one, the upper critical field of Nb_3Al is about 32 T much higher than that for Nb_3Sn and the

other is its high strain tolerance. Its T_c at 18.8 K is comparable to that of Nb_3Sn. Multifilamentary Nb_3Al composite wires were produced first time by ENEA (Frascati) in collaboration with IMI in Italy following the JR method. The conductor was meant to upgrade the SULTAN test facility by constructing three insert coils one each for the SULTAN partners, ECN–Petten, SIN Villigen and ENEA. Fine multifilamentary composite wires produced by the JR method were heat treated at 750–850 °C for prolonged period during which Nb_3Al forms through direct reaction between Nb and Al. The JR technique was described in Sect. 6.4.6. It has the advantage that no intermediate heat treatment is required and that Al and Nb are very uniformly distributed across the filament cross section. The Nb_3Al wire prepared by this technique yielded a non-Cu $J_c = 1.9 \times 10^5$ A/cm^2 (11 T, 4.2 K). ENEA had also plans to fabricate Nb_3Al Rutherford cable carrying a current of 12 kA and produce a field of 12 T in a toroidal coil for NET reactor.

6.5.2 Phase Diagram of Nb–Al System

The phase diagram of the binary phase of Nb and Al is shown [45] in Fig. 6.34. The phase diagram of Nb–Al has a similarity with the Nb–Sn system in so far as the

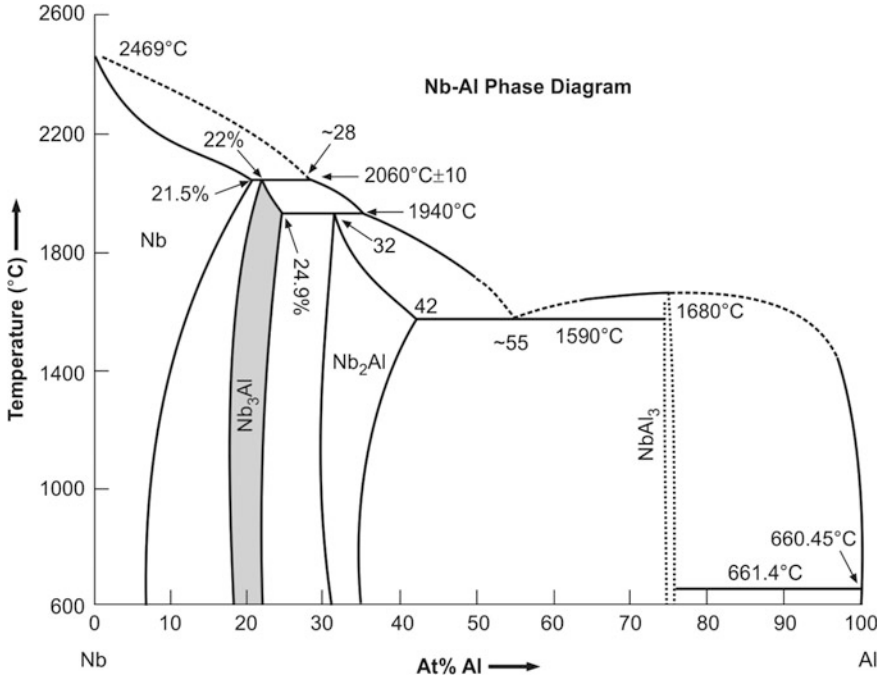

Fig. 6.34 The binary phase diagram of Nb and Al [45] (Reproduced by permission of Taylor and Francis Group, LLC, a division of Informa plc and Takao Takeuchi)

A-15 phase is formed by a peritectic reaction from bcc phase + liquid to A-15 phase at 2,060 °C. The bcc solid solution phase Nb(Al)ss however extends over a wide range of composition. The solubility limit of Al is 21.5 at.% at 2,060 °C and 9 at.% up to 100 °C. On both sides, that is, Al-rich side as well as Nb-rich side the phase limits of the A-15 phase depend strongly upon temperature. On the Al-rich side the A-15 phase includes the stoichiometric composition at the second peritectic temperature of 1,940 °C. This limit, however, shifts to lower Al concentration of 21.5 at.% at 1,000 °C. The Al content on the Nb-rich side varies from 19 at.% at 1,500 °C to 22.5 at.% at the peritectic temperature. This extensive variation of A-15 phase stoichiometry at low temperatures creates problem in fabricating Nb_3Al conductors with acceptable J_c and B_{c2} values. Even the stoichiometric bulk Nb_3Al (3:1) material has low T_c of 12 K when heat treated at below 1,000 °C. This T_c, in fact, corresponds to a Al-rich limit of 21 at.% Al. Low temperature heat treatment below 1,000 °C is thus ruled out for fabricating Nb_3Al wire conductors. The ternary Cu–Nb–Al phase diagram too is complicated and has proved to be a big hurdle in adopting the so called bronze technique to produce MF Cu–Nb_3Al stabilized conductors. Several unwanted ternary phases are formed which block the tie line routes between Cu-Al bronze and the Nb solid solution through the A-15 Nb_3Al phase. It was, in fact, this failure of conventional bronze process being not applicable to Nb_3Al wire fabrication, that caused long delay in developing alternate technique for the commercial production of Nb_3Al.

Nb_3Al has the β-wolfram (β-Tungsten) crystal structure similar to that of Nb_3Sn shown in Fig. 6.21 with the difference that Sn atoms are now replaced by Al atoms. The lattice parameter, of Nb_3Al is, $a = 5.183 \pm 0.002$ Å.

6.5.3 Mass Production of JR Nb_3Al Conductors by JAERI for ITER

In the previous section we understood why the bronze process failed to materialize for this material. For successful manufacturing our strategy has to be twofold. One, that the A-15 stoichiometric composition should be attained at high temperature ($\sim$1,900 °C) by forming a bcc solid solution $(3Nb.Al)_{SS}$ and should be retained by quenching fast ($\sim 10^4$ °C/s.) the alloy though is in bcc phase. Diffusion to form A-15 phase at such high temperature would lead to large size grains and poor J_c. To keep the grain size small a heat treatment for Nb–Al diffusion has to be kept below 1,000 °C. This three-step procedure thus leads to perfect stoichiometric composition (25 at.% Al) leading to high T_c and high B_{c2} which will give high J_c at higher fields. Further, low temperature diffusion process will leads to fine grains enabling the conductor to carry large transport current in low field. The process thus fulfills the twin objective of fine grains and high B_{c2}. We describe this technique in some detail below.

As described earlier, the JR process is a reliable process to make long length A-15 MF superconductors. Thin sheets of Nb and Al are laminated and wound over a Cu rod and encased in a Nb sheet. The composite billet is extruded and drawn to hexagonal shaped JR sub-elements. These sub-elements are stacked together in the desired geometry in a Cu tube and processed to wires of required diameter.

Figures 6.35 and 6.36 show the cross sections of the strands and of the CICC developed [46, 47] by the Japan Atomic Energy Research Institute (JAERI) in collaboration with Sumitomo Electric Co. for ITER magnets. Figure 6.35 is the cross-section of a strand 0.81 mm in diameter with 96 JR processed sub-elements and Fig. 6.36 on the other hand is the cross section of the CICC with 1,152 such strands. These JR processed wires are heat treated at a temperature of 750 °C to facilitate the formation of Nb_3Al through the diffusion reaction. A non-Cu J_c of $\sim 1.0 \times 10^5$ A/cm^2 (12 T, 4.2 K) has been attained. JAERI established the facility to process 70 kg billets producing JR Nb_3Al wires of length as much as 16 km and weighing about 1,000 kg. This conductor has been used for an insert coil of the ITER central solenoid producing a field of 13 T at 4.2 K. The hysteresis losses are found to be limited to 600 mJ/cm^3 at ±3 T and a residual resistivity of the chrome-plated wire less than 1.6×10^{-10} Ωm.

JAERI has since tested successfully a stain less steel (SS) jacketed JR-processed Nb_3Al CICC conductor in a 'react and wind' form carrying a current of 46 kA at 13 T, 4.2 K as a candidate for the TF coils of the ITER. No J_c-degradation is observed up to a strain level of 0.4 %. The Nb_3Al coil was tested as an insert in the bore of the ITER central solenoid model coil. This coil was successfully operated at a current of 46 kA producing a field of 13 T. This has established the efficacy of this conductor for its intended use.

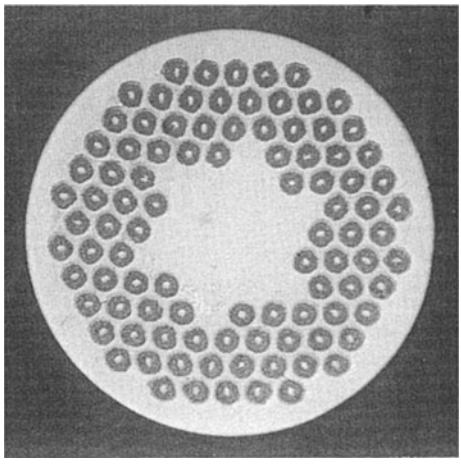

Fig. 6.35 Cross-section of a 0.81 mm dia. strand with 96 sub-elements of Nb_3Al processed by JR technique, for the insert coil of the central solenoid of ITER [46] (With permission from Elsevier)

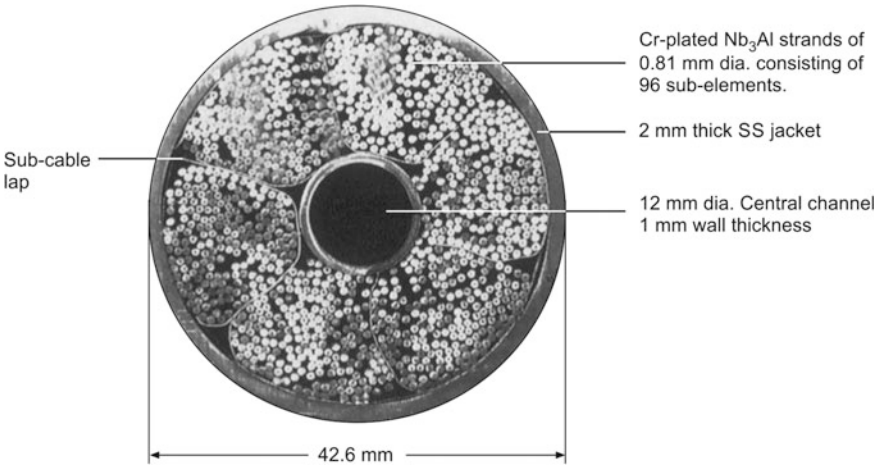

Fig. 6.36 The cross-section of the JR processed Nb_3Al–CICC for ITER TF coils (13 T @ 46 kA) [47] (With permission from Elsevier)

6.5.4 The Rapid Heating, Quench and Transformation (RHQT) Technique

Though JAERI has been successful in developing Nb_3Al CICC by JR method suitable for ITER applications, yet the technique suffers from an inherent problem. Nb_3Al phase has been produced by JAERI by a direct diffusion reaction between Al and Nb at a comparatively lower temperature of 750 °C at which the phase composition deviates from the normal A-15 stoichiometry. The upper critical field in these conductors is ~22 T significantly lower than the expected value of 30 T. Alternatively, diffusion can be carried out at high temperature (~1,800 °C) but coarser grains, formed at this temperature, lower the J_c thus annulling any benefit from high B_{c2}.

The twin objective of fine grains and perfect stoichiometric composition can best be met by the Rapid Heating, Quench and Transformation (RHQT) technique developed at NRIM (NIMS) and pioneered by Takeuchi [48, 49]. In this technique, a metastable bcc super saturated Nb-solid solution containing 25 at.% Al, that is, (3Nb.Al)ss is obtained at high temperature and quenched fast to retain its composition. In the next step this bcc super saturated solid solution is transformed in to A-15 phase through a suitable heat treatment carried out at ~800 °C. Here, the transformation only changes the crystal structure (from bcc to A-15) and not the composition, our twin objective of fine grains and perfect composition is thus met intelligently. After trying liquid quenching technique in the beginning, NIMS finally perfected the so called RHQT technique [49] for the manufacture of long lengths of Nb_3Al tapes/wires.

The schematic diagram of the system developed at the NIMS to produce long lengths of Nb_3Al conductor is shown in Fig. 6.37. In this technique the precursor multifilamentary Nb_3Al wire is prepared by the usual JR method. Foils of Nb and Al are laminated together and are spirally wound on a Nb-rod and wrapped around by a Nb sheet at the outside. The composite is encased in a Cu can which should be removed after the extrusion and drawing processes are complete. The standard multifilamentary wire thus has the Nb-matrix only. NRIM and Hitachi cable Ltd. Produced 2.6 km wire using a 50 kg billet of the size 140 mm × 450 mm. As shown in the figure the precursor wire is fed from pay-off reel to a Cu wheel (working as an electrode) and then to a pulley dipped in molten Ga and is collected on another spool. A uniform RHQ treatment along the length of the wire is crucial for this scale up system. The wire is Ohmic-heated between the copper wheel and Ga bath to a temperature of about 1,950 °C where the bcc solid solution extends to 25 at.% Al. The wire is then quenched in the molten Ga-bath kept at ~50 °C followed by annealing at ~800 °C to transform the bcc solid solution to A-15 Nb_3Al phase. The speed of the moving wire is kept 20 m/min. The bcc (3Nb.Al)ss solid solution is ductile at room temperature and therefore enables convenient cabling and winding before the final annealing for phase transformation (Fig. 6.37).

Copper stabilizer is incorporated with the wire after quenching by mechanical cladding. Drawing the wire at room temperature in the bcc phase has been found to

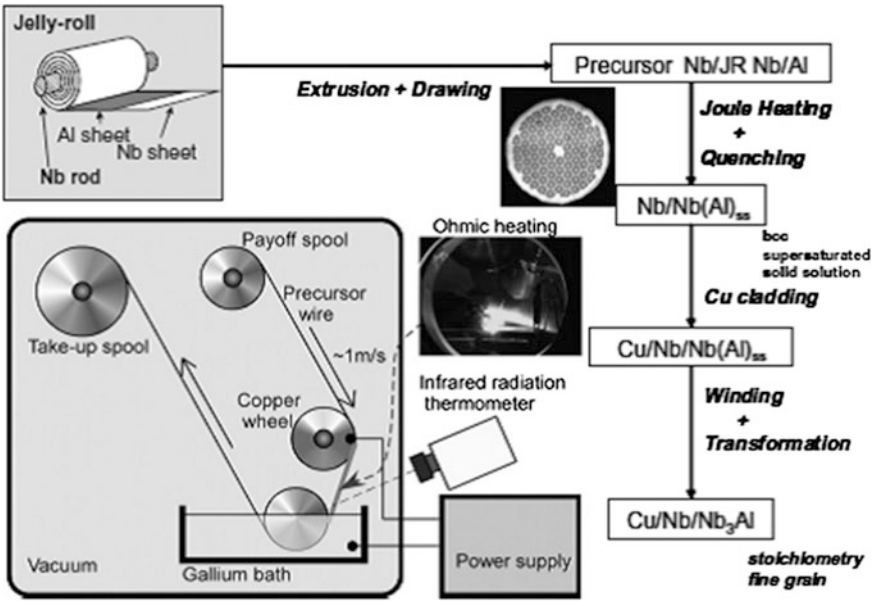

Fig. 6.37 Schematic diagram of the RHQT technique developed at NIMS for the production of long length Nb_3Al conductors. The JR Nb_3Al precursor wire is Ohmic-heated to 1,950 °C, quenched to 50 °C in Ga-bath and annealed at 800 °C [49] (*Courtesy* T. Takeuchi and with permission from Elsevier)

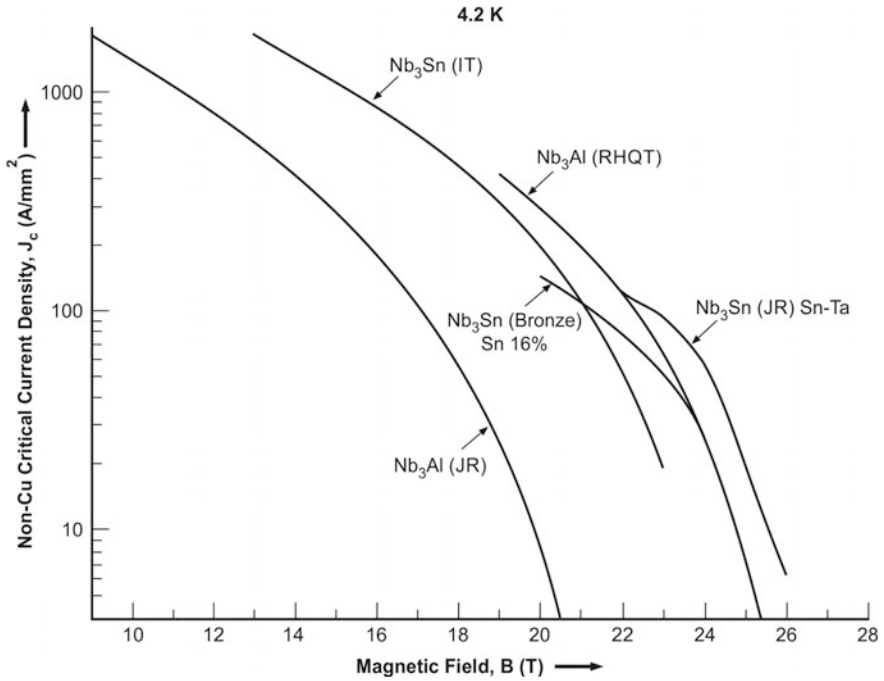

Fig. 6.38 Comparison of non-Cu, J_c of RHQT processed JR Nb_3Al wire with some recent data on Nb_3Sn wires prepared by different techniques. The superiority of RHQT wire is quite noticeable at 20–22 T field [25] (With permission from Alex Braginski (ESNF) and K. Tachikawa)

increase J_c by a factor of two in the annealed wire. For comparison, the non-Cu J_c of the RHQT wire has been plotted against field together with three recent Nb_3Sn wires in Fig. 6.38. Evidently, the RHQT Nb_3Al wire stands out to be superior to other wires in the field range of 20–22 T. The J_c of this wire is surely much higher than the ordinary JR-processed wire by JAERI.

A test insert (Fig. 6.39) coil of RHQT Nb_3Al wire has been successfully tested at NIMS producing a field of 19.5 T at a current of 242.3 A in a background field of 15 T provided by a combination NbTi/Nb_3Sn magnet [49]. The technique is now being used for making Nb_3Al cables for next generation high field particle accelerators magnets [50] because of its high strain tolerance. For the up-gradation of the luminosity of the Large Hadron Collider (LHC), a 27 strand Rutherford cable (13.93 × 1.84 mm) has been developed using the JR method and RHQT technique by NIMS in collaboration with KEK and the Fermi Laboratory. The wire has been prepared using Ta-matrix with a matrix ratio = 0.8, in place of the Nb-matrix which had caused large magnetic instabilities in low fields. Figure 6.40 is the cross section of this 27 strand Rutherford cable.

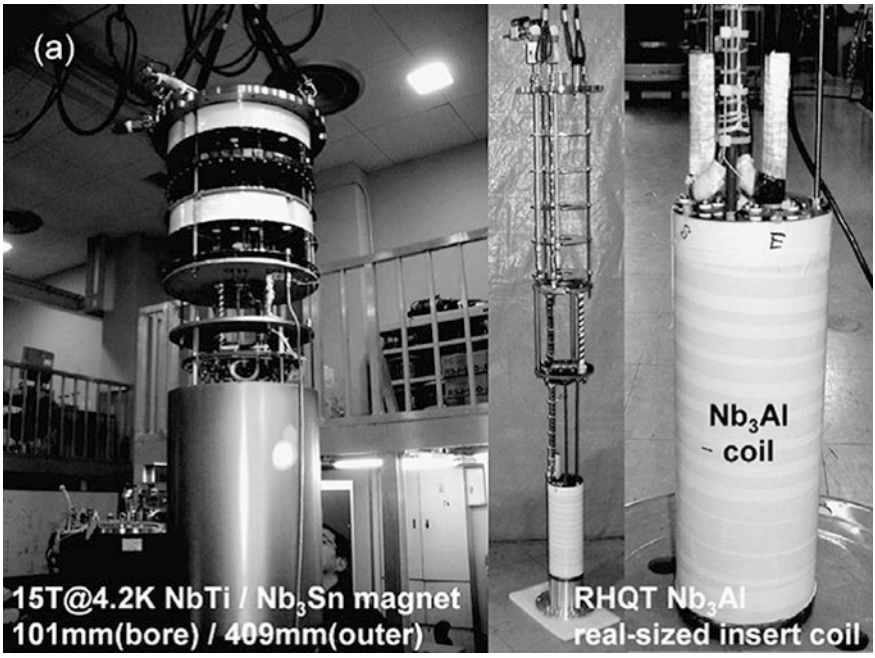

Fig. 6.39 A RHQT Nb_3Al insert coil built at NIMS, Japan. The coil produced a field of 19.5 T in a background field of 15 T generated by a Nb–Ti/Nb_3Sn combination magnet [49] (*Courtesy* T. Takeuchi and with permission from Elsevier)

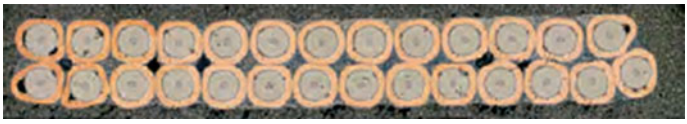

Fig. 6.40 A typical cross-section of a 27 strand Rutherford cable fabricated by a number of institutions in US and Japan

6.6 The V_3Ga Tapes/MF Superconductors

6.6.1 The Phase Diagram of V_3Ga

Superconductivity in the A-15 intermetallic V_3Ga superconductor was discovered by Matthias et al. [51] in 1956. In contrast to world wide development of Nb–Ti and Nb_3Sn superconductors, work on the development of V_3Ga superconductor has been followed religiously in Japan at NRIM only, though laboratory studies have been carried out at few other places too. As discussed earlier in this chapter V_3Ga has a great potential to carry much larger transport current compared to Nb_3Sn at

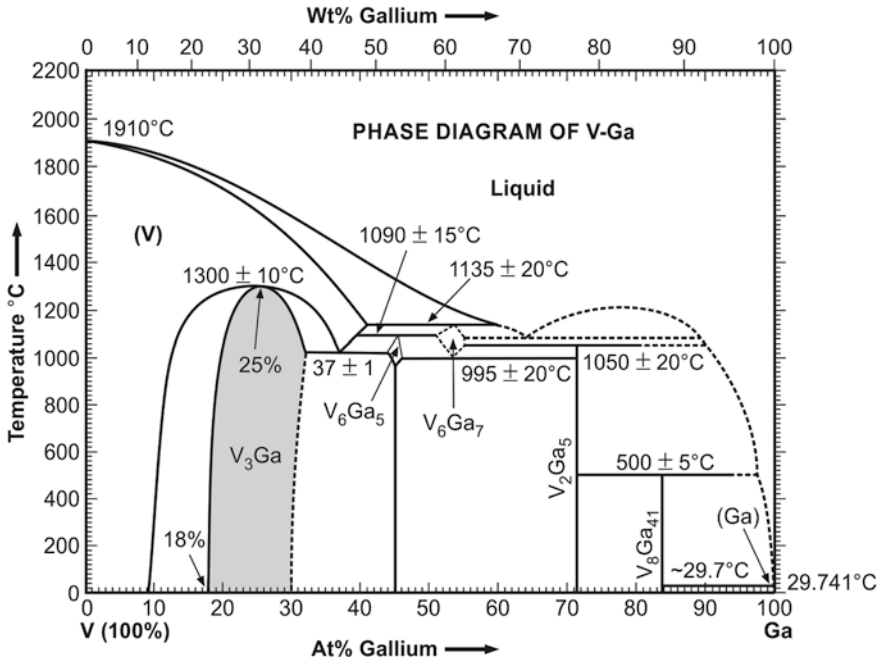

Fig. 6.41 The V–Ga binary phase diagram [52] (With permission from Springer, copyright © 1981, Springer)

high magnetic fields. V_3Ga also has better mechanical properties and is less sensitive to strain. It has an added advantage that one needs lower heat treatment temperature for the formation of V_3Ga layer, of the order of 600 °C. The decomposition temperature of V_3Ga is 1,300 °C which is much lower than 2,100 °C for Nb_3Sn. Thus for the same grain size V_3Ga has to be heated at lower temperature.

The binary phase diagram of V–Ga [52] is shown in Fig. 6.41. V_3Ga has a wide range of composition from 21.3–31.5 at.% Ga at 1,010 °C, however falls to 21–29 at.% at a lower temperature of 600 °C. This wide range of composition of the A-15 phase makes it an attractive material for application. The highest T_c recorded for the stoichiometric V_3Ga is 15.2 K. T_c decreases as one moves away from the 3:1 stoichiometry. V–Ga system has several other intermetallic compounds which are Ga-rich. These compounds are V_6Ga_5, V_6Ga_7, V_2Ga_5 and V_8Ga_{41}. However, only compound V_3Ga crystallizes in β-tungsten (Cr_3Si) structure and displays superconductivity. The lattice parameter of V_3Ga is a = 4.186 Å. This crystal structure persists up to 20 K below which it undergoes a martensitic transformation quite similar to in several A-15 Nb and V based superconductors.

6.6.2 V_3Ga Diffusion Tapes

The importance of V_3Ga as a high field practical superconductor was realized by Tachikawa at NRIM as early as 1960s. They developed a surface diffusion technique [53] to fabricate long length of flexible V_3Ga tapes. The process consists of two steps. In the first step, a 50 μm thick V-tape is passed through a molten Ga-bath heated at 500–600 °C and then through a tube furnace kept at 800 °C. During this process about 10 μm thick layers of V_3Ga_2 and VGa_2 are formed on both sides of the V-substrate. In the second step the tape is electroplated with a 5 μm thick Cu layer and heat treated at 650 °C. Cu diffuses fast in to V_3Ga_2 and VGa_2 to form a ternary Cu–V–Ga alloy of low melting point (700–800 °C) which supplies Ga to form a thick layer of V_3Ga. High J_c in Zr doped tapes were obtained for tapes heat treated at 650 °C for 100 h. Tapes had approximately 30 μm thick V sandwiched between 8–10 μm V_3Ga layers on either side and outer Cu–Ga layer.

Indeed world's first highest field (17.5 T) was produced [25] in 1976 by a superconducting magnet which used V_3Ga as a central coil prepared by the surface diffusion technique at NRIM. The background field was provided by the outer Nb_3Sn coils. Figure 6.42 shows the magnet with support system without the cryostat on the left and the complete system under operation on the right. The magnet was

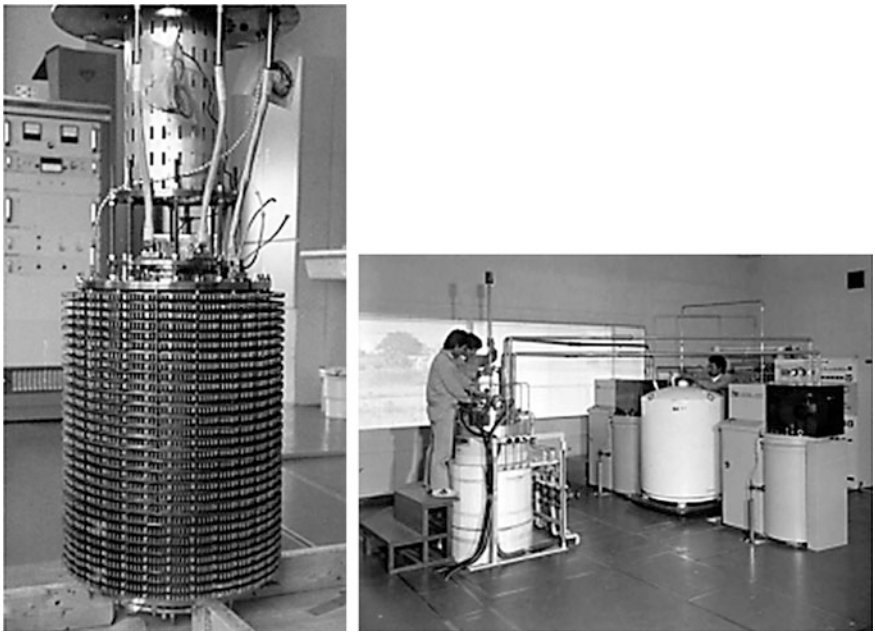

Fig. 6.42 World's first 17.5 T superconducting magnet operated at NRIM, Japan in 1976. Innermost coil used V_3Ga diffusion tape [25]. *Left* The magnet without the LHe-cryostat. *Right* The magnet under operation with two He-liquefiers (*Courtesy* K. Tachikawa and permission from Cryogenics and Superconductivity Society of Japan)

cooled down with two helium liquefiers perhaps because large liquefiers may not have been available around the time. It had a working bore of 31 mm, outer diameter 400 mm and the height 600 mm.

6.6.3 Bronze Processed V_3Ga MF Conductors

One out-come of the surface diffusion technique used for making V_3Ga tapes was the exemplary role played by Cu in the growth of the V_3Ga layer through its addition to Ga. This finding led Tachikawa to propose the so called bronze process [27] for the production of MF V_3Ga wires. The technique has already been discussed in Sect. 6.4.3 for the MF Nb_3Sn superconductors. The methodology is the same except the Nb-core is now replaced by V-core and the Cu–Sn matrix by the Cu–Ga (15–20 at.%) matrix. As discussed earlier, heat treatment temperature for the formation of V_3Ga layer is smaller at 600–650 °C. Significant improvement in J_c of V_3Ga has been achieved by adding elemental impurities to core and/or to the matrix and also by changing the fabrication geometry. Tachikawa et al. [54] reported an improved $J_c = 1 \times 10^5$ A/cm^2 (20 T, 4.2 K) by adding simultaneously 6 at.% Ga to the V-core and 0.5 at.% Mg to the Cu–Ga (19 at.%) matrix as shown in Fig. 6.43. The enhancement of J_c is primarily caused by grain refinement of V_3Ga

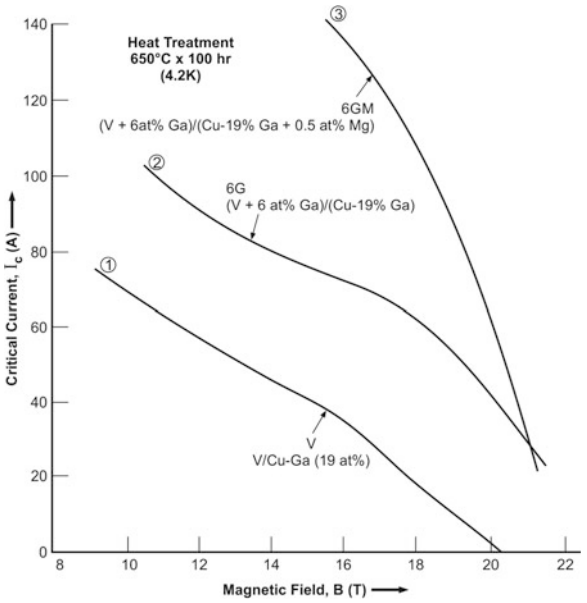

Fig. 6.43 I_c values of the bronze V_3Ga composite tapes plotted against magnetic field. 3G and 6G samples have 3 and 6 at.% Ga respectively in the V-cores. M represents 0.5 at.% Mg addition to the Cu–Ga (19 at.%) matrix [24, 54] (*Courtesy* K. Tachikawa)

and an accelerated layer growth. In these attempts efforts have been made to achieve two objectives. First, that, Ga has high solubility in V ($\sim$8 at.%) at 600 °C. A significant amount of Ga migrates from the matrix and gets dissolved in to V-core before V_3Ga formation starts. This reduces the availability of Ga for V_3Ga layer formation. The pre-addition of 6 at.% of Ga in V-core prevents the depletion of Ga in the matrix and consequently results in an accelerated layer growth and a better stoichiometry of V_3Ga. The second objective is to restrict the grain growth through Mg addition to the matrix which increases the pinning strength and J_c.

High J_c values of V_3Ga were also reported by Sharma et al. [55, 56] by fabricating monofilamentary and multifilamentary Cu–V_3Ga composite wires and tapes by reversing the geometry of the starting billet and using Ga and Mg additions. Figure 6.44 shows two types of configurations in which the composite billets were prepared. Configuration-1 is the normal one in which the V-core is kept inside the Cu–Ga matrix. Configuration-2 is a sort of a reverse geometry. The matrix is now used as core inside a V-tube with Cu-cladding. Since the matrix has a larger thermal expansion coefficient than V, V_3Ga is formed under compression at 600 °C, the reaction temperature in configuration 2. The layer growth is much faster in this new configuration. The addition of 6 at.% Ga in V and 0.5 at.% Mg in Cu–Ga matrix were also used in both the configurations. The typical V_3Ga thickness for a 0.65 mm dia. mono-core composite wire heat treated at 600 °C for 212 h is 1.9 μm prepared in configuration-1, 2.2 μm when prepared in configuration-2 and 4.7 μm when prepared in new geometry (configuration-2) and with Ga and Mg additions. The Mg-addition leads to fine grains and accelerated V_3Ga growth through grain boundary diffusion. The critical current I_c versus B plots for these materials with additives and in two different geometries can be seen in Fig. 6.45. At all fields and up to 16 T the I_c is higher for configuration-2 compared to those prepared in conventional configuration-1 and still higher for Ga and Mg addition. The best J_c of V_3Ga turns out to be 7.0×10^5 A/cm^2 (15 T, 4.2 K). The typical V_3Ga layer formed in a sample prepared in configuration-2 and heat treated at 600 °C for 212 h is shown in Fig. 6.46. Note that the Cu–Ga matrix is now inside the V-tube as a core and that a very thin layer ($\sim$2 μm) of V_3Ga is formed. It is this $\sim$2 μm thick V_3Ga layer which carries the entire super current out of the whole cross section of the wire.

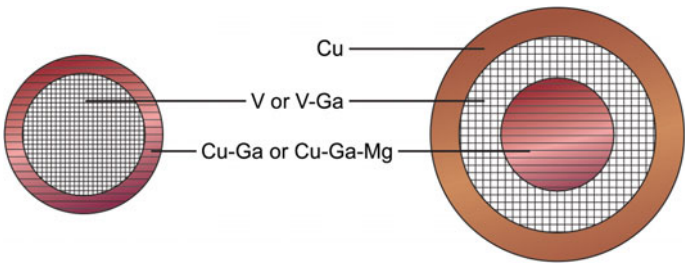

Fig. 6.44 The composite billets prepared in two different configurations. Configuration-1 has V-core in Cu–Ga matrix, configuration-2 has matrix inside the V-tube and cladded with Cu [55] (With permission of Elsevier)

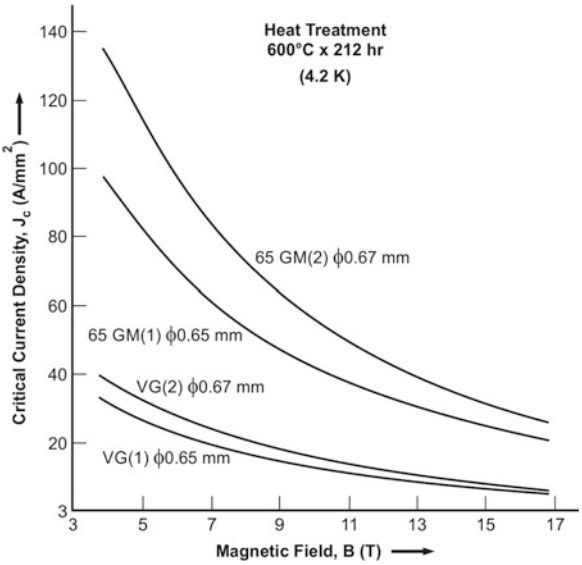

Fig. 6.45 Critical current, I_c of bronze processed V_3Ga composite wires (heat treated 600 °C × 212 h) plotted against field. Samples (1) are prepared in conventional geometry and (2) in reverse geometry. 65GM samples have 6 at.% Ga in V and 0.5 at.% Mg in Cu–Ga (19 at.%) matrix [55] (With permission of Elsevier)

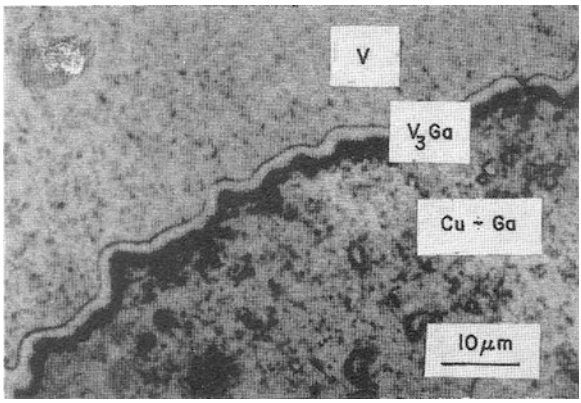

Fig. 6.46 A typical V_3Ga layer formed in a configuration-2 sample heat treated 600 °C for 212 h. Cu–Ga matrix has been used as core inside the V-tube. It is this thin V_3Ga layer which carries entire supercurrent [55] (With permission of Elsevier)

The results of these studies were used in fabricating Cu–V_3Ga composite wires with 19 composite cores [56]. Each core was now a V-tube filled with the matrix and finally cladded with a Cu-sleeve. The composite was drawn to wires and rolled to tapes. The geometrical cross-section of the composite is shown in Fig. 6.47a.

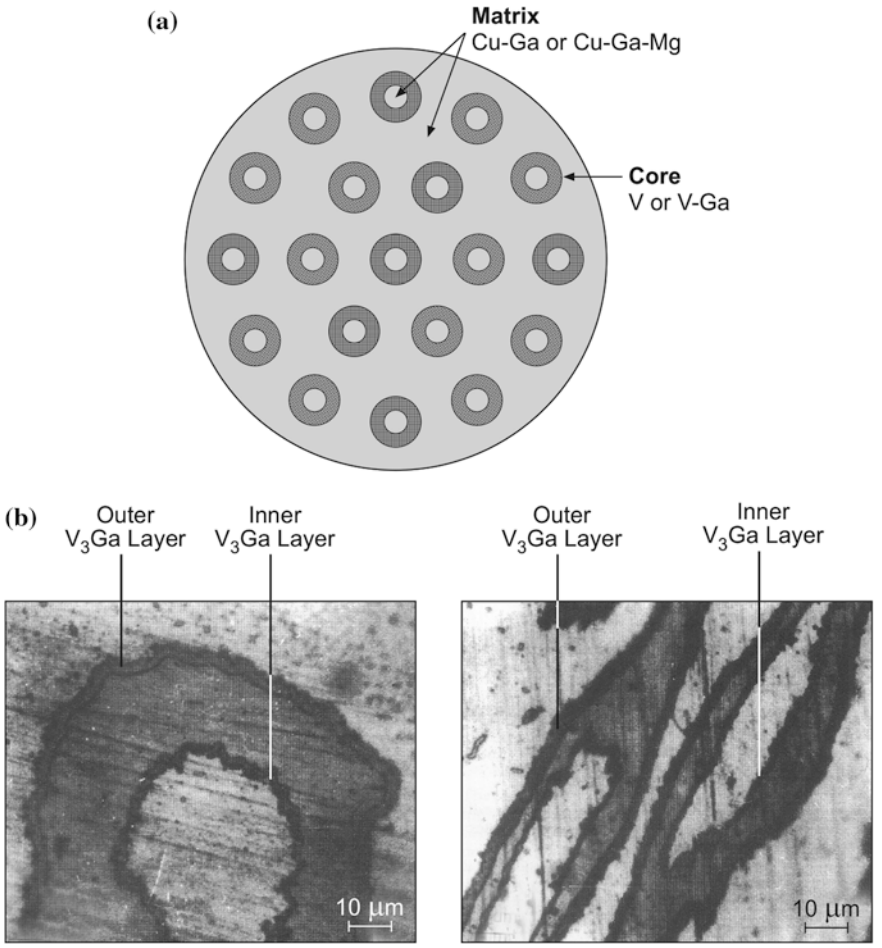

Fig. 6.47 **a** Geometrical cross-section of the billet with 19 composite cores. Each core is a V (or V–Ga) tube filled with Cu–Ga (or Cu–Ga–Mg) Matrix [56] (With permission of Elsevier). **b** V_3Ga layers are formed on both the side of the core. The composite billet was drawn to wires and also rolled to tapes [56] (With permission of Elsevier)

Two layers of V_3Ga are now formed on either side of the V-tubes as shown in Fig. 6.47b. The inner layer has a much faster growth rate compared to the outer one per unit matrix volume to surface area ratio and reaches saturation in shorter time. The overall J_c of this 19-core composite wires were significantly higher than those with conventional 19-core wires. Beneficial effect of Ga and Mg addition increasing J_c was confirmed in these studies too.

The bronze-processed Cu–V_3Ga composite MF wires/cables were manufactured by Furukawa Electrical Co. [57] on a commercial scale in 1974. Wires were prepared by bronze process using a matrix of Cu–Ga (19 at.%) and 55 V-cores. Some

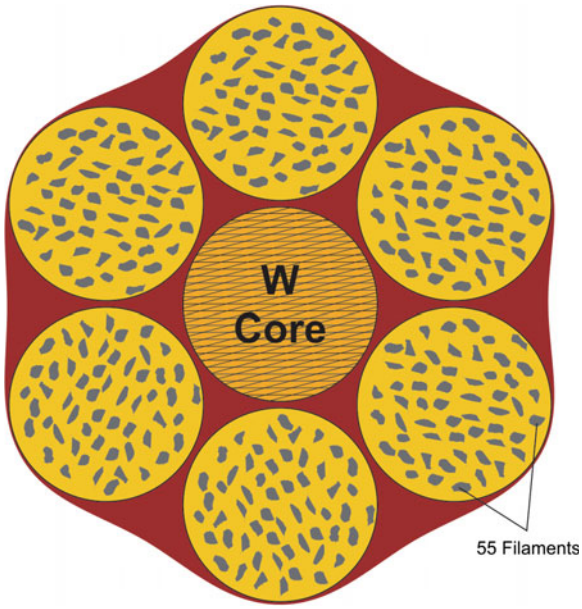

Fig. 6.48 The geometrical scheme of the cross-section of *six twisted* wires Cu–V_3Ga each having 55 filaments manufactured by Furukawa Electric Co. in 1970s by bronze-process. In the centre is a tungsten core (for strength), Overall $J_c = 3.3 \times 10^4$ A/cm^2 (15 T, 4.2 K)

unspecified percentage of Zr too was added to the V-cores. The wires were drawn to 0.12 mm dia. size. Six of these wires were twisted with tungsten wire at the centre with a pitch length of 5 mm. The tungsten core provides mechanical strength to the cable. The geometrical cross-section of the cable is shown in Fig. 6.48. The cable had a final diameter of 0.37 mm and the filament dia. about 10 μm. A heat treatment of 700 °C × 100 h. resulted in a V_3Ga layer of 2.9 μm thick. The cable was impregnated with In. An overall $J_c = 3.3 \times 10^4$ A/cm^2 (15 T, 4.2 K) and $B_{c2} = 21$ T were obtained. No degradation in J_c was observed down to a bending dia. of 20 mm. A 13 T magnet with 50 mm bore was successfully operated using this MF V_3Ga wire. The bronze technique thus works well for V_3Ga composites similar to Nb_3Sn.

6.6.4 The PIT–V_3Ga Conductors for Future Fusion Reactors

As of today, Cu–Nb_3Sn composite wires and cables are universally used for high field magnet applications, however, interest in the revival of V_3Ga conductor is growing rather fast. This is because of the two superior properties of this compound vis-à-vis Nb_3Sn. V_3Ga has intrinsically better mechanical properties and a much shorter decay time of induced radioactivity. The later characteristic property is most

relevant at the present time in the context of its application in future advanced fusion reactors. Advanced fusion reactors or power plants will have high magnetic fields to confine and maintain burning deuterium (D)–tritium (T) fusion plasma in steady state. It is estimated that burning plasma will generate 14 MeV fusion neutrons during D–T reaction. These neutrons will stream to penetrate superconducting magnets via the numerous ports provided in the reactor for various inserts. Nb_3Sn magnets are considered to be safe for ITER as the neutrons penetrating the magnets will be of the order of 10^{11} nm^{-2} s^{-1} (>0.1 MeV). Since future reactors will require long steady state operation to produce power, neutron streaming and penetration will increase by orders of magnitude. The magnets will thus be operated in harder neutron irradiation environment than the ITER. Studies show that the decay time of induced radioactivity of the nuclide of ^{94}Nb nuclear transformed from ^{93}Nb is over 10,000 years. The estimated half life is $\sim 2 \times 10^4$ years. The decay time of all the V-superconductors, on the other hand, is of the order of 10 years.

Realizing the merit of V_3Ga superconductor for its excellent property of the short decay time for induced radioactivity, Hishinuma et al. [58] at the National Institute for Fusion Science (NIFS), Japan have preferred to produce Cu–V_3Ga composite wires by the powder-in-tube (PIT) technique and using high Ga-contents. Ingots of Cu–Ga (25, 30, 40 at.%) were cast at 1,020, 940 and 810 °C respectively. These ingots were milled to powder and filled in a V-tubes (6 mm ID and 10 mm OD). The composite billets were rolled and drawn to wires of dia. 1.04 mm. The wire samples were heat treated under vacuum at several temperatures ranging from 600 to 900 °C. The optimum heat treatment temperature found was 700 °C and time $\sim$50 h. Thick layers of V_3Ga are formed during heat treatment. The V_3Ga thickness measured were 20, 40 and 50 μm for the Ga-contents of 25, 30 and 40 at.% respectively, In the two samples of 25 and 30 at.% Ga pure V_3Ga forms via the solid-solid phase reaction. In the 40 at.% Ga sample V_6Ga_5 phase was formed probably by the excessive release of Ga from the Ga-rich liquid phase and then V_3Ga was formed by the diffusion reaction between the V_6Ga_5 phase and the V-sheath. Best superconducting parameters are obtained for 30 at.% Ga samples heat treated at 700 °C for 50 h. The J_c of the V_3Ga layer is plotted against field B in Fig. 6.49. The best value of $J_c = 4 \times 10^4$ A/cm^2 (4×10^2 A/mm^2) (17 T, 4.2 K) is obtained for the 700 °C heat treated sample. Peak effect in J_c–B behaviour is observed for higher temperature of heat treatment. Perhaps the fluctuation of Ga concentration in these samples bring down J_c in high field region. The grain growth due to higher temperature heat treatment, on the other hand, brings down J_c in low field region. Much higher J_c and B_{c2} of V_3Ga can be expected with suitable elemental additions in PIT technique similar to achieved in the bronze technique.

Our discussion on conventional practical superconductors shows that NbTi and Nb_3Sn will remain the work horse for all time to come for field generation of 8–9 and 15–16 T respectively. Nb_3Al seems to be the material close to commercial production sooner than we expect and will be used for generating field in the range of 19–20 T. Commercial production of V_3Ga seems imminent in near future as the work on future advanced fusion reactors and accelerators progresses. There are other potential superconductors listed in (Table 6.1), namely A-15, Nb_3Ga, Nb_3Ge,

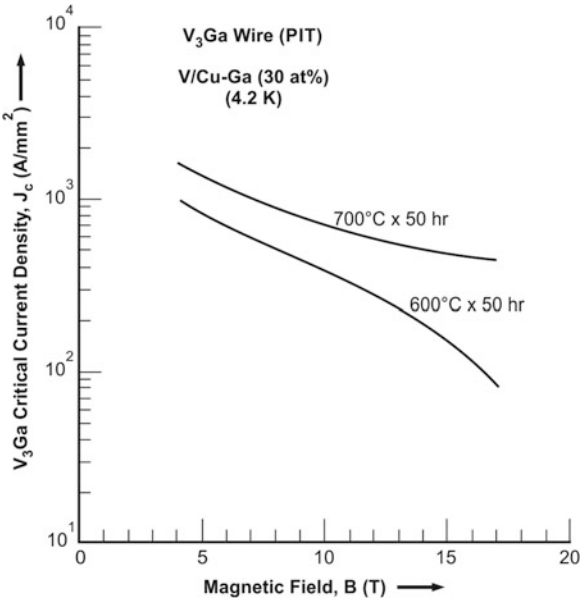

Fig. 6.49 The V_3Ga layer J_c versus B for a monofilamentary PIT wire. Best J_c obtained for heat treatment at 700 °C for 50 h and for a matrix Cu–Ga (30 at.%) [58] (© IOP Publishing. Reproduced by permission of IOP Publishing)

V_3Si, C-15 (Laves phase) V_2 (Hf, Zr), NbN and Cheveral phase $PbMo_6S_8$ which have some advantage or the other over rest of the materials. How do we know which of these might emerge commercially viable in time to come to meet the exigencies of the future programmes.

6.7 2G REBCO Wires/Tapes—The Superconductor of the Future?

High hopes were generated, first time, to use YBCO for high field superconducting magnets and operate them at 77 K but the results were disappointing. The critical current in bulk YBCO superconductor drops down sharply with the application of magnetic field for a variety of reasons. One important reason is that these materials happen to be grainulus with grain boundaries which are weakly superconducting or even insulating. High critical current densities have however been reported in epitaxially grown YBCO films [59] and in YBCO single crystals [60]. This resulted in high expectation of developing this material with high critical current densities needed for high field applications. The critical current within the grain has been found to be quite high $\sim 10^6$ A cm^{-2} at 77 K. After a few years of intensive research, the focus of R&D activity shifted from research institutes to industry for

their commercial production. American Superconductors, Furukawa, SuperPower and Sumitomo are some leading companies marketing HTS wires, tapes and current leads.

The straight forward method to fabricate flexible wires and tapes with powder materials is the usual powder-in-tube technique or the so called PIT technique. Thermal stability criterion requires superconductor to be co-processed with high conductivity material like copper but cuprates HTS have been found to be reacting with copper on heating. The author through a systematic study [61] had found in 1988, silver to be a safe material for processing YBCO wires and tapes. Silver addition as much as 60 at.% was found neither affecting the crystal structure of YBCO nor the T_c. Ag tubes have therefore been used to fabricate YBCO wires and tapes. Since silver is too soft a material, Ag-alloys have been especially developed to process wires to have high mechanical strength. Weak superconductivity in grain boundaries proved to be the stumbling block in achieving reasonably high transport J_c in cuprates.

The strategy adopted to make wires with high J_c has therefore been to deposit highly oriented thin film of YBCO on biaxially textured substrates and suitably laminate with high conducting hardened metal for stability and strength. The scheme of various layers deposited is shown in Fig. 6.50. Sophisticated techniques such as Ion Beam Assisted Deposition (IBAD), Rolling Assisted Biaxially Textured Substrate (RABiTS) and Inclined Substrate Deposition (ISD) have been employed by various R&D laboratories. American Superconductors (AMSC) markets this product under the brand name 344 SC copper stabilized YBCO 2G HTS wire. The two techniques used for the production of the 2G superconductor, IBAD and RABiTS were developed under DAE (USA) programme at Los Alamos National Laboratory (LANL) and the Oak Ridge National Laboratory (ORNL).

The LANL perfected IBAD process. It involves pulse laser deposition of the preferentially oriented buffer layer on the top of commercial hastelloy tape. Four ion beams are used to grow YSZ crystals with one orientation on top of the ceramic oxide buffered hastelloy. Excellent lattice match between YBCO and YSZ leads to highly oriented YBCO film. The ORNL follows RABiT which involves the fabrication of long lengths of bi-axially textured Ni tapes. Suitable oxide buffer layers are then grown to transfer the orientation to the YBCO layer. In both the processes

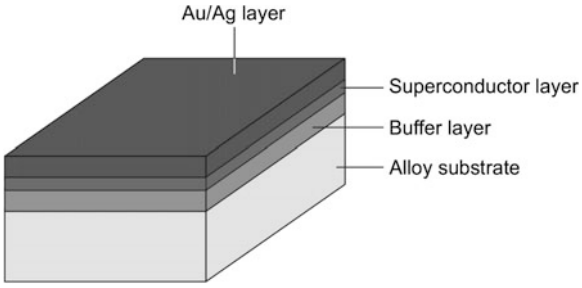

Fig. 6.50 General scheme of deposition used for producing second generation 2G REBCO wires

YBCO is deposited using PLD. 2G tapes have J_c better than traditional Nb–Ti and Nb_3Sn when used at 64 K. The temperature (64 K) is conveniently provided by pumped liquid nitrogen. It is far superior than the old BSCCO-2223 tapes. Even along the c-direction, J_c in 2G tapes at 64 K and 8 T field is much higher than the J_c value for the first generation BSCCO-2223 at 77 K and zero field.

Figure 6.51 shows the architecture of the 2G HTS tape manufactured by SuperPower. Preferentially oriented buffer layers are grown on the hastelloy C 276 substrate by IBAD/magnetron sputtering over which (RE)BCO film of 1 μm thickness is deposited by Metal Organic Chemical Vapour Deposition (MOCVD) technique. A 2 μm silver layer is deposited next by sputtering. The composite tape is finally laminated on both sides with 20 μm thick layers of hardened high conducting copper which provides strength and stability. The hastelloy C 276 substrate provides high mechanical strength to the tape. The stress limit rises to 700 MPa and the yield stress to 970 MPa (77 K) @ 0.92 % strain. High I_c value of 310 A/cm width (77 K) for a 1.1 μm thick HTS film have been obtained by doping with Zr and by introducing nano defects. These defects create efficient pining sites and increase J_c. A world record of magnetic field of 27.4 T was established in 2009 at NHMFL (Florida State Uni.) using this 2G HTS central coil in a background field of 19.9 T. Later in 2012 NHMFL has generated a field of 32 T (@4.2 K) using 2G REBCO tape in a background field of 20 T provided by the resistive magnet.

The lift factor defined as I_c(B, T)/I_c(Sf, 77 K), the ratio of the critical current I_c at a field and temperature to the value at self field and 77 K of the SuperPower 2G wires are plotted in Fig. 6.52 in two orientations. The current, I_c in *B*//*ab* plane orientation shows very little drop with magnetic field compared to the *B*//*c*-axis orientation up to 9 T. The lift factor goes up by a factor of more than 6 as the temperature is lowered from 77 to 4.2 K. In *B*//*ab* plane I_c goes up to still high values. A significant improvement in critical current has also been obtained in these tapes with the addition of Zr.

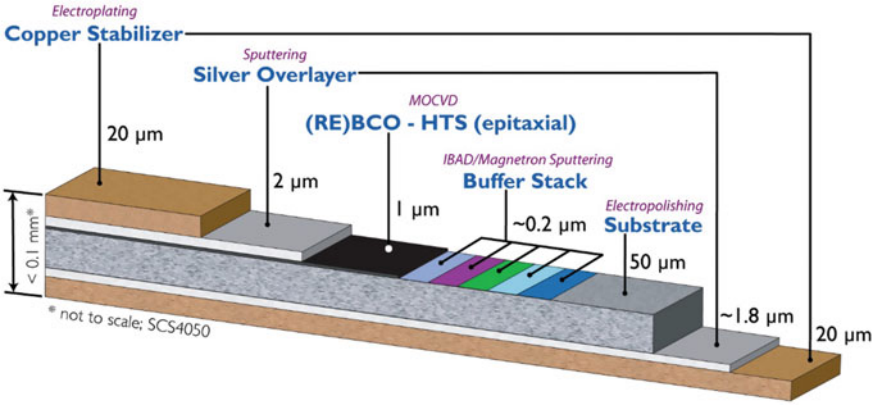

Fig. 6.51 The architecture of the 2G HTS (REBCO) tape conductor, manufactured by SuperPower (Copyright SuperPower Inc. 2014, image provided courtesy of SuperPower)

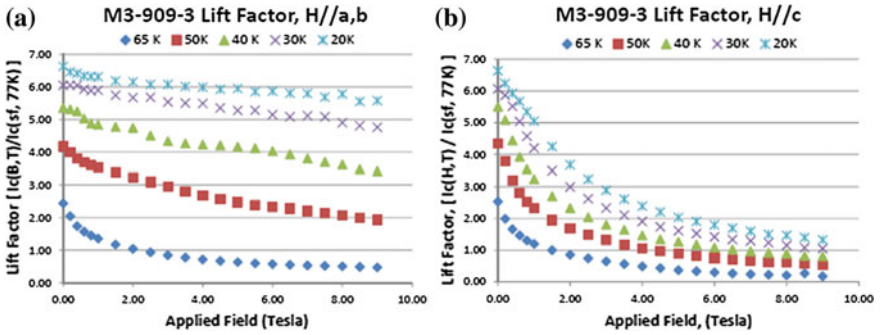

Fig. 6.52 The I_c–B behaviour of SuperPower 2G HTS tapes. The lift factor $I_c(B, T)/I_c(\text{Sf}, 77\ \text{K})$ has been plotted for the SP wire ID M3-909-3 at 65, 50, 40 and 20 K in field parallel to *ab*-plane (**a**) and field parallel to *c*-axis (**b**) (H in the figures is the applied magnetic field) (Copyright SuperPower Inc. 2014, images provided courtesy of SuperPower)

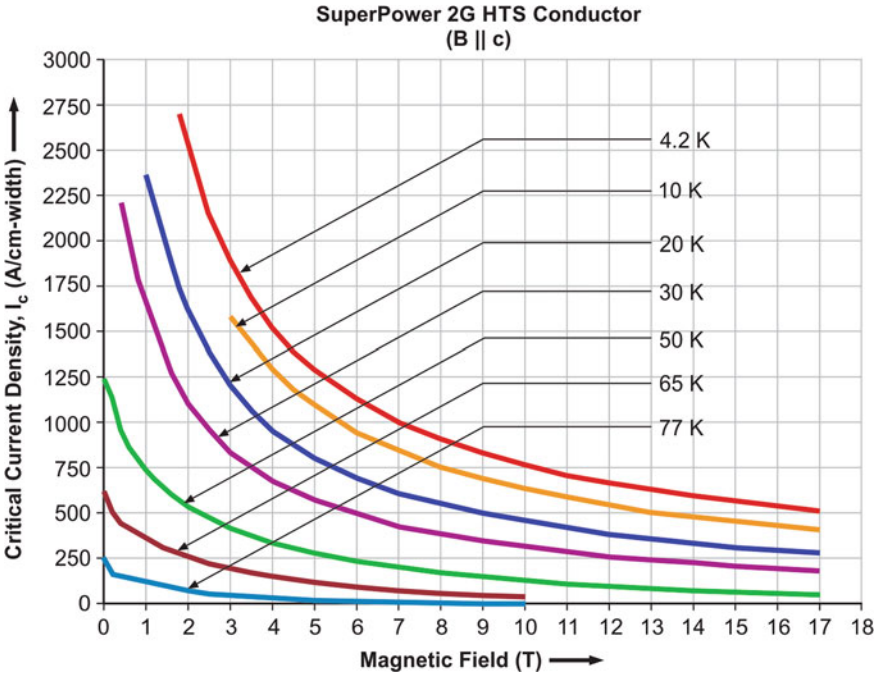

Fig. 6.53 The I_c–B behaviour of SuperPower 2G HTS tapes in B//c orientation. Notice J_e = 560 A/mm^2 (15 T, 4.2 K). In B//a–b orientation Je will go up by a factor of 5–6 (Copyright SuperPower Inc. 2014, images provided courtesy of SuperPower)

Figure 6.53 is the I_c versus B plots (*B*//*c* axis) of SuperPower 2G wires at different temperatures between 77 and 4.2 K. This wire is an AP (Advanced Pinning) type. $BaZrO_3$ nano columns were introduced into the REBCO layer and engineered along

the *c*-axis to enhance the in-field performance. At low fields the enhancement of I_c at reduced temperature is very significant. At 4.2 K the wire carries a current of 500 A/cm width at a field of 17 T which establishes the efficacy of the material as a future high field conductor. The engineering current density J_e of these wires measured at NHMFL up to 30 T field is $\sim$2,000 A/mm^2 at 4.2 K in B//a–b orientation. This value is far beyond the values for best Nb_3Sn conductors.

The AMSC make 2G wire is 0.2 mm thick, 4.5 mm wide and laminated on both sides with hardened copper. The maximum tensile stress (room temp.) is 200 MPa, the maximum tensile strain is 0.3 % and carries an engineering current (J_e) of 90 A ($\sim 10.2 \times 10^3$ A cm^{-2}) at 77 K. The critical current tends to decrease when long lengths of wire are produced.

A comparison of J_c of most of the practical conductors conventional as well as HTS wires from various sources and prepared with different techniques is shown in Figs. 6.54 and 6.55. A uniform J_c of $\sim$300 A/mm^2 over long length of conductor from AMSC prepared by the MOD/RABiTS technique appears to be very encouraging. The superiority of J_c (64 K) of YBCO wires prepared by IBAD or RABiTS in comparison with conventional superconductors, Nb–Ti and Nb_3Sn (4.2 K) in magnetic field can be seen [62] in Fig. 6.54. YBCO indeed stands out to be the future material of choice for high magnetic field when operated at 64 K. Refrigeration to such temperature can be comfortably provided by a conventional cryo-cooler.

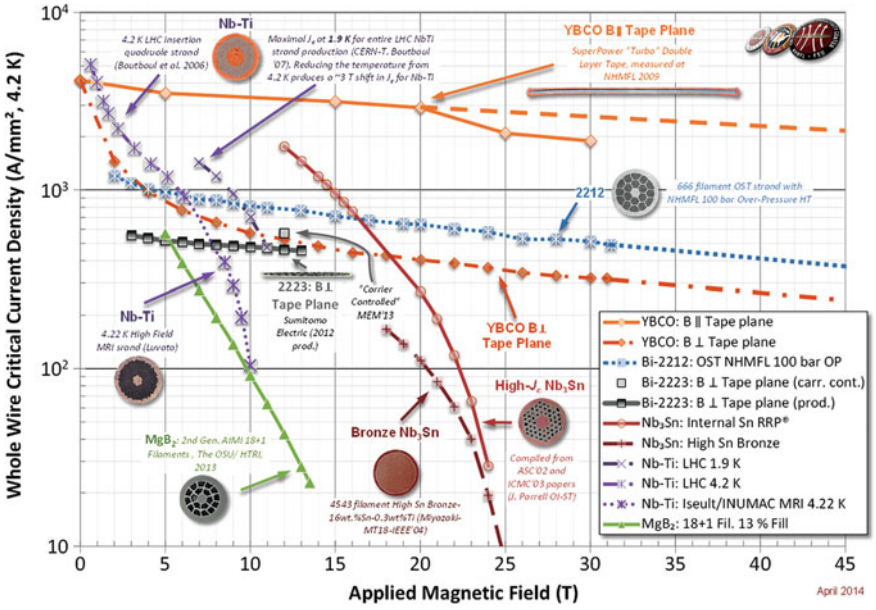

Fig. 6.54 Superiority of J_c (64 K) of 2G REBCO wires prepared by IBAD or RABiTS over conventional superconductors, Nb–Ti, and Nb_3Sn at 4.2 K. BSCCO and MgB_2 too are left behind [62–74] (*Courtesy* Peter J. Lee, National High Magnetic Field Laboratory)

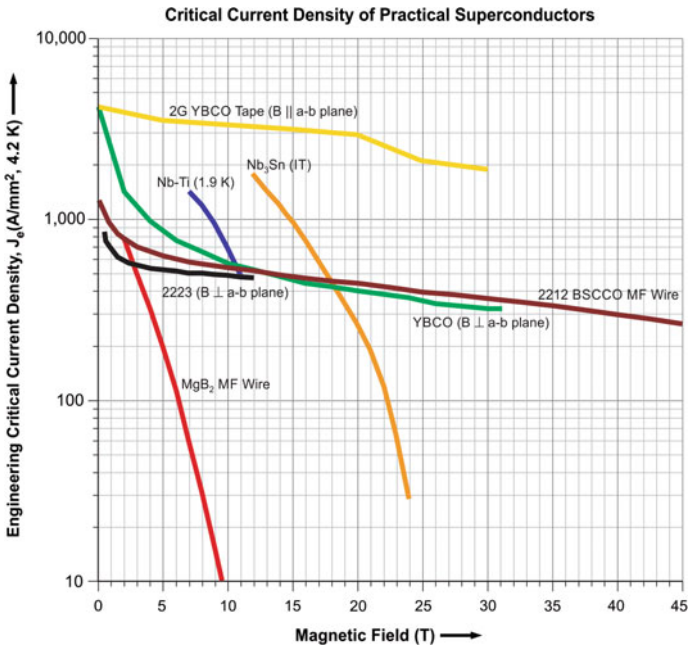

Fig. 6.55 Same as Fig. 6.54 with distinct curves plotted for better clarity. Superiority of J_c (64 K) of 2G REBCO wires over conventional Superconductors like Nb–Ti, and Nb_3Sn is convincing [62–74] (*Courtesy* Peter J. Lee, National High Magnetic Field Laboratory)

Over the years, 2G conductors have shown impressive improvement in J_c and uniformity over longer lengths. Record fields have been produced by the coils of 2G over the successive years peaking at 35.4 T in 2011 at NHMFL. The conductor is produced in the form of tape 4 and 12 mm wide and 0.1 mm thick. The architecture of the tape is custom made to suite specific application. Obviously the J_e of the 2G YBCO is way above the values of the conventional superconductors and might be a substitute for Nb_3Sn in not so distant a future. Figure 6.54 has been provided by Peter Lee of the NHMFL, Florida. The details of the samples and their sources are provided in references [63–74].

References

1. M.N. Wilson, *Superconducting Magnets* (Clarendon Press, Oxford, 1983)
2. M.N. Wilson, Cryogenics **48**, 381 (2008)
3. P.F. Smith, M.N. Wilson, C.R. Walter, J.D. Lewin, *Proceedings of the Summer Study on Superconducting Devices* (Brookhaven National Laboratory, Upton, 1968), p. 967
4. P.R. Critchlow, E. Gregory, B. Zeitlin, Cryogenics **11**, 3 (1971)
5. P.R. Critchlow, Zeitlin, J. App. Phys. **41**, 4860 (1970)

6. J.K. Hulm, R.D. Blaugher, Phys. Rev. **123**, 1569 (1961)
7. B.T. Matthias, Superconducting device consisting of a niobium and titanium composition. US Patent No. 3 167 692, filed, 24 April, granted 26 Jan 1965
8. T.G. Berlincourt, R.R. Hake, Bull. Am. Phys. Soc. **7**, 408 (1962)
9. T.G. Berlincourt, R.R. Hake, Superconductivity at high magnetic fields and current densities in Ti-Nb alloy. Post deadline paper at the Washington Meeting, Am. Phys. Soc. (23–26 April 1962)
10. H.T. Coffey, J.K. Hulm, W.T. Reynolds et al., J. App. Phys. **36**, 128 (1965)
11. J.E. Kunzler, B.T. Matthias, Superconducting magnet consisting of a niobium-zirconium composition. US Patent No. 3 281 736, filed 24 April 1961, granted 25 Oct 1966
12. T.G. Berlincourt, R.R. Hake, D.H. Leslie, Phys. Rev. Lett. **6**, 671 (1961)
13. T.G. Berlincourt, Cryogenics **27**, 283 (1987)
14. http://boulder.research.yale.edu/Boulder-2000/lectures/larbalestier/larbalestier3.pdf. PPT
15. A.V. Narlikar, D. Dew-Hughes, J. Mat. Sci. Eng. **1**, 317 (1966)
16. H. Krauth, Fabrication and Applications of NbTi and Nb_3Sn Superconductors. Vacuumschmelze GmbH & Co. KG "Niobium, Science & Technology": Proc. Int. Symp. Nb 2001, Orlando, Florida, USA, 2–5 Dec 2001. http://cbmm.com.br/portug/sources/techlib/science_techno/table_content/sub_3/images/pdfs/014.pdf
17. E. Gregory, Cryogenics **27**, 290 (1987)
18. G. Hardy, J.K. Hulm, Phys. Rev. **89**, 884 (1953)
19. B.T. Matthias, T.H. Geballe, S. Geller, E. Corenzwit, Phys. Rev. **95**, 1435 (1954)
20. J. Charlesworth, I. MacPhail, P. Madsen, J. Mater. Sci. **5**, 580 (1970)
21. J.E. Kunzler, E. Buehler, F.S.L. Hsu, J.H. Wernick, Phys. Rev. **6**, 89 (1961)
22. R.G. Sharma, J. Sci. Ind. Res. **42**, 64 (1983)
23. R.G. Sharma, Cryogenics **27**, 361 (1987)
24. K. Tachikawa, Cryogenics **48**, 337 (2008)
25. K. Tachikawa, *European Superconductivity News Forum IESNF*. 16 April 2011, pp. 1–30
26. A.R. Kaufman, J.J. Pickett, Bull. Am. Phys. Soc. **15**, 883 (1970)
27. K. Tachikawa, Proc. Int. Cryog. Eng. Conf. (ICEC-3), (Lliffle Science and Technical Publications, Surrey, 1970), p. 339
28. E. Nembach, K. Tachikawa, J. Less Common Metals **19**, 359 (1969)
29. M. Hong, I.W. Wu, J.W. Morris Jr et al., Adv. Cryog. Eng. **28**, 435 (1982)
30. T. Miyazaki, H. Kato, T. Hase et al., IEEE Trans. App. Supercond. **14**, 975 (2004)
31. H. Sakine, Y. Iijima, K. Tachikawa, J. App. Phys. **53**, 5354 (1982)
32. K. Kamata, H. Moriai, N. Tada et al., IEEE Trans. Magn. **21**, 277 (1985)
33. T. Kiyoshi, S. Matsumoto, A. Sato, IEEE Trans. App. Supercond. **15,** 1330 (2005)
34. K. Okuno, H. Nakajima, N. Koizumi, IEEE Trans. App. Supercond. **16**, 880 (2006)
35. K. Tachikawa, K. Miyashita, K. Sugiyama et al., *2T-Class 50 Hz AC Magnet of 50 mm Bore Made by Bronze-Processed Submicronic Filament New Nb_3Sn Cables*, eds. by D. Dew-Hughes, R.G. Scurlock, J.H.P. Watson. Proc. ICEC 17 (IOP, Bristol, 1998), pp. 439–442
36. Y. Hashimoto, K. Yoshijaki, M. Tanetia, *Proceedings of the Fifth International Cryogenic Engineering Conference* (IPC Science and Technology Press, Guildford, 1974), p. 332
37. B.A. Zeitlin, G.M. Ozeryansky, K. Hemachalam, IEEE Trans. Magn. **MAG-21**, 293 (1985)
38. K. Egawa, Y. Kubo, T. Nagai, T. Sone et al., Adv. Cryog. Eng. (Mater) **50B**, 403 (2004)
39. Y. Kubo, K. Egawa, T. Nagai, T. Sone et al., IEEE Trans. App. Supercond. **16**, 1232 (2006)
40. W.K. McDonald, C.W. Curtis, R.M. Scalan et al., IEEE Trans. Magn. **MAG-19**, 1124 (1983)
41. K. Tachikawa, T. Ando, H. Sasaki et al., IEEE Trans. App. Supercond. **21**, 2533 (2011)
42. C.C. Tsuei, Science **180**, 57 (1973). IEEE Trans. Magn. **MAG-11**, 272 (1975)
43. R.G. Sharma, N.E. Alekseevskii, J. Phys **D8**, 1783 (1975)
44. R.G. Sharma, Y.S. Reddy, M.M. Krishna, Indigenous development of A-15 superconductors through in situ technique. Workshop on Superconducting Magnets and Cryogenics, ICFA, Brookhaven National Laboratory, Upton, New York, USA (12–16 May 1986), pp. 127–131

45. Handbook of Superconducting Materials, eds. by A. D.A. Cardwell, D.S. Ginley, ISBN 07503 04324 (Vol. 1), 2003, Fig. 3.3.4.1(a), p. 674. Contribution B 3.3.4 Processing of Low T_c Conductors: The Composite Nb_3Al, Author Takao Takeuchi
46. Y. Yamada, N. Ayai, A. Mikumo et al., Cryogenics **39**, 115 (1999)
47. N. Koizumi, Y. Takahashi, Y. Ninoya et al., Cryogenics **42**, 675 (2002)
48. T. Takeuchi, Topical review 'Nb_3Al conductors for high-field applications'. Supercond. Sci. Technol. **13**, R101 (2000)
49. T. Takeuchi, A. Kikuchi, N. Banno et al., Cryogenics **48**, 371 (2008)
50. K. Tsuchiya, A. Kikuchi, T. Takeuchi et al., IEEE Trans. App. Supercond. **21**, 2521 (2011)
51. B.T. Matthias, E.A. Wood, E. Cobbnzwit, J. Bala, J. Phys. Chem. Solids **1**, 188 (1956)
52. The Ga-V (Gallium-Vanadium) System, Bull. Alloy Phase Diagrams **2**, 201 (1981)
53. K. Tachikawa, Y. Tanaka, Japan J. App. Phys. **5**, 834 (1966)
54. K. Tachikawa, Y. Tanaka, Y. Yoshida, et al., IEEE Trans. Magn. **Mag-15**, 391 (1979)
55. R.G. Sharma, Y. Tanaka, K. Tachikawa, Cryogenics **21**, 165 (1981)
56. R.G. Sharma, Y. Tanaka, K. Tachikawa, Cryogenics **25**, 381 (1985)
57. Y. Furuto, T. Suzuki, K. Tachikawa, Y. Iwasa, App. Phys. Lett. **24**, 34 (1974)
58. Y. Hishinuma, A. Kikuchi, Y. Iijima et al., Supercond. Sci. Technol. **20**, 569 (2007)
59. P. Chaudhuri, R.H. Koch, R.B. Laibowitz et al., Phys. Rev. Lett. **58**, 2684 (1987)
60. T.R. Dinger, T.K. Worthington, W.J. Gallagher, R.L. Sandstorm, Phys. Rev. Lett. **58**, 2687 (1987)
61. R.G. Sharma, Y.S. Reddy, S.R. Jha et al., Pramana J. Phys. **30**, L75 (1988)
62. R. Gupta, *PPT Superconducting Magnets for Particle Accelerators* (RISP, ISB, Korea, Aug 22 2012) (slide no. 9). http://www.bnl.gov/magnets/staff/gupta/Talks/RISP/HTS-MAG-RISP.pdf
63. YBCO: Tape, ∥Tape-plane, SuperPower "Turbo" Double layer (tested NHMFL 2009). Source: Aixia Xu and Jan Jaroszynski, June 2009. 20 T depression due to He bubble, dashed line estimates true performance
64. YBCO: Tape, ⊥ Tape-plane, SuperPower "Turbo" Double layer (tested NHMFL 2009). Source: Aixia Xu and Jan Jaroszynski, June 2009
65. Bi-2223: B ⊥ Tape-plane "DI" BSCCO "Carrier Controlled" Sumitomo Electric Industries (MEM'13 presented by Kazuhiko Hayashi)
66. Bi-2223 (2012 production): B ⊥ Tape-plane "DI" BSCCO (measured at NHMFL by Jianyi Jiang and Dmytro Abraimov Oct. 2013)
67. D.C. Larbalestier, J. Jiang, U.P. Trociewitz, F. Kametani, C. Scheuerlein, M. Dalban-Canassy, M. Matras, P. Chen, N.C. Craig, P.J. Lee, E.E. Hellstrom, Isotropic round-wire multifilament cuprate superconductor for generation of magnetic fields above 30 T. Nat. Mater. (2014) (Advance online publication). doi:10.1038/nmat3887 (Bi-2212: OST 2212 wire with 100 bar over-pressure HT at NHMFL. 25 % SC)
68. T. Boutboul, S. Le Naour, D. Leroy, L. Oberli, V. Previtali, Critical current density in superconducting Nb-Ti strands in the 100 mT to 11 T applied field range. IEEE Trans. Appl. Supercond. **16**(2), 1184–1187 (2006). doi:10.1109/TASC.2006.870777 (Nb-47Ti: 0-6 T—1.8 and 4.2 K)
69. Nb-47Ti: 5-8 T 1.8 K Maximal: Nb-Ti: Max @4.2 K for whole LHC NbTi strand production (CERN-T. Boutboul '07)
70. H. Kanithi, D. Blasiak, J. Lajewski, C. Berriaud, P. Vedrine, G. Gilgrass, Production Results of 11.75 Tesla Iseult/INUMAC MRI Conductor at Luvata. IEEE Trans. Appl. Supercond. **24**, 1–4 (2014). doi:10.1109/TASC.2013.2281417 (Nb-47Ti: 4.22 K for 11.75 T Iseult/INUMAC MRI)
71. J.A. Parrell, Y. Zhang, M.B. Field, P. Cisek, S. Hong, High field Nb_3Sn conductor development at Oxford Superconducting Technology. IEEE Trans. Appl. Supercond. **13**(2), 3470–3473 (2003). doi:10.1109/TASC.2003.812360 (Nb_3Sn (RRP®): Non-Cu J_c Internal Sn OI-ST RRP® 1.3 mm)
72. J.A. Parrell, M.B. Field, Y. Zhang, S. Hong, Nb_3Sn conductor development for fusion and particle accelerator applications. AIP Conf. Proc. **711**, 369 (2004). doi:10.1063/1.1774590

73. T. Miyazaki, H. Kato, T. Hase, M. Hamada, Y. Murakami, K. Itoh, T. Kiyoshi, H. Wada, Development of high Sn content bronze processed Nb_3Sn superconducting wire for high field magnets. IEEE Trans. Appl. Supercond. **14**(2), 975–978 (2004). doi:10.1109/TASC.2004.830344 (Nb_3Sn (High Sn Bronze): T. Miyazaki et al. MT18—fig3)
74. G.Z. Li, M.D. Sumption, J.B. Zwayer, M.A. Susner, M.A. Rindfleisch, C.J. Thong, M.J. Tomsic, E.W. Collings, Effects of carbon concentration and filament number on advanced internal Mg infiltration-processed MgB_2 strands. Supercond. Sci. Technol. **26**(9), 095007 (2013). doi:10.1088/0953-2048/26/9/095007 (MgB_2: 18 Filament—The OSU/HTRI C 2 mol% AIMI ("Advanced Internal Mg Infiltration") 33.8 % Filament to strand ratio, 39.1 % MgB_2 in filament)

Chapter 7
Building Laboratory Superconducting Magnets

Abstract This chapter gives tips to the researchers how to design, build and operate standard superconducting solenoid magnets in the laboratory and use them for physical property measurements. Broad parameters discussed are the design dimensions, homogeneity, current lead optimization, current supply, quench protection and persistent switches. Multifilamentary Cu/Nb–Ti conductor is the universal choice for building (multi-section) magnets producing field up to 8 T (4.2 K). Additional field is produced by using inserts of A-15 Nb_3Sn conductor, usually of the 'wind and react' type. Specific examples of the design, fabrication and operation of a 7 T Nb–Ti magnet, a 11 T Nb–Ti/Nb_3Sn combination magnet and a 6 T cryofree magnet, built in author's laboratory, have been discussed. Delicate steps followed during winding, tension adjustment, controlled high temperature reaction, preparation of current contacts and the final impregnation of the Nb_3Sn magnet have been elaborated. The chapter presents all salient features of a superconducting magnet and the latest developments made in achieving record fields in conventional and HTS magnets.

7.1 The Solenoid Magnets: Introduction

The fact that superconductors carry current without dissipation, has made them ideal for building magnets. A magnet coil is, however, a common component of any electro-technical machine. Attempts have been continuously made to develop superconductors that can produce higher and higher magnetic field. The motivation to produce high magnetic field has come from such diverse applications as listed below.

R.G. Sharma, *Superconductivity*, Springer Series in Materials Science 214,
DOI 10.1007/978-3-319-13713-1_7

- Magnetic field is a versatile thermodynamic parameter like pressure and temperature which can manipulate phase diagram of magnetic materials wherein electrons spins can order ferro or antiferromagnetically and alter the behaviour of a material.
- Magnetic field is an essential tool for scientific research in several disciplines like condensed matter physics, material science, atomic and molecular physics, life sciences and chemistry. Whenever the field was raised by a significant step, a new phenomenon was discovered or a high precision device built.
- High magnetic field enables the observation of Quantized Hall Effect (QHE) and Fractional Quantum Hall Effect (FQHE) in quantized electron energy levels. QHE is already in use internationally for resistance standard.
- Unprecedented field stability and very high fields available with superconducting magnets has made high resolution Nuclear Magnetic Resonance (NMR) spectroscopy a powerful tool to study structure of large and complex molecules. 1 GHz NMR spectrometers (23.5 T field) are now commercially available (Fig. 10.6).
- Whole-body Magnetic Resonance Imaging (MRI) based on NMR principle is extensively used in non-destructive and non-invasive imaging of living systems. Magnetic Resonance Imaging (MRI) has become an important diagnostic tool with radiologists and has benefited the society at large.
- Superconducting magnets are playing pivotal role in high energy particle accelerators and fusion reactors. The success of Large Hedron Collider (LHC) can be attributed to a large extent to superconducting magnets. The success of on-going projects like International Thermonuclear Energy Reactor (ITER) and International Linear Collider (ILC) too is equally dependent on the perfection to which the magnets will be built.

7.2 A Brief History of Superconducting Magnets

Kammerlingh Onnes realized the importance of superconducting materials for producing high magnetic field soon after the discovery of superconductivity but his dream of producing high field using Pb-wire remained unfullfilled because of the inherent limit of low critical field, B_c of this material. The first superconducting magnet was built at Physics Laboratory in Leiden Uni. by winding Pb wire (Fig. 7.1a) but the results were too disappointing. Magnets became a possibility in mid 1950s after the discovery of type II superconductors with high upper critical field, B_{c2} values. Yntima [1] built a successful superconducting magnet for producing low temperature by adiabatic demagnetization of a paramagnetic salt. He wound a fine enameled strained Nb-wire (dia. 0.05 mm) over a soft iron core and produced a field of 0.7 T in a pole gap of 2.78 mm. The number of turns of Nb-wire were 4,296. The Nb layer was covered by another layer, that of the bare Cu wire of 0.46 mm diameter, having 183 turns. He wound magnets using cold-worked as well

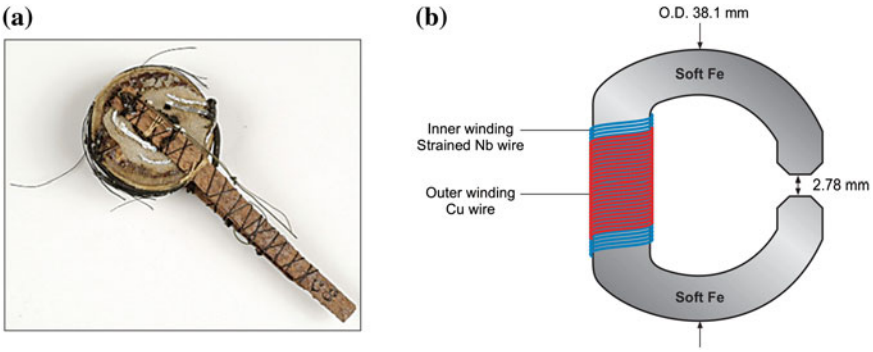

Fig. 7.1 **a** World's first superconducting magnet wound with Pb-wire at Leiden Physics Laboratory in 1912. *Image Courtesy* of Museum Boerhaave, Leiden, The Netherlands (2011) http://www.aps.org/meetings/march/vpr/2011/imagegallery/supercoil.cfm. **b** World's first successful superconducting magnet wound by Yntima using strained Nb-wire at Uni. of Illinois in 1954 producing a field of 0.71 T (adapted and modified from [1])

as annealed Nb-wires and found that cold-worked wires carry larger current compared to annealed wires and produce higher field. This was perhaps the first indication that defects introduced in superconductors enhance the critical current via the mechanism of flux pinning.

An important event was the development of a 9.2 T magnet by Coffey et al. [2] using three sections of Nb–Ti wire in a background field of 5 T provided by two-section Nb–Zr coil. High field superconducting magnets, however, became possible only after the discovery of A-15 superconductors. The year 1961 proved to be a turning point in the history of superconducting magnet development when Kunzler et al. [3] at Bell Lab showed conclusively that field in excess of 10 T were possible using Nb_3Sn conductor. Nb_3Sn magnets in pancake structure were built using flexible tapes of Nb_3Sn deposited on hastelloy tapes either by Sn-diffusion technique or the chemical vapour deposition (CVD) technique in 1960s. These magnets were, however, not stable against flux jumps. The emergence of Cu-stabilized multifilamentary (Nb–Ti and Nb_3Sn) wires and cables in 1970s laid a strong foundation for real high field superconducting magnet technology. Continuous improvement in the J_c values of Nb_3Sn conductor through improved mechanical deformation techniques and metallurgical processing has led to an all time high magnetic fields. Multi-section (Nb–Ti/Nb_3Sn) magnets producing 20 T field are commercially available. The use of HTS (Bi-2223 or 2G YBCO) inserts has pushed this value to still higher fields in excess of 22 T. A 32 T superconducting magnet has been designed, fabricated and tested at NHFML, Florida State University [4, 5]. The magnet uses two sections of Nb–Ti, and three sections each of Nb_3Sn and YBCO conductors. Other advances in producing very intense field have recently been made at BNL and NHFML, BNL produced a field of 16 T by a REBCO stand alone magnet. NHFML generated a record field of 35.4 T [6] using a REBCO insert in a background field of 31 T provided by a resistive 20 MW magnet. The insert contributed a field of 4.4 T.

During last decade and a half 'conduction-cooled' or 'cryo-free' superconducting magnet systems have flooded the research laboratories which do away with the use of liquid helium for magnet cooling. Instead, the magnet system is cooled by closed cycle refrigerators (CCR). This has been possible for two reasons. One, that CCR of 1.5 W cooling @ 4 K are commercially available and second, that HTS current leads capable of carrying thousands of Ampere current have been commercialized. Superconducting leads do not generate Joule-heating and have poor thermal conductivity. Cooling need of the magnet system is comfortably met with the CCRs. Cryo-cooled magnets capable of generating high field up to 20 T have found their way in research laboratories. These magnets are hooked-up with a large variety of physical and magnetic measurement systems.

7.3 Unique Features of a Superconducting Magnet

The winding of a superconducting magnet is quite an intricate exercise because of the peculiar behaviour of a superconductor carrying large current in high magnetic field and the large mechanical forces encountered by the conductor. We discuss below some of these peculiarities.

- In a superconducting magnet the magnet current is a function of temperature and the magnetic field. The maximum current that a coil can carry depends upon the maximum field experienced by the superconductor. The operating temperature for most magnets is 4.2 K provided by liquid helium bath. For enhanced fields the magnet is operated at a reduced temperature of 1.8 K.
- Superconducting wires are produced in the form of multifilaments embedded in high conductivity copper by a multi-step process. This is needed to overcome stability problems, discussed in detail in Sect. 6.2.
- The magnet wire is subjected to mechanical load primarily due to winding tension and the bending strain.
- Differential thermal contraction of the constituent materials of the magnet gives rise to stress when cooled to operating temperature.
- There is stress internal to the conductor because of the sharp change of temperature from reaction temperature to operating temperature.
- Since these magnets generate strong fields the conductor experiences large radial Lorentz force which gives rise to hoop stress (=BJR) which can be severe in large size magnets.
- The J_c of superconducting wires has a very strong stress-strain characteristic. Strain under load can bring down J_c drastically.
- Any micro-movement of the conductor under large Lorentz force can generate heat sufficiently high to drive the conductor to normal state and quench the magnet. To prevent such movement of the conductor the magnet is always impregnated with a suitable low temperature compatible epoxy or bees wax.

- The magnet is always susceptible to quench for a variety of reasons such as insufficient cooling, exceeding the current beyond J_c, too high current ramp rate or for any unforeseen thermo-mechanical disturbance. During the quench, the stored energy of the magnet (=½ LI^2) released can burn the magnet. This energy therefore has to be dumped outside of the magnet. A fool-proof quench protection system is therefore integrated with the superconducting magnet to save it from burn-out.
- Notwithstanding the extreme care that is needed to build superconducting magnet systems, the magnet industry has seen an unprecedented growth over last five decades. This is because of the distinct advantages these magnets have over the normal copper-iron electromagnets. Since iron core in a normal electromagnet saturates at around 2 T, superconducting magnets are indispensable when intense magnetic field is required. These magnets are very compact, occupy little space, are light in weight and consume very little energy. No elaborate water cooling system is required either. Superconducting magnets are traditionally operated in liquid helium bath but small size magnets are increasingly cooled by cryocoolers.

7.4 Design Considerations of a Solenoid Magnet

An excellent paper on the method of optimization of winding parameters of a superconducting solenoid magnet has been published by Boom and Livingston [7] as early as in 1962. The calculation method is based upon the classical theory of Fabry [8, 9]. Quite a few good books [10–14] too have been published at different times which have been serving the community well for designing and constructing laboratory superconducting magnets for almost all types of applications. Several computer programmes for different applications are available for various aspects of magnet design.

Superconducting magnets widely used for research are almost exclusively solenoids. It will therefore be most appropriate if we describe the design of such a magnet in detail. Let us consider a solenoid as shown in Fig. 7.2 with a working bore $2a_1$, outer winding dia. $2a_2$ and the winding length 2ℓ. The current I produces a central field B_0 and a maximum field, B_M close to the inner winding layer.

The axial field of an infinite length solenoid is given by

$$B_0 = J\,\lambda\,a_1 F(\alpha,\,\beta) \tag{7.1}$$

where B_0 is the axial field in the mid-plane, J the current density of the conductor, λ the space factor (total conductor cross section divided by the total winding cross section), $\alpha = a_2/a_1$, the ratio of the outer winding diameter to inner winding diameter, $\beta = 2\ell/2a_1$, the ratio of the winding length to inner winding diameter and $F(\alpha, \beta)$ is a geometry dependent quantity called field factor, shape factor or Fabry parameter and is given by

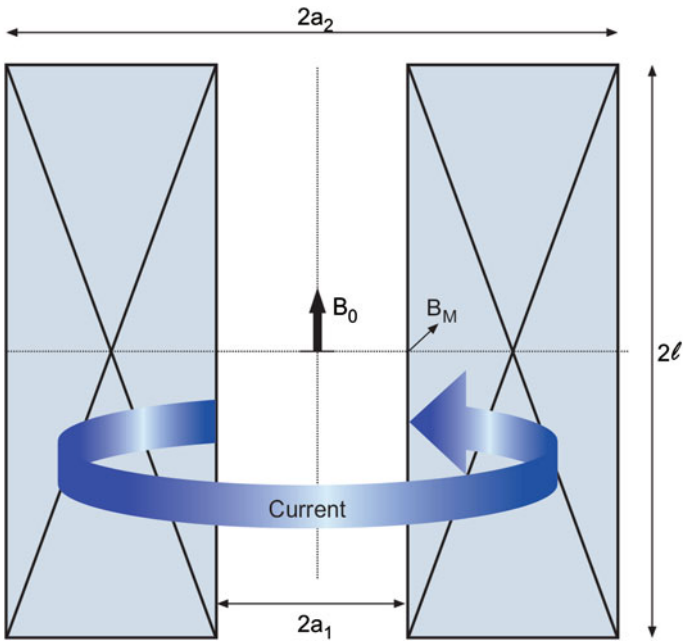

Fig. 7.2 A solenoid magnet of inner dia. $2a_1$, outer dia. $2a_2$ and a winding length 2ℓ. The axial field is B_0 and the maximum field B_M at the innermost winding layer

$$F(\alpha, \beta) = \mu_0 \beta \ln \left[\frac{\alpha + \left(\alpha^2 + \beta^2\right)^{1/2}}{1 + \left(1 + \beta^2\right)^{1/2}} \right] \tag{7.2}$$

To start designing a solenoid magnet, we select the working bore and then the inner winding dia. $2a_1$, after taking the thickness of the former into account. We then select the central axial field, B_0. The current density J is found out from the I_c-B plot of the conductor intended to be used. λ usually varies from 0.7 to 0.9 depending upon the voids in the winding and non-superconducting stuff such as interlayer insulation etc. used. The value of field factor, $F(\alpha, \beta)$ is now determined. Interestingly, for one value of $F(\alpha, \beta)$ several combinations of α and β are possible to yield the same field as shown in Fig. 7.3. It is possible to choose a combination values of α and β which corresponds to the minimum winding volume. Unfortunately, this geometry leads to a short and fat coil which in turn leads to a poor field homogeneity and consume more conductor. For high field homogeneity we must select parameters α and β away from minimum volume condition using larger value of β. The maximum axial field is experienced on the inner most layer of the winding. It is this field which ultimately restricts the operating current of the magnet and not the central field. In Fig. 7.4 we have plotted the maximum field experienced by the conductor at the inner most layer, B_M for a central field of 6 T and for

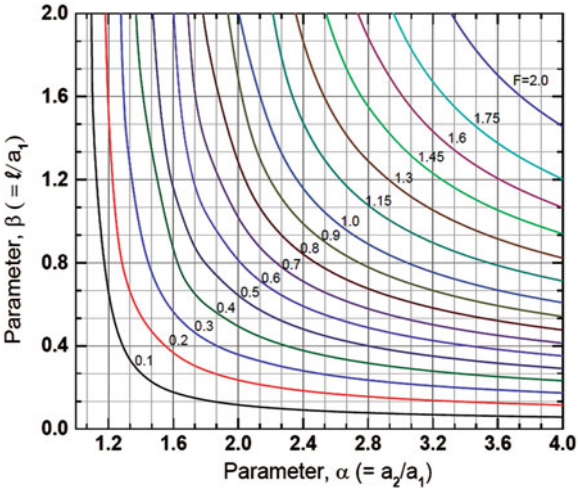

Fig. 7.3 Febry parameter, $F(\alpha, \beta)$ *curves* plotted as a function of α and β. Several combinations of α and β are possible for a given value of $F(\alpha, \beta)$ and thus for a magnet to produce a particular field (*Courtesy* Soumen and Vijay)

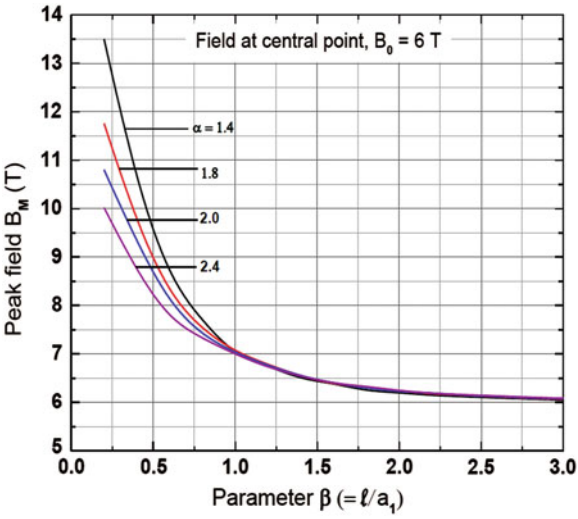

Fig. 7.4 Peak field B_M versus β plots for different values of α = 1.4, 1.8, 2.0 and 2.4 for a 6 T magnet. Field homogeneity improves with increasing β and appears to saturate beyond β = 3 (*Courtesy* Vijay, Phaneendra and Soumen)

different values of α(=1.4, 1.8, 2.0 and 2.4). Boom and Livingston [7] have plotted the homogeneity curves represented by the ratio, $k = B_M/B_0$ (ratio of peak field to the central field) as a function of α and β. It is clear from the figure that for high homogeneity one has to choose α and β values such that the B_M/B_0 ratio is as close to 1 as possible. This means β has to be much larger than that given by the minimum volume criterion. This is clearly seen from Fig. 7.4 that for a 6 T axial field the peak field rises sharply for β values less than 1 for all values of α. The peak field is reduced for β greater than 1 and becomes close to the central field B_0 for β = 3. Such a magnet will consume lesser quantity of conductor and yield high homogeneity. This results from the fact that the maximum field or the peak field is

now much reduced and the magnet can be operated at a higher current producing higher field. The central axial field B_0 increases as we move away from the centre along the radius, becomes maximum (B_M) close to the inner most winding layer and decreases thereafter and even becomes negative close to the outer edge of the winding. This means that a smaller operating magnet current is now chosen corresponding to B_M instead of the central field B_0. Since the outer layers of the winding are exposed to decreasing field, the conductor is capable of carrying much larger current than the inner part of the winding. It is therefore advisable to wind the magnet in multi-sections, outer sections operating at larger current densities than the inner ones. Better still, if we use different dia. wires in different sections and run them at the same current, that is, at different current densities as dictated by the J_c-B plots of the conductor. Such a magnet will consume lesser quantity of conductor and yield high homogeneity. This results from the fact that the maximum field or the peak field is now much reduced and the magnet can be operated at a higher current producing higher field. One should therefore use thicker wire for the inner and thinner wire for the outer sections. We built several 7–8 T Nb–Ti magnets in two sections using 0.75 mm dia. wire for the inner section and a 0.54 mm for the outer section and running them in series using the same current supply.

7.4.1 Specific Example of a 7 T Superconducting (Nb–Ti) Magnet

Let us take an example of designing a 7 T Nb–Ti magnet to be used as an insert to a 100 mm neck dia. liquid helium storage vessel [15]. To keep the outer diameter of the magnet smaller than 100 mm (LHe-vessel neck dia.) we chose a thicker Cu/Nb–Ti wire (0.75 mm dia.) and a high operating current $\sim$210 A. We started with a former of clear bore of 46 mm and the inner winding dia. ($2a_1$) of 50 mm. We used a 45 filament Cu/Nb–Ti wire supplied by Vacuumschmelze. This wire had an I_c = 245 A at 7 T field and we take 85 % of this value, that is 208 A as the operating current. λ, the space factor is taken to be 0.78, a value we find consistently in many of our magnets wound using a fiber-glass cloth as inter-layer material. J is obtained by dividing 208 by area cross-section of the wire (0.4418×10^{-6} m^2) which turns out to be 470×10^6 A m^{-2}. By putting the appropriate values in (7.1) the function F (α, β) comes out to be 0.76255×10^{-6} for a field of 7 T. Using the B_M/B_0 plots for different combinations of α and β in Fig. 3.3 of Wilson [12] we selected a ratio k (B_M/B_0) to be 1.0112 such that the peak field at the inner winding layer is just 7.078 T low enough to allow a safe operating current of 208 A. We now select from the same figure a combination of α = 1.665 and β = 3 compatible with this field ratio. Thus the outer winding diameter of the coil, $2a_2$ becomes = 83.25 mm and the winding width = 16.6 mm. Since β is to be 3 a winding length 150 mm has been chosen. One layer will have 200 turns and there will be 22 layers in all. The total number of turns thus becomes = 4,400. The parameter details of the magnet are reproduced in Table 7.1.

The former was made out of SS and a layer of fiber glass cloth was wrapped on the bare surface of the former before starting winding. Thin G-10 sheets were fixed on the inside of the two SS end flanges. The flanges and the central pipe of the former had perforations to allow LHe to seep and cool the winding. The wire terminals were taken out through the top end flange at an easy slop. A schematic diagram of the former and the winding is shown in Fig. 7.5. Winding was carried out on a modified lathe with 0.75 mm pitch and rotating at a comfortable speed of 18 rpm. Each layer was very tightly wound and had 200 turns. A tension of 1 kg was uniformly maintained throughout the winding. To prevent possibility of wire movement under Lorentz force during operation of the magnet precaution should be taken not to leave gap in the winding. We always wind an even number of layers so that the second terminal of the wire can also be taken out from the top flange. After the winding, the two terminals of the wire were secured in position and the magnet was vacuum-pressure impregnated in bees wax.

The magnet was suspended from a top flange using G-10 supports and radiation shields. Two vapour cooled optimized current leads also terminate at the top flange for connecting with the power supply. Figure 7.6a shows the bottom part and Fig. 7.6b the top part of the magnet assembly. A relief valve is provided at the top flange for He-gas to escape in the event of a pressure build-up in the LHe vessel. Helium gas flow through the current leads is regulated using a control valve which is connected to the recovery line. A He-gas flowmeter, in the gas recovery line measures the He-gas evaporation rate. The magnet assembly pre-cooled with liquid nitrogen is gently and slowly lowered into the LHe-storage vessel and experiments can be performed rather quickly as compared with conventional magnets operated in dedicated LHe-dewars which need time to be ready for operation.

Table 7.1 Parameters of the 7 T solenoid magnet of insert type

Parameter	Value	Parameter	Value
Working bore	46 mm	Conductor used	Cu/Nb–Ti (MF)
Inner winding dia. $2a_1$	50 mm	Cu:Nb–Ti	1.8:1
Outer winding dia. $2a_2$	83.25 mm	Conductor dia.	0.75 mm
Winding width w	16.6 mm	No. of filaments	45
Winding length, 2ℓ	150 mm	Filament dia.	38 μm
Parameter α	1.665	Inductance	0.4 H
Parameter β	3	Field at 208 A	7 T
Function $F(\alpha, \beta)$	0.76255×10^{-6}	Field factor	29.71 A/T
Field homogeneity	0.094 % (10 mm DSV)	Quench field at 210 A	7.1 T
No. of layers	22	Stored energy at 210 A	8.8 kJ
Total no. of turns	4,400	Impregnating material	Bees wax
Conductor length	0.9 km	Inter-layer material	Fiber glass cloth

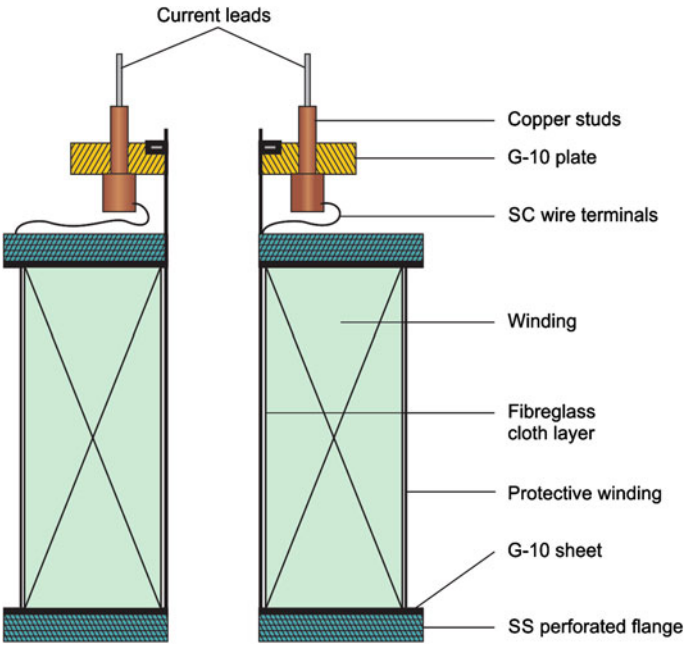

Fig. 7.5 Schematic diagram of the former and the winding of a 7 T magnet of the insert type

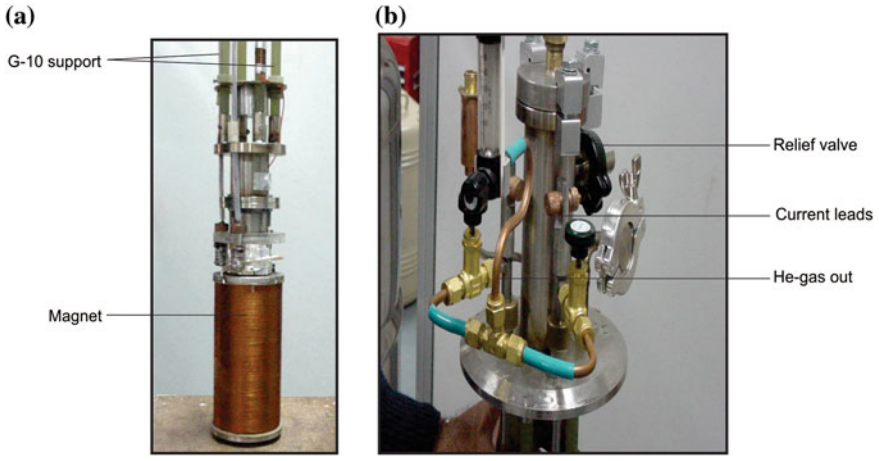

Fig. 7.6 **a** The 7 T magnet and the *bottom* part of it's support system. **b** *Top view* the flange, seen in the picture fits on to the *top* of the LHe-vessel neck, He-gas flows through the current leads and is collected via a gas flow meter [15] (*Courtesy photo* IUAC Delhi)

The axial field variation with the distance from the mid-plane is plotted in Fig. 7.7. The inset shows the axial field homogeneity of 0.098 % in a 10 mm DSV (diameter spherical volume). The radial component of the axial field along the axis remains zero.

Figure 7.8 shows the plots of the magnetic field lines using Poisson Superfish computer programme. Three distinct features can be noted from this figure. First, that the density of magnetic field lines increases as one moves away from the mid plane along the radius of the magnet. It becomes maximum at the inner-most winding layer. It is for this reason, that the axial field peaks at the inner winding layer. Second, that the density of lines of force decreases thereafter and becomes zero close to the outermost layer. The zero-field region is indicated in the figure. Thirdly, the lines of force bend near the ends of the magnet, (this is true for any finite length solenoid as ours) and reverses the field direction beyond the outer most layer. The Lorentz force, generated by the interaction of perpendicular current and magnetic field ($B \times I$), at the outer layer will therefore reverse the direction and will tend to compress the coil from outside. There is already a Lorentz force acting on the inner-most layer compressing the coil. As one moves away along the radius this force decreases and then changes direction. Bending at the ends also introduces a radial component of the field which produces an axial Lorentz force tending to compress the coil axially. A magnet is therefore like a pressure bottle similar to a high pressure gas cylinder trying to explode. This pressure is $=B^2/2\mu_0$ and for a field

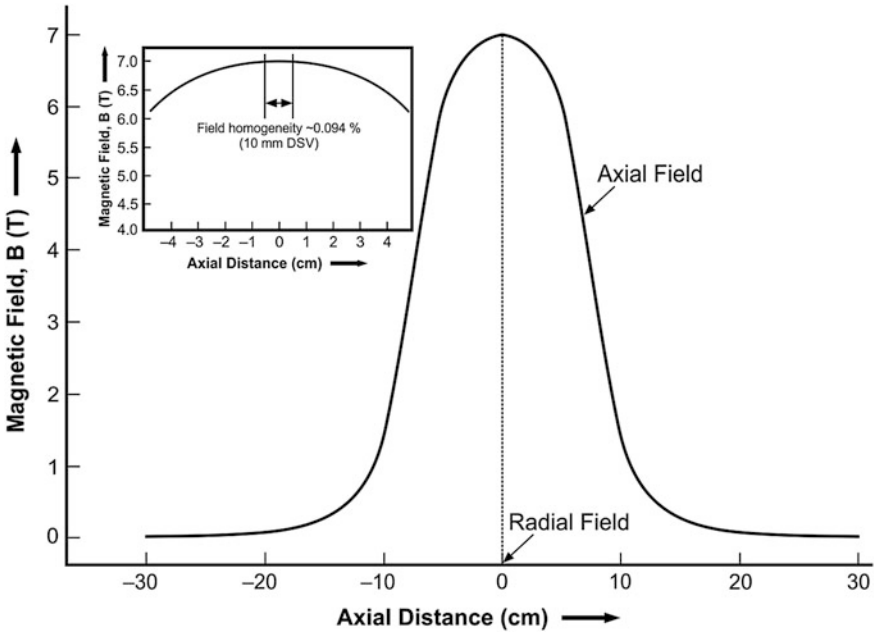

Fig. 7.7 The axial field profile of the magnet at 7 T. The inset shows a field homogeneity of 0.098 % in a 10 mm DSV. The radial field along the axis is nearly zero [15]

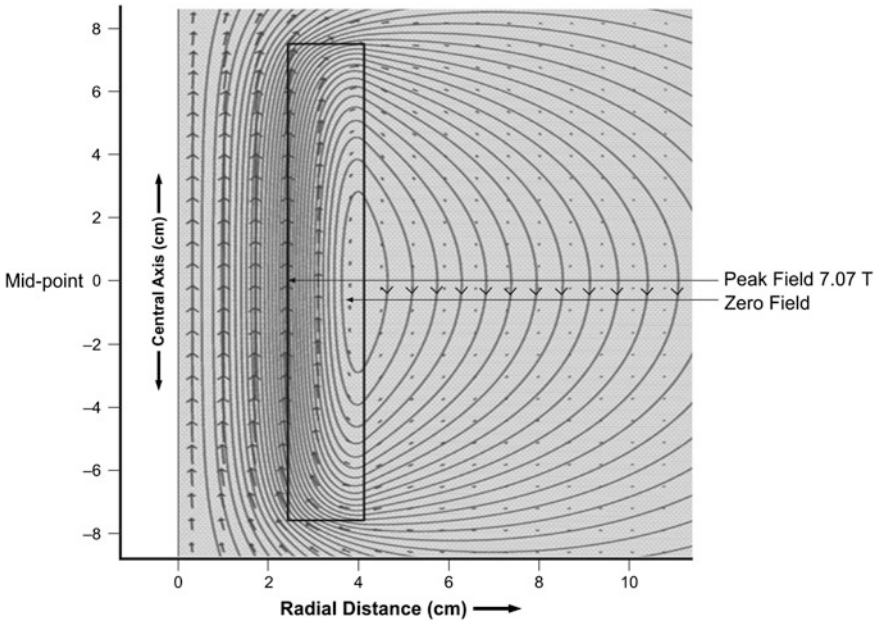

Fig. 7.8 Field profile of the 7 T magnet plotted by using Poisson Superfish computer programme. Note the peak field region and the zero field region [15]

value of 10 T it turns out to be as high as 4×10^7 N/m^2 which is close to the yield strength of copper. Large Lorentz force also gives rise to large hoop stresses tending to explode the magnet. Reinforcement of the magnet-winding is thus extremely important. The fact that peak axial field occurs at the inner most layer, implies that the critical current density, J_c of the conductor chosen should be with respect to this field and not the field at the centre.

7.4.2 Optimization of Vapour-Cooled Current Leads

The current lead is a critical component of a superconducting magnet system in so far as it is the biggest source of heat leak to the LHe-bath. The current lead carries large current and consequently generates large amount of Joule heat. This heat is transported to He-bath. Heat is also transported from the top plate at room temperature to the bath though the leads by thermal conduction. The dimensions of the current leads can, however, be optimized for a given current such that the heat leak to the bath is minimum. Copper current leads have been universally used because of its being a good electrical conductor. Paradox, however, is that any good electrical conductor also happens to be a good conductor of heat. The thermal conductivity (k) and the

electrical resistivity (ρ) of a metal are related through the Weidemann- Franz Law, namely $k_{(T)}\,\rho_{(T)} = L_0 T$ where L_0 is the Lorenz number = 2.45×10^{-8} WΩK^{-2}. So it does not matter what material one chooses for current leads, SS or copper. In SS the Joule heating will be very high but heat conduction to the bath will reduce, SS being a poor thermal conductor of heat. In copper leads it will be just reverse, that is, Joule heating will reduce but thermal conduction will be very high. The length and cross section of the leads are optimized such that heat leak is reduced to minimum for a given lead current. Once the length of the current lead is chosen it is the cross section of the leads which is determined through the optimization procedure. The heat transport to the bath will, however, increase for smaller or higher operating current. To reduce the heat leak further, evaporated out-going helium vapours are used to cool the current leads. As shown in Fig. 7.9 the He-vapours from the cryostat are forced to flow spirally past the copper leads encased in a SS tube. The annular space between the leads and tube is packed with fiber glass roving to create fine multiple channels for efficient heat exchange.

Optimization of the current leads is done using steady state energy balance equation:

$$\frac{\mathrm{d}}{\mathrm{d}x}\left[k(T)A\frac{\mathrm{d}T}{\mathrm{d}x}\right] - \mathrm{f.m.}C_{\mathrm{P}}\frac{\mathrm{d}T}{\mathrm{d}x} + I^2\frac{\rho(T)}{A} = 0 \tag{7.3}$$

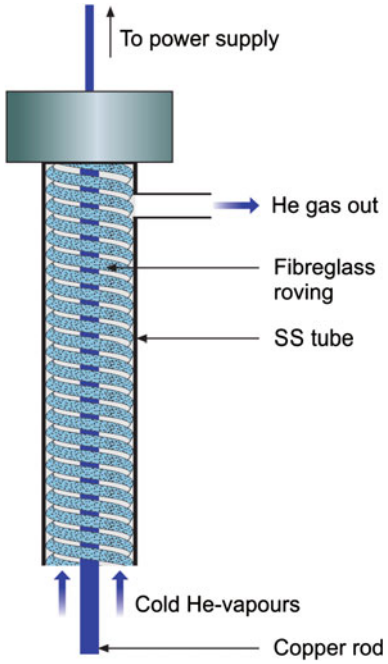

Fig. 7.9 The schematic design of the vapour-cooled current leads [15]

where A is the area cross section of the lead, C_p the specific heat at constant pressure and can be assumed constant, f is the efficiency of the heat transfer between the leads and vapours, I, the operating current and m (kg/s) the mass of liquid helium boil off by the heat leak from the lead. We optimized the leads with cross Section 0.3 cm^2 and length 75 cm for a current of 200 A. For our shape factor $(IL/A) = 3.5 \times 10^6$ A/m the minimized heat leak through the current lead comes out to be 1.04 mW/A. Thus the total heat flow to the He-bath by the two current leads at 200 A current turns out to be 0.4 W. The flow rate of the He-gas escaping from the top of the magnet system is regulated through a valve depending upon the lead-current. He-gas coming out of the top flange is found to be at room temperature establishing the efficacy of our optimization calculations.

7.4.3 Magnet Quench

Quench is a term used for a superconducting magnet when, all of a sudden, it turns normal (resistive) during the operation. This transition from superconducting state to normal state invariably occurs whenever any of the three parameters, temperature, magnetic field or current exceeds its critical value. This happens even if a minute part of the winding becomes resistive. The Joule heating (I^2R) across this resistive part will spread rather fast to the entire winding turning the magnet normal and dumping the stored energy ($\frac{1}{2}LI^2$) into the LHe-bath. This heat evaporates large amount of liquid helium and raises the temperature of the magnet far above the bath temperature. In extreme cases this dissipation of energy can burn the magnet. The occurrence of quench can, however, be minimized by stabilizing the magnet through a careful design and winding. The conductor therefore is chosen with appropriate filament size and Cu:SC ratio.

One can comfortably prevent quench caused by excessive current or poor cooling by keeping the current below the critical limit and maintaining LHe-level. The tricky part is the quench caused by the micro movement of the conductor in the winding under the influence of large Lorentz forces and by the release of strain energy. It will happen even if enough precautions are taken during winding. The quench is quite common due to wire movement during the virgin run. Let us consider a small heat pulse in the conductor in a very small part of the conductor. The heat will travel through a conductor longitudinally in both the directions at a rate determined by its thermal conductivity. We can assume near negligible dissipation in transverse direction because of inter-layer insulation and thermal contact resistance etc. If the heat dissipation from the ‘hot spot’ is faster than the generation of heat the normal zone will collapse and the magnet will be stable. If the heat dissipation is slower, the normal zone will grow and spread throughout the winding thus quenching the magnet. Interestingly, the time scale involved in quench are in the range of μ and m s. In fact, there is a critical size of the normal zone, called as minimum propagation zone (MPZ) for a given conductor which will initiate quench. This is discussed in the next section.

7.4.3.1 The Minimum Propagating Zone

To understand the concept of minimum propagating zone (MPZ) let us consider a superconductor of area cross section A carrying a current at a density J generates heat Q_{gen} due to some disturbance and raises the temperature locally of a small length ℓ to a value above T_c. turning it normal. The MPZ area and the temperature profile are shown in Fig. 7.10. The heat generated over a short length, ℓ, will travel through the superconductor longitudinally in both the directions. The heat generated in this normal region (I^2R) due to Ohmic heating will be

$$Q_{\text{gen}} = J^2 A\, \ell\, \rho \tag{7.4}$$

where ρ is the resistivity of the superconductor in normal state. This heat will travel along both the directions at a rate determined by the thermal conductivity of the normal region.

Thus the heat dissipated away Q_{Diss} will be, determined by the thermal conductivity of the normal region.

$$Q_{\text{Diss}} = 2\,k\,A\,(T_c - T_B) \tag{7.5}$$

Here k is the thermal conductivity of the conductor and T_B the bath temperature. The factor of 2 enters because of the heat being dissipated in two directions. Under

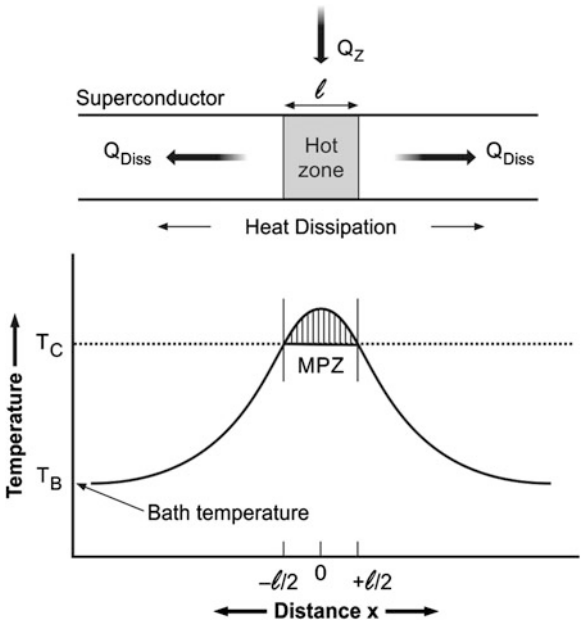

Fig. 7.10 The concept of minimum propagation zone (MPZ) and the temperature profile

equilibrium condition the two equations can be equated and we get the expression for ℓ as;

$$\ell = \left[\frac{2k(T_c - T_B)}{J^2\rho}\right]^{\frac{1}{2}} \tag{7.6}$$

If the size of the hot zone is less than ℓ, heat generated will dissipate away and the hot spot will disappear but will grow if the size exceeds ℓ.

To have an idea of the magnitude of MPZ in Nb–Ti, let us assume a $J = 4 \times 10^8$ A m^{-2}, T_c (6 T) = 6.71 K, T_B = 4.2 K, the electrical resistivity, $\rho = 6.5 \times 10^{-7}$ Ω m and thermal conductivity, $k = 0.1$ W m^{-1} K^{-1}, the MPZ, ℓ turns out to be just 2 μm. A simple calculation will show that for bare Nb–Ti the heat required to trigger quench is tiny, just of the order of 10^{-9} J. The problem has, however, been solved by producing composite superconductors with fine filaments embedded in high conducting copper which has a thermal conductivity of about 400 W m^{-1} K^{-1}. This topic has already been discussed in Chap. 6.

7.4.3.2 Quench Voltage and Temperature Rise

A solenoid magnet, in general, is a pure inductance in its normal operation. Part of the winding, however, turns resistive during a quench. This resistive part is shown in Fig. 7.11 as R_Q. During the normal magnet operation the power supply voltage is nearly zero. Small voltage develops during ramp-up (charging) and ramp down (discharging) with opposite polarity. The power supply is turned-off as soon as a quench is detected. Large voltage is generated within the resistive winding which

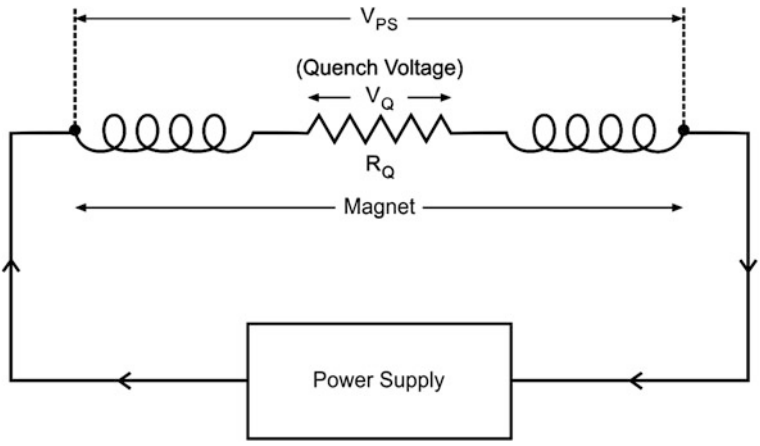

Fig. 7.11 Part of the magnet winding goes resistive (R_Q) and develops huge voltage across this part. Voltage across magnet terminals is restricted to power supply voltage, V_{PS}

can burn insulation and even lead to arcing within the winding. The expression for quench voltage V_Q can be found out from the following equations.

$$V_Q = I R_Q - M \, dI/dt \tag{7.7}$$

and

$$L \, dI/dt = I R_Q \quad (V_{PS} \text{ being zero}) \tag{7.8}$$

where I is the magnet current at the time of quench, R_Q is the resistance of the quenched part, L, the self inductance of the magnet and M, mutual inductance between the resistive part and the rest of the inductance of the magnet.

$$\text{From the two equations } V_Q = I R_Q(1 - M/L) \tag{7.9}$$

V_Q is often of the order of few hundreds or thousands of volts. In the worst scenario, ignoring M, the internal voltage will be

$$V_Q = I R_Q \tag{7.10}$$

With time R_Q will increase and so will M, but the current will fall. The internal voltage will therefore rise to a peak and then fall.

It is extremely important to estimate maximum temperature reached at the point of quench initiation in the winding and keep it restricted, in any case below room temperature. An exact estimate is tedious as the quench process is too fast taking place in a fraction of a second. As the temperature rises the physical properties like resistivity and specific heat keep changing by orders of magnitude. We may follow Maddock and James [16] for the estimation of the maximum temperature and write heat balance equation of the unit volume of the winding.

$$J^2(t) \, dt = C(T) \, dT/\rho(T) \tag{7.11}$$

where $J(t)$, the current density which changes with time t, ρ, electrical resistivity, dt time duration, d, the density and $C(T)$ specific heat at temperature T. All the quantities are averaged over the total winding cross-section. By integrating the above equation we find

$$\int_0^\infty J^2(t) dt = J_0^2 t_d = \int_{4..2}^{T_{MAX}} \frac{dC(T)}{\rho(T)} dT = F(T_{MAX}) \tag{7.12}$$

that the maximum temperature, T_{MAX} is solely dependent on material properties and can thus be worked out by substituting the relevant values in (7.12). J_0 is the initial current density and t_d the decay time of the current after the quench. T_{MAX}

should always be kept under safe limit, in any case well below room temperature. After fixing the maximum upper limit of temperature we can find the decay time of the current and calculate the value of the dump resistance in the protection circuit.

7.4.4 Quench Protection

We have just seen in the previous section that a quench can lead to very serious consequences and destroy a magnet if not protected intelligently. Suppose a magnet with 10 H inductance and running at a current of 200 A quenches in 1 s, it will induce a voltage of 2 kV. The stored energy equal to 0.2, MJ if released in the winding, will burn the winding and can even melt the conductor. Protection circuits are therefore integrated with the magnet so as to dump the energy stored in unquenched part of the winding into an external device and save the magnet. Two types of protection circuits are most popular and used by the scientific community and by the manufacturing companies. These are, one the resistor protection circuit and the other is resistor-diode protection circuit. We briefly discuss them below.

7.4.4.1 Resistor Protection Circuit

This circuit is very simple and cheap. An external low value dump resistance, R_D as shown in Fig. 7.12, is connected across the magnet. The resistance is selected such that the time constant is small for the current to decay and the induced voltage is moderate not exceeding a few kV. Table 7.2 shows the value of time constant, τ ($=L/R_D$) and induced voltage ($=L\ dI_0/dt$) corresponding to the dump resistance of 0.5, 1.0, 10 and 100 Ω for the 7 T magnet discussed in Sect. 7.4.1. The magnet had an inductance of 0.4 H. I_0 is the magnet current at the start of the quench, 210 A in this case. As soon as a quench appears, the power supply detects an increasing

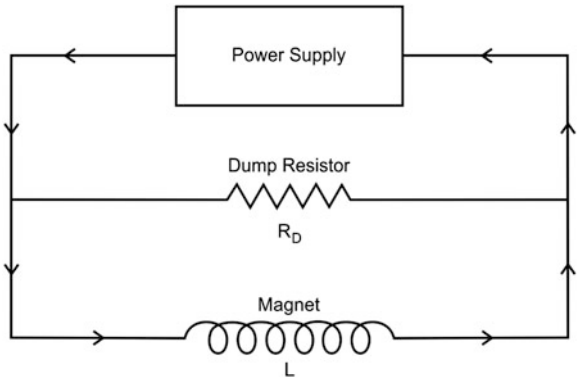

Fig. 7.12 Magnet quench protection by dump resistor, R_D

Table 7.2 Induced voltage corresponding to dump resistance value

Dump resistor R_D (Ω)	Time constant τ (s)	Induced voltage V (volts)
0.5	0.8	105
1.0	0.4	210
10	0.04	2,100
100	0.004	21,000

voltage and switches off automatically. The stored energy is rapidly dumped into R_D according to

$$I = I_0 e^{-(R_D/L)t} = I_0 e^{-(1/\tau)t} \tag{7.13}$$

where t is the time and τ, the time constant. The dump resistor value is kept small as dictated by the requirement of low T_{MAX} and low maximum voltage V_{MAX}, limited to Ohmic voltage across R_D. There is, however, one drawback with the use of resistor that during the ramp-up and ramp-down of the current, the induced voltage drives a current through the dump resistor dissipating heat. This heat will evaporate liquid helium and at high ramp rates can lead to dangerous pressure build-up in the cryostat if the resistor is kept under LHe-bath. As an example, suppose we charge our magnet of 0.4 H inductance and having 0.5 Ω dump resistance across it to 210 A in 1 min, the induced voltage will be 1.4 V. A current of 2.8 A will flow through the resistor dissipating 3.92 W energy. This energy, if released into the LHe-bath will evaporate 5 l/h liquid helium. If the magnet is to be ramped repeatedly this dissipation will add up to very high value and will evaporate large amount of liquid helium. On the other hand, if the same magnet is charged to full current in 10 min the dissipation will be as low as 0.04 W and will evaporate just 52 ml of LHe per hour. To prevent this dissipation from entering the LHe-bath, the dump resistor should be mounted on a radiation baffle in vapour phase. This arrangement assumes greater importance while dealing with large magnets dumping huge energy into the LHe-bath during a quench.

When a magnet is wound in multi-sections, each section is protected against quench by incorporating separate dump resistance across each section. The total stored energy of the magnet is thus divided amongst the sections. In the event of any mishap only the section affected will be damaged.

7.4.4.2 Diode-Resistance Protection Circuit

A better alternative for quench protection is the diode-resistance technique which prevents current flow through the resistor under the influence of induced voltage during ramping up and ramping down. As shown in Fig. 7.13, a set of special diodes is connected in series with the dump resistor. These diodes should be highly reliable, able to function at 4.2 K and sustain current during quench. The number of diodes in the circuit should be chosen such that the forward conducting voltage of the diodes is

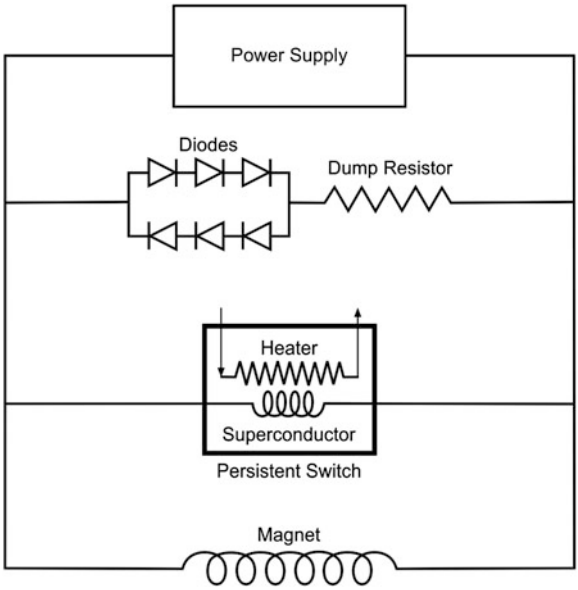

Fig. 7.13 The schematic of a diode-resistor quench protection system for a superconducting magnet. A persistent switch is also shown and connected across the magnet

of the order of few volts. They should not switch on and allow the current to flow through the resistor due to the voltage developed during ramping up and ramping down. Since we need both polarities during ramping we use two sets of back to back diodes in an arrangement shown in Fig. 7.13. This arrangement enables the current in either direction during a quench. At the initiation of quench, the voltages starts rising until the diodes 'switch on' allowing the current to flow through the resistor. The peak voltage is then reached in the resistor. Since in normal operation no current flows through the circuit, this protection system can as well be mounted in LHe-bath. This does away with the need of heavy current leads dumping heat into the bath. Helium evaporation is thus drastically curtailed. In the case of very large magnets we have to have a re-look if the protection system, with or without diodes, should at all be mounted in LHe-bath. During the quench the energy dissipated may cause excessive helium vapour built-up to dangerous level. External dump resistors may be a better option for the protection of huge magnets used in accelerators and fusion reactors. This will be discussed in the next two chapters.

7.4.5 The Persistent Switch

Shown in Fig. 7.13 is also a persistent switch used to run the magnet in persistent mode at a fixed field with power supply switched-off. The switch is connected in parallel with the magnet. The switch has a small non-inductive (bifilar) superconducting winding of 10–100 Ω room temperature resistance and a heater wound over

it. The switch is encased and impregnated with epoxy. To have the superconducting wire of manageable length the wire has a Cu–Ni resistive matrix. During the start-up of the magnet, the heater is 'switched-on' turning the persistent switch normal. The resistance of the switch becomes much higher than the magnet resistance such that the current flows through the magnet and not through the persistent switch. As the current is ramped up the voltage $V = Ir + L\,\mathrm{d}I/\mathrm{d}t$ is seen increasing. Here the first term is the voltage drop across lead resistance 'r' and the second term is induced voltage due to the charging of the magnet. After the required field is achieved, the heater current is 'turned-off'. It is necessary to note down this current. After a pause of 10–20 s the current from the power supply to magnet is reduced to zero. As current through the leads decreases, current through the switch increases to the magnet current level. The current now flows through the magnet in a close-loop and the magnet runs in persistent mode. In NMR and MRI magnets the current leads are de-mountable and are removed once the magnet is put in persistent mode.

A reverse procedure is followed while de-energizing the magnet. Power supply is 'turned-on' and the current raised to the value, at which the magnet was put in persistent mode. The switch heater is now turned-on and the main current is ramped down to the new value as per the new desired field. The switch can be 'turned-off' again to put the magnet in persistent mode. An auxiliary 50 mA power supply is usually in-built in the main power supply for the operation of the persistent switch.

The fabrication of a persistent switch is straight forward and simple but the functioning of the switch strongly depends upon quality of the superconducting joints. Ideally, the joints should have zero resistance. In fact, the jointing technique is a top guarded secret of the manufacturers. The usual steps involved are to etch away the copper cladding of the MF wire, de-oxidize the filaments of the two terminals and twist them. Twisted terminals can be encased in a Nb–Ti sleeve and squeezed under high pressure. This sleeve can be electron-beam welded along the length. There are many variants of this procedure followed by individual laboratories and the commercial establishments. Jointing is more tricky in case of brittle Nb_3Sn and HTS magnets as joints need controlled post heat treatments.

The field does decay with time but quite slowly depending upon the inductance, the design of the switch and the number and quality of the joints. A stability of 10 ppm/h is attained quite comfortably. For high resolution NMR spectroscopy applications, the field stability has to be improved to 0.1 ppm/h and even better.

7.4.6 Training of the Magnet

Training of the magnet is an important part of the magnet operation. Commercial magnets are trained at the factory site before being shipped and need no further training. More often than not, a magnet quenches at a current much below its designed value in the virgin run. The problem is fixed through 'training' the magnet. The specific heat of the superconductor at 4.2 K is small, of the order of 10^{-4} J/g/K and therefore, any tiny thermo-mechanical disturbance in the magnet

can generate heat and form a hot spot which might drive the temperature of the superconductor beyond its T_c. If this hot spot does not subside and propagates, it can lead to quench. Further, a superconducting magnet is a complex composite of several materials like the metallic conductor, the former, inter layer insulation and epoxy used for impregnation. Their thermal contraction coefficients are widely apart. During cool down there is a mismatch in thermal contraction and large stresses are frozen-in. Fracture could occur when large Lorentz forces are built up. Cracks in the epoxy can release strain energy sufficient to cause quench.

Once the strain energy is released, the quench will occur during re-energization at the next level of strain and the magnet can be charged to higher current value. Similarly, the winding adjusts itself against micro movements of the conductor during successive energizations. Experimentally, in the first run of the magnet built in the laboratory, one sweeps the current at low rate to a small value say 10 A/min, stays for a few minute at this level, ramp-down the current to zero. Next time charge the magnet to higher current and ramp-down to zero. This way in a finite number of steps, one goes to the highest designed current. In several of our magnets we did not observe the quench of the magnet during training phase. This must have been due to a perfect winding and good impregnation. Figure 7.14 is a typical training curve of a magnet where the current was ramped-up and ramped-down to a smaller current in steps without inducing quench.

We built many 7 and 8 T magnets in 1970s using many types of impregnating materials like silicon grease, bees wax and epoxy. We have preferred vacuum impregnation route in some and wet winding in others. Both performed admirably well. We found wet-winding, using wax as well as epoxy to be a superior technique. Wet-winding ensures impregnation between each layer and each turn, even though it is a bit messy process. Other advantage is that one can use a filler material with epoxy or wax to reduce the mis-match of the thermal contraction coefficients of the constituents. Filler is not practical in vacuum impregnation technique as the

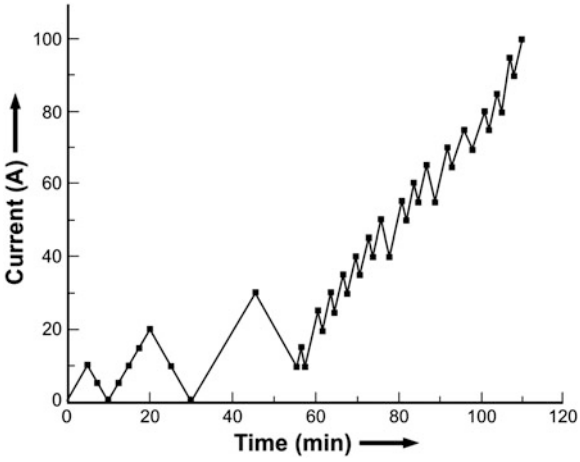

Fig. 7.14 Ramping-up and ramping-down the current in steps during 'training' of a magnet [15]

material has to have low viscosity and has to flow through fine channels. We got excellent results using wet-winding technique using stycast (2,850 FT from Emerson and Cuming) mixed with 20 % Al_2O_3 powder in our cryo-free magnet. As mentioned earlier in many magnets we used fiber glass cloth as the inter-layer which allows free flow of impregnating material during vacuum impregnation process.

7.5 Magnet Power Supply

The superconducting magnet power supply has many features which are unique and quite distinct from the ordinary dc power supplies. Under normal operation it supplies power at low voltage and high current to a high inductance and almost zero resistance load but the magnet can go from pure inductive to pure resistive state during a quench. The power supply detects the quench and switches-off automatically. Circuit design allows variable sweep rates (A/min) for ramping-up and ramping-down the current in a step in the magnet. Four quadrant output capability permits smooth and continuous current reversal through zero current and smooth magnetic field reversal. The power supply can be programmed to sweep magnet current at predetermined different rates at different current levels without user intervention. The voltage limit can be adjusted which in turn puts a limit upon the sweep rate. The supply senses the voltage directly across the magnet bypassing the current leads.

It also has an auxiliary circuit to supply current (0–100 mA) to the heater of the persistent switch. Some supplies also have provision of bi-polarity to supply current in either direction to reverse the direction of the magnetic field. Supplies have computer compatibility using RS 232 or IEEE interface. The power supply has many in-built safety features. It ramps down the current automatically in the event of the detection of power loss and a temperature rise. There are safety interlocks for persistent switch enable/disable and for changing important magnet parameters and limits.

Most power supplies these days are of ‘switching mode’ type which are light in weight and occupy less space. They run in constant current mode instead of constant voltage mode. Power supplies based on linear topology permits operation with less electrical noise and low drifts than switch-mode superconducting magnet power supplies. For high field stability, the current drift at static field should be extremely low for which power supplies based on linear topology are superior. They generate smooth field that is nearly free from offending electromagnetic signatures. Clean field background allows greater resolution in many precision measurements. Modern supplies have firmware module which enables the supply to remember the current at which the magnet was put in persistent mode. This eliminates human error related to the opening of the switch at a wrong current value.

The block diagram of a superconducting magnet power supply system which consists of a switching mode power supply and a programmer built at our Centre (IUAC) [17] several years ago is shown in Fig. 7.15. The programmer consists of a controlled ramp generator and a feedback loop to control power supply. Controlled ramp generator generates desired control signal ramps in the form of straight lines. Controlled loop first generates an error corresponding to current nonlinearity by comparing magnet current with the desired ramp function. This error is then compared with the voltage feedback to compensate for current ramp nonlinearity and voltage drops in the leads. PI type control loop has been developed to improve transient stability performance of the system. The programmer allows a ramp rate between 0 and 10 A/s and an automatic ramp down of magnet current in case of quench. A large rectifier provided at the back of the supply limits the high voltages generated during the magnet quench. These power supplies have been used at the Centre for more than a decade without trouble.

7.6 High Homogeneity Field

We observed in Fig. 7.7 that the field decreases along the magnet axis as we move along the Z-direction away from the centre. The typical field homogeneity obtainable through the judicious selection of the parameters α and β, is limited to about 1 in 10^3 in 10 mm DSV. This homogeneity is, however, quite inadequate for a variety of applications. In principle, field homogeneity can be improved by lowering the peak field at the centre of the magnet by missing certain number of turns in the middle part of the magnet or by adding extra coils at the two ends to enhance the field on either side of the centre. Use of these compensating coils can raise the homogeneity to 10^{-5}–10^{-6} level. NMR magnets need still higher homogeneity of the order of 10^{-9} which is provided by a set of a large number of superconducting 'shim coils' to compensate higher order field expansion terms. We will discuss them in the context of the magnets used in NMR spectrometer in Chap. 10.

Before we discuss the compensating coils to improve the field homogeneity, let us find how the field varies along the axis. To calculate field at point S, a distance Z (Fig. 7.16) away from the centre along the axis. We can make use of the (7.1) and (7.2) and divide the solenoid magnet into two parts as shown in Fig. 7.16, each part being half of a solenoid. The field at the end of the solenoid magnet can be taken as half of the field at the centre. The field at the point S can thus be written as:

$$B_z = \frac{1}{2} J \lambda a_1 [F(\alpha \cdot \beta_1) + F(\alpha \cdot \beta_2)] \tag{7.14}$$

where $\alpha = a_2/a_1$, $\beta_1 = (\ell - Z)/a_1$ and $\beta_2 = (\ell + Z)/a_1$. It is to be noted that β_1 becomes negative for $Z > \ell$, for points outside the end point of the magnet, $F(\alpha, \beta_1)$ should therefore be taken as $F(\alpha, -\beta_1)$, or $= -F(\alpha, \beta_1)$. Following Montgomery [10] the

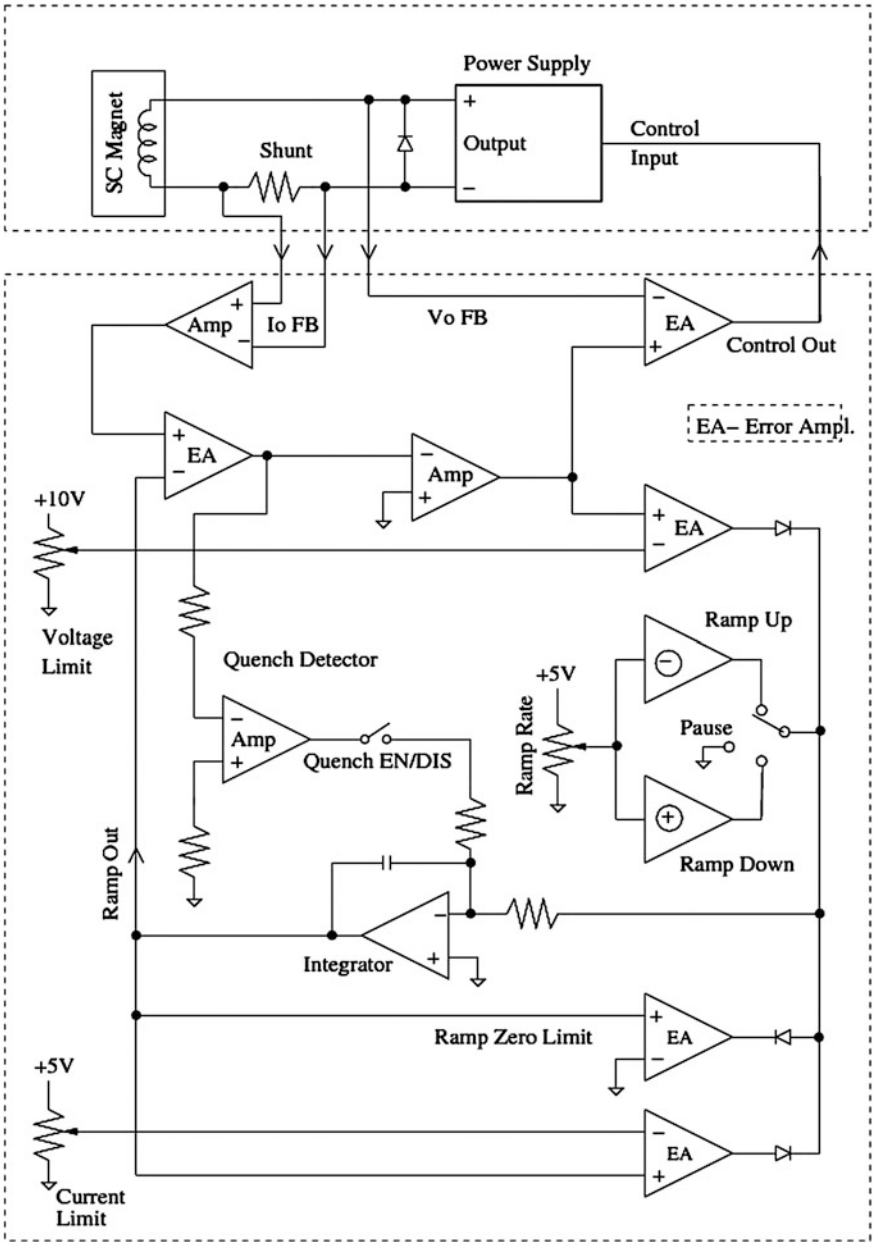

Fig. 7.15 The block diagram of a superconducting magnet power supply system consisting of a switching mode power supply (6 V, 100 A) and the programmer [17] (*Courtesy* Rajesh Kumar, IUAC Delhi)

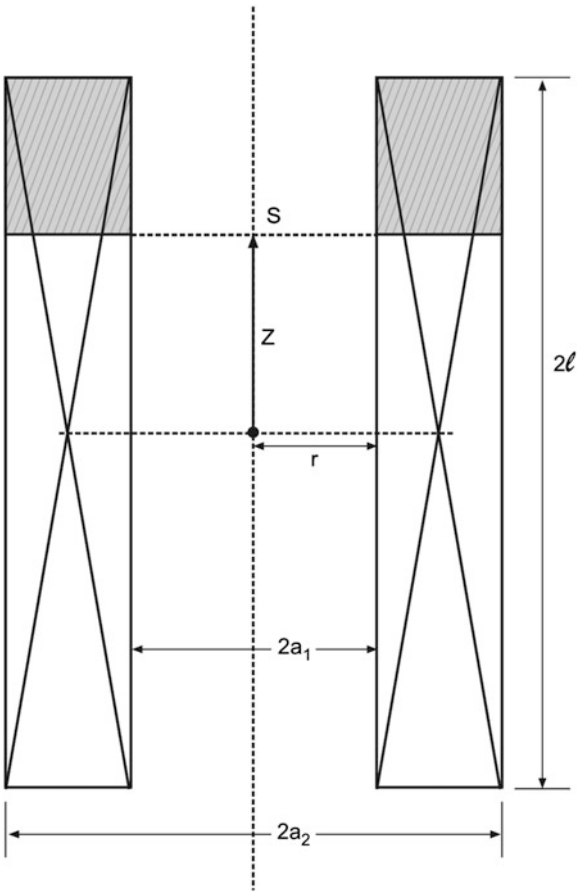

Fig. 7.16 To find field at a distance Z from the centre, magnet is divided into two parts each one-half of a solenoid. β for the two solenoids will now be $(\ell + Z)/a_1$ and $(\ell - Z)/a_1$

axial and radial components of the axial field in a centrally symmetric solenoid can be written as the expansion series as:

$$B_Z(Z,0) = B_0\left[1 + E_2\left(\frac{Z}{a_1}\right)^2 + E_4\left(\frac{Z}{a_1}\right)^4 + E_6\left(\frac{Z}{a_1}\right)^6 + \cdots\right] \tag{7.15}$$

$$B_Z(0,r) = B_0\left[1 - \frac{1}{2}E_2\left(\frac{r}{a_1}\right)^2 + \frac{3}{8}E_4\left(\frac{r}{a_1}\right)^4 - \frac{5}{16}E_6\left(\frac{r}{a_1}\right)^6 + \cdots\right] \tag{7.16}$$

where the error coefficients E_n are given from the standard formula for the coefficients in a Taylor series:

$$E_{2n} = \frac{1}{B_0}\left(\frac{1}{(2n)!}\right)\frac{d^{2n}B_Z(Z,0)}{d_Z^{2n}} \quad Z = 0 \tag{7.17}$$

The values of these coefficients can be determined by taking the derivative of the field (7.14) with respect to Z, that is, along the axis and evaluating them at $Z = 0$. First few E_{2n} dominant terms have been given by Montgomery [10] (Table 8.2, p. 236). It is noticed from (7.15) and (7.16) that near the centre where r/a_1 is small, the E_2 term dominates and the deviation of the field in the radial direction is only half of that along the axis. For a simple solenoid E_2 term is always negative. The field along the axis decreases but increases in the radial direction until $r = a_1$. It decreases thereafter because of certain boundary conditions.

7.6.1 High Homogeneity Field by Compensated Coils

Field expansion (7.15) and (7.16) indicate very clearly that in a solenoid magnet the inhomogeneity in the axial field along longitudinal and radial directions come from the higher order terms in these equations. To get high homogeneity fields it is therefore imperative to get rid of the successive terms in these equations. Larger the number of terms eliminated, higher is the homogeneity of the field. This can be achieved by subtracting a smaller coil from the main coils so as to cancel higher order terms. These compensating coils operate at the same current level as the main coil. Compensating coils will look like a gap or will appear as a notch in the main winding. The number of terms to be cancelled depend upon the number of variable geometrical parameters chosen for the compensating coil. For example, with one of the variable parameters α and β keeping same for both the coils and varying the other parameter, we can cancel one term, E_2. The magnet will be compensated to fourth order similar to a Helmholtz coil. With two variable parameters α and β one can cancel two terms, E_2 and E_4 compensating the main coil to sixth order. This compensating coil can be incorporated either at the inner winding bore or at the outer winding bore and are referred to as 'inside notch' and 'outside notch' respectively.

The fourth order compensation geometry is shown in Fig. 7.17, which is just a Helmholtz coil. Here the missing coil is the gap in the middle of the main coil. The main coil as also the gap has the same value of $\alpha(\alpha = \alpha_c = a_2/a_1)$ but different values of parameter β. As seen in Fig. 7.17 β for the main coil is ℓ/a_1 while for the correction coil β_c is ℓ_c/a_1. Here the subscript 'c' indicates the parameters for the compensating coil.

For sixth order compensation (E_2 and $E_4 = 0$), both 'inside notch' and 'outside notch' geometry are possible and are shown in Fig. 7.18. Shaded areas are the missing part or the so-called compensation coils. In sixth order (inside notch) again has the same a_1 as for the main coil. The modified field expression for the combined coil can now be written as

$$B_z(Z,0) = J\lambda a_1 \Big[F_0(\alpha,\beta) - Fc(\alpha_c,\beta_c) + \{F_0 E_2(\alpha,\beta) - F_0 E_2(\alpha_c,\beta_c)\}(Z/a_1)^2 + \{F_0 E_4(\alpha,\beta) - F_0 E_4(\alpha_c,\beta_c)\}(Z/a_1)^4 \ldots\Big] \tag{7.18}$$

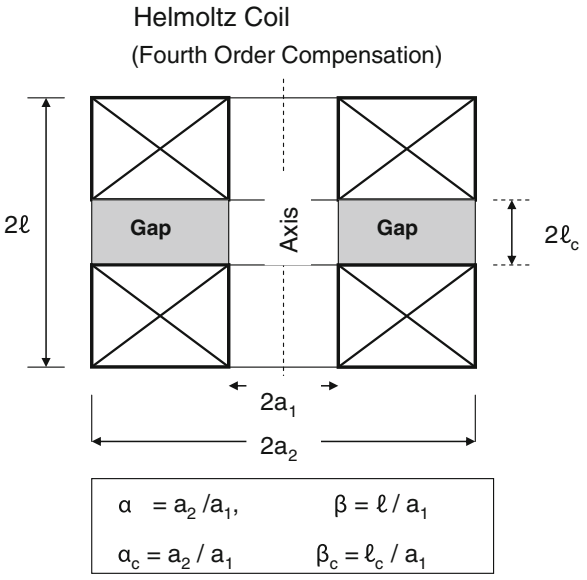

Fig. 7.17 Graphical representation of the fourth order compensation. Note same value of α for the main coil as well as for the compensating coil but different values of β and β_c

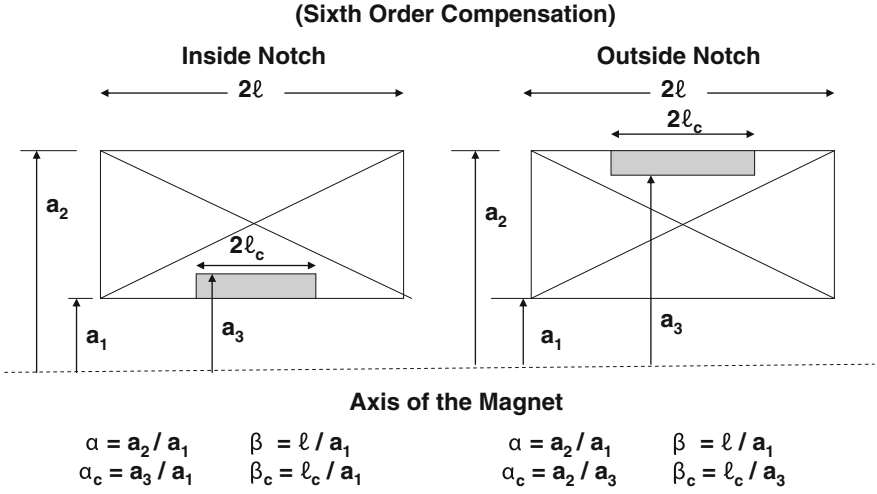

Fig. 7.18 Graphical representation of sixth order compensation, 'inside' (*left*) and 'outside' (*right*). Missing turns are shown shaded. Values of α, β and α_c, β_c have also been written

For fourth order compensation the terms $F_0\, E_2(\alpha, \beta)$ and $F_0\, E_2(\alpha_c, \beta_c)$ are equal and opposite in sign and therefore cancel out. The field uniformity improves. The functions $F\, E_2(\alpha, \beta)$ and $F\, E_4(\alpha, \beta)$ when plotted against β for different values of

α show a peak which means that there are two values of β for each value of the functions $F_0\ E_2(\alpha, \beta)$ and $F_0\ E_2(\alpha_c, \beta_c)$ for the same value of α. The smaller value of β on the left of the peak yields β_c for the small compensating coil. Since the inner diameter of the compensating coil (both fourth order and sixth order, inside notch) is the same as that of the main coil the corresponding length of the compensating coil can be calculated from β_c.

Figure 7.19 shows the contours of constant FE_2 and FE_4 intersecting at two points. Intersection at $\alpha = 3$ and $\beta = 2$ corresponds to the main magnet and the second intersection at $\alpha_c = 1.87$ and $\beta_c = 1.33$ corresponds to the sixth order compensating coil. The cancellation of the first two terms, FE_2 and FE_4 thus leads to much more field homogeneity than the fourth order Helmholtz coil. It is important to control the dimensions of the compensating coils very precisely, within 2 % of the calculated value, homogeneity being extremely sensitive to the errors in choosing the dimensions. This sensitivity is significantly reduced by choosing β much larger than the minimum coil volume criterion. The magnitude of the higher order terms to be cancelled is significantly reduced.

Very useful tables for the design of the compensating coils have been given by Montgomery [10] for fourth order, for sixth order compensation inside notch and outside notch. We made a few Nb–Ti magnets of the sixth order compensation using these tables in early 1970s. One, rather long and low field (2.35 T) solenoid magnet with $\alpha = 1.224$ and $\beta = 3.38$ we built [18] using outside notch gave us an homogeneity of 3×10^{-6} in 10 mm SDV.

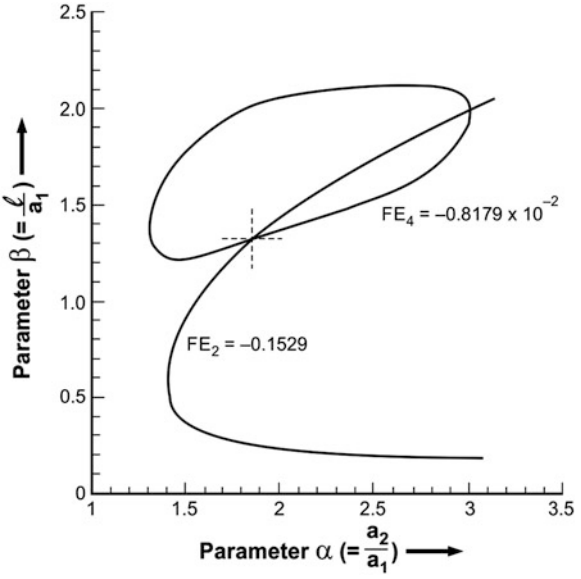

Fig. 7.19 The contours of constant FE_2 and FE_4 intersecting at two points Intersection at $\alpha = 3$ and $\beta = 2$ corresponds to the main magnet and the second intersection at $\alpha_c = 1.87$ and $\beta_c = 1.33$ corresponds to the sixth order compensating coil [10] (*Courtesy* D.B. Montgomery "Solenoid Magnet design")

7.7 Nb_3Sn Magnets

For field production above 9 T and at 4.2 K, our option is limited to the A-15 Nb_3Sn superconductor. With the availability of Nb_3Sn conductors produced by improved techniques and elemental additions (Chap. 6), field higher than 21 T have been produced [19] in 1990s. In general, such high field magnets consist of a number of concentric solenoids. The outermost solenoid is a Nb–Ti coil providing a background field of 8 T. The inner coils are wound using Nb_3Sn, $(Nb, Ti)_3Sn$ and $(Nb, Ta, Ti)_3Sn$ conductors. First 1 GHz (1,000 MHz) NMR spectrometer (BioSpin) was installed by Bruker in 2009 in France which has a superconducting magnet producing a field of 23.5 T. 930 MHz spectrometers using superconducting magnets are in use for some years at Tsukuba Magnet Laboratory, National High Magnetic Field Laboratory, Florida and many such other places. High field magnet usually produce 20–21 T field using a combination of Nb_3Sn coils and an inner-most coil of high T_c Bi-superconductor. This Bi-2223 coil is now being replaced by superior 2G-RBCO coils. Standard Nb_3Sn magnets going up to 20 T are now manufactured by cryogenic industries and are usually integrated with various measurement systems.

Building Nb_3Sn magnets is quite difficult as compared to Nb–Ti magnets. The main reason being the extreme brittleness of this material. Commercial multifilamentary cryo-stabilized Nb_3Sn wires and cables are by and large available in pre-reacted form, that is, with Nb-filaments in Cu–Sn bronze matrix. The wire is ductile enough to be wound into a coil. The coil is then heat reacted at high temperature under controlled conditions whereby Sn from the matrix diffuses into Nb-filaments to form intermetallic Nb_3Sn. The magnet is then impregnated as usual but extreme care is required to handle the reacted magnet.

7.7.1 Construction Details of an 11 T Magnet

As an example we take-up the construction of an 11 T magnet which we built [20] many years ago as an exercise. The magnet is a combination of an outsert of Nb–Ti coils and an insert of Nb_3Sn coil. The Nb–Ti outsert magnet provides a background field of about 7.2 T and the rest generated by the insert Nb_3Sn coil. The magnet coils were designed as per the standard procedure described in Sect. 7.4. In brief, the magnet had a working bore of 50 mm and a total of three sections. Outer two sections were wound using MF Cu/Nb–Ti wires. The Nb–Ti magnet had a clear bore of 100 mm to accommodate Nb_3Sn coil. It's winding length was 220 mm. All the actual dimensions of all the coils and other magnet parameters [21] have been listed in Table 7.3. We used a Nb–Ti wire of 0.75 mm diameter for winding the inner coil and 0.54 mm for the outer coil of the Nb–Ti outsert. Both the coils were wound one over the other on the same former. The formers for Nb–Ti magnet as well as for Nb_3Sn magnet were made out of SS 304. The cylindrical part of both the formers were uniformly perforated to allow liquid helium to cool the inner parts of

Table 7.3 Parameters of a 11 T superconducting magnet [21] working bore Dia. = 50 mm

Sr. no.	Parameter	Inner most coil (Nb_3Sn)	Outer coil (Nb–Ti)	
			Inner section	Outer section
1	Inner winding dia.	56.6 mm	110.6 mm	148.8 mm
2	Outer winding dia.	100 mm	148.5 mm	180.5 mm
3	Winding length	170 mm	220 mm	220 mm
4	Parameter α	1.766	1.34	1.21
5	Parameter β	3.00	1.99	1.48
6	Parameter $F(\alpha, \beta)$	0.873×10^{-6}	0.36828×10^{-6}	0.21149×10^{-6}
7	Conductor used	Nb_3Sn	Nb–Ti	Nb–Ti
8	Conductor dia.	0.85 mm	0.75 mm	0.54 mm
0	No. of filaments	6,000	54	54
10	No. of layers	20	22	26
11	Total no. of turns	3,863	6,458	10,584
12	Field at 90.5 A	2.395 (T)	Field by Nb–Ti coils 7.315 (T)	
13	Final field with 90.5 A in Nb–Ti coils and 140 A in Nb_3Sn coil		11.03 (T)	
14	Conductor length (approx.)	1 km	2.65 km	5.6 km
15	Interlayer material	Fibre glass cloth		
16	Impregnation (vacuum)	Bees wax		
17	Quench protection	Through dump resistor		

the coil. Similarly, the two end flanges of both the magnets had perforation and also curved radial slots enabling again cooling by liquid helium and taking the end terminals of the coils out. For Nb_3Sn coil we used a bronze-processed 'wind and react' wire of 0.85 mm diameter supplied by Vcuumschmelze, Germany. We had no choice of choosing wire diameters optimized for the same current but had to use the wires available and we could procure.

7.7.2 Winding the Background Nb–Ti Magnet

The winding of the Nb–Ti magnet was carried out as outlined in Sect. 7.4 except that now the magnet was wound in two sections. The inner coil was wound using 0.75 MF Cu/Nb–Ti wire. As Table 7.3 shows a total of about 2.65 km of wire was used and wound in 22 layers and 6,458 turns in all. Fiber glass cloth was used as inter-layer material. The outer section was wound on the inner section using MF Cu/Nb–Ti wire of 0.54 mm diameter. We used about 5.6 km of this wire in 26 layers and 10,584 number of turns. The end terminals of the coils were wrapped over the copper studs which had spiral grooves. Sufficient length of the wires was wrapped and soldered with Pb–Sn solder. This was to make very low resistance joints. Vapour-cooled current leads were taken out to the top plate of the cryostat. The three current terminals at the top plate enabled us to operate the two coils either in series or individually. The magnet was vacuum-impregnated in bees wax following the standard procedure.

7.7.3 Winding the Nb_3Sn Magnet

Winding the Nb_3Sn magnet is rather tricky. This is for several reasons. The first one is that since the wire is finally to be reacted at high temperature, it does not have the usual electrical insulation. The wire is covered with a glass sleeve which is quite fragile. Handling the wire during winding is thus a difficult task. Glass cloth was used as interlayer. The space factor 'λ' in Nb_3Sn coil is smaller than in the case of Nb–Ti coils. As shown in Table 7.3 the magnet had a clear working bore of 50 mm and an inner winding diameter of 56.6 mm. Here again we preferred SS-304 former. The winding length was 170 mm. A bronze processed Cu–Sn/Nb wire of 0.85 mm diameter with glass sleeve cover was used for winding. The wire had 6,000 filaments. In all, we had 20 layers and a total of 3,836 number of turns.

7.7.4 Preparation of Current Terminals

Before carrying out heat treatment, it is essential to fix the coil terminals on to a pair of copper studs without removing the glass sleeves from the wires. Figure 7.20 shows the Nb_3Sn coil before heat treatment (a) and after the heat treatment (b). It is seen clearly from these figures that the wire terminals of the coil have been taken

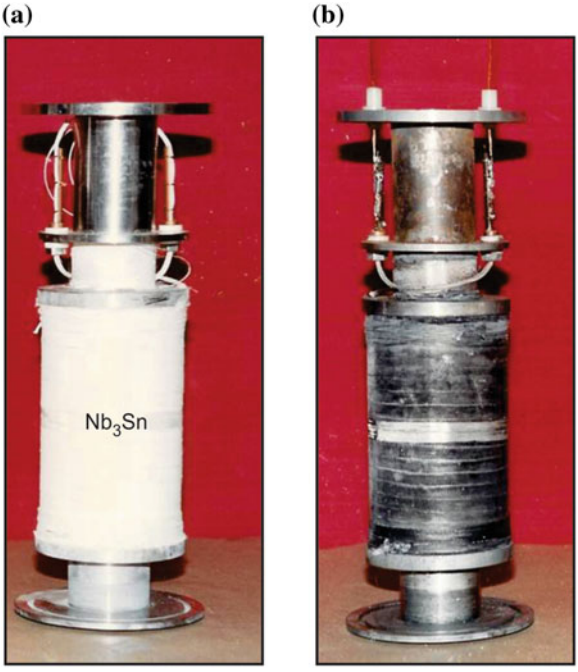

Fig. 7.20 The Nb_3Sn coil before heat treatment (**a**) and after heat treatment (**b**). Note how the coil terminals have been taken out through the metallic flanges using ceramic spacers to prevent electrical shorts [21] (*Photo courtesy* NPL Delhi)

out through the ceramic bushes fixed in the metal flanges to prevent electrical contact. The two long copper studs have a central hole and half circular cross-sections. The coil terminals are tied with the help of a copper wire on to these two studs at several places. The precaution to be taken here is that the glass sleeve should be in place along the entire length of the wire. At no place the superconducting wire should come in contact with the copper studs. If by chance it happens the Sn from the bronze wire will diffuse into copper studs during the heat treatment and stoichiometric Nb_3Sn will not form, making the magnet unusable.

7.7.5 Heat Treatment and Impregnation

Now comes the most critical phase of the magnet fabrication. The pure Nb-filaments embedded in Cu–Sn bronze have to be converted into Nb_3Sn filaments. Before going in for heat treatment of the magnet we kept the magnet under running water to get rid of starch coated on glass sleeve and glass cloth. Earlier through some preliminary study on the heat treatment of the short sample of the bronze wire we found the glass sleeve to be charred and covered with thick layer of carbon. Significant amount of starch was washed out from the magnet winding by the process we followed. As discussed in detail in Chap. 6, a two-step heat treatment is advisable to get high critical current density in the wire. A long heat treatment at comparatively lower temperature enables the formation of small size grains in the Nb_3Sn compound which is a prerequisite for all A-15 superconductors to have high J_c. This treatment should be followed by a second heat treatment for a shorter period but at higher temperature to improve stoichiometry of the Nb_3Sn which in turn raises the upper critical magnetic field B_{c2} and thus J_c.

Another important step in the heat reaction is that there should be no trace of oxygen in the reactor. The heat treatment must be carried out either in vacuum or under inert gas atmosphere. For all our Nb_3Sn magnets we carried out heat treatment under flowing high purity argon gas. The reactor chamber was thoroughly pumped and flushed several times with Ar-gas after the magnet was loaded into the reactor. The magnet was kept at a temperature of 120 °C for many hours to get rid of moisture. Out of a few options of heat treatment schedules given by the supplier of the wire we chose a two step process. The magnet was kept at 570 °C for 120 h followed by another heat treatment of keeping the magnet at 700 °C for 80 h after which the magnet was furnace cooled. The real challenge comes at this stage, how to handle the brittle magnet right from the stage of taking it out of the reactor, making current contacts and carrying out impregnation. To make electrical contacts of the coil terminals with the copper studs, the glass sleeve is very carefully removed and the reacted wire is cleaned. These bare wire terminals are now soldered with the Cu-studs using (Pb–Sn) solder along the full length. The next step is the impregnation of the magnet using either bees wax or the epoxy in a way similar to the Nb–Ti magnets. After the impregnation handling of the magnet becomes easier.

7.7.6 Assembly of Magnet Coils and Operation

The Nb_3Sn magnet is nested inside the Nb–Ti magnet and rigidly fixed in position. The combined magnet is then suspended from the support structure consisting of radiation baffles, liquid helium level sensor, LHe-fill line and G-10 support rods. A ll the three sections of the magnet were protected against quench independently by separate dump resistors which were mounted in the vapour phase. Separate vapour-cooled current leads were taken out from the two magnets such that they can be energized independently as well as jointly by making series connection outside the cryostat at the top plate. The combined magnet is shown in Fig. 7.21 and the whole magnet assembly along with the support system in Fig. 7.22.

Standard procedure for the operation of the magnet can now be followed to cool down the magnet system to 4.2 K and energize. Two power supplies were used because of the mismatch of the currents in the two magnets. The Nb–Ti magnet produced a field of 7.315 T at a current of 90.5 A, whereas the Nb_3Sn magnet generated an additional field of 3.715 T at a current value of 140 A. A total field

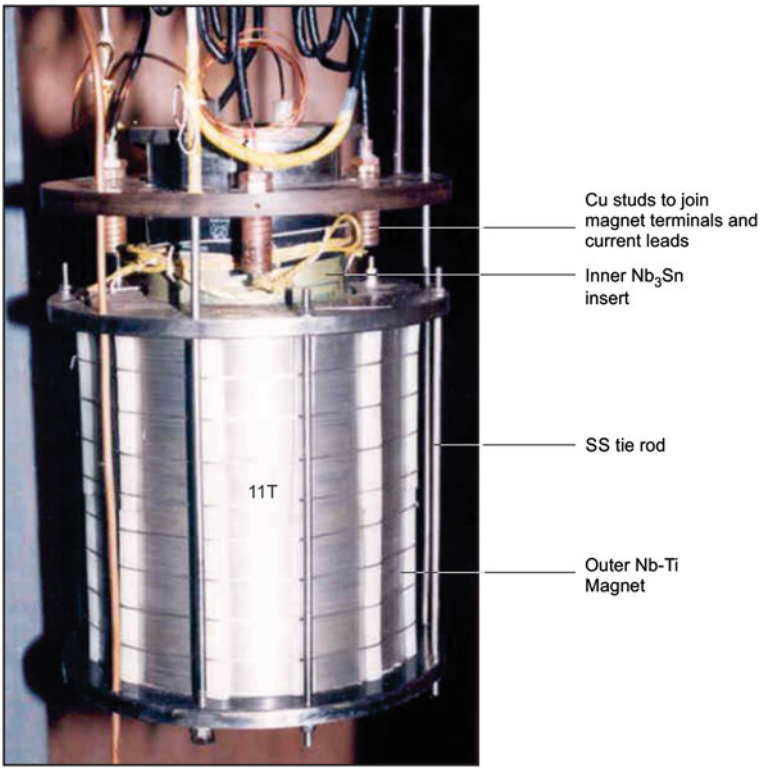

Fig. 7.21 The 11 T Nb–Ti/Nb_3Sn magnet made in author's laboratory in early 1990. The outer coil seen is the Nb–Ti magnet with tie rods. Liquid helium fill-line and level meter too are seen on the *left*. Nb_3Sn insert coil is in the *centre* [21] (*Photo courtesy* NPL Delhi)

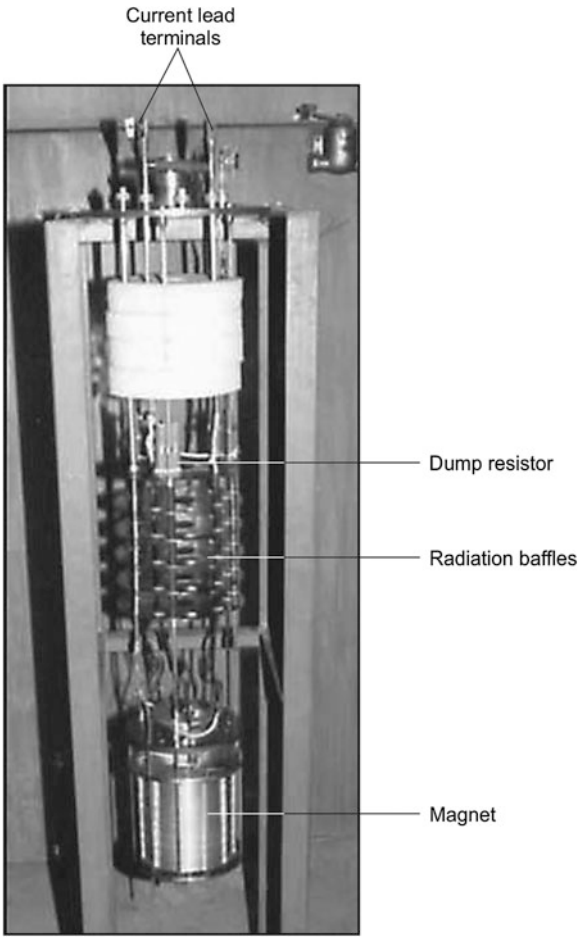

Fig. 7.22 The Nb–Ti/Nb_3Sn magnet along with the support system [21] (Photo courtesy NPL Delhi)

of 11 T is thus achieved as per the objective of this magnet. During the training, we ramped-up and ramped-down the field in steps of 10 A, no quench occurred in any of the coils. The *I–B* profiles of the Nb–Ti magnet, the Nb_3Sn magnet and the two in combination are plotted in Fig. 7.23.

7.8 Intense Field Magnets

7.8.1 A 21.1 T Superconducting Magnet Built by NIMS

Great strides have been made in the production of fields of the order of 20 T and above using the combinations of two metallic superconductors, namely the Nb–Ti and the A-15 Nb_3Sn. Having built world's first highest field 17.5 T all

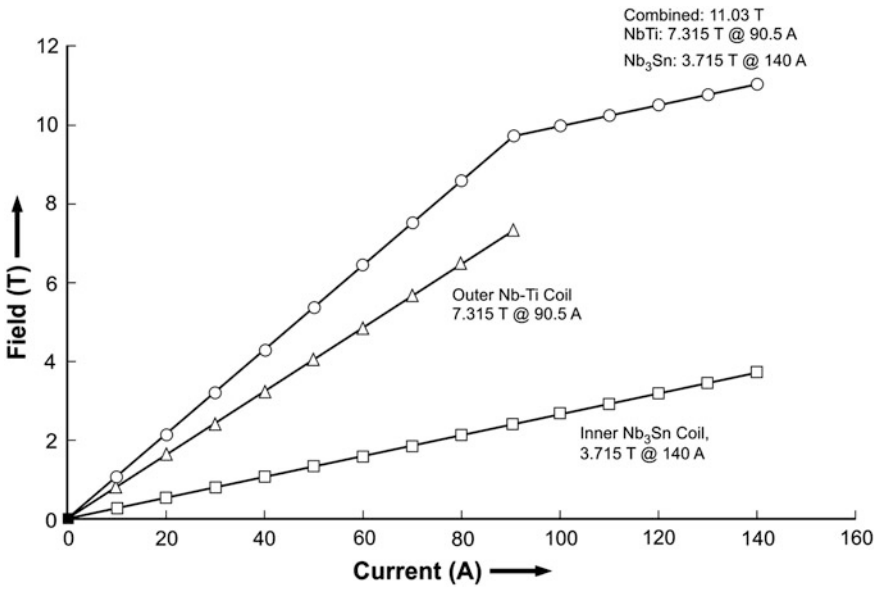

Fig. 7.23 The field versus current relationship for the Nb–Ti (*middle curve*) and Nb_3Sn magnet (*lower curve*). The *I-B* profile of the combined magnet is the *top curve* producing a field of 11 T [21]

superconducting magnet [22], the NRIM, Japan now called NIMS (National Institute of Material Science), has been a forerunner in enhancing this field steadily to higher than 21 T. The 17.5 T magnet was built using Nb_3Sn and an insert coil of V_3Ga developed by NRIM by diffusion process. With the improvement in J_c of Nb_3Sn through elemental additions, V_3Ga has been pushed to the background by Nb_3Sn which is comparatively cheaper also. The field was increased to 21.1 T [23] by NIMS in 1994 by using coils of Nb–Ti, (Nb, Ti)$_3$Sn and (Nb, Ta, Ti)$_3$Sn conductors. This magnet was an improvement over the earlier magnet built by NIMS [24] producing a field of 20.33 T in a clear bore of 44 mm. The new magnet replaced the inner most coil by a coil which was wound using (Nb, Ta, Ti)$_3$Sn conductor and following a 'wind and react process'. This conductor had much lower copper ratio of 0.48 in place of the earlier conductor which had a ratio of 0.8. This meant a much higher current density. Yet another innovation carried out was the removal of the SS former of this inner most coil. This made available a larger working bore of 50 mm and also prevented high stress between the former and the coil.

The new (Nb, Ta, Ti)$_3$Sn conductor was developed at NIMS wherein 0.5 at.% Ta has been added to Nb and 0.6 at.% Ti to the Cu–Sn matrix. These composite cores are bundled together in a Cu–Sn bronze tube and processed. These processed MF strands are stacked together in a Cu-tube, for stability, with a Nb diffusion barrier and reduced to desired size of the conductor. The outer-1 coil was wound using a Cu-stabilized rectangular cable having 11 twisted strands of (Nb, Ti)$_3$Sn and the

Table 7.4 Parameters of the 21 T Magnet built in 1994 at NIMS (data compiled from [23] with permission from Elsevier)

Magnet coil	Inner most $(Nb, Ta, Ti)_3Sn$	Middle $(Nb, Ti)_3Sn$	Outer-1 $(Nb, Ti)_3Sn$	Outer-2 (Nb–Ti)
Inner coil dia.	50 mm	180 mm	380 mm	801 mm
Outer coil dia.	151.2 mm	291.8 mm	725.6 mm	1175.8 mm
Coil length	220.3 mm	463.5 mm	1,230 mm	1,293.6 mm
Coil form	solenoid	31 double pancakes	40 double pancakes	41 double pancakes
Total no. of turns	1,760	1,364	1,520	2,296
Conductor dimensions	2.42 × 2.0 mm	6.0 × 2.0 mm	13.4 × 8.15 mm 11 strand ract. cable	13.8 × 6.0 mm 19 strand ract. cable
Process	Bronze process wind and react	Bronze process wind and react	Bronze process react and wind	Normal commercial process
Operating current	350 A	910 A	4,717 A	4,717 A
Field produced	2.5 T	3.6 T	Total (Both Coils) 15 T	
Total field	21.1 T @ 4.2 K			

outermost coil using a Cu-stabilized rectangular conductor of 19 twisted strands of Nb–Ti. The complete parameters of the magnet are given in Table 7.4.

The total magnet system is housed in a cryostat with two separate chambers in vacuum. The outer chamber houses the two outer coils and the inner chamber remaining two inner coils. The two outer coils were connected in series and jointly produced a field of 15 T. The middle coil generated an additional field of 3.6 T at an operating current of 350 A. The inner-most coil was run on an independent power supply and added another 2.5 T. The operating temperature was maintained at 1.8 K. The total field produced was 21.16 T, the highest ever reported using only the metallic superconductors, that is, without the use of a HTS insert coil. The complicated nature and the shear size of such magnet can be gauged from Fig. 7.24 where the assembly of a 21 T magnet [25] is going on at TML (NIMS). This particular magnet produced a field of 21.5 T field at 1.8 K in a clear bore of 61 mm good enough to accommodate an inner HTS coil to produce still higher fields.

7.8.2 Ultra High Field Superconducting Magnets

The production of very high or ultra high magnetic field is limited not so much by cost as by the stringent requirement of the superconducting material to carry high current in presence of intense magnetic field and to withstand very large electromagnetic forces (=BJR). Low Temperature Superconductors (LTS) based

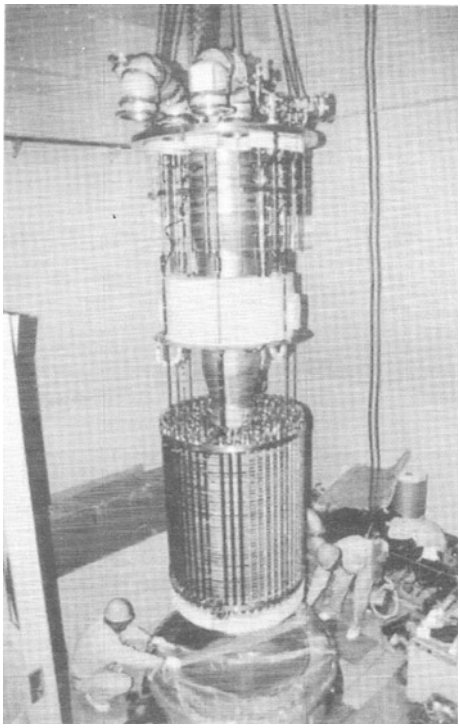

Fig. 7.24 The on-going assembly of the outer coils of a 21.5 T superconducting magnet at the Tsukuba Magnet Laboratory, Japan [25] (With permission from Elsevier)

magnets discussed in the last section seem to have saturated once at 21.5 T even when we operate them at superfluid helium temperature (1.8 K). The only hope to raise further this limit appears to be the HTS conductors. Even though, the dream of producing high magnetic field at 77 K has not been realized so far, yet these materials have shown promise in pushing the field limit well beyond 21.5 T, only if HTS magnets are operated at 4.2 K, their B_{c2} being very high. Their critical current values are very high at large field when operated at such low temperatures. One problem peculiar to HTS is the strong anisotropy of J_c with magnetic field direction. The current has to flow parallel to the wider surface of the tape conductor and the magnetic field should be parallel to the c-axis. Since the magnetic lines bend at the edge of the magnet, the field no longer remains parallel to the c-axis. The critical current density of the conductor decreases with angle of field orientation. J_c at the magnet-end and not at the mid-plane should therefore be found out after the dimensions of the coils are frozen. The conductor intended to be used is to be thoroughly characterized for its J_c with respect to field orientation. This is not the problem with LTS magnets. The next step is to produce these superconductors sufficiently flexible and with high stress tolerance through cladding with high strength material. Technology to produce HTS in long length needs to be upgraded.

The driving force to produce ultra high magnetic field using superconducting magnets has come from researchers from solid state physics, chemistry and the life

sciences. Availability of such intense magnetic field will lead to new phenomena, hitherto undiscovered in a variety of solids and also open up possibility of building ultra high field NMR spectrometers with unprecedented resolution. It will then be possible to study extremely complex molecular structure of proteins and similar species. The strategy to attain high field has been to generate maximum possible field by the suitable combination of the Nb–Ti and Nb_3Sn coils and using an inner most HTS coil as an insert. For highest field the magnet is operated at 1.8 K. Until recently, BSCCO 2212 and 2223 have been the favorite materials for winding the magnet coils. But during last few years REBCO coated superconductors with superior performance have been developed and marketed by a number of companies in USA and Japan. Record high field have been produced using these combinations. Below we discuss very briefly the most notable developments that have taken place in past few years.

7.8.3 A 24 T Magnet Using GdBCO Insert Coil

A team led by S. Matsumoto at TML, Japan had produced a record breaking field of 24 T in 2011. The details of this, all superconducting 4.2 K magnet, have been published recently [26]. The inner most coil has been wound using GdBCO thin film wire produced by Fujikura Ltd. Japan and vacuum-impregnated in wax. The beauty of the magnet is that it operates at 4.2 K instead of 1.8 K which is so much simpler to handle than a superfluid. The coil generates a field of 6.8 T at a current level of 321 A and a an electromagnetic force BJR of 408 MPa. The coil has a clear bore of 40 mm and is nested in a combination magnet of Nb–Ti and Nb_3Sn generating together a background field of 17.2 T. Some of the parameters of this magnet system are given in Table 7.5.

Table 7.5 Some parameters of the 24 T magnet coils [26] (With permission from Shinji Matsumoto and IOP)

Coil	Unit	Inner most coil
Conductor (tape)		(Gd–Ba–Cu–O)
Coil inner dia.	mm	50.27
Coil outer dia.	mm	112.80
Coil height	mm	88.33
Conductor dimensions (w × t)	mm × mm	5.00 × 0.15
Total no. of layers		124
Total no. of turns		2,010
Total conductor length	m	515
Operating current	A	360
Central field by the inner coil	T	7.6
Background field by Nb–Ti and Nb_3Sn coils	T	17.2
Total central field	T	24.8

As mentioned above a background field of 17.2 T is provided by a combination of Nb–T and Nb_3Sn outserts. The middle coil is a Nb_3Sn coil with 135.2 mm inner dia., 318.4 mm outer dia. and has a height of 440 mm. It produces a field of 8.2 T at an operating current of 241.1 A. The outermost coil is a Nb–Ti coil with an inner dia. of 330.3 mm, outer dia. 516.8 mm and a height of 710 mm. It produces a field of 9.0 T at an operating current of 241.1 A. The highest central field produced thus turns out to be 24. 8 T @ 4.2 K.

7.8.4 Recent High Field Magnet Developments at FSU

7.8.4.1 A 26.8 T YBCO Insert Coil

Yet another important development towards the goal of achieving 30 T field by using HTS inserts took place at FSU in 2007. The NHMFL in collaboration with SuperPower produced a coil using coated YBCO tape conductor. The coil produced a record field of 7.8 T in a background field of 19 T generated by a 20 MW, 20 mm bore resistive magnet [27] and yielded a combined field of 26.8 T. The coil had a clear bore of only 9.5 mm but it did establish the possibility of generating field in excess of 30 T HTS insert coil operated at liquid helium temperature, 4.2 K.

7.8.4.2 A Record Field of 32 T

FSU has already designed a whole superconducting magnet using inner insert coils of REBCO coated superconductor to produce a record field of 32 T in a 32 mm bore. It has already tested a REBCO insert coil producing a total field of 32 T [4, 5] in a 32 mm bore in a background field of 20 T generated by a resistive coil. This happens to be a world record of field produced by a combination of superconducting and resistive magnets at the present time. This is a landmark development and deserves to be discussed a bit in detail. These efforts were aimed at technology demonstration and resolve problems related to conductor behaviour under conditions of high field and high mechanical stresses, its I_c-B behaviour vis-à-vis field orientation and strain effect, the quench protection, the jointing of the conductor crucial to the stability of field required in NMR type applications and so on.

The first prototype of the 32 T magnet [28] has already been fabricated and tested in a back ground field 15.14 T produced by a set of Nb–Ti and Nb_3Sn LTS coils. The central REBCO coils generated a field of 17.4 T. The photograph of the REBCO coils with its support structure is shown in Fig. 7.25. Important parameters of the 32 T magnet are given in Table 7.6.

The paper [28] does not identify the rare earth 123 compound used for inner coils. It can be conjectured that various options of rare earth-123 compounds might have been evaluated. Two REBCO HTS coils nested one inside the other have been used. The inner HTS coil has an inner dia. 40 mm and outer dia. 140 mm and

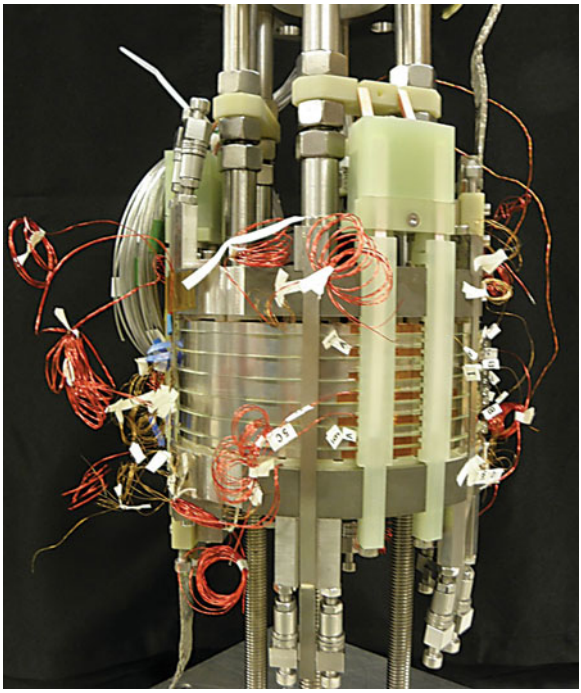

Fig. 7.25 A photograph of the 6-module prototype of coil 1 of the 32 mm bore multi-section 32 T showing the support structure and the instrument wiring [28] (*Courtesy*, H.W. Weijers, W. D. Markiewicz and D.C. Larbalestier, National High Magnetic Field Laboratory)

Table 7.6 Important parameters of the 32 T magnet (data compiled from [4, 28])

Parameter	Unit	Value
Working cold bore	mm	32
Total central field	T	32
Outer dia. of the HTS outer coil(2)	mm	232
Field by inner HTS coil (1) @ 180 A	T	11.0
Field by outer HTS coil (2) @ 180 A	T	6.4
No. of modules in coil (1) and coil (2)		20 and 36
Dimensions of REBCO tape conductor	mm × mm	4.1 × 0.17
Piece length for coil 1 and coil 2	m	60 and 110
Total conductor length used in coil (1)	m	2,758
Total conductor length used in coil (2)	m	6,621
Background field by Nb–Ti/Nb_3Sn coils	T	15.0
Operating current	A	180
Maximum conductor current density	A/mm^2	334
Maximum ramp rate (0–180 A)	A/sec	1
Maximum hoop stress	MPa	297
Design hoop stress	MPa	400

consists of 20 modules of double pancakes. The outer HTS coil has an inner dia. 164 mm and an outer dia. of 232 mm and consists of 36 double pancake modules. These dimensions are good enough to accommodate a dilution refrigerator. Availability of such high field and mK temperature range will undoubtedly open new frontiers of research in condense matter physics.

The HTS conductor is the coated tape of the size about 4.1 mm × 0.17 mm uninsulated. The tape conductor is co-wound with an insulated SS insulated tape which provided turn to turn insulation as well as mechanical strength through reinforcement. A double layer of G-10 provides module to module insulation and also sandwiches the encapsulated heaters used for quench protection. The inner and the outer HTS coils generate a field of 11 and 6.4 T respectively at an operating current of 180 A. The total stored energy in the two coils is 267 kJ and another 1.06 MJ is added due to the mutual inductance of the HTS coils and the LTS coils. The LTS magnet system along with the cryostat will be supplied by Oxford Instruments. The design allows the use of the LTS magnet system in stand-alone mode providing a field of 15 T in 250 mm cold bore. Both the magnet systems the REBCO and the LTS run on two separate power supplies and protected independently against quench.

The design of such magnet needed a vast amount of data on the conductor behaviour under extreme conditions of field, operating current and mechanical stresses, which was just not available. Quench protection to save the magnet at such high fields becomes a challenge. For stable fields extremely low resistance joints need to be developed. Since no such data existed, thorough studies were undertaken by FSU to generate first time data on numerous parameters crucial to the design of such a magnet.

The studies were aimed at investigating J_c/B behaviour of HTS at 4.2 K and variation of J_c with field, temperature, strain and field orientation. These parameters are critical to the magnet design. Crucial and unique to HTS, is the variation of J_c with field orientation. At the magnet ends, the field lines curve and make an angle with the direction of the field. J_c decreases with the angle and this variation has to be found out. It turns out that the limiting operating current of the inner HTS coils is not determined at high field mid-plane but at the magnet end. In this particular magnet design the field orientation angle is 18° at the magnet edge. A mathematical model [29] has been developed to study angular dependence of the J_c of REBCO tape under high magnetic field.

These studies have brought out interesting facts about HTS needed for magnet construction. These are summarized below.

- REBCO tapes have good irreversible strain of 0.6 % which stays at the lap joints of the tape if the overlapping length is more than 60 mm. For a given strain value the stress decreases as the amount of copper layer is kept 40–100 μm thick on a 50 μm thick Hastelloy tape. The tape also becomes soft with the addition of copper.
- The bare HTS tapes and wires supplied by the manufacturers need suitable electrical insulation. Metal oxide, UV-cured epoxy and Kapton have been

studied. The SS co-wind with a turn insulation was found to be a good winding technique. Sol-gel and UV cured epoxy have been found good as turn insulation on the SS strip. SS co-wind not only enhances mechanical strength but makes tape handling far more easier.

- Dry winding in double pancake structure involving number of steps and a large number of joints has been followed successfully. The winding is quite convenient as the REBCO tapes possesses large bending strain tolerance.
- The coils were operated at an average current density of 1.8 to 2×10^4 A/cm^2 (taking into account conductor thickness, copper fraction, inter pancake spacers and SS co-wind).
- The maximum stress in the winding was 400 MPa and the maximum strain 0.4 %.
- Winding lengths of the coils are determined as per the field and field uniformity requirement. Longer winding also cuts down radial component of the field. Inner coil uses a conductor length of 150 m per module and the outer coil 220 m.
- Passive quench protection system, good for LTS magnets, is no good for HTS because of the very low quench propagation velocities, high operating current densities and current sharing temperatures. The quench protection is provided by heaters distributed throughout the coils which have been found to be most effective. A quench detector activates the protective heaters the moment a quench is detected. Outer LTS coils have usual passive protection of resistors and diodes.
- The outer LTS coils and the inner HTS coils run on two separate power supplies.

After these exhaustive studies the magnet coils were designed, reduced-height prototypes fabricated and finally tested experimentally. The prototype coils have been successfully operated at current values higher than needed for 32 T field. It is expected that 32 T magnet will soon be a users' facility which will serve the world community for next 20 years or more.

7.9 Cryo-Free Superconducting Magnets (CFSM)

The biggest fall-out of the discovery of high temperature superconductors was the development of HT current leads capable of transporting large currents without Joule heating when operated below T_c. This development together with the availability of two stage Gifford-McMahon (GM) closed cycle refrigerator (CCR) of 1.5 W @ 4 K capacity led to the development of CFSM producing high fields. The HTS current leads have the twin advantage, one that there is no Joule heating across the leads and two that they behave nearly like a thermal insulator as superconductors have poor thermal conductivity, about 500 times smaller than OFHC. Since there is no hassle of producing and transferring liquid helium to the system, these

magnets have found wide spread popularity in a short time. A world record of 27.5 T by a hybrid magnet using a cryo-free outsert and the resistive magnet as an insert was established by IMR, Tohoku University, Sandai some years ago. Presently, CFSM producing field up to 20 T are available in the market.

The feasibility of a cryo-free magnet was reported by Hoenig [30] in 1983 who produced a field of 3.3 T using Nb_3Sn conductor and a 10 K two stage CTI-1020 CP Cryodyne cryocooler. This 12 kg Nb_3Sn magnet was operated at 14 K and produced a field of 3.3 T at a current density of 6×10^4 A/cm^2. It was, however, during 1990s when the HTS current leads became commercially available that massive development of CFSM, the world over, took place. There are numerous publications on CFSM we will just mention a few of them. A 6 T, 220 mm wide bore (room temperature) CFSM has been built by Watazawa et al. [31] using two sections of Nb–Ti coils. The weight of the magnet was 120 kg and had two sections. The inner section produces a field of 1.4 T and the outer section 4.6 T, both operating at a current of 152 A. Bi-2223 tubular current leads (ID = 20 mm × OD = 23 mm) have been used between the first and the second stage of the CCR. Two 4 K, GM cryocoolers were used to cool down the system. At the operating current of 152 A the heat load at the first stage turns out to be 42.8 W and 0.61 W at the second stage. The respective temperature at the two stages are 45 and 4.9 K. The magnet had an inductance of 35 H and a stored energy of 400 kJ.

Watanabe et al. [32] built a 52 mm room temperature bore CFSM which produced a field of 11 T. This magnet was the combination of an outer Nb–Ti coil and an inner Nb_3Sn coil and uses Bi-2223 current leads (same as in [31]). The magnet was cooled by a pair of 4 K GM cryocoolers. The coils were operated at 6 K at a current of 150 A which generated a central field of 11 T. The magnet parameters are given in Table 7.7. Each coil is protected against quench by a pair of diodes and a resistor of 2.9 Ω placed close to the respective coil. During the quench about 35 %

Table 7.7 Parameters of a 11 T cryo-free superconducting magnet (data compiled from [32])

Parameter	$(Nb, Ti)_3Sn$	Nb-47 wt% Ti
Conductor dimensions	0.9 mm (dia)	0.76 × 1.5 mm
No. of filaments	54	1,050
Filament dia.	90 μm	22 μm
Cu: SC ratio	0.87	1.9
Coil inner dia.	86 mm	187 mm
Coil outer dia.	177 mm	281 mm
Coil height	222 mm	225 mm
Operating temp.	6 K	6 K
Operating current	150 A	150 A
Field generated	6.4 T	4.6 T
RT Bore	52 mm	
Total central field	11 T	
Total inductance	19 (H)	
Total stored energy	215 kJ	

of the total stored energy of 215 kJ is adiabatically absorbed by the magnet system and the protective diode-resistor system. Coil temperature rises by 50 K. The magnet was charged up to 130 A at a ramp rate of 3 A/min, up to 140 A at 2 A/min and finally at 1 A/min up to 150 A. The ac loss mainly comes from the hysteresis in the superconductor and is of the order of 30 mW. The equilibrium temperatures at a field level of 10.5 T are, 4.8 K for both the coils, 4.7 K at the cold end (stage II) of the cryocooler and 59 K at the warm end of the current leads.

Of late, pulse tube cryocoolers (PTC) with 1.5 W cooling capacity have become commercially available. PTC have the advantage that there is no moving part in it like the displacer in the GM cryocooler. They are thus free from mechanical vibrations and from electromagnetic noise. These PTCs are preferred for experiments where vibrations are not acceptable and the noise level has to be small. Secondly, the life cycle is going to be much higher than 10,000 h. of free maintenance of the GM cryocoolers. The PTCs do consume large power in so far as about 6.5 kW power is required to produce 1.5 W of cold compared to 0.25 to 1 kW power required to produce 1 W of cooling by liquid helium. This cost is, however, more than off-set by net saving in helium cost and heavy investment if one has to install helium liquefaction facility.

A 5 T Nb–Ti magnet with room temperature bore of 50 mm was built by Giebeler et al. [33] in 2004 using a two stage PTC with a cooling capacity of 0.4 W @ 4.2 K. It is a compact 12 kg magnet, 190 mm in height and produces a field of 5 T at a charging current of 35 A. The PTC cools down the magnet to 2.7 K in 44 h. The minimum temperature attained is 2.4 K. The temperature stability at the first and second stage are 5 and 0.1 K respectively over a period of 21 days. The magnet runs in persistent mode. The persistent switch is cooled by the second stage of the PTC.

We would like to take-up the design and operation of a CFSM a bit in detail now. As an example, we again take up the construction of our own 6 T, 50 mm room temperature magnet which we built at our centre some years ago. Before we do that, let us discuss the crucial issues involved in the design and operation of a cryo-free magnet and which are generally not reported being a propriety item of the manufacturers.

7.9.1 Important Considerations for CFSM System Design

- The most important and foremost issue is that there is no longer a liquid helium bath which has large capacity to cool the magnet and absorb heat rather quickly. Cryo-free magnets are cooled by the second stage of the CCR through thermal conduction which is a slow process and depends upon the quality of the thermal contacts. A small thermal disturbance, if not dissipated to the CCR fast enough, may raise the temperature locally and quench the magnet.
- A thermal analysis of all heat loads to the two stages of the CCR must be carried out carefully before embarking on the design. Total heat loads should be reasonably below the refrigeration capacity of the two respective stages.

- The thermal shield and the magnet, the two heaviest components of the whole system, are cooled by the first stage and the second stage of the CCR respectively by thermal conduction only. Thermal contacts have therefore to be nearly perfect with least thermal resistances.
- Flexible OFHC braids often serve ideal material for thermal connections whether fixed mechanically or through soldering. Flexibility prevents stresses in the system during thermal cycles.
- The magnet should preferably use former made of copper. The former must have perforations and should have a slit along the entire length (including flanges) to minimize the eddy current heating during ramp-up and ramp-down of the magnet.
- The magnet is cooled via the top and bottom flanges of the former in thermal contact with the second stage. Cooling of coil starts from the outer and inner layers. Inter-layers should be avoided as this will slow down the thermal conduction making the layer to layer heat transfer inefficient.
- We recommend wet winding using stycast epoxy mixed with 15–20 wt% aluminum nitride (ALN) powder. Wet winding ensures fool-proof impregnation and ALN powder improves the thermal conductivity of the stycast. ALN also reduces the mismatch of the thermal contraction coefficients of the epoxy and the conductor, minimizing cracking under Lorentz forces during cooling.
- Since there is no bath to keep the magnet temperature constant, operating temperature has to be estimated at the target field. The magnet temperature rises from the zero current state as the magnet current is ramped up. A good temperature margin (>1 K) should be maintained between the operating temperature and the current sharing temperature.
- The maximum heat to the system comes from the current leads. In CFSM the current leads are hybrid, a combination of copper leads from room temperature to thermal shield and HTS leads from shield to the magnet connected with the second stage of the CCR. Heat input to the thermal shield consists of heat conducted from the room temperature top plate and also due to Joule heating within the copper leads. The copper current leads therefore should be optimized for the operating current to minimize Joule heating.
- Between the shield and the magnet, the current leads are HTS leads generating practically no heat. These leads are joined to the copper current leads. These contacts should have very low electrical resistance to minimize Joule heating. These joints should be anchored to the shield through spacers of material like ALN which are not only good electrical insulator but also good thermal conductor. The lower ends of the HTS leads are connected to the magnet and the second stage of the CCR.
- The performance of the CCR and the HTS leads deteriorate in presence of the magnetic field. A field profile of the magnet should therefore be carried out in advance so that the HTS leads and the CCR heads are positioned in low field areas where the stray field is below 0.1 T.
- An efficient quench protection system similar to one used with the bath-cooled magnets has to be designed such that the magnet temperature does not exceed

40–50 K after the quench. In these systems there is no helium gas pressure build-up at quench in contrast with the bath-cooled magnets.

7.9.2 The Design and Winding of the Magnet

To discuss the construction details of a CFSM system, we take up the example of a 6 T, 50 mm warm bore Nb–Ti magnet we built [34, 35] in our laboratory. The design considerations for the bore dia., field strength, current and number of turns and layers are the same as for any bath-cooled magnet, discussed in detail in Sect. 7.4. The major consideration here is that the operating temperature of the magnet is to be calculated from heat loads coming to the magnet from different sources for the given field, the three critical parameters of the conductor, T_c, J_c and B_{c2} being inter-dependent. The operating current is then chosen from the conductor I_c-B plots.

To have a warm bore of 50 mm we chose the inner winding dia. of 104 mm and a winding length of 200 mm on the basis of field homogeneity criterion. The outer winding dia.comes out to be 137 mm. At an operating current of 102 A the magnet should produce a field of 6 T. This current is 68 % of the short sample I_c value supplied by the manufacturer. We emphasize that the J_c and B_{c2} values quoted are at 4.2 k and at zero current. Similarly, T_c value is always quoted in zero field and zero current. For CFSM we have to find out the current sharing temperature, T_{cs} which is higher than zero current T_c. The current sharing temperature, T_{cs} is defined as the temperature at which the current starts flowing partly through copper. As the magnet current rises T_{cs} too starts rising. The temperature window to operate magnet becomes narrower. Values of T_c and T_{cs} can be estimated at different fields using following equations given by Lubell [36].

$$T_c(B) = T_c(0) - [1-(B/14.5)]^{0.59} \tag{7.19}$$

$$T_{cs}(B) = T_b + [T_c(B) - T_b]\left(1-J_{op}/J_c\right) \tag{7.20}$$

where $T_{cs}(B)$ is the current sharing temperature at a field B, T_b the operating temperature, J_{op} the operating current and J_c the critical current. The T_{cs} values and also the temperature margin for operating the magnet at 6 T field has been evaluated for different operating currents and are listed in Table 7.8. For an operating current of 102 A and an operating temperature of 4.2 K the T_{cs} for this 6 T magnet is 5 K. Thus the temperature margin ΔT is only 0.8 K. However if the magnet is operated at 3.3 K the ΔT goes up to 1.7 K. The T_c of Nb–Ti at 6 T is 6.71 K. The operating temperature should therefore be as low as feasible by reducing the heat leaks to the two stages of the CCR to a minimum. T_{cs} thus becomes an important input parameter for the magnet design calculations,

Table 7.8 Current transfer temperature T_{cs} at 6 T and different operating currents and the temperature margin, ΔT for Supercon 0.54 mm dia. Nb–Ti wire with I_c = 150 A @ 6 T, 4.2 K

Operating current (A)	% of I_c	T_b (K)	$T_c(B)$ at B = 6 T (K)	T_{cs} (K)	$\Delta T = T_{cs}–T_b$ (K)
50	33.3	4.2	6.71	5.86	1.67
90	60	4.2	6.71	5.204	1.0
102	68	4.2	6.71	5	0.8
135	90	4.2	6.71	4.45	0.25
150	100	4.2	6.71	4.2	0

The magnet is wound on a electro-tough pitch (ETP) copper former with a slit along the entire length. The slit reduces heat generation due to eddy current induced in the former during charging and discharging of the magnet. A layer of thin Kapton tape was wrapped on the former surface to make it electrically insulating. Supercon 0.54 mm dia. Cu/Nb–Ti wire was used for coil winding. We preferred wet winding using stycast epoxy mixed with ALN (aluminum nitride) powder as filler to improve it's thermal conductivity and reduce mismatch in thermal contraction values of the epoxy and the conductor. Since the cooling of the coil proceeds layer to layer, no inter-layer has been used which would have hampered layer to layer conductance. All the parameters of the magnet are given in Table 7.9.

Table 7.9 Parameters of a 50 mm warm bore CFSM built at author's laboratory [34, 35]

S. no.	Magnet parameter	Unit	Value
1.	Inner winding dia.	mm	104
2.	Outer winding dia.	mm	137
3	Winding length	mm	200
4	Inter-layer		None
5	Impregnation (wet winding)		Stycast with filler
6	Conductor used		MF Cu/(Nb–Ti)
7	Wire dia.	mm	0.54
8	No. of filaments		54
9	Filament dia.	μm	38
10	Cu/Nb–Ti ratio		2.0 ± 0.2:1
11	Total conductor length	km	4.1
12	No. of layers		32
13	No. of turns/layer		370
14	Peak field	T	6.2
15	Current at peak field		105.3
16	Field factor (T/A)		0.0588
17	Stored energy at peak field	kJ	31.04
18	Quench protection (dump resistor)	Ω	0.5

7.9.3 Current Lead Design

The optimization of the copper part of the hybrid current leads is crucial in so far as it determines the heat input to the top plate of the thermal shield and its temperature. This directly affects the minimum temperature reached at the second stage and hence the operating temperature of the magnet. Please remember that there is no helium vapour cooling available like in bath cooled magnets. Optimization of conduction cooled current leads can be done using following equations given by the McFee model [37].

$$\frac{Q_{\mathrm{OPT}}}{I} = \sqrt{L_0\left(T_W^2 - T_C^2\right)} \tag{7.21}$$

$$\left(\frac{IL}{A}\right)_{\mathrm{OPT}} = \frac{1}{\sqrt{2}} \int_{T_c}^{T_W} \frac{k(T)dT}{\sqrt{L_0\left(T_W^2 - T_c^2\right)}} \tag{7.22}$$

where Q_{OPT} is the optimized heat flow, L_0 the Lorenz number, T_W and T_c are the temperatures at the warmer end and the colder end of the copper lead respectively. I is the lead current, L and A are the length and the area cross-section of the lead respectively. $k(T)$ is the temperature dependent thermal conductivity of the lead material. Using (7.21) Q_{OPT} for a lead carrying current between 300 and 33 K comes out to be 47 mW/A. Substituting appropriate values of the different parameters, in (7.22) the lead parameter, IL/A for copper of RRR 150 purity turns out to be 4.5×10^6 A/mm^2. Thus for a current lead of area cross-section 15 mm^2 and optimized for 85 A, the length should be 800 mm. Calculations show that for values of RRR 50 to RRR 300 the lead parameter is same at all temperatures from 300 K down to 30 K.

7.9.4 The Cryostat Design

The CFSM system is schematically shown in Fig. 7.26 which basically consists of a wide body SS vacuum chamber. The CCR sits off-the-centre on the top plate of the chamber. The top plate of the cylindrical thermal shield, made out of ETP copper, was suspended from the top plate of the chamber using G-10 strips. This plate is thermally connected to the first stage of the CCR using copper braids. Indium gaskets have been used at all the contact interfaces to reduce thermal resistance. The magnet is mounted on a slotted ETP copper plate which is thermally anchored, mechanically, to the cold head of the second stage of the CCR through sixteen semi flexible copper strips (20 mm × 2 mm). Apiezon N grease mixed with copper powder is used at the interface to improve thermal conduction. The magnet, weighing about 15 kg, is supported by G-10 strips from the top of the shield as

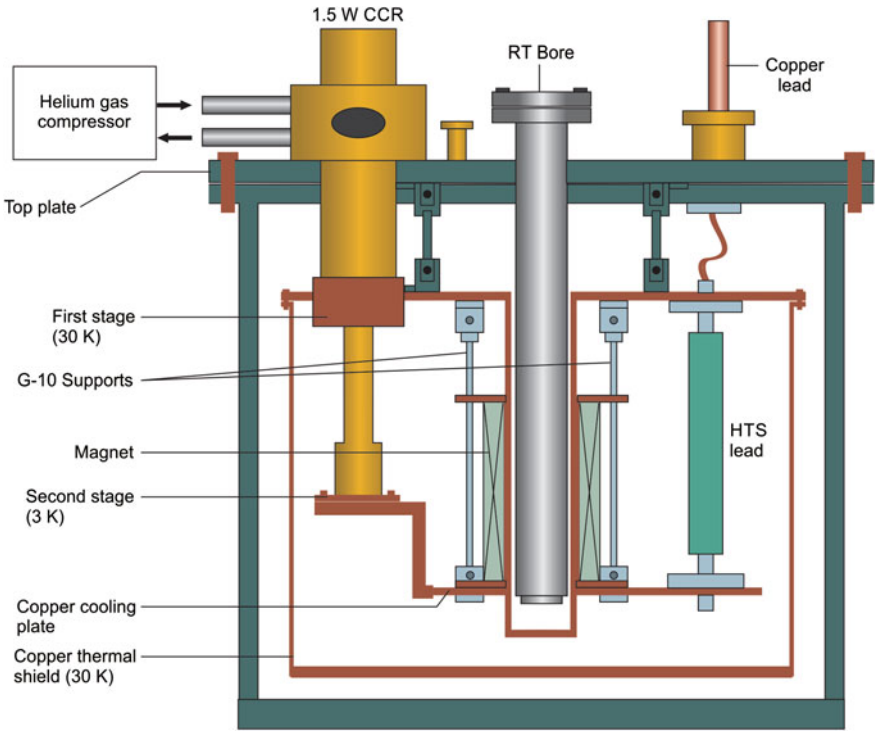

Fig. 7.26 A schematic diagram of a 6 T CFSM system built in author's laboratory at IUAC [34, 35]

shown in Fig. 7.26. The total thermal mass directly cooled by the second stage cold head is about 17 kg which consists of the former, Nb–Ti coil and the heat transfer plate. A pair of hybrid current leads. consisting of pure copper leads in the warmer region (between top plate and the shield) and HTS leads in the colder region (between shield and the magnet) are used to charge the magnet. The copper part of the leads was optimized for an operating current of 102 A between 300 and 35 K using Mcfee model [37]. The dimensional parameter, (*IL*/*A*) for copper of RRR 150 turns out to be 4.4×10^{-6} A/mm^2. For a 15 mm^2 cross-sectional area the length of the lead has to be 650 mm. The heat load per lead works out to be 4.7 W. It is a good idea to simulate the experiment in advance with a dead mass of weight equal to the magnet and find out the different heat loads static and dynamic with and without the magnet current. This will help to know the temperature of the shield and optimize the copper current leads correctly. We carried out such simulation for this magnet [38]. The complete assembly of the system is shown in Fig. 7.27. The entire system hangs from the top plate of the vacuum chamber. Copper current leads (in braid form) are joined with the copper braid terminals of the HTS inside a copper bush with lead-tin solder. These joints are thermally anchored to the top plate of the thermal shield and electrically insulated through the use of ALN disc spacers.

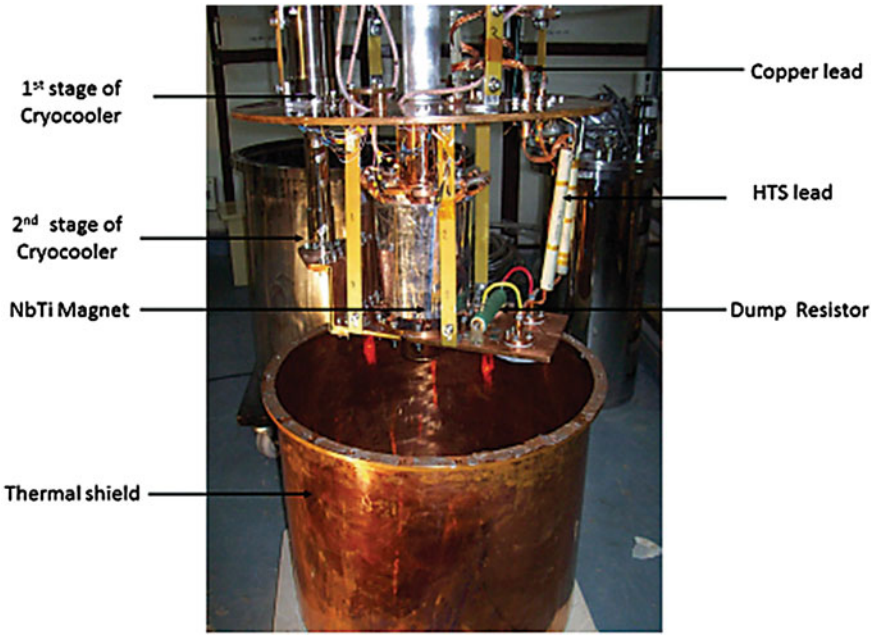

Fig. 7.27 The photograph of the inner assembly of the 6 T CFSM built at IUAC. The top plate of the vacuum chamber and thermal shield, HTS current leads and shield chamber, are visible (*Courtesy* IUAC Delhi)

Similarly, the lower ends of the HTS leads (copper braids) are soldered to Nb–Ti wire terminals and anchored to the heat transfer plate using same type of copper block and ALN spacer. This plate is already thermally connected with the second stage of the CCR.

Figure 7.28 is the photograph of the complete CFSM system with central RT bore and all feed thrus. The Bi-2223 HTS leads, (model CSL-7/120.1) were bought from CAN Superconductors. The conductive heat leak through the lead pair between 64 and 4 K is 20 mW. Silicon diode temperature sensors have been mounted at several locations of the system to monitor temperature for carrying out thermal analysis later.

7.9.5 Operating the Magnet

It is advisable to test the magnet and train it in a liquid helium bath cryostat before being installed in the cryo-cooled chamber. This 6 T magnet was tested in bath cryostat and energized at a slow rate 3A/min. The first quench occurred at 80.1 A (4.7 T), second at 87.2 A (5.15 T) and third at 99 A (5.85 T). Finally, the magnet produced a field of 6.2 T at a current of 105.2 A without quench. After the training,

Fig. 7.28 The photograph of the complete CFSM system with central RT bore and all feed-thrus (*Courtesy* IUAC Delhi)

the magnet was charged at a sweep rate of 30 A/min to 6 T without quench. The B-I_{op} data obtained and quench positions are plotted in Fig. 7.29. After the magnet was tested and trained up to 6 T it was dismounted from the test cryostat and was transferred to its new destination within the vacuum chamber. The performance details can be found in [39]. All the components of the system in the final configuration are shown in Fig. 7.27. After ensuring all the lead connections, proper mounting of the thermal transfer plates to the two stages of the CCR, the vacuum chamber was evacuated to 10^{-5} mbar. The magnet cools down to a minimum of 3.3 K in 15 h. The vacuum at this temperature improves to 10^{-9} mbar. The equilibrium temperatures of the cold head, magnet cooling plate and the copper anchor recorded are 2.75, 3.1 and 4.5 K respectively. The difference between the temperatures of the cold head and the outer layer of the magnet is only 0.6 K. The thermal shield temperature stabilizes at 35. 7 K.

The magnet was energized in steps of 10 A at a ramp rate of 3 A/min. up to 102 A corresponding to the field 6 T. Magnet quenched at 87 A and 102 A during the first run of this system. Temperature of the magnet rose to 41.5 and 54 K after the quench at the two current values respectively. Magnet, however, cools down to

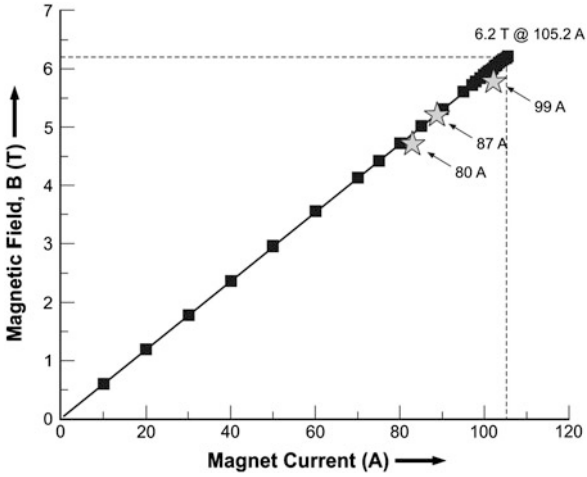

Fig. 7.29 Training of the magnet in liquid helium bath. Maximum field produced 6.2 T @ 105.2 A. Magnet quenched at 80, 87 and 99 A during training [39]

3.3 K, the operating temperature in just 40 min. We find the maximum workable ramp rate to be 6A/min. Beyond this value the heat generation caused by the AC losses and the induced eddy currents exceeds the heat extraction rate of the CCR. This is because of the inherent thermal resistances at the current lead joints. At 102 A current the magnet stabilizes at 4 K and the cold head at 3.13 K. Temperature at the lower end lead joint too goes from 4.5 to 6.6 K at 102 A. This temperature rise is due to the Joule heating of the copper braid which connects the HTS lead with the magnet. With a resistance of 10 μΩ the braid generates 210 mW of heat at 102 A. Estimates show that static heat load at the first stage without lead connection is only 14.6 W and goes up to 19.8 W after lead connections but no current and to 25.3 W at 102 A in the leads.

An elegant and systematic electro-thermal analysis of the heat load transferred to the two stages of the CCR by various sources has been carried out by Kar et al. [40]. The entire magnet system from room temperature to magnet has been reduced to a network of electrical and thermal resistances as detailed in Fig. 7.30. Electrical contact resistances of all the joints were measured experimentally. Thermal resistances were calculated from the measured temperatures at appropriate places and using thermal conductivity of the material. It turns out that the heat input to the first stage comes mainly from the optimized copper current leads followed by warm end cu-braid, Cu–Cu joints and Cu–HTS joints. All these heat inputs show an increase with magnet current. Similarly high heat input to the second stage comes from heating of the lower copper braid, followed by Cu–HTS joints and Cu–Nb–Ti joints, all again going-up with the increase of magnet current. Heat generated in HTS leads is less than 5 mW and stays current independent.

Above discussion clearly establishes the fact that it is extremely important to design the hybrid current leads meticulously so that the heat inputs to the two stages of the CCR are well within their cooling powers. All the inter-lead joints should have low contact resistance producing minimum heat. Anchoring to thermal shield

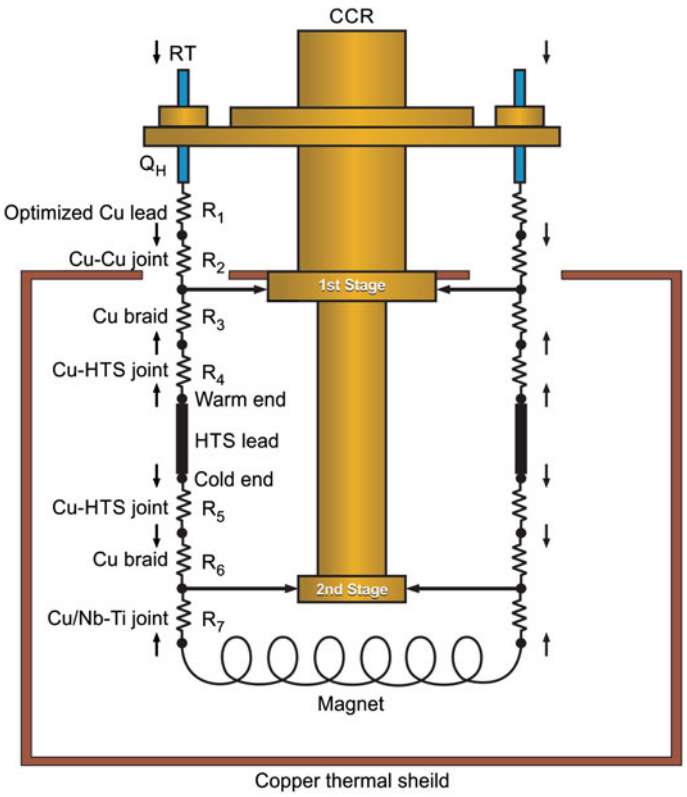

Fig. 7.30 The resistance network model used to calculate heat loads to the first and second stage of the CCR, generated by various resistances and joints [38]

and magnet cooling plate have to be perfect. Technology to built cryo-free magnets producing field up to 20 T is well established by now. Looking at the great developments that are taking place in the production of superior quality HTS conductors in long lengths and similar development in high power CCRs, a day is not far when cryo-free magnets producing 30–50 T field will be a reality and much sooner than expected.

References

1. G.B. Yntema, IEEE Translations on Magnetism, **MAG-23**, 390 (1987)
2. H.T. Coffey, J.K. Hulm, W.T. Reynolds et al., J. App. Phys. **36**, 128 (1965)
3. J.E. Kunzler, E. Buehler, F.S.L. Hsu, J.H. Wernick, Phys. Rev. **6**, 89 (1961)
4. W.D. Markiewicz, D.C. Larbalistier, H.W. Weijers et al., Magnet Technology, MT-22, 2CO-8, (2011), IEEE Trans. App.Supercond., **22**, 4300707 (2012)

5. U.P. Trociewitz, M. Dalban-Canassy, M. Hannion et al., Appl. Phys. Lett. **99** (20), 202506 (2011)
6. Ulf P. Trociewitz, M. Dalban-Canassy, M. Hannion et al., 35.4 T field generated using a layer-wound superconducting coil made of (RE)$Ba_2Cu_3O_{7-x}$ (RE = Rare Earth) coated conductor, http://arxiv.org/ftp/arxiv/papers/1110/1110.6814.pdf
7. R.W. Boom and R.S. Livingston, Proc. IRE **50**, 274–285 (1962)
8. Ch. Fabry, L'Eclairage Electrique **17**, 133 (1898)
9. Ch. Fabry, J. Phys. **9**, 129 (1910)
10. D.B. Montgomery, *Solenoid Magnet Design* (Wiley, New York, 1969)
11. H. Brechna, *Superconducting Magnet System* (Springer, New York, 1973)
12. M.N. Wilson, *Superconducting Magnets* (Clarendon Press, Oxford, 1983, 1986, 1989)
13. Y. Iwasa, *Case studies in Superconducting Magnets- Design and Operational Issues* (Plenum Press, New York, 1994)
14. K.H. Mess, P. Schmüser, S. wolff, *Superconducting Accelerator Magnets* (World Scientific Hemberg, 1996)
15. S. Kar, Rajesh. Kumar, Manoj Kumar et al., Ind. J. Cryo. **32**, 131 (2007)
16. B.J. Maddock, G.B. James, Proc. IEE **115**, 543 (1968)
17. Rajesh Kumar, S.K. Suman, A. Mandal, INPAC -2011, http://www.iuac.res.in/InPAC2011/proceedings/InPAC2011%20Proceedings/poster16Feb2011.html
18. R.G. Sharma, Y.S. Reddy, R.B. Saxena et al., in *A Superconducting Magnet System for 100 MHz NMR Spectrometer, Advances in Instrumentation* eds. by B.S. Ramprasad, S. Ashokan, K. Rajanna, N.C. Shivaprakash. Proceedings of International Conference Instrumentation (ICI-1996), August 8-10, Bangalore, India
19. T. Kiyoshi, M. Kosuge, K. Innoue, H. Maeda, Phys. B **216**, 196 (1996)
20. R.G. Sharma, Y.S. Reddy, M.M. Krishna et al. *News item NPL Develops Nb_3Sn Magnet Technology* (NPL (India) Technical Bulletin, April 1992), p. 14
21. R.G. Sharma, R.B. Saxena, M.A. Ansari, *An 11 T Nb–Ti/Nb_3Sn Magnet* (Research Report, NPL (India), 2003)
22. K. Tachikawa, Y. Tanaka, K. Inoue et al., 17.5 Tesla Superconducting Magnet. J. Cryogenic Soc. Japan **11**, 252 (1976). (in Japanese)
23. M. Oshikiri, K. Inoue, T. Kiyoshi et al., Phys. B **201**, 521 (1994)
24. T. Kiyoshi, K. Inoue, K. Itoh et al., IEEE Trans. App. Super. **3**, 78 (1993)
25. T. kiyoshi, M. Kosuge, K. Inoue, H. Maeda, Physica, **B 216**, 196 (1996)
26. S. Matsumoto, T. Kiyoshi, A. Otsuka et al., Supercond. Sci. Technol. **25**, 025017 (2012)
27. D. Larbalestier, New Magnet Lab. record promises more to come, News and press releases, August 7, 2007 www.magnet.fsu.edu/mediacenter/news/pressreleases/2007august7.html
28. H.W. Weijers, W.D. Markiewicz, A.J. Voran et. al., IEEE Trans. App. Supercond. **24**, 5 (2013)
29. D.K. Hilton, U.P. Trociewitz, H.W. Weijers, D.C. Larbalestier (FSU, To be published)
30. M.O. Hoenig, IEEE Trans. Magn. **MAG**-19, 880 (1983)
31. K. Watazawa, J. sakuraba, F. Hata et al., IEEE Trans. Magn. **MAG-32**, 2594 (1996)
32. K. Watanabe, S. Awaji, J. Sakuraba et al., Cryogenics, **36**, 1019 (1996)
33. F. Giebeler, G. Thummes, K-J. Best, Supercond. Sci. Technol. **17**, S-135 (2004)
34. S. Kar, P. Konduru, R. Kumar et al., Advances Cryo. Engg. **57A**, 597 (2012)
35. S. Kar, P. Konduru, R. Kumar et al., Advances Cryo. Engg. **57A**, 909 (2012)
36. M.S. Lubell, IEEE Trans. Magn. **19**(3), 754 (1983)
37. R. McFee, Rev. Sci. Instrum. **30**, 98 (1959)
38. S. Kar, A. Chaudhury, P. Konduru et al., Ind. J. Cryog. **35**, 246 (2010)
39. P. Konduru, S. Kar, M. Kumar et al., Ind. J. Cryo. **36**, 81 (2011)
40. S. Kar, P. Konduru, R.G. Sharma et al., IEEE Trans. Appl. Super. **23**, 4800507 (2013)

Chapter 8
Superconducting Magnets in Accelerators

Abstract Particle accelerators and high field superconducting magnets had been the greatest promoters of each other. In accelerators, RF power is used to boost the beam energy through the use of superconducting (RF) cavities. Bending, focusing and steering of the beam is provided by superconducting magnets. Fundamentally, an accelerator can either be of circular type or linear. Circular accelerators like LHC (Large Hedron Collider) are suitable for heavy ions like protons because the energy loss caused by synchrotron radiation in a circular accelerator varies inversely to the fourth power of the mass of the ion. Brief discussion on the superconducting colliders built and operated, namely, Tevatron, HERA, SSC, RHIC prior to LHC have been given in the chapter. LHC magnets have been discussed in greater details. LHC, world's most powerful particle accelerator has been in operation since 2009 and has yielded vast data and has confirmed the existence of Higgs boson. Parameters of the collider magnet system and the specifications of the conductor used are presented. Innovative magnet designs and development of superior conductors have been included. Linear accelerator, is the choice for light particle like electrons and positrons. An international effort has been made to build a 31 km long linear collider named ILC (International Linear Collider) for colliding electrons and positrons with a collision energy of 500 GeV ($\sim$1 TeV in future). The chapter ends with a brief description of the magnets in cyclotrons. World's first superconducting cyclotron of the class K-500, world's biggest cyclotron, K-1200 (both at MSU) and the world's biggest ring cyclotron, RIKEN SRC K-2500 have been described. K-1200 can accelerate U to 90 MeV and the SRC K-2500 up to 350 MeV.

8.1 The Accelerators

Great advancement made in the development of superconducting magnet technology led to their application to particle accelerators enabling them to go to higher and higher beam energy. High energy accelerators, in turn, have been responsible for the unprecedented growth in the production of superconducting cables carrying

R.G. Sharma, *Superconductivity*, Springer Series in Materials Science 214,
DOI 10.1007/978-3-319-13713-1_8

several thousands of ampere current with high stability and low a c losses. It looks, as though, the two technologies have been moving in tandem.

In an accelerator, the beam is accelerated by pumping RF through superconducting radio frequency (SCRF) cavities (mostly Nb) to produce high voltage gradient. High energy accelerators built are mainly either of circular or linear configuration. In both types of accelerators the beam is accelerated in an array of SCRF cavities but differ in several other aspects. In a circular accelerator, the beam travels through the SCRF cavities arranged in a nearly circular path. Dipole magnets are used for bending the beam by producing appropriate and very precise field transverse to the beam path. As the beam particles travel through the cavities repeatedly they gain energy and their velocity increases. The accelerating field in the cavity too is adjusted accordingly. For higher energy the magnetic field has to be adjusted to keep the particle moving in the same trajectory. Once the velocity approaches relativistic value equal to the speed of light, c, the RF frequency stays constant. This design of accelerator has been followed in colliders in which two energetic beams traveling in opposite directions collide to produce particles that were not seen before. The most famous of such colliders is the LHC (Large Hadron Collider) build and operated at CERN (European Organization for Nuclear Research) to accelerate two protons traveling in counter clockwise directions to acquire an ultimate energy of 7 TeV and collide to produce a collision energy of 14 TeV. LHC installed in a 27 km long tunnel used earlier by the LEP (Large Electron-Proton Collider) has been successfully operating since Sept. 2009. The first collision between two 3.5 TeV beams was observed in March 2010 and the long sought after Higgs boson was observed in Nov. 2012.

The difficulty with the circular accelerators, however, is that the relativistic particles emit radiation while traveling perpendicular to the field in the bending region. This results in a significant loss of energy as the energy loss is found to be proportional to E^4. The size of the machine is therefore greatly increased. Further, the energy loss also scales with the rest mass of the radiating particle as $1/m^4$. For this reason alone the energy in LEP never reached beyond 200 GeV even after up-gradation till it was retired in Nov. 2000. Circular accelerator are thus suitable to accelerate heavy particles only, like protons in LHC.

Linear accelerators (linac) are preferred to accelerate light particles like electrons and positrons. Here the beam is accelerated in a straight line trajectory. The energy is proportional to the accelerator length as the beam travels through a cavity only once. In a linear collider two beams are accelerated in two opposite directions and made to collide at the intersection point (IP) and discarded into the beam-dump. A new bunch is used each time. The advantage of the linac is that there is no energy loss due to synchrotron radiation. The energy is proportional to the number of RF cavities and the gradient of each cavity but does not depend on particle mass. Maximum luminosity is obtained by increasing the frequency of collision and reducing the area cross-section of the beam.

Cyclotrons are yet another type of accelerators which can accelerate heavy ion like U to high energies up to 350 MeV and the superconducting magnets again play a pivotal role in achieving such high energies. The ion circulate spirally under the

influence of a vertical magnetic field and an RF across two gaps between two dees. The RF frequency matches with the cyclotron frequency of the charged particle and accelerate it each time it crosses the gap. The beam is finally extracted through an extraction system and used to bombard targets for the production of radio isotopes.

In this chapter we will focus on the role of superconducting magnets in both these types of accelerators with special reference to LHC and the future ILC.

8.2 Role of Superconducting Magnets in Accelerators

Superconducting magnets have become the essential part of all types of accelerator design. Successful operation of LHC owes much to the high field superconducting magnets used along its 27 km circumference. LHC is using more than 1,600 superconducting dipole and quadrupole magnets in addition to other magnets. The future ILC (International Linear Collider) will have as many as 715 superconducting quadrupole magnets and 1,374 correctors. Besides many other types of magnets, the dipole magnets and quadrupole magnets constitute the backbone of any high energy accelerator. To achieve transverse field the dipoles are made of long saddle shaped coils or the simpler racetrack coils and are installed in two halves all along the entire curved part of the ring. Quadrupole superconducting magnets are used to keep the beam well-focused. In addition, there are higher order magnets, the correctors, to compensate for the field errors arising in the main dipoles and quadrupoles. These field errors are caused by the persistent magnetization currents generated in superconducting filaments during field ramping and also by the manufacturing errors/tolerances.

Circular accelerators are built in long underground circular tunnels so that the beam keeps circulating to get repeated acceleration in SRF cavities by the accelerating voltage. The beam energy obtainable in a relativistic accelerator is approximately given by the equation $E = 0.3\ B_{\text{dipole}} \times R$, where E is the energy in TeV, B_{dipole}, the dipole field in tesla and R the effective radius of the tunnel in km. For high energies, therefore it is imperative to have very long tunnels and high magnetic field depending on the budget available. All pervading Nb–Ti/Cu cables have been used in almost all the modern high energy accelerators. This superconductor has an upper limit of producing field of 9 T when operated below 2 K. For field 10–15 T, attempts are being made to develop Nb_3Sn magnets. Some proto type Nb_3Sn dipoles and quadrupoles have already been built and tested primarily at Fermi Lab. (USA).

An excellent and comprehensive book has been written by Mess, Schmuser and Wolff [1] on all aspects of superconducting accelerator magnets. Readers will find detailed description of field calculations, design and construction of the magnets, quench protection, electromagnetic forces, mechanical and field accuracies, collaring and warm and cold yoke. A useful review article had also been published earlier by Schmuser [2].

8.3 High Energy Accelerators Using Superconducting Magnets

Below we give a brief account of all the superconducting accelerators built prior to LHC. The experience gained through the operation of these accelerators led to the design and construction of the most powerful accelerator LHC which promises to unravel the mystery of matter.

8.3.1 Tevatron

Tevatron was the first high energy hadron collider built at Fermi National Accelerator Laboratory (FNAL), near Chicago, USA using superconducting magnets and commissioned in 1983. It was a proton–antiproton collider which achieved an energy of 1 TeV. It had warm iron yoke putting less low temperature load but high heat input to the cold mass. The entire EM forces are taken by the collars. It accelerated protons and anti-protons in a ring of 6.3 km circumference. By 1987, it attained a beam energy of 0.9 TeV thus a collision energy of 1.8 TeV, the highest energy ever attained till that time. It used 774 dipoles each 6 m long, 224 quadrupoles magnets and several correcting magnets. The dipoles generated a field of 4.4 T at 4.4 K. Cu/Nb–Ti cables had been used for magnet coils. Tevatron has been shut since September, 2011 especially because Large Hadron Collider (LHC) at CERN started operation and will be producing much higher collision energy (7 + 7 TeV). Nevertheless, Tevatron has become a trend setter for building high energy beam colliders using high field superconducting magnets. Over more than two and half decades of operation, this collider yielded profound data of 500 trillion collisions from year 2001 onwards. The analysis of the data led the Fermi Lab. team of researchers to believe strongly the possible existence of all illusive Higgs Boson which has since been confirmed from LHC's data.

8.3.2 HERA (Hadron Electron Ring Accelerator)

Soon, the technology of building hadron collider using superconducting magnet was adopted by DESY (Deutsches Electronen Synchroton), Hemberg, Germany to built their electron—proton beam collider, HERA. The accelerator started operations in 1989 and continued until it was shut down in 2007. Unlike the Tevatron the HERA had a cold iron yoke enclosing the high strength Al-alloy ($AlMg_{4.5}Mn$) collars. It was installed in a tunnel 6.3 km long and up to 25 m deep underground. It had two storage rings mounted one at the top of other. Normal room temperature magnets had been used in the electron storage ring which ran below the proton storage ring. Superconducting magnets have, however, been used in the proton ring

only. The proton ring employed 422 main dipole magnets to provide 5.3 T field for beam bending and 244 main quadrupoles for beam focusing. Four dipoles, four quadrupoles, six sextupoles and correction magnets were grouped together as one 47 m long module along the curved path. These magnets had two layered coils and operated at 4.2 K. The electron ring used conventional magnets, 456 main dipoles providing a field of 0.17 T and 605 main quadrupoles. One dipole, one quadrupole, one sextupole and a few correction dipoles were grouped into a 12 m long module. Old accelerators were used to pre-accelerate the proton beam. The last accelerator was PETRA which accelerated the electron beam to 14 GeV before injection into HERA. Sixteen four cell cavities with an accelerating field of 5 MV/m were used to accelerate the beam to a final energy of 0.92 TeV.

8.3.3 SSC (Superconducting Super Collider)

The SSC was the most ambitious collider project conceived during mid 1980s in USA and finally sanctioned in 1991. The project was, however, abandoned due to high cost involved, just 2 years later. It was aimed at accelerating proton to 20 TeV energy thus producing a collision energy of 40 TeV. It was to be a chain of five accelerators pre-accelerating proton to 2 TeV before being finally injected into the SSC. It was to be a two race track like rings with 70 cm separation. More than a total of 9,600 superconducting magnets were envisaged to be used. These included 7,860 main dipoles, 1,360 main quadrupoles, many corrector magnets and 648 special magnets for directing beams to six collision points. The design and development work on dipoles was carried out by Fermi Lab. and BNL (Brookhaven National Lab). The R&D work on quadrupoles was done by LBL (Lawrence Berkeley Laboratory). The dipoles were 16.6 m long to produce a field of 6.6 T at 4.35 K, whereas the quadrupoles were 3.3 m long and to produce a field gradient of 230 T/m at 4.35 K. The dipoles were two layered Cosine θ coils wound using Cu/Nb–Ti cable with an inner diameter of 4 cm. Coils were collared and closed with a split yoke consisting of lamination of the arc accurately die-punched sheets of low carbon steel and 1.5 mm thick. Yoke too formed the part of the cold mass cooled by supercritical helium at 4.15 K at 4 atm. pressure. Many full scale magnets were built and tested successfully for their critical performance as per the quality assurance codes. Many problems related to quench and training were solved. Alas ! the project was dropped soon after it was sanctioned for lack of funds.

8.3.4 RHIC (Relativistic Heavy Ion Collider)

RHIC was built by Brookhaven National Lab, (BNL), Upton, USA. It has been under operation since 1999. Until 2010 it was the highest energy collider in the world, now taken over by LHC at CERN. But it is the only collider which

accelerates spin polarized protons. Positively charged heavy ions and/or protons circulate in opposite directions at 99–99.5 % of the speed of light, in two independent rings, hexagonal-shaped and 3.8 km in length. A total of 1,740 superconducting magnets have been used in the two rings. Dipoles produce a field of 3.46 T at an operating current of 5.1 kA. Out of 1,740 magnets, 396 are the main dipoles and 492 quadrupoles. Rest of the magnets are the corrector magnets. The dipole magnet is 9.45 m long, the coil I.D. 80 mm and O.D. 100 mm. The inner and outer diameters of the yoke are 119.4 and 266.7 mm respectively. An important feature of the magnets of RHIC is that there are no separate collars between the coils and the yoke. The yoke itself serves the purpose of collars and provide required pre-stress to the coil. The yoke is the part of the cold mass. The collision between gold ions resulted in a record temperature of more than 4 trillion K creating conditions that might have existed moments after the 'big-bang'. It has six intersection points where the heavy ions up to gold collide and produce an energy of 0.1 TeV per beam. RHIC upgrade will facilitate collisions between positively charged and negatively charged particles.

8.3.5 LHC (Large Hadron Collider)

LHC is the world's largest particle accelerator, built by CERN at Geneva Switzerland. It has a tunnel 27 km long and 50–175 m deep underneath the border between France and Switzerland. At full potential it will accelerate proton beams rotating in opposite directions to an energy of 7 TeV. Two proton beams will then collide at four intersection points and produce a collision energy of 14 TeV. LHC has so far attained a level of 4 TeV/beam. It will attain its full potential of 7 TeV/beam by the end of 2014. Proton beams are pre-accelerated by old SPS (Super Proton Synchrotron) to 450 GeV before being injected into the LHC. SPS uses normal magnets. The yearly data generated is several peta-bytes which is analyzed in 140 computing centres spread over 36 countries and connected by the world's largest computing grid.

The LHC has used about 6,000 superconducting magnets, out of which 1,232 are the main dipoles along the curved path of the beam pipe. These are 15 m long with 56 mm inner diameter. The number of quadrupole magnets is about 400 and the rest are different types of magnets including multi-pole corrector magnets. All the magnets are divided into 8 sectors for operation powered by 8 power supply systems. Each sector has 154 main dipoles and 45 quadrupoles. The dipoles produce a field of 8.34 T. To produce such high fields using Cu/Nb–Ti cables the magnets are operated at a reduced temperature of 1.9 K using superfluid ^{4}He. The conductor is a Rutherford cable 15.2 mm wide with 36 strands of 0.825 mm diameter and each strand having 6,425 filaments of 6 μm dia. One unique feature of LHC is that the main magnets around the two beams are collared together and contained in one yoke. This makes the cold mass a compact system and much economical.

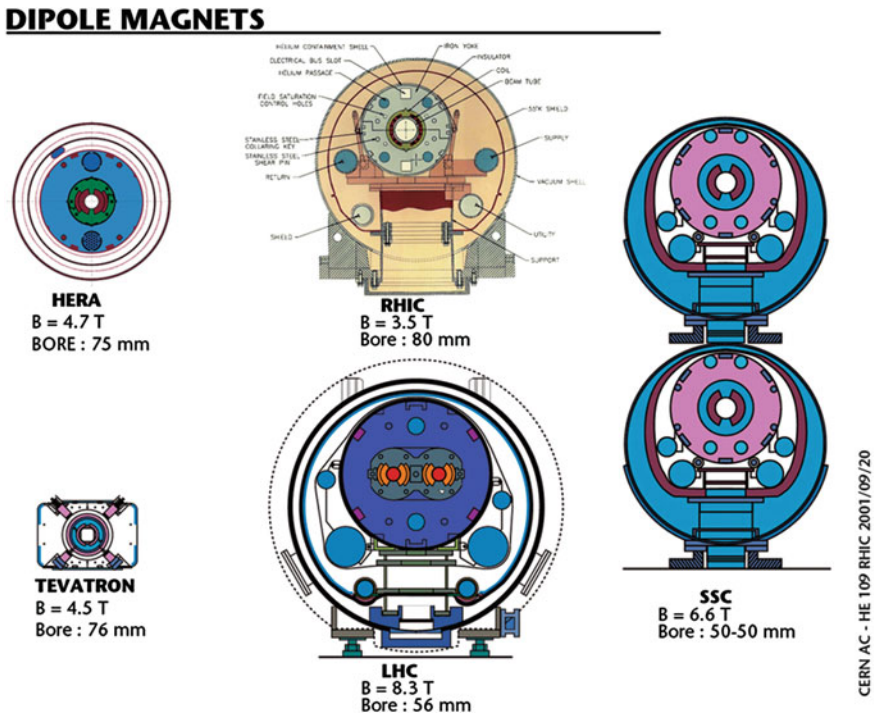

Fig. 8.1 Schematic cross-section of the main dipoles of the five accelerators discussed in Sect. 8.3 (*Source* [3]) (*Courtesy* Lucio Rossi, CERN Photo Library and with permission from "CAS")

Schematic cross-sections of the main dipole magnets of these accelerators are reproduced in Fig. 8.1.

8.4 Unique Features of the Accelerator Magnets with Special Reference to LHC

In this section we will discuss important characteristics of the accelerator magnets with a special reference to LHC which has been built with several new features over the past accelerators. A good number of papers have been published by Lucio Rossi of CERN on all aspects of LHC magnets and cryogenic system. I refer to a few of them [3–7]. The magnets are the most critical components of any accelerator. A dipole magnet is far more longer than its aperture, the conductor therefore runs parallel to the beam except a small part which bends at the coil ends. It is built in two halves with current flowing in opposite directions and producing required field in a direction transverse to the beam as shown in Fig. 8.2. Dipole magnets are not straight, instead they follow the curvature of the beam pipe. The deviation from a

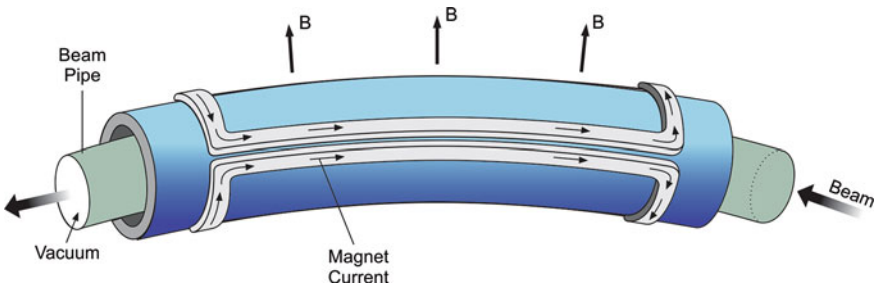

Fig. 8.2 Dipole magnets produce transverse field to bend the beam along the curved path. Current in the two halves of the coil flows mostly longitudinally except short coil ends and in opposite directions

straight line is, however, so small in comparison with the dipole magnet length that it is hardly noticed. This curvature makes the design of the magnets quite complicated and difficult. Computer codes like TOSCA, ANSYS, POISSON, DXF and ROXIE have been developed and used for magnet designs. ROXIE (Routine for the Optimization of magnet X-sections, Inverse software programme Package) was developed by Rossenschuk [8, 9] for LHC magnets and is widely used by many institutions for magnet design. It is a versatile and easy to use programme. It is used to give integrated design of a superconducting magnet, including the conceptual design, optimized field, coil ends design, end spacers, cross-sections of the coils, collars and the iron yoke and produces detailed drawings. 'End spacers' design is interfaced with CAD-CAM for the five axes CNC milling machines to produce these pieces. It has the capability of tracing manufacturing errors which affects the field quality.

8.4.1 The Coil Geometry

A perfect dipole field can be produced [1] by a current sheet with surface current density distribution of azimuthal type varying as Cosine ($n\varphi$). One obtains dipole, quadrupole and sextupole field for n = 1, 2, and 3 respectively. For perfect dipole field such a coil geometry is obtained by the intersection of two cylinders [10] and also by the intersection of two ellipses (shaded parts) carrying equal volume current densities but in opposite directions as shown in (Fig. 8.3a, b). A perfect quadrupole field can similarly be obtained by the intersection of two crossed ellipses as shown in Fig. 8.3c each quadrant carrying equal current densities but reversing the current polarity in alternate segments. A very common and well known geometry of the current shell generating dipole field is shown in Fig. 8.4a and the current shell generating quadrupole field is shown in Fig. 8.4b. The value of the limiting angle φ of a dipole is kept 60° which eliminates sextupole (n = 3) but higher multipoles like decapole (n = 5) and 12-pole do exist. These higher multipoles can only be

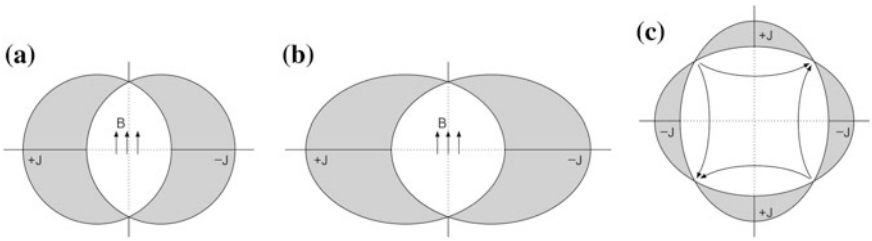

Fig. 8.3 **a** A perfect dipole field by intersecting two cylinders or, **b** a perfect dipole field by two intersecting ellipses (both carrying uniform current but in opposite directions), **c** a quadrupole field generated by the intersection of two crossed ellipses

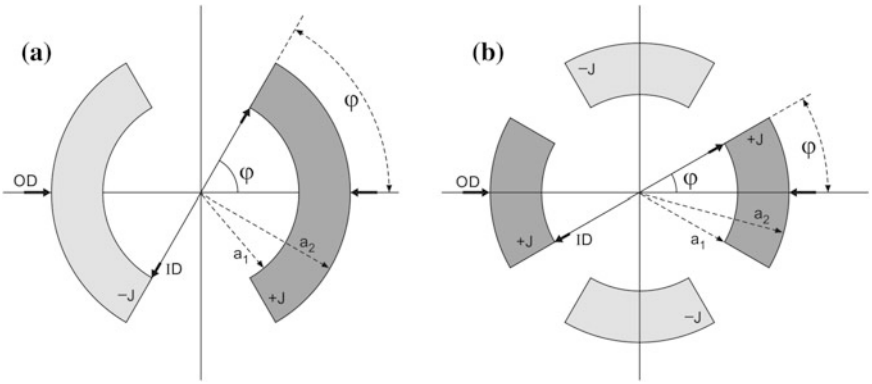

Fig. 8.4 **a** Current shell geometry with dipole symmetry and **b** quadrupole symmetry

eliminated of by winding the shells in two layers. Similarly, the quadrupole current shells are wound in two layers to eliminate higher order multipoles (Fig. 8.4b). The limiting angle of the quadrupole shell φ is 30° and for a sextupole 20°. The field homogeneity is further improved by introducing longitudinal wedges in the windings.

In a perfect dipole with a current density of $J \cos \varphi$, the field B is proportional to J and ΔR ($B \propto J \times \Delta R$) where ΔR is the coil thickness. To keep the volume of the coils within reasonable limits, we have to look for high J_c conductor for a given beam aperture. Further, these magnets are wound in two layers and since the outer layer experiences lower field, one can operate the outer coil at much higher current compatible with the field. This reduces the coil volume too. Operating the two coils at different current levels will, however, be complicated because it requires two separate power systems and quench protection/detection systems.

Designing the coil ends is difficult as these are raised above the longitudinal winding. Bending of the conductor at the ends has to be carried out accurately and should be below the permissible strain limit of the conductor. The bends are of the shape of a saddle. To keep the end winding in position suitable spacers machined

from fiberglass-epoxy composites are inserted. Coil ends are impregnated with resin to fill the gaps between spacers and the winding and to obtain good finished surface for collaring.

8.4.2 The Collars

The Dipole magnet-coils are wound in two halves over the beam tube, both repelling each other. At high J_c and high field these coils experience huge lateral force ($=J \times B$) with a large horizontal component, which is not self supported like in a solenoid winding. This force is huge, of the order of several MN at the level of the field produced. The two halves are thus held together mechanically by strong clamps referred to as collars. Collaring is carried out in a large press to compress the coils to 100–120 MPa so that the collars remain compressed to a pressure of 60–90 MPa after the pressure is released. In LHC, the two dipoles around the two beam pipes, are housed in a single cold mass system. Both the dipole coils are collared together and called "twin". The collars used in LHC are made of stamped laminations of austenitic steel. HERA at DESY has used collars made of laminations of a strong Al–Mg–Mn alloy. The two halves are held in position together using pins and dowel rods The collar material has to remain non-magnetic even after thermal cycling to LHe temperatures, cold worked during stamping or after welding. Protection sheets have been used between the coils and the collars which also provide ground insulation. Sometimes, very thin 3–5 mm skin spacers have been used in place of collars and all the compression to the coil is provided by the outside yoke. The field enhancement too increases because of closer proximity of the yoke with the coil. Quadrupole coils are collared individually.

8.4.3 The Yoke

The compression by collars is further enforced by the iron yoke fitted outside the collars. The yoke is used to reduce the fringe field out side the magnet to below 10 mT. At the same time, the yoke also enhances the magnet field. Warm (room temperature) as well as cold (cooled to LHe-magnet temperature) yokes have been used in different accelerators. Enhancement of field is higher when the yoke is part of the cold mass because of the close proximity of the yoke with the coil. Cold yoke only require more cryogen and the magnet system takes little more time to cool down, which is not very important because accelerator magnets are not warmed-up and cooed-down frequently. Moreover fast cooling is not desirable to prevent excessive thermal stresses. Enhanced field, however, allows the use of smaller operating current in the coil, which results in the reduction of stored energy and the consequent enhancing protection against quench. One drawback of the cold yoke is that the shrinkage in soft iron yoke is larger than in the coil after cool-down and

therefore larger pressure has to be applied while compressing the yoke. Second problem could be the saturation of the yoke which may generate higher order poles and distort the field. This has to be well accounted for during the design stage itself. Recall that RHIC does not use collars at all, instead, the coils are compressed directly by the yoke.

In LHC, the yoke is 600 mm thick and made into two halves and put around the collars. The yoke is of cylindrical shape consisting of 1.5 m long packs of stamped laminations compressed together to a density of 98.5 %. A cylindrical shell in two halves and of 10 mm thick 316 LN steel then surrounds the yoke. Welding is carried out simultaneously on top and bottom parts under a pressure of 400 tons. After mounting electrical systems in place the two end parts too are welded. All along the length of a dipole a total welding of 16 m is carried out. This 316 LN SS cylinder also forms part of the LHe-cryostat.

8.4.4 The Magnets

The magnets constitute the most critical part of an accelerator and more so the dipoles which produce high field, quite close to the limit of Nb–Ti conductor. These magnets operate at high current. To minimize heat input to the cryostat the number of current leads are cut down to minimum. All the magnets in one sector are therefore connected in series and powered by a single sector power system using only one pair of current leads. The twin magnets and common collar and the yoke are installed in the same liquid helium cryostat. This whole assembly is commonly referred to as the "cold mass". A schematic cross-section of the cold mass is shown in Fig. 8.5. The dipole characteristic parameters are tabulated in Table 8.1. The stringent requirement of all the dipole magnets in the lattice is that they ought to produce almost identical field in magnitude as well as in quality. The field strength and the harmonic contents of all the dipoles must be same within the range of the order of 10^{-4} (one unit). This means that the coils of two poles (top and bottom) of each dipole have to be identical and so should be for all the dipoles built at different locations. Each coil is wound in two layers using two different cables running at different current densities but same operating current. The geometrical dimensions of the two layers of all the magnets have to match within a variation of less than 100 μm. Small variation can cause appreciable change in the main field and the higher harmonics. These requirements call for precision winding and should be perfectly reproducible in all magnets.

The photograph in Fig. 8.6 shows the cutaway cross-section of the twin aperture dipole magnet used in LHC. Each dipole is about 15 m long. All the dipole magnet systems (cold mass) alone occupy close to 20 km length of the tunnel.

The stringency of field uniformity equally holds for quadrupoles which too are wound in two layers and using the same cable as used for winding the outer layer of the main dipoles. A small shortfall (<10 %) in the focal strength of a magnet can, however, be compensated by successive quadrupoles.

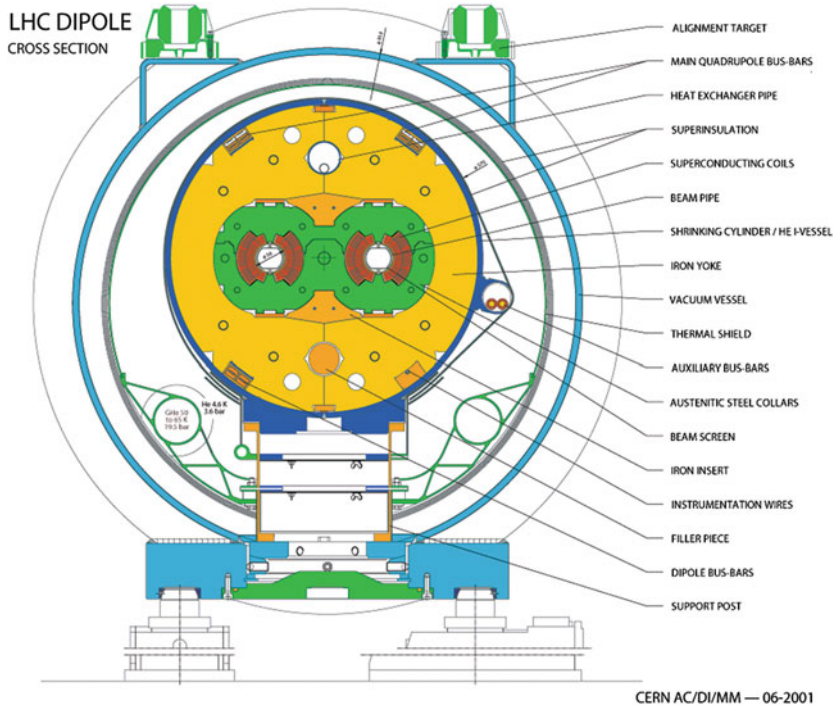

Fig. 8.5 The cross-section of the compact cold mass of the main LHC dipole. The two dipoles of the two oppositely circulating beams are coupled together by a single austenitic steel collar and compressed within the same iron yoke [3] (*Courtesy* Lucio Rossi, CERN Photo Library and with permission from "CAS")

Table 8.1 Important parameters of the main LHC dipole (data compiled from [5, 6])

Parameter	Unit	Value
Operating field	T	8.33 (can operate up to a max. 9.00 T)
Operating current	kA	11.85
Operating temperature	K	1.9
Coil aperture	mm	56
Distance between the two aperture axes	mm	194
Stored energy/channel	MJ	3.5 @ 8.33 T
Magnet length	m	14.3
Cold mass length	m	15.18
Cold mass O. D.	mm	570

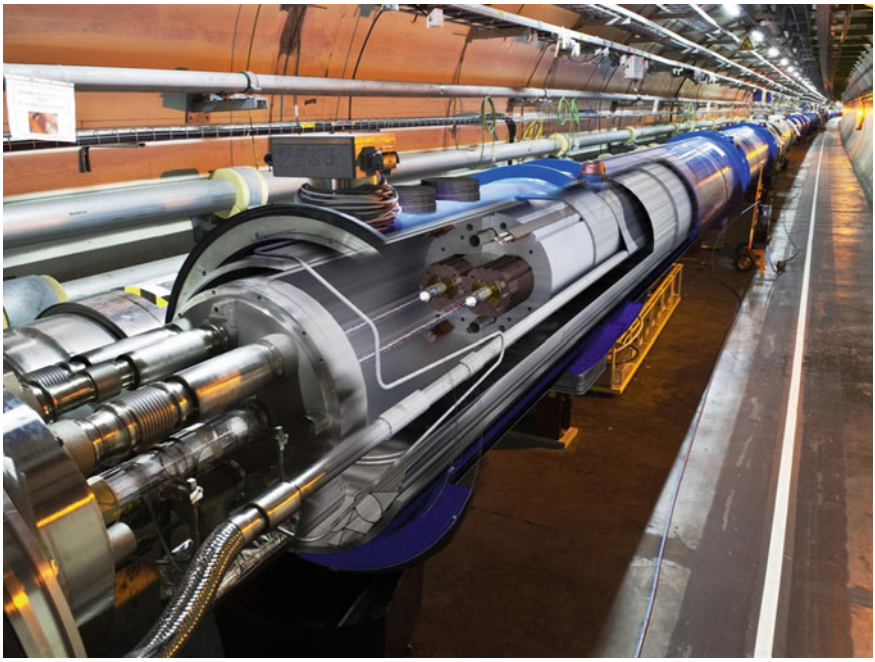

Fig. 8.6 A cutaway cross-section of a twin aperture dipole magnet mounted in a 27 km long tunnel. All the dipoles together occupy nearly 20 km length of the tunnel (CERN Photo courtesy Ph. Lebrun)

8.4.5 The Superconductors

So far, the most favoured superconductor for all the accelerator magnets have been the Cu/Nb–Ti (Rutherford type) cables because of its superior mechanical properties and comparative insensitivity to stresses. The production procedures for manufacturing large quantities of Nb–Ti conductor are well established and standardized since the material is being produced commercially over last four decades. In an accelerator, the quantity of conductor used for winding large number of magnets is huge and cannot be supplied by a single manufacturer. For field uniformity and field reproducibility, the total quantity of conductor produced by all the manufacturers has to be uniform within a small tolerance limit. LHC has used something like 1,200 tons of cable, out of which the Nb–Ti is about 400 tons.

The quality control of the conductor starts from the compositional uniformity of the basic material, Nb–Ti, its processing, uniformity of filament size, the strand size and finally the braided cable dimensions. The strand diameter has to be uniform within 1 μm and the cable size to ±6 μm. The uniformity of the size of the cable is crucial to the conductor positioning in the coil and ultimately the field profile. To prevent degradation in the overall I_c of the cable, the strands must be compacted to no less than 90 %. Equally crucial is the uniform distribution of current among the

strands and the inter-strand resistance of a cable. CERN has devised an ingenious and cost effective technique for the production of Rutherford cable used for LHC. The strands are coated with a Sn–Ag alloy before they are cabled. The cable is then oxidized by heating it under controlled conditions in air. The technique, in fact, has proved a turning point in the successful production of Rutherford cable for LHC. The contact resistance is low also because the coil is pre-stressed to 80–100 MPa.

The most important parameter of the cable is its over-all critical current density, J_c usually referred to as J_{Eng} (engineering critical current). This takes into account the total cross-section of the cable which consists of superconducting and non-superconducting components like, copper, filament barrier and bronze in case of Nb_3Sn. The microstructure of Nb–Ti is to be well controlled to benefit from the effective flux pinning. For stability, a copper to Nb–Ti ratio of 1.5–2 has been used for accelerator magnets. To boost J_{Eng} further, a much lower ratio of 0.7–0.8 is being planned for future magnets with no deterrent to conductor stability and/or the quench protection.

To keep the inductance and the stored energy within limits these magnet coils are optimized for high currents somewhere in the range of 10–13 kA. One has to keep in mind that the transverse field produced by (cosine θ) type coils is smaller than that produced by a simple solenoid coil for the same J_c and same coil thickness. The field in a solenoid is $B = \mu_0 J t$ whereas for a cosine θ coil it is $B = \frac{1}{2} \mu_0 J t$ (cos θ). Here J is current density and t the winding thickness. Rutherford cable capable of carrying such large current have invariably been used for accelerator magnets. Each cable has few tens of strands with high I_c value, braided together in a rectangular shape (see Fig. 6.10). The cable has a high compaction density of about 90 %. The main parameters of the cable and the strand used for LHC dipoles are tabulated in Table 8.2.

Well microstructured Nb–Ti with effective pinning optimally has been serving well as high I_c conductor for accelerator magnets, nevertheless, suffer from the big problem of persistent (magnetization) current which can distort the field. These superconductors retain magnetization even when the field from its maximum value of 8.33 T is ramped down to the lowest injection value of 0.54 T. Since the critical current density is very high of the order of 10 kA/mm^2, the persistent magnetization current can be significant and can damage the field quality drastically. The magnetization scales as $M \propto J_c D_{eff,}$ where D_{eff} is the effective diameter of the filament

Table 8.2 Parameters of the strands and the Cu/Nb–Ti Rutherford cable used for LHC dipoles (data compiled from [5, 6])

Strand			Cable		
Parameter	Unit	Value	Parameter	Unit	Value
Diameter	mm	0.825	Width	mm	15.1
Filament diameter	μm	6	Thickness @ 70 MPa	mm	1.48 ± 0.006
No. of filaments		6,425	No. of strand		36
Cu/Nb–Ti ratio		1.9–2.0	Inter-strand resistance	μΩ	20–80
I_c @ 1.9 K	A	380 @ 7 T	I_c @ 1.9 K	kA	12.97 @ 7 T

and J_c the critical current density. D_{eff} sometimes can be much more than the geometrical diameter, if the filaments touch each other or are coupled together in metal matrix due to small inter-filament separation. In such cases the filaments are usually cladded with a barrier like Nb. Since we cannot afford a drop in J_c, we must reduce the filament diameter to the extent possible. For LHC application a filament diameter of 6–7 μm was found ideal and selected. Still smaller filament diameter leads to much lower J_c values.

8.4.6 Training

Training of accelerator dipoles assumes special importance because of the low Cu: Nb–Ti ratio of the conductor used and the coil running at very high current density. It is almost impossible that the magnet attains its peak field and the peak operating current in the virgin run. The large EM forces cause some movement in the coil winding, the strand or the cable and quench the magnet at a current which may be much lower than the maximum operating current for which the magnet is designed. In successive runs the magnet quenches at increasingly high currents. After a few cool down cycles the magnet reaches a saturation point where the maximum current and field are achieved. The magnets are therefore 'trained' before being installed at their designated locations. The final quench current and the quench field so attained after training should be reproducible each time the magnet is operated and thermally recycled to room temperature. All the magnets are operated at a level little below the quench current values to make allowance for small variation in the performance of such a large number of magnets.

The training process is most expensive one as it involves huge quantity of liquid helium for such a large number of magnets but cannot be done away with. It is important that the training is irreversible and the magnets do not quench after their installation below the quench current value. A premature quench in a single dipole may cause a chain reaction, of the sort, and affect rest of the 154 dipoles which are connected in series in one sector. If one magnet quenches, energy from all other magnets in the sector has to be discharged safely. A quench in one magnet may result in the increase of temperature of all other magnets in a sector, above T_c, turning them normal. LHC did face this problem in Sept. 2008 within 9 days of its first operation, when one main dipole magnet in sector 3–4 quenched due to a faulty electric connections and consequent mechanical damage and release of LHe. This resulted in the damage of 50 expensive magnets. It took 14 months to repair the damage and to bring back LHC to life in Nov. 2009.

At last, LHC succeeded in discovering all evasive Higgs Boson, first predicted by Peter Higgs together with five other physicists in 1964. The first indication came in July. 2012 and the final announcement of the confirmation of Higgs particle was made in March 2013. Peter Higgs and Francois Englert were awarded the 2013 Nobel Prize in physics. The particle has a mass 125 GeV/c^2, zero spin and zero electric charge. Its decay time is found to be 1.56×10^{-22} s.

8.4.7 The Quench Protection

Since quench cannot be ruled out in a superconducting magnet it is very important to provide a most reliable and fool-proof quench protection system for accelerator magnets especially when the magnets are operating at high field. No sooner the hot spot is detected, the current should decay fast and the stored energy should spread over the entire coil so as not to allow excessive heating at the hot spot. Quench protection in LHC type magnets is tricky because each magnet has large stored energy and a large number of them, 154 are connected in series and energized by a common source. Normal protection systems were found inadequate. LHC magnets have superconducting bus bars in parallel with magnet coils. In the event of a quench Joule heat dissipation starts at the hot spot and the voltage increases. As soon as the voltage exceeds the opening voltage of the by-pass diodes, the current gets diverted into the superconducting bus bars. This prevents excessive heating and rise in temperature beyond acceptable limit of room temperature. The current decays over a time constant ($=L/R$) which in LHC magnets is too large, R being very small. R is kept small because the quench propagation in the LHC conductor is slow at 20 m/s and dR/dt = 10 mΩ/s. Large time constant means it will take a long time to stop heat dissipation at the hot stop risking the magnet safety.

Dumping energy in an external resistor will need high resistance ($\sim 1\ \Omega$) for LHC magnets which will induce high voltage of the order of 10 kV across the magnet which is too high and well above the prescribed limit of 1 kV. LHC magnets are protected by activating the SS strip heaters mounted between the coil winding and the collars. This helps in spreading the quench to the larger part of the coil and rather fast. The resistance R rises and the time constant decreases. The stored energy thus spreads uniformly across the whole coil without excessively increasing the temperature at the hot spot. This also avoids thermal gradients and consequent unwanted stresses in the coil. Since the resistive voltage and the inductive voltage have opposite polarity, they balance each other to great extent. As a result, the voltage rise in LHC during the quench does not exceed beyond 600 V.

The main parameters of all the superconducting colliders discussed above are summarized in Table 8.3.

8.5 High Field Magnets for Future Accelerators

The quest of high energy community to achieve higher beam energy has never ceased. While world's largest accelerator, LHC at CERN was being built R&D on developing still high field superconducting magnets had continued at CERN and other places notably in USA. The aim has been to build 15 T magnets in immediate future and 20 T magnets for a distant future. Obviously, in today's scenario, the only conductor available is the brittle A-15 Cu/Nb_3Sn composites. The next candidate for fields higher than 15 T could be Nb_3Al [11] of the same family. Other

Table 8.3 Summery of the superconducting collider

Parameter	Unit	Tevatron FNAL (USA)	HERA[a] DESY (Germany)	SSC TEXAS (USA)	RHIC BNL (USA)	LHC CERN (Europe)
Year of operation		1987	1989	Proposed 1991	1999	2009
Present status		Shut 2011	Shut 2007	Dropped 1993	Working	Working
Tunnel length	km	6.3	6.3	87.1	3.8	27
Colliding species		p^+–p^-	e^-–p^+	p^+–p^+	Ions-proton	p^+–p^+
Collision energy	TeV	1.8	0.92	40	0.2 (Au-p^+)	14
Main dipoles		774	422 proton ring only)	7,860	396	1232
Main quadrupoles		224	244 (proton ring only)	1,360	492	400
Dipole field	T	4.4	5.3	6.6	3.46	8.34
Operating temp.	K	4.4	4.2	4.35	4.6	1.9
Conductor used		Cu/Nb–Ti	Cu/Nb–Ti	Cu/Nb–Ti	Cu/Nb–Ti	Cu/Nb–Ti
Collar used		Yes	Yes	Yes	No, yoke only	Yes
Yoke (iron)		Warm	Cold	Cold	Cold	Cold

[a] HERA has proton ring and electron ring one over the above. Proton ring has superconducting magnets and the electron ring normal magnets. The electron ring has 456 normal dipole magnets (1.7 T) and 605 quadrupole magnets

option is to use high T_c superconductors like Bi-2223 or 2G YBCO after they are produced in sufficient lengths by cost effective technique and meet the stringent characteristic parameters set for accelerator magnets. Major efforts in this direction have been going on at several places like CERN, FNAL, BNL, LBNL, University of Twente (NZ) and other such places individually as well through mutual collaborations. So far these efforts have been directed towards using Nb_3Sn superconductor albeit produced by different techniques.

8.5.1 The Nb_3Sn Conductor for Accelerator Magnets

The biggest challenge to High Field Accelerator Magnet (HFAM) programme stems from the brittle nature of the Nb_3Sn. The conductor is manufactured in preformed (Nb filaments in a Sn composite matrix) state. It is only after the coil is wound that the superconducting compound Nb_3Sn is formed in the final stage through a controlled heat treatment, what is generally termed as "wind and react" technique. So far, this reaction temperature is quite high in the range of 650–700 °C

which poses several problems related to electrical insulation and application of pre-stress etc. The "react and wind" technique which is feasible for HTS like Bi-2223 and YBCO tape conductors is being pursued at some places. Extensive R&D efforts are being made to study the effect of bending dia. on J_c of Nb_3Sn. One option being tried is to react the cable under bend position at a certain diameter so that the degradation by final diameter winding is cut significantly.

Nb_3Sn also suffers from poor ultimate tensile strength as compared to Nb–Ti and therefore needs re-enforcement. Cables with SS core have been produced and used for accelerator magnets. Conductors produced by four different techniques, namely, the MJR (Modified Jelly Roll), the ITD (Internal Tin Diffusion), PIT (Powder-In-Tube) and RRP (Restack Rod Process) have been used for making model dipoles and quadrupoles by FNAL or in collaboration with BNL and LBNL [12]. We have discussed these techniques in some detail in Chap. 6. Conductors with $J_c \sim 2{,}500$ A/mm^2 with a filament dia. of less than 50 μm and a Cu/Nb_3Sn ratio between 1 and 1.5 have been used for magnet fabrication. To keep persistent current under control the filament dia. should be reduced further to $\sim$20 μm or still below. Further, the Cu/Nb_3Sn ratio needs to be brought down to 50–60 % which in turn demands very effective quench protection procedures. Fine filaments seems to be possible with PIT technique. After over a decade of extensive research it is now feasible to have magnets producing a nominal field of 12 T and the maximum field of 15 T. More R&D efforts are needed to build 15 T nominal field magnets. These studies have generated plethora of useful data on coil design, conductor evaluation, mechanical structure, coil pre-stress, quench performance, field quality and coil performance. These studies will go long way in establishing a reliable Nb_3Sn technology for 15 T and higher accelerator magnets.

8.5.2 Nb_3Sn Accelerator Magnets Development at FNAL

In the context of Nb_3Sn magnet development programme for future high energy accelerators it will be appropriate to discuss the high field programmes pursued at Fermi Lab. [12] for LHC IR upgrade, Muon Collider Storage Ring and future high field accelerators. Fermi Lab. while developing this technology also had collaboration with BNL and LBNL. It built approximately 20 dipoles and 35 quadrupole magnets in 1, 2 and 4 m lengths and later another 14 quadrupoles, all 4 m long. Magnets have performed well up to a nominal field of 12 T and a maximum field of 15 T. Vast data with regard to cable parameters, collaring technique, pre-stress, mechanical structure, field quality and quench behaviour has been generated. This data has indeed laid the foundation for future development of Nb_3Sn accelerator magnet programme.

Fermi Lab. built base line dipoles for VLHC (Very Large Hadron Collider), generating 10–11 T field @ 4.5 K, in an aperture of 43.5 mm. The coil was two layer shell type with a mechanical structure which had a cold iron yoke 400 mm

thick and a SS skin 10 mm thick but had no collars. It also developed Nb_3Sn quadrupoles for the LHC luminosity upgrade under the US-LARP (LHC Accelerator Research Programme) having an aperture of 90 mm and providing a nominal field gradient of 200 T/m. This value is the same as in the 70 mm aperture of the present LHC Nb–Ti quadrupoles. These magnets will also be operated at 1.9 K. These quadrupoles too have a two layer shell type coils with a 25 mm thick SS collar, a 400 mm thick cold iron yoke and a 12 mm thick SS skin.

For dipoles, keystoned Ruherford cable 14.24 × 1.8 mm size with 27/28 strands of dia. 1 mm was used. For quadrupoles, similar cable of the dimensions 10.05 × 1.26 mm, with 27 strands of 0.7 mm dia. each was used. The keystone angles of the two cables were 0.9 and 1.0° respectively. The maximum field generated by the dipoles was 12.05 T @ 4.5 K and a peak field of 12.6 T at the coil. The quench current was 21.06 kA. The quadrupoles operated at 1.9 K provided a field gradient of 233 T/m with a peak field of 12.1 T at the coil. These values were obtained at a quench current of 14.07 kA. The characteristic parameters of the cables used and the performance parameters of the dipoles and quadrupoles [12] are given in Table 8.4. To prevent persistent currents caused by magnetization, the filament size should be kept below 20 μm without lowering J_c. The eddy current effects are dependent upon the twist pitch of the strand and of the cable, the matrix resistivity and the inter-strand resistivity. These effects have been suppressed by the insertion of a SS core in the cable which increases the inter-strand resistance and also by having well twisted strands.

The strands used in cables for the magnets were made following three different methods, namely, MJR, PIT and RRP. The J_c of the strands produced by the three techniques was in the range of 2–2.8 kA/mm^2 and filament size 50–100 μm. The insulation studied, were the ceramic tape, S-2 glass sleeve and E-glass tape. Ceramic insulation proved to be the best from the coil fabrication point of view but it is rather thick and more expensive of the three. Ceramic tape was used for all the dipoles and S-2 and E-glass sleeve for quadrupole magnets.

Table 8.4 Characteristic parameters of the Nb_3Sn cables and the performance parameters of the model dipoles and quadrupoles built at FNAL cables used are produced by MJR, PIT and RRP techniques (data compiled from [12])

Parameter	Unit	Dipoles	Quadrupoles
Cable (keystoned Rutherford) size with SS core	mm	14.24 × 1.80	10.05 × 1.26
Keystone angle	degrees	0.9	1.0
Number of strand		27/28	27
Strand diameter	mm	1	0.7
Filament dia.	μm	~20	~20
Maximum field @ 4.5 K	T	12.05	
Field gradient @ 1.9 K	T/m		233
Peak field at the coil	T	12.6 (4.5 K)	12.1 (1.9 K)
Quench current	kA	21.6	14. 07

To handle the coil processing, FNAL used a ceramic binder which after curing holds rigidly all the components of the coil like wedges, pole blocks etc. and enhances the mechanical strength of the electrical insulation. During heat treatment, this binder turns into fine ceramic particles serving as filler material during the impregnation of the coil. So far the magnets have been impregnated with epoxy CID 101 K. Efforts are on to find an epoxy which is more resistant to hard radiation.

Brittle Nb_3Sn coils and the need for pre-stress pose serious challenge to the mechanical structure design. A thick SS shell structure was used for some magnets and a SS collar supported by SS skin for others. Two Al-clamps pre-stress the dipole coils to 20 MPa at room temperature. The final pre-stress of 100–120 MPa at 4 K is provided by the yoke and the skin. In quadrupole magnets, the coils are stressed to 30–35 MPa by the collars and to final pre-stress of 110–150 MPa by the SS skin. Control spacers have been used to prevent over-compression during yoking.

8.5.3 EuCARD Nb_3Sn Dipole Magnets

The EuCARD (European Coordination for Accelerator R&D) project is aimed at developing technologies for future accelerators in Europe with higher energies and higher luminosities. Its Work Package-7 relates to the development of high field Nb_3Sn magnets for accelerators. One of the key objectives of this work package is the fabrication of a 1.5 m long dipole magnet with a 100 mm aperture and a bore field of 13 T. This will replace the present Nb–Ti based dipole magnet of FRESCA, the Cable Test Facility at CERN and has been code named as FRESCA-2. The magnet was put under operation in 2013.

The detailed design of the model FRESCA-2 dipole has been given by Milanese et al. [13] and a status report at the end of 2012 has been published by Ferrasin et al. [14]. A block layout has been preferred for the coil design in place of a cos θ configuration. It has two coils each having two layers. The first coil (inner) consisting of layer 1 and layer 2 has 36 turns and is wound over a Ti pole with 100 mm diameter hole. The second coil (outer) consisting of layer 3 and layer 4 is wound with 42 turns around an iron-pole. Each coil has a double pancake structure and wound using single length of the conductor, reacted and impregnated separately. Insulating inter-layer shims (0.5 mm) and inter-coil shims (1.5 mm) are used. The coil ends are bent upwards at an angle of 17° to make room for the 100 mm aperture as shown in Fig. 8.7. The bent coil ends are supported by steel wedges.

FRESCA2 design phase has been funded by the European Commission under the framework of EuCARD under the Grant Agreement n° 227579.

The salient feature of the design of FRESCA-2 is the use of the so-called ‘bladder and key’ concept developed earlier by LBNL. Horizontal and vertical pads have been used between the coils and the yoke made of 5.8 mm iron laminations compressed by SS end-plates. The pads transfer the entire force to the split iron yoke. The iron yoke covers the entire coil length and is fitted into a 65 mm thick pre-tensioned (with bladders) cylindrical shell made of a 7075 Al-alloy. Ultimately,

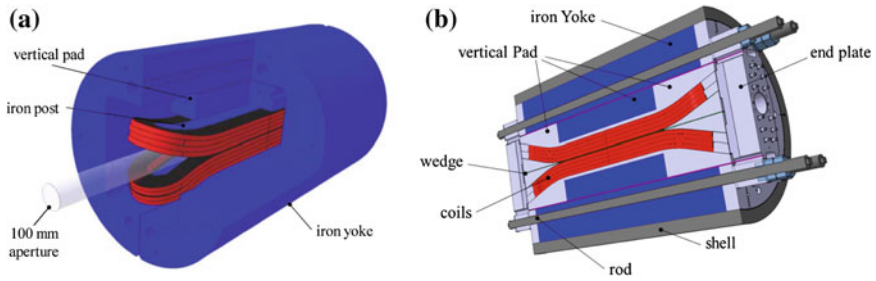

Fig. 8.7 **a** A cutaway sectional view of the FRESCA-2 dipole coils and the beam aperture. The coil ends are bent upwards supported by wedges [13], **b** a longitudinal cross-section of the FRESCA-2 dipole coils (© CEA/IRFU, P. Manil, J.F. Millot)

the entire force is taken care of by the shell. The shell shrinks more than the other parts of the assembly during cool-down and pre-compresses the coil further. The mechanical support design of FRESCA-2 ensures sufficient pre-compression on the coil to counter Lorentz force effectively as the current keeps rising during the energization of the magnet. It also keeps the peak stress under limit in the cool-down state. In the cool-down state the maximum horizontal stress observed is 150 MPa at 13 T field.

The presence of iron vertical pads close to the second coil (layer 3 and 4) and the iron yoke makes a significant impact on the field strength inside the bore as well as on the peak field at the coils. The target field of 13 T is achieved at a magnet current of 10.8 kA instead of at 12.8 kA, that would have been required without iron. It also reduces the peak field from 13.9 to 13.2 T. Lorentz force, however, remains unaffected. The fringe field at a distance of 1 m, too, decreases from 150 to 100 mT.

The cable used for winding is a Rutherford cable of the size 20.90 × 1.82 mm (pre-reacted) with 40 strands of 1 mm diameter. Each strand contains 192 filaments of ∼48 μm diameter and a Cu/Nb_3Sn ratio of 1.3. Strands are produced by PIT method as well as by the RRP technique. The magnet design takes into account the cable size increase during reaction. The cable size after reaction turns 21.32 × 1.89 mm. The strand reaches a critical current density, J_c = 2,450 A/mm^2 (4.2 K, 12 T) and 1,400 A/mm^2 (4.2 K, 15 T). Cabling brings down the J_c by about 5 %. The cable is insulated with a 0.2 mm thick braided S2 glass fiber. The strand and cable parameters are given in Table 8.5.

The stored energy of the FRESCA-2 magnet is extremely high, 4.6 MJ (Table 8.5) and therefore quench protection system becomes a critical part of this project. An efficient protection system, based on dump resistors and quench heaters, has been provided. The external dump resistor is of 95 mΩ so that the voltage at the magnet terminals does not exceed 1 kV. The heaters are SS strips 25 μm thick and 12 mm wide. These heaters are mounted on the outer surface of each layer covering nearly 50 % of the surface area available. The response time from the initiation of quench to activating heaters is expected to be less than 40 ms and the maximum temperature to be 150 K.

Table 8.5 The parameters of the magnet and strand/cable used for FRESCA-2 dipole produced by PIT technique (data compiled from [12–14])

Cable/strand parameters	Unit	Value	Magnet parameters	Unit	Value
Cable type		Rutherford	Aperture diameter	mm	100
Cable size (before reaction)	mm	20.9 × 1.89	Outer diameter of the magnet	m	1.03
Cable size (after reaction)	mm	21.32 × 1.89	No. of turns in layer 1 and layer 2		36
No. of strands		40	No. of turns in layer 3 and layer 4		42
Strand diameter	mm	1	Bore field (4.2 K)	T	13
No. of filaments		192	Magnet current at 13 T	kA	10.9
Filament dia.	μm	~45	Stored energy (13 T)	MJ	4.6
Cu:SC ratio		1.3	Quench protection		Resistors and heaters
Strand J_c (4.2 K, 15 T)	A/mm^2	1,400	Coil fabrication		Wind and react

8.6 Common Coil High Field Dipole Magnets—A New Approach (LBNL)

Although Nb_3Sn based dipole magnets are being built and tested for future VLHC application, a parallel programme of looking for altogether a new innovative design for the high field dipoles has been going on at few select places. The motivation for a new design stems from the requirement of reducing the cost of the superconducting magnets. In particle accelerators, a dipole magnet is the single most expensive component and challenging from fabrication point of view. So far, all the dipoles have been built on cos θ design which involves many complicated steps till the final assembly. The factors on which the new design should take into account are that the design should be simpler, cost effective and should yield desired high field with minimum quantity of the conductor. At the same time, the new design should aim at minimizing field harmonics and the peak field. It should have a much simplified and compact mechanical structure. The design must be of modular form enabling easy coil repair or replacement when required.

An innovative design, the so called "Common Coil Design" earlier proposed by Gupta [15, 16] is being pursued actively at LBNL. This design is also sometimes referred to as 2-in-1 dipole. The salient feature of the common coil design is that the coils are of simple racetrack type and a single pair of coils provides opposing high field to both the apertures aligned now in vertical direction (one over the other), making it most cost effective. The bend diameter of the coils is thus much larger than in LHC design as this is now determined by the separation between the two apertures and not by the small aperture diameter. This is extremely crucial for the

Nb_3Sn conductor which is very brittle. Use of "React and Wind" Nb_3Sn conductor also becomes a possibility. LBNL has already demonstrated [17] successfully a 6T prototype dipole magnet (RD-2) based on common coil design and using Nb_3Sn conductor. This magnet used a Rutherford cable of the size 12.34 × 1.45 mm containing 30 strands of Nb_3Sn 0.808 mm dia. manufactured by Teledyne Wah Chang Albany. The strand J_c was only 610 A/mm^2 (12 T, 4.2 K). This was the precursor to the later 15–16 T racetrack dipole magnets built at LBNL.

LBNL built and tested [18] its first 14 T racetrack common coil dipole (RD-3) using Nb_3Sn conductor with a J_c of 2,000 A/mm^2 supplied by Oxford Technologies. At 14 T the total horizontal Lorentz force turns out to be ~12 MN over a 780 mm coil length which tries to push the coil windings apart. The mechanical support structure was designed to withstand such large forces. The inflatable bladder and interference key system has been employed for RD-3. The design of the cross-section of the RD-3 dipole is shown in Fig. 8.8. The bladders installed between the coil pack and the iron yoke work as an internal press compressing the coil packs to 70 MPa. It also provides a tension of 155 MPa to the surrounding 40 mm thick aluminum shell. Next, the keys are inserted and the bladders are deflated and removed leaving a tension of 140 MPa on the aluminum shell. This stress rises to 250 after cool-down due to the thermal mismatch between the yoke and the shell. The magnets use 3 modular coils. The two 10 mm aperture beam pipes are inserted between the coils.

During training, first quench occurred at 8.1 T and the field reached 14 T after 35 quenches. No quench occurred up to this field after thermal cycling. Quenches below 13.7 T were found to be caused by conductor movement in the inner coil module located in high field region and quenches above this field originated in the outer coil modules. A record field of 14.7 T was achieved which was close to the

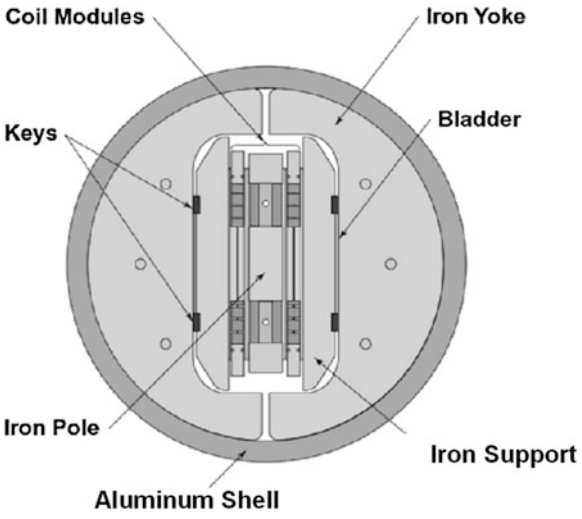

Fig. 8.8 The cross-section of the 14 T common coil dipole magnet built at LBNL (RD-3) [18] (*Courtesy*, Lawrence Berkeley Nat'l Lab)

short sample limit of the conductor in the two coils. No degradation in J_c was thus observed by cabling or due to Lorentz forces. The mechanical structure too withstood the forces as per the prediction made by TOSCA and ANSYS models.

8.7 The 15 T HD-2 Dipole

LBNL continues to carry forward the common coil dipole development programme with the ultimate aim of generating a field of 16 T in a bore of 40 mm dia. LBNL built one racetrack type dipole, code-named HD-1 which generated 16 T in a bore dia. of 8 mm. The next target was to increase the bore dia. to 35 mm and generate a field of 15 T. LBNL achieved [19, 20] 15 T in a 36 mm dia. bore field in a 1 m long dipole, code-named HD-2. The design is again based on the simple racetrack coil geometry, the block-coil module configuration and the bladder-interference key technology. The cross-section of HD-2 is shown in Fig. 8.9. HD-2 has two double layer coil modules. Each module has two layers. Coil 1 is wound on a Ti-alloy pole having a central cut-out for the bore pipe and has 24 turns. Coil 2 has 30 turns wound on another Ti-alloy pole. The coil ends are flared and supported by Al-bronze wedges with a central cut-out for the beam pipe. The two coils are separated by a SS mid-Plane sheet 1.37 mm thick.

A Rutherford Nb_3Sn cable (22 × 1.4 mm) of 'Wind and React' type consisting of 51 strands of 0.8 mm dia., Cu/SC ratio 0.94 has been used. Strands were supplied by 'Oxford Superconducting Technologies' and the cable was fabricated at LBNL. The strand with 54/61 sub-elements was produced by RRP technique. Strand J_c was 2,800–3,000 A/mm^2 (4.2 K, 12 T). The support structure is quite similar to the

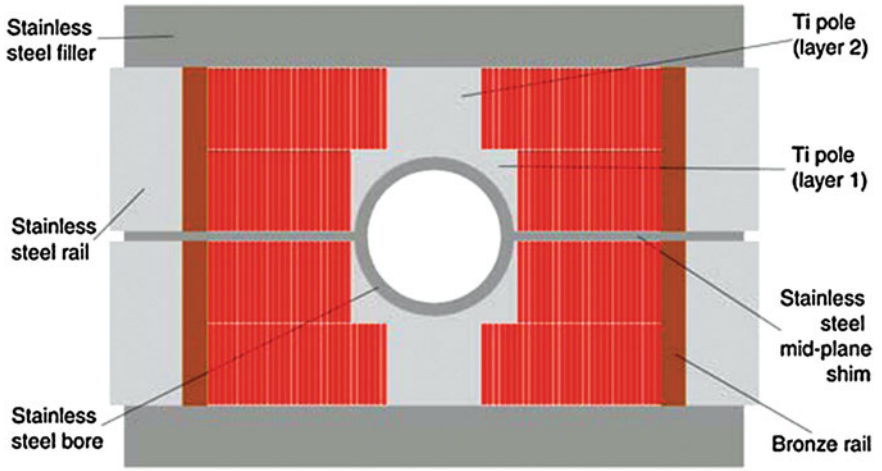

Fig. 8.9 The schematic of the cross-section of the HD-2 dipole magnet [20] (*Courtesy*, Lawrence Berkeley Nat'l Lab)

dipole RD-3 and consists of the outer 41 mm thick Al-shell pre-tensioned using inflatable bladders and the interference keys. The iron yoke is made in two halves with 50 mm thick laminations.

HD2 produced an accelerator quality bore field of 15 T at 4.2 K. Field harmonics have been suppressed to acceptable level. The design could suppress persistent current induced effects quite significantly.

8.8 Work on the Design of 15 T Nb_3Al Dipole

Yet another programme on the design and development of a 15 T dipole [21] based on coil block concept is going on using Nb_3Al superconducting cable. This work is being carried out under a collaboration between FNAL (Fermi National Accelerator Laboratory), NIMS (National Institute for Material Science) and KEK (High Energy Accelerator Research Organization). A Rutherford cable (13.93 × 1.84 mm) containing 28 strands (1 mm Dia.) of Nb_3Al produced by the so called, RHQT (Rapid Heating Quench and Transformation) process is slated to be used for the dipole. The RHQT technique has already been discussed in Sect. 6.5.4, Chap. 6. The strand has a non-Cu J_c of 1,000 A/mm^2 (15 T, 4.2 K). The filament dia. is 50 μm and the Cu ratio 0.5. Nb_3Al is known to have much larger B_{c2} and has better stress tolerance than the Nb_3Sn conductor. NIMS has already produced a field of 19.5 T in a background field of 15 T using this material. The dipole has been designed using ROXIE and the stress analysis carried out using ANSYS. The total stress at the mid-plane due to Lorentz force is 85.4 MPa and the horizontal stress at the outer surface of the block coils is 67 MPa at 4.5 K. Both are well within the tolerance limit of the conductor.

We thus find that even after the successful operation of LHC efforts continue to go to higher fields and higher energies. Unconventional simple and cost-effective coil designs are being investigated. A-15 Nb_3Sn magnets might replace Nb–Ti magnets in near future and focus then might shift to Nb_3Al for certain applications. HTS like 2G YBCO conductors may also become candidate for accelerator magnets once they meet the established criteria for accelerators and their reliability is proven. Production cost too has to be within affordable limits. The biggest fall-out of accelerator programme has been the emergence of the state-of-art technologies for the manufacture of high current efficient superconductors.

8.9 Linear Colliders with Special Reference to ILC

As discussed in Sect. 8.1, linac is a preferred option for accelerating light particles like electrons and positrons, as the energy loss due to synchrotron radiation is no longer a major problem. In 2004, the International Committee on Future Accelerator (ICFA) had recommended superconducting RF cavity (SCRF) technology for

future accelerators. The three large accelerators, namely, NLC (Next Linear Collider) at SLAC, GLC (Global Linear Collider) in Japan and TESLA (Terra Electronvolt Energy Superconducting Accelerator) in Germany decided to pool their efforts together and build ILC (International Linear Collider). In ILC, electrons and positrons will be accelerated in linear accelerators in opposite directions and collide with a collision energy of 500 GeV which could be up-graded to 1,000 GeV (1 TeV) later. It will be 30 km long to start, with a provision of extending up to 50 km. The site of location of the ILC is expected to be one of the two sites selected in Japan's mountainous regions, Kitakami (Tohoku Prefecture) or Sefuri (Kyushu Prefecture). A schematic diagram of ILC [22] is shown in Fig. 8.10. Electrons are produced by striking a gallium-arsenide photocathode with a nanosecond laser. The electrons are also made to move through a helical undulator to create photons. These photons in turn produce a pair of electron and positron when they strike a titanium target. The positrons proceed to be accelerated in the main linac whereas the electrons and the remaining photons are dumped. Positrons are accelerated in a separate linac. After acceleration both the beams collide and the fragments are picked up by two detectors.

Evidently the collision energy of the ILC, initially at 500 GeV, is much smaller than the collision energy of LHC, but use of smaller particles, electrons and positrons with higher accuracy results in an unprecedented precision. It is expected that the ILC can analyze the data accurately and can verify if the Higgs boson is the same as predicted by the Standard Model of particle physics.

8.9.1 Superconducting Magnets in ILC

The ILC Reference Design Report (RDR) [23] was presented in 2007. As per the design report superconducting magnets will be used in ILC to transport beam all along the accelerator length. ILC will use 2,333 superconducting magnets out of a

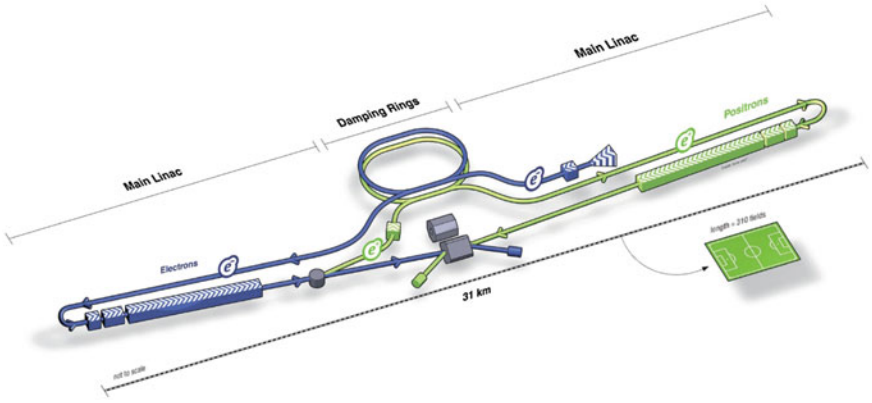

Fig. 8.10 A schematic layout of the ILC [22] ILC conceptual diagram (© ILC GDE)

total of more than 13,000 magnets which will be used in the entire machine. The main superconducting magnets are: 715 quadrupoles to focus the beam and 1,374 dipole correctors to steer the beam. In addition, there are 12 sextupoles, 14 octupoles, 16 simple solenoids, 160 wigglers and 42 undulators. To a large extent, the success of the collider will depend upon the precision with which the magnets are designed, manufactured and positioned. The field quality for most of the length of the collider should be few parts in 10^4 the beam size being only 6 nm × 600 nm. In a linear accelerator, the magnets must meet several stringent requirements such as discussed below.

The magnet centre field stability should stay within an accuracy of 5 μm during the operation of the quadrupoles and the beam based alignment (BBA) process up to a 20 % change in the focusing field. Beam alignment is extremely critical in this accelerator to keep on track such a small size beam for collision. Horizontal and vertical dipole correctors are used in the quadrupole magnets to correct all magnet centre deviations caused by field variation and the BBA.

The magnetic centre stability is influenced by a number of factors such as the mechanical misalignment of the magnets, the magnetization effects in the magnets, the hysteresis effects in the iron core and its saturation, thermal deformations in magnet on cooling, Lorentz forces and the coupling between the coils of the quadrupole and dipole. The dipole correctors need to be programmed to restore magnet centre under all circumstances.

Since the magnets are mounted close to SCRF cavities they have to be effectively shielded to limit the fringe field on the cavities below 1 μT during cooling. This is required to prevent flux trapping in the cavities. During normal operation, the fringe field should not exceed 10 μT. A cut-view of the cross-section of ILC cryomodule can be seen in Fig. 8.11. The cavity and other components of the cryomodule are seen in the picture.

Fig. 8.11 A cut-view of the cross-section of ILC cryomodule. Cavity and other components are seen in the *picture* (© Rey.Hori/KEK)

8.9.2 The ILC Quadrupole and Dipole Correctors

We have just seen in the last section that the quadrupole/dipole corrector magnets play a crucial role in the success of the beam transport in ILC. Superferric quadrupole magnet design has been chosen by RDR for ILC. In this design the field is substantially enhanced even after the iron core is saturated. The design and fabrication of the model quadrupole magnet has been carried out by Kashikhin et al. [24] at the Fermi Lab. The field in the quadrupole is produced by a set of 4 rectangular race track coils. The design optimization has been done using OPERA 2-D and 3-D codes. Since field region of interest is limited to 5 mm radius only, the core and coil positions are not very critical. The conceptual cross-section of the Q pole magnet is shown in Fig. 8.12.

The details of the Q-pole magnet and the conductor used for winding are given in Table 8.6. The coils wound are of race track geometry which have the advantage of showing low superconducting magnetization effect. The coils have been wound using a single strand Nb–Ti wire with a filament size of 3.7 μm. The winding is done on a SS former with channels. Kapton insulation is provided to the winding to prevent ground shorts. The coil of each pole consists of 700 turns. The coil is vacuum-pressure impregnated with epoxy inside a mould. The yoke is made of laminations precisely cut out of a 1.5 mm thick sheet of AISI 1006 steel. Two (single lamination) flat iron sheets are fixed at the two ends of the magnet for magnetic shielding to limit the fringe field on the SCRF cavities to 1 μT. The quadrupole magnets will be mounted inside the cryomodules close to the SCRF cavities. As shown in the conceptual design in Fig. 8.13 the quadrupole is mounted below the centre support. Some SRF cavities including one 9-cell cavity and the Q-pole magnets are also shown in the figure.

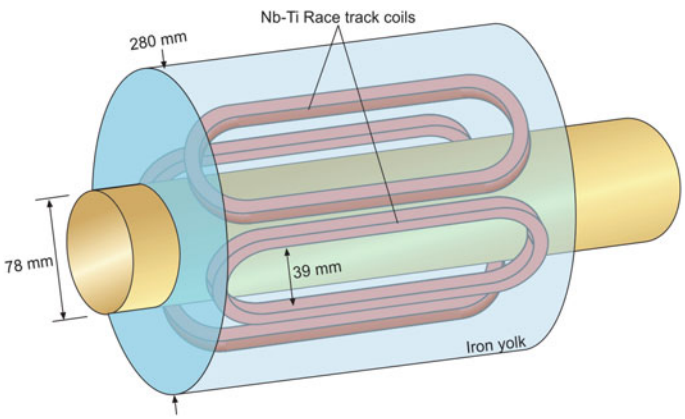

Fig. 8.12 A conceptual design of the quadrupole magnet for ILC consisting of four race track coils around the beam pipe (concept from [24])

Table 8.6 The quadrupole magnet parameters and conductor specifications for a beam energy of 250 GeV (data compiled from [24, 25])

Quadrupole magnet parameters and conductor specifications		
Parameter	Unit	Value
Magnet aperture	mm	78
Magnet length	mm	680
Yoke outer diameter	mm	280
Integrated field strength	T	36
Peak gradient	T/m	54
Peak current in Q-pole and dipole correctors	A	100
Magnet stored energy	kJ	40
Magnet centre stability at BBA	μm	5
Field non-linearity at 5 mm radius	%	0.05
Conductor used		Nb–Ti
SC wire dia.	mm	0.5
Filament dia.	μm	3.7
Cu/Nb–Ti ratio		1.5
Coil maximum field	T	3.3
SC wire I_c @ 5 T and 4.2 K	A	200
Operating temp.	(K)	2
No. of turn/pole of Q-pole coil		700
No. of turns/pole of dipole corrector		100

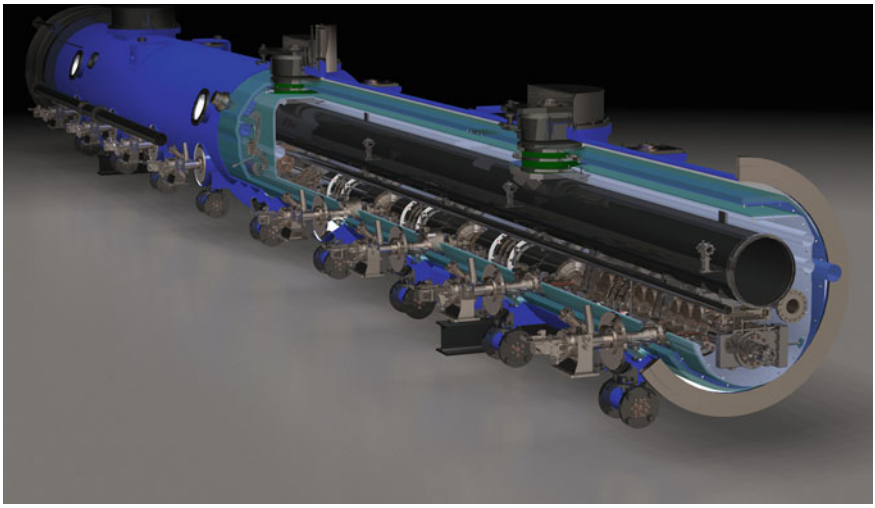

Fig. 8.13 ILC showing the location of SCRF cavities and the quadrupoles focusing magnets inside the cryomodule (*Courtesy* Fermi Lab.)

The model quadrupole magnet has been tested at Fermi Lab. by Kashikhin et al. [25]. The magnet centre stability shifts by ±2.5 μm for a current range of 3–10 A. The studies on the coupling effects between quadrupole and dipole corrector coils have been carried out by connecting them in series. This eliminates current imbalance between the two sets of coils. The magnet needs multiple training because of the multiplicity of various Lorentz forces. The magnet is protected against quench by an external resistor of 10 μΩ and coil heaters. The quench is detected by voltage taps in 50 ms with a heater response time of 100 s. The maximum temperature raise during quench is restricted to safe limit, 74 K. and the induced voltage to below 1 kV.

Recently, Kashikhin et al. [26] at Fermi Lab. have come out with an innovative design and fabricated a split-quadrupole magnet with the same dimensions. The need for modifying the design arose from the requirement of assembling the magnet under extremely clean conditions as they are installed between the SCRF cavities inside the cryomodules. In the new design the magnet is split along the vertical plane and is installed around the beam line without exposing the beam pipe to room temperature contamination. A four race track and superferric coil design was followed. In the new design the magnet is not cooled in a liquid helium bath but is conduction cooled using cryomodule liquid helium supply and gas return lines. The newly designed quadrupole produced 20 % higher field gradient than the rated value. The design is being improved further to reduce magnet centre shift.

Of late, Kashikhin [27] has come out with an interesting proposal to reduce the number of power supplies needed for operating the ILC quadrupole/corrector magnets. This proposal can improve the magnet centre stability and significantly enhance the operational reliability of the magnets. In the RDR design each magnet in the accelerator runs on a dedicated power supply and separate sets of bus-bars and current leads. In the new approach suggestion has been made to group a certain number of magnets and power the group with a single power supply. Further, the magnets, quadrupoles and dipole correctors should run in persistent mode using superconducting persistent switches. In this arrangement each magnet is energized to the required field level by a single power supply by opening the persistent switch and locking after regulating the magnet current by closing the switch. The process is repeated for every individual quadrupole as well as for the dipole corrector and are put in persistent mode of operation one by one. The new design will not only reduce the cost but will also add to the reproducibility and reliability of operation as the field stability in persistent mode is extremely high.

8.9.3 The Wiggler Magnets

The luminosity performance of the ILC requires extremely low emittance e^- and e^+ beams with high bunch charges. As per the RDR, ILC will use damping rings equipped with superconducting wiggler magnets to damp the beams effectively.

A wiggler magnet provides a sequence of transverse fields with alternate polarity and forcing the charge particles (e^- and e^+) to wiggle up and down emitting EM radiation. Crittenden et al. [28] have developed an OPERA based finite element ILC model for the design of the wiggler magnets. They followed a CESR (Cornell Electron Storage Ring) wiggler magnet design with a few changes in the parameters. About 54 magnets, each 2.2 m long, with a peak field of 1.51 T for 5 Hz mode and 2.16 T for the 10 Hz mode will be used to provide damping for the required horizontal emittance in each ring. These magnets will operate at 4.5 K. The wiggler magnets are of the superferric type where the coil is wound over a iron pole. There are 14 poles, 30 m period and a pole gap height of 7.62 cm.

8.9.4 The Undulator

The superconducting undulator will be used to generate positron source using the electron beam in the linac itself. The helical undulator will be placed in the main electron accelerator at a point of 150 GeV beam energy. The undulator produces synchrotron radiation and polarized photons which in turn produce positrons by impinging on a Ti target. Model coil is a double helical coil wound on a copper tube of ID 5.85 mm and OD 6.35 mm which produces helical transverse field. The undulator has 42 modules each with two magnet coils. The length of the field is 2×1.74 m. The axial field is 0.86 T at a nominal current of 250 A. The period is 11.5 mm. The tolerances to maintain alignment are very tight because of the small aperture. The winding is done on a SS former with grooves using a 0.4 mm dia. Nb–Ti wire. A SS yoke has been used which enhances the field by 10 % and also provide mechanical support.

8.9.5 Other Superconducting Magnets

In addition to the magnets discussed above, the collider will have 12 sextupoles, 14 octupoles and 16 solenoids serving the interaction region (IR), the beam delivery system (BDS), the e^-–e^+ source region and the ring to main linac (RTML) region.

The fabrication and installation of such a large number of magnets with great precision is a big challenge. The design details discussed above are as per the RDR which was largely based upon concepts and is subjected to modification. The 'ILC Final Design Report' has been submitted to ICFA on June 12, 2013 simultaneously at Tokyo, Geneva and Chicago, the representative cities of three continents, Asia, Europe and USA. Several modified versions of the focusing magnets are being studied at BNL, Fermi Lab. and SLAC laboratories.

8.10 Superconducting Magnets in Cyclotron

8.10.1 The Cyclotron

Superconducting magnets have played equally important role in the development of yet another type of particle accelerators, the cyclotron. Cyclotrons have been very successful in accelerating light to very heavy particles like U to high energies equivalent to K values of 2,500 MeV. Here K value represents the energy in MeV of a proton to which it can be accelerated in a cyclotron. Since a nuclei contains many protons and neutrons the nuclei energy will be much smaller. The beam injection in a cyclotron is done using either a linear accelerator or an ECR source. This class of accelerators have been very popular in the study of nuclear physics, production of radioisotopes used as tracer elements and particle therapy for the treatment of cancer.

A cyclotron uses a pair of hollow electrodes which are of the shape of 'D' (dee) arranged in opposite configuration with a gap as shown in Fig. 8.14. These electrodes are held between the poles of a magnet which produces a uniform vertical

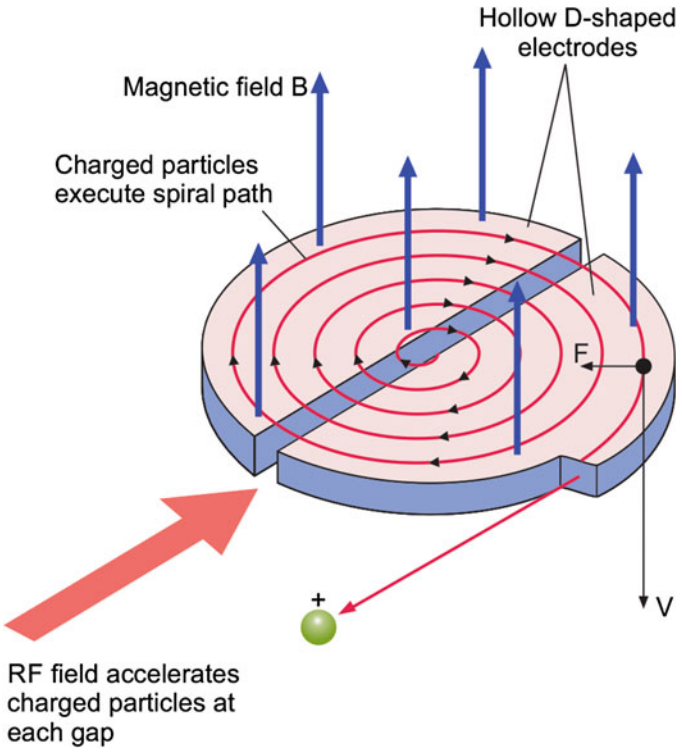

Fig. 8.14 In a cyclotron a charged particle executes a spiral trajectory under the influence of a RF field and a perpendicular uniform magnetic field

field. An alternating voltage, in MHz range, is applied to the electrodes. An ion source kept in the gap at the centre produces ions which get attracted by the first electrode. The ions execute circular motion inside the electrode (in magnetic field) and get attracted across the gap by the second electrode when they emerge from the first electrode because of the opposite polarity of the second electrode. The ions again execute circular motion in the second electrode and get accelerated in the gap by the first electrode. Ions after acceleration gain energy and move in a larger circle. This process of acceleration in gaps continues and the ions continue to travel in circles of increasing radii till they exit from the dee through an extraction route. To achieve this condition the RF frequency must match the cyclotron resonance frequency so that the ions are in phase with the RF to get repeated acceleration. This intense beam can be used to bombard a variety of target materials to produce rare radioisotopes or to conduct nuclear physics experiments. Powerful cyclotrons need high magnetic field which can be provided by a superconducting magnet alone.

The orbital motion to the ions in a magnetic field such as in a cyclotron, is provided by the Lorentz force which acts as the centripetal force:

$$qvB = mv^2/r \tag{8.1}$$

$$r = mv/qB \tag{8.2}$$

where r is the radius of the dee, m mass of the particle, v the particle velocity, q the charge of the particle and B the magnetic field. The time taken by the ion to execute half a circle in a dee will be

$$t = \pi r/v \quad = \pi m/qB \tag{8.3}$$

The cyclotron time period thus will be

$$T = 2t = 2\pi m/qB \tag{8.4}$$

And the cyclotron frequency

$$f = qB/2\pi m \tag{8.5}$$

The maximum kinetic energy can be obtained by calculating the maximum velocity at the periphery of the dee, that is, by replacing 'r' by 'R' the radius of the dee:

$$E_{max} = {}^1/_2\left(mv^2\right) = {}^1/_2\left(mq^2B^2R^2/m^2\right) \tag{8.6}$$

$$= q^2B^2R^2/2m \tag{8.7}$$

This cyclotron frequency (8.5) is constant only for low non-relativistic velocity where 'm' is constant. For high velocities the relativistic mass increases and

therefore the cyclotron frequency decreases. For continuous acceleration either the frequency has to decrease like in a synchrocyclotron or the magnetic field be increased as the particles move towards the perimeter of the dees. So the cyclotron is now isochronous wherein the magnetic field increases with radius to keep the angular frequency of the particle constant.

8.10.2 Cyclotron Magnet

A cyclotron has 4 major subsystems [29], the injection system, the magnet system, the RF system and the extraction system. Each of these subsystems have to be compatible with others and are designed through a sustained iteration process till the construction stage. Our discussion will be restricted to magnet part which certainly is the most critical subsystem of the cyclotron as a whole. As shown [29] in Fig. 8.15 the magnet is a long solenoid nested in a rather thick iron yoke and having top and bottom iron pole caps and a large gap. In an isochronous cyclotron the magnet provides axial field to the particle for circular motion as well as an axial focusing to the beam which becomes critical as the velocity approaches relativistic values (>0.5 c). For axial focusing the field should increase azimuthally as the spiral radius increases. This is achieved by creating hills (high field) and valleys (low field) at the pole tips which too are spiraled to improve focusing further. In a superconducting magnet and high field region the pole tips are fully saturated which results in the enhancement of field at the hills by 1.5 T, higher than the field in the valleys. This saturation or the complete alignment of the magnetic moments is in fact equivalent of a surface current of 450 kA on a 250 mm thick ordinary steel pole

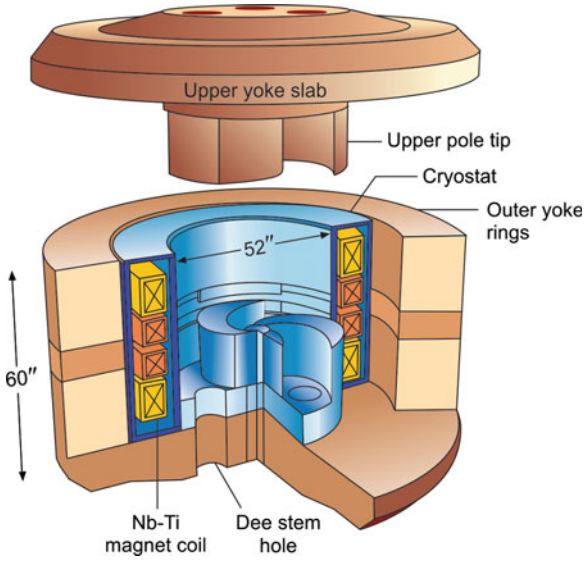

Fig. 8.15 A sketch and dimensions of the MSU cyclotron K-500, world's first superconducting cyclotron [29, 30] (*Courtesy* Marti Felix and Gelbke Konrad, NSCL, Michigan State University)

tip and with no cost. The azimuthal width of the valley and the hill is kept same so as to benefit from maximum focusing effect.

The next consideration about the magnet design is the number of hills or the so called 'sectors'. The thumb rule is that good axial focusing at the centre is obtained by a smaller number of sectors but to operate the cyclotron at high beam energies a larger number of sectors are needed. For example, 200 MEV/nucleon seems to be the upper limit to which the K-800 cyclotron of MSU, with three sectors, can accelerate a beam. For higher energies one has to use either four sectors or three inner sectors breaking into six outer sectors. To keep the magnetic field to be isochronous and maintain azimuthal field variation for focusing, trim coils are often used. For variable energy, the magnetic field profile has to remain synchronous so that the beam does not go out of phase with the accelerating voltage. This may need large adjustment in the radial field increase ranging from almost 1–20 % in K-800 class of cyclotron depending on the beam being accelerated. This is best achieved by dividing the main coil into two or more no. of coil pairs symmetric to the median plane and exciting them at different currents.

8.10.3 Some Landmark Superconducting Cyclotrons

We list below some of the well known superconducting cyclotrons built and operated in Europe, Japan and USA.

1. K-500 NSCL, MSU (USA) 1982
2. K-520 Chalk River (Canada) 1985
3. K-500 (TAMU) Texas A&M Uni. (USA) 1985
4. K-1200 NSCL, MSU (USA) 1989
5. K-800 LNS, Catania (Italy) 1994
6. K-600 (AGOR), KVI (Orsey-Groningen), 1996
7. K-2500 RIKEN Ring Cyclotron, RIKEN (Wako, Japan), 2006
8. K-500 VECC (Kolkata, India) (First beam line acceleration 2009)

Below we discuss three trend setting cyclotrons, namely, K-500, K-1200 and K-2500 mentioned above.

8.10.3.1 K-500 Cyclotron at NSCL (Michigan State University)

World's first superconducting cyclotron K-500 was built and operated at National Superconducting Cyclotron Laboratory, MSU, USA in Nov. 1981 and the first beam was extracted in August 1982. Since then many cyclotrons have been built ranging up to very high energies up to K-2500. Some of these cyclotrons have been listed in the previous section. The MSU design of the cyclotron got popularity and was followed by a number of laboratories. The schematic diagram of the cross-section of the cyclotron is shown in Fig. 8.16. The cyclotron is 2.184 m tall and

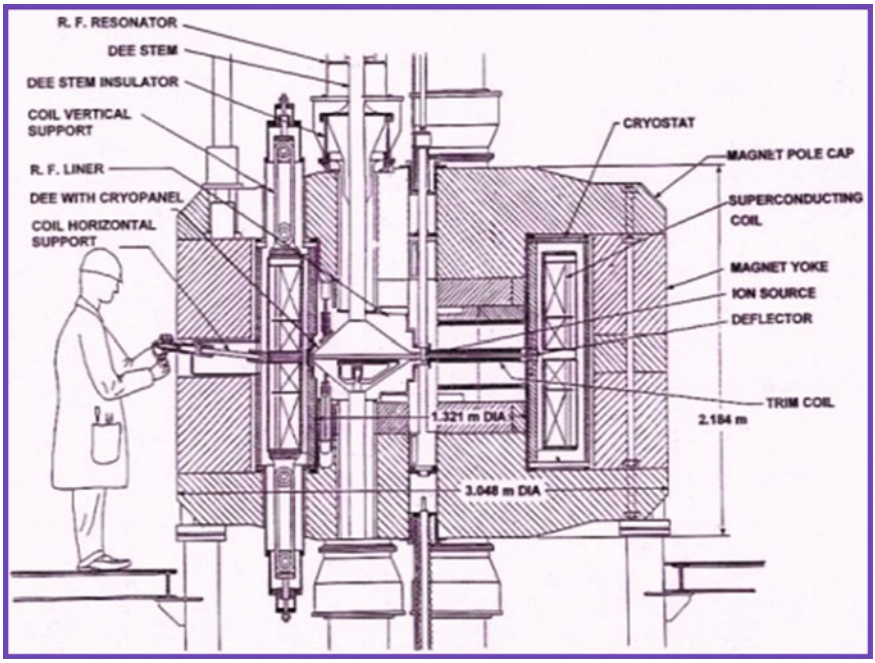

Fig. 8.16 The schematic cross-section of the K-500 cyclotron (MSU) [29] (*Courtesy* Marti Felix and Gelbke Konrad, NSCL, Michigan State University)

3.048 m wide (dia.). The magnet has two pairs of superconducting coils on either side of the median plane placed symmetrical, namely, α coils close to the centre and β coils away from the centre. The α and β coil sets are energized independently which allows proper adjustment of the isochronous field for all the beam energies and the central field. The magnet is installed in an annular cryostat with thermal shields and diagnostic tools. After welding, the magnet becomes an integral part of the annular cryostat as a single unit. The magnet operates in liquid helium at 4.2 K and produces field up to 5 T. The gap between the two coil sets allows different type of radial insertions in the median plane especially the extraction elements.

8.10.3.2 K-500 Cyclotron (VECC, Kolkata)

The K-500 superconducting cyclotron built at VECC [31], Kolkata is based upon the MSU design already shown in Fig. 8.15. The design parameters of the cyclotron are given in Table 8.7. The main magnet is divided in four coils, two identical pairs of α coils and β coils on either side of the median plane. Both the α coils and β coils are energized by two different power supplies. The α coils are short coils placed closure to the median plane and the larger β coils away from the median plane.

Table 8.7 The design parameters of the α and β coils of the main magnet of the K-500 (VECC, Kolkata [31]) (data compiled from PPT presentations)

Parameters of the α coils			Parameters of the β coils		
Parameter	Unit	Value	Parameter	Unit	Value
No. of α coils		2	No. of coils		2
Inner dia.	mm	1,521	Inner dia.	mm	1,521
Outer dia.	mm	1,793	Outer dia.	mm	1,793
Coil height	mm	162	Coil height	mm	327
No. of layers/coil		36	No. of layers/coil		36
No. of turns/coil		1,083	No. of turns/coil		2,234
Inductance of coils	H	13.8	Inductance of coils	H	27.6
Designed coil current	A	800	Designed coil current		800
Weight of coil	kg	690	Weight of coil	kg	1,410
Aluminum banding	mm	2.48 × 5.13	Aluminum banding	mm	2.48 × 5.13
No. of layers		10	No. of layers		10
No. of turns/layer		62	No. turns/layer		32
Total cold mass				ton	8
Main magnet frame dimensions (height)				mm	2,184
Main magnet frame dimensions (dia.)				mm	3,048
Weight of the main frame				ton	100
Total stored energy				MJ	22

All the coils have same inner and outer diameter and wound on a common SS former. The α and β coils are separated by an insulating 10 mm thick glass epoxy laminate spacer which has six segments of 60° each. The spacer has alternate grooves spaced at 2° pitch for liquid helium flow and for lead entry and exit. The former surface is electrically insulated with layers of mylar followed by a layer of 40 mil × 13 mm wide NEMA G-10CR laminate placed at a gap of 13 mm to allow the flow of liquid helium. Flange spacers of G-10 glass epoxy laminate with grooves of 2° pitch and 13 mm wide alternating ducts are used at the two ends of the former. These ducts provide liquid helium cooling channels. For inter-layer insulation also G-10 spacers, (180 in number) have been used, providing axial flow channels. Since during operation the winding is subjected to large EM forces, to prevent cable movement the winding is carried out under tension of 2,000 psi. The terminal of the magnet coils and the current leads are taken out through the top flange of the former. The two α coils and the β coils are connected in series to form two pairs and are operated using two separate power supplies. After insulating the coils with several layers of mylar, ten layers of aluminum (5052—H34 grade) banding (2.48 mm × 5.13 mm) were wound on the coils at a high tension of 20,000 psi. This banding increases the compressive stress on the coils significantly. The space between the two pairs of coils in the median plane is used for a variety of horizontal inserts.

The magnet former is welded shut inside the annular helium vessel such that the former itself acts as the inner wall of the helium container. The helium container is surrounded by an annular 80 K thermal shield and finally suspended inside a vacuum tank using G-10 vertical and horizontal support links. Many ports such as vacuum port, refrigeration ports and ports for current leads and other diagnostic tools are provided at the top of the vacuum container. The helium container is shown in Fig. 8.17a. The whole assembly is now positioned in a magnet frame which is one half of the iron yoke and weighs about 100 tons. The yoke carries top and bottom pole caps and three pole tips of sector shape, spaced at 120°. The lower half of the yoke is shown in Fig. 8.17b. Each pole tip has 13 trim coils wound over them for fine tuning of the field for different radii. A forged steel of AISI 1020 grade has been used for the fabrication of the yoke components including pole caps. All the components have been machined to a precision of 1.6 μm for perfect mating. Cylindrical symmetry around the axis and mirror symmetry of the two halves on either side of the median plane has been achieved using VTB machine.

The conductor used is a 1.2 mm multifilamentary wire of Nb–Ti (46 %) composition. The complete specifications of the conductor used are given in Table 8.8. The wire is embedded in the groove of a copper bar of dimensions 2.794 × 4.978 mm and filled with Pb–Sn soft solder. Since the maximum single length of the cable available was limited to 6 km three joints were made in each β coil and two joints in α coils. Special technique was developed to prepare low resistance joints. A total of 35 tons of cable has been used. The VECC cyclotron machine with beam line system is shown in Fig. 8.18. First beam acceleration took place in August 2009.

The quench protection system uses external dump resistors and consists of two independent circuits one each for α and β coils. The circuit (Fig. 8.19) enables the dumping of the stored energy in the resistors either in a slow-dump mode (4 A/min) or in a fast-dump mode (15.3 A/s) in different situations. The slow dump is activated in the event of a power failure. However, whenever some cryostat parameters exceed the acceptable limit such as liquid helium level, current lead voltage or

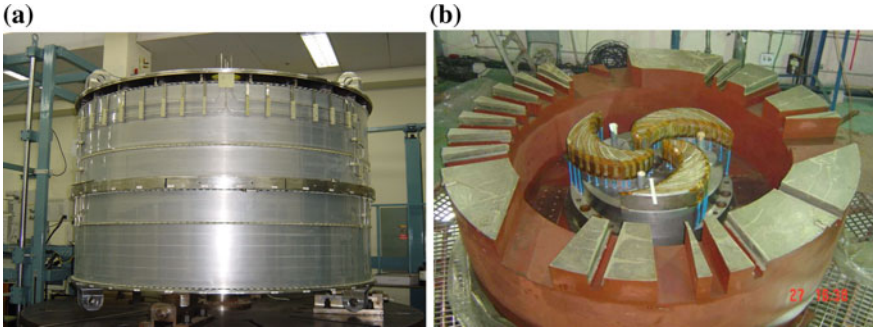

Fig. 8.17 **a** The annular helium vessel housing the magnet coils. **b** Lower half of the yoke with bottom pole caps and three sector shaped pole tips. Each pole tip has 13 trim coils (*Courtesy* D. Srivastava and S. Saha, VECC, Kolkata)

Table 8.8 The specifications of the conductor used for winding coils for K-500 (VECC, Kolkata, [31]) (data compiled from PPT presentations)

Parameter	Unit	Value
Type of conductor		MF (Nb–46 % Ti) wire soldered in a Cu-channel
Cable outer dimensions	mm	2.794 × 4.978
MF–Nb–Ti wire dia.	mm	1.20
No. of filaments		500
Filament dia.	μm	40
Cu/SC ratio in the wire		1.3
Overall Cu/SC ratio in the cable		20
Overall current density	A/mm^2	58
Critical current @ 5.5 T, 4.2 K	A	1,030
Conductor yield strength	MPa	117
Max. conductor single length	km	6
Total length of conductor used	km	35

Fig. 8.18 VECC superconducting cyclotron with beam line system (first beam line acceleration in August 2009) (*Courtesy* D. Srivastava and S. Saha, VECC, Kolkata)

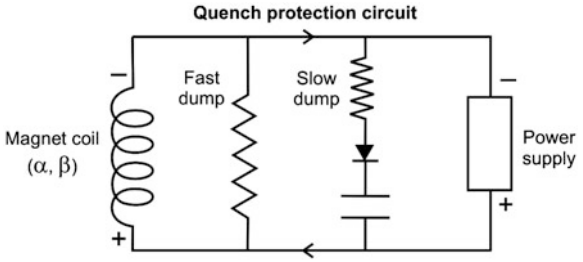

Fig. 8.19 Quench protection circuit provides slow and fast discharge of energy in external dump resistors in different situations

strain related force etc. the energy will dissipate in fast dumping resistors. The magnet system was first operated in 2009. A field of 4.8 T was achieved at the pole tips (hill region) at a radius of 0.55 m by charging α and β coils to 550 A current.

8.10.3.3 K-1200 Cyclotron (NSCL, MSU)

NSCL built yet another powerful cyclotron, K-800 [32, 33] as a booster to K-500 which went into operation in 1988. The new cyclotron performed superbly and provided excellent focusing power and was renamed K-1200 a year later in 1989. K-1200 continues to be world's highest energy superconducting cyclotron in its class. The design envisaged a beam energy of 200 MeV/nucleon for fully stripped light ions and 30 MeV/nucleon heavy ions depending upon the charge state of the ions injected. Even though, the design was based upon the use of K-500 as an injector yet the option was kept to operate K-1200 in stand alone mode using ECR ion source injector. All important parameters of the cyclotron and the conductor used in magnet construction are given in Table 8.9.

The design of K-1200 is similar to K-500 but differs in respect of several parameters. For example, the pole diameter was increased from 2.05 to 2.1 m, hill gap increased from 62.5 to 75 mm and the hill width from 46° to 51° at the outer radii. The distance between the two α coils increased from 75 to 100 mm making larger space for radial insertions especially for the magnetic channels of the extraction system. The pairs of α and β coils are powered by two independent power supplies like in K-500 to adjust the isochronous field for all ions and the main magnetic field. For most relativistic ions and for energies approaching focusing limit, current in β coils may be negative with respect to α coil and the average field increases by 20 % from $R = 0$ to $R = 1$ m. For non-relativistic ions these coils are positive with respect to α coils and the average field B_{ave} is almost constant with radius. Figure 8.20 is a photograph of K-1200 during the assembly procedure. The picture shows the lower half of the yoke with several radial penetrations related to the beam extraction system and other diagnostic tools. The coil and lower hills too are visible.

Table 8.9 Important parameters of K-1200, the magnet coils and the conductor (data compiled from [32])

Parameters of K-1200 cyclotron, the magnet and conductor		
Parameter	Unit	Value
Operating field	T	3–5
Pole diameter	m	2.1
No. of sectors used		3
Minimum hill gap	mm	75
Maximum valley gap	mm	900
Yoke inner diameter	m	2.95
Yoke outer diameter	m	4.375
Yoke height	m	2.875
No. of trim coils		22
Max. current in any trim coil	A	400
Max. power in any trim coil	kW	70
Peak dee voltage	kV	200
K value at 5 T		1200
RF frequency range	MHz	9–27
Number of coil pairs		2 (α and β)
Inner coil diameter	m	2.275
Outer coil diameter	m	2.575
Height of α coil (closer to median plane)	mm	400
Height of β coil (away from median plane)	mm	262.5
Separation between α coils	mm	100
Al-alloy banding thickness	mm	50
Inner dia. of vacuum tank	m	2.1125
Outer dia. of vacuum tank	m	2.925
Total height of cryostat	m	1.725
Conductor used (embedded in Cu-channel)		Nb–Ti (monolithic)
Conductor dimensions	mm	5.175 × 3.75
Overall Cu:SC ratio		25:1
Max. nominal current	A	1,000
Total inductance including mutual inductance at J_α = 3,500 A/cm^2	H	88.8
Total stored energy	MJ	61
Weight of the magnets	ton	280

The magnet operated in a range of 3–5 T field with a magnetic rigidity of 5 T m (K-1200). The magnet coils were run at a maximum current density of 3,500 A/cm^2. A monolithic Nb–Ti wire of the size 1.1 mm × 1.65 mm embedded in a copper channel (in a groove filled with solder) has been used for winding. The dimensions of the cable are 5.175 mm × 3.75 mm. A set of 21 trim coils have been used to have required B_{ave} v/s R slope. These coils have been wound on the pole

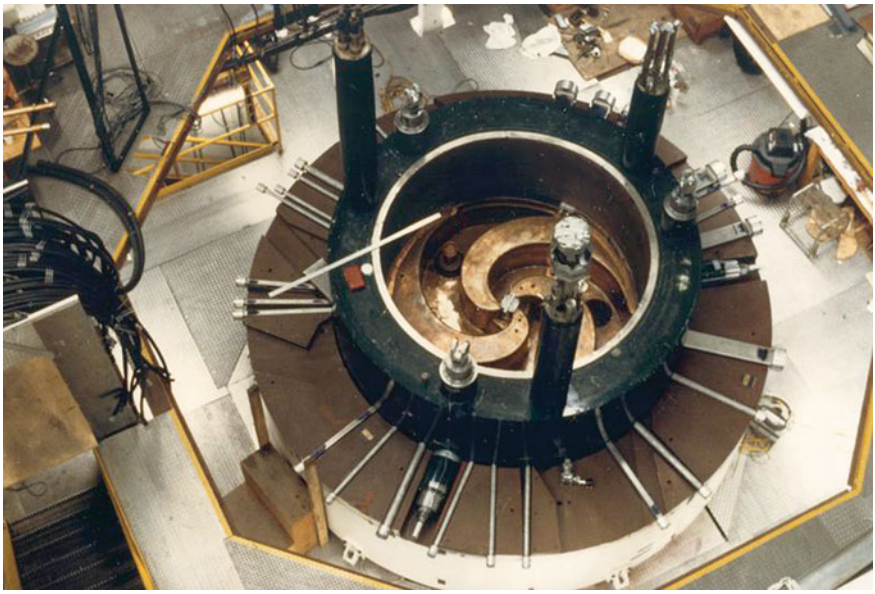

Fig. 8.20 K-1200 during the assembly process, the return yoke, the penetrations associated with the extraction elements (radial tubes) and the coil as well as the lower hills are seen in the *picture* (*Courtesy* Marti Felix and Gelbke Konrad, NSCL, Michigan State University)

tips using conventional copper conductor. A set of thick and heavily spiraled steel pole tips with three-fold symmetry provides vertical focusing. The gap between the valleys is 0.9 m. The sector area has a central hole of 175 mm which increases to 250 mm in the poles. This cyclotron happened to be first to have used a vertical injection and a ECR source for injection. There are 42 holes of dia. 18.75 mm, on the two sides of the each hill for the leads from the 21 trim coils. Holes have also been provided for feeding RF. The number of trim coil layers has been reduced from two to one and the gap between the hills increased to 75 mm. This enables easy slide of the deflector inwards at lower fields and helps in the extraction system. Nine magnetic channels and two electrostatic deflectors have been used in the extraction system.

The cyclotron went on stream and the first beam of $^{20}Ni_{3+}$ with 18 MeV energy was extracted successfully on June 6, 1988. The cyclotron performance was in excellent agreement with design calculations and the beam followed the highly intricate trajectory accurately. The beam spot was 4 mm well within the calculated value of 5 mm. The construction of the cyclotron was indeed most challenging because of much larger EM forces, a very intricate extraction system, much tighter pole tip spiral and a much larger size isochronous cyclotron with a magnet rigidity of 5 T m.

In 2001, K-1200 was coupled [34] to k-500 at the injection stage through an intermediate coupling line with a magnetic system. An ECR source injects the beam

into K-500 which accelerates the beam to 17 MeV/nucleon which in turn is injected into K-1200. The ions pass through a thin foil stripper which increases the charge state by a factor of 2.5. The beam is finally accelerated to 200 MeV/nucleon. It thus became possible to accelerate light ions to high intensities and heavy ions to large energies. This upgraded version can accelerate the U beam to 90 meV/nucleon and in stand alone mode can accelerate U beam to 25 MeV/nucleon. The cyclotron can as well be operated in stand-alone mode using ECR source producing very high charge state. The cyclotron produces radio active ion beam and is used by a vast community of nuclear scientists from across the globe.

8.10.3.4 K-2500, RIKEN Superconducting Ring Cyclotron

The RIKEN superconducting ring cyclotron (SRC) is the most important accelerator of the RIKEN radioactive ion beam factory (RIBF) project in Japan. The beam energy from the old ring cyclotron K-540 is boosted using a cascade of ring cyclotrons with K values of 570, 980 and 2,500 MeV. The final beam energy goes up to 440 MeV/nucleon for light ions like carbon and 350 MeV for very heavy ions like U. The high energy beam of heavy ions are then converted into high intensity radioactive ion beam through the fragmentation of stable isotopes. RIBF is world's unique facility which provides most intense radioactive ion beams of all the elements across the periodic table. Figure 8.21 is a complicated picture showing the organization of sector magnets and various other components constituting the ring.

The K-2500 SRC [35, 36] is 19 m in diameter and 8 m in height. The main components of the SRC are six sector magnets, one flat-top RF cavity, four main RF cavities, an injection system and an extraction system. The beam from the previous cyclotron is injected into the SRC at a radius of 3.56 m. Important parameters of the SRC and the sector magnets are given in Table 8.10. Each sector magnet is 7.2 m long, 6 m in height and has a sector angle of 25°. Each sector magnet module comprises of a pair of main coils, four sets of superconducting trim coils, thermal shield, thermally insulating supports and the cryostat. The magnet is operated at 4.5 K. In addition, there are 22 pairs of normal conducting trim coils, warm poles and warm yoke. Each sector magnet weighs $\sim$800 tons. The total cold mass of all the six sector magnets is 140 tons which needs three weeks to cool to 4.5 K from room temperature. A unique feature of the construction of the SRC is the use of 1 m thick iron slabs for an effective radiation and magnetic shielding. These slabs cover the valley regions between the two adjacent sector magnets and also vertically along the sides between the top and bottom slabs. This minimizes the inverse-direction stray field which influences beam deflection power in the valley. The decrease in leakage field brings down the magneto-motive force at the peak bending power. In all, the iron slabs weigh around 3,000 tons. The SRC itself becomes massive weighing 8,300 tons. The beam is finally extracted at a radius of 5.36 m. The maximum field produced is 3.8 T which accelerates U^{+88} to an energy of 350 MeV and is a world record.

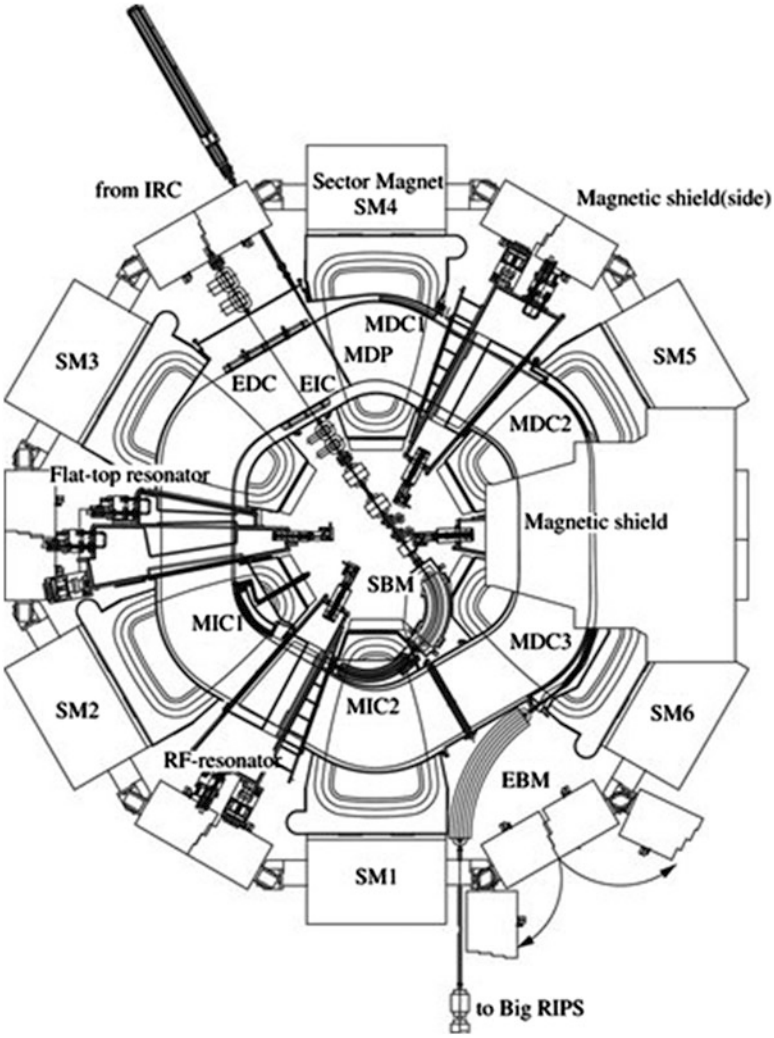

Fig. 8.21 The layout of the six sector magnets of the RIKEN K-2500 superconducting ring cyclotron (SRC) [35] (*Courtesy* Hiroki Okuno and with permission of Oxford University Press on behalf of Physical Society of Japan)

The cable used for winding the main coils of the sector magnet and the superconducting trim coils is of a Nb–Ti Rutherford type with an outer dimensions of 15 mm × 8 mm. The stabilizing cladding material is an aluminum alloy containing about 1,000 ppm Ni which increases the yield strength of this alloy from 44 to 55 MPa. The maximum operating current for the main magnet is 5,000 A and for the trim coils 3,000 A. The main coil has a solenoid winding with 396 turns and generates a magneto-motive force of 4×10^4 AT (Ampere Turn). Inter-turn and inter-layer fiberglass reinforced plastic (FRP) spacers have been used in the

Table 8.10 Important parameters of RIKEN K-2500 SRC and the magnet (data compiled from [35, 36])

Parameter	Unit	Value
Outer dia. of SRC	m	19
Height of SRC	m	8
Injection radius	m	3.56
Extraction radius	m	5.36
Total weight	ton	8,300
No. of sector magnets		6
Sector angle	degree	25°
Poles and yoke		Warm
No. of main coils		2
No. of SC trim coils		4 sets
Max. sector field	T	3.8 @ 5 kA
Total stored energy	MJ	235
Length of sector magnet	m	7.2
Height of sector magnet	m	6
Weight of a sector magnet	ton	800
Conductor used		Nb–Ti
Type of conductor		Rutherford
Cable outer dimensions	mm	15 × 8
Jacket material		Al-alloy
Yield strength of Al-alloy	MPa	55

horizontal and vertical gaps to insulate the conductor electrically as well as to provide cooling channels for the conductor. About 50 % area of the cable is left exposed. For trim coils also the same conductor has been used. Four sets of trim coils, installed in the beam accelerating area of the sector magnet, are wound in a double pancake structure. The wide and thin trim coil is sandwiched between two Al-alloy plates having grooves. These grooves serve as cooling channels for the forced flow of two phase helium. A control dewar mounted at the top of the SRC supplies liquid helium to all the six sector magnets in a close loop mode. A refrigerator with a capacity of 620 W at 4.5 K and 400 W at 70 K has been used which is far more than the heat load of the total cold mass (140 tons).

The injector system too has a superconducting bending magnet (SBM) [37] for bending the beam before injection into K-1200. This magnet generates a field of 3.8 T along the beam trajectory having a curvature of 1.21 m at a current of 363 A. The special features of the magnet are the flat coil geometry, iron poles used as former for coil winding and the iron yoke in two parts, one H-shaped cold yoke and another C-shaped warm yoke. The total cold mass is only 3 tons. A monolithic Nb–Ti conductor of the dimensions of 2.4 mm × 0.8 mm has been used for winding. The coil is finally vacuum epoxy impregnated.

The demand for superconducting magnets for application to accelerators will continue to grow. Focus, however, may shift to A-15 class of superconductors like

Nb_3Sn and Nb_3Al for their superior performance and to the high T_c superconductors in the near future. MgB_2 is a new superconductor which is economical and stands chance of becoming a good candidate for application to accelerators. High T_c superconductors and MgB_2 have the added advantage that they can operate on cryo-coolers in place of liquid helium.

References

1. K.H. Mess, P. Schmuser, S. Wolff, *Superconducting Accelerator Magnets* (World Scientific, Singapore, 1996)
2. P. Schmuser, Rep. Prog. Phys. **54**, 683 (1991)
3. L. Rossi, Very high field magnets, in *Proceedings CAS* (*CERN Accelerator School*), Erice, Italy 8–17 May, 2002, ed. by S. Russenschuk, G. Vandoni. Course lecture, pp. 177–195
4. L. Rossi, IEEE Trans. Appl. Supercond. **12**, 219 (2002)
5. L. Rossi, IEEE Trans. Appl. Supercond. **13**, 219 (2003)
6. L. Rossi, Cryogenics **43**, 281 (2003)
7. L. Rossi, IEEE Trans. Appl. Supercond. **14**, 153 (2004)
8. S. Russenschuk, Electromagnetic design of superconducting accelerator magnets, in *Proceedings CAS* (*CERN Accelerator School*), Erice, Italy 8–17 May 2002, ed. by S. Russenchuk, G. Vandoni. Course lecture, pp. 71–151
9. S. Russenschuk, ROXIE—a computer code for the integrated design of accerator magnets, http://accelconf.cern.chg/accelconf/e98/PAPERS/TUP11H.PDF
10. I.I. Rabi, Rev. Sci. Instrum. **5**, 78 (1934)
11. T. Takeuchi, A. Kikuchi, N. Banno, H. Kitaguchi et al., Cryogenics **48**, 371 (2008)
12. A.V. Zlobin, arxiv.org/ftp/arxiv/papers/1108/1108.1869.pdf
13. A. Milanese, M. Devaux, M. Durante et al., IEEE Trans. Appl. Supercond. **22**, 4002604 (2012)
14. P. Ferrasin, M. Devaux, M. Durante et al., Report No. CERN-ATS-2013-022, in *Applied Superconductivity Conference*, *ASC 2012*, 7–12 Oct 2012, Portland, Oregon, USA
15. R. Gupta, A common coil design for high field 2-in-1 accelerator magnet, in *Proceedings of the 1997 Particle Accelerator Conference*, vol. 3, p. 3344 (1997)
16. R. Gupta, Common coil magnet system for VLHC, in *Proceedings of 1999 Particle Accelerator Conference*, vol. 5, p. 3239 (1999), https://accelconf.web.cern.ch/accelconf/p99/PAPERS/THP120.PDF
17. S.A. Gaurlay, K. Chow, D.R. Dietderich et al., Fabrication and test results of a prototype, Nb_3Sn superconducting racetrack dipole magnet, in *1999 Particle Accelerator Conference*, NY, March 1999, SC MAG 628, LBNL# 41575
18. R. Benjegerdes, P. Bish, D. Byford et al., Fabrication and test results of a high field, Nb_3Sn superconducting racetrack dipole magnet, in *Proceedings of the 2001 Particle Accelerator Conference*, Chicago, pp. 208–210, http://escholarship.org/uc/item/76w9q3sg#page-1, LBNL, 2LC03SC-MAG#764 LBNL-49901
19. P. Ferracin, S.E. Bartlett, S. Kaspi et al., IEEE Trans. Appl. Supercond. **16**, 378 (2006)
20. P. Ferracin, S. Caspi, D.W. Cheng et al., http://www.escholarship.org/uc/item/4n89827c (e scholarship, LBL, Publication 29 Sept 2008)
21. R. Yamada, G. Ambrosio, E. Barzi et al., Design study of 15-Tesla RHQT Nb_3Al block type dipole magnet, FERMILAB-CONF-05-426 TD (2005)
22. J.C. Thompkins, V. Kashikhin, B. Parker et al., in *Particle Accelerator Conference*, *2007* (PAC07), 25–29 June 2007, Albuquerque
23. N. Phinney et al., International linear collider reference design report, ILC-REPORT-2007-001
24. V.S. Kashikhin, N. Andreev, M.J. Lamm et al., IEEE Trans. Appl. Supercond. **18**, 155 (2008)

25. V.S. Kashikhin, N. Andreev, G. Chlachidze et al., IEEE Trans. Appl. Supercond. **19**, 1176 (2009)
26. V. Kashikhin, N. Andreev, J. Kerby et al., IEEE Trans. Appl. Supercond. **22**, 4002904 (2012)
27. V. Kashikhin, IEEE Trans. Appl. Supercond. **22**, 4003904 (2012)
28. J.A. Crittenden, M.A. Palmer, D.L. Rubin, Wiggler magnet design development for the ILC damping rings, in *Proceedings of IPAC 2012*, New Orleans, Louisiana, USA, TUPPR 065, http://accelconf.web.cern.ch/accelconf/IPAC2012/papers/tuppr065.pdf
29. H.G. Blosser, Design, construction and operation of superconducting cyclotron. Lecture Notes of 1986 RCNP Kikuchi Summer School on Accelerator Technology, Osaka, pp. 39–78, 20–23 Oct 1986
30. H.G. Blosser, IEEE Trans. Nucl. Sci. **NS-26**, 2040 (1979)
31. S. Saha, J. Chaudhury, G. Pal et al., Cryogenics **49**, 235 (2009)
32. F.G. Resmini, G. Bellomo, H.G. Blosser et al., IEEE Trans. Nucl. Sci. **NS-28**, 2749 (1981)
33. J.A. Nolen Jr., Nucl. Instrum. Methods Phys. Res. B **40/41**, 870 (1989)
34. R.C. York, H.G. Blosser, T.L. Grim et al., The NSCL coupled cyclotron project-overview and status, http://www.nscl.msu.edu/∼marti/publications/overview_ganil_98/overview.pdf
35. H. Okuno, N. Fukunishi, O. Komigaito, Prog. Theor. Exp. Phys. 03C002 (2012)
36. Y. Yano, Nucl. Instrum. Methods Phys. Res. B **261**, 1009 (2007)
37. H. Okuno, S. Fujishima, T. Tominaka et al., IEEE Trans. Appl. Supercond. **14**, 275 (2004)

Chapter 9
Superconducting Magnets in Fusion Reactors

Abstract A fusion reactor is an artificial sun created under laboratory conditions of high temperature and pressure to produce inexhaustible energy. When two nuclei of hydrogen isotopes are forced to fuse, under high temperature and high pressure, the reaction produces huge amount of energy and the heavier atoms of helium. The tokamak concept for magnetic confinement of plasma in a fusion reactor made the use of superconducting magnets most attractive and a natural choice. This chapter gives an account of the fusion process, the Lawson-Criterion for realizing 'ignition', different methods of plasma confinement and the superiority of tokamak concept. In a tokamak plasma is confined in a torus by an axial field generated by a set of toroidal coils distributed around the torus and a poloidal field generated by a set of poloidal coils. A high field central solenoid induces current in the plasma to heat it to high temperature through ramping of the field. This current in turn also produces poloidal field. We discuss the superconducting magnet systems built for most important fusion reactors so far, namely, T-7 of Russia, Tore Supra of France, JT-60 SA of Japan, KSTAR of Korea, EAST of China and SST-1 of India. The magnet systems of ITER, has been discussed in greater details. Two tokamaks, namely, TFTR of USA and JET at Culham UK both using normal magnets have also been included for they had many firsts and the data collected from them contributed significantly to the design of ITER. Two more futuristic reactors, the stellarator W7-X being built in Germany and IGNITOR an Italian–Russian joint fusion reactor being built in Russia have also been included towards the end of the chapter.

9.1 The Fusion Reaction

The sun and stars produce their own energy through a hydrogen-hydrogen fusion reaction under conditions of high pressure (high gravitational pull) and high temperature. At high temperature hydrogen gas converts into plasma and the positively charged nuclei so formed fuse together under high pressure. Under such condition,

R.G. Sharma, *Superconductivity*, Springer Series in Materials Science 214,
DOI 10.1007/978-3-319-13713-1_9

the attractive nuclear force overcomes the Coulomb repulsion between the positively charged nuclei forcing them to fuse. The fusion reaction produces heavier nuclei of helium and releases huge amount of energy. This huge energy is a consequence of the loss of a small mass during the reaction which gets converted into energy ($E = mc^2$). Fusion scientists were keen (since around 1930s) to create the conditions of the sun in the laboratory and use fusion as an inexhaustible source of energy for future. The big challenge is that how to create massive gravitational pull, such as available on the sun, inside a laboratory. One option is that we raise the temperature of the plasma to $\sim 10^8$ K, about 6 times higher than the sun temperature. The other condition to be met is that the plasma should remain dense enough for long intervals so that the fusion continues and reaches 'ignition' stage as the new fuel is continuously fed. In other words, the re-deposition of fusion energy back into plasma must exceed the energy lost by the plasma to the reactor walls by conduction and radiation. This is referred to as 'self sustaining plasma' or the so called 'ignition' and is attained in a laboratory under controlled conditions.

The present efforts are focused on the fusion reaction between the two heavy isotopes of helium, namely, deuterium (D) and tritium (T) which yields much higher fusion energy compared to D-D or H-D fusion. Deuterium is most abundant in sea water but tritium is not available in nature. It is radioactive but has a small half-life of 12 years. Tritium, however, can be produced in the fusion reactor itself through by reacting lithium with neutrons generated in fusion reaction ($^1n_0 + {}^6Li_3 = {}^3T_1 + {}^4He_2$). The D-T reaction is schematically shown in Fig. 9.1. In a

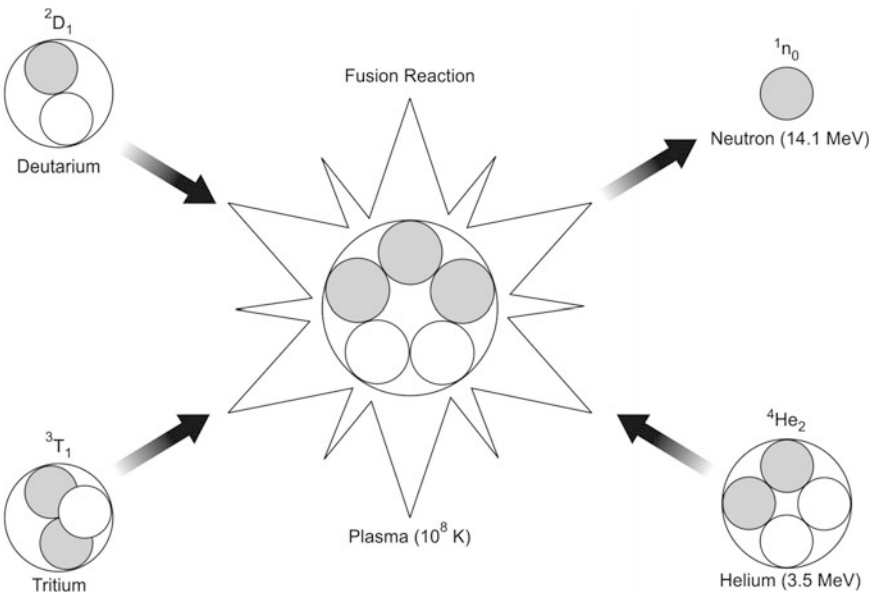

Fig. 9.1 Fusion Reaction: two isotopes of hydrogen, deuterium and tritium fuse under condition of high temperature and produce high energy, 14.1 MeV neutrons and helium atoms

fusion device, the energetic (14.1 MeV) neutrons are absorbed by a thick blanket containing lithium which gets heated-up. In a power producing reactor this heat will be used for the production of steam for rotating turbines in a conventional power plant.

Fusion is attractive because it does not release polluting obnoxious gases like the fossil fuels do. There is no chain reaction either like in fission and no possibility therefore of a 'melt-down' or 'run-away'. Any interruption in the control system in heating of the plasma will automatically terminate fusion. The fusion product is helium which is not radioactive or toxic.

9.2 Plasma Ignition

The 'Lawson's Criterion' [1] stipulates that the plasma can reach the 'ignition' stage only if the triple product of plasma temperature (T), the plasma (electron) density (n_e) and the energy confinement time (τ_E) fulfills the following condition:

$$n_e T \tau_E \geq \frac{12 k_B}{E_{ch}} \frac{T^2}{\langle \sigma v \rangle} \tag{9.1}$$

where k_B is the Boltzmann constant, $E_{ch,}$ energy of the charged fusion product, σ, fusion cross section, v, the relative velocity and $\langle \sigma v \rangle$ the average of Maxwellian velocity distribution at temperature T. The above 'triple product' value for a D-T reaction, on a 50:50 basis, turns out to be

$$n_e T \tau_E \geq 10^{21} \text{ keV s/m}^3 \tag{9.2}$$

This condition has not been achieved in any reactor so far, though ITER is designed to attain this triple product value. The energy confinement time, τ_E is defined as the rate at which a system losses energy to its surroundings and is given by

$$\tau_E = \frac{W}{P_{loss}} \tag{9.3}$$

where W is the energy density (per unit volume) and P_{loss}, the power loss density (rate of energy loss per unit volume).

Lawson had assumed that the fusion energy loss is mostly caused by conduction and radiation (Bremsstrahlung). His calculations show that the plasma temperature in a D-T reaction has to reach 30 million degrees and for a D-D reaction it has to reach 150 million degrees. In practice, plasma is heated by a combination of techniques. Most highly developed techniques are heating by inducing current in electrically conducting plasma by ramping field in a central solenoid, by EM radiation (in radio frequency and microwave frequency range) using ICRH and ECRH techniques and by high energy neutral beam injection.

High temperature causes turbulence in plasma which tends to escape to the walls of the container and thus lower the plasma temperature. To sustain the plasma, the fusion materials are to be added continuously and prevent plasma escape to the reactor walls by suitable confinement technique with a long energy confinement time, (τ_E). Two types of confinements have been studied in depth, the inertial confinement and the magnetic confinement. We briefly discuss these techniques below.

9.3 Plasma Confinement

9.3.1 The Inertial Confinement

In inertial confinement, the plasma is confined by its own inertia and the energy confinement time (τ_E) is only about 1 ns, thus limited to pulse operation only. This means that the break-even point (where the fusion energy is equal to the energy spent in fusion reaction) in an inertial confinement will reach only at a very high plasma density, about 10^{30} particles/M^3 (100 times the density of a liquid). Such high densities are achieved by compressing mm size solid fuel pellets by focusing an intense laser or a particle beam on to the pellet. The inertial confinement [2] is schematically shown in Fig. 9.2. These techniques are often referred to as 'laser-fusion' and 'particle beam-fusion' respectively. Laser fusion became popular during 1970s but has been taken over by the magnetic confinement in the following years. In the rest of the chapter we will restrict our discussion to 'magnetic confinement', only.

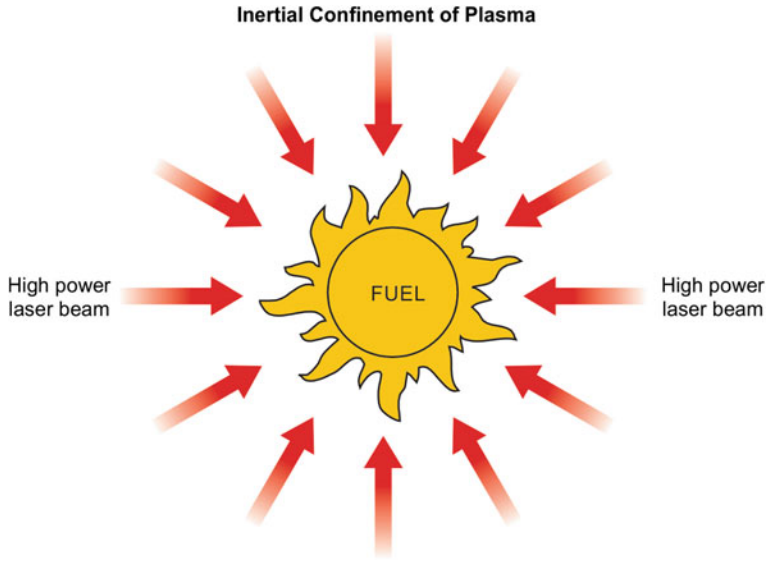

Fig. 9.2 Principle of inertial plasma confinement (dense plasma but short confinement time)

9.3.2 The Magnetic Confinement

In magnetic confinement, the plasma, having a charge, makes helical path along the field direction and is confined for long period of time. Since the plasma has a density of 10^{21} particles/M^3 only, orders of magnitude smaller than the density of air at room temperature, it must have an energy confinement time of at least 1 s. This simply means that the energy of plasma should be replenished every 1 s.

Magnetic confinement together with high temperature ($\sim$100,000 °C) stands out to be the best option for stabilizing plasma in the laboratory and a substitute for the gravitational pressure on the sun. Magnetic confinement is based on the principle that the charged particles in the plasma travel in a helical path along the direction of the magnetic field as shown in Fig. 9.3. Several configurations of magnetic confinement were proposed and tried but three major configurations were pursued and developed over last few decades with varying degree of success. These are 1. magnetic mirror, 2. stellerators and 3. tokamaks.

9.3.3 Magnetic Mirror

The magnetic mirror confinement is a simpler technique. It employs a cylindrical magnet with an axial field. The axial field does prevent plasma escape in the radial direction but they can escape from the two ends. This escape can be eliminated by plugging the ends magnetically and electrostatically. In this configuration the magnetic field at the ends is increased by placing two coils as shown [3] in Fig. 9.4. Such an arrangement creates a 'constriction' at the ends with stronger field at the two ends and a weaker field in the middle. The plasma with charged particles slows down and gets reflected from the ends or the so called 'magnetic mirrors'. However, plasma particles possessing very high speed can still escape through the mirrors. Such particles can be stopped by providing electrostatic end plugs. A pair of additional plasma sections are added at the two ends beyond the magnetic mirrors.

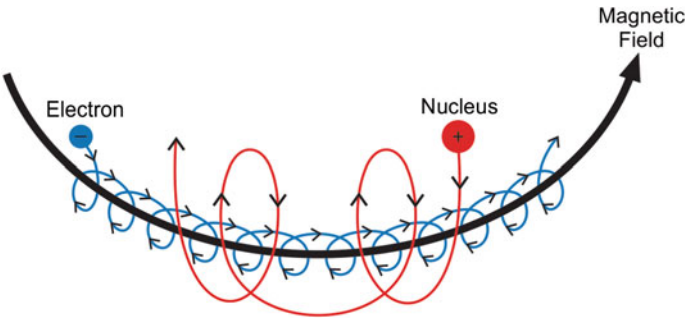

Fig. 9.3 Principle of magnetic confinement. Charged particles of the plasma circulate around the magnetic field and move along the axis (low density plasma but long confinement time)

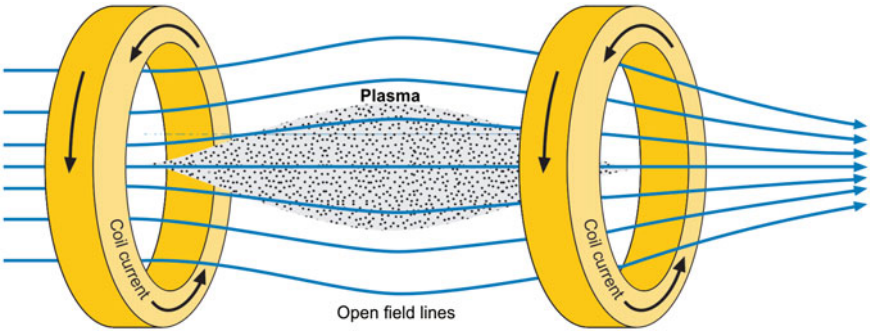

Fig. 9.4 Schematic diagram of a magnetic mirror configuration with magnetic lines. The two end coils with strong field create a 'constriction' for plasma at the ends (adapted from [3])

Plasma in these sections generates a potential barrier which prevents the plasma escape. Such a configuration is termed as 'Tandem Mirror'. A tandem mirror test facility (TMTF) [4] was built by Lawrence Livermore National Laboratory in 1986 but was closed immediately after.

9.3.4 The Stellarators

The concept of stellarator was proposed by Lyman Spitzer [5] in 1950 under a secret project 'Matterhorn' at Princeton, USA and the device was built the very next year but the project was de-classified in 1961 only, under a new name, Princeton Plasma Physics Laboratory (PPPL). Spitzer proposed a new and simpler technique to prevent the escape of plasma from the two ends by bending the solenoid into the form of a torus and closing the two ends. In this configuration, the winding at the inner edge is tight and close to each other but gets farther apart at the outer edge. As a consequence, the magnetic field at the outer edge is weaker than at the inner edge and is thus no longer uniform. Spitzer modified the geometry by stretching out the torus converting it into the shape of a race-track coil and twisting one end by 180° so as to form a figure of '8'. In such a geometry, the downward drift of the plasma particles in one curved section is counter balanced by the upward drift in the other curved section. The net drift is thus greatly reduced but is not 'perfect'. Like magnet mirror confinement the stellarator too is a low plasma density and high confinement time device. Here the strategy has been to use differing magnetic field such that the net force on the torus is neutralized. It uses helical coils which may be continuous or discrete around the torus. A typical stellarator magnet is shown in Fig. 9.5.

The remarkable advantage that a stellarator offers is that a steady state operation of the reactor is possible after the ignition has been achieved. The superconducting coils need not be pulsed or the energy be stored. There are no current disruptions either. The design also makes large aspect ratio possible and does not need

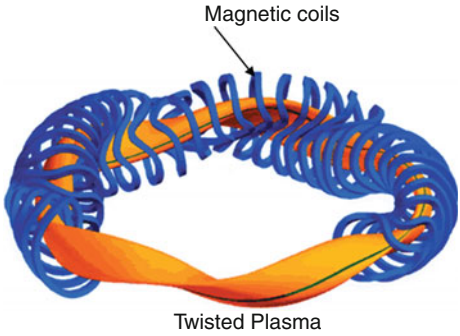

Fig. 9.5 Magnetic coil configuration in a stellarator (*Courtesy* Thomas Klinger, Max-Planck Institute for plasma Physics)

complicated correction coils for shaping the field and position control coils. It gained popularity in 1950s and 1960s but lost the race to tokamaks in 1970s. Tokamaks were built in many countries independently. Finally, these countries joined hands to pool together their vast experience and resources in building ITER (International Thermonuclear Experimental Reactor) in France. Interest in stellarator reactors has, however, revived in recent time in view of the complexities involved in building tokamak devices. Some of the important reactors being built are 1. W 7-X (Wendelstein 7-X), Germany, 2. HSX (Helically Symmetric Experiment), USA, 3. LHD (Large Helical Device), Japan. A review on stellarators was published by Beidler et al. [6] in 2001.

9.3.5 The Tokamak

The concept of magnetic confinement of high temperature plasma was given by Soviet scientists (now Russian) Igore E. Tamm and Andrei D. Sakharov of Kurchatov Institute, Moscow in 1950 (see [1–3] in [7] of this chapter) while working in a secret project on controlled thermonuclear reactor at 'Arzamas-16 Nuclear Centre'. The abbreviation 'tokamak' has been taken from the Russian term 'Toroidalnaya Komneta s Magnetiymi Katushkami' which in English translates into 'Toroidal Chamber with Axial Magnetic Field'. Beginning 1951, Sakharov had worked out the tentative parameters of a toroidal thermonuclear D-D fusion reactor of 900 MW power. The dimensions read like, major radius 12 m, minor radius 2 m, field 5 T, plasma density $3 \times 10^{20}/m^3$ and plasma temperature $\sim$100 keV (1,000 million °C). These values when extrapolated to D-T fusion reaction are close to the modern D-T tokamak dimensions. The confinement was proposed by a combination of a toroidal field and a field produced by a current circulating in the plasma itself. The work on thermonuclear fusion was declassified in 1954. A good account of the contribution of the Russian scientists to tokamak development has been given by Smirnov [7].

9.3.5.1 Magnetic Field in a Tokamak

High temperature plasma in a toroid is confined by a combination of two fields, one a poloidal field produced by the current circulating in the plasma and another an axially symmetric strong magnetic field parallel to the current. The axial field is produced by a set of toroidal coils spaced around the torus. The resultant field is a helical field around the circular plasma and close to the surface (Fig. 9.6). It is this helical field which confines the plasma. The toroidal field can be calculated using Ampere's Law. A toroidal magnet is a group of coils each carrying same current. The magnetic field inside a torus at any distance from the centre is uniform because of the symmetry. If the number of coils is N each carrying a current I, the magnetic field will be;

$$B = \frac{\mu NI}{L} = \frac{\mu NI}{2\pi R} \qquad (L \text{ being} = 2\pi R) \tag{9.4}$$

where R is the distance of the plasma axis from the centre. Thus we find that the toroidal field is inversely proportional to the distance from the centre. The field therefore at the outer periphery is weaker than at the inner radius. The role of the strong toroidal field is to suppress the main magnetohydrodynamic instabilities. The cross-section of the magnetic surface in a plane passing through the axis (Fig. 9.6b)

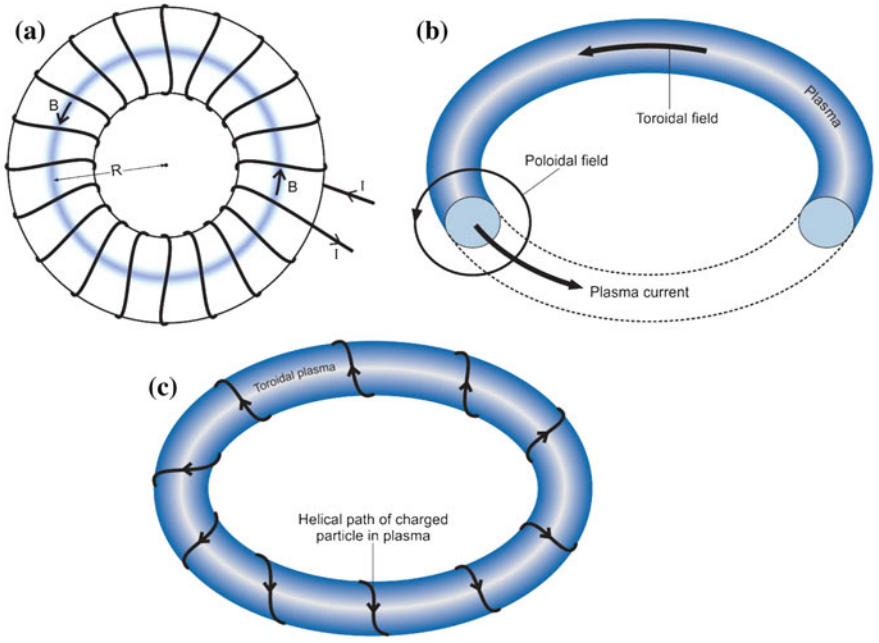

Fig. 9.6 **a** Toroidal field produced by coils wound around the torus. **b** Poloidal field produced by the current flowing in the plasma. **c** The helical path followed by the charged particles in the plasma

can be considered only approximately circular. Plasma equilibrium analysis shows that at a high toroidal field magnetic surface shape deviates significantly from a circle. Further, the field in a tokamak is also not perfectly symmetric. The toroidal field is produced by a number of coils spaced around the torus. The coils cannot be brought too close because enough space is required for the insertion of a large number of diagnostic instruments and vacuum ports. Still with a larger number of coils the field symmetry obtained is quite good, the field oscillations are well within the acceptable limit.

Plasma equilibrium on macroscopic scale is another crucial aspect of a tokamak. Even though the superposition of toroidal field and poloidal field leads to good plasma containment, yet under the influence of electrodynamic forces the plasma current loop tend to expand outwards. The laws of electrodynamics say that a ponderomotive force acts on a current carrying conductor such that it tends to increase its inductance. In a circular conductor it will mean that the radius of the plasma loop will increase. To maintain the equilibrium this expanding force is to be balanced by applying additional magnetic field parallel to the major axis of the toroid. A perpendicular magnetic field $B_{\perp}$ interacts with I and creates a force = $2\pi RIB_{\perp}/c$ which acts on the entire length of the plasma loop. This interacting force of the supplementary current carrying coils producing vertical field will act inwards to counter balance this expanding force with a correct choice of sign. Besides, tokamak devices use a conducting toroidal casing which compensates the internal forces expanding the loop. Eddy currents are produced in the metal casing when the current carrying loop moves outwards. These eddy currents interact with loop current and give rise to a force which acts inwards. The real breakthrough in fusion research came in 1958 in USSR when they achieved plasma temperature and confinement time in a doughnut shaped vessel called tokamak. The world's first superconducting tokamak T-7 too was built in USSR in 1978 [8] but it used only toroidal magnets as superconducting. Other magnets were normal magnets.

Present day tokamaks use all the magnets superconducting to reduce power consumption. Figure 9.7 shows the scheme of different magnets used in present day tokamak device. Magnetic confinement of plasma is realized by a set of toroidal coils arranged equidistant around the torus, and a set of poloidal coils mounted around the toroidal coils. A central solenoid (CS) produces high field which induces current in plasma when ramped. This in turn heats the plasma and generates poloidal field. The CS, in a way, acts as a primary of a transformer and the plasma as the secondary. This induced current causes Ohmic heating of the plasma. The Ohmic heating is, however, not enough to raise the plasma temperature to the required level. It can raise the plasma temperature to only 20–30 million °C. Additional heating is provided by using EM high frequency waves like ECRH (electron cyclotron resonance heating), ICRH (ion cyclotron resonance heating) in the 40–55 MHz frequency range and neutral beam injection as shown in Fig. 9.8. A neutral beam has to have a large kinetic energy ($\sim$1 MeV) to heat the plasma. Since neutral atoms cannot be accelerated by an electric field, a positively charged ^{2}D beam is first accelerated to high energy and then allowed to pass through a ^{2}D gas cell called 'ion beam neutralizer' where it picks-up the lost electron to become

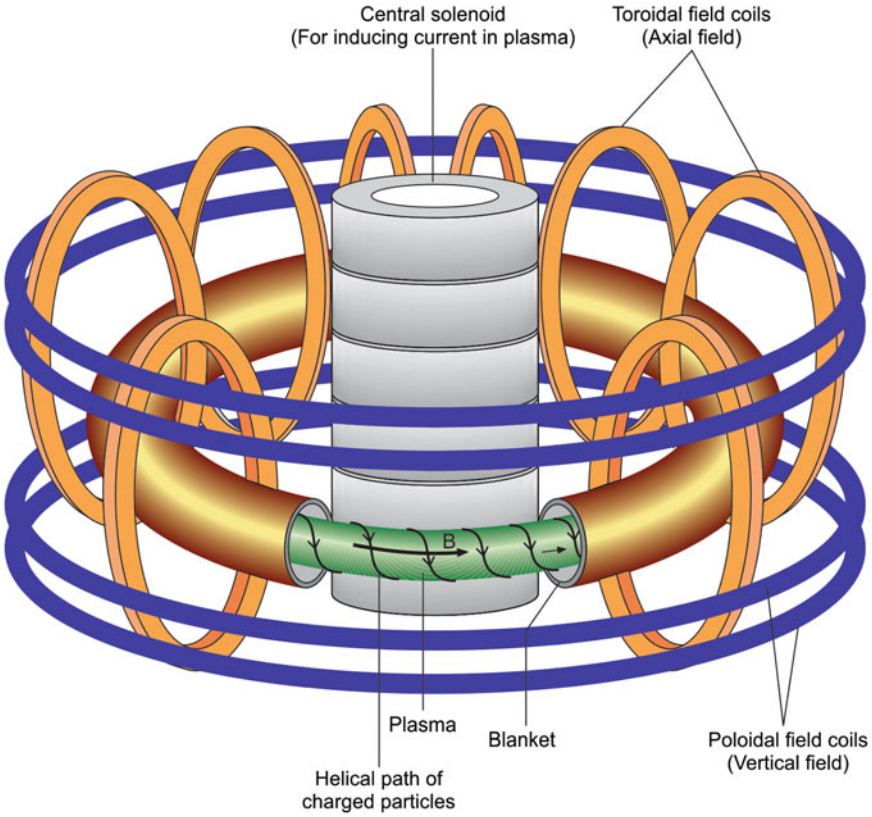

Fig. 9.7 Magnetic confinement of plasma realized by a set of toroidal, and poloidal coils. A central solenoid induces current in plasma which, in turn heats the plasma and generates poloidal field

neutral again. Neutral beam is injected into the plasma stream where it collides and transfers energy to plasma and heats it up. Till now, more than 200 fusion reactors of different sizes, using magnetic confinement techniques, have been built and operated world over. Some of them are still working. More advanced tokamaks and stellerators are being built in Europe, Asia and USA. In the following sections we will discuss the magnet systems of some of the important fusion reactors.

9.4 Important Superconducting Tokamaks

High triple fusion product require large confinement time and thus high magnetic field. Such fields can be generated by superconducting magnets only. Use of these magnets enable operation in continuous mode and also results in a substantial saving of power, an important factor to cross the breakeven point. Many superconducting toroidal magnets were built, (T-7 to T-20) in Russia (Moscow), Toresupra in France

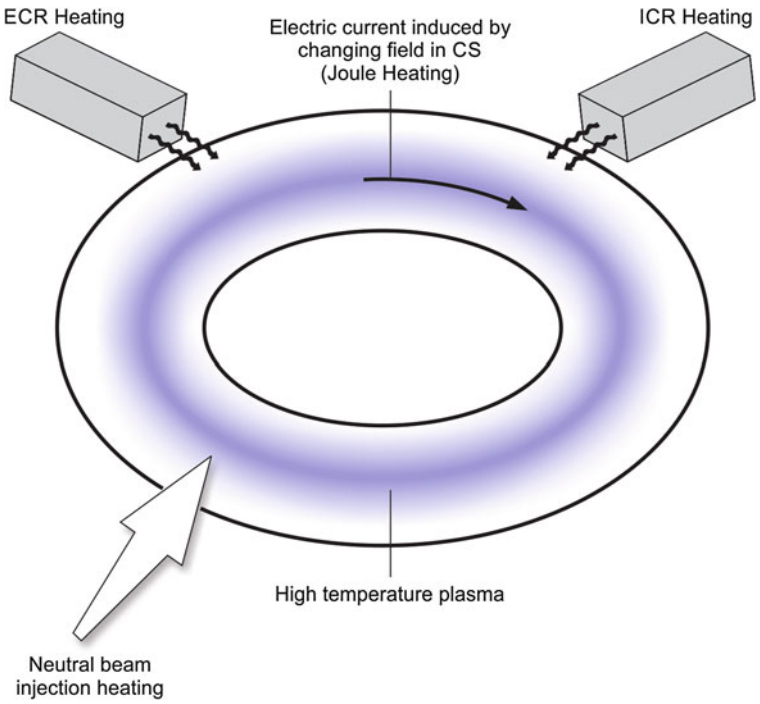

Fig. 9.8 Three different modes of plasma heating. Electric current through plasma is induced by the changing magnetic field in the central solenoid. Additional heating done by ICR, ECR and neutron beam injection

(Cadarache), and JT-60 (Japan Torus) in Japan (Naka). Some of them are operational and others not. HT-7 (Hefei Tokamak) in China (Hefei) was the first fully superconducting tokamak in the world. The working superconducting fusion reactors are (T-7, T-15) at Kurchatov Institute, Russia, Tore Supra in France, Triam 1-M and LHD in Japan and HT-7 in China. New fusion reactors that have come-up recently are EAST in China, K-STAR in Korea, SST-1 in India and JT-60 SA in Japan. Fusion reactors, JET (Joint European Torus) at Kulham, UK and TFTR (Toroidal Fusion Test Reactor) at Princeton Plasma Research Laboratory (PPPL, USA) though non-superconducting, contributed greatly to our present day understanding of fusion. JET achieved 16 MJ fusion energy first time surpassing the 10.7 MW achieved by TFTR, but remained well below the breakeven point, where the fusion energy produced is equal to the power spent in operating the machine. JET used 50:50 deuterium and tritium fuel mixture similar to TFTR and has the distinction of developing the remote handling system for tritium first time. TFTR is no longer in operation. PPPL also built a spherical torus 'NSTX' (Next-Step Spherical torus Experiment) in 1999 with spherical plasma with a central hole but had to stop in 2008 because of the lack of funding. New fusion reactors based on stellarator concepts of magnetic confinement (Wendelstein 7-X) is being built at Greifswald in

Germany. The experience accumulated over last 50 years on these reactors has finally culminated in building world's biggest tokamak fusion reactor, ITER, an international effort and a precursor to a power plant, DEMO to be build in 2030s. We will discuss very briefly some of these tokamaks in the following sections.

9.4.1 Tokamak Development in USSR/Russia

As mentioned in the previous section, the concept of tokamak confinement originated in the then Soviet Union (USSR) at the Kurchatov Institute in Moscow. A large number of tokamaks, small and big were built to carry out research on specific problems related to plasma physics which involve plasma temperature, plasma parametric stability, different modes of heating and conductor selection for magnets. The parameters of some of the important tokamaks built at Kurchatov institute are tabulated in Table 9.1. The first tokamak was built in 1958 designated as tokamak T-1 which used only Ohmic heating. A picture of this historic tokamak is shown in Fig. 9.9a. Other important milestone was the first ever use of superconducting toroidal [8] magnet in tokamak T-7.

The tokamak T-7 used a total of 48 double pancake coils having 60 turns each for its toroidal magnet [9]. All the coils are connected in series but not evenly distributed around the torus. The coils are grouped in 24 modules each consisting of two coils and joined at the nose end making an angle of 6°. These modules are spread around the torus spaced at an angle of 9° with each other. These angles make enough hatch area available to have ports for various types of inserts and diagnostic tools. Each coil was

Table 9.1 Some of the early tokamaks built in USSR/Russia (data collected from [7])

Tokamak name	Year of start/ operation	Major radius (m)	Minor radius (m)	Toroidal field B_{tor} (T)	Plasma current	Salient feature
T-1	1958	0.67	0.17	1.5	100 kA	First tokamak of the world, only Ohmic heating
T-7	1978	1.22	0.35	4.0		First-ever superconducting tokamak (toroidal only SC)
T-8	1976	0.28	0.048	0.9	24 kA	World's first 'D' shaped toroidal coil elongated plasma
T-10	1975	1.5	0.40	5.0	0.65 MA	Ohmic + ECRH (4 MW) 1987
T-15	1988–1995	2.43	0.78	3.5	1.0 MA	World's first Nb_3Sn toroidal coils, heating – Ohmic + NB (9 MW) + ECRH (6 MW) + ICRH (6 MW), Pulse 1.5 s

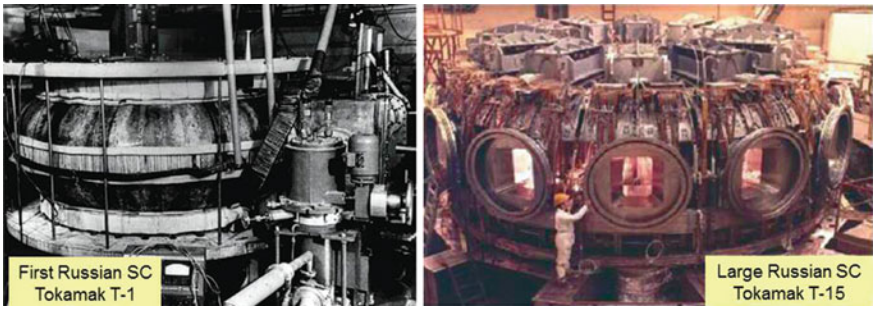

Fig. 9.9 *Left* World's first superconducting tokamak, T-1 fusion reactor built at Kurchatov Institute (USSR/Russia) in 1954 [7]. *Right* Large Russian superconducting tokamak, T-15 fusion reactor built at Kurchatov Institute (USSR, Russia) in 1988, now undergoing up-gradation to support ITER and DEMO [7] (both pictures with permission from "Nuclear Fusion" IAEA)

wound using 200 m of an electroplated Nb–Ti strip conductor with nine 2 mm dia. cooling channels. One channel of each coil is taken out side the system and connected in parallel to the helium distribution network to allow forced flow @ 8 g/s of supercritical helium (SHe) at 4.5 K for cooling. Copper shells 15 mm thick cooled by liquid nitrogen surround the toroidal coils. The shells not only serve as thermal shields but also as a magnetic shield to the windings against eddy currents produced by field variation in the poloidal coils. The magnet produces a field of 3 T at the plasma axis at a current of 6 kA. The maximum field at the conductor is 5 T. The magnet is protected against quench by an external dump resistor of 0.17 Ω. The magnet dumps the stored energy at a discharge voltage of 5 V persisting for a minimum duration of 0.2 s. This avoids the possibility of magnet discharging due to any spurious and harmless voltage of a smaller duration. The coils are strengthened by an arch frame reinforced by 96 winding rings. This frame is cooled by liquid helium (LHe) to reduce heat input to the coil shell thus minimizing the vapour phase content in LHe. The parameters of T-7 tokamak are given in Table 9.2.

Soon Artisimovich and Safranov [10] came-up with a brilliant idea of an elongated plasma cross-section which yielded enhanced plasma stability. This led to the development of a 'D' shaped toroidal coil first time. A number of reactors, T-8, T-9 and T-12 TBD were built with 'D' shaped toroidal coils which established the efficacy of the magnetic field in the formation of an equilibrium plasma in an elongated shape and an efficient use of the magnetic volume. T-10 was a bigger tokamak (3 m × 0.8 m) built in 1975 with a plasma field of 5 T. In 1987, extra 4 MW of power was added to the plasma using an ECR source. All the accumulated experience was used to built tokamak T-15 of larger size (4.86 m × 1.56 m) and is shown in Fig. 9.9b. Heating to plasma was provided by neutral beam injection, NBH (9 MW), ECRH (6 MW) and ICRH (6 MW). T-15 operated in 1988 at a field level of 3.6 T and a plasma current of 1.0 MA. It was first time that Nb_3Sn conductor was used for winding toroidal coils. Both the tokamaks T-7 (HT-7U) and T-15 are operational.

Table 9.2 Specifications of world's first superconducting Tokamak T-7 (data compiled from [7])

Parameter	Unit	Value
Year of operation		1978
Present status		1992 transferred to China, named HT-7U
Major radius of torus,	(m)	1.22
Inner radius of vacuum chamber	(m)	0.35
No. of toroidal double pancake coils		48
Average radius of pancake	(m)	0.50
Winding width	(cm)	15
No. of turns in a coil		60
No. of coil modules		24
Superconductor		Nb–Ti electroplated strip 200 m per coil
Operating temperature (forced flow of SHe)	(K)	4.5
Field at torus axis	(T)	3
Maximum field at the conductor	(T)	5
Field volume	(m^3)	6
Operating current	(kA)	6
Average current density at 3 T	(kA/cm^3)	1
Stored energy at 3 T	(MJ)	20
Quench protection	(Ω)	0.17 (ext. resistor)
Total cold mass	(ton)	12
Refrigerator capacity	(W)	400

Tokamak T-15 is undergoing up-gradation programme (2008–2020) [11] to carryout R&D in support of the ITER and DEMO programmes. The up-gradation aims at raising the plasma energy to 10 keV (>100,000,000 °C), modify poloidal coils to divertor mode, raise the plasma discharge time up to 1,000 s in stages and increase the plasma heating to 20 MW using different modes. Extra poloidal coils will be installed inside the vacuum chamber so as to increase the plasma elongation (K) to 1.5 and triangularity (δ) to 0.3. Since with the existing system of room temperature poloidal coils, the limit to plasma discharge time is 25 s, these coils will be replaced by superconducting poloidal coils to achieve the discharge time to 1,000 s.

9.4.2 TFTR (Tokamak Fusion Test Reactor), Non-superconducting, PPPL, USA

TFTR built at PPPL (Princeton Plasma Physics Laboratory) is not a superconducting tokamak but has an important place in the development of fusion reactors in so far as it has many firsts and is an important link to the modern reactors. This was

the first fusion reactor which used deuterium and tritium mixture (in 50:50 ratio) as fuel and produced a fusion power of 10.7 MW at a power density of 2.8 MW/m^3. Some of the TFTR parameters are shown in Table 9.3.

TFTR used water-cooled normal conductor magnets [12]. The toroidal magnet has 20 coils at 18° interval. Each coil is a double pancake with 44 turns. The magnet generates a field of 6 T at the major radius of 2.6 m (centre of plasma) for a flat top time of 4 s. The pulse interval is a minimum 300 s and the magnet has to sustain 300,000 full-power pulses. Each coil of the magnet is encased inside Ti-cells to transmit the forces to the support structure outside. Coils are cooled by 10 °C chilled water and to protect the electrical insulation the coil temperature is not allowed to go beyond 65 °C. The whole tokamak is made in ten modules each spaced at 36° angle apart. Each module consists of a 36° segment of the vacuum vessel and two toroidal coils. This configuration allows remotely controlled removal and replacement of coils in a module in the event of a malfunctioning of the coils after the operation with tritium. It produced first time fusion power at a level of 10.7 MW. Figure 9.10 is a photograph of TFTR which operated from 1982 to 1997 at PPPL.

TFTR had its last and final run [13] on April 4, 1997. During its operation (1982–1997), it not only achieved its most of the scientific and technical objectives but surpassed them. During this period TFTR produced a total of 80,000 plasma shots which included more than 1,000 shots of D-T plasma. It firmly established the feasibility of a fusion reactor with deuterium and tritium mixture fuel reaching the ignition stage albeit in a pulse mode. It also proved the efficacy of the magnetic confinement of the plasma and made way for more advanced tokamaks inching towards power generation.

Table 9.3 Parameters of TFTR (PPPL, USA) (data compiled from [12, 13])

Parameter	Unit	Value
Year of start of operation		1982
Year of final operation		1997
Plasma major radius	(m)	2.6
Plasma minor radius	(m)	0.9
Nature of magnets		Normal magnets
No. of toroidal field coils		20
Toroidal field at plasma centre	(T)	6
Coil configuration		Spiral winding, double pancake
No. of turns in a coil		44
Toroidal coil current	(kA)	73.3
Coil coolant		Water
Plasma current	(MA)	3
Heating pulse duration	(s)	4
Fusion power (1994)	(MW)	10.7
Auxiliary plasma heating	(MW)	51 (NB-40), RF (11)
Fuel used		D + T

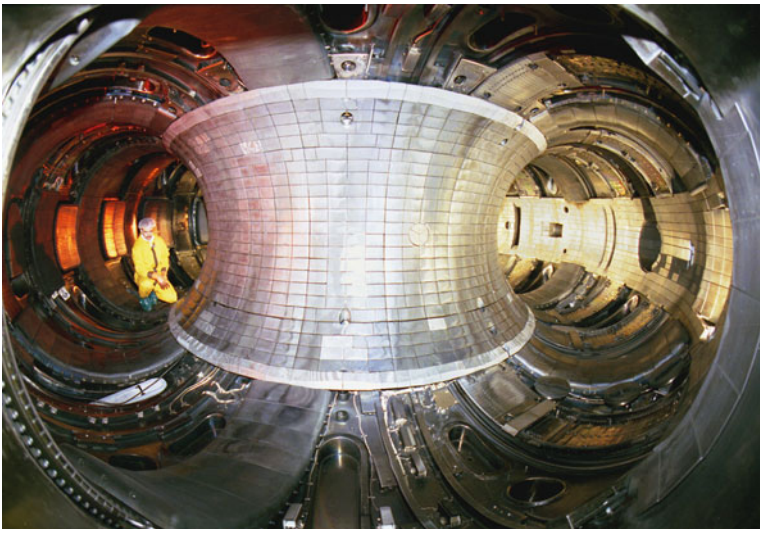

Fig. 9.10 TFTR at PPPL (Princeton Plasma Physics Laboratory, USA) (*Courtesy* Mirium Edvardse, Princeton Plasma Physics Laboratory)

9.4.3 JET (Joint European Torus), Non-superconducting, Culham, UK

JET [14, 15] tokamak too has normal copper magnets but is a ongoing large and most powerful tokamak which has a number of landmark achievements to its credit. It has been working under EFDA (European Fusion Development Agreement) and used by over 40 laboratories from EURATOM associations. It may be called as the predecessor of ITER as over the years it has changed to ITER like experimental configuration to provide feedback to ITER in key areas. In 2006 JET changed its magnet to ITER like configuration. During 2009–2011, the carbon-lined plasma container was replaced with beryllium container to prevent neutron retention in carbon. The experience gained and data collected on plasma physics from JET operation has surely given a boost to the international efforts to the ultimate realization of fusion power. Its construction began in 1978, produced first plasma in 1983 and released fusion energy in 1991. It established a world record of generating 16 MW (@ 65 % of the input power) fusion power for 1 s in 1997 using deuterium and tritium fuel mixture. JET also has the distinction of having the capability of remote handling of tritium. Table 9.4 gives the main specifications of the JET tokamak. Figure 9.11 shows the interior of the JET tokamak (left) and the cut-away view of the magnet coil structure (right).

Up-graded JET is fully geared to find solution to problems related to plasma physics and engineering expected to be encountered in ITER operation. JET has been very successful in establishing the reliability of remote controlled handling

Table 9.4 Parameters of JET (Culham Center for Fusion Energy, UK) (data compiled from [14, 15])

Main Parameters	Unit	Value
Year of first plasma		1983
Present status		On-going
Plasma major radius	(m)	2.96
Plasma minor radius	(m)	2.1 (vertical) 1.25 (horizontal)
Plasma current	(MA)	3.2 (circular plasma) 4.8 (D-shaped plasma)
Plasma volume	(m^3)	200
Fusion power (up-graded)	(MW)	20
Toroidal field at plasma centre	(T)	4
Plasma sustains for	(s)	5–30
Flat top pulse length	(s)	20–60
Auxiliary heating	(MW)	NB-34 ICRH-10 LHCD-7
Plasma container walls		Beryllium/Tungsten
Weight of TF coils	(ton)	384
Weight of the vacuum vessel	(ton)	100
Fuel used		D + T

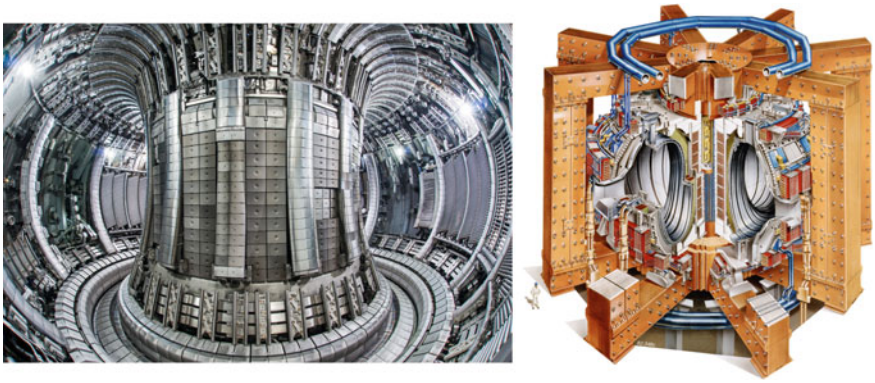

Fig. 9.11 *Left* Interior of JET tokamak. *Right* A cut-away view of the coil structure of toroidal and poloidal magnets of JET (*Courtesy* Nick Holloway, "EFDA JET")

and replacement of components inside the tritium infected vacuum vessel. A futuristic and more compact device named MAST (Mega Ampere Spherical Tokamak) is being developed at CCFE, Culham to help ITER. Spherical tokamak provides improved magnetic confinement and better stability of plasma and at a lower cost. It confines plasma at a higher pressure and low aspect ratio than in a tokamak for a given confinement field. Fusion power being proportional to plasma pressure square, fusion power can be produced in a smaller device and with high stability. Spherical tokamaks, however, need very careful designing of the magnet system and the vacuum vessel.

9.4.4 Tore Supra (NRC, Cadarache, France)

Tore Supra is a large superconducting tokamak run by Euratom-CEA Association at 'Nuclear Research Centre', Cadarache, France. It started operation in 1988 and since then has carried out extensive research on problems related to plasma physics and technical issues concerning engineering design of the plasma container and other components of the tokamak system. The research has been somewhat complementary to JET. It provided crucial inputs to the final design of the ongoing ITER tokamak programme and continues to play supporting role for the success of ITER and the later versions like the DEMO. A photograph of Tore Supra is shown in Fig. 9.12.

The tokamak has 18 superconducting toroidal coils [16–19] built in 6 modules of 3 coils each and are suitably spaced around the vacuum chamber and joined together to complete the torus. The three coils, each insulated electrically, are mechanically interlocked using strong insulated shear keys to make a rigid structure as shown in Fig. 9.13. Each coil is wound in a 26 double pancake structure. Each pancake is separated by electrically insulting spacers which allows large contact area between the winding and the superfluid. The coil becomes rigid after curing and is enclosed in a thin (2 mm) SS casing with perforated glass spacers and ground insulation in between. The casing serves as a superfluid helium (1.8 K) vessel as well. The void volume inside the winding though is filled with superfluid helium,

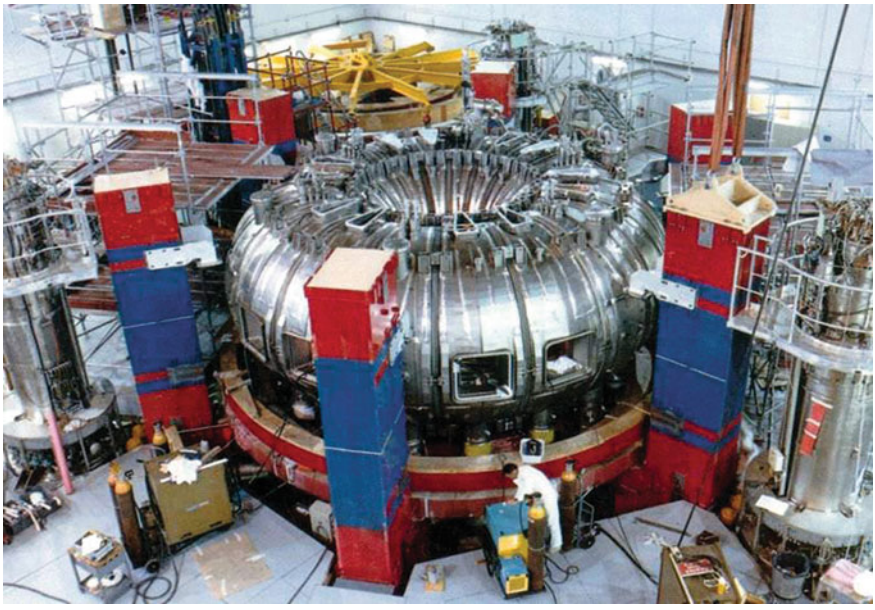

Fig. 9.12 Tore Supra tokamak (Cadarache, France) [17] (*Courtesy* Valerie Lamaison and J-L Duchateau) (Copyright CEA-IRFM, Institute for Magnetic Fusion Research)

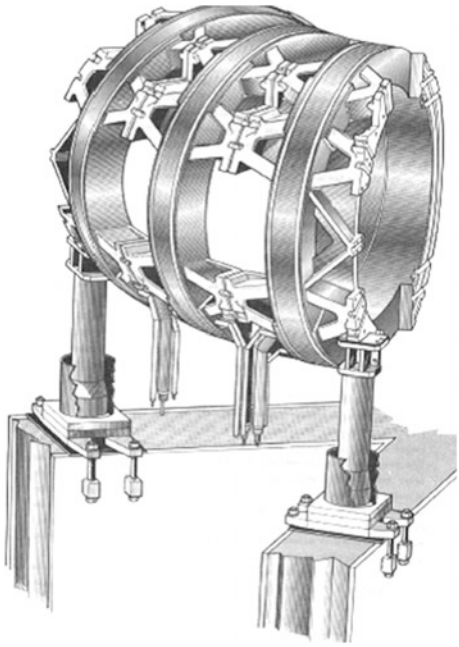

Fig. 9.13 One module of 3 superconducting coils of the toroidal magnet of Tore Supra joined together rigidly by shear keys. There are 6 such modules to complete the torus [17] (Copyright CEA-IRFM, Institute for Magnetic Fusion Research, courtesy, Valerie Lamaison)

the individual turns are insulated by pre-impregnated fiber glass tape co-wound with the conductor. This thin casing in turn, is enclosed in a thick SS mechanically strong casing with the inter-layers of polymic alumina chalk. The thick casing provides mechanical strength against the radial forces caused by the toroidal field. It also acts as a vacuum jacket around each coil and a magnetic shield against the field fluctuations. The thick casing is cooled separately to 4.5 K by pressurized (1.5 MPa) supercritical helium. Most of the heat dissipation takes place in this casing minimizing heat load on the coils which operate at 1.8 K. A cut-away cross-section of the coil [17] is shown in Fig. 9.14. The insulation can withstand a voltage of 5 kV. Complete specifications of plasma, toroidal coils and the conductor are given in Table 9.5.

Each of the six modules is assembled as a complete 1/6th segment of the torus, that is, containing inner vessel, thermal shield, the magnet system, the outer thermal shield and the outer cryostat vessel. All the modules are assembled to make a complete torus. Each module is a rigid entity capable of withstanding the forces experienced during magnet operation.

The tokamak was designed for a toroidal field of 4.5 T at the plasma axis. The peak field at the conductor turns out to be 9 T. Nb_3Sn would therefore have been the ideal choice. The complexity of high temperature heat reaction involved in Nb_3Sn magnets especially during those years in 1980s prevented the use of this conductor. Instead, copper stabilized low loss Nb–Ti conductor to be operated at 1.8 K was preferred. The Nb–Ti conductor has a cross-section of 5.6×2.8 mm^2 with a single strand with 11,000 filaments each of 23 μm diameter. The conductor carries a

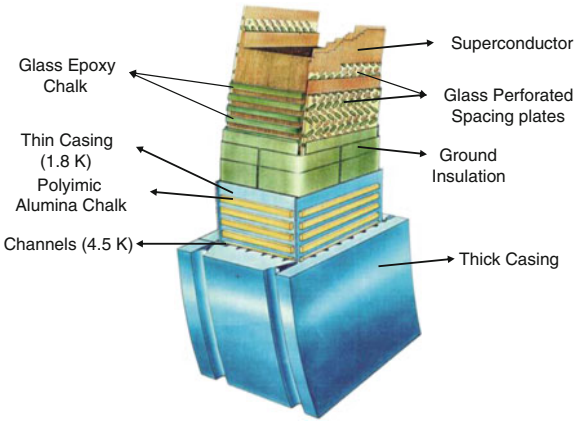

Fig. 9.14 A cutaway view of the toroidal coil of Tore Supra. Note the two cooling channels, one for 1.8 K superfluid, inside the thin case for cooling the winding and the other for 4.5 K supercritical helium, to cool the outer thick casing [17] (Copyright CEA-IRFM, Institute for Magnetic Fusion Research, courtesy, Valerie Lamaison)

current of 1,400 A at 9 T field at 1.8 K. The composition of the conductor is Nb–Ti (46.5 wt%) 29 %, copper 62 % and Ni 9 %. The filaments are co-processed in a resistive matrix of copper and cupronickel instead of pure copper to minimize ac losses. A total of 45 tons of conductor measuring 622 × 494 m has been used. The toroidal magnet weighs 160 tons. The stored energy is 600 MJ.

The poloidal coils are the normal non superconducting water-cooled copper magnets and mounted outside the toroidal magnet and the cryostat. Changing magnetic field in the poloidal coils induces current which heats the plasma. The effect of the poloidal field on the toroidal field results in two opposite torques around the axis of the torus which can go up to 99 MN on one half (upper or lower) of the torus in the event of a plasma current disruption. This gives rise to shear stress between the coils which is taken care of by the system of insulated inter-coil keys. The toroidal field causes a centripetal force which stresses greatly the inner vault and the insulating components between the coils. These stresses ultimately are transmitted to the thick casing. Radial magnetic field generates hoop stresses in the winding which too are passed on to the thick casing. The windings operate under high compression. The thick casing is thus shrink-fitted to the rigid winding to rule out any mismatch of thermal contraction after cool-down.

The toroidal coils are protected against quench by 18 dump resistors of 2.5 Ω each in series with as many coils to keep the current equal in each coil. A set of resistances, 5 Ω each is also connected in parallel with each coil to limit the voltage. The quench can be detected by monitoring voltage on the coil and also by noticing increase in pressure inside the cooling channel of each coil. The magnet coil discharges in 14 s and limits the voltage across the coil to 3,500 and ±1,750 V to

Table 9.5 Parameters of Tore Supra and toroidal magnet specifications (data compiled from [16, 17])

Parameter	Unit	Value
Year of start of operation		1988
Present status		On-going
Overall diameter	(m)	11.5
Overall height	(m)	7.2
Plasma major radius	(m)	2.25
Plasma minor radius	(m)	0.70
Plasma current, I_P	(MA)	1.7
Plasma heating	(MW)	Ohmic -2, NBI -10, ICRH -9, LHH -6
Plasma hold time	(minute)	Up to 6
Plasma volume	(m^3)	24
No. of toroidal coils		18
No. of modules of toroidal coils		6 with 3 coils each
Toroidal field at the plasma centre	(T)	4.5
Maximum field on conductor	(T)	9.0
Operating current	(A)	1,400
Operating temperature	(K)	1.8
Magnetic structure temperature	(K)	4.5, supercritical LHe
Total weight of magnet	(ton)	160
Magnet stored energy	(MJ)	600
Conductor specifications		
Conductor used		Nb–Ti (46.5 wt%)
Nb–Ti:Cu:Cu–Ni ratio		0.29:0.62:0.09
Conductor dimensions	(mm)	(2.8 × 5.6)
Number of strands		1 with 11,000 filaments
Filament diameter	(μm)	23
Total Nb–Ti conductor used	(m)	622 × 494 lengths
Total weight of superconductor	(ton)	45

ground. The quench protection system has been further improved and the coil and ground voltages have been brought down further.

After 25 years of its first plasma discharge (1988), Tore Supra has appeared in 2013 in its new incarnation 'WEST' (Tungsten (W) Environment in Steady State Tokamak) for testing the efficacy of the tungsten divertor to be used in ITER. WEST will investigate issues related to the operation of actively cooled tungsten divertor components in a fusion reactor and its influence on plasma performance. It will test the technology of high heat flux removal which will be implemented in ITER. Several modifications are slated to be carried out.

9.4.5 JT-60 SA (Japan Torus—60 Super Advance), JAERI, Naka, Japan

JT-60 SA is the biggest and wholly superconducting tokamak being built at Naka, Japan under the "Broader Approach" (BA) agreement between Japan Atomic Energy Agency (JAEA) and the Euratom. The tokamak is designed in ITER configuration as its satellite facility for a successful start-up of ITER leading to energy production by DEMO. JT-60SA, in fact, will be a replacement of JT-60 and its later upgraded version JT-60U at the same site. JT-60 SA may as well be called a real mini replica of ITER. We will therefore discuss this tokamak a bit in detail.

JT-60 (JapanTorus-60) [20], though a non-superconducting tokamak had been a very successful fusion reactor and played key role like the JET and Tore Supra in the design of ITER. It achieved a record triple product value of 1.77×10^{28} K s m^{-3} ($= 1.53 \times 10^{21}$ keV s m^{-3}) in 1994. It did use D–D fuel but the extrapolation of their results to D–T fuel showed that the energy produced will cross the breakeven point with a Q factor of 1.25. The ignition, however, requires a minimum of $Q = 5$ and higher. JT-60 does not have the tritium handling facility like the JET. Some important parameters of JT-60 are given in Table 9.6. A cutaway view of the JT-60 SA device is reproduced in Fig. 9.15. The figure shows the locations of the toroidal coils, equilibrium coils, the central solenoid, the vacuum vessel, the plasma and the cryostat. A large number of ports for diagnostic instruments and tools is a common feature of any fusion machine.

JT-60 SA [21] is being built with an objective to achieve steady state plasma for 100 s under condition of high β, flexible low aspect ratio (2.5–3.1) and plasma shape. The plasma current would go up to 5.5 MA for low aspect ratio. The tokamak is expected to produce a minimum of 6,000 pulses under normal operation and 12,000 pulses under reduced performance conditions. The magnet system of JT-60 SA is quite similar to that of ITER. All the magnets are superconducting, to achieve steady state. Use of normal copper magnets requires intermittent long cool-down of the coils due to excessive heating and high thermal stresses. It consists of

Table 9.6 Some parameters of JT-60 fusion reactor (data compiled from [20])

Parameter	Unit	Value
Year of start of operation		1985
Year of close of operation		2010
Toroidal field	(T)	4.0
Plasma major radius	(m)	3.4
Plasma minor radius	(m)	1.0
Plasma volume	(m^3)	90
Plasma current	(MA)	3
Plasma duration	(s)	28.6
Toroidal field	(T)	4.0
Heating power	(MW)	40 (NBI) 15 (RF)
Fuel used		D + D

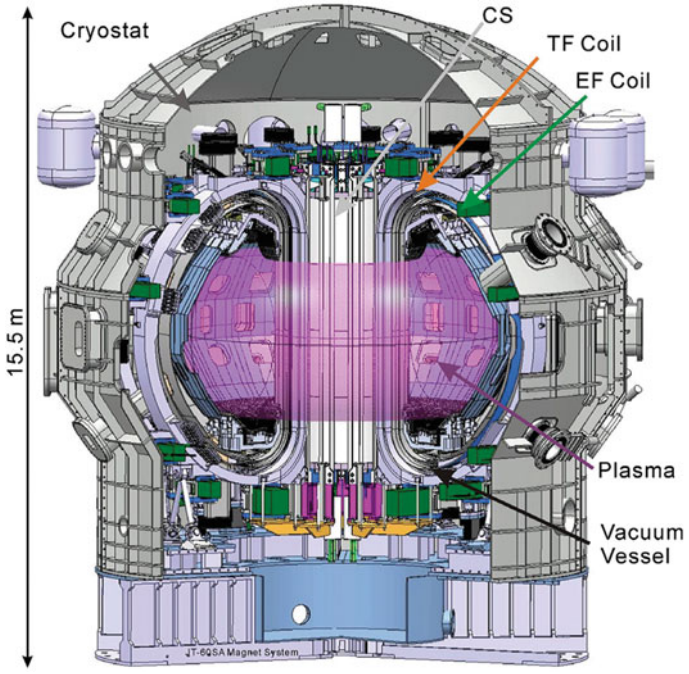

Fig. 9.15 A cutaway view of the JT-60 SA device showing locations of TF, EF, CS, plasma and vacuum vessels, cryostat and the ports [19] (With permission from 'Elsevier')

18 toroidal coils to confine the plasma. It has 6 plasma equilibrium field coils which provide vertical stability to plasma and position equilibrium of the plasma current. A central solenoid consisting of four stacked solenoid modules controls the plasma shape by increasing the plasma current through the ramping of the field. Figure 9.16a shows the total magnet system and Fig. 9.16b, a typical 'D' shaped toroidal coil with gravity supports and inter-coil mechanical parts for joining with other coils. The other requirements of the up-gradation are the 41 MW heating and current drive system and a divertor which can carry 15 MW/m^2 heat flux. The main parameters of the tokamak are given in Table 9.7.

The toroidal coils have been built by Euratom under the (BA) agreement. The TF coils are wound using a rectangular SS jacketed Nb–Ti cable-in-conduit conductor (CICC) of the dimensions 22 mm × 26 mm consisting of 324 strands and 162 copper wires without central spiral. To reduce ac losses, either the strands are coated with nickel or the Cu–Ni barriers are used inside the strand matrix which brings down the inter-strand coupling. Each toroidal coil has 6 double pancakes with 6 turns each. Every winding package has electrical insulation wrapped around and finally vacuum-pressure impregnated. The dimensions of a winding pack are 345 mm (toroidal) × 150 mm (radial). This pack is enclosed in an AISI austenitic steel casing which withstands most of the EM forces generated in the magnet system and provide support to the equilibrium coils. The geometry and the

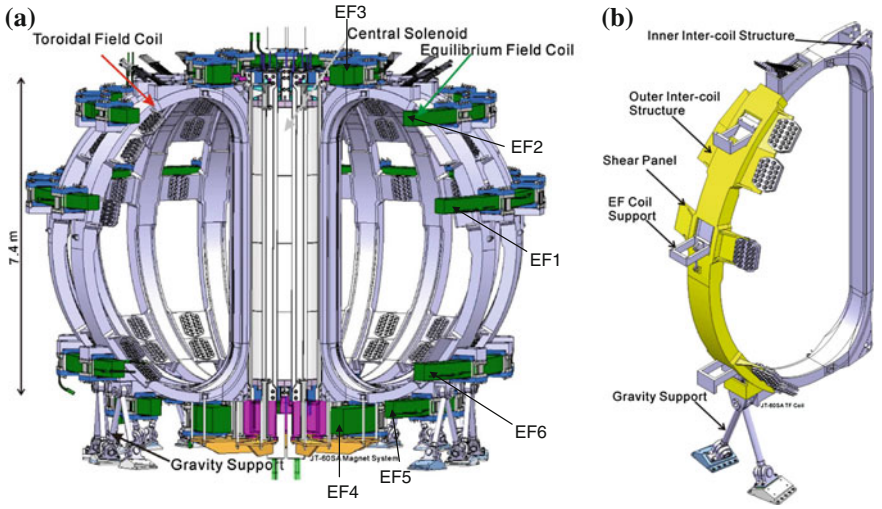

Fig. 9.16 **a** Toroidal coils, equilibrium coils and central solenoid of the JT-60 SA tokamak [21]. **b** The 'D' shaped toroidal coil with ground supports and inter-coil jointing mechanical pieces [21] (With permission from 'Elsevier')

Table 9.7 Main plasma parameters of JT-60 SA tokamak (data compiled from [21])

Parameters	Unit	Value
Scheduled year of start		2019 (first plasma expected)
Major plasma radius, R	(m)	3.06
Minor plasma radius, a	(m)	1.15
Aspect ratio		3.1
Plasma volume	(m^3)	127
Plasma current	(MA)	5.5
Plasma duration	(s)	100
Plasma elongation, κ		1.76
Triangularity, δ		0.45
Plasma heating power	(MW)	34 (NBI) 7 (ECRH)
Fuel to be used		D + D

dimensions of the casing are extremely precise, strictly within permissible tolerances so that they are positioned properly and provide necessary mechanical support to the magnet system.

The toroidal magnet produces a field of 2.69 T on the plasma axis at an operating current of 25.7 kA. The coils are cooled to 4.8 K by the forced flow of supercritical helium at a flow rate of 4.8 g/s. The peak field at the conductor turns out to be 6.5 T. The stored energy is 1.06 GJ. Three pairs of current leads are used to energize the magnet. The parameters of the toroidal magnet and the conductor used are given in Table 9.8. All the 18 toroidal coils and their casings have been manufactured in

Table 9.8 Specifications of the toroidal magnet and the conductor used in JT-60 SA (data compiled from [21–24])

Parameter	Unit	Value
No. of toroidal coils		18
No. of double pancakes in a coil		6
No. of turns in a pancake		6
No. of turns/coil		72
No. of current lead pairs		3
Toroidal field at plasma axis	(T)	2.69
Peak field on conductor	(T)	6.4
Operating current	(kA)	25.3
Operating temperature	(K)	4.8 (SCHe)
Mass flow rate of He	(g/s)	4.8
Stored energy in TF coils	(GJ)	1.06
Total weight of the toroidal magnet (including structure)	(ton)	700
The conductor		
Conductor used		Nb–Ti/Cu/Cu–Ni
No. of strands/copper wires		324/162
Void volume		34 %
Cable dimensions	(mm)	22 × 18
Conductor jacket dimensions	(mm)	26 × 22
Jacket material		SS 316 LN
Total conductor length	(km)	24.4 (=74 × 0.33)

Italy [22] and delivered at NAKA. Nine coils and 18 casings have been built by ENEA and nine coils wound by CEA. The implementing agencies for the design and manufacturing of the TF coils were JAEA (Japan Atomic Energy Agency) Japan and F4E (Fusion for Energy) Europe. The test results on the TF coils match closely with the conceptual design calculations [23, 24]. Various computer codes have been used in the design of the coils. The maximum field at the winding has been verified using codes TOSCA (by ENEA) or TRAPS (by CEA), mechanical loads/stress analysis using finite element code ANSYS and Gandalf, nuclear heating of the casing and the winding pack computed using MCNP-4C Monte Carlo code for D-D neutron emission rate of 4.0×10^{17} n/s and TRAPS code for computing eddy current losses in the jacket housing the winding pack.

The Central Solenoid (CS) consists of four identical coil modules CS1 (top) to CS4 (bottom) stacked together vertically with insulation in between except between central modules CS2 and CS3 which are connected in series. The solenoid is supported by the TF coils for which TF coil attachments are provided at the bottom and the top of the solenoid. There is a centering mechanism for positioning and to counter the dynamic horizontal forces. The support structure of the CS has a set of tie plates located at the inside and outside diameters of the solenoid to pre-compress the stack vertically. This is required to maintain the integrity of the stacks as the modules CS1 and CS4 at the two ends tend to move away from the central modules

CS2 and CS3 when the plasma discharge is close to the end of flat-top. The modules can be energized separately to accomplish the plasma shape. The terminals and bus bars are taken outside the solenoid to the terminal box which is connected to the supply and return lines for helium. The pre-loaded support structure is cut into segments and isolated electrically so as to minimize ac losses.

The CS produces a field of 8.9 T and is wound using Nb_3Sn (W&R) conductor. The conductor consists of a 21 mm dia. cable inserted into a 27.9 mm × 27.9 mm squire-shaped jacket of SS 316 LN with a central hole. The parameters of the CS magnet and the conductor used are listed in Table 9.9. The jacket allows the heat treatment of the coils at 650 °C (×100 h). The cable has 216 Nb_3Sn strands produced by a multi-stage process and 108 copper strands cabled around a central cooling spiral of 7 mm i.d. and 9 mm o.d. The cooling spiral greatly enhances the extraction of excessive heat. Generated due to ac losses during a break down.

The six EF coils are mounted on to the 18 TF coils which provide total support to the EF coils and the CS. The sizes and positions of the EF coils are determined as per the plasma requirements and the need for enough space for inserts and ports around the vacuum vessel. The coils are fixed with flexible support plates which enable the radial displacement of the coils. The divertor coil EF4 experiences the maximum field, 6.2 T. All the coils are subjected to rapid field change up to 2.0 T/s. The EF coils are wound using a CICC Nb–Ti conductor in pancake structure. The winding pack of the small bore coils have double pancakes while large bore coils have single pancakes. All the coils are operated at a current of 20 kA. The operating temperature for EF4 is 5 and 4.8 K for rest of the coils. Two different jacketed CICC conductors detailed in Table 9.10 have been used to wind the coils. depending upon the peak field to which they are exposed and the operating

Table 9.9 The parameters of the central solenoid and the Nb_3Sn conductor of JT-60 SA (data compiled from [21])

Parameters	Unit	Value
Overall height	(m)	9.5
Nominal peak field	(T)	8.9
Operating current	(kA)	20
Operating temperature	(K)	5.1 (SHe)
No. of solenoid modules		4
Total conductor length	(km)	11.5 (unit length 352 m)
No. of current lead pairs		4
Total weight of CS and structure	(ton)	92
Conductor used (CICC)		Nb_3Sn (W&R)
No. of Nb_3Sn strands		216
No. of copper strands		108
Void fraction	(%)	34
Cable diameter	(mm)	21
Conductor size (after jacketing)	(mm)	27.9 × 27.9
Central cooling spiral dia.	(mm)	7 (id) × 9 (od)

Table 9.10 Some parameters of the three representative EF coils of JT-60 SA; Nb–Ti (CICC) conductor used for all EF coils and cooled by forced flow of supercritical helium (data compiled from [21])

Parameter	Unit	EF1	EF4	EF6
Winding diameter	(m)	11.638	3.838	10.108
Peak field	(T)	4.8	6.2	4.8
Operating current	(kA)	20	20	20
Operating temperature	(K)	4.8	5.0	4.8
Cable diameter	(mm)	19.1	21.8	19.1
Conductor dimensions	(mm)	25 × 25	27.7 × 27.7	25 × 25

temperature. These conductors were optimized for 6.2 T (EF4) and 4.8 T (E1 and E6) peak fields. The diameters of the EF coils differ widely as per their locations around the toroidal coils, coils EF1 and EF6 being of largest sizes.

9.4.6 KSTAR (Korean Superconducting Tokamak Reactor), NFRI, Daejeon

KSTAR is a all-superconducting magnet fusion reactor [25], operating at National Fusion Research Institute (NFRI), Daejeon, Republic of Korea since 2008, and has many similarities with ITER. It is a steady state fusion reactor with high performance plasma and with a capability of confining plasma for 300 s. Figure 9.17 is a schematic diagram of the position of toroidal, poloidal and central solenoid together with the vacuum vessel. It has 16 TF coils and 14 PF coils. Eight of the PF coils (PF1–PF4) are located in the central solenoid magnet system and six PF coils (PF5–PF7) are outside the TF coil system. All the TF coils and smaller dia. PF coils (PF1, PF2, PF3, PF4 and PF5) are wound using CICC Nb_3Sn conductor (wind and react type) and the larger PF coils PF6 and PF7 coils are wound using CICC Nb–Ti conductor. The requirement for conductor for TF coils and PF coils is, however quite different. The TF coils run in static mode and therefore the conductor must have high current density, greater than 750 A/mm^2 at 12 T and 4.2 K (the HP-I criterion). The PF coils, on the other hand, have to operate in pulse mode and should have low hysteresis losses meeting HP-II criterion (loss should be less than 250 mJ/cc at 3 T cycle). KSTAR developed a Nb_3Sn conductor which meets both the criteria simultaneously (HP-III) and has been used for all the coils except PF6 and PF7.

The conductor has more than 3,000 filaments carrying high current and low hysteresis. To have low ac loss performance the strands are coated with a $\sim$2 μm thick resistive layer of chrome. This chrome layer remains intact during the long period of heat treatment of the coil. In the fist step two superconducting strands and

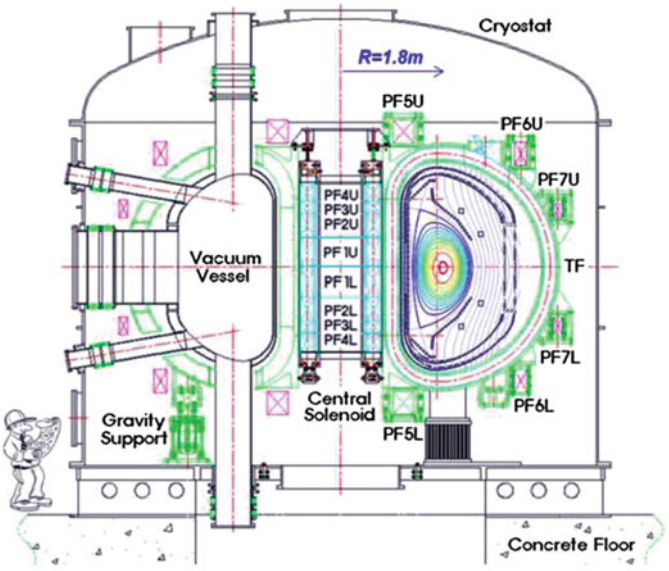

Fig. 9.17 A schematic diagram of KSTAR fusion device indicating the position of the superconducting magnets (toroidal, polloidal and CS.) and the Vaccum vessel [25] (*Courtesy* Yeong-Kook Oh, NFRI, Daejeon, Korea)

one OFHC copper wire are cabled together to form a triplet. These triplets are further cabled in 3 × 3 × 3 × 3 × 6 and 3 × 4 × 5 × 6 configurations to 486 strands cable for TF coil and 360 strands cable for PF coils respectively. Each cable is wrapped with a 30 mm × 0.05 mm SS strip with 20 % overlapping and jacketed in an incoloy 908 casing. The cladding material has been chosen to prevent large strain in the conductor due to the mismatch of the thermal contraction during cooling. The main design parameters of the KSTAR and the TF coil are given in Table 9.11.

Most coils have winding in single length of conductor without a joint inside the coil except the large coils PF6 (upper and lower) which have one joint each inside the winding. After the winding, coils are subjected to a three-step heat-treatment, (460 °C × 100 h) + (570 °C × 200 h) + (660 °C × 240 h) under inert atmosphere wherein Sn diffuses into Nb filaments to form Nb_3Sn layer. The final heating is done at 660 °C for the formation of stoichiometric (3:1) Nb_3Sn. Electrical and ground insulation is then provided using Kapton, S2-glass tapes, S2-glass roving and G-10 pieces (shaped to fill the voids). Quench detecting sensors are also mounted at designated places.

The magnet structure is strong enough to withstand large Lorentz forces experienced during the operation. KSTAR uses high strength STS 316LN stainless steel for its 16 TF structures, one CS structure and 80 PF structures. The TF coils are subjected to in-plane force of as much as 15 MN when charged to the nominal current of 35.2 kA. Similarly the PF coils, the CS and plasma current too exert an

Table 9.11 Specifications of the KSTAR, the TF coils and the conductor (data compiled from [25])

Parameter	Unit	Value
Year of start of operation		2008
Major plasma radius	(m)	1.8
Minor plasma radius	(m)	0.5
Plasma current	(MA)	2.0
Plasma volume	(m^3)	17.8
Plasma cross-section	(m2)	1.6
Plasma shape		DN, SN
Plasma elongation, κ		2.0
Plasma triangularity, δ		0.8
Plasma hold time	(s)	300
Auxiliary heating	(MW)	28
Plasma fuel		H + D
Specifications of the toroidal coils and the conductor		
Total no. of toroidal coils		16
Overall height of the coil winding	(m)	4.2
Overall width of the coil winding	(m)	3.0
No. of pancakes used in a coil		8
No. of turns/pancake		7
Toroidal field at plasma axis	(T)	3.5
Peak field at the coil	(T)	7.2
Operating temperature	(K)	4.5 SHe-forced flow cooled @ 5 bar
Operating current	(kA)	35.2
Stored energy	(MJ)	470
Superconductor material		Nb_3Sn (W&R)
No. of strands		486
No. of filaments		3,000
Maximum single conductor length	(km)	1.8
Cold mass of the toroidal magnets	(ton)	150

out-of-plane force of 2.6 MN/m. The CS structure is designed such that it applies 15 MN (at 5 K) vertical compressive force on the CS coils to nullify the repulsive forces between the coils. The 6 PF coils are mounted on to the 16 TF coils at 80 locations. The structure designed to absorb the difference in the thermal contraction of the TF and PF coils during cooling to cryogenic temperature. A bird eye view of the KSTAR reactor is shown in Fig. 9.18. The first phase of the operation of KSTAR has been successfully completed in 2012. In its 2011 campaign [26] KSTAR has already achieved 3.5 T toroidal field at an operating current of 35.2 kA with a temperature rise of only 0.1 K. A plasma inductive current of 1 MA has already been achieved by ramping the poloidal field. The data obtained on KSTAR tokamak will go a long way to support the operation of ITER and DEMO.

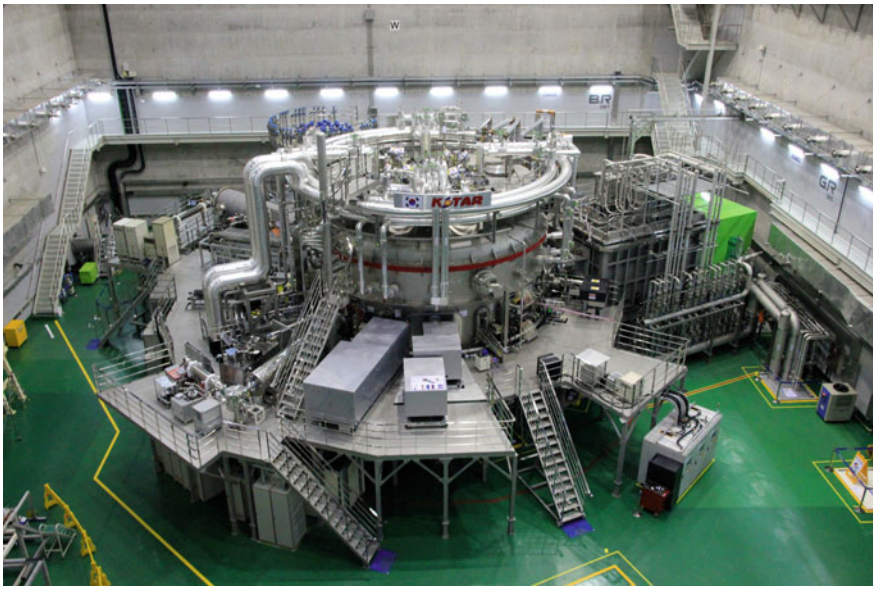

Fig. 9.18 A bird *eye view* of the of KSTAR [25] (*Courtesy* Yeong-Kook Oh, NFRI, Daejeon, Korea)

9.4.7 EAST (Experimental Advance Superconducting Tokamak), IPP, China

EAST is a wholly superconducting experimental fusion reactor built and completed in 2003 at the Institute of Plasma Physics (IPP), Chinese Academy of Sciences, Hefei, Anhui Province in East China. It started operating in September 2006. The reactor is an outcome of the rich experience, the Chinese fusion scientists gained on their earlier fusion reactor HT-7 [27, 28]. Reactor HT-7 was a modified version of Russian tokamak, T-7 bought from Kurchatov Institute, Moscow by China and modified with Russian help at Hefei. The details of the HT-7U (upgrade) can be found in [28]. The results obtained from R&D programme of EAST will boost further the global efforts in realizing fusion power.

EAST is focusing on the technologies related to design, fabrication and testing of large superconducting magnet systems and the design and production of CICC conductors. Plasma facing materials such as multi-element doped carbon and thick gradient SiC coating on carbon based materials have also been developed. Other areas on which IPP is focusing is the development of low activation ferritic/martensitic steel, CLAM, the (Chinese Low Activation Maretensitic) steel. A special structural material for blanket RAFM (a Chinese version for reduced activation ferritic/martensitic steel) also has been developed. The major parameters of EAST [29] and the TF coils are given in Table 9.12.

Table 9.12 Major parameters of EAST (data compiled from [28, 29])

Parameter	Unit	Value
Year of start of operation		Sept. 2006
Height of the tokamak	(m)	10
Diameter of the tokamak	(m)	8
Total weight of EAST	(ton)	400
Plasma major radius, R	(m)	1.85
Plasma minor radius, a	(m)	0.45
Plasma elongation, κ		1.6–2
Plasma triangularity, δ		0.6–0.8
Plasma current	(MA)	1.0
Plasma discharge duration	(s)	0–1,000
Plasma heating (non-inductive)	(MW)	7.5 (ICRH–3 MW) (LHCD–4 MW) (NBI–0.5 MW)
Plasma configuration		SN/DN/pump limiter
Plasma fuel		H + D
Specifications of the TF magnet system and conductor		
No. of TF coils		16
Dimension of a TF coil	(m)	3.5 × 2.6
Field at plasma axis	(T)	3.5
Peak field at the coil	(T)	5.8
Operating current	(kA)	14.5
Total stored energy	(MJ)	300
Operating temperature	(K)	4.5 (SHe forced flow)
Conductor used		Nb–Ti CICC
Conductor size	(mm)	20.4 × 20.4
No. of SC strands		120
Diameter of SC strand	(mm)	0.85–0.87
Diameter of Cu strand	(mm)	0.98
Cable configuration	(2SC + 2Cu) × 3 × 4 × 5 + 1 CCC[a]	
Coating material for strands		Pb-30Sn-2Sb
Temperature margin ($^{b}T_{CS}$–T_{OP})	(K)	1.88

[a] *CCC* central Cu cable
[b] *TCS* current sharing temperature

A schematic cutaway cross-section of EAST depicting the total CS, TF and PF magnet system, thermal shields and the cryostat is shown in Fig. 9.19. EAST has an overall height of 10 m and diameter 8 m and weighs 400 tons. EAST has 16 toroidal coils, 3 pairs of poloidal coils of the CS system and three other pairs. Both of the biggest poloidal coils outside the TF coils have the diameter of 6.65 m. The PF coil system stores a maximum energy of 50 MJ. Each TF coil is of the size 3.5 m × 2.6 m and a weight of 10 tons. TF coils operate at 14.5 kA and produces a plasma axis field of 3.5 T. The peak field at the TF coil is 5.8 T. The TF magnet

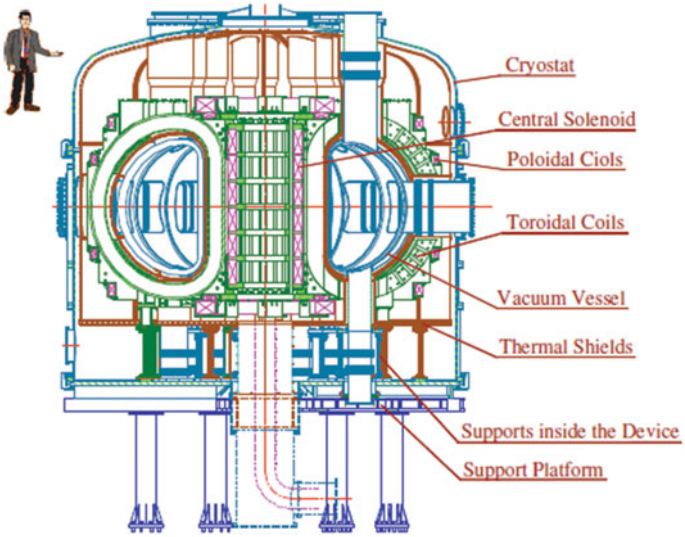

Fig. 9.19 A cutaway *cross-sectional view* of the EAST machine showing the positions of TF, PF and CS coils position [29] (*Courtesy* Jiangang Li, Institute of Plasma Physics, CAS, Hefei, P.R. China)

system has a stored energy of 300 MJ. The TF coils are 'D' shaped with 5 arcs and one straight leg so as to have a coil free of bending moment. Like any other reactor EAST has used IPP design and produced CICC Nb–Ti conductor with high stability, high current density and low a c losses suitable for pulse operation. For TF coils the conductor has been made in a configuration (2SC + 2Cu) × 3 × 4 × 5 + 1 CCC (central copper cable). The SC strands were coated with 2 μm thick Pb-30Sn-2Sb soldering material. For four big PF coils, another CICC configuration, viz; (1SC + 2Cu) × 3 × 4 × 5 + 1 CCC was used. In this cable the SC strands were coated with 3 μm thick Ni layer. Special CICC Nb–Ti conductors were designed and produced by IPP to fulfill the requirement of TF as well as for PF coil magnet systems.

All the coils have been wound in pancake structure and jacketed in very strong casing of 316LN which has a yield stress of 1,500 MPa below 80 K. The finite element analysis yields a maximum stress on the TF coil as 350 MPa. The casing of the TF coils have to withstand a centripetal force as large as 1,300 tons. The casing is built in a box structure and on the straight part of the coil. The case plate is as much as 58 mm thick. Sensors for quench detection are placed at the select places in the winding. Fiber glass 0.5 mm thick is wrapped around the conductor and 1 mm thick on the pancakes for electrical insulation. A 6 mm thick multilayer glass tape provides ground insulation to the coils which are finally vacuum impregnated. A photograph of EAST along with its all auxiliary systems is shown in Fig. 9.20.

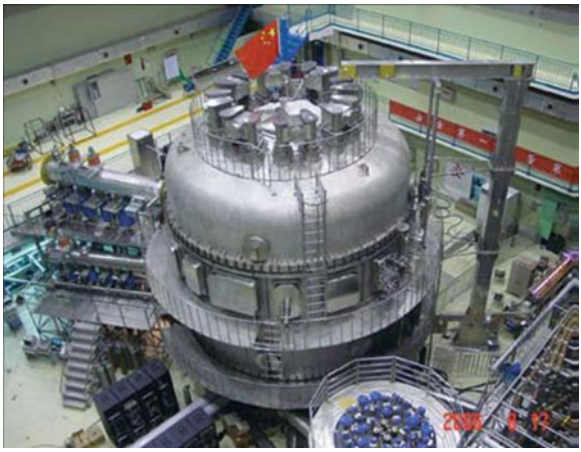

Fig. 9.20 EAST superconducting tokamak built at IPP (Chinese Academy of Sciences), Hefei [27] (*Courtesy* Jiangang Li, Institute of Plasma Physics, CAS, Hefei, P.R. China)

9.4.8 SST-1 (Steady State Superconducting Tokamak-1), IPR, Gandhinagar, India

SST-1 is a superconducting Tokamak designed and commissioned at the Institute for Plasma Research (IPR), Gandhinagar, India in the western state of Gujarat. It is a modest size tokamak [30–32] designed to study physics and technology to achieve long duration (1,000 s) steady state hydrogen plasma with significant elongation (1.7–2.0) and triangularity (0.4–0.7) in double null (DN) divertor configuration. SST-1 is expected to sustain a current of 220 kA. The parametric details of the SST-1 tokamak are given in Table 9.13. The auxiliary heating consists of LHCD (1.0 MW), ICRH (1.0 MW), ECRH (0.2 MW) and NBI (0.8 MW). The total heat input, however, would not exceed 1 MW at any given point of time because of the limited heat extraction capability of the first wall of the SST-1 plasma container.

Superconducting Toroidal (TF) and Poloidal (PF) magnets have been used in SST-1 to confine and shape the plasma. SST-1 has sixteen superconducting TF coils and nine superconducting PF coils. Additionally, there are nine resistive coils known as Ohmic transformer coils (OT) and compensating coils (TR) to assist in creating the plasma, a pair of vertical field coils (VF) to provide the initial equilibrium to the plasma column formed and two in-vessel PF coils to provide the shape and radial control to the initial plasma column apart from a pair of in-vessel fast feedback coils designed to. The relative positions of these coils can be seen in Fig. 9.21. The 16 TF coils are toroidally placed around the torus 22.5° apart The TF coils have been wound using Nb–Ti/Cu Cable-in-Conduit-Conductor (CICC) in double pancake configuration. Each TF coil has six double pancakes and each double pancake has eighteen turns. The details of the TF coil parameters and the conductor specifications are given in Table 9.14. The ‘outer dimensions of the jacketed CICC are 14.8×14.8 mm^2. The jacket is made of non-magnetic SS 304L. The CICC has 135 strands of diameter 0.85 mm each and having Cu:Nb–Ti ratio of

Table 9.13 Main parameters of the SST-1 Tokamak (data compiled from [30])

Parameter	Unit	Value
Year of completion		2012
Year of First Plasma		2013
Major radius	(m)	1.1
Minor radius	(m)	0.2
Plasma elongation, κ		1.7–2.0
Plasma triangularity, δ		0.4–0.7
Maximum designed Field at plasma centre	(T)	3.0
Plasma current	(kA)	220
Plasma hold time	(s)	1,000
Plasma configuration		Double null
Plasma temperature	(keV)	1.5
Plasma density (average)	(/cm^3)	1×10^{13}
Plasma fuel		H + H
Pre-ionization	(MW)	0.5 (ECRH, 42 GHz)
Plasma heating	(MW)	1.0 (LHCD, 3.7 GHz) 1.0 (ICRH, 22–91 MHz) 0.2 (ECRH, 84 GHz) 0.8 (NBI @80 keV)

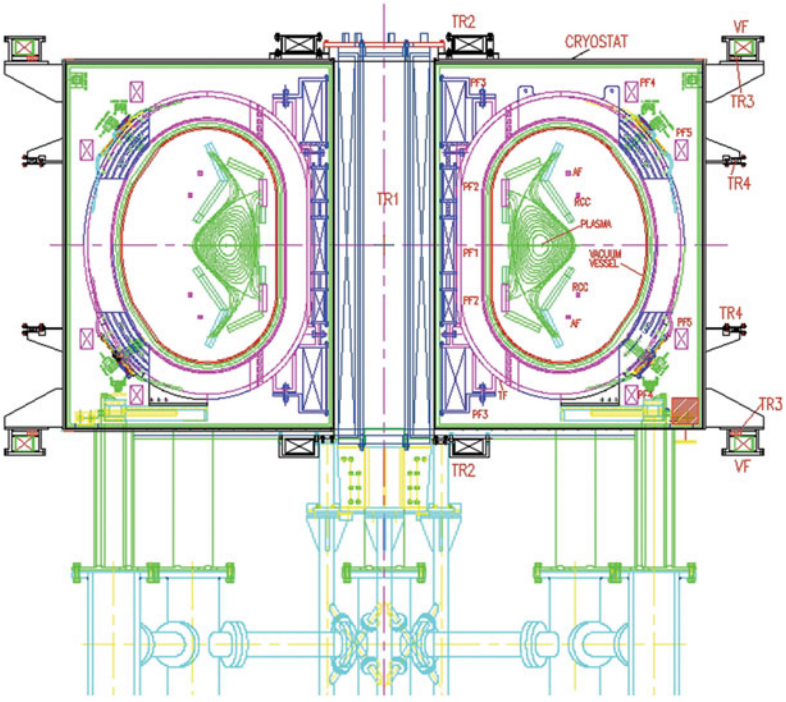

Fig. 9.21 A schematic of the cross-section of the SST-1 and the support structure (*Courtesy* SST-1 Team, 2014 IPR)

Table 9.14 TF coils and conductor parameters of SST-1 (data compiled from [30])

Parameter	Unit	Value
No. of TF coils		16
Maximum Toroidal field at plasma centre	(T)	3
Max. field at the coil	(T)	5.16
Max. field ripple at the plasma edge	(%)	2.0
TF Coil configuration		6 double pancakes
No. of turns/coil		108
Coil current	(kA)	10
Stored energy in TF system	(MJ)	56
Cooling media		Supercritical forced flow @ (4.5 K, 4 bar) or Two phase flow
Refrigeration capacity	(W)	650 + 200 l/h for the Current leads
Energy dump time of TF magnets	(s)	12
Max. dump voltage	(V)	1,200
No. of PF coils		9 (8 coils in 4 pairs and one single)
Conductor specifications		
Conductor used		Nb–Ti
Conductor size	(mm)	14.8 × 14.8
No. of strands in the cable		135
Cu:Nb–Ti ratio in a strand		5: 1
Strand diameter	(mm)	0.86
No. of filaments/cable		1224
Filament diameter	(μm)	10
Jacket material		SS304L (1.5 mm thick)
Void fraction	(%)	38

5:1. The strands are twisted in four stages with the pitch of 40, 75, 130 and 290 mm respectively. The strand has a total no of 1,224 filaments, each of an average diameter of 10 μm. Six double pancakes in the winding pack of each of the TF coil are insulated and then consolidated together after which a ground insulation was put over the consolidated winding pack. The winding pack was finally shrunk fitted into an appropriate casing fabricated from non-magnetic SS 316LN. The SST-1 TF casing comprises of inner and outer rings and side plates, all welded together. All the sixteen TF coil cases in SST-1 machine shell assembly are wedged at the inner legs forming an inner cylindrical vault. All the outer legs of all the TF coils are joined together through a mechanical structure known as outer-inter-coil-structure (OICS). These arrangements in TF coil assembly in SST-1 withstand the centering force as well as the overturning torque acting on the TF coil system resulting from the interaction of the transport current with the magnetic field. The TF coil casings in SST-1 are robust enough to take care of the thermal stresses during the cool-down as well as the entire electromagnetic (EM) forces during the operation. Liquid nitrogen cooled thermal shield kept at 80 K have been used between the TF coils

and the vessel. Similarly, thermal shield has been placed between the TF coils and the outer cryostat with a vacuum gap.

The coils are cooled to 4.5 K using forced flow helium. The helium is fed to the coils from inside in the high field region. A large number of joints between the CICC have been made between the double pancake terminations as well as between the coils. Low sub-nano ohm DC 'hand-shake' type joints have been developed using copper termination blocks and low melting Sn–Ag solder as a filler. The joint resistance was typically $\sim$0.3–0.4 nΩ at 4.2 K for a current of 10 kA. Large number of sensors have been used in the magnet for quench detection. The coils are protected against quench through the use of dump resistors.

The SST-1 tokamak has nine superconducting PF coils and two copper resistive coils inside the vessel for plasma shaping and equilibrium with the option of a wide range of elongation and triangularity. Provision has been made for double null and single null operation at a nominal plasma current of 220 kA and advanced plasma configurations at 330 kA. The nominal currents and positions of the PF coils have been worked out using a code based on ideal MHD equilibrium, free boundary and axi-symmetric model. PF coils in SST-1 too have been wound using the same conductor as used for the TF coils. The PF coils are supported on the casing of the TF coils.

All the SST-1 magnets were tested [31] individually in a dedicated LHe cryostat for its performance during 2010–2011 successfully. The first plasma in SST-1 was observed on June 20, 2013 assisted with ECRH pre-ionization at second harmonic. The TF field has since been raised to 2 T for 20,000 s at the plasma center (3.8 T at the TF magnet winding pack). The plasma current has been jacked up to 75 kA for a pulse length of 430 ms.

9.4.9 The ITER (International Thermonuclear Experimental Reactor), Cadarache, France

9.4.9.1 Objectives of ITER

ITER is an international collaborative project and the culmination of all the efforts that the fusion reactor community around the world have been putting in for over four decades. ITER is designed to produce fusion power of 500 MW, ten times the input power (Q = 10) and will be the biggest ever tokamak based fusion reactor built so far. ITER will not produce power but test all the relevant technologies needed for the power generating reactor, DEMO to be built in 2030s. The objectives include igniting plasma (self sustaining), verifying tritium breeding concepts from the neutron-lithium reaction and developing efficient technique to extract heat from the fast neutrons, generated in the D-T reaction. For this purpose ITER will evaluate various modules of the blanket designed to slow down and absorb fast neutrons reliably and efficiently. This neutron energy appears as heat which is extracted by the coolant to run the turbines.

ITER means "way" in Latin and is the result of a broad understanding reached between the two presidents, Reagan of US and Gorbachev of Soviet Union in 1985 at a IAEA meeting. The design work proceeded between 1988 and 1998 and the project was accepted in 2001. The project is funded by seven countries, European Union (EU), US, Russia, Japan, China, Korea and India. EU is funding the project to the extent of 45 % and the rest is shared by the other partners (9 % each). The building activity is in full swing at the moment at Cadarache, France and the production/fabrication of parts of the total system is going on in many countries. The assembly started in 2013 and is scheduled to be completed by 2015. The first plasma is expected in 2022 and the D-T operation should start in 2027.

9.4.9.2 ITER Design

ITER is a fully superconducting tokamak consisting of 18 toroidal coils, 6 poloidal coils, one central solenoid and 9 pairs of correction coils (CC). Correction coils are needed to correct the error fields generated by the imperfections in the manufacturing and/or assembly stages and to stabilize the plasma. All the TF coils are being built by EU and Japan, the CS in six identical modules by US and the poloidal coils by EU, Russia and China. PF1 and PF6 are being built by EU and Russia and PF2 to PF5 will be fabricated by China. The 9 pairs of CC and 31 feeders too will be

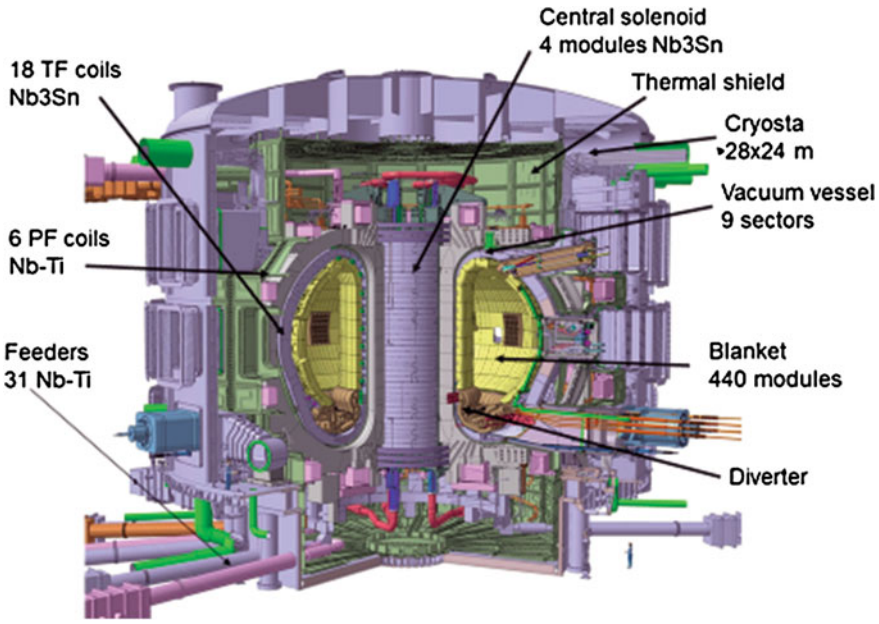

Fig. 9.22 A *cut-view* of the ITER machine [33] (*Credit* © ITER Organization, http://www.iter.org/) (*Courtesy* Carlo Sborchia and Amoud Devred)

supplied by China. These feeders include Nb–Ti CICC bus bars and Bi-2223 HTS current leads. India is fabricating the LN2 and LHe supply lines and the cryostat. Figure 9.22 is the cut-view of the ITER [33] which shows the 'D' shaped TF coils and the CS along with several feeders and inserts. The main parameters of the ITER are listed in Table 9.15. The scheme of the PF and CS is shown in Fig. 9.23 [34] and the entire magnet coil system is shown in Fig. 9.24.

Since the peak field in the TF coils is 11.8 and 13.5 T in the CS magnet, Nb_3Sn CICC conductors have been used for these two magnets. The peak field in PF coils and CC coils is, however, limited to 6 and 4.2 T respectively, Nb–Ti CICC conductor has therefore been used. All the coils are cooled by the forced flow of supercritical helium entering the coil terminals at 4.5 K. Both the conductors have the CICC configuration and the strands are Cr-coated. The general process followed for the manufacture of the CICC conductors used for coil winding for ITER magnets is depicted schematically [33] in Fig. 9.25.

About a 1,000 multistage superconducting strands, each with a predetermined copper fraction, are twisted around a central cooling spiral tube. SS wraps have been used at the sub-cable stages to reduce ac losses. The cable is then inserted inside the SS 316L tubes which are butt welded and extruded as circular jacket for

Table 9.15 The main parameters of ITER (data compiled from [35, 36])

Parameter	Unit	Value
Year of start of operation		2022 as scheduled
Plasma major radius	(m)	6.2
Plasma minor radius	(m)	2.0
Plasma volume	(m^3)	840
Plasma surface	(m^2)	678
Plasma current	(MA)	15
Plasma average temperature	(keV)	20
Plasma average density	($/m^3$)	10^{20}
Plasma inductive burn time	(s)	300
Average neutron wall loading	(MW/m^2)	0.57
Vertical elongation, κ		1.7–1.85
Triangularity, δ		0.33–0.49
Plasma heating	(MW)	173 (auxiliary-73, current drive-100)
Field at plasma axis	(T)	5.3
Peak field	(T)	11.8
Current leads (Bi-2223 HTS)I_c	(kA)	70
Cryostat height	(m)	29.3
Cryostat diameter	(m)	28.6
Weight of the magnet system	(ton)	10,150
Weight of the cryostat	(ton)	820
Weight of the machine	(ton)	23350 (magnets + vac. vess. + cryostat)
Fusion power	(MW)	500

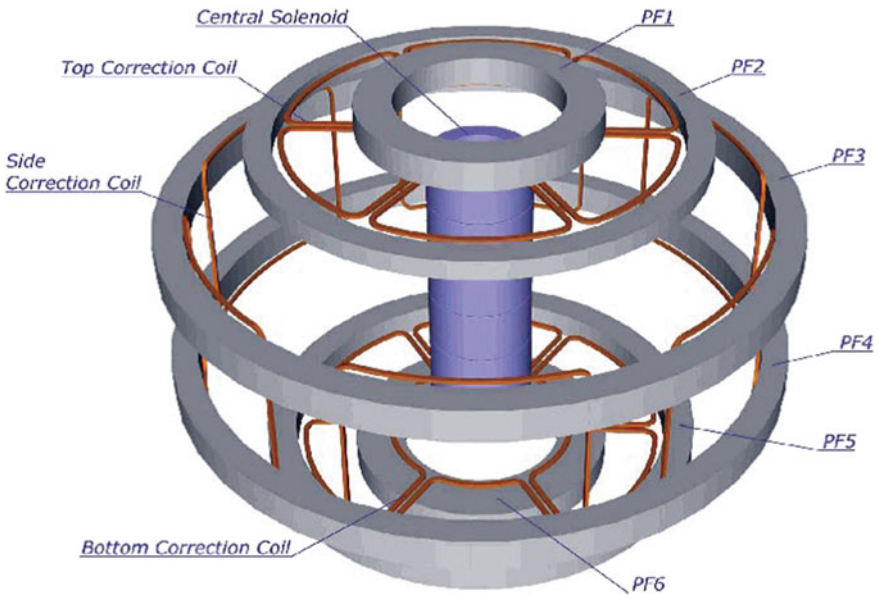

Fig. 9.23 The scheme of PF and CS coils of the ITER [34] (*Credit* © ITER Organization, http://www.iter.org/) (*Courtesy* Carlo Sborchia and Amoud Devred)

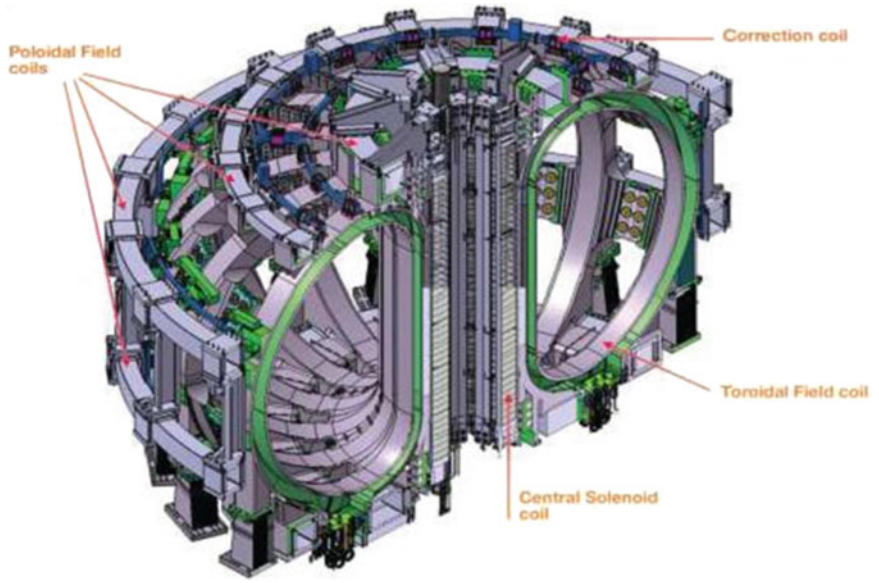

Fig. 9.24 Schematic of the magnet system consisting of CS TF, PF and CC coils of the ITER [35] (*Credit* © ITER Organization, http://www.iter.org/) (*Courtesy* Carlo Sborchia and Amoud Devred)

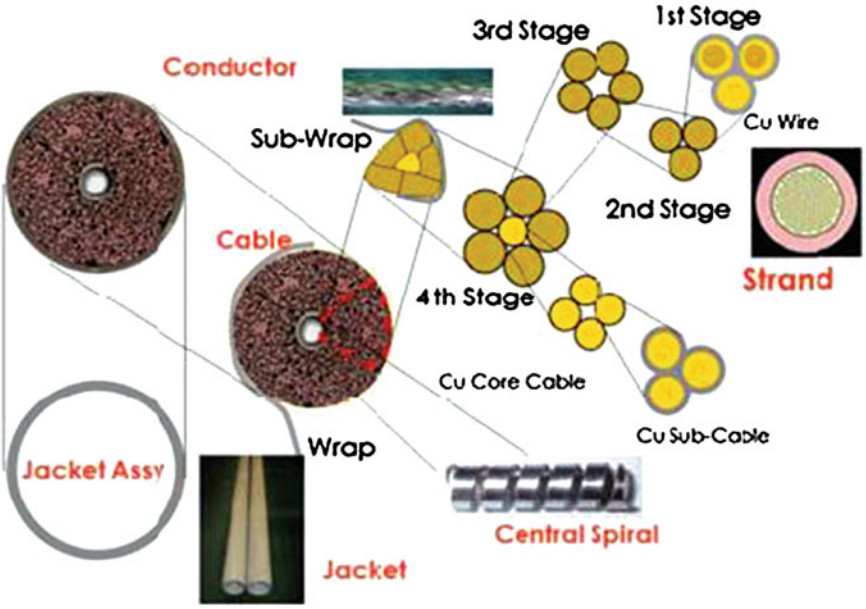

Fig. 9.25 The process through different stages of cabling for CICC cables used for ITER magnet coils [33] (*Credit* © ITER Organization, http://www.iter.org/) (*Courtesy* Carlo Sborchia and Amoud Devred)

the TF coils and as square jacket for the other coils. The jacket material for the CICC Nb_3Sn for CS modules is Incoloy Alloy 908. The operating current requirement for the TF coils is 68 kA and 45 kA for the CS and PF coils. The CC coils use a cable with only about 300 strands and without the central channel as they operate at a lower current level of 16 kA. The conductors have a void volume of about 29 %, which facilitate SHe flow for cooling. Table 9.16 gives the specifications of the TF, CS and PF coils [33, 37] and the conductors used. HTS Bi-2223 current leads with a critical current of 70 kA will be used to power the magnets. The use of HTS leads results in a 25 % of saving of energy. The total cryogenic power requirement is estimated to be 64 kW.

9.4.9.3 The TF Coil Winding Pack

Each TF coil consists of 7 double pancakes (DPs) wound with Nb_3Sn conductor. The winding of the coils and maintaining the dimensional and geometrical accuracies is a complicated procedure because the winding packs (WPs) are heat treated. The winding has to take into account the conductor elongation (about 0.05 %) due to heat treatment. The winding is carried out in a mold to hold the conductor shape during heat treatment. After the winding, the conductor terminations and helium inlets are

Table 9.16 Main parameters of the TF, PF and CS coils of the magnet system of the ITER (data compiled from [33, 37])

Parameter	Unit	TF coil	PF coil	CS coil
No. of coils		18	6	6
Conductor used		Nb_3Sn	Nb–Ti	Nb_3Sn
No. of double pancakes		7	8(PF1,3,4,5) 6 (PF2) 9(PF6)	
No. of turns/coil or WP		134	115–459	549
Operating temperature (supercritical helium)	(K)	4.5	4.5	4.5
Max. operating current	(kA)	68	45	45
Nominal peak field	(T)	11.8	6.0	13.0
Total stored energy	(GJ)	41	4	7
Electrical discharge time constant	(s)	15	18	11.5
Total weight of the coils (with case and structure)	(ton)	5,364	2,163	954
Length of the coil centre line	(m)	34.1	25–27	10.7
WP conductor length	(m)	4,570	6,009–14,067	6,019
Total conductor length	(m)	82,260	63,142	36,114
Conductor unit length	(m)	760/415	387–879	903/601
SC strands/total strands		900/1,422	1440, 1152 and 720 (SC)	
Sc: Cu ratio		1	1–2.3	1
Strand plating thickness	(μm)	2	2	2
Strand diameter	(mm)	0.82	0.73	0.83
Cable diameter	(mm)	43.7	35–38	43.7
Jacket		SS 316LN (circular)	SS 316LN (square)	JK2LB (square)
Void fraction	(%)	29		
SHe mass flow rate in conductor	(g/s)	8	8–14	8
SHe mass flow rate in structure	(kg/s)	2.5		

formed by opening the conductor jackets. Each DP has two terminations and each winding pack has 6 DP to DP joints. The coils are now heat treated (650 °C × 200 h) under controlled inert atmosphere. The mold is removed and radial plates (RP) are inserted between the two single pancakes by creating gap. The RP is made out of a high strength thick plate of austenitic steel SS 316LN with finely machined grooves to fit the conductor. This procedure is to be carried out extremely carefully within the conductor strain limit of 0.1 %. The conductor is insulated with a thin wrap of glass cloth by lifting it gently and the gap in the groove is filled with glass cloth shims. A perforated cover plate (CP) is fixed by laser welding to lock the conductor in the groove. The perforation in the CP enables the epoxy flow during the vacuum-pressure

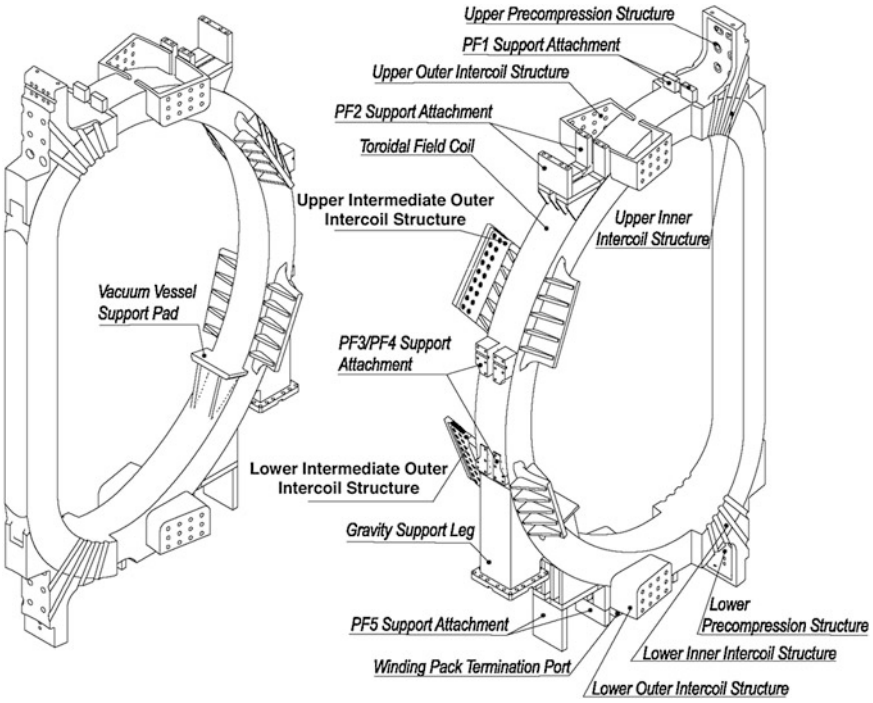

Fig. 9.26 The TF coil with casing and various support structures [34] (*Credit* © ITER Organization, http://www.iter.org/) (*Courtesy* Carlo Sborchia and Amoud Devred)

impregnation. Electrical insulation is provided to the conductor and ground insulation to the DP and impregnation carried out.

The TF coil casing is the next most critical part of the tokamak as it carries all the support structure for a large number of PF coils, the CS and many other components. As shown in Fig. 9.26 the casing carries upper and lower pre-compression structures, upper and lower, inner and outer inter-coil structures, support structure for all the PF coils, gravity support leg structure and terminal port for the WP. The WP is inserted in the casing and the space between the WP and the casing is filled with epoxy. A two step process, that is, laser root technique (LRT) followed by submerged arc welding (SAW) technique has been used for welding the casing parts. The casing is finally closed with the plates and welded using the same technique.

9.4.9.4 The PF Coil Winding Pack

The PF coils too are fabricated in a double pancake (DP) structure. The DPs are wound, electrically insulated and epoxy impregnated. They are stacked together and again impregnated to complete the WP. The winding packs of PF1, PF3, PF4 and

PF5 have 8 DPs, PF2 has 6 DPs and the PF6 has the maximum number, 9 DPs. Before a DP is impregnated about 5 m of the conductor ends are kept un-bonded by an anti-adhesive wrap. This wrap is removed after the impregnation. These conductor ends are used for making flexible terminations for making joints. A glass cloth layer is inserted between the DPs to facilitate the resin flow and bonding during impregnation. The inlet and outlet SHe ports are now joined to the cooling pipes which are ground insulated and joined with the cooling system network.

PF coils use Nb–Ti CICC conductors. Since different PFs experience different peak field the cables with different specifications [37] have been produced and used for winding the PF coils. Coils PF1 and PF6 have the highest peak field than the other PF coils. The conductor for PF1 and PF6 has therefore larger no. of superconducting strands (1,440) compared to other coils, 1,152 for PF5 and 720 for rest of the PFs. Nb–Ti and Cu strands are cabled like a rope but without a central spiral and jacketed in SS 316LN with a square cross-section. The strands in these conductors are coated with Ni. The conductors are manufactured in 5 cabling stages as indicated in the table. The starting stage is always a triplet (2 or 3 SC strands + one copper strand). The cable in last but one stage is wrapped with a thin SS tape in a helical fashion with gaps. The tape limits the coupling currents and the gap facilitate SHe flow for cooling. A detailed account of the conductor production has been given by Devred et al. [38].

9.4.9.5 The CS Coils

The CS magnet is a solenoid consisting of 6 coil modules stacked vertically one over the above. Each of the 6 coils is wound using a bare CICC Nb_3Sn conductor in the form of either a quadpancake (QP) or a hexapancake (HP). Spacers are used between the successive turns and between the pancakes for the insertion of insulation. The parameters of the CS coils and the conductor used are given in Table 9.16. The conductor jacket is opened at appropriate locations to make provision for SHe inlet and outlet as well as for the terminations. The hexapancakes/quadpancakes under proper clamping system are then heat treated (650 °C × 200 h) and glass insulation is provided turn to turn and pancake to pancake after removing the spacers extremely carefully. The entire module is now ground insulated. The module is inserted into a mould and epoxy impregnated keeping the SHe inlet and outlet ports open. The CS with high strength top hangers, central compression flanges and lower centering system together with the conductor cross-section is shown in Fig. 9.27.

The modules with their bus bars extensions are stacked together vertically using a strong and slotted support system. The modules are pre-compressed using a set of super nuts and bolts and by pulling on all the tie plates by tightening the bolts with matching tensile load on every tie plate. The bolts are finally unscrewed to release the load on the thread after the shims are introduced between the tie plates and the

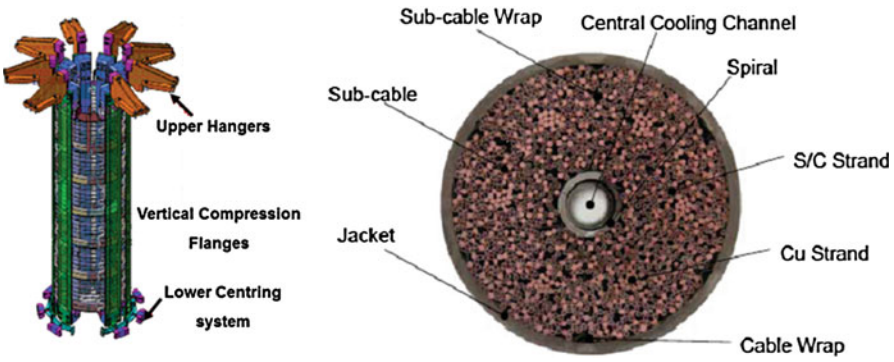

Fig. 9.27 The CS (*left*) and the CICC Nb_3Sn conductor cross-section (*right*) used for CS coils winding [35] (*Credit* © ITER Organization, http://www.iter.org/) (*Courtesy* Carlo Sborchia and Amoud Devred)

key blocks and the horizontal screws are tightened. The CS is supported on the inboard vault structure of the TF coils.

A very comprehensive review titled "Challenges and status of ITER conductor production", running into 39 pages and written by Amoud Devred et al. has just appeared [39] about the status of conductor production for different types of ITER magnets. The huge amount of conductor required by ITER being far above the present production capacity of the manufacturers, a large number of suppliers have been involved. The uniformity of the conductor parameters produced at different locations is a challenging task. It will be first time that Nb_3Sn conductor will be used on such a massive scale and exposed to unprecedented large EM forces and high level of stresses during thermal cycling all through its life time. All the technical problems envisaged during quality assurance and quality control during production and procurement have been solved.

9.4.9.6 Final Assembly of ITER

The tokamak is to be assembled in 9 sectors each consisting of a pair of TF coils and 1/9th of the cryostat including the vacuum vessel and the thermal shield. Feedthroughs and ports are to be provided in the inter-space between the TF coils. PF5 and PF6 coils will be mounted in position on a temporary structure in the lower part of the cryostat. Gravity support, lower pre-compression rings and various other components of the support structure too will be fixed in position. The 9 sectors will then join together to form the torus. Eventhough all the parts are custom machined within the tolerance limits, yet shimming may have to be used at places during the assembly.

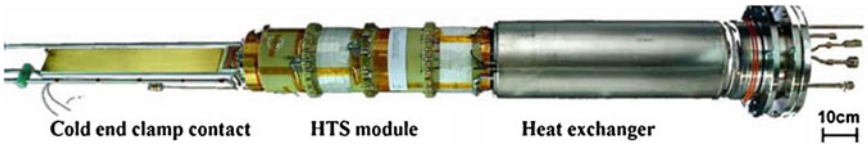

Fig. 9.28 70 kA HTS (Bi-2223) current leads for ITER [35] (*Credit* © ITER Organization, http://www.iter.org/) (*Courtesy* Carlo Sborchia and Amoud Devred)

The remaining PF coils and the upper, lower and side correction coils will be installed at appropriate places on the TF coil cases. All the remaining feeders are then to be mounted at this stage through the bottom and the side ports. ITER has a total of 31 feeders, 26 for coils, 3 for the structure and 2 for instrumentation. In the final stage of the assembly will be the installation of the CS which is separately assembled and pre-compressed along the central axis of the tokamak. The CS will finally be lowered in the central bore of the machine and rigidly fixed at the bottom of the TF coils.

9.4.9.7 HTS Current Leads

ITER needs about 60 current leads to transport a total current of 2,500 kA. HTS current leads are proposed to be used to reduce the heat load and save on the cryogenic cost. This will result in a 25 % reduction in the cryogenic power (18 kW @4.5 K). The current leads capable of carrying 70 kA have already been developed and tested by Heller et al. [40] at Karlsruhe Institute of Technology (KIT). A schematic diagram of the current lead is shown [35] in Fig. 9.28. The current leads are made using a stack of Bi-2223 tapes clad in a Ag–Au alloy sheet. These current leads have been optimized for 80 K, the temperature at which the thermal shields is cooled by SHe. The leads have been successfully tested up to 70 kA. Optimization at 80 K also makes the option of using liquid nitrogen a possibility. The current leads have three main components, a copper heat exchanger, an HTS module and the bottom cold end clamping.

We summarize the main parameters of the important superconducting tokamaks discussed in above sections in Table 9.17. Tore Supra, K Star, EAST and SST-1 are already in operation and yielding useful data. The other superconducting tokamak, JT-60 SA will start operation soon. It is hoped that the experience gained from these reactors will enable ITER to reach its goal as planned.

Table 9.17 Comparison of main parameters of some of the important superconducting tokamaks including ITER

Parameters	Unit	T-7 (USSR)	Tore Supra (France)	JT-60 SA (Japan)	K STAR (Korea)	EAST (China)	SST-1 (India)	ITER (France)
Year of Start		1978	1988	2014	2008	2006	2013	2022
Major radius	(m)	1.22	2.25	3.06	1.8	1.85	1.1	6.2
Minor radius	(m)	0.35	0.70	1.15	0.5	0.45	0.2	2.0
No. of TF coils		24 × 2	18	18	16	16	16	18
Toroidal field	(T)	3.0	4.5	2.69	3.5	3.5	3.0	5.3
Peak field	(T)	5.0	9.0	6.4	7.0	5.8	5.1	11.8
Operating current	(kA)	6.0	1.40	25.3	35.2	14.5	10.0	45
Stored energy	(MJ)	20	0.6	1,060	470	300	56	51,000
Cooling media		SHe	SHe	SHe	SHe	SHe	SHe	SHe
TF conductor	CICC	Nb–Ti	Nb–Ti	Nb–Ti	Nb_3Sn	Nb–Ti	Nb–Ti	Nb_3Sn
Plasma current	(MA)		1.7	5.5	2.0	1.0	0.22	1,5000
Plasma elongation	κ		1.76	1.76	2.0	1.6–2.0	5.2	1.7–1.85
Plasma triangularity	δ		0.45	0.45	0.8	0.6–0.8	1.7–2.6	0.33–0.49
Plasma volume	(m^3)		24	127	17.8			840
Plasma heating	(MW)		27	41	28 (Aux)	7.5 (Aux)	3(Aux)	173
Plasma fuel			D + D	D + D	H + D	D + T?	H + H	H + D + T

9.4.10 Other Fusion Devices Under Construction

Notwithstanding the ongoing construction of ITER and the preparation for futuristic DEMO, efforts are going on to build fusion devices at various places to test alternative approach to produce fusion power. We discuss two such initiatives below.

Table 9.18 Main parameters of W7-X stellarator and the CICC Nb–Ti conductor used for magnet coils (data compiled from [42, 43])

Parameter	Unit	Value	Parameter	Unit	Value
Year of start		2015	Conductor		Nb–Ti (CICC)
Major radius	(m)	5.5	No. of strands		243
Minor radius	(m)	0.53	Strand dia.	(mm)	0.57
No. nonplanar coils		50	No. of filaments/strand		144
No. of planar coils		20	Cabling configuration		3 × 3 × 3 × 3 × 3
Field on the axis	(T)	<3	Cu: SC ratio		2.6
Stored energy	(MJ)	600	Void fraction	%	37
Plasma pulse length	(min)	30	Conductor I_c	(kA)	35 (4 K, 6 T)
Plasma volume	(m^3)	30	Temperature margin	(K)	1
Plasma heating	(MW)	15–30	Total length of strands	(km)	15,000
Dia. of the cryostat	(m)	16	Total conductor length	(km)	60
Height of the device	(m)	4.5	Max. single length of conductor	(m)	120–130 (PC) 150–170 (NPC)
Weight of the device	(ton)	725	Jacket Material		(AlMgSiO5)
Cold mass	(ton)	425	Jacket dimensions	(mm)	16 × 16
Cooling media		SHe			

9.4.10.1 W7-X (Wendelstein 7-X) Stellarator, Greifswald, Germany

The W7-X Stellarator fusion device is an alternative to a tokamak system to confine plasma magnetically. W7-X is a steady state reactor being built at the Max-Planck Institute for Plasmaphysik (IPP), Greifswald, Germany [41–43]. The stellarator is wholly superconducting, consisting of 50 non planar coils, 20 planar coils, 121 bus bars and 14 current leads. In contrast to tokamak which uses dc and ac fields the stellarator uses only dc field because PF modulation for plasma positioning and start-up is not needed. It also offers steady state operational capability and prevents fast plasma disruption which dumps energy on the wall. The main parameters of the machine and the CICC Nb–Ti conductor used for winding magnet coils are given in Table 9.18. All the coils are divided into 5 nearly identical modules and together form a toroid. Each module has two mirror symmetric half modules. One half module consists of 5 non planar and 2 planar coils. All the coils in a half module are designed and shaped differently to meet the requirement of a five fold symmetry of the machine and the flip symmetry installation of the two identical halves of the module. The coils are rigidly joined together and mounted on to a cast steel central support ring. The magnet system and all the component systems are housed in a 16 m dia. cryostat which has plasma vessel, outer vessel and 254 ports. These ports are used for the installation of diagnostic instruments, heating, water supply to in-vessel components and pumping. All the magnets are grouped in 7 electrical circuits each energized by a power supply. Fourteen hybrid current leads are used to power the coils. In addition to the superconducting coils, 5 water-cooled normal

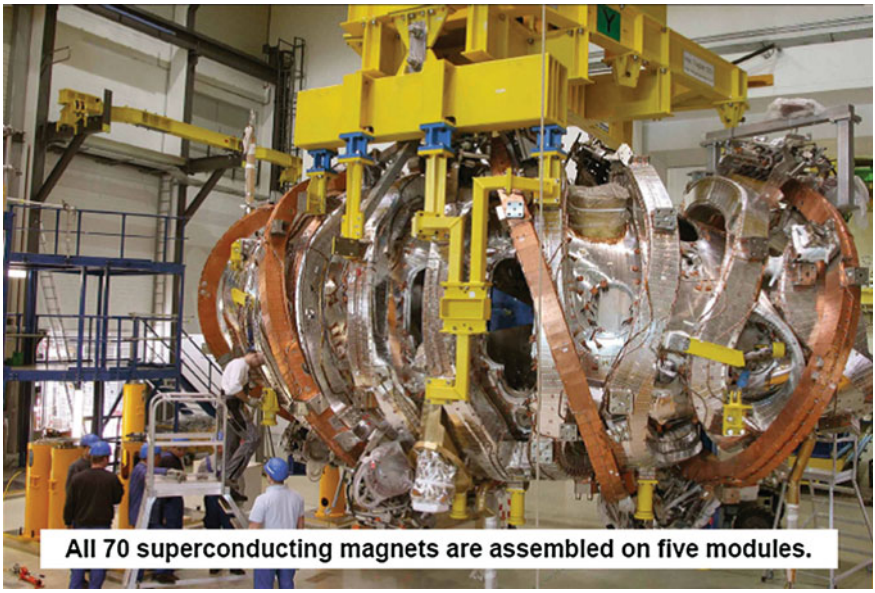

Fig. 9.29 All 70 SC magnets (50 non-planar, 20 planar) of the W7-X stellarator assembled in 5 modules [42] (*Courtesy* Thomas Klinger, *credit* Max-Planck Institute for plasma Physics)

conducting saddle shaped trim coils are used outside the cryostat to fine tune the edge magnetic field. Four coils are of the size 3.6 m × 3.3 m and one coil 2.82 m × 2 m. The coil assembly is seen in Fig. 9.29.

A Nb–Ti CICC conductor has been used for all the superconducting coils. The cable has 342 strands of 0.57 mm diameter and each strand has 144 Nb–Ti filaments. The Cu to non-Cu ratio is 2.6. The conductor has a critical current value of 35 kA at 4 K and 6 T field. The coils are cooled by the forced flow of supercritical helium. The void available for the SHe flow is 37 %. In all, 390 double layer lengths of 120–130 m for the planar coils and 150–170 m for the non planar coils were used for winding.

The non planar coils provide a combination of helical field and the toroidal field and thus play a key role in providing magnetic confinement in stellarators. Each non planar coil has 6 double layers consisting of a total number of 108 turns and uses a single length of conductor. All the 6 double layers are connected in series electrically and in parallel hydraulically for cooling. SHe inlets are connected to the coils on the high field side (inner most layer). The coil is vacuum-pressure impregnated using fiber glass and hot curing epoxy in a rigid mould. The 5 mm thick insulation provides a ground insulation of 6 kV. The winding pack thus formed is inserted in a strong SS case cast in two halves. The case is strong enough to withstand large EM forces. After the insertion of the coil the two halves are welded and the gap between the coil pack and the case is filled with quartz sand and cold curing epoxy. In the final stage, 1,100 copper strips are welded around the case

and these are soldered to the four cooling pipes. This arrangement provides an effective cooling shield to the winding pack. The nominal current for the coil operation is 17.6 kA dc. A non planar coil has the dimensions of about 3.5 × 2.5 × 1.5 m and weighs close to 5.5 tons.

The planar coils are installed around the non planar coils at an angle of 20° from the vertical axis. These coils are used to move the plasma inward or outward and to configure the magnetic field. Coils are fabricated much in the same way as the non planar ones with some different features. Same CICC Nb–Ti conductor has been used to wind the coils. All the coils are divided into two (10 coils each) different configurations. The winding pack now has 3 double layers each with 12 turns and connected in series electrically. The double layers are connected in parallel hydraulically to the cooling channels. Electrical insulation with a ground voltage of 4 kV dc is achieved with glass fiber and cold curing epoxy similar to that used for the non planar coils. Each coil weighs about 3 tons and has an outer dia. of 4 m. The casing for the WP is prepared using a SS plate cut into rings (outer and inner) and two annular plates, one each for the bottom and the top. After the impregnated WP is inserted between the inner and outer rings top and bottom plates are screwed tightly. To pre-compress the coil the case is heated to 150 °C and the coil inserted. The gaps are filled with G11 pieces and glass epoxy and cured. All the coils are protected against the radiation heat flux from the outer vessel by welding copper plates to the case and thermally connecting them to the cooling channels. Ninety six plates (100 mm × 2 mm) with gaps have been used. The gaps reduce the eddy current heating during the fast ramping of the field.

Superconducting bus bar system has been used for connecting the coils with the current leads. The bus bars (121 nos.) are 4.5–16 m long, made of the same conductor but machined to 17 mm dia. for flexibility, insulated with kapton tape wrapped with epoxy resin impregnated glass fiber tape. The insulation can withstand a voltage of 13 kV dc. The bus bars are designed to carry current up to 18.2 kA and withstand load up to 17 MPa under extreme quench condition. Hybrid current leads consisting of a copper heat exchanger at the warm end, HTS Ag–Au/Bi-2223 current leads in the middle and the Cu/Nb_3Sn rods at the lower end, have been developed. The current leads join the room temperature bus bar system to the superconducting parts inside the cryostat. The current leads are mounted at the bottom of the machine with HTS part at the top. Each current lead weighs 260 kg. Voltage and temperature sensors are fixed on the leads at select locations. Current leads have been successfully tested up to a current of 20 kA.

The W7-X stellarator is indeed an extremely complicated reactor being developed at Greifswald and an expensive one. However, if the machine can produce 30 min duration steady state plasma, stellarator concept will be an alternate route to power generation.

9.4.10.2 IGNITOR (Italian-Russian Collaboration), ITP, Triniti, Russia

The Italian company ENEA (New Technologies, Energy and Environment) and the Institute for Tokamak Physics at Triniti, Russia entered into an agreement in 2010 to build a tokamak 'IGNITOR' fusion reactor [44, 45]. The tokamak is a revival of the Alcator series of fusion machines built by MIT in USA and Frascati Torus Programme in Italy in 1970s. The IGNITOR will be built in Russia at Triniti near Moscow and the core of the machine will be supplied by Italy. IGNITOR relies upon the use of high magnetic field and high plasma energy density in a compact system such that the state of ignition is achieved without external heating. It is a compact machine. It has a major radius of 1.32 m much smaller to ITER. The energy density is, however, twice to that in ITER. This high energy density is sufficient to heat the D-T plasma to an ignition temperature of 11 keV for a confinement time of 0.6 s. This device will weigh only 700 tons in comparison to ITER which will be 19,000 tons. Main parameters of the tokamak are listed in Table 9.19. The tokamak will have 24 toroidal coils. The ignition is attained at lower fusion power under conditions of high magnetic field and high current in a compact configuration with only Ohmic heating. The key elements of tokamak are TF coils, the mechanical structure, the PF coils, the CS, vacuum vessel and the surrounding cryostat. Figure 9.30a is the conceptual 3D picture of the exterior of the machine [45] and Fig. 9.30b, the cross-section showing position of the toroidal, poloidal coils and the central solenoid. Plasma chamber and various other components too can be seen.

One important feature of IGNITOR will be that MgB_2 conductor will be used first time for winding the largest poloidal coil P-14 which has a dia. of 5 m. The coil will operate at 10–15 K cooled by cryogenic He gas and will produce 4–5 T field at

Table 9.19 Some parameters of the IGNITOR fusion device (data compiled from [44–45])

Parameter	Unit	Value	Parameter	Unit	Value
Plasma major radius	(m)	1.32	Toroidal field	(T)	13
Plasma minor radius	(m)	0.47 × 0.86	No. TF coils		24
Aspect ratio		2.8	Max. poloidal field	(T)	6.5
Plasma stored energy	(MJ)	11.9	Poloidal current	MA	9
Plasma current	(MA)	11	ICRH power	(MW)	0
Plasma elongation, κ		1.83	Ohmic power	(MW)	11.2
Plasma triangular, δ		0.4	Toroidal plasma current	MA	11
Plasma volume	(m^3)	10	Energy confinement time	(s)	0.62
Plasma temp.	(keV)	11	Peak power load on the wall	MW/m^2	1.8
Plasma fuel		D + T	Conductor used for PF, P-14—MgB_2		

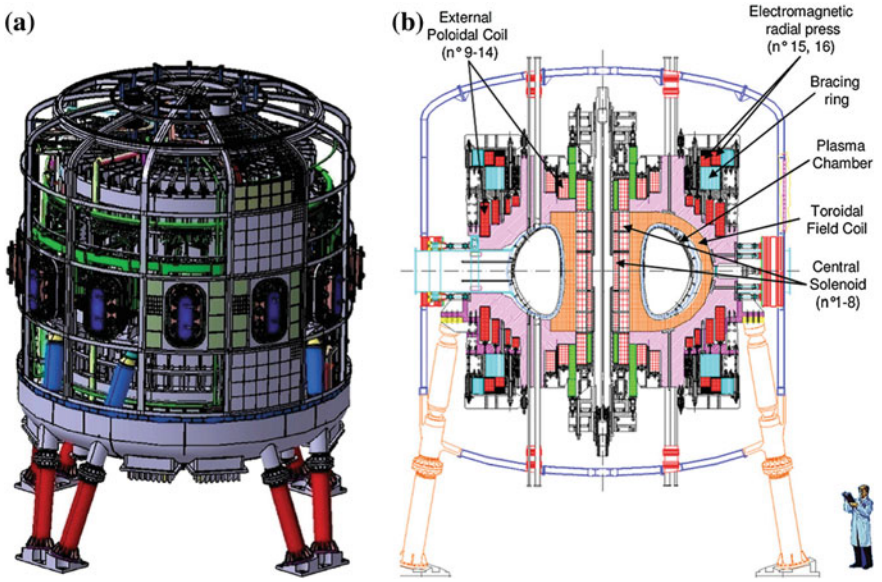

Fig. 9.30 **a** A conceptual 3D picture of the IGNITOR showing its exterior. **b** The cross-section of machine showing the locations of magnet coils and ports [45] (*Courtesy* Bruno Coppi and with permission from IAEA)

the coil location. The MgB_2 cable will be a circular conductor of dia. 31.55 mm having 336 strands of dia. 1.13 mm wrapped around a copper tube facilitating the He-flow. Each strand has 37 filaments in a Ni-matrix. For enhanced stability the strand will be coated with a 30 μm Cu-layer.

The dream of realizing power through fusion has always been a decade away. The ITER, a giant effort being made by the international community and at huge cost might ultimately break this passé and pave the way to build DEMO with high degree of confidence. Next two decades are going to be crucial when we get the final answer to the power generation through fusion. Superconductivity will continue to play the leading role in this endeavour. In the wake of these developments, there has been unprecedented growth of production of quality cables with high critical current, high field and low ac losses. This trend is bound to continue and possibly high T_c superconductors might replace the conventional superconductors and sooner than expected.

References

1. J.D. Lawson, Some criteria for a power producing thermonuclear reactor. Proc. Phys. Soc. **B70,** 6 (1957)
2. S. Prager, in *Magnetic Confinement Fusion Science-Status and Challenges*, PPT, University of Wisconsin, Feb 2005, http://fire.pppl.gov/aaas05_prager_mfe.pdf

3. Magnetic Confinement Fusion, http://library.thinkquest.org/17940/texts/magnetic_confinement/magnetic_confinement.html
4. R.H. Bulmer, Tendam Mirror System for the Mirror Fusion Test Facility, in *Proceedings of the 8th Symposium on Engineering Problems of Fusion Research*' (1979), p. 744, http://adsabs.harvard.edu/abs/1979epfr.conf..744B
5. L. Spitzer, D. Grove, W. Johnson et al., USAEC Report NY0-6047 (1954)
6. C.D. Beidler, E. Harrmeyer, F. Herrnegger et al., Stellerator Fusion Reactor—An Overview, in *Toki Conference. ITC-12*, Dec 2001, http://fire.pppl.gov/itc12_wobig_paper.pdf
7. V.P. Smirnov, Tokamak foundation in USSR/Russia 1950–1990. Nucl. Fusion **50**, 014003 (2010)
8. A.A. Bagdasarov et al., in *Proceedings of the 10th Conference on Controlled Fusion and Plasma Physics*, Moscow, Russia, 1981, A-19
9. D.P. Ivanov, V.E. Keilin, B.A. Stavissky et al., IEEE Trans. Magn. **MAG-15**, 550 (1979)
10. L.A. Artsimovich, V.D. Safranov, Sov. Phys. JETP Lett. **13**, 72 (1972)
11. G.S. Kirnev, V.A. Alkhimovich, O.G. Filotov et al., Superconducting Tokamak T-15 Upgrade, FT/P7-3, www-naweb.iaea.org/napc/physics/fec/fec2006/paper/ft_p7-3pdf
12. G.E. Smith, W.F.B. Panchard, TFTR Toroidal Field Coil Design, http://www.osti.gov/bridge/servlets/purl/5154253-mqn8cX/5154253.pdf
13. A. von Halle and the TFTR Group, Final Operations of the Tokamak Fusion Test Reactor (TFTR), in *Proceedings of the 17th IEEE/NPSS Symposium*, vol. 1, 6–10 Oct 1997, pp. 65–69
14. Joint European Torus, http://en.wikipedia.org/wiki/Joint_European_Torus
15. JET's main Features, www.efda.org/jet/jet's-main-features
16. Equipe TORE SUPRA, IEEE Trans. Magn. **25,** 1473 (1989)
17. Jean-Luc Duchateau (CEA Cadarache) PPT, The superconducting TF magnetic system of Tore Supra, http://www-fusion-magnetique.cea.fr/matefu/school_2/Wednesday/duchateau-Toresupra.pdf
18. J.L. Duchateau, J.Y. Jouneaux, B. Gravil, Fusion Sci. Technol **56**, 1092 (2009)
19. H. Rogalla, P.H. Kes (eds.), *100 Years of Superconductivity* (CRC Press, New York, 2012)
20. JT-60, http://en.wikipedia.org/wiki/JT-60
21. K. Yoshida, K. Tsuchiya, K. Kizu et al., Physica C **470**, 1727 (2010)
22. A. Cucchiaro, Italian Contribution to the JT-60 SA Project, http://www.fusione.enea.it/PROJECTS/realizationJT60SA/index.html.en
23. K. Kiju, K. Tsuchiya, T. Ando et al., IEEE Trans. Appl. Supercond. **17**, 1348 (2007)
24. A. Pizzuto, L. Semeraro, L. Zani et al., IEEE Trans. Appl. Supercond. **18**, 505 (2008)
25. Y.-K. Oh, K. Kin, K.-R. Park, Y.-M. Park, Superconductor Application to the Magnetic fusion devices for the steady–state plasma confinement achievement, in *Superconductors—Properties, Technology and Applications*, INTECH, 2012, ed. by Y. Grigorashvili, ISBN: 978-953-51-0545-9, http://www.intechopen.com//books/superconductors-properties-technology-and-applications/superconductor-application-to-the-magnetic-fusion-devices-for-the-steady-state-plasma-confinement-ac
26. M. Kwon, Y.K. Oh, H.L. Yang et al., Nucl. Fusion **51**, 094006 (2011)
27. Y. Wan, China's Ambitious Path to Fusion Power, an Interview dated Dec 1, 2010, 21st Century Science and Technology, Spring 2011, p. 47
28. Y.N. Pan, P.D. Weng, Z.M. Chen et al., IEEE Trans. Appl. Supercond. **10**, 628 (2000)
29. S. Wu, Q. Huang, J. Chen, Y. Wu, Fusion Reactor Technologies Development in ASIPP, PPCA2-I, http://www-pub.iaea.org/MTCD/publications/PDF/P1250-cd/papers/ppca2-i.pdf
30. Y.C. Saxena S. Pradhan, PPT, in *20th IAEA Fusion Energy Conference*, 1–6 Nov 2004, http://www.cfn.ist.utl.pt/20IAEAConf/presentations/T5/4T/FT_3_4Ra/talk_FT_3_4Ra.pdf
31. S. Pradhan, IEEE Trans. Appl. Supercond. **22**, (2012). doi:10.1109/TASC.2011.2174951
32. S. Pradhan, K. Doshi, A. Sharma et al., IEEE Trans. Appl. Supercond. **24**, (2013). doi:10.1109/TASC.2013.2290380
33. N. Mitchell, A. Devered, P. Libeyre et al., IEEE Trans. Appl. Supercond. **22**, 400809 (2012)
34. Summery of the ITER Final Report, July 2001 by Director ITER (G A0 FDR 4 01-06-28 R 0.2), http://www-pub.iaea.org/MTCD/publications/PDF/ITER-EDA-DS-22pdf

35. Carlo Sborchia, PPT Lecture on "Fusion Reactor Engineering", Politecnico of Turin (I), 31 January, 2011, http://staff.polito.it/roberto.zanino/sub1/teach_files/current_topics/lect_sborchia.pdf
36. Joseph V. Minervini, PPT, in "*Superconducting Magnets for Fusion and ITER Project" American Nuclear Society- Northeast Region Meeting*, Wellesley, MA, 18 April 2002, http://local.ans.org/ne/archives/Superconducting_Magnets%20-%20Joseph_Minervini_April_18_2002.pdf
37. H. Rajainmaki, A. Bonito-Oliva, C. Sborchia et al., in *The ITER Magnet System: Status of Design and Procurement*, PPT, Summer School, Kullaa, 17 June 2008, http://www.prizz.fi/sites/default/files/tiedostot/linkki1ID360.pdf
38. A. Devred, I. Backbier, D. Bessette et al., IEEE Trans. Appl. Supercond. **22**, 4804909 (2012)
39. A, Devred, I. Backbier, D. Bessette et al., Supercond. Sci. Tech. **27**, 044001 (2014)
40. R. Heller, W.H. Fietz, R. Lietzow et al., IEEE Trans. Appl. Supercond. **16**, 823 (2006)
41. T. Kupiszewski, O.R. Christianson, Conceptual Design of Superconducting Magnet Coils, http://aries.ucsd.edu/LIB/REPORT/SPPS/FINAL/chap4.pdf
42. T. Klinger, in *Stellerators Difficult to Build? The Construction of Weldelstein 7-X,* PPT, http://www.iter.org/doc/www/content/com/Lists/Stories/Attachments/680/ITER_W7X.pdf
43. T. Rummel, K. Riβe, G. Ehrke et al., IEEE Trans. Plasma Sci. **40**, 769 (2012)
44. B. Coppi, A. Airoldi, F. Bombarda et al., Critical Physics Issues for Ignition Experiments, MIT (RLE) Report PTP 99/06, http://www.ifp.cnr.it/publications/1999/PTP9906.pdf
45. B. Coppi, A, Airoldi, R. Albanese et al., Nucl. Fusion **53**, 104013 (2013)

Chapter 10
Other Applications of Superconducting Magnets

Abstract One area in which superconductivity has directly benefited the society is the health care. Magnetic Resonance Imaging (MRI), built around a superconducting magnet is widely used world over for diagnostic purposes like imaging soft tissues of human body. MRI is based on the principle of Nuclear Magnetic Resonance (NMR). High resolution NMR spectrometers used for studying structure of most complex molecules require high magnetic field, high homogeneity and high temporal stability. Superconducting magnets are run in persistent mode with power supply disconnected and produce field with unprecedented stability. Compensating and shim coils provide high homogeneity. 1 GHz (23.5 T) NMR spectrometers are commercially available with Nb–Ti/Nb_3Sn magnets operating at 1.5–1.8 K. Another potential application, though not very popular, is Superconducting High Gradient Magnetic Separator (SHGMS) used to reduce magnetic impurities to ppm level in a variety of minerals. Superconducting Magnet Energy Storage (SMES) is an ideal device to store large amount of energy and releasing it to the grid for load leveling and to balance short duration transient faults. It is used as an attractive pulse power source in strategic applications. Superconducting magnet in persistence mode stores an energy equal to $\frac{1}{2}LI^2$. Large SMES with stored energy in TJ range for power network system and medium energy 400 MW (70 GJ) SMES for FEL guided weapons were designed but not built. Micro 5 and 10 MVA SMES have been built and put in use in Japan. All the SMES are designed and built with Nb–Ti superconductors. Attention is now focused on the design of magnets for all the applications based upon 2G REBCO coated conductor which promises high critical current at elevated temperature, 30–50 K. All these HTS devices will be conduction cooled using cryocoolers and will become commercially competitive.

10.1 Introduction

In the last three preceding chapters we kept our discussion confined to the use of superconducting magnets in research laboratories, in accelerators and in fusion reactors. Superconducting magnets, however, have several commercial but critical

R.G. Sharma, *Superconductivity*, Springer Series in Materials Science 214,
DOI 10.1007/978-3-319-13713-1_10

applications where there is no alternative to these magnets. We wish to pick up a few specific applications, namely, the Nuclear Magnetic Resonance (NMR)/Magnetic Resonance Imaging (MRI), Superconducting High Gradient Magnetic Separator (SHGMS) and Superconducting Magnet Energy Storage (SMES). NMR spectroscopy, today is the most powerful technique to study the structure of most complex molecules in all physical, chemical and biological systems and an essential tool in a pharmaceutical R&D laboratory. NMR spectrometer needs intense magnetic field with high homogeneity over the sample volume and high temporal stability. Such stringent requirements can only be met by a superconducting magnet. MRI is based upon the principle of NMR and is used by the radiologists to get the images of the soft tissues in different organs of the human body. The quality of pictures obtained in MRI is far superior to any other technique like X-rays or the computer tomography. MRI has turned out to be a most popular diagnostic tool in the hospitals affecting greatly the health care of the society.

HGMS are increasingly used by the mineral industry for the removal of magnetic impurities, especially with low susceptibility and small particle size, from mineral ores that are needed for quality products. SHGMS had been popular with the pottery industry for Kaolin Clay purification and find application in desulphurization of coal, recovery of uranium from copper tailings, waste water treatment and for the recovery of useful oxides from fly ash. Not very high field is required for HGMS but the power saving in continuously operating plants is quite significant.

SMES is yet another promising area for the use of superconducting magnets for the storage of power when surplus and discharging it during the peak demand hours. SMES are used for load leveling and against short duration voltage dips preventing long and costly shut downs in a variety of industry. Several proto-type SMES were made at different times and at different places and connected to the city grid to establish the viability of such systems. The interest has been revived now since 2G HTS with good critical current versus magnetic field behaviour are commercially available. HTS based SMES can be operated at 30–50 K which can be conduction-cooled using cryocoolers. The use of expensive liquid helium and the associated hassle is thus done away with.

10.2 Nuclear Magnetic Resonance (NMR)

Nuclear Magnetic Resonance (NMR) is a physical phenomenon observed in a nuclei, which has an odd number of protons and/or neutrons and a nuclear spin, I½ or its odd integral multiple. When such a nuclei is placed in a magnetic field (B_0) it absorbs and re-emits electromagnetic radiation. In a constant magnetic field these nuclear spins get aligned either parallel or anti-parallel to the field, thus occupying two energy states, one at higher energy (anti-parallel) and another at lower energy (parallel). The lower energy state is slightly more populated than the upper energy state (this difference being of the order of five nuclei in a total of two million

hydrogen nuclei). If the nuclei is now irradiated with a RF field of frequency matching with the Larmer frequency (resonance condition), the energy is absorbed and induces a transition from lower energy state to higher energy state. In other words the nuclear spin flips from parallel to anti-parallel state. After the pulse duration, the spin system relaxes back and re-emits the radiation which is recorded as NMR signal. The RF field is applied in a direction perpendicular to the static magnetic field because the signal strength gets maximized. An NMR spectrum is usually acquired in a continuous wave (CW) mode by varying the frequency of the RF radiation but keeping the external magnetic field constant. In an actual experiment the sample is taken in the form of a solution in a ~ 5 mm dia. tube held at the centre of the room temperature bore of the magnet dewar. The sample tube is spun to average out any magnetic field variations and the tube imperfections. The RF antenna and the signal detection coil surround the tube.

In the applied field the nuclei (like an elementary magnet) precesses around the field, with an angular frequency

$$\omega_{\mathrm{I}} = 2\pi v_0 \tag{10.1}$$

called the Larmer frequency. The Larmer frequency depends upon the strength of the static magnetic field as:

$$\omega_{\mathrm{I}} = \gamma_{\mathrm{I}} B_0 \tag{10.2}$$

here γ_{I} is called the gyro-magnetic ratio. Whenever the RF frequency matches the Larmer frequency, the system is in 'resonance' and the interaction is strong yielding a strong NMR signal. We see from (10.2) that higher the static magnetic field higher is the Larmer frequency. In fact, the gyro-magnetic ratio is highest for hydrogen (proton) and a proton frequency of 100 MHz corresponds to a static magnetic field of 2.35 T. The higher the resonant frequency higher is the spectral resolution. It is for this reason that attempts have been continuously made to reach higher and higher magnetic field.

10.2.1 Magnet Features and Present Status

The magnet constitutes the most vital and expensive part of any NMR system. The main requirements of the magnet used in NMR system are:

1. The magnetic field has to be strong enough, compatible with the Larmer frequency of (mostly) proton. Higher the frequency higher is the spectral resolution. NMR spectrometers of 1 GHz frequency with a magnetic field of 23.5 T are commercially available now.
2. The field homogeneity across the sample volume has to be very high. In NMR the field in-homogeneity should be restricted to about 1 ppb and in MRI

magnets to about 1 ppm. The sample volume in NMR is few mm^3 but in MRI it is several litres.
3. The field should have high temporal stability. This is achieved in superconducting magnets by operating them in persistent mode and removing current supply and the leads. This mode of operation also cuts down helium boil-off significantly. Field stability depends strongly on the quality of superconducting joints.
4. The magnet must be shielded so as to reduce the stray field to 0.5 mT level at a distance of about 2 m.
5. To reach highest possible field, the magnet needs to be operated at reduced temperature usually at 1.5–1.8 K.

All these stringent conditions can only be met using superconducting magnets. The technology of magnet construction has evolved considerably over last three decades. The first superconducting magnet was built by Oxford Instruments for a JEOL DELTA-GSX 270 NMR system which was installed by JEOL, USA in 1979. The magnet used a Nb–Ti conductor and produced a field of 6.3 T compatible with 270 MHz proton frequency. Oxford Instruments also built first magnet which was operated in persistent mode for a 600 MHz spectrometer in 1987. With the availability of high current conductors, developed in the wake of giant projects in accelerators and fusion reactors, NMR spectrometers have been continuously upgraded to higher frequencies. Thus a 900 MHz spectrometer was built by Bruker BioSpin [1] and installed at Scripps research Centre, San Diego, USA in 2001. A 930 MHz (21.9 T) NMR spectrometer [2] was built at NIMS, Japan in 2005. World's highest frequency, 1 GHz NMR spectrometer 'AVANCE 1000' was built and installed by Bruker BioSpin [3] at CRMN, Lyon, France in July 2009. The major players among the manufacturers of NMR spectrometer are Bruker, Varian, JEOL and Hitachi. MRI scanners use wide bore magnets for whole body imaging but the field is limited to 3 T. Higher field 7 T MRI scanners are mostly used for research on animals.

Like in all other applications, Nb–Ti conductors have been exclusively used for NMR magnets up to 400 MHz (9.4 T) spectrometers. High frequency spectrometers use the combination of Nb–Ti and Nb_3Sn coils to produce the desired field. Outer coils of Nb–Ti provide the background field and the inner coils of Nb_3Sn produce additional required field. Such a combination can produce a maximum field of 21.1 compatible with 900 MHz proton frequency. The design of the magnet is optimized to use full potential of the conductor exposed to a particular field. The magnet therefore consists of a large number of Nb–Ti and Nb_3Sn coils all nested one inside another and each coil operating at maximum current level. To produce highest possible field from such a combination the magnet is operated at reduced temperature of 1.5–1.8 K. The 1 GHz NMR spectrometer [3, 4] has been built using this option. Yet another record breaking 1.3 GHz (30 T) NMR spectrometer has been planned [5] at the NHFML, FSU making use of the BSCCO and/or YBCO superconductor as the inner most coils and operating at liquid helium temperature. High T_c superconductors do carry large current in presence of high magnetic field at temperatures below 50 K. There are some concerns yet to be resolved with regard to

their production in sufficient lengths, uniformity, anisotropy, high temperature heat treatment, mechanical strength and inter-diffusion of the matrix and the core material. These issues have already been discussed in detail in Sect. 7.8.4.2.

10.2.2 The Magnet and Shim Coil Design

The outstanding feature of an NMR magnet is to produce required field with homogeneity in ppb range. The dimensions of the magnet are primarily determined by the twin objective of generating required field with high homogeneity and to provide a room temperature standard working bore of 52–54 mm. As discussed in Chap. 7, the winding length to inner diameter ratio, that is, β is kept large to have high homogeneity. The outer diameter is fixed by the number of layers needed to generate the required field which in turn will be determined by the I_c value of the conductor. To utilize the full current carrying capacity of the conductor the main magnet consists of several coils using conductor of appropriate I_c values. Sophisticated computing programmes are available to choose such a design. Errors are, however, introduced often at several stages of fabrication, winding, installing and the presence of magnetic materials in the surrounding building structures. Field homogeneity is restored by providing a number of shim coils which correct the axial and radial field inhomogeneities. The main magnet is wound with large β value which gives a normal homogeneity of the order of 10^{-5}. Use of compensating coils (inner or outer) raises the homogeneity to ppm range. Homogeneity is further improved by a few orders by the use of bipolar axial and radial shim coils. Another set of coils is used to minimize the stray field outside the cryostat. The NMR magnet system thus has a number of coil sets, the main magnet, the compensating coils, the shim coils and the shielding coils. Shielding coils operate with reverse current so as to cancel out the fringe field outside the magnet cryostat.

The field in-homogeneity are caused by the presence of higher order terms in the field expansion. The magnetic potential on the NMR sample kept at the centre of the magnet can be written as:

$$V = \sum_{n=1}^{\infty} \sum_{m=0}^{m=n} r^n P_n^m(\cos\theta)\left[A_n^m \cos m\varphi + B_n^m \sin m\varphi\right] \tag{10.3}$$

where $P_n^m \cos\theta = \sin^m\theta\left(\frac{\partial^m}{\partial^m \cos\theta}\right)[P_n(\cos\theta)]$ is the Legendre polynomial of nth order and degree m.

The axial component of the field B_Z can therefore be written as:

$$B_Z = \frac{\partial V}{\partial Z} = -\cos\theta\left(\frac{\partial V}{\partial r}\right) + \sin\theta\left(\frac{\partial V}{\partial \theta}\right) \tag{10.4}$$

$$= \sum_{n=1}^{\infty} \sum_{\mathrm{m}=0}^{m=n} r^{n-1} \left[(n-m) \cos\theta . P_n^m(\cos\theta) + \sin\theta . P_n^{m+1}(\cos\theta) \right] x \left[A_n^m \cos m\varphi + B_n^m \sin m\varphi \right] \tag{10.5}$$

In cartesian coordinate the first term in the expansion series of B_Z turns out to be:

$$\begin{aligned} B_Z = {} & A_1^0 + 2A_2^0 z + 3A_2^1 x + 3B_2^1 y + (3/2)A_3^0\left(2z^2 - x^2 - y^2\right) + 12A_3^1 zx + 12B_2^1 zy + 15A_3^2\left(x^2 - y^2\right) \\ & + 30B_3^2 xy + 4A_4^0 z\left[z^2 - (z/3)\left(x^2 + y^2\right)\right] + (15/2)A_4 x\left(4z^2 - x^2 - y^2\right) \\ & + (15/2)B_4^1 y\left(4z^2 - x^2 - y^2\right) \end{aligned} \tag{10.6}$$

Shim coils are wound to eliminate the first eight terms. Each term is independent of other not affecting the field produced by other coil. Shim coils can be wound inside as well as outside the main solenoid magnet. A bipolar power supply is used to regulate the current in the shim coils in either direction. Axial corrections are provided by eliminating Z and Z^2 terms. Z term is eliminated by using a pair of circular coils placed symmetric about the mid-plane (xoy plane) and fed with opposite current. Z^2 term is eliminated by winding one pair each of circular coils symmetric to the mid-plane (xoy plane) and with reverse currents. The exact position of a shim coil is found by equating the relevant term to zero and calculating the angle of the arc from the centre of the mid-plane. Given the diameter of the shim former the vertical distance of the shim coil from the mid-point is found out. An experimental 100 MHz NMR magnet system [6, 7] was built in author's group decades ago. For locating the exact positions of the 6 sets of shim coils we followed the article published by Sauzade and Kan [8] and made use of the angles calculated by the authors.

The shim coils to provide radial correction are saddle-shaped, wound in the form of arcs to eliminate xy, zx, zy and $x^2 - y^2$ terms. The angle and the location of these arcs are again found out from the (10.6). We had used aluminum former for the main solenoid and separate fiber glass epoxy formers for the shim coils. The exterior of this magnet with radial shim coils is seen in Fig. 10.1a. To get rid of zx term we used eight arcs four on either side of the xoy plane with opposite current polarity at angles (0°–120° and 180°–300°). Similarly, the zy term is eliminated by having eight arcs but shifted by an angle of 45° with respect to the zx coils. So the new arcs are wound at angles of 45°–165° and 225°–345°. The $x^2 - y^2$ term is eliminated by eight pairs of arcs symmetric to the xoy plane as well as to the $x = y$ and $x = -y$ planes and with current in opposite direction. The angles of the arcs thus are 0°−90°, 90°–180°, 180°–270° and 270°–360°. The xy term also has eight pairs of arcs but rotated by an angle of 45° around the oz axis with respect to the $x^2 - y^2$ coils. Thus the new arcs are wound at angles 45°−135°, 135°–225°, 225°–315°, 315°–45°. The schematic of the shim coils is shown in Fig. 10.2.

We had cut grooves in the shim formers for winding shim coils. The z and z^2 coils had 8 layers and each layer had 14 turns. Radial shim coils had 10 turns each. The shim coils used a 0.279 mm dia. Nb–Ti wire of Supercon make. All the shim coils were connected in series and energized by a single bipolar shim power supply (SPS)

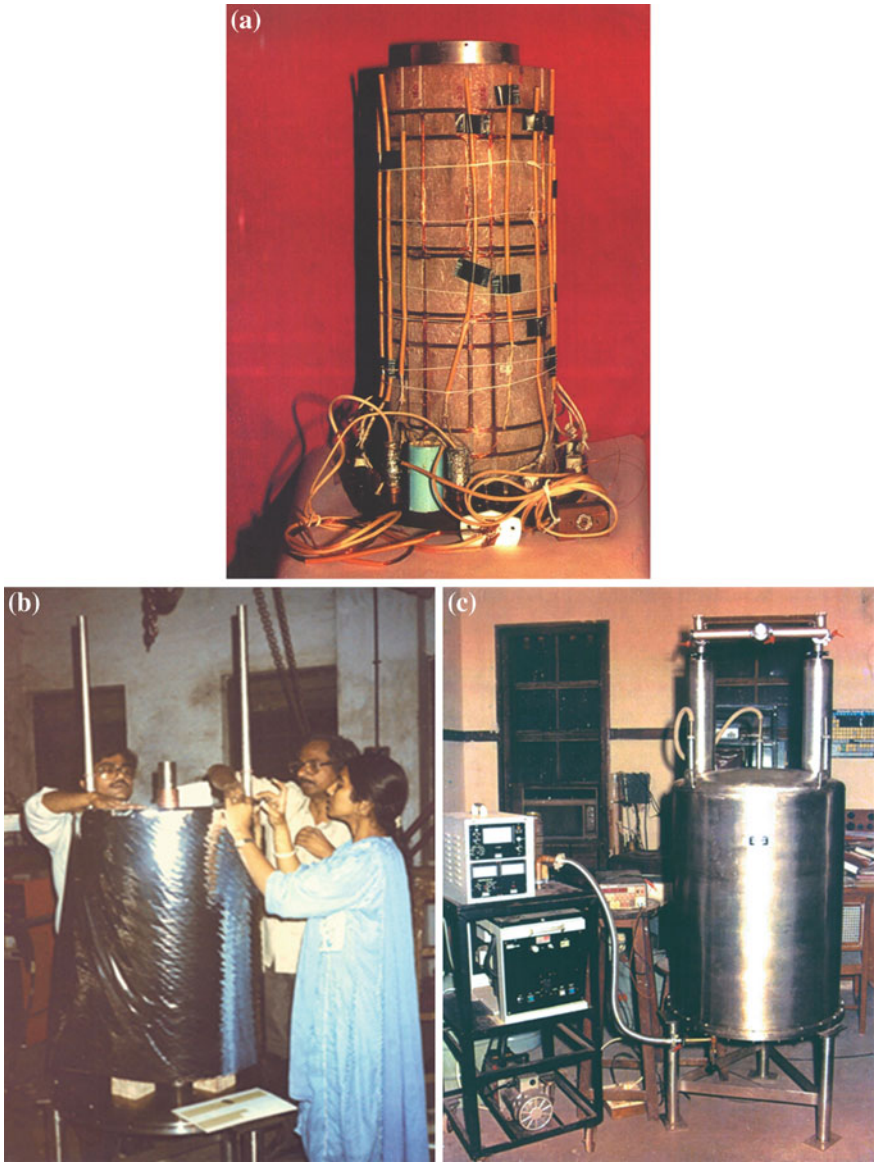

Fig. 10.1 **a** An NMR magnet exterior showing shim coils, superconducting joints and persistent switches for the main magnet and the shim coils. **b** B. Sarkar, Y.S. Reddy and R. Rajput winding the superinsulation. **c** The NMR cryostat after the installation of the magnet inside [6, 7] (*Photos courtesy* NPL Delhi)

of ±25 A as shown schematically in Fig. 10.3. Since the main magnet and all the shim coils have to operate in persistent mode, we developed persistent switches in-house. Two sets of switches were developed one for high current main magnet and another

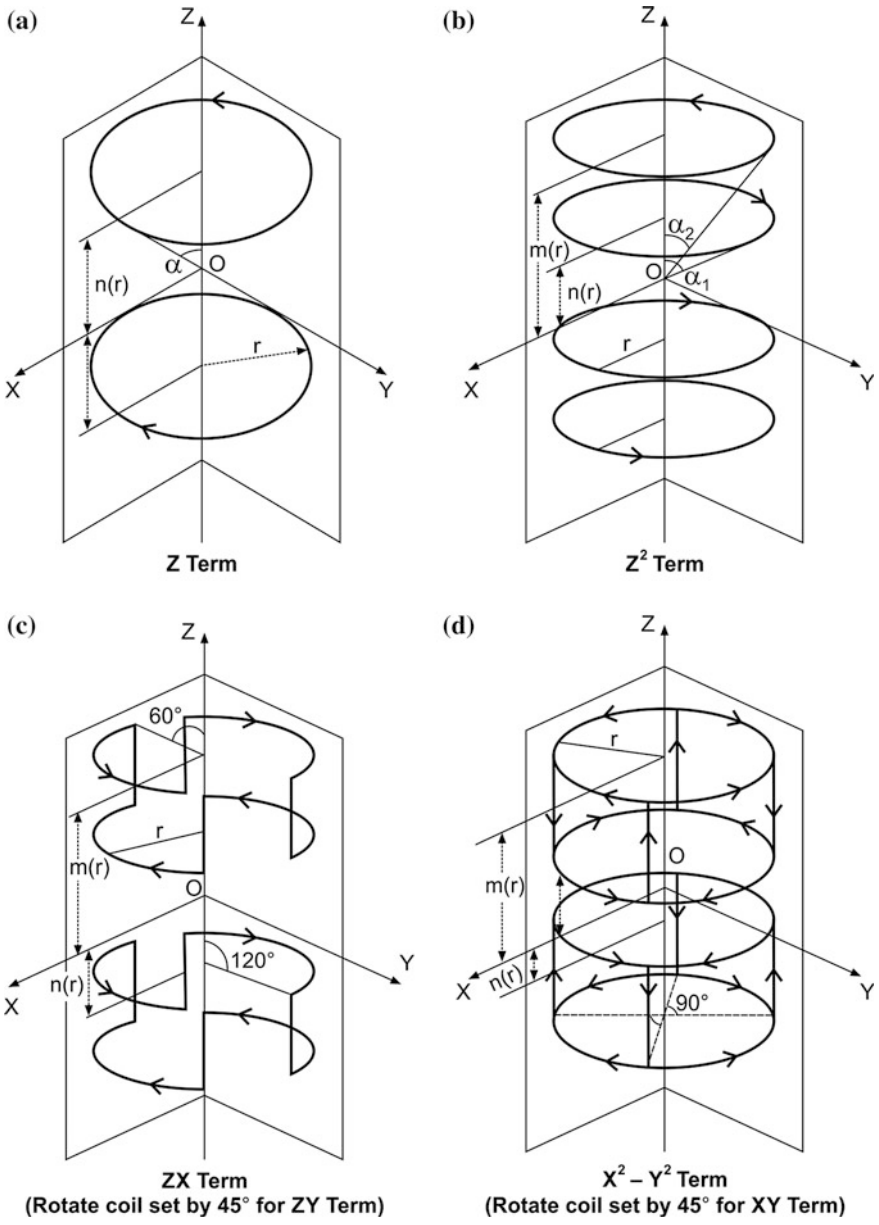

Fig. 10.2 The scheme of circular and saddle shim coils of the NMR Magnet [7]

for low current shim coils. We used a Nb–Ti wire in a resistive Cu–Ni matrix Vacry flux 5001 with a dia. of 0.455 mm. It had a room temperature resistance of 2 Ω/m. All the shim switches had an overall dimension of 30 mm × 10 mm. The switch resistance was 7 Ohms and the heater resistance 120 Ohms to have high current capacity, the

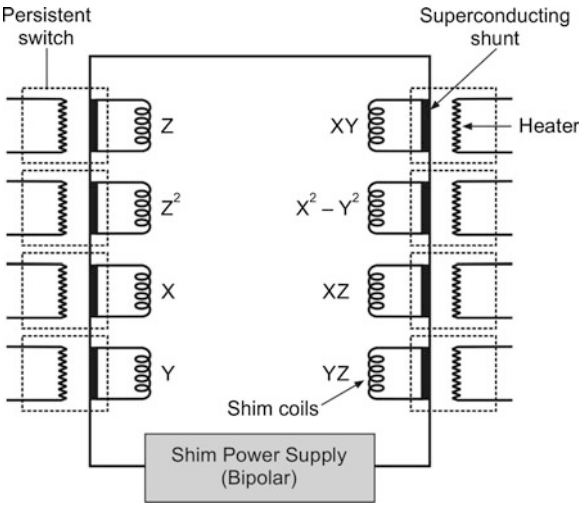

Fig. 10.3 Schematic of the shim coils circuit. All the shims are connected in series and energized by a ±25 A power supply. Each shim coil is provided with a persistent switch

main magnet switch was wound with two wires joined together. All the switches had bifilar non-inductive winding. All the switches were epoxy molded and fixed on an insulated platform at the bottom of the magnet.

The main magnet had a winding length of 380 mm and an inner winding diameter of 112.3 mm. The magnet was 6th order compensated with outer compensating coils. Shims were wound outside. The outer most diameter of the magnet was 137.5 mm. We used a copper stabilized 0.35 mm dia Nb–Ti wire of Outokumpu make for winding the main magnet. In all, we used 11 km of wire. Since the operating field was small (2.35 T only) and the magnet had to run in persistent mode we opted for a mono-filamentary wire with the core dia. of 186 μm. The large filament size came handy in making superconducting joints. The magnet had 25 layers each having 1,091 turns. Fiber glass cloth was used as inter-layer which allows free flow of the impregnating medium.

10.2.3 Jointing of the Wires

A perfect superconducting joint (non-dissipative) between different coil sections is the key technology needed for achieving high stability of the magnetic field, so essential for any NMR/MRI system. Manufacturers have developed their own techniques which is a propriety item. We briefly discuss the technique we followed and quite successfully. The joint has to be made between the superconducting filaments only without the involvement of the matrix. The matrix material, usually copper and/or a cu-alloy is removed carefully by acid etching. The exposed filaments are now thoroughly cleaned and de-oxidized. The filaments of the terminals are twisted together and inserted in a Nb–Ti tube and crimped. This joint can be welded using e-beam or spot welded over the entire length in vacuum or in an inert

atmosphere. We wrapped the twisted length with a thin Nb–Ti thin foil (rolled from a rod) and spot-welded all along the length under inert atmosphere. We developed a special vacuum system for carrying out this spot welding process. The joints should be coated with epoxy to prevent oxidation. We did observe deterioration in the performance of the bare joints when exposed to atmosphere. It is important that the critical current at the joint should not be below the I_c value of the conductors. The joints should therefore be evaluated by critical current measurements in magnetic field. All the joints must be located in the cryostat in region of low magnetic field.

The jointing, however, becomes complicated when Nb–Ti wires/cables are jointed with other superconductors like Nb_3Sn and to HTS conductors commonly used in high frequency systems. Both these materials need controlled high temperature heat treatment for conversion to high T_c phase. During the process of welding the superconducting phase may get disturbed because of the change in stoichiometry or in the oxygen contents of the HTS. One technique of jointing Nb–Ti and Nb_3Sn conductor has been described by Williams et al. [9]. In this technique, a small hole is drilled in the centre of a compact composite of 90 % Nb and 10 % of Sn and the exposed Nb-filaments of the unreacted Nb_3Sn wire are pushed in. After the reaction the composite surface is polished and flattened Nb–Ti filaments are spot welded to the surface of the composite through the Nb_3Sn layer of a (RCA CVD tape). The welded length is coated with epoxy for protection against oxidation. Most such techniques are in fact developed by the manufacturers and the details are usually not published.

10.2.4 The NMR Cryostat

The NMR cryostat shown in Fig. 10.1b is a standard design and was also followed by us [6, 7]. The magnet system is mounted at the bottom of an annular liquid helium vessel suspended by two long SS wide bore pipes and connected together at the top by a horizontal pipe which has a pressure release valve and a bursting disc. One of the pipes is used for filling LHe, the return line and for taking out the leads from the LHe level meter. The second pipe is used for inserting a 30 pin de-mountable current probe which connects to the 30 pin socket fixed at the bottom of the pipe. The current probe is removed after the magnet and the shim coils are charged and put in persistent mode. The cryostat has a standard room temperature bore of 52 mm. The LHe shell is surrounded by an annular 20 K vapour cooled Cu thermal shield and an outer annular liquid nitrogen shell. The LN2 vessel is suspended from the top by three SS tubes which are also used for filling LN2 and for the exhaust. The schematic diagram of the cryostat shown in Fig. 10.4. It had an overall dia. of 0.748 m and a height of 1.535 m. The LHe vessel has a capacity of 190 l. The cryostat was designed for a re-fill time of 100 days. Separate thermal shields are provided around the room temperature central bore tube. The whole system is housed in a vacuum chamber with a vacuum port at the bottom. Multi layer insulation is used at appropriate places in the vacuum space to minimize the LHe evaporation. The present day cryostats utilize the total enthalpy of

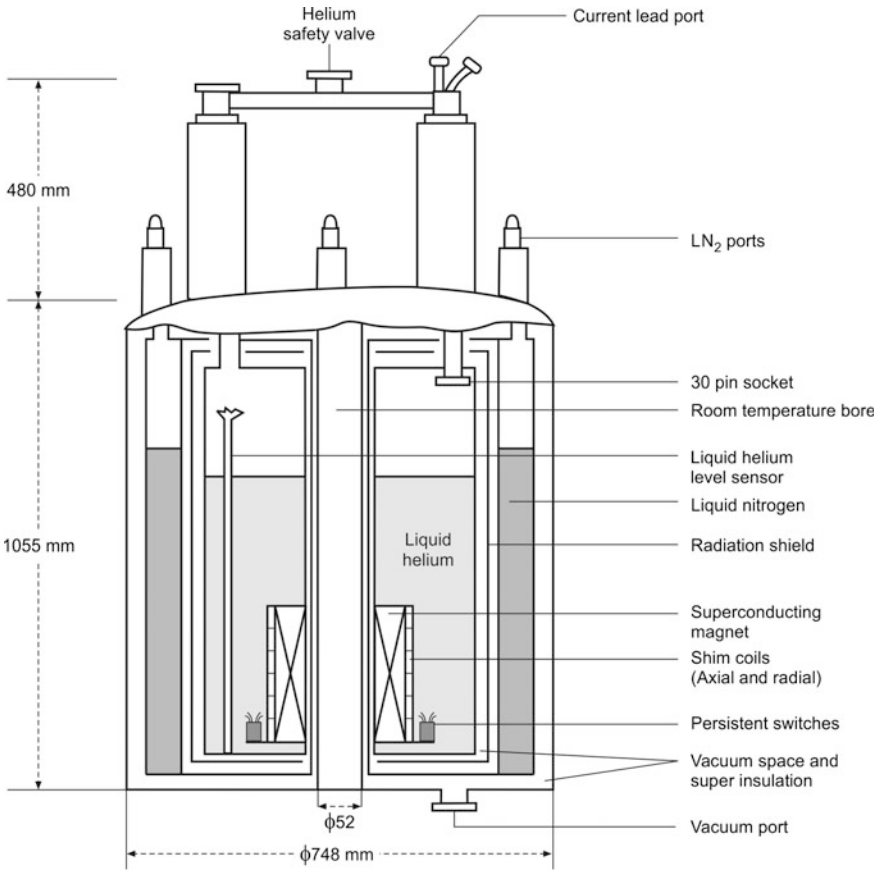

Fig. 10.4 A schematic diagram of the NMR cryostat with dimensions. 20 K shield is not shown in figure [7]

the evaporated helium and are very efficient. With the installation of the cryo coolers to re-condense the evaporated helium the refill time is almost unlimited.

10.2.5 The Operation

NMR magnets are charged by the supplier at the time of commissioning and put under operation. The power supply is disconnected and taken back. The spectrometer is then used for studies by the user community for years on. We briefly discuss the steps needed to start virgin run. The vacuum space is pumped under condition of baking. It is important to insert the 30 pin current probe before starting the cooling phase to prevent blocking of 30 pin socket due to ice formation. Liquid helium is transferred to the cryostat which is already pre-cooled with LN2. The magnet, after it reaches

equilibrium temperature, is charged to the required field by 'switching on' the heater and opening the persistent switch. The field in the sample space is monitored by using an NMR Gauss meter. After the field has stabilized at the designated value the heater is 'switched off' and the magnet runs in persistent mode. Shim coils are now energized one by one by opening the relevant switch and adjusting the current in either direction to a value at which the NMR peak becomes sharpest. The shim current is locked at this value by 'switching off' the heater current, that is, by closing the persistent switch. All other shims are energized in a similar way in steps. The SPS is now 'switched off'. 30 pin current probe can be removed now from the cryostat. A probe with a cascade of radiation shields is now inserted in this column to prevent radiation losses. This tube is finally sealed to prevent moisture from entering the cryostat. The spectrometer is ready for measurements. We were able to attain a field stability of 0.22 ppm/h in our demonstration NMR magnet [7]. Very higher field stability is available in commercial spectrometers.

10.2.6 Some Innovative Developments

10.2.6.1 Bruker's "UltraStabilized^{TM}" Cryostat for 2 K Operation

The magnetic field produced by the combination magnets of Nb–Ti and Nb_3Sn reached an upper limit of 21.1 T (900 MHz) when the magnet is operated at 4.2 K. For higher frequency NMR spectrometers HTS conductors is an option, at least for the inner most coil, but this possibility still seems to be some years away. Bruker has been able to build 1 GHz (23.5 T) NMR spectrometer by operating the Nb–Ti/Nb_3Sn magnet system at a reduced temperature of 2 K. The critical current of both the materials at a given field is significantly higher at reduced temperature. For example the I_c of a typical Nb–Ti conductor used for 9.4 T (400 MHz) field goes up from 100 A at 4.2 k to 400 A at 1.8 K. In case of Nb_3Sn conductor the available current density J_c at 17 T is about 76 A/mm^2 at 4.2 K but goes up to about 155 A/mm^2 when operated at 1.8 K. This property of the conductors offers two great advantages. One, that, it is possible to go to higher fields and two, that the quantity of conductor used will be reduced. This will make the whole magnet system very compact.

NMR spectrometers run for years on in a continuous mode and need long term stability of temperature independent of LHe level and evaporation rate etc. Bruker developed a new UltraStabilized^{TM} cryostat based on an innovative design [1]. Most of the features and the exterior appearance of this cryostat are the same as the conventional systems but differs in the design of the LHe vessel. The LHe container is no longer a single vessel but consists of two vessels joined together through a narrow channel to maintain the same pressure. The upper vessel is filled with LHe at 4.2 K but the lower vessel housing the magnet is cooled to 2 K. The pressure inside both the vessels is kept slightly higher than the ambient pressure to prevent ice formation due to any possible air leak in the vessels. A bath temperature of 2 K corresponds to a He-vapour pressure of 30 mbar and to prevent such a low pressure

over the LHe bath, the temperature, 2 K and below, is produced by the expansion of LHe into a heat exchanger unit via a J-T valve. Thus only the heat exchanger unit is pumped to pressure below 30 mbar for maintaining temperature of 2 K and lower in the lower LHe-bath. The LHe flow through the J-T valve and the pumping speed is determined by the heat load from the sub-cooled 2 K bath. The bath temperature remains constant because the heat load in the bath due to the operation of the magnet is equal to the heat transfer from the bath to the heat exchanger. The temperature of the bath does no longer depend upon the ambient pressure.

The temperature stability of the lower bath thus depends upon the stabilities of the J-T valve and the pumping speed settings both of which determine the amount of helium flowing through the J-T valve. The schematic diagram of this UltraStabilized^{TM} cryostat is reproduced in Fig. 10.5. Unprecedented temperature stability

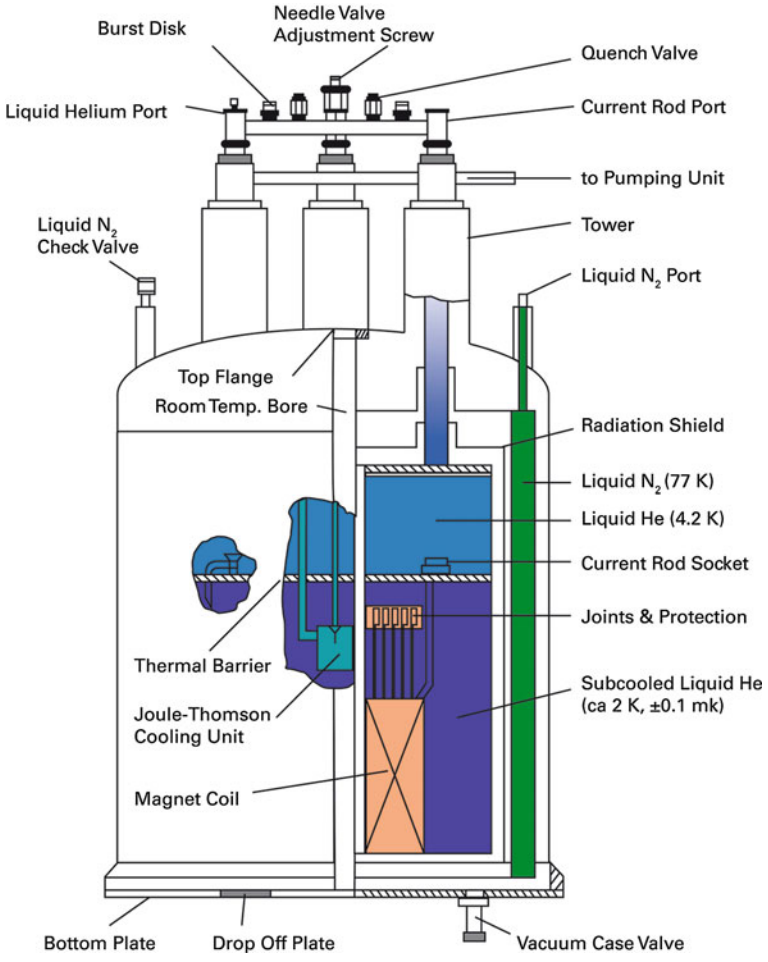

Fig. 10.5 A schematic of the "UltraStabilized^{TM}" Cryostat for 2 K operation of the magnet of High Frequency NMR spectrometer (*Courtesy* Kuemmerie Rainer, "copyright by Bruker (© Bruker)")

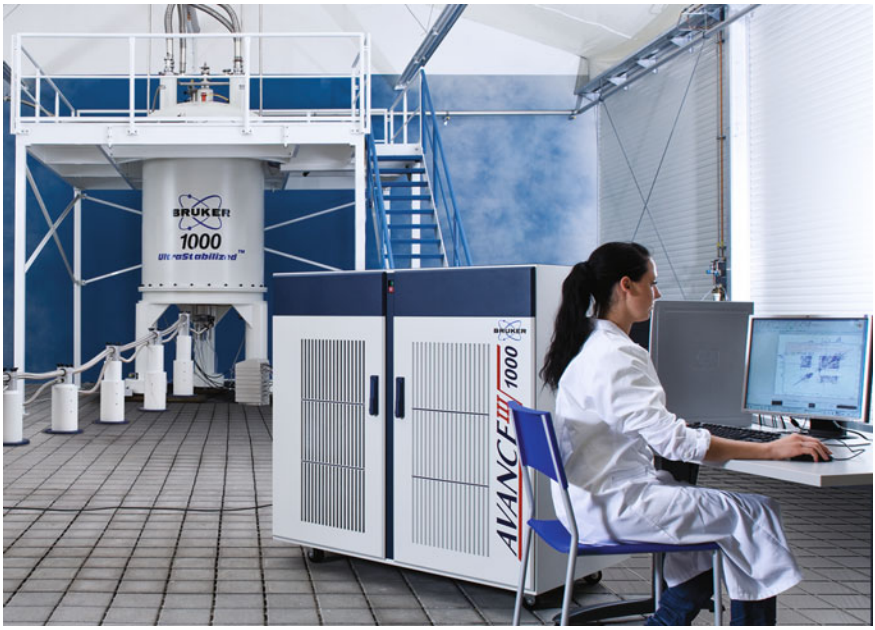

Fig. 10.6 "AVANCE 1000" A 1 GHz NMR Spectrometer marketed by Bruker BioSpin (Bruker's Rheinhafen facility in Karlsruhe (Germany) (*Courtesy* Kuemmerie Rainer, "copyright by Bruker (© Bruker)")

of 0.1 mK has been attained in this design. The J-T valve can be adjusted over a wide range of flow rates from high cooling power, required during the cool-down and charging of the magnet, to low cooling power sufficient for the normal operation over long periods. The cryostat is highly efficient. It makes full use of the enthalpy of the helium gas escaping from the valve in cooling the insert pipes and the radiation shields. The pumped out gas gives away it's entire cold to the sub-cooled system and leaves the cryostat almost at room temperature. World' highest field 1,000 MHz frequency, "AVANCE 1000" commercial NMR spectrometer (Fig. 10.6) marketed by Bruker BioSpin used this UltraStabilized^{TM} cryostat.

10.2.6.2 JEOL's 'Zero Boil-off Magnet for NMR System'

JEOL USA Inc. has just introduced [10] a magnet system for NMR over a wide range of magnetic field 9.4 T (400 MHz)–21.8 T (930 MHz) with near negligible boil-off of liquid helium through the use of cryocooler for re-condensing the evaporated vapours. It needs maintenance once in 2 years without disturbing the magnet operation or the NMR signal quality. In the event of a power outage the LHe reservoir keeps the magnet going for 4 h.

10.2.6.3 A Split NMR Magnet System

Hitachi in collaboration with NIMS has introduced [11–13] a new concept in developing a high sensitivity solution NMR spectrometer. First option to go to high sensitivity NMR system is to produce highest possible magnetic field. Further improvement in the sensitivity can be attained by using a cryogenic probe with a solenoid-shaped antenna coil. It is, however, not possible to accommodate this sample probe and the solenoid-shaped antenna detector together in the NMR system of conventional design. Hitachi has come up with a novel idea and designed a split magnet system with two room temperature bores, one bore horizontal, another vertical and the two bores crossing each other at the centre. Figure 10.7 is a schematic diagram [12, 13] of this split magnet. The liquid sample tube is inserted through the vertical bore from the top and the solenoidal antenna coil through the horizontal bore.

The main magnet in this design is divided into two multi-layer solenoids separated by a gap which provides the vertical bore. The field produced by the magnet, B_0 is along the horizontal direction. The magnet has several new features as compared with the conventional design. The magnet has shim coils inside as well outside the magnet. The shim coils used have periodically wavy shape. The main magnet has a total of 18 main coils and 2 self shielding coils. The 6 inner pairs are wound using Nb_3Sn conductor and 3 outer pairs of Nb–Ti conductor. The self shielding coil too is wound using Nb–Ti conductor. The innermost coil in the present magnet operates at a fixed negative current for improved field homogeneity. The parameters of the magnet and the cryostat are given in Table 10.1.

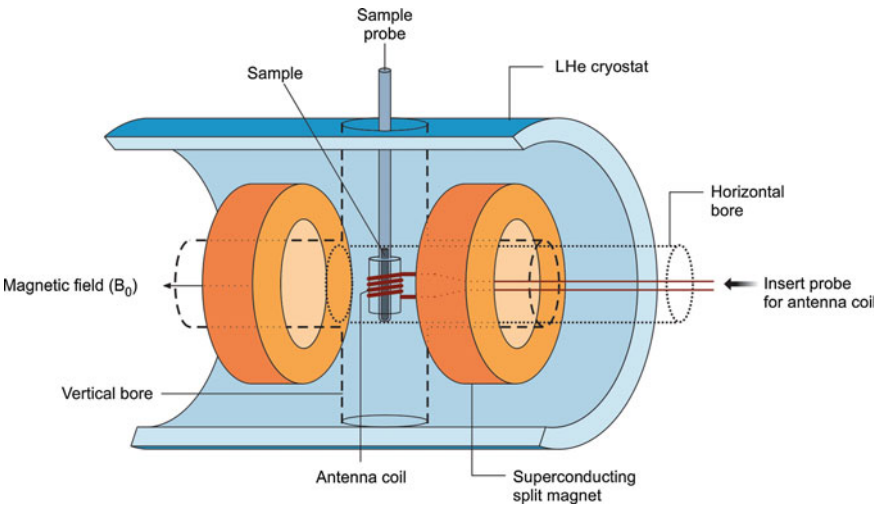

Fig. 10.7 A schematic diagram of a split magnet of an NMR system having a vertical and a horizontal bore (adapted and modified from [11–13])

Table 10.1 Specifications of the Hitachi 600 MHz NMR spectrometer built with split magnet design (data compiled from [11–13])

Parameter	Unit	Value
Main magnetic field strength	T	14.1
Conductors used		Nb–Ti and Nb_3Sn
No. of inner Nb_3Sn coils		12 (6 pairs)
No. of outer Nb–Ti coils		6 (3 pairs)
No. of shielding coils		2 (1 Pair)
Operating current	A	297
Stored energy	MJ	10
No. of inner shim coils		28
No. of outer shim coils		10
No. of Nb_3Sn/Nb–Ti joints		24 (main magnet) 56 (shim coils)
No. of Nb–Ti/Nb–Ti joints		32 (main Magnet) 78 (shim coils)
Horizontal bore dia.	mm	54
The cross-bore material		Al

The cross-bore is made of 3 concentric aluminum pipes. The outer pipe is in contact with the LHe vessel at 4.2 K, the middle one with the thermal radiation shield and the innermost remains at room temperature. The magnet is protected against quench by a passive protection system of resistors and the heaters. The resistance heaters are connected in parallel with each coil close to the next coil. Once a coil quenches, its heater heats the next coil and raises the temperature of this coil. This coil too quenches and heats up the next coil. This way all the coils of the magnet quench distributing the large stored energy evenly among all the coils. The temperature increase of each coil is thus restricted within limits.

As seen from the table the magnet system has a large number of superconducting joints, 24 between Nb_3Sn and Nb/Ti conductors and 32 between Nb/Ti and Nb/Ti conductors. The shim coil joints are in much larger number 56 and 78 respectively for the two types of joints. Since the stored energy is very high 10 MJ, extreme precautions are taken for magnetic field stability and the structure to support large hoop stresses. The field homogeneity can be improved to tens of ppm charging the innermost coil with current of reverse polarity. Homogeneity improves to better tan 1 ppm with the shim coils activated. The field drift of the magnet system is less than 1 Hz/h.

10.2.6.4 Possible 1.3 GHz (30 T) NMR Spectrometer

The National High Magnetic Field Laboratory, Tallahassee, has planned [5] to break the 1 GHz barrier and build a 1.3 GHz NMR (30 T) spectrometer in near future. It is obvious that such a magnet needs a large number of coils of conventional materials Nb–Ti and Nb_3Sn and the innermost coils have to be made out of

multi-core HTS conductors, BSCCO or REBCO tapes or round wires. HTS do carry current with high densities in presence of very high magnetic field but only if they are operated at LHe bath temperature. The production technology of these materials has, however, not developed to a level when they can be used straight away for NMR application. Various issues expected to come up for building a such a magnet are being sorted out at the NHMFL through well planned R&D efforts as discussed in Chap. 7.

A 30 T magnet will have a background field of 20 T provided by the combination of the conventional Nb–Ti and Nb_3Sn coils. The inner HTS magnet will have a number of concentric coils to add another 10 T. For high homogeneity, the NMR magnets have to have longer winding length and therefore need large quantity of HTS conductor and long single length with high uniformity. The HTS conductor should also have high tolerance to bending strain as the diameter of the inner coils will be small. The conductor also needs to be characterized for the strain effect on the critical current density. Besides, The HTS conductor must be suitably reinforced and cladded with high strength material to withstand large EM forces generated at 30 T field. Silver-magnesium alloy cladding alone may be inadequate as it can withstand a maximum stress of 150 MPa only.

A 'wind and react' technique is generally followed for these ceramic core conductors. These conductors need heat treatment at high temperature, close to 900 °C under oxygen atmosphere. This adds to the problem of selecting the right electrical insulation and preventing the inter-diffusion of the ceramic core and the cladding material. The temperature profile to be followed has to be carefully chosen because the reaction temperature (900 °C) is quite close to the melting point of silver. A 'react and wind' technique is yet to be perfected where one can use such conductors without developing cracks.

These HTS materials also display large anisotropy of critical current density, J_c and the critical field. The material has to be produced in MF tape configuration with aligned grains and the current must flow in the ab plane where the J_c is high. A pancake winding is a preferred choice.

One can save a lot on the conductor quantity and make the magnet compact by operating the magnet at 1.8 K. It is then possible to benefit from the maximum current carrying capacity of all the three conductors, Nb–Ti, Nb_3Sn and the HTS.

Since the stored energy in a 30 T magnet will be tremendously high, an effective quench protection system has to be provided. A passive circuit of quench resistors and heaters similar to the one developed at Bruker and discussed in the previous section can provide good protection.

The NHFML group [5] has already carried out most of these studies on the characterization and evaluation of prospective conductors for their critical parameters. NHFML has already tested magnets producing field up to 32 T with an ultimate aim to design a 1.3 GHz NMR spectrometer.

10.3 Magnetic Resonance Imaging (MRI)

10.3.1 Introduction

MRI is perhaps the best application of superconductivity which directly affected the humanity across the globe. It is a common tool with the radiologist in diagnostic hospitals for imaging various soft tissue parts of the human body and for detecting tumors. The concept of NMR imaging used in present day MRI systems was proposed by Paul Lauterbur [14] as early as 1973. MRI exploits the presence of vast amount of hydrogen (protons) in a human body as the water content in a human body is said to be about 80 %. When protons in the tissues of the body, aligned in a static magnetic field (B_0), are subjected to resonant RF excitation, they absorb energy. Proton relaxes back and emits resonant signal which is a characteristic of the tissue. The signal is picked-up by a receiver located inside the magnet bore and is used to construct the image using Fourier transform. Since the NMR signal frequency is proportional to the magnetic field the whole tissue can be mapped by assigning different values of the proton frequency to different proton locations in the sample using well computed field gradient. All MRIs use proton NMR for mapping proton density which is different in different types of tissues. The images show contrast which helps in identifying these tissues and the changes occurring in a sample tissue. MRI turns out to be an ideal technique for soft tissue regions of the body such as brain, eyes and soft tissue part of the head. Since bones have low density of protons they appear as dark regions.

Under the field gradient along the Z axis, the (spin-flip) frequency of the emitted NMR signal increases as one moves across the sample tissue from the lower field to a higher field direction. Different frequencies observed from different proton areas are separated using Fourier transform and the location of the target protons identified. To locate the position of protons in other directions (x and y) rotating field gradient coils are used to obtain 2D images.

10.3.2 The Elements of an MRI Scanner

A superconducting magnet is the heart and most expensive part of an MRI scanner. MRI magnets need high homogeneity and high temporal stability similar to NMR spectrometers. However, the magnetic field requirement in the present day MRI scanners for clinical use is limited to 3 T only. Another major difference with NMR magnet is that sample size is much larger. The sample now is a human body part and thus the magnet needs an homogeneity of 10 ppm over a SDV of 50 cm. The magnet assembly is schematically shown in Fig. 10.8. The main magnet is superconducting, cooled to LHe temperature and mounted in an efficient cryostat with a horizontal bore to accommodate the patient. Inside the main magnet is a set of

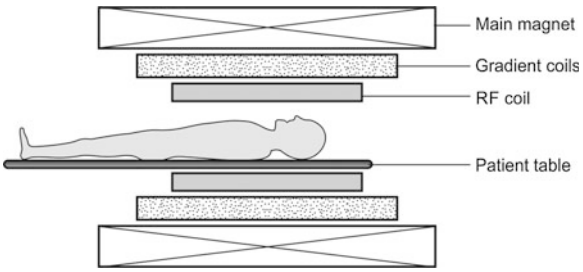

Fig. 10.8 A schematic diagram of a MRI scanner consisting of the main magnet, the gradient coils, the RF coil and the patient table

gradient coils for changing the field along the X, Y and Z directions required for imaging. Inside the gradient coils are the RF coils producing the field B_1 for rotating the spin by an angle dictated by the pulse sequence. These coils also detect the signal emitted by the spins inside the body. At the centre is a patient table which is computer controlled.

The typical length of the magnet is 1.6–2.0 m and a clear bore of 0.9–1.0 m. The LHe capacity of the MRI cryostat is typically 1,700 l. In the older systems the LHe vessel was surrounded by a liquid nitrogen (77 K) annular container which worked as a thermal buffer between room temperature and 4.2 K. In modern MRI scanners the 77 K container has been replaced by a thermal shield cooled by the cryocoolers. Cryo-coolers are also fitted with the LHe cryostats which re-liquefy the evaporated He-gas. The LHe refill time has thus increased to 3–4 years. Another development that has taken place in recent times is the introduction of active shield coils which reduce the stray field to below 0.5 mT at a distance of 3–4 m.

The design of an MRI magnet has evolved over the decades to become more friendly to claustrophobic patients, provide better picture quality and reduce cost, capital as well operational. We briefly describe the primary requirements of an MRI magnet. The magnet has to produce an axial horizontal magnetic field of desired strength with a homogeneity of 10 ppm over 50 cm DSV. The stray field inside the scanner room should not be more than 0.5 mT so that the magnetic field does not interfere with the functioning of the auxiliary equipment or risk the personnel in the room with a pacemaker. The design must be based on an operating current well below the current density, I_c to prevent quench. The threshold for quench therefore should be high and an efficient fool proof protection system needs to be provided. The entire magnet structure consisting of the magnet coils, the former, the cryostat and other components used in the magnet assembly should be able to withstand high stresses produced by the large Lorentz forces and cooling.

Attention is now focused on designing short magnets producing high field for reducing the perception of claustrophobia. To attain high homogeneity in short magnet is indeed a challenge.

10.3.3 Evolution of MRI Magnet Design—A Brief Description

Starting with the cylindrical design the technology of MRI magnet design has undergone many refinements and many groups proposed a variety of design procedures and geometries. Garrett [15] proposed a design for a high homogeneity field based on the compensation of the higher order (6th–20th) terms in the spherical harmonic expansion. Figure 10.9 shows the schematic coil configuration of a compensated concentric multi solenoidal MRI magnet. The design was widely followed in early MRI magnets. In later years quite a few unconventional approaches were made at number of centres based on hybrid techniques [16, 17]. They combined different aspects of the results of finite element, analytical, variational technique and other numerical methods to obtain optimized design of a high homogeneity MRI magnet. Crozier and Doddrell [18] proposed compact magnet design based upon stochastic optimization. Zhao et al. [19] proposed a multi-layer current density approach to optimize the design. Sinha et al. [20] too have developed a code based on a combination of analytical and numerical methods for a short MRI actively shielded magnet with minimum conductor, inductance and ampere turns. The code is flexible and can be used for a variety of geometries. Most recently, Lvovsky, Strautner and Zhang have published [21] a detailed review on possible novel configurations of the future MRI magnets.

Doddrell and Zhao [22] have a US Patent on an innovative MRI magnet design. In this design the winding is split into a multi layer coils and also axially separated. Such a geometry results in extra degrees of freedom to optimize the design of short length magnets with high field homogeneity and minimum conductor volume. The design also minimizes maximum field, excessive stress on the conductor and the stray field outside the magnet. One such design envisages the first layer consisting of four coil pairs, the second layer coil consisting of two pairs and the third and outermost two coil pairs. While the current direction in coils of the first and second layers is positive, that of the third (outer) layer coils is negative. Thus in a 3 T

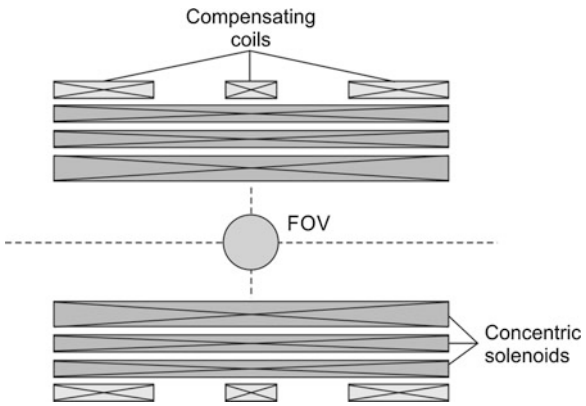

Fig. 10.9 Schematic coil configuration of compensated coaxial multi solenoid MRI magnet

magnet the first layer coils generate a field of +2 T, the second layer coils +3 T and the coil layer 3 generates a field of −2 T. One can in fact further split the coils into sub-coils to adjust different parameters of the magnet.

All the attempts to design an MRI magnet have been aimed at attaining high homogeneity field in a large 'field of view' (FOV), ∼50 cm DSV. In general, two distinct magnet designs are followed, a compensated solenoid type and a discrete multi-coil type.

10.3.4 Compensated Solenoid Magnet Design

The design has been popular in the first generation MRI scanners. The coil is wound uniformly across the entire length of the cylindrical former. The winding is divided in a number of sections each wound with optimized graded conductor. This design reduces the peak field to central field (B_{peak}/B_0) ratio and also the stress. The homogeneity of the field is enhanced by winding a number of optimized compensating coils outside the main magnet as shown in Fig. 10.9. Attaining high homogeneity especially in large FOV and short magnets becomes a challenge and so does the stress management. In principle, several multiple coil configurations are possible to yield required field with high homogeneity and low stray field. In practice, a trade-off is made in choosing the design which optimizes the overall dimensions of the machine and keeps the conductor volume and stress level within acceptable limits. In spite of a perfect optimized design inhomogeneities are often caused by a variety of factors like, manufacturing tolerances, winding process, mismatch of thermal contraction of the former and the winding during cooling or the movement of winding due to Lorentz force. To correct these harmonic errors magnetic shimming is mandated to be used in the MRI magnet system just as in NMR magnets and discussed in Sect. 10.1.2. In principle, shim coils can be passive or active (superconducting). In passive shimming shim trays with iron pieces are fitted in slots at predetermined positions either on the magnet bore or in the gradient coil assembly. In addition, there are low field resistive shim coils fitted in gradient coils which are specific to a patient.

Active shimming is provided by a set of superconducting coils wound over the main magnet in the form of circular arcs and racetracks at various azimuthal positions symmetric to the centre along the z-axis. These shim coils are connected in series and energized by a single bipolar power supply through the use of superconducting persistent switches. The main advantage of using active shims is that they can compensate for large tolerances arising during magnet fabrication without adding too much weight. The disadvantage, however, is that the shim coils are located outside the magnet, that is, far away from the FOV, they are not very effective for high order ($n > 6$) harmonic errors. Some limited passive shimming too is provided together with the active shimming, referred to as 'hybrid shimming'. Different combinations of shimming techniques are employed by the manufacturers to meet the stringent uniformity requirement of the magnetic field.

Use of active shielding coils also adds to the complexity of winding because of large dipole moment of the long solenoid, high stress and the field inhomogeneity caused by the shielding coil. The design is now restricted to 7 and 9.4 T Nb–Ti high field research magnets where it is crucial to keep B_{peak}/B_0 ratio low. These magnets are usually long up to 3 m compared to standard 3 T clinical scanner which is about 1.5 m long.

10.3.5 Multi-coil Magnet Design

Another traditional design of an MRI magnet is in the form of discrete coils centrally symmetric along the z-axis. The number of coils to be used depends on the number of harmonics to be eliminated and the positional angles of the coils. For example, a six-coil magnet can eliminate harmonic errors up to 12th order [15]. The B_{peak}/B_0 ratio and stresses in the coils can be tuned by choosing coil shapes and SC/Cu ratio. Figure 10.10 is a schematic of the modern day clinical MRI scanners with three symmetric pairs of coils placed along the z-axis constituting the main magnet. The design must also provide effective shielding of the magnet such that the stray field inside the scanning room is reduced to below 0.5 mT. The stray field in MRI magnets tends to be large because of the large dipole moment. Both the types of shielding, passive and active are possible. For passive shielding iron is used outside the cryostat but has several disadvantages. Passive shielding adds to the magnet weight adversely and is designed for a specific central field. Active shielding is provided by a set of superconducting coils which are coaxial with the main magnet coils but of larger diameter. The current through these coils is in reverse direction which produces a negative field. Active shielding, however increases the conductor use, the size of the cryostat and the LHe inventory. The advantage is that active shield, operates at different central field and do not affect the homogeneity since the coils maintain current-field linearity relationship. The positions of different types of coils are indicated schematically in Fig. 10.10. To maintain field homogeneity extra set of shim coils (axial and transverse) are to be used for which extra former is used.

Irrespective of the coil designs followed most other subsystems inside the cryostat are common. All the joints must be superconducting with a contact resistance of less than 10^{-10} Ω to ensure a drift of less than 0.1 ppm/h. These joints and the persistent switches should be mounted in low field regions. Protection system consists of dump resistors, diodes, quench protection switches and coil heaters. In the event of quench the switch must open to divert the current through the coil heaters to spread stored energy within the entire magnet to prevent excessive increase in temperature locally. Current leads are normally detachable and are removed after the magnet goes into persistent mode. This cuts down the heat load to the LHe bath substantially. Most commercial scanners have LHe 4.2 K bath fitted with cryocoolers to recondense evaporated He. The LHe refill time has thus increased to 3–4 years. These cryostats have a single 40–60 K radiation

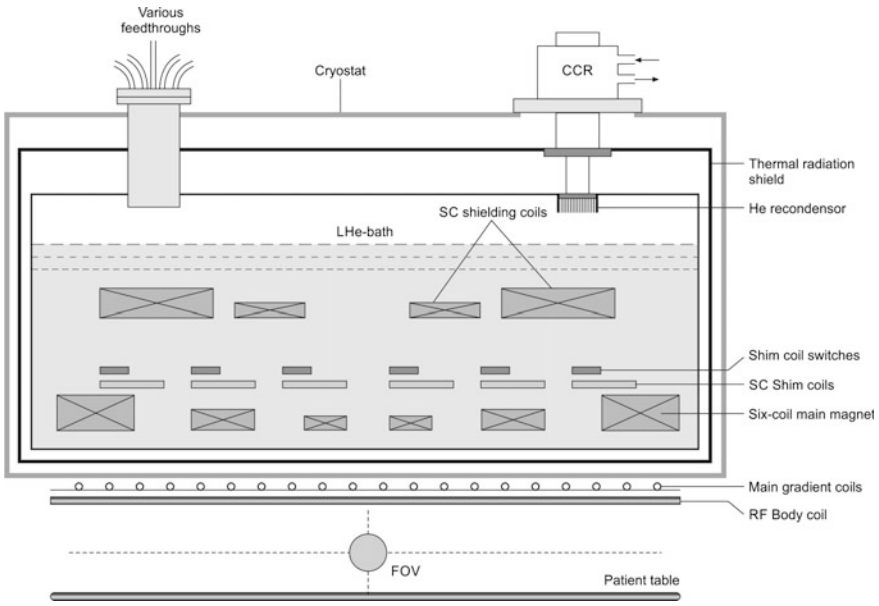

Fig. 10.10 Schematics of a discrete six-coil main magnet with superconducting shims and shielding coils for an MRI scanner (only upper half shown)

thermal shield instead of two (10 and 80 K) shields used earlier. This together with improved superinsulation has resulted in reducing the overall dimension of the cryostat.

10.3.6 Some Recent Developments in MRI Scanners

With the popularity of clinical use of MRI scanners for whole body (WB) imaging growing at a fast pace most manufacturers have focused on innovative design of the magnet systems and the scanners keeping patient comfort as top priority. The present trend is to build wide bore 70 cm and short magnet scanners so that the patient head can be kept outside the magnet and the shoulders be accommodated well. Small bore magnets can be more useful for anatomy of body parts like head. Efforts are being made to produce MRI scanners with split-open magnet configuration. The human body in this system is kept in the gap between the two poles of the magnet instead of confining inside a cylindrical coil. The gap can be vertical or horizontal. Some of the open-split MRI scanners in the market are 0.5 T Sigma-SP interventional shown in Fig. 10.11, 0.7 T open Speed both from GE, 1.0 T Panorama from Phillips, 1.2 T Oasis from Hitachi and an MgB_2 0.5 T Open Sky from Paramed. The scanners are patient friendly but expensive because two LHe cryostats are to be built for this configuration. 3 T standard scanner will not be able to compete with cylindrical scanner.

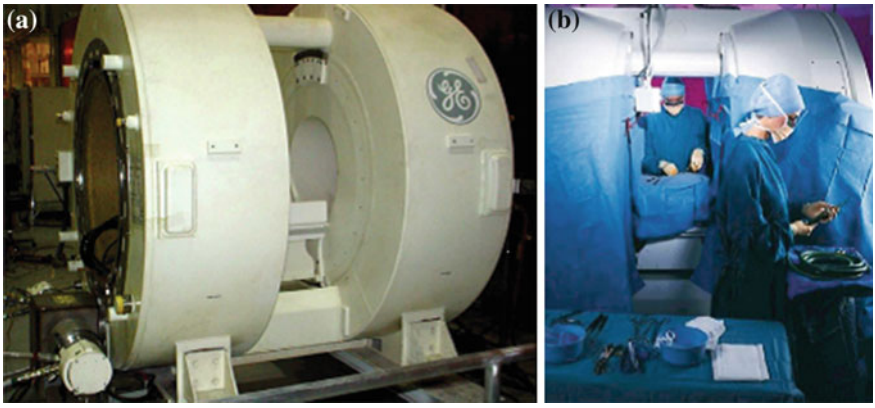

Fig. 10.11 First 0.5 T whole body interventional conduction cooled MRI using Nb_3Sn magnets [21]. **a** Magnets have access for patient and the surgeons. **b** MRI Scanner 'Sigma-SP' during surgery procedure (*Courtesy* Ernst W. Srautner, GE Global Research and with permission from IOP)

Hopes are also pinned on HTS magnets in coming years since they can be conduction cooled by using crycoolers and operated at 20–50 K. By this time solution to most of the issues with HTS, discussed in Sect. 10.1.6.4, has been found through rigorous studies carried out at NHFML. Single length conductor production will have to be stepped up and material cost be reduced to a reasonable level. MgB_2 stands a better chance to be used for MRI magnets with its attractive T_c of 39 K. Paramed has commercialized a 0.5 T Open Sky MR scanner using MgB_2 magnet. The scanner has a fully open vertical gap and provides total comfort to claustrophobic patients, a child or an elderly person. The magnets operate at 20 K and are conduction cooled by cryocoolers. With the continuous improvement in the critical current performance of the MgB_2 conductor it is hoped that commercial 3 T MRI scanners will soon be available for clinical use. A 3 T compact MgB_2 magnet system [23] for MRI is being developed at GE Global Research. Siemens and Oxford Instruments have developed proto type 0.2 T MRI system using BSCCO-2223 HTS magnet with a horizontal pole gap. R&D work on a large variant of conventional and non conventional configurations of magnets has been going on at several places. A detailed account of these efforts has been published recently in a review by Lvovsky et al. [21].

10.4 Superconducting High Gradient Magnetic Separator (SHGMS)

10.4.1 Principle of Magnetic Separation

Magnetic Separation had been a well established technique for the separation of magnetic materials with differing properties, largely in mineral industry. With the development of superconducting magnet technology in 1970s magnetic separation

found potential application in diverse fields like mining, manufacturing, medicine and pollution control. Magnetic separation is achieved by a combination of a magnetic field B_0 and a field gradient ∇B. The force on a magnetizing particle of volume V_P and susceptibility χ kept in a magnetic flux B_0 and a field gradient ∇B is given by

$$F_m = \frac{\chi V_P}{\mu_0}(B_0.\nabla B) \tag{10.7}$$

where μ_0 is the permeability of air. The magnetic acceleration will be

$$A_m = (F_m/m) = \frac{\chi}{\rho_P}(B_0.\nabla B) \tag{10.8}$$

where ρ_P is the particle density. Since for most of the minerals $\chi = 0.1–1.0$ SI units, the product $(B_0.\nabla B)$ should be between 1 and 100 T^2/m to overcome the gravitational force F_g and the fluid drag F_d which oppose the separation. F_g and F_d are given by

$$F_g = \rho_P.V.g \tag{10.9}$$

$$\text{and} \quad F_d = 6.\pi.b.\eta.v_{br} \tag{10.10}$$

where $g = 9.8$ m/s^2 is acceleration due to gravity v_{br} is the relative velocity of fluid with respect to the particle, b the radius of the particle assumed to be spherical. η is the viscosity of the medium. For larger particle, especially in air, the gravitational force dominates. For separating small particles we must use smaller flow velocity and/or higher field and field gradient. The magnetic separator are designed in a way such that it creates a force strong enough to deviate the particles from the fluid flow. The separator can broadly be divided into two categories. In the first category (Fig. 10.12a) the field gradient is produced by the magnet pole faces themselves whereby the magnetic particles get collected in the high field region. In the second category the magnet produces a uniform field and the gradient is created by introducing secondary poles (Fig. 10.12b). The magnetic particles are captured by these secondary poles and the material can be released by switching off the field and recovered. The raw mineral is first crushed or milled to liberation size of the process material and can either be fed directly into the separator for dry separation or in the form of a slurry for wet separation. It is evident from (10.7) that for particles of colloidal size and which are weakly magnetic one needs a high uniform magnetic field and a high magnetic field gradient created by a filter matrix.

Even though the technology of high gradient magnetic separator (HGMS) was introduced in 1930s, it found popularity in kaolin clay industry to enhance its brightness by the removal of darker magnetic components much later. Like all other magnet applications the superconducting magnet technology made the HGMS technique economically attractive. State-of-art systems for Kaolin clay purification

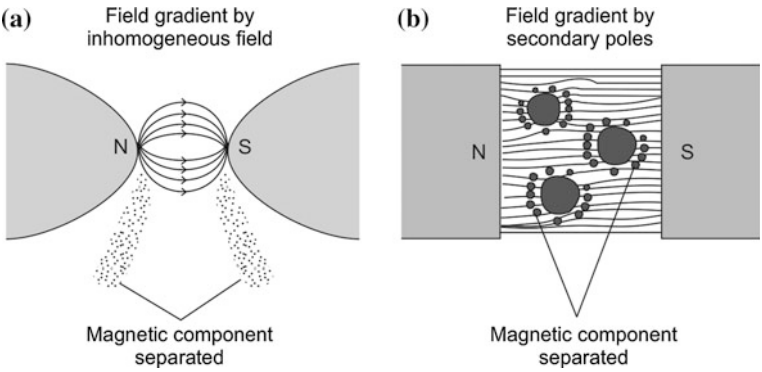

Fig. 10.12 Two principal techniques used for magnetic separation

became available in 1989 with almost no "dead-time" and without operational failures. SHGMS only needs periodic refilling of liquid helium. The refill time too has increased drastically with the use of cryocooler re-condensers and many systems are working in remote locations in the mine areas. S-HGMS have been developed [24–28] for a variety of applications built and used for varied applications.

10.4.2 SHGMS Magnet Design

The magnets used in large capacity SHGMS has a room temperature horizontal bore similar to MRI magnets except that it does not require high field homogeneity. The field strength is limited to 5 T in the present applications. Figure 10.13 is a schematic diagram of a demonstration 5 T SHGMS author's NPL group built in collaboration with BHEL (R&D), a Public Sector Undertaking around 1990. It has a vertical RT bore of 100 mm housing a 96 mm dia. SS 316 container filled with SS 430 ferromagnetic wool with a fiber dia. of 45 μm at a density of 2–5 %. The cryostat was of a tail shape to reduce LHe inventory. The magnet was built in five sections using 0.74 and 0.54 mm Nb–Ti wires and vacuum epoxy impregnated. Each section was separately quench protected by dump resistors. The magnet produced a field of 5 T at a current value of 120 A. It had a field uniformity of 5 % in a SDV of 150 mm. The parameters of the magnet built for this SHGMS are given in Table 10.2. The cryostat had a LN2 precooling vessel and a 78 K thermal shield. The tail part of the cryostat had a 25 mm thick ferromagnetic shield to reduce the stray field to <0.5 mT at a distance of 1 m (at 4.5 T field level). This is to prevent malfunctioning of the process control system and the magnetic operation due to the movement of ferromagnetic material in the vicinity.

Figure 10.14 is a flow diagram of the filtration process using process material in the form of slurry. The entire process is PLC controlled. Energization and de-energization of the magnet is synchronized with the opening and closing of the

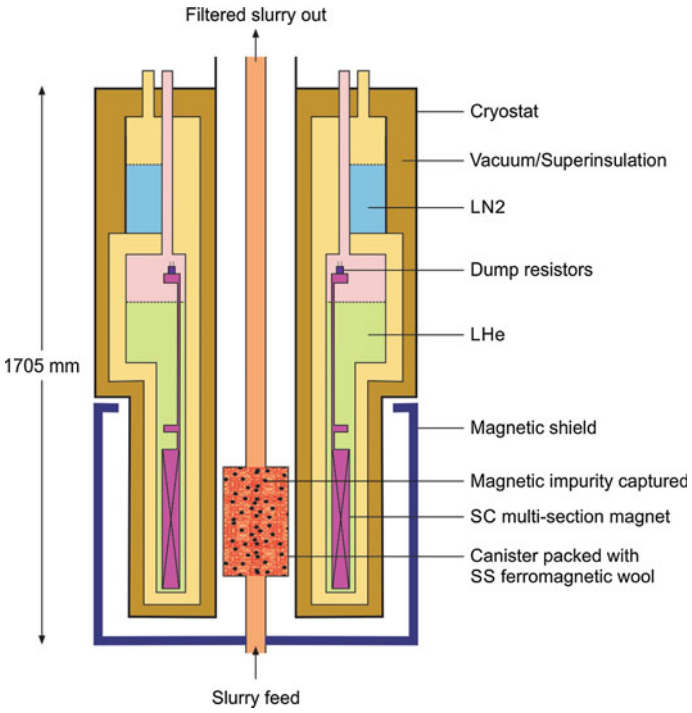

Fig. 10.13 A schematic diagram of a demonstration SHGMS system [29]

Table 10.2 Some parameters of the magnet of the SHGMS discussed above [29]

Parameter	Unit	Value
Central magnetic field	T	5
Inner bore diameter	mm	160
Magnet winding length	mm	320
Warm bore diameter	mm	100
Field homogeneity over 15 mm DSV	%	5
Conductor used		Cu/Nb–Ti
Conductor diameter	mm	0.75 and 0.54
Quench protection		Dump resistors
Stray field at 1 m	mT	<0.5
Shield material		25 mm thick commercial iron

relevant solenoid valves. On the extreme left is a 200 l slurry tank with a stirrer. Mineral to be filtered is ground to about 5 μm size and mixed with water (2–5 %) with the addition of a deflocculant such as sodium bicarbonate or hexametaphosphate. This is done to control pH value and to prevent particles from agglomerating during the slurry process. After the magnet is energized to desired field the slurry is

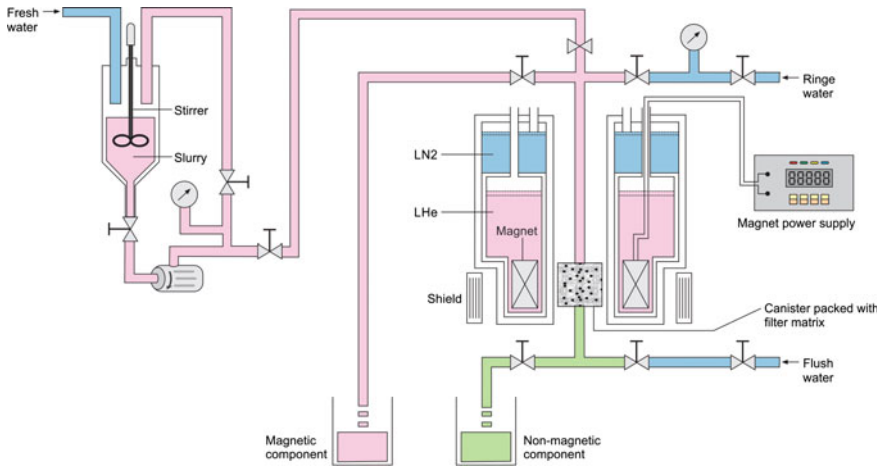

Fig. 10.14 The flow diagram of SHGMS with slurry handling system [29]

pumped into the filter matrix through top or bottom distributing header. After filtration the slurry is collected into three separate containers (not all shown in the figure) viz; (1) the concentrate, the desired material released by rinse water (2) middling which consists of magnetic and non-magnetic components and can be recycled. (3) the tailings, the reject component. System was used extensively for removing magnetic impurities of micron size from a variety of minerals with excellent results [29]. Some of the minerals processed were ball clay, wolframite, magnesite, synthetic rutile and iron ore slime. Optimization were carried out with respect to flow velocities, different magnetic fields, different densities of filter matrix and multiple filtrations for obtaining high grade material. The system was designed for batch processing only. Industrial systems use large horizontal RT bore magnets and run in continuous mode on a 24 × 7 basis. In such systems two reciprocating canisters packed with filter matrix move in and out of the magnetic field on a continuous basis. The magnets are operated in persistent mode consuming little power.

10.4.3 Recent Developments

A 2,000 ton/day SHGMS has been developed [30, 31] at Osaka University to recycle waste water from a paper industry. The waste water contains suspended solid (SS), glue, colourant, dye and cohesion agents which increase the chemical oxygen demand (COD) to 2,000–3,000 ppm level and cannot be discharged without being treated. SHGMS has been found to be most viable technique economically and treated water is re-cycled. The magnet has a RT bore of 400 mm, length

680 mm and produces a field of 2 T at a current of 100 A. The magnet uses Nb–Ti conductor. The system has proved to be very successful and reduces the COD to 100 ppm, turbidity from 200–300 NTU (nephalometric turbity unit) to 2–10 NTU, and SS (suspended solid) from 200–400 to 20–40 mg/l. The parameters of this SHGMS and the magnet are given in Table 10.3. The system is compact too, occupying just 6 m × 6 m space. The cost of SHGMS is 1/6th–1/10th of the conventional activated sludge system (Table 10.4).

More recently Ning et al. [32] at the Institute of High Energy Physics (CAS) have built a 300 mm bore, 5.5 T SHGMS for Kaolin clay. The magnet used a Nb–Ti conductor of the size 1.28 mm × 0.83 mm, a Cu:Nb–Ti ratio 4:1, filament dia. 80 μm with a tensile strength 400 MPa and a yield strength of 245 MPa. The magnet coil has an inner dia. of 400 mm, an outer dia. of 474 mm and a length of

Table 10.3 Parameters of SHGMS built at Osaka University for recycling paper industry waste water (data compiled from [30, 31])

Parameter	Unit	Value
Capacity	Ton/day	2,000
Magnet field	T	2
Operating current	A	100
RT bore of the magnet	mm	400
Magnet length	mm	680
Conductor used		Cu/Nb–Ti
Reduction in COD (chemical Oxygen Demand)	ppm	From 2,000–3,000 to 100
Reduction in turbidity	NTU[a]	From 200–300 to 2–10
Reduction in SS (suspended solid)	Mg/l	From 200–400 to 20–40

[a] *NTU* nephalometric turbity unit

Table 10.4 Parameters of SHGMS built at IHEP (CAS) for Kaolin clay (data compiled from [32])

Parameter	Unit	Value
Magnet field	T	5.5
Peak field	T	5.6
Operating current	A	150
Magnet bore inner diameter	mm	400
Magnet outer diameter	mm	474
Magnet length	mm	815
Conductor used		Cu/Nb–Ti
Conductor dimensions	mm	1.28 × 0.83
Filament diameter	mm	80 μm
Cu: SC ratio		4:1
Hoop stress	MPa	150
Stray field at 1 m radially	mT	<5
Shield (octagonal) material		Iron
No. of canisters with filter matrix		2

815 mm. The coil former is 10 mm thick. The magnet produces a central field of 5.5 T at a current of 150 A which is 75 % of the short sample value. The maximum field is 5.6 T. An iron octagonal shield has been used which reduces the stray field to below 5 mT at a radial distance of 1 m and an axial distance of 1.2 m.

Extreme care is taken to control hoop stress due to large Lorentz force. A bandage 14 mm thick consisting of 15 layers of 1 mm dia. SS wire has been used. Stress simulation was carried out by developing a code using 2-D Finite Element Method (FEM) based on ANSYS software. During simulation the hoop stress has been kept restricted to 150 MPa only whereas the maximum overall allowable hoop stress of Nb–Ti is 350 MPa. A pre-stress of 70 MPa was applied on the coil and a pre-stress of 100 MPa applied to the bandage. Stress and strain behaviour of the coil during winding, cool down and charging has been studied in detail. The SHGMS has two canisters with filter matrix reciprocating in the magnet bore. During the time one canister is being filtered in the magnetic field the other canister is cleaned.

In recent time attention has been focused to build conduction cooled systems which can operate in remote areas where LHe supply is difficult. Quantum Design Inc. has marketed a conduction cooled 5 T SHGMS system [33] with reciprocating canisters for Kaolin clay. The magnet of this system has a bore of 203 mm and produces a field of 5 T with a uniformity of 10 % over 406 mm. This long range of uniformity enables the system to process 30–40 tons of material per day depending upon the quality of clay and the desired level of purity. The magnet is cooled by a 1.5 W GM cryocooler and uses a ‘energy smart technique’ which brings down the operating cost rather dramatically. Virgin cooling of the magnet takes about 45 h. No cryogenic fluid is used. The magnet has non-dissipative HTS current leads which makes the system power efficient. The system has two canisters reciprocating rapidly using a servo drive. An ingenious design of the canister allows to maximize effective filter volume enhancing the processing capacity of the system to 10,000–15,000 tons/year. The system is of modular type such that several modules can be combined together to raise the production capacity to desired level. Routine maintenance of an individual unit can be carried out without any interruption to the clay processing by other units.

10.5 Superconducting Magnet Energy Storage (SMES)

10.5.1 Introduction

SMES is yet another important application of superconducting magnets. It is a unique device for load-leveling and for the stabilization of utility system which stores and converts electric energy directly with >95 % cyclic efficiency. SMES does not convert electric energy into mechanical or chemical energy and vice versa. Compared to other energy storage devices like pumped hydro and compressed air which need large time for the energy conversion from mechanical to electrical, SMES has very small response time and delivers power almost instantaneously and

can charge/discharge unlimited number of times. The device does not possess either the highest power density or the highest energy density but has good balance between the two, crucial for certain applications. Further, there is no energy loss in SMES the only loss is about 2–3 % in the inverter/rectifier system. SMES finds application mainly in UPS (Uninterrupted Power Supply), PPS (Pulse Power System) and FACTS (Flexible AC Transmission System). Large number of big [34] and small [35, 36] size SMES have been built since late 1980s and operated mostly in USA and Japan. Some of them were even abandoned [37] in favour of more economical electrical systems. The status of SMES as in 2008 has been reviewed by Tixador [38]. SMES based UPS with power rating in MW range are in use in power sensitive semiconductor chip fabrication and liquid crystal units in USA and Japan. These industries need ultra clean power and protection against voltage dips to prevent costly shut downs. Even though high capital cost of SMES has prevented it to become as popular as NMR and MRI, yet they are increasingly used in several dedicated civil and military applications. Recent induction of HTS based conduction cooled SMES [39] in power conditioning system by Gesellschaft fur Innovative Energiemwandlung und Speicherung (EUS) for improving power quality locally seems to be very promising.

Two main characteristics of SMES, namely, high power density and a fast discharge time make them attractive for use in metal forming, for EM launchers in weaponry and as a pulse power source. SMES has, however, low energy density of the order of 10 kJ/kg and thus is more useful as a power source. The energy density is limited by mechanical structure needed to counter large EM forces. Other advantages are very large number of charging and discharging possible, high conversion efficiency and there are no moving parts involved.

One very important element of a SMES system is the Power Conditioning System (PCS), an interface between the magnet and the power utility system. PCS broadly consists of an ac to dc rectifier and dc to ac inverter which changes the ac from the power utility to dc and feeds the magnet. A dc-dc chopper, linked to a voltage source inverter, is used to charge and discharge the magnet and for balancing the voltage dip. Conventionally, the power is transmitted at high voltage and low current and the magnet operates at high current (several kA) and low voltage, a step-down transformer is therefore used. Unwanted harmonics are suppressed through the use of passive filters. A digital controller controls various functions of the SMES such as the detection of a voltage dip, voltage balance and the smooth functioning of instrumentation. It also regulates the output voltage and the frequency in stand-alone mode when there is no supply from the utility and SMES is the only source to a strategic application.

10.5.2 Magnet Design in SMES

The energy storage capacity of a SMES solely depends on the size of the magnet and the critical current of the superconductor used. The magnet thus happens to be

the heart of a SMES and a most expensive component since it requires large quantity of the conductor, a LHe cryostat, refrigeration system like cryocoolers and the electronic control system for power supply and quench protection. Magnet shielding, passive or active, too is required to reduce stray field below the acceptable level. Other important component is the PCS just described in Sect. 10.4.1. The outstanding capability of a superconducting magnet to operate in persistent mode, makes it an ideal energy storage device. Since there is no dissipation of energy the current and the magnetic flux in the magnet remains constant. The energy stored in a magnet is $\frac{1}{2}LI^2$ where L is the inductance of the magnet coil and I, the coil current. When the persistent switch is opened the stored energy can be transferred to the desired load by lowering the current in the magnet coil. SMES thus serves as a current source in contrast to a capacitor which serves as a voltage source. The energy is the product of mean power and the discharge time. The discharge time is strongly dependent on application. For example, a magnet is designed for short discharge time of msec to sec if used for the protection of a sensitive electric load against voltage dips. On the other hand, the magnet must be designed for long discharge time if used for load leveling in a grid. Long discharge time may vary from hours to weeks.

The optimization of magnet design is aimed at achieving maximum possible stored energy for a given amount of conductor with the least probability of a quench. The peak field on the conductor should not exceed 7 T for Nb–Ti conductor. The magnet can either be designed in a solenoid form or in the form of a toroid. A toroid does have the advantage of low stray field because the entire field is contained within the magnet bore itself. This has two benefits, (1) the size of the support structure is reduced and (2) the toroidal SMES can be installed close to the utility or the load. The design helps in reducing the external magnetic forces and thus the dimensions of the mechanical structure. Further, the toroidal coils always perform under compression by the outer hoop stress and the two discs at the bottom and the top. Mechanical forces start dominating as the SMES size increases and the toroidal design then becomes a preferred option. A toroidal magnet is realized by using a number of coils wound in pancake structure and distributed along the circumference of the torus. The earlier large SMES had small aspect ratio solenoids with 100 m diameter buried under the earth and supported by rocks. The toroidal SMES, however, stores just 50 % of the energy that a solenoid SMES can store using the same amount of conductor volume. Another problem with this design is that the magnet coil experiences a large radial force towards the axis in addition to longitudinal and transverse forces. Quench in such magnets causes imbalance in the force distribution making the protection complicated. The magnet coil must be epoxy impregnated to prevent any movement during ramping. Since the magnet can release energy very fast, the coil should be able to withstand large voltage. The conductor and the interlayers must have thick insulation layer and spacers respectively. High power, being the product of the current I and the voltage V_{max}, needs high current as also very good electric isolation for high voltages. Multiple solenoid coil design is yet a third option where the stray field problem is quite small but it consumes much larger quantity of the conductor for a given energy density.

A solenoidal design of the magnet is ideal for commercial small (micro) SMES which is simpler to fabricate. Mechanical support and quench protection can also be managed easily. The magnet should preferably be built with an even number of solenoids in a modular fashion either in a four solenoid configuration in squire arrangement or in six coil configuration in an hexagonal arrangement. This design helps in reducing the stray field appreciably. The solenoid design should be optimized for minimum conductor volume when the diameter to height ratio is 5. Passive iron shield as well as active superconducting shield are employed to reduce the stray field. The active shield coils are wound over the main magnet with current in a reverse direction to cancel the field outside.

10.5.3 Factors Affecting SMES

10.5.3.1 The Mechanical Structure

Though the stored energy ($=B^2/2\mu_0$) in a magnet, generating a field B, is proportional to the square of the field strength, yet the maximum energy it can store is ultimately limited by the strength of the mechanical structure. A robust structure is required to contain the large Lorentz forces generating high stress. The ratio of the stored energy W to the minimum mass of the structure, M_m for a solenoid magnet as given by virial theorem ($W/M_m = \sigma/d_{sm}$) turns out to be 12.5 kJ/kg for steel for a working stress of 100 MPa for a finite length solenoid. Here σ is the working stress and d_{sm} is the density of structure material. High strength, low density Al-alloys with density of about 1/3rd of steel can enhance the working stress a bit but the energy to mass ratio remains largely unaffected. The magnet conductor, chosen for winding, too must be capable of withstanding expected high stresses and deformations without degrading its superconducting critical parameters like the critical current, I_c.

To contain large Lorentz forces two techniques have been followed. In the first technique, the magnet system is buried under ground where the forces are transmitted to rocks and the reinforcement. In the second technique, the cold structure of the magnet itself supports the forces. Support material can be fiber-glass reinforced epoxy which is cryogenic compatible. The second technique is more economical and is pursued for SMES systems up to a GJ range of energy.

10.5.3.2 The Conductor

Like many other applications the conductor should have high engineering critical current density, J_e in high magnetic field, should provide safe temperature window for operation, and well stabilized in a conducting matrix. The conductor must have sufficient reinforcement to withstand large forces. Since the magnet charges and discharges rapidly, there are ac losses in the coil conductor and eddy current losses

in the cryostat. Low ac loss conductors with resistive barrier around the conductor filaments are to be used. Low loss CICC conductors are ideally suited for use in SMES. Cryostat too is designed to cut the eddy current losses to a minimum. So far all the SMES have been manufactured with Nb–Ti conductor and operated at 4.2 K LHe bath. Operation of the magnet at reduced temperature, 1.8 K increases J_c and reduces the conductor amount. Use of HTS current leads inside the cryostat cuts down the heat load to the LHe bath significantly. With the induction of the cryocoolers as recondensers inside the cryostat the LHe refill time has increased enormously.

MgB_2, a 39 K superconductor, though much cheaper than the Nb–Ti does not seem to be a potential material for future SMES because its operating temperature 10–15 K is not very significantly higher than 4.2 K of the Nb–Ti.

Cryogenic cost can be expected to reduce drastically if the Nb–Ti magnets were to be replaced with HTS magnets which can be operated at much higher temperatures (20–50 K). HTS magnets can be conduction cooled by the cryocoolers thus doing away with the use of LHe. The second generation (2G-REBCO) coated conductors do hold the potential of replacing Nb–Ti in the near future, once the conductors are manufactured in sufficient lengths and with a reasonable cost. The advantage of the 2G conductor is that they can be operated at 50 K instead of at 20 K required for the first generation BSCCO conductors. Other advantage with the use of HTS is that the magnet is very stable because of the high heat capacity of the conductor, about two orders of magnitude higher at 50 K compared to that at 4.2 K. At such high temperatures thicker electric insulation can be used which can withstand high voltage. An increase in the operating voltage will increase the power of the SMES system. The insulation thickness has to be optimized such that the temperature gap ΔT between the conductor and the cooling media remains low. Quench protection should take into account the slow propagation velocity of the hot spot (normal zone) in HTS which can raise the local temperature and can even damage the coil. Innovative protection system will have to be designed.

10.5.4 Some Examples of SMES

10.5.4.1 Very Large SMES

Why the SMES technology did not find wide acceptability by the power distribution sector for balancing the load in the electricity distribution network was that the scale of power is in range of GWhr which required gigantic size of superconducting magnets around 1 km in diameter. Building a magnet of this dimension poses sever problems related to mechanical structure, the conductor amount, LHe cooling, and the cryostat. Large Lorentz forces have a radial outward component trying to expand the coil and an axial component symmetric to the central vertical line. Strong mechanical structure has to be designed to withstand these forces and the weight of the magnet.

Table 10.5 Specific parameters of a large SMES (data compiled from [34, 38])

Parameter	Unit	Value
Peak stored energy	TJ	18.9
Peak power	MW	1000
Magnet diameter	m	1000
Magnet height	m	19
Aspect ratio		0.019
Maximum field	T	5.18
Peak field	T	6.69
Magnet current	kA	200
Operating temp.	K	1.8
Magnet configuration		4 layers coil
Cool down hoop stress	MPa	345
Refrigeration load/day	MWhr	120
Status		Designed only

One large SMES system of 1,000 MW capacity was designed [34, 38] under the Strategic Defense Initiative (SDI) in USA in 1987. The specific parameters of this big device are given in Table 10.5. The magnet had a designed diameter 1 km, a height of 19 m and a stored energy of 18.9 TJ. The system was to operate at 1.8 K at a current level of 200 kA producing a working field of 5.18 T. It was planned to be installed inside a trench in mild rock near the surface. Fiber-glass reinforced epoxy (G-10CR) struts with graded thickness were to be used as the bottom support to the magnet to take care of the thermal contraction during cool-down. The sequence of fabrication was something like this. The helium outer vessel, the struts and the vacuum vessel were to be fabricated onsite in the trench. The coil was to be wound on the inner side of the helium outer vessel in segments. Helium vessel wall was to be fabricated next after winding each signet of the coil and the helium vessel sealed. The vertical supports between the helium vessel and the inside wall of the vacuum vessel complete the assembly. It was proposed to use CICC conductor with LHe flow through the conductor. Separate LHe vessel was not provided for. A network of tubes for carrying LHe for cooling and for heat extraction was, instead to be fabricated. The device was, however, not constructed and remained confined to design stage only.

10.5.4.2 Medium Scale (400 MW) DNA-SMES

The Defense Nuclear Agency (DNA) of USA under the SDI initiative took up a 400 MW SMES programme [40] for use as a pulse power (short duration high power) source for Free Electron Laser-directed energy weapons as well as for load leveling and stabilization in power network in 1987. The Electric Power Research Institute (EPRI) proposed [37] an Engineering Test Model (ETM) for this dual use 400 MW SMES. Two teams, Bechtel and Ebasco came out with two different

designs. The key design parameters of the 400 MW SMES as proposed by the two Teams are given in Table 10.6. In the Bechtel design the magnet diameter was 129 m and the height 7.5 m. A 200 kA CICC Nb–Ti conductor which had very low ac losses, was planned to be used. The critical current of the conductor was 303 kA at 1.8 K and in 5 T field. The CICC conductor with LHe flow channel does not need LHe vessel making the construction of the cryostat less complex. A high current conductor such as this, reduces the total amount of conductor required and also keeps the operating voltage within a safe limit of 10–12 kV. Higher operating voltage involves the risk of arcing. Further, the magnet coil was to be operated at a reduced temperature of 1.8 K when the conductor can carry much larger current and save on the conductor cost. He-II ensures uniform temperature of the conductor and faster heat extraction because of its extremely high thermal conductivity. The saving in conductor cost turns out to be orders of magnitude higher than the increased cost of the extra refrigeration need for He-II. A two layer coil design also allows easy access to inspection and repair of the winding. HTS current leads were to be used because of their poor thermal conductivity and non dissipative properties. Fiber-glass reinforced epoxy (G-10CR) struts were to be used as the bottom support to the magnet to take care of the thermal contraction during cool-down. The magnet was proposed to be built inside a steel lined concrete reinforced trench.

Containing Lorentz forces in such large size magnets is a challenge. Stresses caused by cooing as well by the Lorentz forces are calculated such that the limit of the yield strength of any of the materials used in the coil pack is not reached. The coil pack needs pre-compression radially inward by about 0.15 % so that the hoop

Table 10.6 Important design parameters of a 400 ETM-SMES as proposed by Bechtel and Ebasco Groups (data compiled from [37, 38, 41])

Parameter	Unit	Bechtel team value	Ebasco/Westinghouse value
Power pulse	MW	400	400
Stored energy	MWhr	20.4 (73 GJ)	20 (70 GJ)
Magnet diameter	m	129	134
Magnet height	m	7.5	4.2
Aspect ratio		0.058	0.00149
Conductor		Nb–Ti	Nb–Ti/Al
Conductor type		CICC	Rutherford cable
Operating current	kA	200	60
Operating temperature	K	1.8 (He-II flow in CICC)	1.8 (He-II bath)
No. of radial layers		2	4
No. of turns		112	32
Power discharge time @ 400 MW	s	100	
Magnet structure material		FRP	G-10CR
Status		Abandoned	Abandoned

stresses developed during cool down in different metal constituents of the conductor (conductor, stabilizer, filament barrier, the central conduit etc.) remain well below their respective yield strength. Pre-compression also reduces tension across the FRP structure joints. The pre-compression procedure must be carried out by shrinking the coil pack in liquid nitrogen and then locking the outer struts. The vacuum vessel should be fabricated and tested outside and then finally fixed in the trench as liner. No gap or air pocket is to be left between the liner and the trench to rule out possibilities of a structure failure. The coil pack will remain accessible to inspection and repair.

The other design was proposed by the Ebasco/Westinhouse team [41]. This design was based upon a 60 kA Nb–Ti conductor with Al stabilization. The magnet has a solenoid configuration. The coil stack is 134 m in diameter and 4.2 m in height (aspect ratio 0.00149). The coil has four layers and each layer has eight turns. G-10CR sheets have been used as turn to turn insulation. To counter the stresses, an axial preload is provided by the insulated SS clamping studs with G-10CR clamping plates. Radial mechanical support is provided by G-10CR finger plates between the walls of the dewar and the outer layers. G-10CR loading bars are used as interlayer. The G-10CR finger plates and the loading bars also serve as good electrical insulation which is extremely important in these devices as large voltage develops during fast charging/discharging and the quench.

10.5.4.3 Micro SEMS for Sensitive Industries

Small size micro SMES units have been built and successfully used in semiconductor and liquid crystal sensitive industries in Japan to provides protection against sudden voltage dip at high power level. The performance of the SMES remains unaffected even after charging and discharging of high power. Commercial 5 and 10 MVA SMES systems has been built [35, 36] by Chubu Electric Power Co. and Toshiba Corporation Power System Co. These devices are operational since 2011. The SMES has a four (even number) pole solenoid configuration. This design has been chosen to reduce the leakage of the magnetic field. Since the duration of the sudden voltage dip is less than 0.5 s the SMES has been designed with a compensation time of 1 s. For the 5 MVA SMES a low ac loss Rutherford Nb–Ti cable with Cu–Ni barrier has been used for coil winding. The coil produces a field of 5.3 T at a current of 2.66 kA and at a temperature of 4.2 K provided by the LHe bath backed by cryocoolers. The key parameters of the 5 MVA-SMES magnet and the conductor are given in Table 10.7. Since SMES operates at a high rated voltage ($\sim$few kV), for safety this voltage is reduced to half the value by grounding the coil with a resistor at its neutral point. The HTS current leads used to carry the required current are a combination of 1 kA class YBCO leads joined together in parallel. The current leads carry a heat load of 3 W to the magnet coils. The leads are capable of withstanding a voltage of 6 kV. The warm ends of the leads were cooled to below 77 K by the use of GM cryocoolers. AIN spacers isolate the leads from the cryocoolers up to a rated dc voltage of 6 kV. A cutaway view of this 5 MVA SMES [35]

Table 10.7 Key parameters of a Small 5 MVA SMES (data compiled from [36, 37])

Parameter	Unit	Value
Rated input and output		3φ, 6600 V, 60 Hz
Peak stored energy	MJ	7.34
Peak power	MW	5.0
Discharge time	s	1
Coil diameter	m	0.53
Coil height	m	0.7
Aspect ratio		1.32
Magnet configuration		Four-pole solenoidal
Maximum field	T	5.3
Rated current	kA	2.657
Operating temp.	K	4.2 (LHe pool boiling)
Rated voltage	kV	2.5
Withstand. voltage	kV	6.0
Conductor/type		Nb–Ti/(Rutherford)
Conductor size	mm	1.67 × 120
No. of strands		27
Strand dia.	mm	0.9
Filament dia	μm	13.5
Cu/CuNi/NbTi		2.25/1.45/1
Critical current	kA	7.9 (5.25 T, 4.2 K)
Present stratus		In use (Japan)

is shown in Fig. 10.15. The SMES was tested successfully from 2003 to 2006 on site. The sudden voltage dips were balanced fast via the power feeding from the SMES without any load on the production line. The same company also marketed 10 MVA SMES units. Three such commercial units are operating in Japan at the moment.

10.5.4.4 High T_c Oxide Superconductor (HTS) SMES

Some BSCCO SMES

Although proto type HTS SMES are still being developed, yet they hold great potential for future. The main advantages of the HTS conductor over the conventional Nb–Ti conductor have already been discussed in Sect. 10.4.3.2. First generation HTS Bi-2223 tapes/wires have been used to construct small 2–3 kJ SMES devices by Hawley et al. [42, 43] primarily to carry out optimization of the design of the magnet, EM stress analysis, mechanical structure issues, current leads and power control circuit. Kalsi et al. [44] at American Superconductor Corporation (ASC) built a 5 kJ SMES using the same Bi-2223 material and was supplied to EUS (Gesellschaft fur Innovative Energieumwandlung und Speicherung), Germany after

Fig. 10.15 A 5 MVA SMES system with four pole solenoid design, built by Chubu Electric Power and Toshiba Corp. Power System Co. Japan. The *inset* on the *left* are the four pole superconducting magnet Coils [36] (With permission from Elsevier)

successful tests in 1996. The EUS used the SMES to devise technology to improve poor power quality in plants where a voltage dip or a short interruption can cause long shut down.

The magnet was built in a solenoid configuration with pancake structure. The pancake structure is ideal for short length conductors and offers an excellent cooling because of large surface exposure. Besides, it is also convenient to replace the conductor in a particular coil. Mechanical support is also superior. The magnetic field direction too is favourable to the critical current under this orientation. The coil inner dia. is 370 mm, the outer dia. 438 mm and the height 98 mm. A pair of bundles of Bi-2223 wires, joined together in parallel, was used as current lead to carry 100 A. The coils were epoxy impregnated. The magnet is housed in a vacuum vessel lined with MLI blanket to minimize radiation heat load. The magnet operates at 20–30 K at 100 A current storing an energy of 5 kJ. The SMES was fully conduction cooled by using two single stage GM cryocoolers, a large cryocooler with 25 W @ 20 K cooling capacity and a smaller one with 45 W @ 65 K capacity. The bigger cryocooler takes care of the heat generated in the magnet due to ac losses caused by the frequent and fast ramping of the current. The magnet can be ramped from zero to 100 A in 2 s. and back to zero in 2 s. The magnet temperature reaches 35 K, the maximum permissible temperature after 100 such ramps or after 400 s. The smaller cryocooler is used to cool the HTS current leads which are anchored to the cold head maintained at 32 K. Magnet withstands a voltage of 200 V. The maximum hoop stress experienced by the magnet is 2.5 MPa only and no extra reinforcement was needed to be provided. The design and performance

parameters of the AMC 5 KW SMES have been compiled and given in Table 10.8. The successful operation of this SMES thus confirms the superiority of the conduction cooled HTS SMES and large units seem feasible with continuous improvement in the quality of the HTS materials.

Experimental prototype SMES using Bi-2223 wires have been designed and tested at several places. A detailed investigation on the optimization of magnet design has been carried out by Wojtasiewicz et al. [45] in Poland using a FLUX 2D software. The design parameters were fixed for a single pancake coil based solenoidal configuration with an outer diameters of the coils of 360 mm and a single length Bi-2223 wire 1,500 m long. Various parameters have been evaluated for different number of pancakes. Different coil radii, number of turns, magnet height and two operating temperatures of 35 and 50 K have been studied. The design selected was a SMES with 14 pancakes, 104 layers, inner dia. 147.8 mm, outer dia. 360 mm, height 93.8 mm. The magnet system has an inductance of 0.76 H, I_c (@35 K) 139 A, B_{max} 0.99 T and stores an energy of 7.36 kJ. A high strength Bi-2223 wire was planned to be used and the magnet was to be cooled using a GM two stage cryocooler. These parameters are given Table 10.9.

A 200 kJ toroidal magnet SMES was designed and optimized by Kim et al. [46] to improve the power quality of a building and to meet strict restriction on stray field. Optimization was done using the so called 1 + 1 evolution strategy (1 + 1 ES) with line element technique. The toroid consisted of 16 pancake modules, each module having three disc shaped pancake coils. The coils use a total of 9.6 km Bi-2223 tape of 4.1 mm × 0.2 mm size. The SMES stores 200 kJ energy at an operating current of 200 A. The SMES has a discharge time of 1.5 s and a maximum voltage of 1 kV. The stray field at a distance of 5 m is only 2.84×10^{-9} T. The system will be conduction cooled by a GM cryocooler. Table 10.10 summarizes parameters of the SMES.

Table 10.8 Design and performance parameters of the AMC 5 KW SMES (data compiled from [44])

Parameter	Unit	Value
Stored energy	kJ	5
Magnet inner dia.	mm	370
Magnet outer dia.	mm	438
Magnet height	mm	98
Peak axial field	T	0.97
Peak radial field	T	0.78
Total ampere turns	kA-turn	140
Effective inductance	H	1
Operating current	A	100
Operating voltage	V	200
Operating temperature	K	20–30
Current leads		Bundle of Bi-2223 wires
Maximun hoop stress	MPa	2.5

Table 10.9 Optimized parameters of a 7.3 kJ (Bi-2223) SMES magnet (data compiles from [45])

Stored energy (kJ)	No. of pancakes	No. of layers	Inner dia. (mm)	Outer dia. (mm)	Height (mm)	Inductance (H)	I_c @ 35 K (A)	B_{max} (T)
7.36	14	104	147.8	360	93.8	0.76	139	0.99

Table 10.10 Design parameters of a 200 kJ toroidal Bi-2223 SMES (data compiled from [46])

Max. stored energy (kJ)	Toroid type	No. of modules	Pancakes in a module	Conductor dimension (mm)	Operating current (A)	Discharge time (s)	Max. voltage (kV)
200	Modular	16	3	4.1 × 0.2	100–200	1.5	1

A 800 kJ Bi-2212 SMES has been constructed as a pulse power source by Tixador et al. [47] at CNRS, France for a DGA (Délégation Générale pour l'Armement) project. In the absence of any specification of the stray field a solenoid design was preferred using a stack of single pancake coils. The innner and outer dia. of the coils are 300 and 814 mm respectively and the height 222 mm. The magnet has a total of 26 pancakes. The dimensions of the magnet were chosen to minimize the conductor volume and to have a flat magnet. A PIT Bi-2212 Nixan conductor cladded with Ag and then with a Ag–Mg sheath was used for winding. Even with Ag–Mg reinforcement the critical stress remains low at 100 MPa. The conductor is further strengthened with an outer SS sheath raising the allowable stress to 170 MPa. Since the magnet is designed to run at a current of over 300 A and the tape has critical current of 100 A, a number of tapes were joined in parallel to carry this current. The pancakes are wound and bonded with slotted copper plates. Copper plates provide good mechanical support to the coils which are epoxy impregnated. The slots in copper plates reduce eddy current losses during ramping. A Kapton tape wrapped around the conductor provides electrical insulation. Hybrid current leads consisting of brass leads between room temperature and an intermediate point and Bi-2212 tubes between this intermediate point and the magnet. The upper ends of the HTS leads together with the thermal shield are kept cooled by a dedicated cryocooler. The quench protection is provided by discharging current in a resistor by opening the power supply connection (during charging) and short circuiting the magnet (during storage mode). The resistor remains connected to the magnet permanently.

The SMES is completely conduction cooled. Two cryocoolers have been used, one for the magnet coils and the other for the current leads and the thermal shield. The SMES operates at 20 K at a current value of 315 A and stores 814 kJ energy. All characteristic parameters of the SMES are given in Table 10.11. The tests show that the ac losses are mainly due to hysteresis. The eddy current losses in the cryostat are minimal. The magnet discharge causes little loss and the temperature increase is limited to 2 K.

Table 10.11 Parameters of 800 kJ HTS SMES (data compiled from [47])

Parameter	Unit	Value
Stored energy	kJ	814
Magnet type		Solenoid
Winding structure		Single pancake
No. of pancakes		26
Coil internal dia.	mm	300
Coil outer dia.	mm	814
Magnet height	mm	222
Conductor used		Bi-2212 (Nexans)
Operating current	A	315
Operating temp.	K	20
B_{max} (longitudinal)	T	5.2
B_{max} (Transverse)	T	2.5
Max. hoop stress	MPa	80
Max. axial stress	MPa	24
Cooling (conduction)		Cryocoolers

2G YBCO SMES

Until recently only one HTS, namely, BSCCO was commercially available in lengths enough to make coils. The drawback with this material, however, is that it supports magnetic field only up to 0.1 T beyond which the J_c drops sharply with magnetic field. This low field corresponds to an energy density of 4 kJ/m^3 only. The 90 K YBCO superconductor has a superior J_c-B characteristic and can support magnetic field up to 5 T which corresponds to an energy density of 10 MJ/m^3. 2G HTS can be operated at still higher temperature, up to 70 K with good J_c. This material is now commercially available as coated (multilayer) tapes and there have been a continuous improvement in conductor length and the critical current at temperature higher than 40 K. Besides, 2G HTS coated conductors have high mechanical strength because of the hastelloy substrate in IBAD process. In recent times a large number of 2G HTS SMES have been designed and simulated and some very small models have been laboratory tested. Yuan et al. [48] at Cambridge University have designed a SMES coil and carried out studies on current and magnetic field distribution and ac losses. The design was based on a 100 m length of Superpower 2G conductor (12 mm × 0.105 mm) with coil inner dia. 80 mm, outer dia. 160 mm, height 12 mm. no. of turns 266 and inductance 20 mH.

A 200 kJ SMES has been conceptually designed by Trillaud and Cruz [49] at UNAM, Mexico using Amperium Cu-stabilized 2G HTS wire for use as UPS for the computer servers to provide power stability during short duration (1–10 s) faults and with long life cycle. A solenoid design of the magnet has been preferred for simplicity and to save on the conductor volume. All the parameters of the SMES and the conductor used are given in Table 10.12. The magnet will have a pancake

Table 10.12 Parameters of 200 kJ 2G HTS SMES and the conductor (data compiled from [49])

Parameter	Unit	Value
Max. stored energy	kJ	252
Usable energy	kJ	200
Magnet configuration		31 pancakes
Pancake inner and outer dia.	m	0.2 and 0.676
Total height of coil	m	0.418
No. of turns/pancake		950
Magnet inductance	H	174.7
Operating current	A	53.8 (80 % Ic)
Operating temperature	K	65
Cooling system		LN2 & CCR recondenser
Conductor used		Cu/2G HTS
Conductor dimension	mm	12 × 0.2
Conductor I_c (77 K, 0)	A	175
Total conductor length	km	4.2
Insulation thickness	μm	50
Max. stress	MPa	33

structure consisting of 31 pancakes and connected in series. The inner dia. of the pancake is kept 0.2 m and the Outer dia, 0.676 m. The inter-coil separation will be 1 mm and the total height of the magnet 0.418 m. The coils are to be wound using 2G HTS 12 mm wide and 0.2 mm thick conductor having 50 μm thick electrical insulation. Each pancake will have a total of 950 turns. The magnet will operate at a current of 53.8 A (80 % of I_c) and at a temperature of 65 K. It will store a total energy of 252 kJ. The SMES is capable of supplying 200 kJ with 52 kJ as spare. It is important to evaluate the operating current from the critical surface (B-T-I) for the operating temperature and for the angle between the magnetic field and the tape (conductor) orientation. The magnet will be housed in a MLI insulated LN2 cryostat fitted with a single stage pulse tube refrigerator (65 W @ 60 K) to recondense evaporated LN2 and to keep a temperature of 65 K. It is expected to take about 56 h to reduce the temperature from 77 to 65 K.

The mechanical structure was designed by performing magnetostatic and mechanical Finite Element Analysis (FEA) for the optimum operating conditions. The maximum stress load due to cooling and the Lorentz force turns out to be at the interface between the former and the coil equal to 33 MPa. This stress load happens to be well below the maximum stress at the I_c degradation, 400 MPa and the Young's modulus of 2G HTS, 165 GPa.

Serious efforts continue to be made to exploit 2G REBCO coated conductors for high mass energy density SMES. It is expected that the 13.4 kJ/kg mass energy density limit set by Nb–Ti magnets can be overcome and raised to 20 kJ/kg in 2G HTS SMES through proper optimization of parameters. Vincent et al. [50] have developed an optimization code for a solenoid based SMES reaching a stored

energy range of 5–50 MJ by taking the constraints of the critical current and mechanical strength of the conductor into consideration. Their calculations show that the mass energy density of 20 kJ/m^2 is achievable with 2G HTS provided it has a current density above 150 MA/m^2 and a stress tolerance higher than 400 MPa. Various solutions are possible for different values of I_e and the inner dia, of the magnet coil. The solution which has low B_{max} is a better option. For high effectiveness and protection, minimum I_e should be selected. The dimensions of the magnets are accordingly determined. The issue of low propagation velocities and increased quench detection time needs careful calculations in this material as well.

The future of 2G REBCO SMES appears to be bright.

10.6 Maglev and Rotating Machines

In this section we mention very briefly two more applications of the superconductors, though very promising but both remained confined to proto type development level and technology demonstration stage, solely for economic reasons. These are Maglev and the rotating machines. The technology could be revived in near future with the commercial availability of high performing HTS conductors.

10.6.1 Magnetic Levitation (Maglev)

Japan had been the leading nation to pursue development of magnetically levitated train using superconducting magnets. The magnets are kept onboard the train and arranged longitudinally in the lower part of the train. Continuous aluminum sheets are embedded inside the concrete track exactly below the magnets. Strong eddy currents are generated in the aluminum sheets due to the magnets moving with the train. These eddy currents produce strong repulsive magnetic field upwards. At a certain speed, the repulsive force exceeds the weight of the train and lifts it off the track by several cms. The friction with the track disappears and the train moves at high speed. Japan Central Railways has attained a speed of 581 km/h for it's maglev train MLX01 in 2003. The trains have not been put in regular service for commuting again for the reason of high cost involved in the usage of LHe. Maglev for regular passenger travel can be a reality sooner than expected in view of the rapid development in the production technology of the HTS.

10.6.2 Motors and Generators

DC homopolar and AC synchronous machines were built using conventional LTS superconductors in the range of a few kW to several MW and tested between 1970s

and 1990s. Super GM of Japan had tested successfully a 70 MW superconducting generator. These machines though not commercialized because of the same reason of the high cost of cryogenic cooling, nevertheless were built and supplied for specific applications. These machines are still preferred where weight and size are the biggest constraints. Similar to other applications, development of high performing HTS has revived interest in these devices. HTS-based devices operating at higher temperature (30–50 K), are bound to revolutionize the entire electrotechnology and will be commercialized in near future. Reputed companies like AMSC, SuperPower, Siemens, GE, Super GM and Relience Electric have been building and supplying high rating motors and generators for specific use to a host of organizations. AMSC has delivered a 36.5 MW 120 rpm motor to ONR for ship propulsion. Weight and volume (space) is at a premium in a ship. Industrial motors of 5,000 hp 1,800 rpm have been built by Siemens. Most generators use superconductor field winding and a normal copper winding for the armature. The superconducting winding produces high magnetic flux without dissipation. The armature has to have an iron-free structure, that is, an air-gap winding. This makes it quite compact. The status of superconducting motors and generators as it existed in 2004 has been reviewed by Kalsi et al. [51].

References

1. G. Roth, Ultra High Field NMR Magnet Design. http://www2.warwick.ac.uk/fac/sci/physics/current/teach/module_home/px388/extra_material/bruker_magnets.pdf
2. T. Kiyoshi, S. Matsumoto, A. Satoet et al., IEEE Trans. Appl. Supercond. **15**, 1330 (2005)
3. Bruker BioSpin, Overview, 23.5 T Standard-Bore, Persistent Superconducting Magnet, The World's First 1 gigahertz NMR. http://www.bruker.com/products/mr/nmr/dnp-nmr/overview.html
4. S.T. Wang, R. Wahrer, F. Anet et al., IEEE Trans. Magn. **30**, 1994 (1994)
5. W.D. Markiewicz, J.R. Miller, J. Schwartz et al., IEEE Trans. Appl. Supercond. **16**, 1523 (2006)
6. R.G. Sharma, Y.S. Reddy, B. Sarkar, R. Rajput, *Design and Winding of the Magnet Coils and Fabrication of Dewar for a 100 MHz NMR System* (NPL, India, 1994) (unpublished)
7. R.G. Sharma, Y.S. Reddy, R.B. Saxena, M.A. Ansari, *A High Homogeneity Superconducting Magnet and a Long Hold Cryostat for NMR Application*, Technical Bulletin, NPL, New Delhi, October, pp. 1–17, (1996)
8. M.D. Sauzade, S.K. Kan, Adv. Electron. Electron Phys. **34**, 1–93 (1973) (Chapter 1, Ed. L. Marton, Academic Press)
9. J.E.C. Williums, S. Pourrranimi, Y. Iwasa et al., IEEE Trans. Magn. **25**, 1767 (1989)
10. JEOL Resonance, *JEOL Resonance Introduces New Zero Boil Off Magnet for NMR System*, A Press Release dated April 17 (2013)
11. T. Suzuki, M. Okada, T. Wakuda et al., J. Phys.: Conf. Ser. **97**, 012133 (2008) (8th European Conference on Applied Superconductivity EUCAS 2007)
12. K. Saitoh, H. Yamamoto, K. Kawasaki, et al., J. Phys.: Conf. Ser. **97**, 012141 (2008) (8th European Conference on Applied Superconductivity, EUCAS-2007)
13. M. Tsuchiya, T. Wakuda, K. Maki et al., IEEE Trans. Appl. Supercond. **18**, 840 (2008)
14. P.C. Lauterbur, Nature (London) **242**, 190 (1973)
15. M.W. Garrett, J. Appl. Phys. **38**, 2563 (1967)
16. S. Pissanetzky, IEEE Trans. Magn. **28**, 1961 (1992)

17. R. Thompson, R.W. Brown, V.C. Srivastava, IEEE Trans. Magn. **30**, 108 (1994)
18. S. Crozier, D.M. Doddrell, J. Magn. Reson. **127**, 233 (1997)
19. H. Zhao, S. Crozier, D.M. Doddrell, Magn. Reson. Med. **45**, 331 (2001)
20. G. Sinha, R. Sundararaman, G. Singh, IEEE Trans. Magn. **44**, 2351 (2008)
21. Y. Lvovsky, E.W. Strautner, T. Zhang, Topical Review, Supercond. Sci. Technol. **26**, 0933001(pp 71), (2013)
22. D.M. Doddrell, H. Zhao, Multi-layer magnet, US Patent 7212004 (2007)
23. S. Mine, M. Xu, S. Buresh et al., IEEE Trans. Appl. Supercond. **23**, 4601404 (2013)
24. H.H. Kolm, IEEE Trans. **MAG-11**, 1567 (1975)
25. Z.J.J. Steckly, IIIE Trans. **MAG-11**, 1594 (1975)
26. S. Nishijima, K. Takahata, K. Saito et al., IEEE Trans. **MAG-23**, 573 (1987)
27. H. Yamashita, K. Fujita, F. Nakajima et al., Sep. Sci. Technol. **16**, 987 (1981)
28. K. Takahata, S. Nishijima, T. Okada et al., IEEE Trans. **MAG-24**, 878 (1988)
29. R.G. Sharma, Y.S. Reddy, *Development of a Superconducting High Gradient Magnetic Separator,* Technical Bulletin, NPL, India, April 1992, pp. 1–8
30. Y. Kakihara, T. Fukunishi, S. Takeda et al., IEEE Trans. Appl. Supercond. **14**, 1565 (2004)
31. S. Nishijima, S. Takeda, IEEE Trans. Appl. Supercond. **17**, 2311 (2007)
32. F. Ning, M. Wang, H. Yang et al., IEEE Trans. Appl. Supercond. **22**, 3700104 (2012)
33. D.D. Jackson, P. Beharrel, J. Sloan, *Industrial-Scale Purification of Kaolin Using a Conduction-Cooled Superconducting High-Gradient Magnetic Separator* (Quantum Design Inc. USA). www.qdusa.com/sitedocs/productBrochures/SHGMS_poster_forEUCAS_2013pdf
34. W. Hassenzhal, IEEE Trans. **MAG-25**, 750 (1989)
35. S. Nagaya, N. Hirano, T. Tanaka et al., IEEE Trans. Appl. Supercond. **14**, 699 (2004)
36. S. Nagaya, N. Hirano, T. Katagiri et al., Cryogenics **52**, 708 (2012)
37. R.J. Loyd, T.E. Walsh, E.R. Kimmy, IEEE Trans. **MAG-27**, 1712 (1991)
38. P. Tixador, Superconducting Magnetic Energy Storage: Status and Perspective, in *IEEE/CSC & ESAS European Superconductivity News Forum*, No. 3, Jan 2008, www.ewh.ieee.org/europe/newforum/pdf/CR5_final3_012008.pdf
39. M. Ferrier, Stockage d' energie dans un enroulement supraconducteur, Low temperature and Electric Pargamon Press, 425–432 (1970)
40. G.W. Ullrich, IEEE Trans. Appl. Supercond. **5**, 416 (1995)
41. J.L. Wu, J.F. Roach, D.C. Johnson et al., Adv. Cryog. Eng. **39**, 813 (1994)
42. C.J. Hawley, S.A. Gower, IEEE Trans. Appl. Supercond. **15**, 1899 (2005)
43. C.J. Hawley, D. Cuiuri, C.D. Cook et al., J. Phys.: Conf. Ser. **43**, 809 (2006) http://ro.uow.edu.au/cgi/viewcontent.cgi?article=7297&context=engpapers
44. S.S. Kalsi, D. Aized, B. Konnor et al., IEEE Trans. Appl. Supercond. **7**, 971 (1991)
45. G. Wojtasiewicz, T. janowski, S. Kozak et al., J. Phys.: Conf. Ser. **43**, 821 (2006)
46. J.H. Kim, S.Y. Hahn, C. Hwan et al., IEEE Trans. Appl. Superconduc. **12**, 774 (2002)
47. P. Tixador, M. Deleglise, A. Badel et al., First tests of 800 kJ HTS SMES http://arxiv.org/ftp/arxiv/papers/0812/0812.3639.pdf
48. W. Yuan, W. Xian, M. Ainslie et al., IEEE Trans. Appl. Supercond. **20**, 1379 (2010)
49. F. Trillaud, L.S. Cruz, IEEE Trans. Appl. Supercond. **24**, 5700205 (2014)
50. B. Vincent, P. Tixador, T. Lecrevisse et al., IEEE Trans. Appl. Supercond. **23**, 5700805 (2013)
51. S.S. Kalsi, K. Weeber, H. Takesue et al., Proc. IEEE **92**, 1688 (2004)

Index

R.G. Sharma, *Superconductivity*, Springer Series in Materials Science 214,
DOI 10.1007/978-3-319-13713-1